From the stellar IMF to large-scale structure formation: How the ΛCDM model is incompatible with observations over all probed astrophysical scales

Dissertation
zur
Erlangung des Doktorgrades (Dr. rer. nat.)
der
Mathematisch-Naturwissenschaftlichen Fakultät
der
Rheinischen Friedrich-Wilhelms-Universität Bonn

vorgelegt von
Moritz Haslbauer
aus
Gmunden, Österreich

Bonn 2024

Angefertigt mit Genehmigung der Mathematisch-Naturwissenschaftlichen Fakultät der Rheinischen Friedrich-Wilhelms-Universität Bonn

1. Gutachter:	Prof. Dr. Pavel Kroupa
2. Gutachter:	Prof. Dr. Karl Menten

Tag der Promotion: 22.05.2024
Erscheinungsjahr: 2024

Don't only practice your art,
but force your way into its secrets,
for it and knowledge can raise men to the divine.
(Ludwig van Beethoven)

To my parents and grand parents

Abstract

Any theoretical framework must be testable and as a consequence falsifiable. Scientific progress is mainly driven by falsifications because identifying and analysing the shortcomings and failures of a theory ideally point the way ahead in which sense a correction is required in order to explain the observations and experimental outcomes. Practically, several independent falsifications by independent research teams are demanded to finally reject an already well-established theoretical framework.

This doctoral thesis tests the current standard model of cosmology (Λ Cold Dark Matter framework) on different astrophysical scales ranging from the local to the early Universe. The Λ Cold Dark Matter (ΛCDM) framework is fundamentally based on Einstein's General Relativity theory and the Cosmological Principle which require the existence of cold dark matter and dark energy. However, neither cold dark matter nor dark energy have been directly detected which together with several tensions of the ΛCDM model with observations entered in one of the greatest crisis in modern cosmology. Testing the ΛCDM model on different astrophysical scales could show if the missing mass problem implies indeed the existence of cold dark matter on galactic scales or rather emerges because of a breakdown of Newton's law of gravity.

In the local Universe, we showed that the spatial and kinematical configuration of the Magellanic Clouds-Milky Way system suggests that Chandrasekhar dynamical friction on galactic scales is much less efficient than predicted by the state-of-the-art hydrodynamical ΛCDM simulation runs of the IllustrisTNG project. The present-day sky-aspect ratio distributions of the galaxy population formed in the hydrodynamical ΛCDM simulation runs of the Illustris, IllustrisTNG, and EAGLE projects disagree with the local observations at the $\geq 12.52\sigma$ confidence level. The simulations overproduce too roundish galaxies while the majority of observed massive galaxies are thin spirals pointing to a failure of the hierarchical merger-driven galaxy evolution in which galaxies grow efficiently through minor and major mergers due to Chandrasekhar dynamical friction on the extended cold dark matter haloes.

On larger scales, we quantified that the locally observed Keenan-Barger-Cowie (KBC) void with a density contrast of about half of the cosmic mean density on co-moving radial distance scales of ≈ 300 cMpc falsifies the ΛCDM framework at the 6.04σ confidence level. Consequently, starting with the initial conditions set by the cosmic microwave background requires a stronger effective gravitational force than obtained from Newton's law of gravity to form deep and extended structures like the observed KBC void. Therefore, we performed semi-analytical simulations conducted within the framework of Milgromian dynamics (MOND) in which the gravitational law gradually changes from Newton's inverse square law to an inverse distance law at accelerations of $\lesssim 10^{-10}\,\mathrm{m\,s^{-2}}$ boosting therewith the formation of structures in the Universe. We showed that the enhanced growth of structures in a MONDian cosmological framework allows the formation of the observed KBC void

from which induced large-scale matter bulk flows resolve in turn the Hubble tension.

The observed Universe may be also more inhomogeneous on Gpc-scales. The almost constant star formation history of the majority of local galaxies challenges the traditional interpretation of the Lilly-Madau plot according to which the evolution of the star formation rate density over cosmic time represents the global star formation history of the Universe. We argued that the peak of the Lilly-Madau plot at redshift $z \approx 1.9$ reflects the imprint of a large-scale overdensity rather than the cosmic noon but more precise measurements of the matter density field would be required in order to affirm this interpretation.

In the early Universe, we showed that the spectroscopically confirmation of observed high-redshift galaxy candidates with derived stellar masses of $M_* \gtrsim 10^9\,M_\odot$ for an invariant canonical stellar initial mass function (IMF) at photometric redshifts of $z_{\rm phot} \gtrsim 10$ by the James Webb Space Telescope (JWST) would imply that the observed stellar mass buildup is inconsistent with the ΛCDM framework. However, the interpretations of photometric measurements and conversion to stellar masses depend on the underlying stellar IMF. We provided the first estimation of the stellar masses of high-redshift galaxy candidates observed by the JWST for a varying galaxy-wide IMF within the integrated galactic IMF (IGIMF) theory according to which the stellar IMF systematically varies with the global star formation rate and metallicity of the galaxy. We calculated that the stellar masses would be about $5-10$ times lower for a varying gwIMF than for an invariant canonical IMF. The state-of-the-art hydrodynamical ΛCDM simulation runs of the Illustris, IllustrisTNG, and EAGLE projects adopt only an invariant canonical IMF such that the stellar mass buildup predicted by the ΛCDM framework for a varying IMF cannot be directly compared with the observations.

The JWST observations illustrate that testing cosmological models requires assumptions about the properties of the stellar IMF. Therefore, we developed the photometric GalIMF (photGalIMF) code as a package of the publicly available chemical galaxy evolution code GalIMF to compute the photometric properties of galaxies in different photometric bands for an invariant canonical but also varying galaxy-wide IMF within the IGIMF theory. This opens the possibility for more precise tests of galaxy evolution and cosmological models.

In conclusion, the performed tests disprove the ΛCDM framework over all probed astrophysical scales ranging from galactic to large-scale structures of the Universe. The tests established a consistent picture of the observed Universe in which dynamical friction on galactic scales is next to absent and structure formation is more enhanced than predicted by the ΛCDM framework. These findings disfavor therewith the existence of extended cold dark matter on galactic scales but rather point to a long-range correction of Newton's law of gravity as provided by MOND. As the interpretation of photometric measurements depends on the properties of the stellar IMF, galaxy evolution and formation models have to be considered in a more holistic picture by bridging stellar population of galaxies with cosmology.

Contents

1 Introduction **1**

2 A brief history of astronomy and cosmological models **7**
2.1 Prehistory . . . 9
2.2 Classical Greek antiquity . . . 11
2.3 Medieval period . . . 15
2.4 Copernican revolution and Newton's law of gravity . . . 17
2.5 Great debate & the nature of galaxies . . . 24
2.6 Modern cosmology & the Λ-Cold Dark Matter model . . . 26
2.7 Precision cosmology & cosmology at crossroads . . . 34

3 The standard Λ-Cold Dark Matter model of cosmology **37**
3.1 Theoretical background . . . 37
3.1.1 Cosmological redshift . . . 38
3.1.2 Friedmann equations and evolution of the cosmological density parameters . . . 40
3.2 Cosmological ΛCDM simulations . . . 43
3.2.1 Millennium simulation . . . 44
3.2.2 Illustris project and Illustris The Next Generation project . . . 44
3.2.3 EAGLE project . . . 45
3.3 Challenges of the ΛCDM model . . . 46
3.3.1 Dynamical friction . . . 47
3.3.2 Core-cusp problem . . . 49
3.3.3 Missing galaxy problem . . . 49
3.3.4 Too big to fail problem . . . 49
3.3.5 Downsizing . . . 50
3.3.6 Angular momentum problem . . . 50
3.3.7 Disk of satellites . . . 50
3.3.8 Dual dwarf galaxy problem . . . 52
3.3.9 Matter distribution on Mpc to Gpc scales . . . 53
3.3.10 Hubble tension . . . 53
3.3.11 Sigma-8 problem . . . 54
3.3.12 Anisotropies . . . 54
3.3.12.1 Hubble diagram . . . 54
3.3.12.2 Deceleration parameter . . . 54
3.3.12.3 Cosmic microwave background . . . 55

3.3.12.4 Galaxy morphology . . . 55
3.3.13 High-redshift galaxies . . . 55

4 Milgromian dynamics (MOND) 57
4.1 Theoretical background . . . 57
4.1.1 External field effect . . . 59
4.2 Cosmological MOND model . . . 59
4.3 Galaxy scaling relations . . . 60
4.4 Challenges for MOND . . . 63
4.4.1 Velocity dispersion of ultra-faint dwarf satellite galaxies . . . 63
4.4.2 Deviations of dSphs from the radial acceleration relation . . . 63
4.4.3 Deviations of galaxy clusters from the radial acceleration relation . . . 63
4.4.4 Missing mass problem of galaxy clusters . . . 63
4.4.5 Lyman-α absorbers . . . 64
4.4.6 Structure formation in the νHDM model . . . 64

5 The galaxy-wide initial mass function 65
5.1 The canonical stellar initial mass function . . . 65
5.2 Towards a varying stellar initial mass function . . . 66
5.2.1 Metallicity dependency of indices . . . 67
5.3 Integrated galaxy initial mass function . . . 69
5.4 Potential challenges for a varying IMF . . . 70
5.4.1 Baryonic Tully-Fisher relation . . . 70

6 Scientific research questions addressed in this thesis 73
6.1 Testing ΛCDM cosmology . . . 74
6.1.1 Local Universe . . . 74
6.1.2 Early Universe . . . 76
6.1.3 Large-scales . . . 78
6.1.3.1 The KBC void and Hubble tension . . . 78
6.1.3.2 The SFHs of local galaxies and the Lilly-Madau plot . . . 80
6.2 Galaxy-wide IMF in a cosmological context . . . 81

7 The KBC void and Hubble tension in the ΛCDM model and Milgromian dynamics 85
7.1 Summary . . . 85
7.1.1 The Hubble tension and KBC void in the ΛCDM framework . . . 86
7.1.2 The Hubble tension and KBC void in MOND . . . 86
7.2 Author contributions . . . 89

8 The morphological distribution of galaxies in the ΛCDM framework 91
8.1 Summary . . . 91
8.2 Author contributions . . . 94

9 High-redshift galaxies in the ΛCDM framework and in light of the IGIMF theory 95
9.1 Summary . . . 95
9.1.1 High-redshift galaxies in the ΛCDM framework . . . 95

9.1.2 JWST and varying IMF within the IGIMF theory . . . 96
9.1.3 Implications . . . 98
9.2 Author contributions . . . 100

10 The Magellanic Clouds in the ΛCDM framework 101
10.1 Introduction . . . 105
10.2 Methods . . . 107
10.2.1 Observations . . . 107
10.2.2 The TNG cosmological simulations . . . 108
10.2.3 Selecting analogues to the MW . . . 109
10.2.4 Selecting analogues to the MCs . . . 109
10.3 Results . . . 110
10.3.1 Phase-space density of the MCs . . . 110
10.3.2 Tracing back analogues to the MCs in light of the MS . . . 114
10.4 Discussion . . . 118
10.4.1 Prior studies on the MCs in ΛCDM . . . 118
10.4.2 First-infall scenario . . . 120
10.4.3 Relating the MCs to the DoS . . . 120
10.4.3.1 Satellites of the LMC . . . 120
10.4.3.2 Alignment of the LMC with the DoS . . . 122
10.4.4 Total mass of LMC analogues . . . 123
10.4.5 The MCs in Milgromian dynamics (MOND) . . . 127
10.5 Conclusions . . . 129

11 The cosmological star formation history of galaxies in the Local Cosmological Volume – evidence for a 5 Gpc-sized underdensity 133
11.1 Summary . . . 133
11.2 Author contributions . . . 135

12 The effect of the environment dependent stellar initial mass function on the photometric properties of star-forming galaxies 139
12.1 Introduction . . . 143
12.2 Methods . . . 146
12.2.1 IGIMF theory . . . 146
12.2.2 Mass-to-light ratio . . . 150
12.2.2.1 Chemical evolution model . . . 150
12.2.2.2 Stellar luminosity evolution . . . 150
12.2.2.3 Star formation histories . . . 152
12.2.2.4 Mass–metallicity relation . . . 153
12.2.2.5 Galaxy evolution in the IMF and IGIMF framework . . . 153
12.2.3 The SFR–Hα-luminosity relation . . . 157
12.2.4 Observational data . . . 159
12.2.5 IGIMF corrected observations . . . 160
12.3 Results . . . 161
12.3.1 Stellar-mass–SFR relation of star-forming galaxies . . . 161

12.3.2 Gas depletion timescale . . . 162
12.3.3 Stellar-mass buildup times . . . 163
12.4 Discussion . . . 166
12.4.1 Stellar-mass–SFR relation of star-forming galaxies for a varying IMF . . . 166
12.4.2 Gas depletion timescales . . . 167
12.4.3 Stellar-mass buildup timescales . . . 167
12.5 Conclusion . . . 168

13 Outlook & Conclusion **171**
13.1 Cosmology at crossroads – distinguishing between different cosmological models . . . 171
13.1.1 Lack of dynamical friction on galactic scales . . . 172
13.1.2 Enhanced structure formation . . . 174
13.1.3 Outlook for distinguishing between ΛCDM and MOND . . . 176
13.2 Galaxy-wide IMF in a cosmological context . . . 177
13.3 Concluding remarks . . . 178

A Paper: The KBC void and Hubble tension contradict ΛCDM on a Gpc scale – Milgromian dynamics as a possible solution **181**

B Paper: The High Fraction of Thin Disk Galaxies Continues to Challenge ΛCDM cosmology **221**

C Paper: Has JWST already falsified dark-matter-driven galaxy formation? **243**

D Paper: The cosmological star formation history from the Local Cosmological Volume of galaxies and constraints on the matter homogeneity **251**

E Appendix: The Magellanic Clouds are very rare in the IllustrisTNG simulations **263**
E.1 Effect of resolution . . . 263
E.2 Different selection criteria . . . 265

F Appendix: The effect of the environment-dependent stellar initial mass function on the photometric properties of star-forming galaxies **267**
F.1 Mass-to-light ratios in different photometrics bands for a canonical IMF . . . 267
F.2 gwIMF for high metallicities . . . 267
F.3 Fitting parameters . . . 268

Bibliography **271**

List of Figures **311**

List of Tables **327**

Acknowledgements **329**

CHAPTER 1

Introduction

"For if we are uncritical we shall always find what we want: we shall look for, and find, confirmations, and we shall look away from, and not see, whatever might be dangerous to our pet theories. In this way it is only too easy to obtain what appears to be overwhelming evidence in favor of a theory which, if approached critically, would have been refuted." (Popper 1957)

The Austrian-British philosopher Sir Karl Raimund Popper (1902–1994)[1] formulated the Falsification Principle as a scientific method to evaluate the viability of a scientific theory. According to the scientific method of the empirical falsification and the concept of the falsifiability of scientific theories, a theoretical framework can only be disproved by experiments and observations but never be verified in its full entirety as this would require an infinite number of tests confirming the theory. Stating an often-quoted example, the observation of a *single* black swan would be enough to reject the null-hypothesis that *all* swans are white. Fortunately, this research question can be answered right away as the black plumage of the swan species named Cygnus atratus mainly observed in Australia clearly falsifies the above null-hypothesis.

Any scientific theory must be predictive and therefore testable and falsifiable as "Every genuine test of a theory is an attempt to falsify it, or to refute it. Testability is falsifiability; but there are degrees of testability: some theories are more testable, more exposed to refutation, than others; they take, as it were, greater risks" (Popper 2014). Moreover, any *viable* scientific theory has to explain the experimental outcomes and observations. The Austrian-British mathematician and cosmologist Sir Hermann Bondi (1919–2005) refines this statement by arguing that "A theory is scientific only if it can be disproved. But the moment you try to cover absolutely everything the chances are that you cover nothing" (Bondi 1967) such that a scientific theory should be defined within a specific range of validity. The development of the "Theory of everything", which would describe the Universe on all scales by connecting general relativity and quantum mechanics, could be considered as the holy grail of physics (if existing at all). Testing and falsifying a theoretical framework is an essential part of scientific progress as a falsification could yield to an extension and/or modification of the tested theory. The word "modification" may not be an appropriate terminology to underline the improvement or extension of an out-dated (falsified) theory as nature itself behaves according to the true ("correct") physical theories.[2] The history of astronomy showed us that sometimes falsifications of well-established

[1] Throughout this thesis the birth and death dates of a person are extracted from the corresponding Wikipedia website.

[2] Private discussions with Pavel Kroupa.

theories and world views even triggered and finally resulted in scientific revolutions as will be briefly discussed in Chapter 2. One needs to be bear in mind that agreement between an observation and a theory does not necessarily imply that the theory provides indeed the correct description of nature which is somewhat exaggerated formulated by the English phrase "even a broken clock is right twice a day". For example, introducing epicycles of planets allowed to explain their apparent retrograde motions but the epicycle theory was not the correct description of planetary motion as we will see in Section 2.4. In practice, the rejection of an already established theoretical framework should never rely only on one single empirical falsification. Several independent falsifications by independent research teams would be required to finally reject a well-established theoretical framework. Ideally, the outcomes of independent falsifications could point the way ahead in which sense a theory has to be modified or rather said "corrected" in order to provide a better understanding and description of nature. Thus, falsification is an essential part in science as "Progress in science comes when experiments contradict theory." (Richard Phillips Feynman, 1918–1988; but see also Gleick 1992)

The main aim of the research projects conducted within the scope of this doctoral thesis is to test the current standard model of cosmology (Efstathiou, Sutherland and Maddox 1990; Ostriker and Steinhardt 1995) on different astrophysical scales. The standard model of cosmology (abbreviated ΛCDM for Λ-Cold Dark Matter model; see Chapter 3 for a more formal introduction and description of the ΛCDM model) is based on the fundamental assumption that Albert Einstein's (1879–1955) General theory of Relativity (Einstein 1915; Einstein 1916) is valid on all cosmological scales which in turn requires the existence of cold dark matter (CDM) in addition to the visible (baryonic[3]) matter and dark energy (Λ) in order to account for the accelerated expansion of the Universe. Originally, the terminology "dark matter" (French: "matière obscure") goes back to the French mathematician and physicist Jules Henri Poincaré (1854–1912) but the establishment of the "dark matter problem" or also known as the "missing mass problem" in astrophysics was mainly driven by observations of high velocity dispersions in galaxy clusters (Zwicky 1933) and flat rotation curves of galaxies (e.g. Babcock 1938; Babcock 1939; Rubin and J. Ford W. K. 1970; Rubin, J. Ford W. K. and Thonnard 1978; Rubin, J. Ford W. K. and Thonnard 1980; Rubin et al. 1985; Bosma 1981), which both suggest an additional unseen ("dark") matter component in the Universe *if* Newtonian dynamics is applied (see Section 2.6 and references therein for a brief historical background of the establishment of dark matter and dark energy). According to the latest analysis of the cosmic microwave background (CMB), baryonic matter makes only up $\approx 5\%$, while dark matter matter accounts for $\approx 26\%$ and dark energy for even $\approx 69\%$ of the energy budget of the Universe (Planck Collaboration XIII 2016; Planck Collaboration VI 2020a).

Over the last decades several candidates for dark matter have been proposed ranging from faint baryons (Carr 1994) in the form of e.g. white dwarfs, brown dwarfs, neutron stars, (primordial) black holes, planets, or even molecular structures (i.e. clumpuscules; Heithausen 2004; Pfenniger, Combes and Martinet 1994; Combes and Pfenniger 1997) to exotic particles beyond the standard model of particle physics (Bringmann 2009; Hu, Barkana and Gruzinov 2000). The interested reader in different dark matter candidates and their searches is referred e.g. to the reviews by Feng (2010) and Cebrián (2023), respectively. Until now (October 2023), neither dark matter nor dark energy have been directly detected meaning that $\approx 95\%$ (!) of the Universe are *dark* or in an other word *unknown* which makes their existence and nature to one of the greatest puzzles not only in modern cosmology and astrophysics but also in physics.

Importantly, the non-detection of the dark matter particle can not be considered as a falsification of

[3] Baryonic matter comprises all particles of the standard model of particle physics.

the existence of dark matter or the ΛCDM model (McGaugh 2015; Kroupa 2015; Kroupa et al. 2023) because such a conclusion would require a non-detection over all possible parameter ranges and the putative dark matter particles might have a cross section for interacting with standard-model-particles of zero, making them entirely undetectable by any laboratory or electromagnetic emission method. However, cosmological theories can be tested by comparing their *a priori* predictions and expectations with observations on different scales. During the last two decades several studies reported tensions between observations and the ΛCDM model (Kroupa et al. 2010; Kroupa 2012; Kroupa 2015; Kroupa et al. 2023, see also Section 3.3 for an overview and the scientific results presented in this thesis) which together with the non-direct-detection of dark matter but also dark energy entered in a major crisis of modern cosmology.

Probably this crisis can be overcome by viewing the missing mass problem from a different perspective. The Poisson equation for gravity states (see also Chapter 4),

$$\nabla \cdot \left(\nabla \Phi_{\rm N}\right) \quad = \quad 4\pi G \rho_{\rm b}\,, \tag{1.1}$$

where $\Phi_{\rm N}$ is the Newtonian potential such that the gravitational acceleration field is $\boldsymbol{g}_{\rm N} = -\nabla\Phi_{\rm N}$ and $\rho_{\rm b}$ is the baryonic matter density. Introducing dark matter as a further matter component would require a "modification" - or as we have learned above - a "correction" of the right-hand side of the Poisson equation by adding the dark matter density to the baryonic matter density. The other but currently also more controversially considered possibility would be to correct the left-hand side by changing the law of gravity and going therewith beyond Newtonian/Einsteinian dynamics. In fact, a correction of Newton's law of gravity has been proposed by the Israeli physicist Mordehai Milgrom (1946–) in 1983. His "MOdified Newtonian Dynamics" or simply "MilgrOmiaN Dynamics" (MOND; Milgrom 1983c) is an acceleration-dependent gravitational law which yields to stronger effective gravitational attractions at accelerations of $\lesssim 10^{-10}\,{\rm m\,s^{-2}}$ compared to Newton's law of gravity addressing therewith the flat rotation curve of galaxies only with the baryonic matter without an additional mass component on galactic scales. Interestingly, MOND can be written in term of the generalized Poisson equation in terms of the p-Laplacian,

$$\nabla \cdot \left[\left(\frac{|\nabla\Phi|}{a_0}\right)^{p-2} \nabla\left(\frac{\Phi}{a_0}\right)\right] \quad = \quad \frac{4\pi G\rho_{\rm b}}{a_0}\,, \tag{1.2}$$

where Φ is the potential and a_0 is Milgrom's constant such that MOND follows for $p = 3$ and Equation 1.1 for $p = 2$ (see Appendix A.1 of Kroupa et al. 2023). Although MOND has successfully addressed many astrophysical observations especially on galactic scales, self-consistently implementing MOND in a cosmological framework remains a challenge (see Chapter 4 and references therein). Naturally, a correction of both the right-hand side and left-hand side of the Poisson equation of gravity would be also a possible scenario (e.g. Angus 2009, and see Section 4.2).

Performing tests of the ΛCDM framework is therefore of great importance as such investigations will point the way forward in which sense galaxy formation and evolution as well as cosmological and gravitational theories have to be corrected in order to overcome the current crisis of cosmology. This thesis is based on six scientific research projects led by the author of the thesis whose results have been published in four peer-reviewed papers and documented in two manuscripts which have been submitted to peer reviewed-journals. The first part of the thesis focused on testing the ΛCDM framework by mainly comparing self-consistent cosmological ΛCDM simulations with observations

of galaxies on small but also on large scales. Investigations on various astrophysical scales are necessary to establish a holistic picture in order to identify more precisely the weaknesses and failure reasons of the model. The main scientific findings of these projects revealed significant tensions on both small and large scales in so far as Chandrasekhar dynamical friction (Chandrasekhar 1942; Chandrasekhar 1943a; Chandrasekhar 1943b; Chandrasekhar 1943c; Binney and Tremaine 2008) is much less effective and structure formation more enhanced in the observed Universe than implied by the ΛCDM framework. In combination with other studies the consistent picture arises in which the existence of cold dark matter on galactic scales is disfavored due to the lack of Chandrasekhar dynamical friction but Milgromian dynamics is favored because of an enhanced growth of structure.

Importantly, the properties of galaxies are not sensitive only to the cosmological paradigm but also to baryonic physics processes which are implemented in galaxy formation and evolution models. A key ingredient of star formation and galaxy evolution is the stellar initial mass function (IMF; Salpeter 1955; Sandage 1957; G. E. Miller and Scalo 1979; Kroupa 2001; Chabrier 2003), which is a mathematical "hilfskonstrukt" (Kroupa et al. 2013) to describe the mass distribution of newly formed stars within a single star-forming event (Chapter 5). Mathematically, the stellar IMF is expressed by

$$\xi_*(m) \equiv \frac{dN}{dm}, \tag{1.3}$$

where dN is the number of stars formed in the mass interval $m, m + dm$. In galaxies, star formation mostly occurs in embedded clusters formed out of giant molecular clouds (Kroupa 2015). Embedded clusters are considered as the fundamental building blocks (Kroupa 2005) such that summing up all IMFs of all embedded clusters within a galaxy gives the galaxy-wide stellar IMF (gwIMF) which is basically the IMF of the entire galaxy. The gwIMF can be computed with the integrated galactic IMF (IGIMF) theory originally formulated by Kroupa and Weidner (2003).

Historically, it has been thought that the stellar IMF is invariant meaning that the shape of the IMF is independent of the physical properties of the star-forming regions but since the 1990s several observations suggest a systematically variation of the stellar IMF with their environmental conditions (see Section 5.2 and references therein) disfavoring stochastic star formation processes (Kroupa 2015). The properties of the stellar IMF is of particular importance in galaxy formation and evolution because it defines not only the distribution of the (visible) stellar matter but also the amount of (non-visible) mass in faint stars, black holes, with dwarfs, or neutron stars showing therewith the historical connection with the missing mass problem (Carr 1994). Moreover, the IMF affects the chemical enrichment of galaxies, the galactic and cosmic matter cycle, and also star-formation tracers used to convert observed luminosities to star formation rates depend on the properties of the IMF (Kroupa and Jerabkova 2019). Thus, the possibility of a varying stellar IMF and gwIMF has to be taken into account in the interpretation of photometric observations (see Section 6.2). Therefore, the second part of the thesis investigates a systematically varying gwIMF within a cosmological context which allows for more precise tests of galaxy evolution and cosmological models bridging therewith the stellar populations of galaxies with cosmology.

The doctoral thesis is organized as follows: Chapter 2 provides a brief historical overview of astronomy mainly focusing on the development and establishment of cosmological models. The Chapters 3 and 4 introduce the basic concepts of the ΛCDM cosmological model and Milgromian dynamics (MOND), respectively. In Chapter 5, the IGIMF theory to compute the gwIMF is described. Along the lines of Sir Popper, each of these three chapters end with observed tensions and potential

challenges for the discussed paradigms and theories. After providing with these chapters the scientific context and theoretical background of the thesis, the conducted research projects and scientific questions addressed during the doctoral studies are outlined in Chapter 6. This includes a discussion of the gwIMF in a cosmological context connecting therewith the different topics covered in this thesis. The Chapters 7-12 and Appendices E-F summarize the main scientific results of the four peer-reviewed publications and two manuscripts (submitted) led by the author of this thesis and states the individual author contributions of these projects. The Appendices A-D include a copy of the four published papers in original form. An outlook for future projects based on the scientific findings gained by this thesis and concluding remarks are finally provided in Chapter 13.

CHAPTER 2

A brief history of astronomy and cosmological models

"Quare liberalia studia dicta sint vides: quia homine libero digna sunt"
(Lucius Annaeus Seneca the Younger in his epistulae morales 88, 2)

Astronomy together with the subjects arithmetic, geometry, music, rhetoric, grammar, and logic formed the Seven Liberal Arts (Latin: "septem artes liberales") in the classical Greek-Roman Antiquity. The Stoic philosopher Lucius Annaeus Seneca the Younger (c. 4 BC–65 AD)[1] praises in his Epistulae morales the Seven Liberal Arts as "quia homine libero digna sunt" (epistulae morales 88, 2; see e.g. Seneca and L. Reynolds 1965) meaning that these disciplines are worth to study for a free person – a person who has not to work for financing the costs of living (see e.g. Tetzlaff 2021, and references therein). In fact, the Seven Liberal Arts strongly influenced the educational system in the Middle Ages but undoubtedly implanted the academic course of the Western culture even up to the present time.

Before we will start our journey through the history of astronomy, I would like to discuss the etymology of the words "Astronomy" and "Cosmology" and some general aspects which we should have to bear in mind when reconstructing the development of cosmological models. First of all, the word "Astronomy" originates from the ancient Greek words "ἄστρον" and "νόμος" meaning "star" and "law", respectively. Due to the advances in technology such as the invention and continuous development of the telescope and the resulting increase of our physical and mental horizon, astronomy is not anymore only limited to the study of the law of stars but describes the formation and evolution of many different objects (e.g. planets, moons, stars, star clusters, galaxies, galaxy clusters, interstellar and intergalactic medium) in the Universe and eventually the Universe as a whole. The latter is nowadays referred to the research field of "Cosmology" which derives from the ancient Greek words "κόσμος" for "world" and "λογία" ("logía") for "study of". The study of the world and therewith the development of cosmological models is inevitably linked with the history of astronomy as new scientific observations and findings shape our conception of the world and yields to a confirmation or revision of scientific models. Although the first - scientific - cosmological models have been already developed by the ancient Greeks (Section 2.2), the English word "cosmology" appeared quite late in the literature. The Glossographia published in 1656 by the lexicographer Thomas Blount (1618–1679) is known as the first book which uses the English word "cosmology" by introducing it as "a speaking

[1] Throughout this thesis the birth and death dates of a person are extracted from the corresponding Wikipedia website.

about the world" (Blount 1670) and describing "cosmical" with "cosmical (cosmicus) of the world, Worldly. In Astronomy we term that the Cosmical ascension of a star, when it ariseth together with the Sun, or the same degree of the Ecliptick [sic!], wherein the Sun abides." (Blount 1670) About 80 years after the publication of "Glossographia", the Latin name "Cosmologia" appeared for the first time in "Cosmologia Generalis" in 1731 by Christian Wolff (1679–1754) (e.g. Luminet 2008; Hetherington 2014).

Reviewing the history of astronomy and the development of cosmology should be always considered within the cultural and technological background of a society. Remarkably, scientific revolutions are linked with historical upheavals which has been noted by the American philosopher Thomas Samuel Kuhn (1922–1996):

> *"Examining the record of past research from the vantage of contemporary historiography, the historian of science may be tempted to exclaim that when paradigms change, the world itself changes with them."* (T. S. Kuhn 1997)

Historical examples have been discussed in the blog post entitled "Update on the Dark Matter Crisis. . . " (No. 50, published on 07.11.2020) by Pavel Kroupa and Moritz Haslbauer published on the science blog "The Dark Matter Crisis – The rise and fall of cosmological hypotheses".

Before but also still in the era of Renaissance (15th and 16th centuries), astronomy and cosmology were strongly influenced by mythological and religious arguments and aspects. Interestingly, the famous German astronomer Johannes Kepler (1571–1630; Section 2.4) was also an astrologer by writing horoscopes for the Bohemian military leader and statesman Albrecht Wenzel Eusebius von Wallenstein (1583–1634). It was in the 18th century when astronomy and astrology were finally treated fully independently from each other maybe also because of the invention of the telescope at the beginning of the 17th century which significantly advanced our understanding of the Universe. Before that, only astronomical objects visible with the naked eye were known with the most prominent objects being the Sun, the Moon, the open star clusters Pleiades also known as The Seven Sisters and the Hyades, and the planets Venus, Mercury, Mars, Jupiter, and Saturn. Assuming that the human eye is able to resolve stars with apparent magnitudes smaller than 6 mag, about 3000 stars can be observed with the naked eye from the northern night sky without any light pollution. All these influences and aspects should be taken into account when discussing the development of cosmological models.

In this respect, the following sections will briefly outline the history of astronomy and the development of cosmological models starting with prehistoric paintings towards space telescopes to probe modern cosmologies. While a substantial part of this mainly focuses on astronomy conducted in the Western culture, it needs to be emphasized that great astronomical achievements have been also established by the Islamic, India, or Chinese astronomy. For example, the Iranian astronomer Al-Sufi (903–986), who was influenced by the contributions of the Alexandrian astronomer Claudius Ptolemy (c. 100–c. 170 AD; Section 2.2) wrote in his famous book "Kitāb suwar al-kawākib" (English: "The Book of Fixed Stars") about the stellar constellations and stars. Chinese astronomy was famous for developing calenders and precise records of stars leading to the identifications of comets, meteor showers, or new shining stars (Latin: "stellar nova") which later turned out to be exploding stars known as Supernovae (SNe). In the early 18th century, the observatory Jantar Mantar (but without optical telescopes)[2] was constructed in Jaipur (India). Interesting though is that the first physical

[2] Private communication with Srikanth T. Nagesh.

models attempting to account for the observed world were suggested in Pre-Roman Greece and later in Renaissance Europe.

This chapter does not claim to be complete and the interested reader may find further information and references on the development of cosmological models e.g. in "Fundamental Ideas in Cosmology" by López-Corredoira (2022). A more general but also very detailed essay of the history of physics can be found in "Kulturgeschichte der Physik" by Simonyi (2001). Bibliographies of famous astronomers are collected e.g. in Krafft (2007). Finally, given that this thesis mainly focuses on the missing mass problem, I would like to refer the reader to the books "The Dark Matter Problem: A Historical Perspective" by Sanders (2010) and "A Philosophical Approach to MOND: Assessing the Milgromian Research Program in Cosmology" by Merritt (2020) for a historical classification. While the followings sections discusses the historical path towards modern cosmology, the theoretical and mathematical background of the current standard cosmological ΛCDM framework and Milgromian dynamics are introduced in the Chapters 3 and 4, respectively.

2.1 Prehistory

The beginning of the history of astronomy is difficult to date but the first astronomical records have been witnessed through cave paintings from the Upper Palaeolithic which occurred about 50000–12000 years ago. In Europe, prehistoric paintings dated around 17000–15000 BC potentially showing astronomical objects have been discovered in the cave of Lascaux in south-western France in 1940. The shaft called "Hall of Bulls" contains a wall drawing of an already extinct aurochs with two prominent black horns as photocopied in the left panel of Figure 2.1. The black dots painted in the head of the aurochs seem to be the stellar members of the open star cluster Hyades with the star Aldebaran representing its eye. In fact, the star Aldebaran has indeed a very prominent reddishly shining appearance on the night sky because of its current evolution stage as a red giant (e.g. Farr et al. 2018). The black painted dots arranged in a straight line below the head of the aurochs could be the belt stars of the Orion constellation while the six (or seven) black dots above the head could be the members of the open star cluster called Pleiades or also known as the Seven Sisters (Rappenglück 1997).

Historically, the Pleiades were of great importance for the agriculture because their appearance on the sky announced the beginning of the harvest during ancient Greek times as witnessed by the poet Hesiod (around 750–650 BC) in his poem "Works and Days":

> *"When the Pleiades, daughters of Atlas, are rising,[a footnote states: "Early in May."] begin your harvest, and your ploughing when they are going to set.[a footnote states: "In November."] Forty nights and days they are hidden and appear again as the year moves round, when first you sharpen your sickle."* (Evelyn-White et al. 2006)

In ancient Greek times, their disappearance from the northern hemisphere around September introduced the upcoming winter period. Nowadays, the Pleiades are visible with the naked eye between April and July. Kroupa (2005) pointed out the interesting coincidence that one can observe the two different evolution phases of the star clusters Pleiades with an age of ≈ 99 Myr and the Hyades with ≈ 500 Myr (see also the computer models of star cluster evolution by Portegies Zwart et al. 2001) at almost the same region on the sky.

Figure 2.1: Prehistoric paintings in the "Hall of the Bulls" (French: "Salle des taureaux") in the cave of Lascaux (France). *Left:* The wall painting prominently shows a bull with two horns. The seven black dots above the head of the bulls might resemble the stars of the open star cluster Pleiades. The stars arranged in one line below left to the head of the bull could be the belt stars of the Orion constellation. The stars in the head of the bull could be the members of the star cluster Hyades with the star Aldebaran being the eye of the bull. Credit: Elke Wetzig (downloaded from Wikipedia on 15.08.2023), CC BY-SA 4.0. *Right:* Prehistoric painting "Shaft scence" in the cave of Lascaux showing a bison, a man with a bird head, and a bird forming the Summer Triangle consisting of the stars Vega, Altair, and Deneb (argument by Michael Rappenglueck as documented e.g. in the BBC article `http://news.bbc.co.uk/2/hi/science/nature/871930.stm` (published on 09.08.2000; website visited on 22.11.2023)). Credit: Peter80 (downloaded from Wikipedia on 15.08.2023), CC BY-SA 3.0.

Another famous wall drawing found in the "Shaft of the Dead Man" in the cave of Lascaux is shown in the right panel of Figure 2.1. The painting consists of a bison (middle right), a man with a bird head (middle left), and a bird (bottom left) which seem to illustrate a mythological scenery but it also has been speculated that arrangement of these three objects reflects the position of the bright stars Vega, Altair, and Deneb which form together the so-called Summer Triangle (e.g. Griffiths and Boroughs 1913; Rappenglück 1997; and see also the argument by Michael Rappenglueck documented in a BBC article[3]).

The left panel of Figure 2.2 presents a current picture of the famous prehistoric stone monument Stonehenge located in Whiltshire (England) which was constructed between 3000 and 2000 BC. The exact usage of Stonehenge is still under debate but it seems to be very likely that it functioned as an astronomical observatory (e.g. Hawkins 1963; Hoyle 1966; Atkinson 1978; Ruggles, Cunliffe and Renfrew 1997). Recently, it has been reported that the Altar stone consists of a different material to the other stones (Bevins et al. 2023) demonstrating the many open questions of Stonehenge.

One of the most famous depiction of astronomical objects from prehistoric times is the Nebray sky disc (in German known as "Himmelsscheibe von Nebra") which was found on the Mittelberg hill closely located to the town Nebra (Germany) in 1999. The right panel of Figure 2.2 shows an image of the Nebra sky disc which has a diameter of about 30 cm on which the full moon or the Sun, the Waxing moon, a cluster of seven stars which are likely the Pleiades, the Sunset and Sunrise, and a Solar barque are painted in Gold (Mozel 2003). The disc has an estimated age of about 3600–3800 years being therewith dated to the Bronze Age (Ehser, Borg and Pernicka 2011).

[3] `http://news.bbc.co.uk/2/hi/science/nature/871930.stm` (published on 09.08.2000; website visited on 22.11.2023)

Figure 2.2: Astronomy in prehistoric times. *Left:* The prehistoric stone monument Stonehenge constructed between 3000 BC and 2000 BC in Wiltshire (England). Credit: Operarius (downloaded from Wikipedia on 15.08.2023), CC BY-SA 3.0. *Right:* Image of the Nebra sky disk (in German: Himmelsscheibe von Nebra) from c. 1800–1600 BCE showing the Full Moon (middle left), the Waxing Moon (right), the seven visible stars of the Pleiades (top middle left), the rising and setting Sun (left and right), and a Solar barque (bottom). The deformations at the left edge of the disk were caused during the archaeological excavations. Credit: Frank Vincentz (downloaded from Wikipedia on 15.08.2023), CC BY-SA 4.0.

2.2 Classical Greek antiquity

In Classical Greek (about 8th century BC till about the 5th century AD), philosophy and natural science experienced a great upswing which yielded to the development of the first - scientific - cosmological models. The reasons for the cultural and intellectual improvements during these times are complex but it seems that the development of a fully phonetic and therewith easier to learn alphabetic script, the sea access which allowed for economic tradings and exchanges with other peoples, and the establishment of a democracy played a key role.[4] Covering all the important contributions to the scientific knowledge and inventions by the ancient Greeks would be beyond the scope of my thesis, but I will review at least some of the most important steps towards the establishment of the Ptolemaic model.

The pre-Socratic philosopher Thales of Milet (c. 626/623–c. 548/545 BC) can be considered not only as one of the Seven Sages of Greece but probably also as one of the very first astronomer and cosmologist by proposing a model of the Universe. He argued that the water is the origin of everything and the Earth is a flat disc which floats on a huge ocean. Based on this model he explained earthquakes by tilts of the earth disc caused by waves on the ocean going therewith beyond the supernatural interpretation of the "Earth-Shaker" Poseidon (O'Grady 2017). The ancient Greek historian Herodotus reported that Thales of Milet correctly predicted a Solar eclipse which occurred on 28.05.585 BC (Krafft 2007) but it is still questionable if this often told story indeed occurred because his model seems to be too inaccurate to make such complicated predictions (e.g. Neugebauer 1969; Querejeta 2013).

Thales of Milet's student Anaximander (c. 610–c. 546 BC) was one of the very first person who proposed the geocentric worldview according to which our Earth is the centre of the Universe. In particular, he described that the Earth has the shape of a cylinder which floats in the centre of an

[4] Private communication with my colleague Nick Samaras.

infinite Universe. Although this of course a wrong description of our Universe, it has to be noted that it is of great intellectual achievement to think about a freely floating massive body in space without based on a solid ground. Anaximander explained further that the Earth is surrounded by three wheels which are filled with fire. Holes in the closest wheel located to the Earth represents the stars, while a hole in the second and third closest wheel refer to the Moon and the Sun, respectively (see e.g. Naddaf 1998, for a discussion on the order of these objects relative to the Earth).

In ancient Greek times, the geocentric model became the established world view with the most important representatives being Anaximander, Plato (428/427 or 424/423–348 BC), Aristotle of Stagira (384–322 BC), and Claudius Ptolemy (c. 100–c. 170 AD). Aristotle's model in which the Earth is surrounded, in this order, by the Moon, Mercury, Venus, the Sun, Mars, Jupiter, Saturn, the fixed stars, and the "Prime Mover", who causes the motions of the other spheres, is schematically illustrated at the left hand side of Figure 2.3. This model had a significant disadvantage because it failed in explaining that planets appear to move first forwards and subsequently backwards on the sky. These so-called retrograde motions of planets are addressed in the model by Claudius Ptolemy by introducing the concept of "deferents" and "epicycles" as visualized at the right hand side of Figure 2.3. In particular, the planet moves on a circular orbits called "epicycle", whose centre itself moves on a circular orbit called "deferent" centered around the "eccentrix". The Earth is slightly off-centered being located at the opposite position of the so-called "equant" from which the centre of the epicycle has a constant angular velocity which should explain the changes of the planet's speed observed from Earth.

Furthermore, Ptolemy wrote the book "Almagest" which lists 1022 stars and astronomical objects (e.g. Pedersen and A. Jones 2010). Till the invention of the telescope in the 17th century (Section 2.4), the "Almagest" was one of the most important astronomical catalogues.

Aristarchus of Samos (310–230 BC) is considered to be the first person who proposed the heliocentric model in which the Sun is placed at the centre of the Universe. However, it took till the Copernican revolution caused by Nicolaus Copernicus (1473–1543) with significant contributions by Johannes Kepler (1571–1630) and Galileo Galilei (1564–1641) to finally replace the geocentric with the heliocentric model (Section 2.4).

Eratosthenes of Cyrene (c. 276–c. 195/194 BC) calculated the circumference of the Earth as schematically illustrated in Figure 2.4. Coincidentally, Cyene is located close to the Tropic of Cancer such that a pole or a Gnomon would not throw a shadow when the Sun is exactly located at the zenit at Solistice. As witnessed by the Greek astronomer Cleomedes it has been told that Erathostenes realized that the Sun's rays hit the ground of a thin and deep well only at a certain time at Solistice. However, at the same time in Alexandria, a pole threw a non-vanishing shadow of $\alpha = 7.2^\circ$ from vertical. Alexandria and Cyene are both roughly located at the same meridian but separated by $\approx 5\,000$ Stadia which corresponds to ≈ 800 km such that Eraosthenes correctly concluded that the Earth has to be a sphere in order to explain his measurements (Van Helden 2010). Using geometry, he then deduced the circumference of the Earth, d_{Earth}, to be

$$\frac{d_{\mathrm{Earth}}}{5000\ \mathrm{Stadia}} = \frac{360^\circ}{7.2^\circ} \tag{2.1}$$

$$d_{\mathrm{Earth}} = 250\,000\ \mathrm{Stadia} \mathrel{\widehat{=}} 40\,000\ \mathrm{km}\,. \tag{2.2}$$

which closely matches today's derived circumference of $\approx 40\,030$ km for a globally-averaged Earth radius of 6371 km (Longhorn and Hughes 2015). Thus, the concept of a non-flat Earth was already

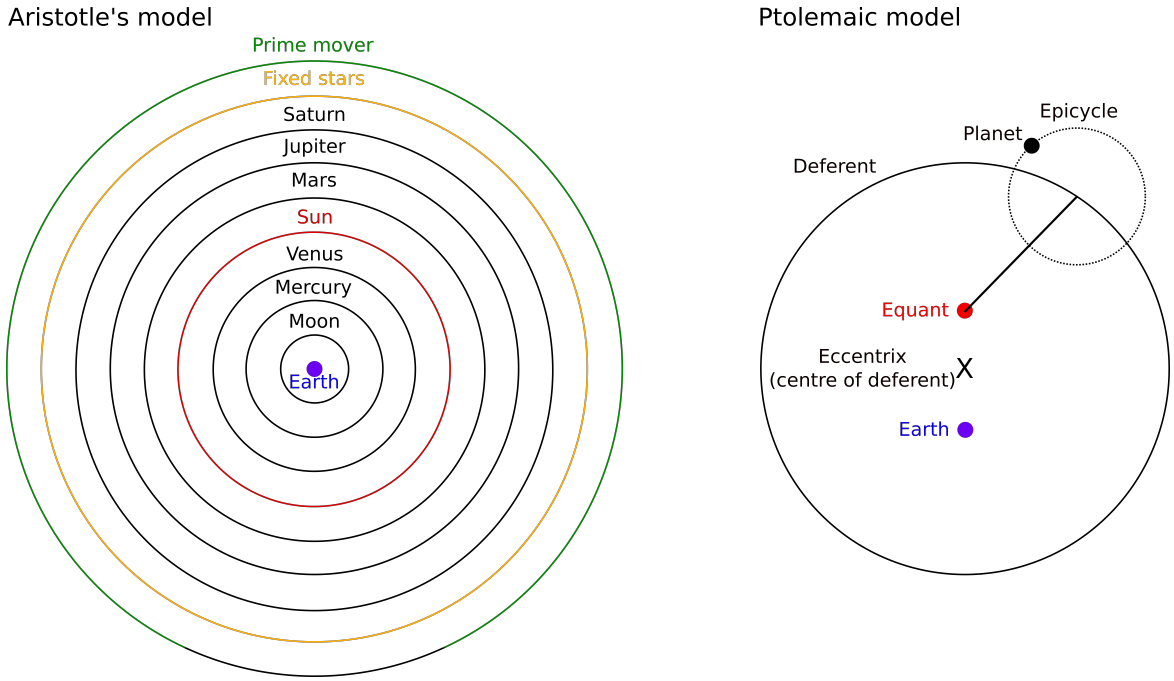

Figure 2.3: Illustration of Aristotle's (left) and Ptolemaic (right) geocentric model of the Universe. *Left:* Aristotle's model assumes that the Earth (blue dot) is at the exact centre of the Universe being surrounded by perfect circles on which move with uniform speed the Moon (first black circle), Sun (red circle), the five planets known at ancient times (i.e. from closest to furthest from Earth: Mercury, Venus, Mars, Jupiter, Saturn; black circles), the sphere of the fixed stars (yellow circle), and the Prime Mover (green circle). *Right:* The Ptolemy model is a modification of the Aristotle's model (left) by introducing "deferents" (solid circle) and "epicycles" (dotted circle) to explain the motion of a planet (black dot). The planet orbits around the centre of the epicycle, which itself follows on a circular motion the deferent. The centre of the deferent is called "eccentrix" (X mark symbol) while the Earth is slightly off-centered. On the opposite position of the Earth is the so-called "equant" (red dot) from which the centre of the epicycle has a constant angular velocity. Note that both diagrams are not to scale. Credit: Illustration made by the author of the thesis, but based on the diagrams presented on the websites `https://www.pas.rochester.edu/~blackman/ast104/aristotle8.html` (left) and `https://www.britannica.com/science/Ptolemaic-system` (right).

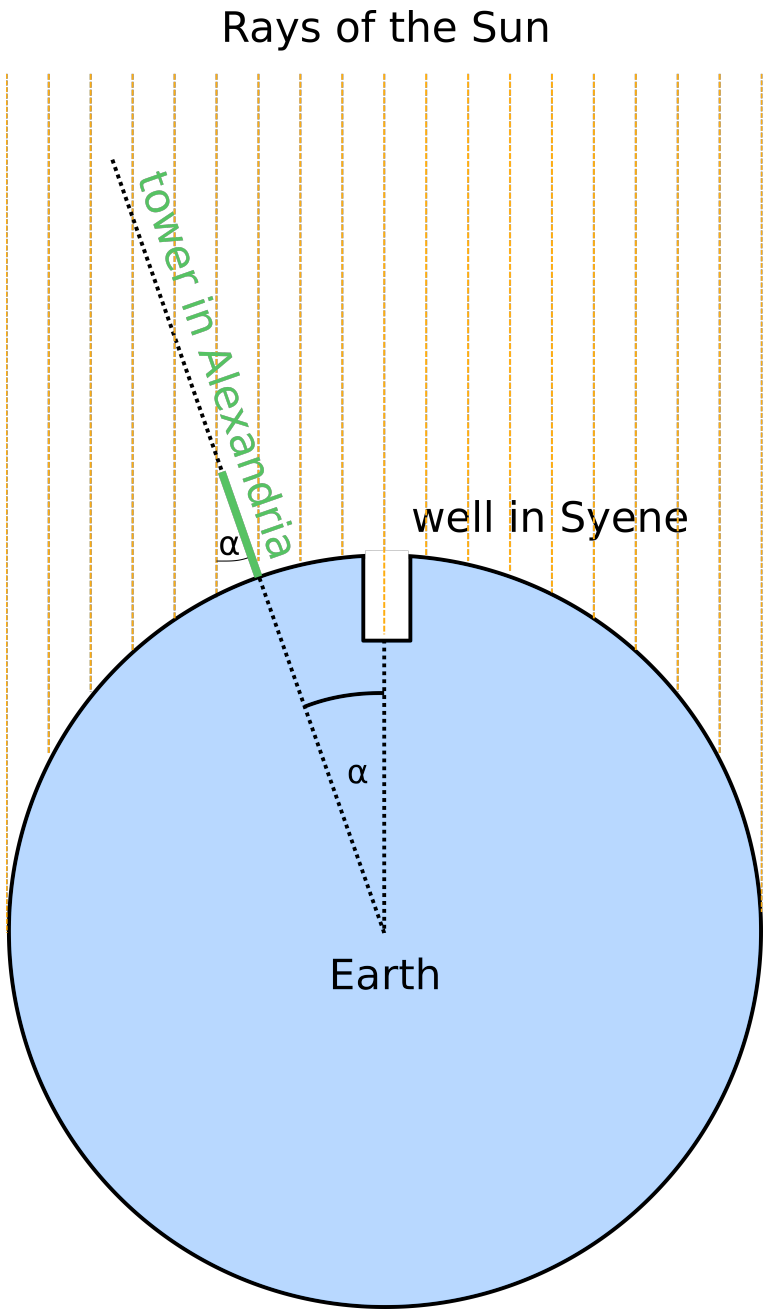

Figure 2.4: Schematically illustration of the derivation of the Earth's circumference by Eratosthenes of Cyrene (c. 276–c. 195/194 BC). Cyene is located close to the Tropic of Cancer such that the Sun ray's fall exactly parallel (orange dashed lines) in a well only at Solistice. Cyence and Alexandria are located roughly at the same meridian and are separated by ≈ 5 000 Stadia which corresponds to ≈ 800 km. At Solistice, a pole or tower located in Alexandria (green solid line) throws a shadow of $\alpha = 7.2^\circ$ from vertical such that Eratosthenes derived a Earth's circumference of $d_{\text{Earth}} \approx 250\,000$ Stadia corresponding to ≈ 40 000 km (see e.g. the documentation in Van Helden 2010). Note that the illustration is not to scale. Credit: figure made by the author of this thesis but based on the image from "cmglee, David Monniaux, jimht at shaw dot ca" from Wikipedia (webpage visited on 13.08.2023), Attribution-ShareAlike 4.0 International (CC BY-SA 4.0 Deed).

established in ancient Greeks and Medival times. In fact, Pythagoras of Samos (c. 570–c. 495 BC) was one of the first who speculated about a spherical Earth (Diller 1949). The wrong assumption that people at these times believed in a flat Earth goes probably back to a mis-interpretation of the book "A history of the Life and Voyages of Christopher Columbus" published in 1828 by the American writer Washington Irving.

Hipparchus of Nicaea (c. 190–c. 120 BC) used the parallax method to calculate a distance between the Earth and Moon of about 60 Earth radii (e.g. Toomer 1974; Krafft 2007) corresponding to about 380 000 km which agreed remarkably well with today's measurement of 356 500 km at the perigee and 406 700 km at the apogee (Murphy 2013). In addition, Hipparchus categorized the stars according to their apparent brightness and position on the sky (Kanas 2009). In 1989, the "HIgh Precision PARallax COllecting Satellite" (HIPPARCOS; Esa 1997) named in honor of Hipparchus was launched to measures the parallaxes and proper motions of stars.

2.3 Medieval period

Astronomy in the Medieval period was mainly influenced by the geocentric world view of Platon, Aristoteles, and Claudius Ptolemy according to which the Earth is the centre of the Universe. The heliocentric model originally proposed by Aristarchos of Samos was for several reasons widely ignored. First of all simply because it may have appeared counterintuitive that the Earth is moving around the Sun and not the Sun around the Earth. Secondly, the heliocentric model predicted parallaxes of nearby stars which were unobservable at those times. The first parallaxes of stars have been measured in the 1830s (Bessel 1838; Henderson 1839; von Struve 1840; and see also Reid and Menten 2020 for a re-analysis of the former three studies). Finally, the heliocentric model was in conflict with the dogma of the catholic church, which considered the Earth and not the Sun as the centre of the Universe.

In general, the scientific development in the Medieval period was significantly inhibited by the belief canon as represented largely by the Catholic church with scientific cosmology being significantly constrained by biblical cosmology. The concept of the "Prime Mover" as a first initiation of all movements has been taken as one of the five arguments for the poof of God by the Italian priest Thomas Aquinas (1225–1274). Interestingly, the prominent opening of the book of Genesis,

> *"In the beginning, God created the heavens and the earth."* (Genesis 1:1)

describes a well-defined beginning of the Universe but the phrase "In the beginning" and not "At the beginning" expresses that God already existed when he or she "created the heavens and the earth". The conflict between belief (i.e. religion) and rational deduction (i.e. science) is a tragic chapter in history as we will see further in Section 2.4.

In Austria, the University of Vienna was founded by the Duke of Austria Rudolf IV (1339–1365) in 1365 which triggered the formation of the "Wiener astronomische Schule" (English: "Vienna astronomical school") with the most prominent representatives being Johannes von Gmunden (c. 1380/84–1442), Georg von Peuerbach (1423–1461), and Regiomontanus (1436–1476). The left panel of Figure 2.5 shows the memorial plague of the astronomer and mathematician Johannes von Gmunden mounted at the city hall of Gmunden, which is not only his but also my own birthplace. Johannes von Gmunden studied in Vienna and became later a pastor in Laa in Lower Austria (Simek and Chlench 2006; Simek and Klein 2012) such that it seems to be unlikely that he performed

observations in Gmunden. Today's observatory of Gmunden is depicted in the right panel of Figure 2.5 and was opened in 1949 and constructed out of a former tower for gunpower which was built in 1844.[5] Johannes von Gmunden was the teacher of Georg von Peuerbach who became the first professor specialized on astronomy in Vienna. Georg von Peuerbach realized several shortcomings in the Ptolemaic model and his lectures collected in the book "Theoricae novae planetarium" (Peuerbach 1508) paved the way for the Copernican revolution in 1543 (Krafft 2007).

Figure 2.5: Astronomy in Gmunden (Austria). *Left:* Memoriam of Johannes von Gmunden (c. 1380/84–1442) mounted in front of the city hall at the Rathaus-Platz 1 in Gmunden. The top plaque reads "Zur Erinnerung an den in dieser Stadt geborenen berühmten Mathematiker und Astronomen Canonicus Johannes von Gmunden eine Zierde der Wiener Universität, an welcher er als Magister und Vice Kanzler 1408 bis 1435 thätig [sic!] war. Er starb am 23. Februar 1442 als Pfarrer von Laa in Nied Oesterr." which translates to "In memory of the famous Mathematician and Astronomer born in this city Canonicus Johannes von Gmunden adornment from the University of Vienna at which he acted as a magister and vice-chancellor from 1408 to 1435. He died in February 1442 as a pastor in Laa in Lower Austria" (translated from German into English by the author of this thesis). The bottom plague announces the timings of the famous "Keramik Glockenspiel" (ceramic bells) at the Gmundner city hall. Credit: Photo taken by the author of this thesis (September 2023). *Right:* Observatory of Gmunden located at the Kalvarienbergweg 3 which was originally a former tower for gunpowder constructed in 1844 and was rebuilt to an observatory by Johannes Eisner (1915–1993) in 1949. Nowadays the observatory is aimed for public guiding tours organized by the club "AURIGA-Traunseeastronomie e.V." led by Hagen Tolle. Credit: Peter Petz

[5] Private communication with Hagen Tolle.

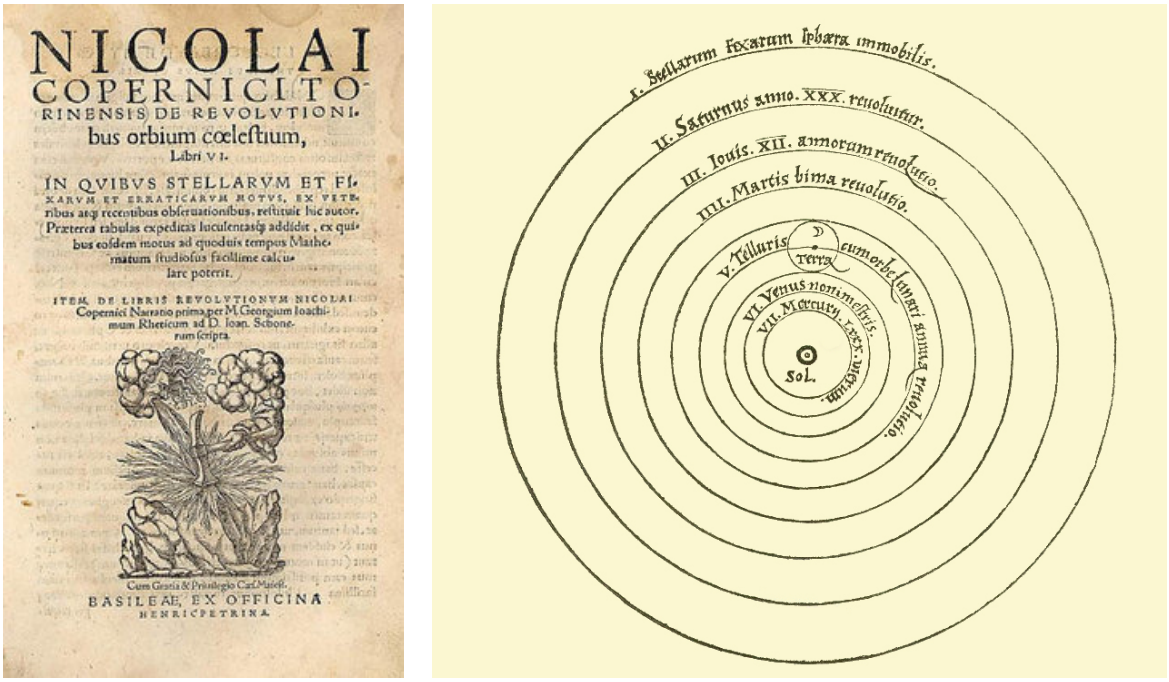

Figure 2.6: "De revolutionibus orbium coelestium" published in 1543 by Nicolaus Copernicus (1473–1543). *Left:* Title page of the 2nd edition (1566) of "De revolutionibus orbium coelestium" (Copernicus and Rhaticus 1566). Credit: Copernicus and Rhaticus (1566) (image of the title page downloaded from Wikipedia on 18.09.2023), Public domain. *Right:* Illustration of the heliocentric model proposed by Nicolaus Copernicus in "De revolutionibus orbium coelestium" in which the Sun is at the centre of the known Universe surrounded (from the inside out) by the planets Mercury, Venus, Earth with Moon, Mars, Jupiter, Saturn, and the fix stars. Credit: Own work from Copernicus 1543 (downloaded from Wikipedia on 18.09.2023), Public domain.

2.4 Copernican revolution and Newton's law of gravity

The "De revolutionibus orbium coelestium" published in 1543 by Nicolaus Copernicus (1473–1543) triggered one of the biggest revolution in astronomy by replacing the geocentric with the heliocentric model in which the Sun becomes the centre of the Universe. Nicolaus Copernicus correctly described the order of the six planets known at this time with the closest planet to the Sun being Mercury, which is followed by the Venus, the Earth with the Moon, Mars, Jupiter, and Saturn as illustrated in the right panel of Figure 2.6. In contrast to the planets and Moon, the stars remain fixed at the outermost sphere. However, this Copernican model still wrongly assumed uniform circular orbits of the planets around the Sun such that smaller versions of epicycles called "epicyclets" were still required to explain the observed planetary motions. Interestingly, Copernicus published his work "De revolutionibus orbium coelestium", which he dedicated to Pope Paul III, briefly before his death, most likely in order to avoid conflicts with the Catholic Church. The rejection from the geocentric towards the helicentric model was heavily criticized by the father of Protestantism, Martin Luther (1483–1546), who stated:

"Der Narr [Nicolaus Copernicus] will die ganze Kunst Astronomiae umkehren!"
(Statement by Martin Luther (Tischreden IV, No. 4630. Weimar 1916) as documented in Zinner, Nobis and Schmeidler 1988)
"This fool wishes to reverse the entire science of astronomy;"
(English translation as documented in T. S. Kuhn 1992)

The Italian astronomer Giordano Bruno (1548–1600) was very much in favor of the Copernican model and further argued that even other stars could be surrounded by planets potentially hosting life similar to the Earth. He considered an infinite Universe without a specific centre and encountered several other conflicts with the catholic church which finally resulted with his sentencing to the stake (see e.g. Bührke 2022).

A technical revolution in astronomy took place at the beginning of the 17th century when supposedly[6] Hans Lipperhey (c. 1570–1619) invented the telescope. In 1609, Galileo Galilei (1564–1642) discovered with a further development of the telescope by Lipperhey the four Galilean moons of the planet Jupiter named after Jupiter's amours Io, Europa, Ganymed, and Callisto. Moreover, Galilei described structures on the Moon, detected the Sun spots which are visible as black spots on the Solar surface, and the phases of the planet Venus. In his book "Sidereus Nuncius" (Galilei 1610) he wrote:

"Est enim GALAXIA nihil aliud, quam innumerarum
Stellarum coaceruatim consitarum congeries;"
(Galilei 1610)
"The Galaxy is nothing else than a congeries of innumerable stars distributed in clusters."
(English translation as given in Galilei 2016)

and realized therewith that the observed stars belong to our own Milky Way galaxy. In fact, nowadays its known that the Milky Way consists of about 100–400 billion stars. Galileo provoked the Catholic Church in his book "Dialogo sopra i due massimi sistemi" (1632) which discusses both the geocentric and heliocentric world views but the fictional representative of the former was named "Simplicio". In 1633, the conflict between Galileo and the Catholic Church escalated in a trial at which he was sentenced to house arrest for the rest of his life.

The heliocentric world view became further established when Johannes Kepler (1571–1630) developed with the help of accurate planetary position measurements from Tycho Brahe (1546–1601) his famous three laws of planetary motion. The story towards Kepler's laws has some dramatic but also anecdotic aspects. Tycho Brahe, who had a quick-tempered and combative character, was working on a hybrid of the geocentric and Copernican models such that he denied to share his accurate measurements with Johannes Kepler. Tycho Brahe's life came to a tragic end after a banquet in Prague during which he could not go to the toilette as this would have been against the rules of good etiquette. This might have led to his bladder rupturing[7] which in turn caused his death forcing Johannes Kepler to get Brahe's data. It has been speculated by others that Tycho Brahe was poisoned, perhaps even by Johannes Kepler (J. Gilder and A.-L. Gilder 2005), but latest findings of an exhumation in 2010 ruled

[6] It is not fully clear if Hans Lipperhey indeed was the first person who invented the telescope (see King 2003).

[7] Pavel Kroupa suggested (private communication) it might have been common to use tourniquets to allow strong drinking, given the strict rule of not being allowed to leave the hall before a banquet was formally ended by the king (or presiding host).

out a death of a mercury poisoning (e.g. Kučera et al. 2017). The tomb of Tycho Brahe is located in the Church of Mother of God before Týn at the old town square of Prague as shown in the left panel of Figure 2.7. With the help of Tycho Brahe's data, Johannes Kepler was finally able to formulate the first two of his laws were published in "Astronomia Nova" (Kepler 1609) and have been developed during his time in Prague from 1607 to 1612, which has been also witnessed at the plague on his former house as shown in the right panel of Figure 2.7. In particular, the first law states that the orbits of planets are ellipses with the Sun at one of the focal points rather than perfect circles as for the Copernikan model. The second law focuses on the speed variations of the planets along their orbits. This is mathematically described by

$$\frac{dA}{dt} = \frac{L}{2m}, \tag{2.3}$$

where dA is the areal element covered at the time dt, and L and m are the angular momentum and mass of the planet, respectively. Thus, planets at the pericentre move faster than at the apocenter of the orbit. His third law was formulated some years later in "Harmonices mundi libri V" (Kepler 1619) describes that the square of the period is proportional to the cube of the semimajor axis of the planet's orbit, which is mathematically expressed via

$$\frac{a^3}{T^2} = \frac{G(M+m)}{4\pi^2} \approx \frac{GM}{4\pi^2}, \tag{2.4}$$

where T is the orbital period, a is the semi-major axis, M the mass of the Sun, and G is the gravitational constant. Therewith, Kepler's three laws of planetary motion finally rejected the epicycle theory.

In Italy, Galileo Galilei had not only performed astronomical observations but had also conducted experiments of rolling objects on inclined surfaces and of free falling objects (probably also from the famous Leaning Tower of Pisa) which made him to conclude that in a vacuum all objects fall with the same acceleration independent of their masses and shapes. Almost 400 years later on the Moon, the astronaut David Scott verified Galileo's experiment during the Apollo 15 mission using a hammer and a feather.[8] Back on Earth and few years after Galileo's experiments, none other than Sir Isaac Newton (1642–1726/27) himself observed an apple falling down from a tree which most likely inspired him to formulate his famous gravitational law as witnessed by the physicist William Stukeley (1687–1765):

[8] See e.g. the video Apollo 15 Hammer-Feather Drop on Youtube.

Figure 2.7: History of astronomy in Prague. *Left:* The tomb of Tycho Brahe (1546–1601) is located next to the altar of the Church of Mother of God before Týn (Kostel Matky Boží před Týnem) which is located at the old town square of Prague (Czech Republic). Credit: Photo taken by the author of the thesis during a research visit in Prague (October 2019). *Right:* House of Johannes Kepler (1571–1630) located in the Karlova street number 4 in Prague (Czech Republic). The plaque above the door states in Czech language "zde žil v letech 1607 až 1612 JOHANNES KEPLER v té době objevil první dva zákony o pohybu planet kolem slunce", which translates: "Here lived from 1607 until 1612 Johannes Kepler. During this period he discovered [the first] two laws concerning the motion of planets around the [S]un." (Wolfgang Volk, http://www.w-volk.de/museum/plaque05.htm (webpage visited on 14.11.2023)). Credit: Photo taken by the author of the thesis during a research visit in Prague (September 2022).

"after dinner, the weather being warm, we went into the garden, and drank thea [sic!] under the shade of some appletrees [sic!], only he, and myself. amidst [sic!] other discourse, he told me, he was just in the same situation, as when formerly, the notion of gravitation came into his mind. "why should that apple always descend perpendicularly to the ground", thought he to him self: occasion'd [sic!] by the fall of an apple, as he sat in a comtemplative [sic!] mood: "why should it not go sideways, or upwards? but constantly to the earths centre? assuredly, the reason is, that the earth draws it. there must be a drawing power in matter. and the sum of the drawing power in the matter of the earth must be in the earths center, not in any side of the earth. therefore dos [sic!] this apple fall perpendicularly, or toward the center. if matter thus draws matter; it must be in proportion of its quantity. therefore the apple draws the earth, as well as the earth draws the apple." "

(Stukeley 1752)[a]

[a] see also the website https://www.newtonproject.ox.ac.uk/view/texts/normalized/OTHE00001 (webpage visited on 17.11.2023)

Newton's intellectual brilliance particularly showed up in his idea to infer from terrestrial experiments the motions of celestial objects as gravity would not only be responsible for the downfalling apple on the Earth's surface but also for the orbit of the Moon (private communication with Pavel Kroupa and see also I. B. Cohen and G. E. Smith 2002). Newton can be therewith considered as the first person who proposed the Cosmological Principle which builds the foundation of modern cosmology (Section 3.1). In 1994, the Austrian-British philosopher Karl Raimund Popper (1902–1994) strongly criticized the Cosmological Principle in saying

"And the "cosmological principles" were, I fear, dogmas that should not have been proposed".

(Statement by Karl Popper as documented in Kragh 2012)

In 1687, Sir Isaac Newton published "Philosophiae Naturalis Principia Mathematica" (Newton 1687) in which he presented his law of universal gravitation. According to Newton's formulation, the gravitational force acting between two bodies with the masses m_1 and m_2 separated by the distance r is given by

$$F_\mathrm{g} = G\,\frac{m_1 m_2}{r^2}\,, \tag{2.5}$$

where G is the gravitational constant being $G = 6.67430 \times 10^{-11}\ \mathrm{m^3\,kg^{-1}\,s^{-2}}$ (Tiesinga et al. 2021). Thus, in Newtonian gravity, the force is inversely proportional to the square of the distance between the two bodies. As discussed further in the Chapters 3 and 4, the theory of gravity is strongly linked with the development of cosmological models as the underlying gravitational law defines the motion of objects and evolution of the Universe (e.g. López-Corredoira 2022). Indeed, the cosmological implications of Newton's law of gravity have been discussed by Richard Bentley (1662–1742) who pointed out that all objects should collapse to a single point within a finite Universe. Newton replied to Bentley's paradox with the very unsatisfactory answer that

> *"a continual miracle is needed to prevent the Sun and the fixt [sic!] stars from rushing together through gravity."*
> (Statement by Sir Isaac Newton as documented in Hoskin 1985)

Astronomical catalogs and surveys build the basis for statistical analysis and the recognitions of variations on the sky. While the "Almagest" published by Ptolemy (Section 2.2) was until the 17th century one of the most important catalogue of astronomical objects, the invention and development of the telescope triggered the construction of new astronomical catalogues. For example, Charles Messier (1730–1817) compiled the "Catalogue des Nébuleuses et des Amas d'Étoiles" (English: "Catalogue of Nebulae and Star Clusters"; Messier 1781) which is nowadays known as the Messier catalogue. Another famous catalogue, which had been continuously extended by including more and more objects, is the "Catalogue of Nebulae and Clusters of Stars" ("CN"; W. Herschel 1786; W. Herschel 1789; W. Herschel 1802) by William (1738–1822) and Caroline Herschel (1750–1848) which was again later updated by the "General Catalogue of Nebulae and Clusters of Stars" ("GC"; J. F. W. Herschel 1864) building the basis for the "New General Catalogue of Nebulae and Clusters of stars" ("NGC"; Dreyer 1888).

William Herschel is also famous for his discovery of the planet Uranus in 1781 (W. Herschel 1781). The planet Neptune was discovered by Johann Galle, Urbain Le Verrier, and John Couch Adams in 1846 (Galle 1846). Pluto was detected at the Lowell observatory in 1930 (Tombaugh 1946). While Pluto was first classified as a planet, the International Astronomical Union (IAU) decided, in Prague in 2006, that Pluto does not fulfill the criteria of a planet and degraded Pluto to the status of a dwarf planet (e.g. M. Brown 2010).

The German astronomer Friedrich Wilhelm August Argelander (1799–1875) performed together with Eduard Schönfeld[9] (1822–1891) the so-called Bonner Durchmusterung ("BD"; English: "Bonner Survey") of 32 500 stars at the "Alte Sternwarte" (English: "Old observatory") in Bonn (Argelander 1903, 2nd edition) as shown in the left panel of Figure 2.8. On a historical side note and connection with Bonn, from my knowledge there are no indications that the Bonner composer Ludwig van Beethoven (1770–1827), who was personally very interested in astronomy, was in contact with Friedrich Argelander. Ludwig van Beethoven owned the book "Anleitung zur Kenntnis des gestirnten Himmels" (Bode 1768) written by German astronomer Johann Elert Bode (1747–1826) and he knew the Austrian astronomer Joseph Johann von Littrow (1781–1840) who was the director of the Vienna observatory from 1819 to 1840 (Lodes 1997; Cooper 2001). The asteroid "1815 Beethoven"[10] discovered by the German astronomer Karl Wilhelm Reinmuth (1892–1979) is named in the composer's honour. An amusing story happened on the 12th of August in 1845. At this day, the statue of Ludwig van Beethoven located at the Münsterplatz in Bonn was inaugurated by Frederick William IV of Prussia (1795–1861). Afterwards he also visited the nowadays known as "Alte Sternwarte" in the Poppelsdorfer Allee 47 in Bonn and asked Argelander the following question (Geffert 2020):

[9] https://www.rheinische-geschichte.lvr.de/Persoenlichkeiten/eduard-schoenfeld/DE-2086/lido/645e0ea85a2d75.80789975 (webpage visited on 21.11.2023)

[10] https://www.minorplanetcenter.net/db_search/show_object?object_id=1815 (webpage visited on 16.11.2023)

> *"Na, Argelander, was gibt es Neues am Himmel?"* (Friedrich Wilhelm der IV, 1845)[a]
> *"Well, Argelander, what's new on the sky"* (Translated by author of this thesis)
>
> [a] see Geffert (2020) and personal communication with Dr. Michael Geffert

on which Argelander replied:

> *"Kennen Majestät denn schon das Alte?"* (Friedrich Wilhelm August Argelander, 1845)[a]
> *"Does Your Majesty already know the previous state?"* (Translated by the author of this thesis)

Argelander's tomb is located at the old cemetery in Bonn which can be seen in the right panel of Figure 2.8.

Figure 2.8: History of astronomy in Bonn. *Left:* Old observatory located in the Poppelsdorfer Allee 47 at Bonn, where Friedrich Wilhelm August Argelander (1799–1875) performed with Eduard Schönfeld (1828–1891) the famous Bonner Durchmusterung from 1859 to 1863. Credit: Photo taken by the author of the thesis (September 2023). *Right:* Tomb of Friedrich Wilhelm August Argelander (1799–1875) at the old cemetery in Bonn. Credit: Photo taken by the author of the thesis (August 2023).

2.5 Great debate & the nature of galaxies

Until the early 20th century the nature and physical properties of galaxies were very much unknown. Immanuel Kant (1724–1804) speculated that galaxies, which appeared as "nebulae" through the telescopes, are located outside of our own Milky Way and even called them "island universes". The discussion on the nature of galaxies finally culminated in the great debate between the two American astronomers Heber Doust Curtis (1872–1942) and Harlow Shapley (1885–1972) in 1920 as documented in Shapley and Curtis (1921). On the one hand, Shapley argued that the nebulae are small and located within (the outer part) of our own Milky Way galaxy, while Curtis on the other hand pointed out that the nebulae are own galaxies outside of the Milky Way:

> *"The evidence at present available points strongly to the conclusion that the spirals are individual galaxies, or island universes, comparable with our own galaxy in dimension and in number of component units."*
> (Heber Doust Curtis in Part II of
> "Dimension and structure of the galaxy" in Shapley and Curtis 1921)

The Great debate finally came to an end when the American astronomer Edwin Hubble (1889–1953) measured the distance to the Andromeda galaxy using Cepheid variable stars which were discovered by Leavitt and Pickering (1912). The great distance of the Andromeda galaxy showed that it must be located outside of the Milky Way galaxy confirming Curti's point of view. This scientific insight was a significant step in the history of astronomy as it showed that there are many other galaxies similar to our own Milky Way and demonstrated the sheer size of the Universe.

On this occasion, I would like to discuss the definition of a galaxy in the modern times. This is in fact a non-trivial task and one would probably come up with different criteria to define a galaxy. Naively, as a first approach one would maybe define a galaxy as a gravitationally bound stellar system. While this is indeed broadly correct, this definition would run into problems when discussing star clusters as these objects significantly differ from galactic systems. A more formal definition is e.g. provided by Forbes and Kroupa (2011) based on the two-body relaxation time (Binney and Tremaine 2008; Kroupa 1998; Forbes and Kroupa 2011), which is the time required to fully loses information about the initial configuration in the distribution of positions and velocities of the stars of a system. The (half-mass) two-body relaxation time in unit of Myr is mathematically expressed by (see equation 6 of Dabringhausen, Hilker and Kroupa 2008)

$$t_{\rm rh} = \frac{0.234}{\log_{10}(M/M_\odot)} \times \sqrt{\frac{M r_{\rm e}^3}{G}}\,, \tag{2.6}$$

where M and $r_{\rm e}$ are the galaxy mass in Solar masses ($M_\odot$) and the effective radius of the galaxy in pc, respectively. G is the gravitational constant being $0.0045\,{\rm pc}^3\,{\rm M}_\odot^{-1}\,{\rm Myr}^{-2}$ in astronomical units. Galaxies typically have $t_{\rm rh} > t_{\rm Hubble} = 13.8$ Gyr, while star clusters $t_{\rm rh} < t_{\rm Hubble} = 13.8$ Gyr (see figure 3 of Dabringhausen, Hilker and Kroupa 2008).

Back in the middle of the 19th and beginning of the 20th century, the different visual appearance of galaxies as e.g. ellipticals, spirals, or irregulars lead to the development of various morphological classification schemes. An early classification scheme was presented by M. Wolf (1908) in which he divided observed galactic (but also planetary) "nebulae" in 23 different groups based e.g. on

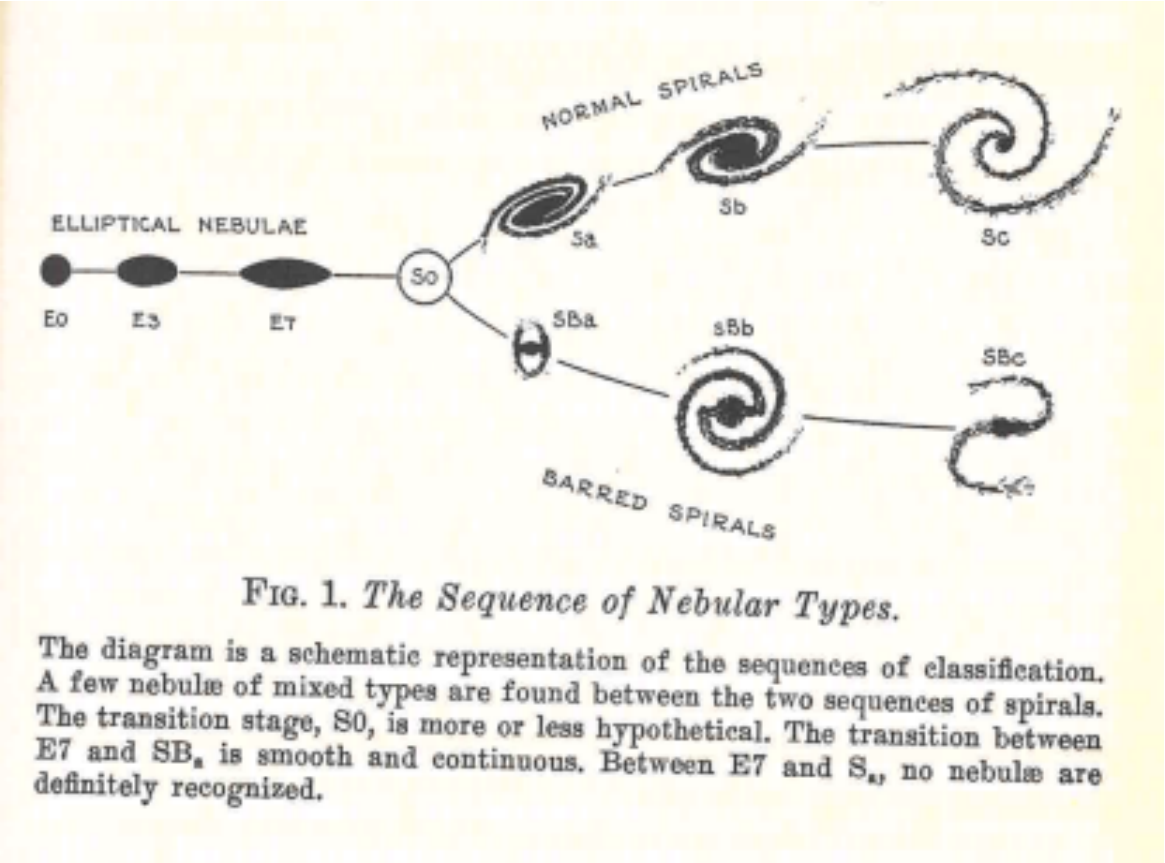

FIG. 1. *The Sequence of Nebular Types.*

The diagram is a schematic representation of the sequences of classification. A few nebulæ of mixed types are found between the two sequences of spirals. The transition stage, S0, is more or less hypothetical. The transition between E7 and SB_a is smooth and continuous. Between E7 and S_a, no nebulæ are definitely recognized.

Figure 2.9: Original Hubble diagram published in Hubble (1936), which divides galaxies in ellipticals (E), lentriculars (S0), unbarred (Sa–Sc), and barred (Sba–Sbc) spirals. This diagram was mainly influenced by the works of John Reynolds and James Jeans (Block and Freeman 2008; Block and Freeman 2015) insofar as J. H. Reynolds (1920) already divided spiral galaxies into seven different groups and Jeans (1928) proposed the tuning fork diagram to distinguish different galaxy types. Credit: Scan of figure 1 of Hubble (1936).

their shapes and intrinsic structures. The most famous galaxy morphological classification scheme is the so-called Hubble-diagram published in Hubble (1936) which is presented in its original form in Figure 2.10. The diagram is designed like a tuning fork for musical instruments in order to group the different types of galaxies. The handle of the tuning fork (left side) is populated with elliptical galaxies which are again subgrouped in E0, E1, E2, E3, E4, E5, and E7 (the original Hubble diagram only shows E0, E3, and E7) categories where the number after the character "E" refers to the degree of their apparent ellipticity. The two prongs (right side) of the tuning fork refer both to spiral galaxies, where one represents the barred spirals labeled as SBa, SBb, and SBc (lower branch) and the other one the unbarred spirals Sa, Sb, and Sc (upper branch). The small letter corresponds to the degree of the winding of the spiral arms whereby "a" describes a tightly and "c" a loosely winded spirals. Galaxies between these two extremes are marked with the letter "b". Lenticular galaxies (S0) are located at the crossing point of the tuning fork.

The history behind the Hubble diagram of 1936 is most remarkable as the underlying main idea goes originally back to John Reynolds and James Jeans (Block and Freeman 2008; Block and Freeman

2015). Firstly, J. H. Reynolds (1920) already proposed to divide spiral galaxies in seven different subgroups. Secondly, the concept of the tuning fork to divide different galaxy types was already published eight years earlier by Jeans (1928). As an interesting side note, James Jeans was a music lover (Block and Freeman 2015) such that one can speculate that Jeans was inspired to split galaxies like a tuning fork which was commonly used to tune music instruments (Block and Freeman 2008; Block and Freeman 2015). Hubble published his work without referencing or acknowledging the work by J. H. Reynolds (1920) or the tuning fork scheme originally introduced by Jeans (1928). The interested reader may find further information about the story behind the Hubble diagram in Block and Freeman (2008) and Block and Freeman (2015).

The classification schemes of galaxies have been revised and further developed over the last decades (e.g. de Vaucouleurs 1959; de Vaucouleurs et al. 1991) whereby nowadays the Hubble diagram, de Vaucouleurs, and the Morgan/Yerkes[11] scheme (Morgan and Mayall 1957; Morgan 1958; Morgan 1959) are commonly used.

2.6 Modern cosmology & the Λ-Cold Dark Matter model

The begin of modern cosmology can be dated with the development of general relativity by the German physicist Albert Einstein (1879–1955) which he published in "Die Feldgleichungen der Gravitation" (English: "The Field Equations of Gravitation"; Einstein 1915) about ten years after his theory of Special Relativity in "Zur Elektrodynamik bewegter Körper" (Einstein 1905). General Relativity provides an entirely new interpretation of the concept of gravity by the curvature of spacetime which the American physicist John Archibald Wheeler (1911–2008) explains with the phrase:

> *"Spacetime tells matter how to move; matter tells space how to curve"*
> (J. A. Wheeler and K. Ford 1998 and see also Misner et al. 2017)

Albert Einstein introduced a cosmological constant to his field equations in order to avoid unstable solutions in which the Universe contracts or expands. Later, he referred to his cosmological constant as his "biggest blunder" (O'Raifeartaigh and Mitton 2018) when observations supported an expanding Universe.

Initially, the scientific community was highly skeptical towards Einstein's General Relativity theory but the situation changed when Sir Arthur Eddington (1882-1944) observed the light deflection of a star by the Sun during a solar eclipse at the west coast of Africa in 1919 (Eddington 1919; Dyson, Eddington and Davidson 1920; and see for a review e.g. Gilmore and Tausch-Pebody 2022). Until today, General Relativity has been confirmed in many experiments e.g. by the detection of gravitational waves propagating with the speed of light (B. P. Abbott et al. 2016; B. P. Abbott et al. 2017) by the Laser Interferometer Gravitational-Wave Observatory (LIGO) or through the imaging of the shadow of the black hole in the M81 galaxy with the Event Horizon Telescope (Event Horizon Telescope Collaboration et al. 2019). In 1921, Albert Einstein was awarded with the Physics Nobel Price "for his services to Theoretical Physics, and especially for his discovery of the law of the photoelectric effect" (The Royal Swedish Academy of Sciences[12]) but astonishingly not explicitly for his theory of Special

[11] Named after the Yerkes Observatory in Wisconsin (United States)

[12] https://www.nobelprize.org/prizes/lists/all-nobel-prizes-in-physics/ (webpage visited on 11.05.2023)

or General Relativity.

First observational evidence showing that galaxies are typically receding from us has been found by the American astronomer Vesto Slipher (1875–1969) who derived the radial velocities of galaxies from their measured spectrum. A spectrum of a galaxy which is moving away from the Earth appears to be redshifted, but blueshifted if moving towards us. The redshift is defined by

$$z = \frac{\lambda_{\rm obs} - \lambda_{\rm emit}}{\lambda_{\rm emit}}, \tag{2.7}$$

where $\lambda_{\rm obs}$ and $\lambda_{\rm emit}$ are the observed and emitted wavelengths, respectively. Slipher (1913) measured that the spectrum of the Andromeda galaxy is blueshifted from which he obtained that Andromeda is moving with 300 km s^{-1} towards our own Milky Way galaxy. However, most of the galaxies he analyzed are redshifted (Slipher 1917) meaning that these galaxies are moving away from us. But galaxies were not known to be extragalactic at that time. The Curtis-Shapley debate took place in 1922 and only in 1926 was their extragalactic nature - them being island universes - finally recognized (see Section 2.5).

The theoretical basis of an expanding Universe was laid by the Russian mathematician and physicist Alexander Alexandrovisch Friedmann (1888–1925) in 1922. In his famous publication entitled "Über die Krümmung des Raumes" (Friedmann 1922), he obtained solutions of Einstein's Field Equation which describe the expansion of an isotropic and homogeneous Universe (see also Section 3.1). Five years later, the Belgium Priest, mathematics, and astronomer Georges Edouard Lemaître (1894–1966) derived independently of Friedmann also solutions for an expanding Universe from Einstein's Field Equations, which he published in French language with the title "Un Univers homogène de masse constante et de rayon croissant rendant compte de la vitesse radiale des nébuleuses extra-galactiques" (Lemaître 1927) which has been translated into English four years later with the title "A Homogeneous Universe of Constant Mass and Increasing Radius accounting for the Radial Velocity of Extra–Galactic Nebulae" (Lemaître 1931). In this study, he has not only presented the theoretical but also the observational evidence for an expanding Universe by showing a linear relation between the observed velocity and distance of galaxies being mathematically expressed via

$$v = H_0 \times D, \tag{2.8}$$

where H_0 is nowadays called the Hubble or Hubble-Lemaître constant (see below), D is the physical (proper) distance between the Milky Way and the galaxy, and v is the radial velocity of the galaxy (see also Section 3.1). Originally, he derived for two different samples expansion rates of $H_0 = 575$ km s^{-1} Mpc^{-1} and 670 km s^{-1} Mpc^{-1} (Lemaître 1927) being significantly higher than today's locally measured value of $H_0 = 73.04 \pm 1.04$ km s^{-1} Mpc^{-1} by Riess et al. (2022). Two years later, Hubble (1929) published the famous Hubble-diagram which is shown in its original form in Figure 2.10 from which he derived a similar value of $H_0 = 500$ km s^{-1} Mpc^{-1} (Hubble 1929).

According to Appenzeller (2009), the terminology "Hubble constant" appeared for the first time in Behr (1951) who explicitly referred to it as the "HUBBLEschen Expansions-Konstante" (English: "Hubble's expansion-constant"). Almost 70 years later, the International Astronomical Union (IAU) finally acknowledged Lemaître's ground-breaking work by officially re-naming the "Hubble law" to the "Hubble-Lemaître law" in 2018.

I would like to emphasize that one should not forget the important contributions by Vesto Slipher,

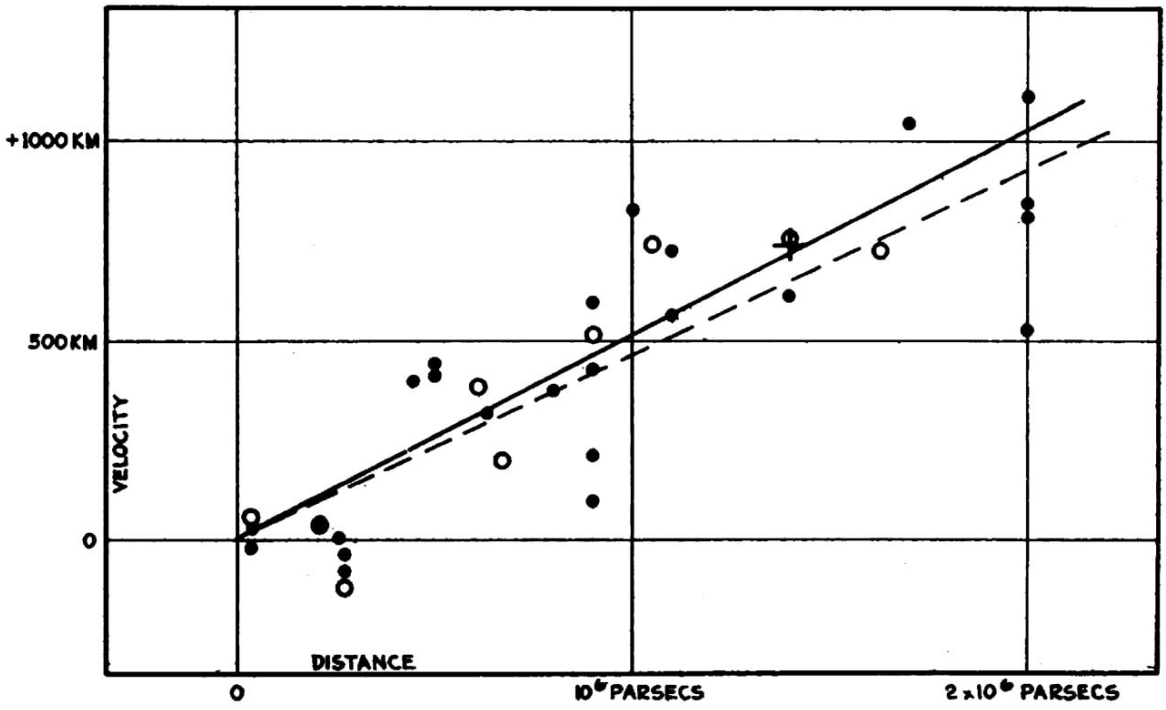

Figure 2.10: The famous Hubble diagram published in this form by Hubble (1929) which shows a correlation between the distance and velocity (redshift) of 24 galaxies (see also Equation 2.8). Note that the unit of the y-axis for the velocity is given in "km" but should be correctly "km/s". It is often stated that this is a typo made by Edwin Hubble (Kirshner 2004), but I would like to highlight that also e.g. Wirtz (1922a), Wirtz (1922b), Wirtz (1924), or Slipher (1917) used in their studies the labeling "km" instead of "km/s" for velocities. Therefore, although the unit "km" for the velocity is incorrect, there is also the possibility that this labeling was "just" a convention or a bad habit in the early 20th century. The x-axis shows the distance from the MW in parsec (1 parsec [1 pc] corresponds to 3.086×10^{13} km). The black circles (solid line) correspond to individual galaxies ("nebulae"), while the open circles are galaxies binned in groups. The black cross refers to the mean velocity and mean distance of 22 nebulae. Hubble (1929) derived a Hubble constant of $H_0 = 500\,\mathrm{km\,s^{-1}\,Mpc^{-1}}$, which is significantly higher than the current locally measured value of $H_0 = 73.04 \pm 1.04\,\mathrm{km\,s^{-1}\,Mpc^{-1}}$ based on Cepheid and SN Ia data (Riess et al. 2022). Credit: figure 1 of Hubble (1929).

Carl Wirtz (Wirtz 1922a and Wirtz 1924 as documented e.g. in Appenzeller 2009; Duerbeck 1989), and Knut Emil Lundmark (Lundmark 1924 and see Steer 2012 for a historical review but without mentioning Carl Wirtz). Thus, both famous diagrams (Figures 2.9 and 2.10) originally attributed to Edwin Hubble are build on significant contributions by others. Sadly, Edwin Hubble appears to have plagiarized the work of Reynolds, Jeans, Slipher, or Lemaître as uncovered in detail by Block and Freeman (2015).

As a historical remark and connection with Bonn, I especially would like to highlight the work by the German astronomer Carl Wilhelm Wirtz (1876–1939) who is the actual discoverer of the expansion of the Universe[13]. Carl Wirtz studied astronomy in Bonn from where he obtained his doctoral degree in 1898 (Joeveer 2007). At the observatory in Strassburg, he performed observations to measure the positions and motions of galaxies (e.g. Wirtz 1911a; Wirtz 1911b; Wirtz 1916; Wirtz 1917). In Kiel, he published two papers which showed that the radial velocity correlates with the apparent magnitude (Wirtz 1922a) and more importantly also with the angular diameter (Wirtz 1924) providing therewith the very first observational evidence for an expanding Universe even before Lemaître and Hubble. An image of Carl Wirtz is presented in the left panel of Figure 2.11. Perhaps the city Bonn or the University of Bonn should consider to acknowledge the scientific contributions of their former astronomy student Carl Wirtz with a memorial plague. Amusingly, during a walk through the Wiesenweg in Bonn, I discovered a construction site barrier on which the name "Karl Wirtz" (but not "Carl") is printed. A picture of this "memorial plague" is shown in the right panel of Figure 2.11.

In the 1930s, one of the greatest question or rather problem in modern physics arose – namely the "missing mass problem". The Swiss physicist Fritz Zwicky (1898–1974) analyzed the Coma galaxy cluster using the virial theorem which states

$$2\,K + U = 0\,, \tag{2.9}$$

where K and U are the kinetic and gravitational potential energy, respectively. Surprisingly, Zwicky (1933)[14] found that the galaxies of the cluster move faster than implied from the visible mass and he writes in his original publication:

> *"[...] die mittlere Dichte im Comasystem mindestens 400 mal grösser sein als die auf Grund von Beobachtungen an leuchtender Materie abgeleitete."*
> (Zwicky 1933)
> *"[...] the average density in the Coma system would have to be at least 400 times greater than that derived on the basis of observations of luminous matter."*
> (Andernach and Zwicky 2017)

from which he concluded further

[13] The story about Carl Wirtz and the Hubble constant is nicely outlined in Appenzeller (2009).

[14] The original work by Zwicky (1933) is written in German but an English and also a Spanish translation can be found e.g. in Andernach and Zwicky (2017) which can be also assessed via https://ned.ipac.caltech.edu/level5/March17/Zwicky/Zwicky_contents.html).

(a) (b)

Figure 2.11: *Left:* Image of Carl Wirtz (1876–1939) who studied astronomy in Bonn and is the actual discoverer of the expansion of the Universe. Credit: Austrian Academy of Sciences Press/Communications in Asteroseismology, Vienna Observatory, Volume 149, December 2008, p. 127/Institut für Astronomie der Universität Wien (downloaded from Wikipedia on 15.09.2023), Public domain. *Right:* Amusing coincidence of the name "K[C]arl Wirtz" printed on a construction site barrier at the Wiesenweg in Bonn. Credit: Photo taken by the author of the thesis in Bonn (June 2023).

> *"Falls sich dies bewahrheiten sollte, würde sich also das überraschende Resultat ergeben, dass dunkle Materie in sehr viel grösserer Dichte vorhanden ist als leuchtende Materie."*
> (Zwicky 1933)
> *"If this should be verified, it would lead to the surprising result that dark matter exists in much greater density than luminous matter."*
> (Andernach and Zwicky 2017)

Thus, Zwicky already used the terminology "dunkle Materie" (English: "dark matter") but to my knowledge, this terminology was firstly introduced much earlier by the French mathematician and physicist Jules Henri Poincaré (1854–1912) in 1906. This happened when the British mathematician and physicist Lord Kelvin (1824–1907) pointed out in his book "Baltimore lectures on molecular dynamics and the wave theory of light" (Kelvin 2010) that

> *"Many of our supposed thousand million stars, perhaps a great majority of them, may be dark bodies; [...]"* (Kelvin 2010)

on which Poincaré disagreed by commenting:

> *"[...] comme son chiffre est comparable à celui que donne le télescope, c'est qu'il n'y a pas de matière obscure, ou du moins qu'il n'y en a pas tant que de matière brillante"*
> (Poincaré 1906a)
> *"[...] since his number is comparable to that which the telescope gives, then there is no dark matter, or at least not so much as there is of shining matter."*
> (Poincaré 1906b)

The so-called "missing mass problem" was later also discovered on galactic scales by the observation of flat rotation curves of spiral galaxies by (Babcock 1938; Babcock 1939; Rubin and J. Ford W. K. 1970; Rubin, J. Ford W. K. and Thonnard 1978; Rubin, J. Ford W. K. and Thonnard 1980; Bosma 1981; Rubin et al. 1985) while a Keplerian rotation was expected according to which the rotational velocity scales with the inverse square root of the distance. Interestingly, the early studies by Babcock (1938) and Babcock (1939) already showed a deviation from a Keplerian rotation in the rotation curve of the Andromeda galaxy:

> *"A new discrepancy is now directly apparent when the rotations of the two systems are compared, for the nearly constant angular velocity of the outer parts of M31 is the opposite of the "planetary" type of rotation believed to obtain in the outer parts of the Galaxy."*
> (Babcock 1939)

Unfortunately, his findings have been and are still widely ignored within the astronomical community (see the discussion in Vanderburgh 2014).

While these observations have been typically interpreted as evidence for a missing mass component in the form of cold dark matter (e.g. Ostriker and Peebles 1973), the Israeli physicist Mordehai Milgrom (1946–) provided in his paper "A modification of the Newtonian dynamics as a possible alternative to the hidden mass hypothesis" (Milgrom 1983c) an alternative scenario in which he proposed a modification of Newton's law of gravity (called MOND) at low accelerations of $\lesssim 10^{-10}\,\mathrm{m\,s^{-2}}$ (see Chapter 4). Remarkably, Fritz Zwicky already discussed in 1937 that the usage of the virial theorem on galaxy clusters also functions as a test of the underlying law of gravity:

> *"It should also be noticed that the virial theorem as applied to clusters of nebulae provides for a test of the validity of the inverse square law of gravitational forces. This is of fundamental interest because of the enormous distances which separate the gravitating bodies whose motions are investigated. Since clusters of nebulae are the largest known aggregations of matter, the study of their mechanical behavior forms the last stepping-stone before we approach the investigation of the universe as a whole."*
> (Zwicky 1937)

Although not a single experiment has directly detected the cold dark matter particle, the concept of a missing mass rather than a correction of the law of gravity became the favored interpretation of

the observations by most of the astronomers. One can only speculate why MOND has been widely ignored by the scientific community but this would be not only beyond the scope of this chapter but also beyond the thesis. However, one reason could be that a non-linear gravitational theory such as MOND is (computationally) much more complicated than the linear theory of Newton. Another reason is that the very first relativistic formulation of MOND called Tensor–vector–scalar gravity (TeVeS; Bekenstein 2004) is inconsistent with gravitational waves traveling at the speed of light as detected with LIGO (B. P. Abbott et al. 2017). Furthermore, MOND provides an accurate description on galactic scales, but still requires an additional mass component on galaxy cluster scales (Section 4.4).

In the middle of the 20th century, two different cosmological paradigms have been discussed among the astrophysical community. On the one hand side, the steady-state theory likely originally proposed by James Jeans (see Section 2.5) and later mainly represented by Hermann Bondi (1919–2005), Thomas Gold (1920–2004), or Fred Hoyle (1915–2001) according to which matter is continuously created in the Universe (Jeans 1929; Bondi and Gold 1948; Hoyle 1948). On the other hand side, the Big Bang theory in which all the matter is created in one event at the beginning of the Universe − the Big Bang. The steady-state theory was finally rejected by the community when Penzias and Wilson (1965) discovered the cosmic microwave background (CMB) which has a black body spectrum at a temperature of about 2.7 K but has been originally predicted with about 5 K by (Alpher and Herman 1948, but see also). Arno Allan Penzias, and Robert Woodrow Wilson were awarded with the Nobel Prize in Physics "for their discovery of cosmic microwave background radiation" (The Royal Swedish Academy of Sciences[12]) in 1978. The Big Bang cosmology was faced by two significant problems, which are known in the literature as the horizon or homogeneity (Rindler 1956) and flatness (Dicke 1969) problems: Firstly, the Universe appears to be homogeneous on large scales although parts of the Universe are causally disconnected. Secondly, the Universe is flat (see Section 3.1) which is only possible for a specific matter density. These fine-tuning problems have been resolved by introducing a inflation phase (Guth 1981; Linde 1982; Starobinsky 1982; Albrecht and Steinhardt 1982) in which the volume of the Universe expands by a factor of 10^{78} between $\approx 10^{-36}$ s to $\approx 10^{-32}$ s (P. Schneider 2015) after the Big Bang. Karl Popper highly criticized the cosmological Big Bang model in 1994 as can be read up in Kragh (2021):

> *"I was a (student) member at the [Vienna] department of theoretical physics when ... Friedmann suggested that Hubble's suggestion could be explained by a simplified Einstein cosmology ... [The] big bang theory became rapidly more and more complicated. And my present view is that the number of auxiliary hypotheses is simply intolerable: according to my theory of science, this is not science. ... And not only is it not stressed by the upholders of the theory that it is all speculation without tests, but it is presented as if the theory were a proven fact. This is horrid; impermissible; against scientific ethics. ... I once was an enthusiastic admirer of (Friedmann's) Big Bang. I am now a disgusted opponent. By contrast, Einstein's General Relativity is a marvelous theory."*
>
> (Statement by Karl Popper as documented in Kragh 2021)

In 1962, the foundation of the European Organization for Astronomical Research in the Southern Hemisphere (or just called European Southern Observatory; ESO) set an important milestone for astronomical research in Europe. ESO hosts several telescopes in Chile (e.g. Schilling and Christensen 2013) while the ESO headquarter is located in Garching bei München (Germany) which is shown in Figure 2.12. Currently, the Extremely Large Telescope (ELT) is under construction at the Cello

Armazones in Chile being with a primary mirror of a diameter of 39.3 m the largest ground-based optical telescope. The first observations are expected for 2028[15], but an artistic image of the ELT can be already seen in the bottom left panel of Figure 2.13.

Figure 2.12: European Southern Observatory (ES0) in Garching bei München (Germany). *Left:* Headquarters of ESO in Garching bei München (Germany). Credit: Photo taken by the author of this thesis during a research visit (October 2022). *Right:* Supernova exhibition next to the ESO headquarter in Garching. Credit: Photo taken by the author of this thesis during a research visit (July 2019).

The advancing technologies during the 20th and 21st centuries yield to several further important observational and theoretical discoveries, which cannot be all covered in this thesis but a brief summary can be e.g. found in López-Corredoira (2022).

The last ingredient to the current standard model of cosmology has been introduced in the 1990s. According to my knowledge, the very first observational evidences for an accelerating expansion of the Universe have been reported by Efstathiou, Sutherland and Maddox (1990), Krauss and M. S. Turner (1995), Ostriker and Steinhardt (1995), and Yoshii and Peterson (1995). Later, Perlmutter et al. (1998) and Riess et al. (1998) independently found an acceleration expansion analyzing Supernovae Ia (SN Ia) data which brought Einstein's "biggest blunder" (see above) - the cosmological constant called Λ - again back into his field equations (see also Section 3.1) but this time not to model a static but rather an accelerated expanding Universe. Thus, the standard model of cosmology is also known as the Λ-Cold Dark Matter (ΛCDM) model and will be formally introduced in the next Section 3.1.2. In 2011, Adam Riess, Brian P. Schmidt, and Saul Perlmutter were honored with the Nobel Prize in Physics "for the discovery of the accelerating expansion of the Universe through observations of distant supernovae" (The Royal Swedish Academy of Sciences[12]). Notably, the study of Yoshii and Peterson (1995) has been widely ignored by having only 41 citations (status as of 24th October 2023) according to the SAO/NASA Astrophysics Data System Abstract Service[16].

[15] According to https://elt.eso.org/about/timeline/ (webpage visited on 14.11.2023)

[16] https://ui.adsabs.harvard.edu/abs/1995ApJ...444...15Y/abstract (webpage visited on 24.10.2023)

2.7 Precision cosmology & cosmology at crossroads

The current era of cosmology is often described as being "precision cosmology", because several space missions have been launched over the last three decades to accurately measure the cosmological parameters of the ΛCDM model (e.g. Cosmic Background Explorer, Wilkinson Microwave Anisotropy Probe, Planck satellite, Extended ROentgen Survey with an Imaging Telescope Array). According to the latest analysis of the CMB by the Planck satellite (Planck Collaboration VI 2020a), the total matter makes up only $\approx 31\%$, while dark energy makes up $\approx 69\%$ of the overall energy budget of the Universe assuming the ΛCDM framework. Because the total constant of dark energy increases in the model - through the increasing volume and thus total vacuum energy - these fractions change with dark energy ultimately overwhelming the energy content. The ΛCDM model thus does not conserve energy and in fact leads to growth towards infinite energy content (Kroupa et al. 2010; Kroupa 2015).

Pioneering work towards cosmological simulations has been achieved by Sverre Johannes Aarseth (1934–) who developed gravitational N-body codes (e.g. Aarseth, Gott and E. L. Turner 1979; Aarseth and Fall 1980). But Sverre Aarseth quickly moved to star-cluster dynamics "[...] because the necessity of introducing dynamically relevant dark matter particles became too speculative in his view." (Kroupa 2012, footnote 2). In 2005, the famous ΛCDM N-body Millennium simulation was published which was then the largest simulation of structure formation ever performed (Springel et al. 2005). A historical overview of cosmological simulations up to 2012 can be found in Frenk and White (2012). In the following years, hydrodynamical ΛCDM simulations of galaxy formation and evolution such as the Feedback In Realistic Environments (FIRE; P. F. Hopkins et al. 2014; P. F. Hopkins et al. 2018; P. F. Hopkins et al. 2023), the Illustris (Vogelsberger et al. 2014a; D. Nelson et al. 2015), IllustrisTNG (Pillepich et al. 2018a; Pillepich et al. 2018b; Pillepich et al. 2019; D. Nelson et al. 2018; D. Nelson et al. 2019; D. Nelson et al. 2019; Marinacci et al. 2018; Naiman et al. 2018; Springel et al. 2018), EAGLE (Crain et al. 2015; Schaye et al. 2015; McAlpine et al. 2016), and most recently the MillenniumTNG (Hernández-Aguayo et al. 2023) projects have been published.

However, the improvements on both the observational and computational side also revealed more and more significant tensions faced by the ΛCDM paradigm (Kroupa et al. 2010; Kroupa, Pawlowski and Milgrom 2012; Kroupa 2012; Kroupa 2015; Di Valentino 2022; Perivolaropoulos and Skara 2022; Kroupa et al. 2023), which are reviewed in Section 3.3 and have been found also in the research projects underlying this thesis. Thus, cosmology is at a crossroads, or even in total crisis, as we will see in the next chapters. Constraining, testing, and eventually falsifying new cosmological and galaxy evolution models require upcoming observations of the local and very early Universe on small but also on large scales. Figure 2.13 shows a compilation of selected telescopes and space missions of the 21st century, which will explore not only the planets and moons of our own Solar systems but also exoplanets or the formation and evolution of galaxies. Consequently, the long history of astronomy and cosmology is still told just as the Greek philosopher Anaxagoras was once saying:

> *"The purpose of life is the investigation of the Sun, the Moon, and the heavens"*
> (Anaxagoras)

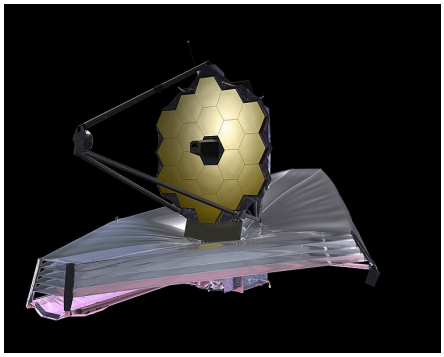

(a) JWST

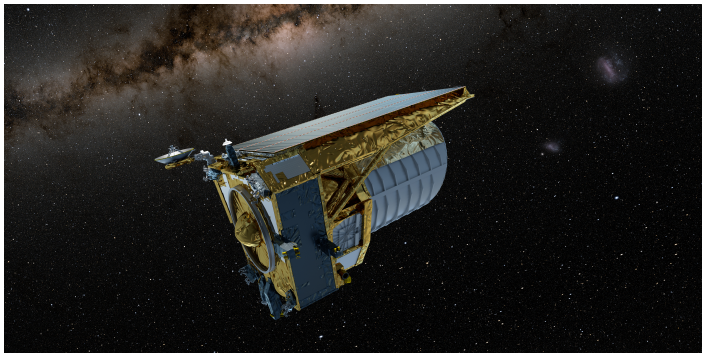

(b) Euclid

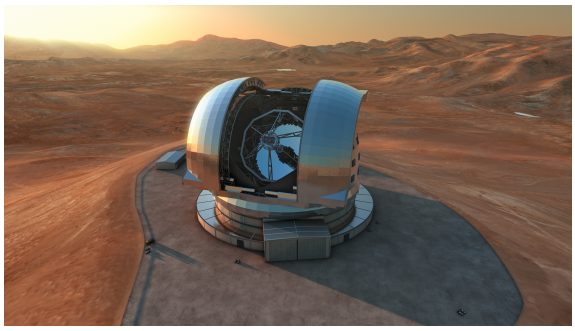

(c) ELT

(d) JUICE

Figure 2.13: Artistic images of selected telescopes and space missions of the 21st century. *Top left (a):* The James Webb Space Telescope (JWST), which is named after the former administrator of NASA James Edwin Webb (1906–1992), was launched in December 2021 and started its science programme in July 2022. Credit: NASA (downloaded from Wikipedia on 30.10.2023), Public domain. *Top right (b):* Euclid, which is named after the mathematician Euclid (fl. 300 BC), was launched in July 2023. Credit: ESA (downloaded from Wikipedia on 30.10.2023), CC BY-SA IGO 3.0. *Bottom left (c):* Rendering of the Extremely Large Telescope (ELT) operated by ESO and located at the Cerro Armazones (Chile). The first light of the ELT is expected for 2028[15]. The primary mirror with a diameter of 39.3 m would allow to study e.g. the formation of galaxies in the very early Universe. Credit: ESO/L. Calçada (downloaded from Wikipedia on 30.10.2023), CC BY 4.0. *Bottom right (d):* The Jupiter Icy Moons Explorer (JUICE) was launched in April 2023 and will explore the moons of the planet Jupiter. Credit: ESA (downloaded from Wikipedia on 30.10.2023), CC BY-SA IGO 3.0.

CHAPTER 3

The standard Λ-Cold Dark Matter model of cosmology

"Science progresses best when observations force us to alter our preconceptions."
(Statement by Vera Rubin as documented in Koupelis and K. Kuhn 2007)

The current standard model of cosmology, also known as the Lambda-Cold Dark Matter (ΛCDM) model, is based on Albert Einstein's theory of General Relativity (GR) and requires the assumptions of a cosmological constant (Λ) associated to dark energy and cold dark matter (CDM). While the existence of dark energy and CDM is up to the present time completely unknown, the ΛCDM framework is widely considered as a successful theory in describing the observed Universe (e.g. P. Schneider 2015) on small but especially on large scales (> 100 Mpc; e.g. Springel et al. 2018). However, over the last two decades more and more observations challenge the ΛCDM model on various cosmological scales (e.g. Kroupa et al. 2010; Kroupa 2012; Kroupa 2015; Di Valentino, Melchiorri and Silk 2020; Di Valentino 2022; Perivolaropoulos and Skara 2022; Kroupa et al. 2023) as investigated also inter alia in the research projects of this thesis.

In this chapter, I will first provide the theoretical background by introducing the Einstein field equations as well as the first and second Friedmann equations (see also e.g. Carroll 1997) and describing the cosmological parameters of the ΛCDM framework (Section 3.1). Secondly, I will give a brief overview of ΛCDM structure formation simulations such as the famous Millennium or the Illustris and EAGLE simulations (Section 3.2), which are assessed to test the ΛCDM model in the Chapters 7-9 and 10. Finally, I will end with an overview of challenges faced by the ΛCDM framework (Section 3.3).

3.1 Theoretical background

The fundamental assumption of the ΛCDM framework is the Cosmological Principle (CP) which states that the Universe is isotropic and homogeneous on cosmological scales. The ΛCDM model predicts to reach homogeneity on scales of $\gtrsim 260\,h^{-1}$ Mpc (e.g. Yadav, Bagla and Khandai 2010), where the dimensionless little h (see e.g. Croton 2013) is defined as $h = H_0/(100\,\mathrm{km\,s^{-1}\,Mpc^{-1}})$. The CP enables to define the Friedmann-Lemaître-Robertson-Walker (FLRW; Friedmann 1922; Lemaître

1927; Lemaître 1931; Robertson 1935; Walker 1937) metric as a description of the geometry of spacetime. The FLRW for a flat Universe in Cartesian coordinates is given by

$$ds^2 \;=\; -c^2dt^2 + a^2(t)\left[dx^2 + dy^2 + dz^2\right]\,, \tag{3.1}$$

where dt is the infinitesimal time coordinate, and dx, dy, and dz are the infinitesimal coordinate elements of the x, y, and z the co-moving components, respectively. c is the speed of light and $a(t)$ is the dimensionless scale-factor, which depends on the cosmic time, t, such that at present time, t_0, the scale factor becomes $a(t_0) = 1$ and $a \to 0$ for $t \to 0$. The physical (proper) distance is given by

$$\boldsymbol{r}(t) \;=\; a(t)\,\boldsymbol{x}\,. \tag{3.2}$$

where $\boldsymbol{x}$ is the co-moving coordinate. Taking the first order time derivation of the above equation yields the velocity

$$\boldsymbol{v}(t) \;=\; \dot{\boldsymbol{r}}(t) \;=\; \dot{a}(t)\,\boldsymbol{x} \;=\; \frac{\dot{a}(t)}{a(t)}\,\boldsymbol{r}(t)\,. \tag{3.3}$$

where the Hubble-Lematîre parameter is defined by $H(t) \equiv \frac{\dot{a}(t)}{a(t)}$. Thus, this is therewith just the famous Hubble-Lemaître law as already introduced by Equation 2.8 in Section 2.6,

$$\boldsymbol{v}(t) \;=\; H(t)\boldsymbol{r}(t)\,. \tag{3.4}$$

More generally, the FLRW metric in spherical coordinates is given by

$$ds^2 \;=\; -c^2dt^2 + a^2(t)\left[d\chi^2 + f_{\rm k}^2(\chi)\left(d\theta^2 + sin^2(\theta)d\phi^2\right)\right]\,, \tag{3.5}$$

where χ is the co-moving radial distance, θ and ϕ are the spherical angular coordinates, and $f_{\rm k}(\chi)$ is the co-moving angular distance depending on the spatial curvature of the Universe k via,

$$f_{\rm k}(\chi) \;=\; \begin{cases} k^{-1/2}\sin\left(\chi k^{1/2}\right) & k > 0\,, \\ \chi & k = 0\,, \\ |k|^{-1/2}\sinh\left(\chi|k|^{-1/2}\right) & k < 0\,, \end{cases} \tag{3.6}$$

where a positive curvature of $k > 0$ corresponds a closed Universe, while a negative curvature of $k < 0$ to an open Universe. A flat Universe refers to $k = 0$ with $f_{\rm k=0}(\chi) = \chi$.

3.1.1 Cosmological redshift

The expansion of the Universe lengthens the wavelength of an emitted photon of an astrophysical object which introduces cosmological redshifts. This effect can be derived from Equation 3.1 which reduces for a radially propagating photon to a null-geodesic of the form

$$ds^2 \;=\; 0 \;= -c^2dt^2 + a^2(t)d\chi^2\,. \tag{3.7}$$

An emitted light ray at time t_e and observed at time t_0 travels along the path χ such that

$$\int_{t_e}^{t_0} \frac{dt}{a(t)} = \frac{1}{c}\chi\,. \tag{3.8}$$

and similarly, a second light ray emitted at time $t_e + \Delta t_e$ and observed at time $t_0 + \Delta t_0$ travels along the same distance χ,

$$\int_{t_e+\Delta t_e}^{t_0+\Delta t_0} \frac{dt}{a(t)} = \frac{1}{c}\chi\,. \tag{3.9}$$

Combining the Equations 3.8 and 3.9 yields

$$\int_{t_e+\Delta t_e}^{t_0+\Delta t_0} \frac{dt}{a(t)} = \int_{t_e}^{t_0} \frac{dt}{a(t)} \tag{3.10}$$

$$\cancel{\int_{t_e}^{t_0} \frac{dt}{a(t)}} + \int_{t_0}^{t_0+\Delta t_0} \frac{dt}{a(t)} - \int_{t_e}^{t_e+\Delta t_e} \frac{dt}{a(t)} = \cancel{\int_{t_e}^{t_0} \frac{dt}{a(t)}}\,, \tag{3.11}$$

which reduces to

$$\int_{t_0}^{t_0+\Delta t_0} \frac{dt}{a(t)} = \int_{t_e}^{t_e+\Delta t_e} \frac{dt}{a(t)}\,. \tag{3.12}$$

$$\tag{3.13}$$

Solving these integrals by assuming that $a(t)$ is constant for small time variations Δt gives

$$\frac{1}{a(t)}\int_{t_0}^{t_0+\Delta t_0} dt = \frac{1}{a(t)}\int_{t_e}^{t_e+\Delta t_e} dt \tag{3.14}$$

$$\frac{\Delta t_0}{a(t_0)} = \frac{\Delta t_e}{a(t_e)}\,. \tag{3.15}$$

By plugging the definition of the wavelength $\lambda = c\Delta t$ in the above Equation 3.15 follows the relation between the wavelength and scale factor,

$$\frac{\lambda_0}{a(t_0)} = \frac{\lambda_e}{a(t_e)}\,, \tag{3.16}$$

which for $a(t_0) = 1$ yields

$$\lambda_0 = \frac{\lambda_e}{a(t_e)}\,. \tag{3.17}$$

Taking into account the redshift definition of Equation 2.7 shows that the scale factor and redshift are related via

$$a(t) = \frac{1}{1+z}\,, \tag{3.18}$$

such that $a(t_0) = 1$ and $z(t_0) = 0$ at present time $t = t_0$, and $a \to 0$ and $z \to \infty$ for $t \to 0$.

3.1.2 Friedmann equations and evolution of the cosmological density parameters

The Einstein Field Equations in tensor notation are given by

$$G_{\mu\nu} + \Lambda g_{\mu\nu} = \frac{8\pi G}{c^4} T_{\mu\nu}\,, \tag{3.19}$$

where $G_{\mu\nu}$ is the Einstein tensor, G is Newton's gravitational constant, c is the speed of light, Λ is the cosmological constant, $g_{\mu\nu}$ is the metric tensor, and $T_{\mu\nu}$ is the energy-momentum tensor. Assuming isotropy and homogeneity, the first and second Friedmann equations can be derived from the Einstein Field Equations,

$$1^{\text{st}} \text{ Friedmann equation:} \quad \left(\frac{\dot{a}(t)}{a(t)}\right)^2 = \frac{8\pi G\rho(t)}{3} - \frac{kc^2}{a^2(t)} + \frac{\Lambda c^2}{3}\,, \tag{3.20}$$

$$2^{\text{nd}} \text{ Friedmann equation:} \quad \frac{\ddot{a}(t)}{a(t)} = -\frac{4\pi G}{3}\left(\rho(t) + \frac{3P(t)}{c^2}\right) + \frac{\Lambda c^2}{3}\,, \tag{3.21}$$

where ρ is the matter density (without the dark energy density) and is the P pressure component. This set of equations describes the time evolution of the Universe. The critical density of a flat Universe (i.e. $k = 0$) is given by evaluating the first Friedmann equation by setting $\Lambda = 0$,

$$\rho_{\text{crit}}(a) \equiv \frac{3H^2(a)}{8\pi G}\,, \tag{3.22}$$

which yields for the present time a value of $\rho_{\text{crit},0} = 1.88 \times 10^{-26}\ h^2\ \text{kg m}^{-3}$ where h is again the dimensionless little defined as $h = H_0/(100\,\text{km s}^{-1}\,\text{Mpc}^{-1})$ (see e.g. Croton 2013). The total mass-energy density (without the curvature density parameter) of the Universe is given by

$$\rho_{\text{tot}}(a) = \underbrace{\rho_{\text{b}}(a) + \rho_{\text{CDM}}(a)}_{\rho_{\text{m}}(a)} + \rho_{\text{rad}}(a) + \rho_{\Lambda}(a) \tag{3.23}$$

where ρ_{b} and ρ_{CDM} are the baryonic and cold dark matter densities, respectively, such that ρ_{m} is the total matter density. ρ_{rad} is the radiation density and ρ_{Λ} is the dark energy density. For practical reasons, the density parameters of the Universe are typically scaled by ρ_{crit},

$$\Omega(a) \equiv \frac{\rho(a)}{\rho_{\text{crit}}(a)} = \frac{8\pi G}{3H^2(a)}\rho(a)\,, \tag{3.24}$$

which yields

$$\Omega_{\rm tot} \equiv \frac{\rho_{\rm tot}(a)}{\rho_{\rm crit}(a)} = \underbrace{\Omega_{\rm b}(a) + \Omega_{\rm CDM}(a)}_{\Omega_{\rm m}(a)} + \Omega_{\rm rad}(a) + \Omega_{\Lambda}(a)\,. \tag{3.25}$$

Consequently, the first Friedmann equation can be re-written in the form of

$$1 = \Omega_{\rm m}(a) + \Omega_{\rm rad}(a) + \Omega_{\Lambda}(a) + \Omega_{\rm k}(a)\,, \tag{3.26}$$

where $\Omega_{\rm k}(a)$ is the curvature density parameter being defined as

$$\Omega_{\rm k}(a) \equiv -\frac{kc^2}{a^2H^2(a)} = \left(\frac{H_0}{H(a)}\right)^2 \Omega_{\rm k,0}a^{-2}\,, \tag{3.27}$$

and the dark energy density being

$$\Omega_{\Lambda}(a) \equiv -\frac{\Lambda c^2}{3H^2(a)} = \left(\frac{H_0}{H(a)}\right)^2 \Omega_{\Lambda,0}\,. \tag{3.28}$$

In order to derive the time evolution of the density parameters, we start with the equation of state (EoS) of a perfect fluid,

$$P = \omega\rho c^2\,, \tag{3.29}$$

where P is the pressure and ω is a dimensionless number. Plugging the EoS in the second Friedmann equation and assuming that ω is a constant it can be shown that the time evolution of ρ has the form of

$$\rho(a) = \rho_0 a^{-3(\omega+1)} \tag{3.30}$$

where ρ_0 present day value of density. In particular, the matter density of the Universe scales with $\rho_{\rm m} \propto a^{-3}$ because both the baryonic and cold dark matter are pressureless implying $\omega_{\rm m} = 0$. The radiation density scales with $\rho_{\rm m} \propto a^{-4}$ as $\omega_{\rm rad} = 1/3$, and the dark energy density is constant over time because recent observations suggest $\omega_{\Lambda} = -1$ (see for a review on the quintessence in Tsujikawa 2013). Thus, the density parameters evolves according to

$$\rho_{\rm m}(a) = \rho_{\rm m,0}a^{-3}\,, \tag{3.31}$$

$$\rho_{\rm rad}(a) = \rho_{\rm rad,0}a^{-4}\,, \tag{3.32}$$

$$\rho_{\Lambda}(a) = \rho_{\Lambda,0}\,, \tag{3.33}$$

and

$$\Omega_{\rm m}(a) = \left(\frac{H_0}{H(a)}\right)^2 \Omega_{\rm m,0}a^{-3}\,, \tag{3.34}$$

$$\Omega_{\rm rad}(a) = \left(\frac{H_0}{H(a)}\right)^2 \Omega_{\rm rad,0}a^{-4}\,, \tag{3.35}$$

$$\Omega_{\Lambda}(a) = \left(\frac{H_0}{H(a)}\right)^2 \Omega_{\Lambda,0}\,, \tag{3.36}$$

which allows to formulate the first Friedmann equation as

$$H^2(a) \equiv \left(\frac{\dot{a}}{a}\right)^2 = H_0^2 \left[\Omega_{\mathrm{rad},0} a^{-4} + \Omega_{\mathrm{m},0} a^{-3} + \Omega_{\mathrm{k},0} a^{-2} + \Omega_{\Lambda,0}\right]. \tag{3.37}$$

The cosmic age of the Universe can be derived by using the definition of the Hubble parameter

$$H \equiv \frac{\dot{a}}{a} = \frac{da}{dt}\frac{1}{a}, \tag{3.38}$$

which rewrites to

$$dt = \frac{da}{aH}. \tag{3.39}$$

Plugging Equation 3.37 and integrating from the time of the Big Bang ($a = 0$) up to the present time ($a(t_0) = 1$) yields the cosmic age of the Universe

$$t_{\mathrm{age}} = \frac{1}{H_0} \int_0^1 \frac{da}{a\sqrt{\Omega_{\mathrm{rad},0} a^{-4} + \Omega_{\mathrm{m},0} a^{-3} + \Omega_{\mathrm{k},0} a^{-2} + \Omega_{\Lambda,0}}}. \tag{3.40}$$

being $t_{\mathrm{age}} \approx 13.8$ Gyr for the above cosmological parameters (Planck Collaboration XIII 2016). Thus, studying the age of the oldest astronomical objects functions as a test of the underlying cosmological paradigm. Recently, Ying et al. (2023) measured an age of the star cluster M92 of 13.80 ± 0.75 Gyr (see also figure 1 and table 1 of Cimatti and Moresco 2023) leaving the possibility that the Universe is older than predicted by the ΛCDM model (Kroupa et al. 2023, and also Chapter 9).

Figure 3.1 shows the time evolution of the cosmological density parameters within the ΛCDM framework assuming $H_0 = 67.74\,\mathrm{km\,s^{-1}\,Mpc^{-1}}$, $\Omega_{\mathrm{m},0} = 0.3089$, $\Omega_{\mathrm{b},0} = 0.049$, $\Omega_{\mathrm{rad},0} = 9.16 \times 10^{-5}$, and $\Omega_{\Lambda,0} = 0.6911$, (Planck Collaboration XIII 2016). According to this parameterization, the total matter-radiation equality occurs at

$$\Omega_{\mathrm{m},0}(1+z)^3 \stackrel{!}{=} \Omega_{\mathrm{rad},0}(1+z)^4 \tag{3.41}$$

$$\Longleftrightarrow z_{\mathrm{eq}} = \frac{\Omega_{\mathrm{m},0}}{\Omega_{\mathrm{rad},0}} - 1 \approx 3371, \tag{3.42}$$

while the total matter-dark energy equality occurs much later at

$$\Omega_{\mathrm{m},0}(1+z)^3 \stackrel{!}{=} \Omega_{\Lambda,0} \tag{3.43}$$

$$\Longleftrightarrow z_{\mathrm{eq}} = \left(\frac{\Omega_{\Lambda,0}}{\Omega_{\mathrm{m},0}}\right)^{1/3} - 1 \approx 0.31. \tag{3.44}$$

Thus, the Universe was radiation-dominated at redshifts of $z \gtrsim 3400$, matter-dominated in redshift range of $3400 \gtrsim z > 0.31$, and is dark energy-dominated since $z < 0.31$. Equation 3.37 reduces for

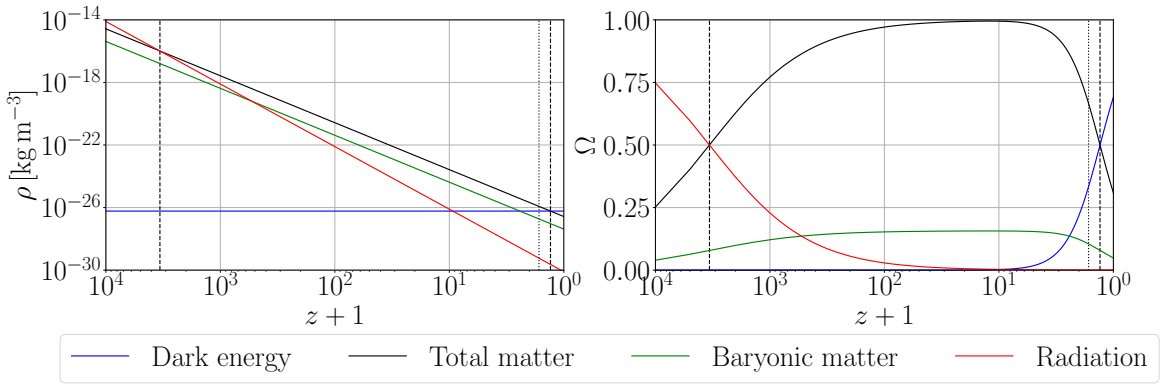

Figure 3.1: Cosmic evolution of the density parameters of the total matter (black), baryonic matter (green), radiation (red), and dark energy (blue) within the ΛCDM framework assuming a standard ΛCDM cosmology with $H_0 = 67.74\,\mathrm{km\,s^{-1}\,Mpc^{-1}}$, $\Omega_{\mathrm{m},0} = 0.3089$, $\Omega_{\mathrm{b},0} = 0.049$, $\Omega_{\mathrm{rad},0} = 9.16 \times 10^{-5}$, and $\Omega_{\Lambda,0} = 0.6911$, respectively (Planck Collaboration XIII 2016). The *left* panel shows the density parameters in the International System of Units (SI), while the *right* panel shows the density parameters scaled by the critical density ρ_{crit} (Equation 3.22). The Universe was radiation dominates at $z \gtrsim 3400$ (Equation 3.42), dark matter-dominated between $3400 \gtrsim z \geq 0.31$, and became dark energy-dominated at $z \leq 0.31$ (Equation 3.44) as highlighted by the vertical dashed lines. The vertical dotted line marks the redshift $z = 0.65$ (Equation 3.47) when the Universe started to accelerate. Credit: figure made by the author of this thesis.

$\Omega_{\mathrm{rad},0} \ll 1$ to

$$H(a) = H_0\sqrt{\Omega_{\mathrm{m},0}a^{-3} + \Omega_{\Lambda,0}}\,. \tag{3.45}$$

Setting the second derivative of the above equation to zero yields,

$$\ddot{a} = \frac{H_0}{2}\frac{2\Omega_{\Lambda,0}a - \Omega_{\mathrm{m},0}a^{-2}}{\sqrt{\Omega_{\mathrm{m},0}a^{-1} + \Omega_{\Lambda,0}a^{2}}} \stackrel{!}{=} 0\,, \tag{3.46}$$

$$\Longleftrightarrow z_{\mathrm{acc}} = \left(\frac{\Omega_{\mathrm{m}}}{2\Omega_{\Lambda}}\right)^{-1/3} - 1 \approx 0.65\,. \tag{3.47}$$

which corresponds to the time when the expansion of the Universe starts to accelerate.

3.2 Cosmological ΛCDM simulations

Testing but also further developing cosmological and galaxy formation and evolution theories require self-consistent simulations for comparisons with observations. In the following three sections, I will briefly summarize the numerical and cosmological parameters of the Millennium, Illustris, IllustrisTNG, and EAGLE simulations, which are assessed for testing the ΛCDM framework. Detailed descriptions of these simulations can be also found in the method sections of the published peer-review papers attached in the Appendices A-C and in the manuscript included in Chapter 10.

3.2.1 Millennium simulation

The Millennium simulation (MS; Springel et al. 2005) is an N-body ΛCDM simulation which evolves the dark matter particles with a resolved mass of $m_{\rm dm} = 1.2 \times 10^8\,M_\odot$ from redshift $z = 127$ up to present time within a cubic simulation box with a co-moving length of 685 cMpc per side. Therewith, the MS was the largest N-body simulation conducted at this time. The MS assumes a ΛCDM cosmology with the cosmological parameters being $H_0 = 73\,{\rm km\,s^{-1}\,Mpc^{-1}}$, $\Omega_{\rm m,0} = 0.25$, $\Omega_{\rm b,0} = 0.045$, $\Omega_{\Lambda,0} = 0.75$, a spectral index of $n_{\rm s} = 1$, and $\sigma_8 = 0.9$ (WMAP-1; Spergel et al. 2003). As the simulation only evolves the dark matter component, semi-anaylcial models of galxy formation have to be applied in the post-processing step in order to model the baryonic physics (e.g Croton et al. 2006; De Lucia et al. 2006; Guo et al. 2011; Croton et al. 2016; Raouf et al. 2017).

The successors of the MS are the Millennium II-simulation (MS-II; Boylan-Kolchin, Springel, White, Jenkins and Lemson 2009), which has a much higher particle resolution of $m_{\rm dm} = 6.9 \times 10^6\,h^{-1}\,M_\odot$ but a smaller box size of $100\,h^{-1}$cMpc per cubic side, and the Millennium-XXL (MXXL; Angulo et al. 2012) simulation with a lower particle resolution of $m_{\rm dm} = 8.456 \times 10^9\,M_\odot$ but with a box size of 4.1 cGpc per cubic side. The MXXL simulation has been analyzed in Chapter 7 and Appendix A.

3.2.2 Illustris project and Illustris The Next Generation project

The Illustris[1] project (Vogelsberger et al. 2014b; D. Nelson et al. 2015) includes a set of hydrodynamical simulations with different box sizes and resolution realizations conducted in the ΛCDM framework with the cosmological parameters being $H_0 = 70.4\,{\rm km\,s^{-1}\,Mpc^{-1}}$, $\Omega_{\rm b,0} = 0.0456$, $\Omega_{\rm m,0} = 0.2726$, $\Omega_{\Lambda,0} = 0.7274$, $\sigma_8 = 0.809$, and $n_{\rm s} = 0.963$ (WMAP-9; Hinshaw et al. 2013). Starting from redshift $z = 127$, the Illustris simulations self-consistently evolves the stellar particles, gas cells, black holes, and dark matter particles up to $z = 0$. The flagship of the Illustris project is the Illustris-1 simulation run which has a co-moving box length of $L = 106.5$ cMpc per cubic side and has a dark matter particle mass of $m_{\rm dm} = 6.3 \times 10^6\,M_\odot$ and an initial baryonic mass resolution $m_{\rm b} = 1.3 \times 10^6\,M_\odot$ but the Illustris project also includes low-resolution simulations, which allow to study numerical effects. The subhalo/halo catalogues and particle data are publicly available and can be downloaded from their website[2].

The Illustris The Next Generation[3] (IllustrisTNG or just TNG; Pillepich et al. 2018a; Pillepich et al. 2018b; Pillepich et al. 2019; D. Nelson et al. 2018; D. Nelson et al. 2019; D. Nelson et al. 2019; Marinacci et al. 2018; Naiman et al. 2018; Springel et al. 2018) advances the original Illustris project (Vogelsberger et al. 2014b; D. Nelson et al. 2015) by implementing e.g. magnetohdydrodynamical and improved baryonic feedback descriptions. IllustrisTNG adopts a ΛCDM cosmology with $H_0 = 67.74\,{\rm km\,s^{-1}\,Mpc^{-1}}$, $\Omega_{\rm b,0} = 0.0486$, $\Omega_{\rm m,0} = 0.3089$, $\Omega_{\Lambda,0} = 0.6911$, $\sigma_8 = 0.8159$, and $n_{\rm s} = 0.9667$ (Planck-2015; Planck Collaboration XIII 2016). The flagships are the TNG50-1, TNG100-1, and TNG300-1 runs as illustrated in Figure 3.2, which have a box size of 51.7 cMpc, 110.7 cMpc, and 302.6 cMpc per cubic side, respectively. The TNG50-1 is the highest resolution realization with a baryonic element mass of $m_{\rm b} = 8.5 \times 10^4\,M_\odot$ and a dark matter particle mass of $m_{\rm dm} = 4.5 \times 10^5\,M_\odot$, TNG100-1 has $m_{\rm b} = 1.4 \times 10^6\,M_\odot$ and $m_{\rm dm} = 7.5 \times 10^6\,M_\odot$, and TNG300-1 has the lowest resolution with $m_{\rm b} = 1.1 \times 10^7\,M_\odot$ and $m_{\rm dm} = 5.9 \times 10^7\,M_\odot$ among these runs. As in

[1] Website of the Illustris project: https://www.illustris-project.org/

[2] Link to the database of the Illustris project: https://www.illustris-project.org/data/

[3] Website of the IllustrisTNG project: https://www.tng-project.org/

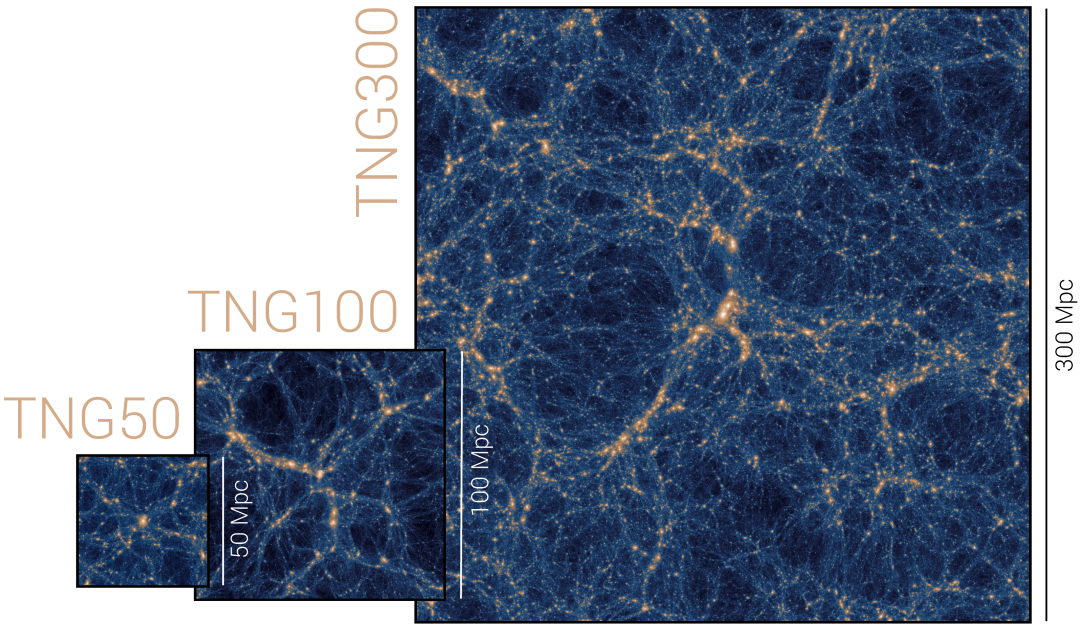

Figure 3.2: The Illustris The Next Generation (IllustrisTNG or TNG) project consists of different simulation runs with different resolution realizations and box sizes. The TNG50, TNG100, and TNG100 runs have 51.7 cMpc, 110.7 cMpc, and 302.6 cMpc per cubic side, respectively (see text). The images show the projected density contrast (the brighter the higher the density contrast) revealing the cosmic web in the simulations. The most massive galaxy clusters form in the knots of the cosmic web. Credit: TNG Collaboration (downloaded from the website of the IllustrisTNG project https://www.tng-project.org/media/ on 10.11.2023).

the case for the Illustris simulations, we also use the lower resolution realizations of the TNG50 and TNG100, TNG300 runs in order to study resolution effects. The data of the IllustrisTNG simulations are publicly available[4].

The simulation runs of the Illustris and IllustrisTNG projects have been assessed in the Chapter 8, while the Chapters 9 and 10 focus on the IllustrisTNG simulations.

3.2.3 EAGLE project

Similar to the Illustris and IllustrisTNG projects, The Evolution and Assembly of GaLaxies and their Environments (EAGLE; Crain et al. 2015; Schaye et al. 2015; McAlpine et al. 2016; The EAGLE team 2017) project[5] is a set of hydrodynamical simulations conducted in the ΛCDM framework. While the Illustris and IllustrisTNG simulations are based on the moving-mesh code AREPO (Springel 2010), the EAGLE simulations run on a modified version of the smoothed particle hydrodynamic (SPH) code GADGET (Springel 2005). Furthermore, the projects assume different baryonic and stellar feedback descriptions. These differences in their computations and physics descriptions allows for a better comparison with observations.

The cosmological parameters of the EAGLE simulations are $H_0 = 67.77\,\mathrm{km\,s^{-1}\,Mpc^{-1}}$, $\Omega_{\mathrm{b},0} =$

[4]Link to the database of the IllustrisTNG project: https://www.tng-project.org/data/

[5]Website of the EAGLE project: https://icc.dur.ac.uk/Eagle/

0.04825, $\Omega_{\mathrm{m},0} = 0.307$, $\Omega_{\Lambda,0} = 0.693$, $\sigma_8 = 0.8288$, and $n_\mathrm{s} = 0.9611$ (Planck-2013 Planck Collaboration et al. 2014). The research projects of this thesis assess the simulation runs labeled Ref-L0050N0752, Ref-L0100N1504, Ref-L0025N0752, and Recal-L0025N0752. The former simulations Ref-L0050N0752 and Ref-L0100N1504 have a box length of 50 cMpc and 100 cMpc per cubic side, respectively, and an initial baryonic particle mass of $m_\mathrm{b} = 1.81 \times 10^6\,M_\odot$ and a dark matter particle mass of $m_\mathrm{dm} = 9.70 \times 10^6\,M_\odot$ (table 2 of Schaye et al. 2015). The simulation runs Ref-L0025N0752, and Recal-L0025N0752 have a smaller box size of 25 cMpc but with $m_\mathrm{b} = 2.26 \times 10^5\,M_\odot$ and $m_\mathrm{dm} = 1.21 \times 10^6\,M_\odot$ a higher particle resolution compared to the other two runs. The Recal-L0025N0752 run uses a different sub-grid parameters in order to match the locally observed galaxy mass function (Schaye et al. 2015; McAlpine et al. 2016; Ploeckinger et al. 2018), which cannot be properly described by Ref-L0025N0752 as it predicts too many galaxies at around stellar masses of $10^9\,M_\odot$. The halo and galaxy (subhalo) catalogues and particle data of the EAGLE project are publicly available[6] and are described in full detail in McAlpine et al. (2016) and The EAGLE team (2017), respectively.

The EAGLE simulations have been analyzed in the Chapters 8 and 9.

3.3 Challenges of the ΛCDM model

The ΛCDM model of cosmology is widely considered as a successful description of the observed Universe, but several weaknesses and challenges have been reported over the last three decades. A weak spot of the theory is the lack of predictive power especially on galactic scales in contrast to Milgromian dynamics (Chapter 4) which is less sensitive to the underlying baryonic and stellar feedback prescription (Nagesh et al. 2023). For example, the ΛCDM model cannot predict the rotation curves of spiral galaxies from the observed matter distribution, although these galaxies make up the majority of observed galaxy types with stellar masses of $M_* \gtrsim 10^{10}\,M_\odot$ (Delgado-Serrano et al. 2010; see also Section 3.3.6 and Chapter 8). This problematic aspect is evident from Figure 3.3 by showing the present-day stellar-to-halo mass ($M_* - M_{200}$) relation[7] for haloes with a central subhalo with $M_* > 10^8\,M_\odot$ in the IllustrisTNG and EAGLE runs. Taking e.g. a Milky Way-like galaxy with $M_* \approx 6 \times 10^{10}\,M_\odot$ (Licquia and Newman 2015), the relation gives a halo mass in the range of $10^{11} \lesssim M_{200}/M_\odot \lesssim 10^{12}$ covering about one order of magnitude and making it therewith impossible to accurately predict its gravitational potential. Note that the scatter of the $M_* - M_{200}$ relation is smaller in TNG50-1 because of the smaller box size (Section 3.2.2). In addition, the dark matter concentration of haloes significantly differs for galaxies with the same halo mass (see e.g. figure 7 of Beltz-Mohrmann and Berlind 2021 for the Illustris, IllustrisTNG, and EAGLE simulation). This is because every galaxy has a different merger history in the hierarchical galaxy evolution model. Thus, it is not possible to predict the rotation curve of any galaxy from their mass distribution assuming the ΛCDM framework. However, the observed matter distribution is closely linked with the rotation curve which is nowadays known as Renzo's[8] rule (Sancisi 2004; Famaey and McGaugh 2012):

[6] Link to the database of the EAGLE project: https://icc.dur.ac.uk/Eagle/database.php

[7] M_{200} is the total halo mass within a sphere with a mean density which is $200 \times \rho_\mathrm{crit}$.

[8] Named after the astrophysicist Renzo Sancisi (Sancisi 2004).

"In the inner parts of spiral galaxies, of high or low surface brightness, there is a close correlation between rotation curve shape and light distribution. For any feature in the luminosity profile there is a corresponding feature in the rotation curve and vice versa. This implies that the gravitational potential is strongly correlated with the distribution of luminosity: either the luminous mass dominates or there is a close coupling between luminous and dark matter. In a similar way, the declining rotation curves observed in the outer parts of high luminosity systems are a clear signature of the stellar disk which either dominates or traces the distribution of mass." (Sancisi 2004)

Other examples which show up the weaknesses of the ΛCDM framework are the functional form and scatter of the observed radial acceleration relation (RAR; e.g. McGaugh, Lelli and Schombert 2016; Lelli et al. 2019) and baryonic Tully-Fisher relation (BTFR; e.g. Tully and Fisher 1977; McGaugh et al. 2000; Lelli et al. 2019) of late type galaxies being introduced in more detail in the upcoming Chapter 4. The RAR describes a tight relation between the observed centripetal acceleration and the centripetal acceleration derived from the observed baryons, while the BTFR is a consequence of the RAR showing a tight correlation between the flat part of the rotation curve and the baryonic mass of the galaxy. Such tight relations are difficult to reproduce in stochastic hierarchical merging models of galaxy formation and evolution and require a fine-tuning of the baryonic feedback processes (Lelli et al. 2017; Ludlow et al. 2017; Keller and Wadsley 2017; Tenneti et al. 2018).

While these aspects are *formally not falsifying* the ΛCDM paradigm as such it shows the weakness of this theory as it loses its predictive power due to the dark matter matter haloes and required fine-tuning of baryonic physics. The following sections briefly discuss some of the most prominent challenges of the ΛCDM model but much more detailed reviews can be found e.g. in Kroupa et al. (2010), Kroupa (2012), Kroupa, Pawlowski and Milgrom (2012), Famaey and McGaugh (2013), Kroupa (2015), Di Valentino (2022), Perivolaropoulos and Skara (2022), or Kroupa et al. (2023). The tensions of the ΛCDM framework identified in this thesis are summarized in the Chapters 7-11.

3.3.1 Dynamical friction

In the ΛCDM framework, primordial galaxies are embedded in extended cold dark matter haloes (see also Figure 3.3). If for example a satellite galaxy interacts with a primordial galaxy such that their CDM haloes overlap, the satellite experiences a gravitational drag by the loss of momentum and kinetic energy redistribution due to encounters with CDM particles. The resulting Chandrasekhar dynamical friction (Chandrasekhar 1942; Chandrasekhar 1943a; Chandrasekhar 1943b; Chandrasekhar 1943c) on a satellite galaxy with mass M and velocity $\boldsymbol{v}$ is given by (see e.g. section 8.1 in Binney and Tremaine 2008)

$$\frac{d\boldsymbol{v}}{dt} = -\frac{4\pi G^2 M \rho \boldsymbol{v}}{v^3} \ln(\Lambda) \left[\mathrm{erf}(x) - \frac{2x}{\sqrt{\pi}} \exp\left(-x^2\right) \right], \tag{3.48}$$

where ρ is the background mass density, erf(x) is the error function, $x \equiv v/\left(\sqrt{2}\sigma\right)$, the CDM particles have a Maxwellian velocity distribution with an one-dimensional dispersion σ, G is the gravitational constant, $\ln(\Lambda)$ is the Coulomb logarithm, and v is the absolute value of the velocity vector, $\boldsymbol{v}$, of the satellite galaxy.

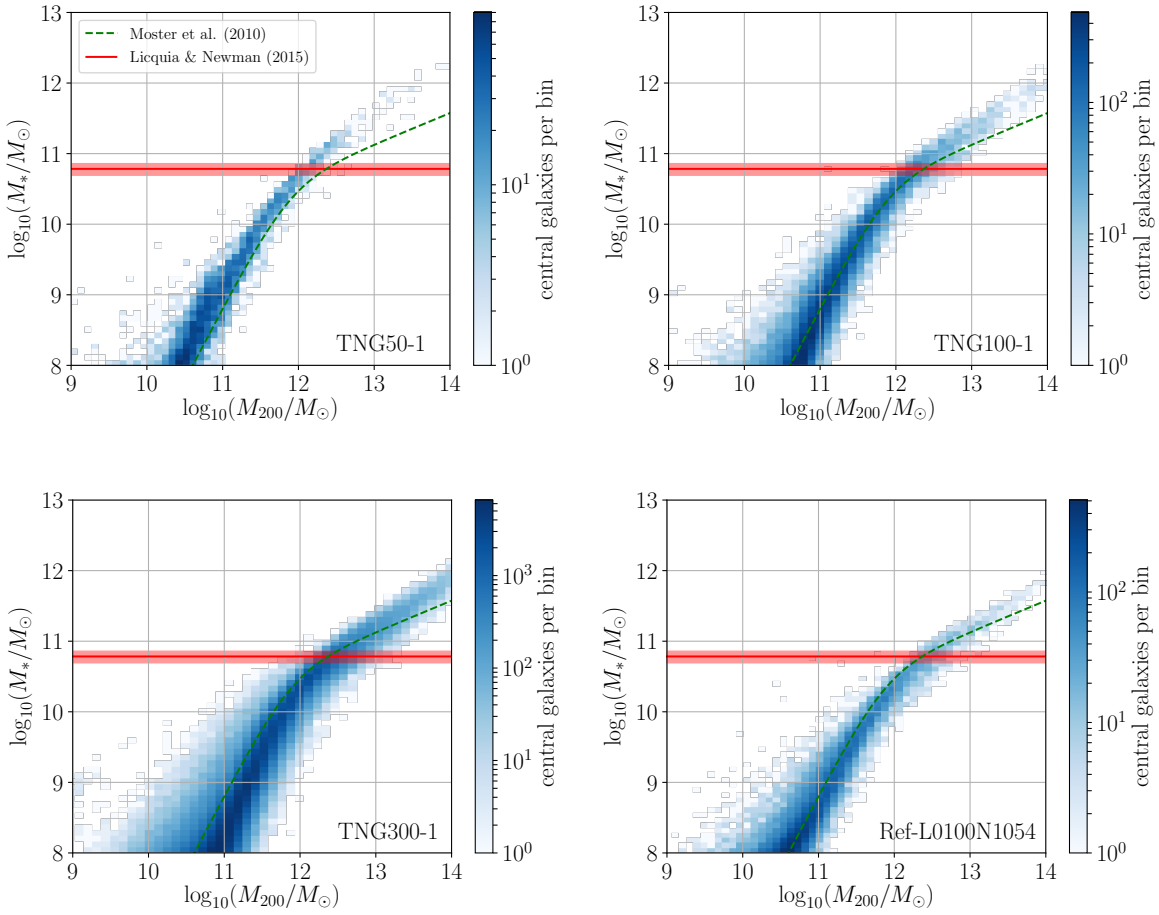

Figure 3.3: The stellar-to-halo mass ($M_* - M_{200}$) relation for haloes with a central subhalo with $M_* > 10^8\,M_\odot$ at redshift $z = 0$ in the flagship runs TNG50-1 (top left), TNG100-1 (top right), TNG300-1 (bottom left), and EAGLE Ref-L0100N1054 (bottom right). The red horizontal solid line marks the MW with a stellar mass of $M_* = (6.08 \pm 1.14) \times 10^{10}\,M_\odot$ (Licquia and Newman 2015) and the red shaded area highlights the corresponding uncertainty. Note that the relation provides a wide range of different M_{200} values for a given value of M_* (see text). The green dashed line refers to equation 2 of Moster et al. (2010). Credit: figure made by the author of this thesis using the IllustrisTNG and EAGE subhalo and halo catalogues (see the Sections 3.2.2-3.2.3).

The lack of dynamical friction on galactic scales has been also reported by other studies (e.g. Angus, Diaferio and Kroupa 2011; Kroupa 2015; Oehm, Thies and Kroupa 2017; Haslbauer et al. 2022; Roshan et al. 2021). For example, Angus, Diaferio and Kroupa (2011) showed that the observed proper motions of the dwarf satellite galaxies Fornax, Sculptor, Ursa Minor, and Carina are not providing viable orbital solutions being consistent with the disk of satellites (DoS; Section 3.3.7) if accounting for dynamical friction.

Oehm, Thies and Kroupa (2017) analyzed the M81 group which consists of the three host member galaxies M81, M82, and NGC 3077. By performing semi-analytical Newtonian models these authors showed that the three galaxies should have merged within a short time scale implying that the galaxies have fallen together from large distances at roughly the same time. Similar conclusions for the case of the spatial and dynamical configuration of the Milky Way-Magellanic Clouds system have been reached in Chapter 10. The observed higher fraction of thin disk galaxies compared to the galaxy population formed in the Illustris, IllustrisTNG, and EAGLE simulations also suggest a smaller merger rate due to the lack of dynamical friction as discussed in Chapter 8 based on Haslbauer et al. (2022).

On kpc scales, Roshan et al. (2021) showed that the bar pattern speed of barred galaxies in the IllustrisTNG and EAGLE simulations slows down due to angular momentum exchange with the cold dark matter particles of the halo conflicting with the observations.

3.3.2 Core-cusp problem

The core-cusp problem is one of the earliest identified challenges faced by cold dark matter models (Dubinski and Carlberg 1991) and emerged when the radial dark matter density profiles of galaxies formed in N-body simulations have been compared with the total matter density profiles derived from the rotation curve of observed galaxies. The dark matter density of simulated galaxies increases with decreasing radial distance forming a "cusp"-like structure but rotation curves of observed galaxies imply a much flatter distribution towards smaller radii representing a "core"-like structure (Dubinski and Carlberg 1991; Flores and Primack 1994; Moore 1994; Gentile et al. 2004).

3.3.3 Missing galaxy problem

Cosmological ΛCDM simulations of structure formation predict a much higher number of (dark matter-dominated) satellite galaxies around their host galaxies than observed (Klypin et al. 1999; Moore et al. 1999; A. Kravtsov 2010). In particular, the Milky Way galaxy host 11 "classical" satellite galaxies (McConnachie 2012) but a Milky Way-like halo should have about 500 satellites (Moore et al. 1999).

3.3.4 Too big to fail problem

The too big to fail problem was identified by Kroupa et al. (2010) and emphasized by Boylan-Kolchin, Besla and Hernquist (2011). The labeling "too big to fail" stems from the American financial market (e.g. Nurisso and Prescott 2017) and refers in astrophysics to the problematic aspect that galaxies formed in the ΛCDM simulations are so massive (or in other words "too big") that they cannot have failed to form observable stars (Bullock and Boylan-Kolchin 2017). However, the observed dwarf galaxies around the Milky Way are not as massive as predicted by the ΛCDM models.

It has been argued that the core-cusp, missing galaxy, and too big to fail can be resolved but this requires a fine-tuning of the baryonic physics (Tomozeiu, Mayer and Quinn 2016).

3.3.5 Downsizing

Downsizing means that observed low mass elliptical galaxies have systematically younger stellar populations by forming over a longer time-span than massive elliptical galaxies conflicting with the hierarchical models of galaxy formation according to which the stellar mass build time scale increases with the mass of the galaxies due to galactic minor and major mergers (e.g. Cowie et al. 1996; Bellstedt et al. 2020).

3.3.6 Angular momentum problem

A long-standing problem of the formation and evolution of galaxies is that (late-type) galaxies simulated in cold dark matter-based simulations suffer from a significant loss of angular momentum over time (e.g. Navarro and Benz 1991; Piontek and Steinmetz 2011; Scannapieco et al. 2012). This problem is directly linked with the morphology of galaxies because a loss of angular momentum thickens the galactic disk such that simulated galaxies appear thicker and too compact compared to observed galaxies (Kroupa 2012).

It has been argued that the angular momentum problem has been resolved in the Illustris-1 simulation due to improved numerical resolutions and baryonic feedback descriptions (Vogelsberger et al. 2014a). Although the simulation indeed produces a mix of different galaxy types as shown in Figure 3.4, my collaborators and I demonstrated in Haslbauer et al. (2022) that not only Illustris-1, but also the runs of the IllustrisTNG and the EAGLE project still fail in reporducing the correct shapes of observed galaxies (Chapter 8 and Appendix B). The fact that the majority of observed galaxies with $M_* > 10^{10}\,M_\odot$ are late-types (Delgado-Serrano et al. 2010), while these simulations overproduce much rounder galaxies resembling more early-types, this problem also suggests that mergers in nature are much less efficient than in the hierarchical ΛCDM galaxy formation model (Section 3.3.1).

3.3.7 Disk of satellites

The spatial and kinematical arrangement of the satellites of the Milky Way galaxy is one of the most prominent and greatest problem of the ΛCDM paradigm (Kroupa, Theis and Boily 2005 and see also e.g. Pawlowski 2021b, Pawlowski 2021a, and Müller 2023 for recent reviews). As discussed in the Sections 3.3.3 and 3.3.8, primordial dwarf galaxies are spherically distributed around the host galaxy in the ΛCDM model. However, the 11 "classical" satellites found out to distances of ≈ 250 kpc (i.e. Sagittarius, LMC, SMC, Draco, Ursa Minor, Sculptor, Sextans, Carina, Fornax, Leo II, and Leo I) are arranged in a thin plane with a root-mean-square height of only 19.6 kpc (Pawlowski 2021b) being perpendicular to the galactic plane of the MW. Moreover, 8 of these "classical satellites" show a kinematic coherence by having aligned orbital poles (Pawlowski 2021b).

Kroupa, Theis and Boily (2005) quantified that "[...] the observed distribution of Milky Way (MW) satellites is inconsistent with their being drawn from a cosmological sub-structure population with a confidence of 99.5 per cent" which corresponds to an equivalent number of standard deviations of 2.81σ for a single Gaussian variable. They further concluded that "[m]ost of the MW satellites therefore cannot be related to dark-matter dominated satellites." (see the abstract of Kroupa, Theis

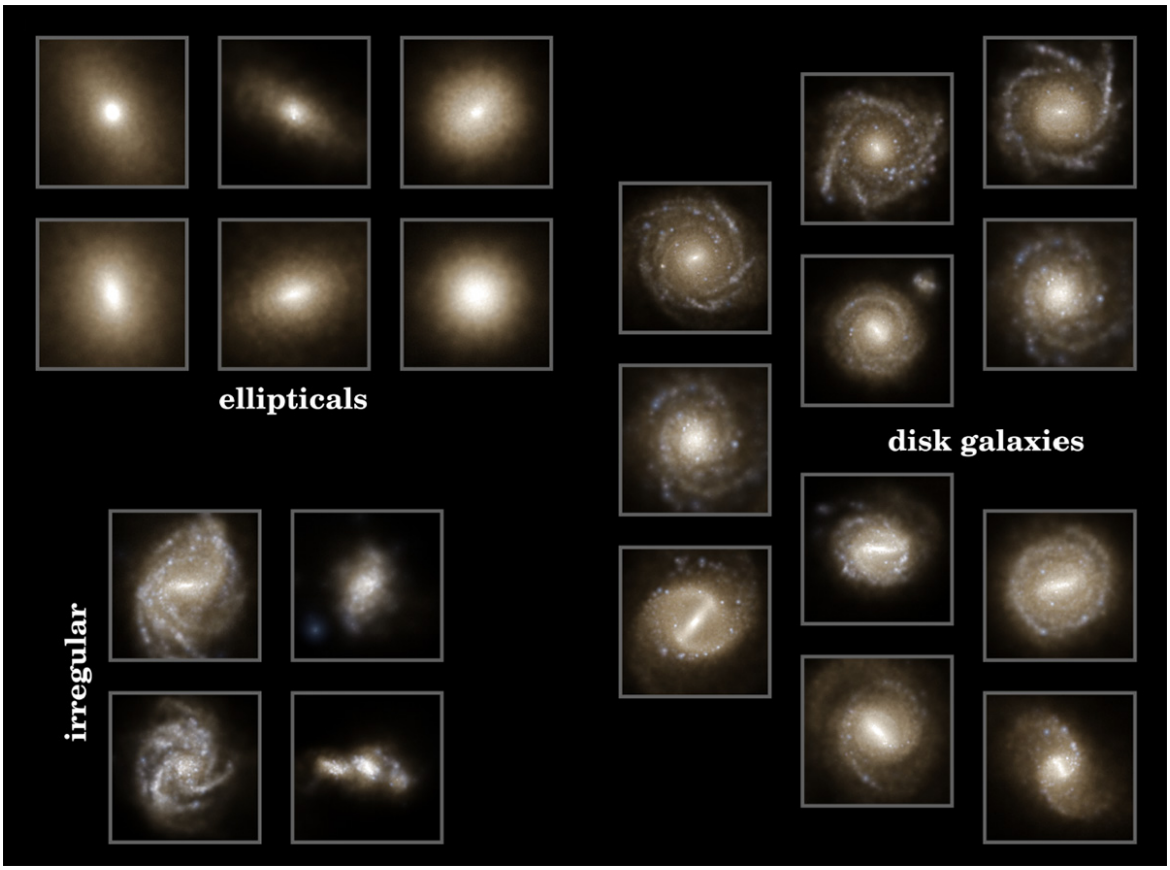

Figure 3.4: Hubble diagram (see also Section 2.5 for a historical overview) based on simulated galaxies formed in the Illustris-1 simulation. The simulation produce a mix of elliptical (top left), barred (bottom right) and non-barred (top right) disk, and irregular (bottom left) galaxies (Vogelsberger et al. 2014a) but cannot reproduce the correct fraction of the observed galaxy types (Haslbauer et al. 2022). This problem is considered in more detail in the Chapter 8 and in the corresponding publications attached in Appendix B. Credit: top panel of figure 1 of Vogelsberger et al. (2014a).

and Boily 2005) More recent analysis even worsened the situation for the ΛCDM framework as the DoS of the MW alone causes a 3.55σ tension based on the TNG100-1 run (Pawlowski and Kroupa 2020; Banik et al. 2021, and the discussion in Chapter 10).

Recently, some studies argued that the DoS of the MW is not posing a serious challenge to the ΛCDM model anymore (e.g. Sawala et al. 2022; Xu, Kang and Libeskind 2023). For example, Sawala et al. (2022) concluded that the DoS of the MW is a short-lived plane which can arise and being therewith consistent with the ΛCDM model. Xu, Kang and Libeskind (2023) basically confirmed the likelihood of the DoS around the MW as quantified by Kroupa, Theis and Boily (2005) because they only found one MW-like system out of 231 candidates in the TNG50-1 run.

However, the situation is even more problematic for the ΛCDM framework because a DoS is not only observed around the Milky Way galaxy but also around the closest major galaxies Andromeda M31 (R. A. Ibata et al. 2013; R. A. Ibata et al. 2014) and Centaurus A (Müller et al. 2018) galaxies and likely also around other galaxies (Müller 2023). In particular, Asencio, Banik and Kroupa (2021) calculated that the DoS of the MW together with the DoS observed around M31 and Centaurus A causes a 5.27σ tension with the ΛCDM framework.

3.3.8 Dual dwarf galaxy problem

The dual dwarf galaxy theorem formulated by Kroupa (2012) and Kroupa (2015) states that there must be two types of dwarf galaxies with different formation channels and physical properties. One are primordial dwarf galaxies (PDGs) which form in the early Universe when baryonic matter streams and condenses into cold dark matter haloes. As a consequence, PDGs are dark matter-dominated and spheroidally distributed around their host galaxies (Section 3.3.3). The other types are tidal dwarf galaxies (TDGs) and ram-pressure dwarf galaxies (RPDGs). TDGs are created out of the tidally stripped gas and ejected stars during galaxy interactions and encounters. The gravitational potential of TDGs would not be strong enough to capture the fast dark matter particles (Okazaki and Taniguchi 2000; Wetzstein, Naab and Burkert 2007) such that TDGs are largely dark matter free (Barnes and Hernquist 1992; Bournaud 2010; Ploeckinger et al. 2018; Haslbauer et al. 2019). RPDGs ("fireballs", Yoshida et al. 2008; Yagi et al. 2010) form out of the stripped gas from an infalling galaxy towards a host galaxy being therewith also largely dark matter free (Kroupa 2012; Haslbauer et al. 2019). TDGs and RPDGs are typically phase-space correlated.

Thus, self-consistent cosmological cold dark matter-based simulations have to produce both dark matter-dominated and -free/-poor galaxies. Indeed, the dual dwarf theorem is valid in the EAGLE (Ploeckinger et al. 2018), Illustris-1 (Haslbauer et al. 2019), and IllustrisTNG (Haslbauer et al. 2019) simulations. Comparing these two types in a stellar radius-mass diagram shows that simulated dark matter-deficient galaxies have systematically smaller stellar half-mass radii than dark matter-dominated galaxies (see figure 9 of Haslbauer et al. 2019). This is because galaxies lacking dark matter have to be more compact in order to remain gravitational bound due to the absence of cold dark matter. However, observed TDG candidates and PDGs do not populate different regions in the stellar radius-mass diagram (see figure 2 of Dabringhausen and Kroupa 2013) conflicting with the ΛCDM predictions (Haslbauer et al. 2019).

Observing galaxies lacking dark matter would indeed be a strong argument for the existence of cold dark matter particles. In fact, van Dokkum et al. (2018) reported that the dwarf galaxy DF2 lacks dark matter observationally confirming the dual dwarf galaxy theorem and contradicting modified gravitational models without the need of cold dark matter (e.g. MOND). However, these authors

have measured the velocity dispersion of the galaxy only based on ten globular clusters. Kroupa et al. (2018) and Haghi et al. (2019) showed that DF2 is very consistent with MOND if taking into account the so-called external field effect predicted by MOND (Section 4.1.1).

3.3.9 Matter distribution on Mpc to Gpc scales

The Local Cosmological Volume (hereafter LV) is defined as a sphere with a radius of 11 Mpc centred around the Milky Way galaxy (Karachentsev et al. 2004; Karachentsev, Makarov and Kaisina 2013). Peebles and Nusser (2010) reported that the spatial distribution of galaxies within the LV[9] conflicts with the ΛCDM exceptions as the LV appears to be too underdense and a significant fraction of massive galaxies are > 2 Mpc above the sheet.

The local Universe is underdense on even much larger scales (e.g. Maddox et al. 1990; Zucca et al. 1997; Karachentsev 2012; Keenan, Barger and Cowie 2013; Rubart and Schwarz 2013; Rubart, Bacon and Schwarz 2014; Böhringer et al. 2015; Karachentsev and Telikova 2018; Böhringer, Chon and Collins 2020; J. H. W. Wong et al. 2022). For example, Karachentsev (2012) calculated an average total matter density within a sphere with radius of 50 Mpc of only $\Omega_{\mathrm{m,loc}} = 0.08 \pm 0.02$ (see also Karachentsev and Telikova 2018) which is 3 – 4 times lower than the value implied from the CMB (Planck Collaboration XIII 2016). Keenan, Barger and Cowie (2013) found that the density on a radial co-moving distance of 300 cMpc is only half of the cosmic mean density, which is known as the Keenan-Barger-Cowie (KBC) void (see also the discussion in Section 6.1.3). We show in Chapter 7, which is based on Haslbauer, Banik and Kroupa (2020), that the KBC void causes a 6.04σ tension with the ΛCDM framework.

An enhanced structure formation is not only imprinted in the local void, but also in overdensities through galaxy clusters. Asencio, Banik and Kroupa (2021) quantified the likelihood of the El Gordo interacting galaxy cluster (ACT-CL J0102-4915; Menanteau et al. 2010; Marriage et al. 2011) with a virial mass of $M_{200} = 3 \times 10^{15}\,M_{\odot}$ and an infall speed of $\approx 2500\,\mathrm{km\,s^{-1}}$ observed at $z = 0.87$ to be at 6.16σ tension with the Juropa Hubble Volume Simulation Project (Jubilee). In a subsequent study, Asencio, Banik and Kroupa (2023) showed that this remains to be a $> 5\sigma$ tension for an updated lower virial mass of $M_{200} = 2.13^{+0.25}_{-0.23} \times 10^{15}\,M_{\odot}$ (Kim et al. 2021) and infall velocities of $> 2300\,\mathrm{km\,s^{-1}}$. The Bullet cluster located at $z = 0.298$ (1E 0657-558, Tucker et al. 1998) causes a 2.78σ tension (Asencio, Banik and Kroupa 2021; see also J. Lee and Komatsu 2010 and Kraljic and Sarkar 2015).

3.3.10 Hubble tension

The Hubble tension is considered as one of the greatest problems in modern cosmology and states that the locally measured Hubble constant H_0 (Equations 3.3-3.4) is with a value of $73.8^{+1.1}_{-1.1}\,\mathrm{km\,s^{-1}\,Mpc^{-1}}$ (Riess et al. 2019; K. C. Wong et al. 2020) about 9 per cent higher than the global value of $H_0 = 67.4^{+0.5}_{-0.5}\,\mathrm{km\,s^{-1}\,Mpc^{-1}}$ (Planck Collaboration VI 2020a) causing a 5.3σ tension (K. C. Wong et al. 2020). Recent reviews on the Hubble tension can be found in Di Valentino et al. (2021) and Di Valentino, Anchordoqui, Akarsu, Ali-Haimoud, Amendola, Arendse, Asgari, Ballardini, Basilakos, Battistelli, Benetti, Birrer, Bouchet, Bruni, Calabrese, Camarena, Capozziello, A. Chen, Chluba, Chudaykin, Colgáin, Cyr-Racine, de Bernardis, de Cruz Pérez, Delabrouille, Dunkley, Escamilla-Rivera, Ferté, Finelli, W. Freedman, Frusciante, Giusarma, Gómez-Valent, Guy et al. (2021). In

[9] Peebles and Nusser (2010) considered a region with an inner radius of 1 Mpc and an outer radius of 8 Mpc around the MW.

Chapter 7, which is based on the publication Haslbauer, Banik and Kroupa (2020), we investigate the Hubble tension in the ΛCDM as well as in the MOND framework (Section 4.2).

3.3.11 Sigma-8 problem

The structure growth parameter is defined as

$$S_8 \equiv \sigma_8 \sqrt{\frac{\Omega_\mathrm{m}}{0.3}}, \tag{3.49}$$

where σ_8 is the root-mean-square density fluctuation within a sphere of radius $8\,h^{-1}$ Mpc. Several studies reported a difference between the locally measured S_8 value and the value derived from the CMB assuming the ΛCDM framework (e.g. Heymans et al. 2021; Di Valentino, Anchordoqui, Akarsu, Ali-Haimoud, Amendola, Arendse, Asgari, Ballardini, Basilakos, Battistelli, Benetti, Birrer, Bouchet, Bruni, Calabrese, Camarena, Capozziello, A. Chen, Chluba, Chudaykin, Colgáin, Cyr-Racine, de Bernardis, de Cruz Pérez, Delabrouille, Dunkley, Escamilla-Rivera, Ferté, Finelli, W. Freedman, Frusciante, Giusarma, Gómez-Valent, Handley et al. 2021; T. M. C. Abbott et al. 2023). For example, the Kilo-Degree Survey (KiDS-1000) found $S_8 = 0.766^{+0.020}_{-0.014}$ (Heymans et al. 2021), which is lower than the value of $S_8 = 0.834 \pm 0.016$ derived from the CMB (Planck Collaboration VI 2020b) causing a $\approx 3\sigma$ tension. Interestingly, Poulin et al. (2023) showed that S_8 increases with redshift. Thus, the local Universe would appear to be even more homogeneous conflicting at first glance with the conclusion reached in Section 13.1.2 that structure formation is enhanced than predicted by the ΛCDM framework. We discuss this so-called σ_8 problem in the light of the Hubble and KBC void in Section 13.1.2 but also in section 4.3 of Haslbauer, Kroupa and Jerabkova (2023).

3.3.12 Anisotropies

The following lists only a small list of observed large-scales anisotropies which question the CP. The interested reader may find further references e.g. in Aluri et al. (2023).

3.3.12.1 Hubble diagram

Migkas et al. (2021) reported a dipole in the Hubble diagram such that the Hubble constant varies from $H_0 = 66.2 \pm 1.6\,\mathrm{km\,s^{-1}\,Mpc^{-1}}$ to $H_0 = 72.7 \pm 1.5\,\mathrm{km\,s^{-1}\,Mpc^{-1}}$.

3.3.12.2 Deceleration parameter

The deceleration parameter is defined,

$$q \equiv -\frac{\ddot{a}a}{\dot{a}^2}. \tag{3.50}$$

Historically, it was assumed that the Universe decelerated such that q_0 was defined as a deceleration term (see the minus sign) but it tuned out that the expansion started to accelerate at $z \approx 0.65$ (Section 3.1.2). The ΛCDM model expects a present-day value of $q_0 = \frac{1}{2}\,\Omega_{\mathrm{m},0} - \Omega_{\Lambda,0} \approx -0.54$ (Planck Collaboration XIII 2016) but a joint analysis from Camarena and Marra (2020) yields $H_0 = 75.35 \pm 1.68\,\mathrm{km\,s^{-1}\,Mpc^{-1}}$ and $q_0 = -1.08 \pm 0.29$ obtained from Pantheon supernovae (Scolnic

et al. 2018) in the redshift range of $0.023 < z < 0.15$ being therewith about two times lower than the ΛCDM predictions (but see the large uncertainty of the observed q_0 value causing a 1.9σ tension). Moreover, Colin et al. (2019) found a dipole in q_0 at a 3.9σ significance.

3.3.12.3 Cosmic microwave background

The CMB shows an anisotropy by having more power on the southern than on the northern ecliptic hemisphere (Eriksen et al. 2004; Maino et al. 2007; Schwarz et al. 2016). The Cold Spot (CS; Vielva et al. 2004; Cruz et al. 2005), which is located at the southern galactic hemisphere, causes a $\approx 3\sigma$ tension with the ΛCDM model (Inoue and Silk 2006; Planck Collaboration et al. 2014; Nadathur et al. 2014, and reference therein). It has been speculated that the CS is the imprint of a void (Inoue and Silk 2006; Inoue and Silk 2007; and see also Haslbauer, Banik and Kroupa 2020 for a further discussion).

3.3.12.4 Galaxy morphology

Javanmardi and Kroupa (2017) showed an anisotropy in the galaxy morphology distribution which aligns with the ecliptic. A causal connection between asymmetry in galaxy morphology distribution and the hemispherical power (see the above point) needs to be investigated (Kroupa et al. 2023). Interesting though is that the northern elliptic hemisphere that has less power in the CMB also has significantly more late-type galaxies whereby the number densities of galaxies are the same in both hemispheres.

3.3.13 High-redshift galaxies

The JWST detected several luminous galaxy candidates with stellar masses of $M_* > 10^9\,M_\odot$ at high photometric redshifts of $z_{\rm phot} > 10$ (e.g. Naidu et al. 2022; Naidu et al. 2022; Labbé et al. 2023). If spectroscopically confirmed, these objects conflict with the stellar mass buildup predicted by the ΛCDM framework (Haslbauer et al. 2022; Boylan-Kolchin 2023; C. C. Lovell et al. 2023) indicating that structure formation is more enhanced and/or that the Universe is older than 13.8 Gyr (Equation 3.40). Upcoming JWST (and also ELT) observations are required in order to assess the significance.

This potential problem for the ΛCDM framework and for a Milgromian cosmological model with a standard expansion history is elaborated further in the Chapter 9 and Section 4.4.6, respectively. Melia (2023) argued that the tension may be resolved in a cosmological model with a constant expansion rate (Melia and Shevchuk 2012) that would increase the age of the Universe to 14.5 Gyr.

CHAPTER 4

Milgromian dynamics (MOND)

"If we accept a departure from the standard laws of physics, we might do away with dark matter."
(Milgrom 2002)

In 1983, the Israeli astrophysicist Mordehai Milgrom published the paper entitled "A modification of the Newtonian dynamics as a possible alternative to the hidden mass hypothesis" (Milgrom 1983c) in which he proposed a generalization of Newton's law of gravity in order to address the rotation curves of galaxies without proposing the existence of cold dark matter. In the same year, Milgrom published two further studies in which he discusses the implications of MOND on galaxies (Milgrom 1983a; Milgrom 1983b). In fact, over the last decades several of his *a priori* predictions have been observationally confirmed but MOND still encounters challenges on galaxy cluster and cosmological scales. Originally, the terminology "MOND" refers to the "MOdification of Newtonian Dynamics" but throughout this thesis I follow the notation introduced e.g. by Kroupa et al. (2022) in which MOND is the acronym for "MilgrOmiaN Dynamics" providing therewith a more accurate naming (see also Chapter 1) as it directly refers to the theory of Milgrom (1983c). The interested reader may find further information about the history and philosophical aspects of MOND in Merritt (2020). A recent review about MOND is given in Banik and Zhao (2022) but see also Famaey and McGaugh (2012).

In this chapter, I will first provide the theoretical concept of MOND (Section 4.1) by introducing the generalized Milgromian Poisson equation and the external field effect. Secondly, I will briefly describe the attempts towards cosmological MOND theories (Section 4.2) by highlighting the MONDian ν-hot dark matter (νHDM) model. This is followed by a discussion on galaxy scaling relations focusing on the connection between the observed baryonic Tully-Fisher relation (BTFR; Tully and Fisher 1977) and MOND (Section 4.3). Finally, I will list some observations potentially challenging MOND and the νHDM model (Section 4.4).

4.1 Theoretical background

Newton's law of gravity is an inverse square law such that the Newtonian gravitational field strength at the distance r from an isolated point mass M in a radial field is

$$g = \frac{GM}{r^2}, \tag{4.1}$$

where G is the gravitational constant. The Newtonian Poisson equation of gravity is given by

$$\nabla \cdot \left(\nabla \Phi_{\rm N}\right) \quad = \quad 4\pi G \rho_{\rm b} \,, \tag{4.2}$$

where $\Phi_{\rm N}$ is the Newtonian potential such that $\boldsymbol{g}_{\rm N} = -\nabla\Phi_{\rm N}$ and $\rho_{\rm b}$ is the baryonic matter density. As discussed in the Chapter 1, applying Newtonian or Einsteinian gravity on astrophysical scales requires the assumption of cold dark matter (Chapter 3) and therefore a correction of the right-hand side of the Poisson equation,

$$\nabla \cdot \left(\nabla \Phi_{\rm N}\right) \; = \; 4\pi G \underbrace{\left(\rho_{\rm b} + \rho_{\rm CDM}\right)}_{\rho_{\rm m}} \,, \tag{4.3}$$

where $\rho_{\rm CDM}$ is the cold dark matter density and $\rho_{\rm m}$ is the total (baryonic and cold dark) matter density.

In general, MOND is an acceleration-dependent long-range correction of Newton's law of gravity such that the gravitational strength scales with the inverse distance at accelerations of $\lesssim 10^{-10}\,{\rm m\,s^{-2}}$. The gravitational field strength, g, at distance r from an isolated point mass M in spherical symmetry is

$$g \; = \; \frac{\sqrt{GMa_0}}{r} \qquad \text{for} \qquad g \ll a_0 \,, \tag{4.4}$$

where G is again the gravitational constant and a_0 is Milgrom's constant, which has been empirically constrained to be $a_0 \approx 1.2 \times 10^{10}\,{\rm m\,s^{-2}}$ (e.g. Begeman, Broeils and Sanders 1991; Gentile, Famaey and de Blok 2011). MOND is a Lagrangian-based theory (Bekenstein and Milgrom 1984; Milgrom 2010) from which the non-linear generalized Poisson equation can be derived. The Milgromian Poisson equation in the deep MOND limit is,

$$\nabla \cdot \left[\left(\frac{|\nabla\Phi_{\rm M}|}{a_0}\right)\nabla\Phi_{\rm M}\right] \; = \; 4\pi G\rho_{\rm b} \,, \tag{4.5}$$

where $\Phi_{\rm M}$ is the MOND potential. The generalized Milgromian Poisson equation requires a transitions function μ between the different MOND regimes

$$\nabla \cdot \left[\mu\left(\frac{|\nabla\Phi_{\rm M}|}{a_0}\right)\nabla\Phi_{\rm M}\right] \; = \; 4\pi G\rho_{\rm b} \tag{4.6}$$

with the boundary conditions $\mu\left(\frac{|\nabla\Phi_{\rm M}|}{a_0}\right) \rightarrow 1$ for $\frac{|\nabla\Phi_{\rm M}|}{a_0} \rightarrow \infty$ and $\mu\left(\frac{|\nabla\Phi_{\rm M}|}{a_0}\right) \rightarrow \frac{|\nabla\Phi_{\rm M}|}{a_0}$ for $\frac{|\nabla\Phi_{\rm M}|}{a_0} \rightarrow 0$. Thus, Equation 4.6 reduces to the Newtonian Poisson equation for accelerations of $g \gg a_0$ and to the deep-MOND limit described by Equation 4.5 for $g \ll a_0$.

Summing up, the assumption of cold dark matter as an additional matter component in combination with the validity of Newtonian/Einstein gravity requires a correction of the right-hand side, while MOND corrects the left-hand side of the Newtonian Poisson equation (Equation 4.2).

4.1.1 External field effect

In MOND, the generalized Poisson equation is non-linear in acceleration (Equation 4.6) such that the internal gravity of a system depends on its surrounding structures which is known as the external field effect (EFE; Milgrom 1986). Consequently, the EFE violates the strong equivalence principle. The observation of rotation curves of non-isolated galaxies favor the existence of the EFE (Chae et al. 2020; Chae et al. 2021).

The EFE plays an important role in structure formation because the surrounding structures influence each other as noted in section 5.2.2 of Haslbauer, Banik and Kroupa (2020). Thus, cosmological MOND simulations have to be large enough in order to achieve an convergence in structure formation but this needs to be studied in upcoming research projects.

4.2 Cosmological MOND model

The first cosmological MOND simulations have been already performed at the turn of the millennium (e.g. Sanders 1998; Sanders 2001; Nusser 2002). While MOND describes accurately the dynamics on galactic scales, it emerged that MOND still requires a further mass component in order to explain the dynamical mass of galaxy clusters (see the discussion of Section 4.4.4) and the angular power spectrum of the cosmic microwave background (CMB) because the amplitude of the third peak of the CMB is understood to be driven by a collisionless matter component. Motivated by the missing mass problem in galaxy clusters, Sanders (2003) argued for a MOND framework with ordinary neutrinos but their existence has been later ruled out by the KArlsruhe TRItium Neutrino (KATRIN) experiment (Aker et al. 2019; Katrin Collaboration et al. 2022) .

Throughout the projects of this thesis, we will only focus on the cosmological MOND framework proposed by Angus (2009) in which the cold dark matter component is entirely replaced by fast collisionless matter in the form of 11 eV c^{-2} sterile neutrinos (ν) which acts as hot dark matter (HDM). This νHDM framework has therefore the same overall mass budget as the ΛCDM model which preservers the standard expansion history, yielding to a similar Big Bang nucleosynthesis (BBN) and angular power spectrum of the CMB to the ΛCDM model (see section 3.1 of Haslbauer, Banik and Kroupa 2020) as compared in the left panel of Figure 4.1. The missing gravitational potential of cold dark matter haloes in the early Universe results in a significantly lack of power on scales of $\lesssim 1$ Mpc at redshift $z = 254.1$ which is shown in the right panel of Figure 4.1 and discussed further in the light of the recent JWST observations in Section 4.4.6 and section 4 of Haslbauer et al. (2022). MONDian effects become dominant at redshifts of $z \lesssim 50$ which enhances the growth of structure because of the stronger self-gravity (Chapter 7).

A more detailed description of the νHDM model is given in Angus (2009) but also in Haslbauer, Banik and Kroupa (2020), Asencio, Banik and Kroupa 2021, Banik and Zhao (2022), and (Wittenburg et al. 2023). Recently, Wittenburg et al. (2023) published the first hydrodynamical cosmological νHDM simulations (see also Section 4.4.6).

Reviewing relativistic versions of MOND is beyond the scope of this thesis but it should be mentioned that the tensor-vector-scalar (TeVeS) gravity of Bekenstein (2004) conflicts with the observational fact that gravitational waves spread out with the speed of light (B. P. Abbott et al. 2016; Boran et al. 2018). This has been corrected in the relativistic MOND theory by Skordis and Złośnik (2019) and Skordis and Złośnik (2021). The interested reader on relativist MOND theories is referred to section 2.6 of Banik and Zhao (2022).

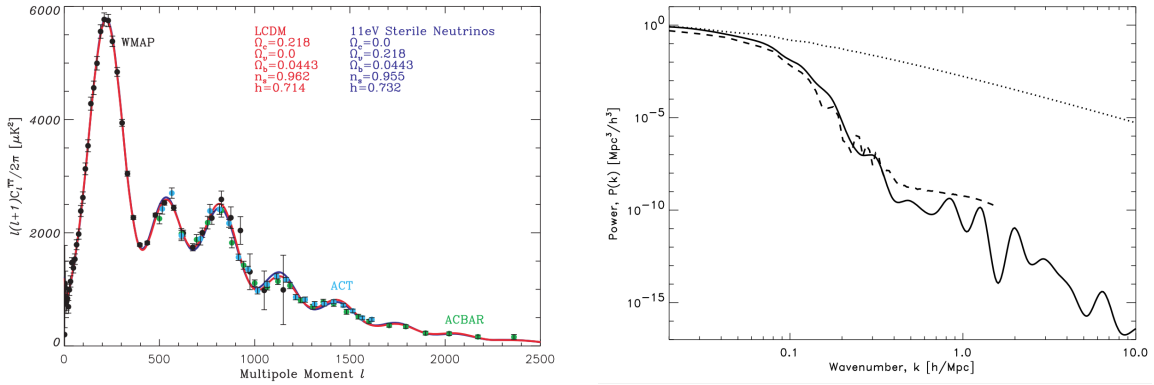

Figure 4.1: *Left:* Angular power spectrum of the cosmic microwave background (CMB) of the ΛCDM model (red line) and the νHDM model (blue line). The cosmological parameters of these models are listed in the top middle (ΛCDM) and top right (νHDM) of the panel. The points refer to the 7-year data release of the Wilkinson Microwave Anisotropy Probe (WMAP-7; black), Atacama Cosmology Telescope (ACT; turquoise data points), and the Arcminute Cosmology Bolometer Array Receiver (ACBAR; green). Credit: figure 1 of Angus and Diaferio (2011). *Right:* Power spectrum of the ΛCDM (dotted line) and the νHDM (solid line) model at redshift $z = 254.1$ using the Code for Anisotropies in the Microwave Background (CAMB). The dashed line shows the power spectrum of the N-body simulation by Angus and Diaferio (2011). Credit: figure 2 of Angus and Diaferio (2011).

4.3 Galaxy scaling relations

Originally pointed out by Milgrom (1983a) and Milgrom (1983b), MOND has several implications for galactic scaling-relations leading to *a priori* predictions as reviewed e.g. in Famaey and McGaugh (2012), McGaugh (2020), or Banik and Zhao (2022).

In the following, we study the BTFR and the radial acceleration relation (RAR; McGaugh, Lelli and Schombert 2016; Lelli et al. 2017) in the light of MOND. Let's consider a test particle on a circular orbit with the speed V_c around the mass M such that the experienced centripetal acceleration is given by

$$g_{\rm cen} = \frac{V_c^2}{r} . \tag{4.7}$$

Combining the Equations 4.4 and 4.7 yields

$$\frac{V_c^2}{r} = \frac{\sqrt{GMa_0}}{r} , \tag{4.8}$$

such that the velocity depends only on the mass of the object via,

$$V_c = (GMa_0)^{1/4} , \tag{4.9}$$

$$\tag{4.10}$$

which is just the observed BTFR of late-type[1] galaxies (e.g. Tully and Fisher 1977; McGaugh et al. 2000; Lelli et al. 2019) as shown in the right panel of Figure 4.2. Observationally, Lelli et al. (2019) found that the observed velocity at the flat part of the rotation curve, $V_{\rm f}$, and the baryonic mass, $M_{\rm b}$, of the galaxy are related via

$$M_{\rm b} \quad \propto \quad V_{\rm f}^{3.85\pm0.09}\,, \tag{4.11}$$

where the power-law index of 3.85 ± 0.09 being slightly lower than the theoretical expectations of Equation 4.10 assuming a canonical (non-varying) IMF (but see also the discussion of the BTFR in the context of a varying IMF within the IGIMF theory in the Sections 5.4.1 and 13.2).

The BTFR follows from MOND but as the BTFR has been discovered by Tully and Fisher (1977) before the invention of MOND (Milgrom 1983c), the BTFR cannot be considered as an *a priori* predication of MOND. However, it needs to be emphasized that nowadays the BTFR covers ≈ 6 order of magnitude of $M_{\rm b}$.

More fundamentally, the BTFR is a consequence of the RAR (McGaugh, Lelli and Schombert 2016; Lelli et al. 2017) as shown in the left panel of Figure 4.2 which describes a tight relation between the observed centripetal acceleration,

$$g_{\rm obs} \equiv \frac{V_{\rm obs}^2(r)}{r} = -\nabla\Phi_{\rm tot}(r)\,, \tag{4.12}$$

and the centripetal acceleration derived from the observed baryons,

$$g_{\rm bar} \equiv \frac{V_{\rm bar}^2(r)}{r} = -\nabla\Phi_{\rm bar}(r)\,, \tag{4.13}$$

where $V_{\rm tot}(r)$ is the observed velocity of the rotation curve and $V_{\rm bar}(r)$ is the velocity implied from the baryonic (stars and gas) component at the galactic distance r. $\Phi_{\rm tot}$ and $\Phi_{\rm bar}$ are the total and baryonic gravitational potentials, respectively. Therefore, $g_{\rm obs} = g_{\rm bar}$ (see the line of identity in the left panel of Figure 4.2) for dark matter-free galaxies (e.g. TDGs; Section 3.3.8) in Newtonian dynamics. The observed RAR can be fitted with an equation of the form (McGaugh 2008; McGaugh 2014; Lelli et al. 2017)

$$g_{\rm obs} = \frac{g_{\rm bar}}{1-\exp\left(-\sqrt{g_{\rm bar}/g_\dagger}\right)}\,, \tag{4.14}$$

where $g_\dagger = 1.20\times10^{-10}\,{\rm m\,s^{-2}}$ for the best-fit (Lelli et al. 2017) implying that dark matter or MONDian affects start dominating at accelerations of $\approx 10^{-10}\,{\rm m\,s^{-2}}$.

The ΛCDM framework has neither predicted the BTFR nor the RAR as briefly discussed in Section 3.3.

[1] Late-type galaxies follow the BTFR, while early-type galaxies the Faber-Jackson relation (Faber and Jackson 1976).

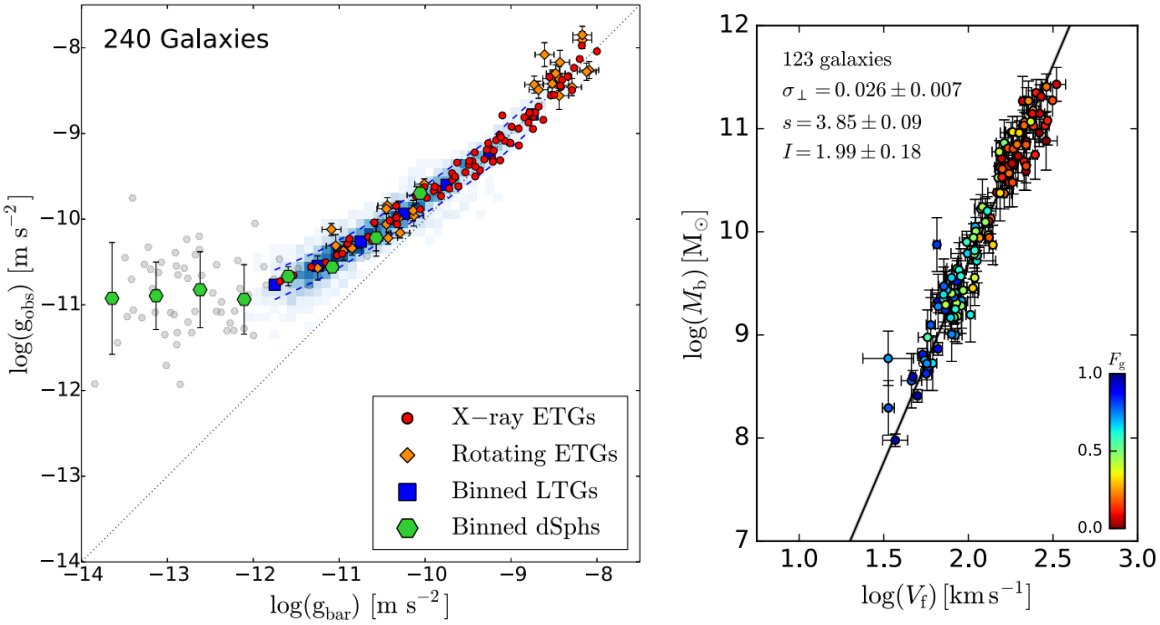

Figure 4.2: *Left:* Radial acceleration relation (RAR) which shows the observed centripetal acceleration, $g_{\rm obs}$ (y-axis), in dependence of the centripetal acceleration implied from the observed baryons, $g_{\rm bar}$ (x-axis), for X-ray ETGs (red circles), rotating ETGs (orange diamonds), binned LTGs (blue squares; see also figure 3 of McGaugh, Lelli and Schombert 2016), and binned dSphs (green hexagons). The dotted black line shows the identity line on which dark matter-free galaxies (e.g. TDGs; Section 3.3.8) are expected to lie if Newtonian dynamics is valid. Credit: left panel of figure 12 of Lelli et al. (2017). *Right:* Baryonic Tully-Fisher relation (BTFR) which shows a relation between the velocity of the flat part of the rotation curve, $V_{\rm f}$, and the baryonic mass, $M_{\rm b}$, for 123 galaxies of the SPARC database. The data are fitted in the $\log_{10}$-space with a linear fit of the form $\log_{10}(M_{\rm b}/M_{\odot}) = s\,\log_{10}(V_{\rm f}/[{\rm km\,s^{-1}}]) + I$, where the best fitting parameters are $s = 3.85 \pm 0.09$ and $I = 1.99 \pm 0.18$. The BTFR has a orthogonal scatter of only $\sigma_{\perp} = 0.026 \pm 0.007$. The colorbar represents the gas fraction of the galaxies defined as $F_{\rm g} \equiv M_{\rm g}/M_{\rm b}$, where $M_{\rm g}$ and $M_{\rm b}$ are the gas and baryonic mass, respectively. The BTFR follows from the RAR but not vice versa (see text). Credit: top left panel of figure 2 of Lelli et al. (2019).

4.4 Challenges for MOND

Although MOND is a very successful (and also predictive) theory, some tensions have been reported on galactic but especially on cosmological scales. The following sections briefly review only some of the most problematic aspects of MOND but a more extended list of potential challenges for MOND is provided e.g. in section 3.2 of Kroupa et al. (2023).

4.4.1 Velocity dispersion of ultra-faint dwarf satellite galaxies

Safarzadeh and Loeb (2021) reported that the line-of-sight velocity dispersion of ultra-faint dwarf satellite galaxies (UFDs) of the MW are inconsistent with MOND (see their figure 1) but these galaxies might not be in dynamical equilibrium causing an overestimation of the line-of-sight velocity dispersion (Kroupa 1997; Kroupa et al. 2023).

4.4.2 Deviations of dSphs from the radial acceleration relation

Some local dSphs deviate from the RAR at low accelerations of $g_{\rm bar} \lesssim 10^{-12}\,{\rm m\,s^{-2}}$ (Lelli et al. 2017; Garaldi et al. 2018; but see also Mercado et al. 2023 for the galaxies DDO154, NGC0055, UGC06667, and UGC02259). Since these data are in the deep-MOND regime, such a deviation of the RAR would pose a serious challenge for MOND. The derived velocity dispersion could be systematically biased if e.g. the galaxies are out-of-equilibrium (Kroupa 1997; Lelli et al. 2017; Garaldi et al. 2018) and/or the number of unresolved binary stars is underestimated (Lelli et al. 2017).

4.4.3 Deviations of galaxy clusters from the radial acceleration relation

P. Li et al. (2023) showed in their figure 5 that their ten analyzed galaxy clusters from the HIghest X-ray FLUx Galaxy Cluster Sample (HIFLUGCS) deviate from the RAR. Similar results have been found by Eckert et al. (2022) for five galaxy clusters of the XMM Cluster Outskirts Project (Eckert et al. 2017). The problem is potentially related to the missing mass problem of galaxy clusters and can be, in principle, caused if the clusters not being in virial equilibrium (see also the following Section 4.4.4). Furthermore, it must be noted that deriving the mass at the cluster's outskirt is a non-trivial task.

4.4.4 Missing mass problem of galaxy clusters

A long-standing problematic aspect of MOND is that the theory still underestimates the gravitating masses of galaxy clusters (The and White 1988; Gerbal et al. 1992) by a factor of about two (Sanders 1994; Sanders 1999; Aguirre, Schaye and Quataert 2001; Sanders 2003; Pointecouteau and Silk 2005). The missing mass problem of galaxy clusters motivated e.g. Sanders (2003) and Sanders (2007) to introduce (sterile) neutrinos as an additional matter component (see also Angus 2009; Angus, Diaferio and Kroupa 2011; Angus and Diaferio 2011) which clusters on galaxy-cluster but not on galactic scales preserving therewith galactic rotation curves but increasing the cluster masses.

Recently, López-Corredoira et al. (2022) argued that the missing mass problem appears because of inappropriate hydrostatic equilibrium assumptions.

4.4.5 Lyman-α absorbers

Aguirre, Schaye and Quataert (2001) reported that Lyman-α absorbers conflicts with MOND without the EFE (Section 4.1.1) but the tension could be alleviated in the case of a large background acceleration field.

4.4.6 Structure formation in the νHDM model

As described in Section 4.2, the cold dark matter component is replaced by fast collisionless matter (hot dark matter) in the form of 11 eV c^{-2} sterile neutrinos in the νHDM cosmological model. Due to the missing gravitational potential of cold dark matter on galactic scales, the νHDM model lacks power especially on < 1 Mpc compared to the ΛCDM model as evident in the right panel of Figure 4.1 based on Angus, Diaferio and Kroupa (2011) but also in the figures 1 and 2 of Wittenburg et al. (2023). As a consequence, the hydrodynamical νHDM model starts to form detectable structures and galaxies only at $z \gtrsim 4$ which significantly conflicts with observations of high-redshift galaxies detected with the HST (Oesch et al. 2016) and more recently with the JWST (e.g. Naidu et al. 2022; Naidu et al. 2022; Labbé et al. 2023) but also with observations of protoclusters at $z \gtrsim 4$ (e.g. Capak et al. 2011; Capak et al. 2011; Walter et al. 2012; Hodge et al. 2013; Oteo et al. 2018; G. C. P. Wang et al. 2021; Alberts and Noble 2022; Morishita et al. 2023). This problematic aspect of the νHDM model has been noted in Haslbauer et al. (2022) but has been recently explicitly demonstrated by Wittenburg et al. (2023) in structure formation simulations.

These inconsistencies of the νHDM model with the observations do not necessarily imply a failure of MOND because the results could also point to a non-standard expansion history which would leave more time to form cosmic structures (Melia 2023).

CHAPTER 5

The galaxy-wide initial mass function

"But the most remarkable discovery in all of astronomy
is that the stars are made of atoms of the same kind as those on the earth."
(Richard P. Feynman in "The Feynman Lectures on Physics"; Feynman, Leighton and Sands 1963)

The properties of galaxies are not only sensitive to the underlying cosmological framework (see e.g. Chapters 3 and 4) but also inter alia on the physical processes on (sub-) galactic scales (Kroupa and Jerabkova 2021; Haslbauer et al. 2022, and see also the Section 6.2 and Chapter 12). A fundamental parameter in galaxy formation and evolution is the stellar initial mass function (IMF) which describes the stellar mass distribution of newly formed stars in a single star-forming event. The stellar IMF is mathematically defined as $\xi_*(m) \equiv dN/dm$, where dN is the number of newly formed stars within the stellar mass interval $[m, m+dm]$. A theoretical framework to compute the stellar IMF for an entire galaxy (which is the galaxy-wide stellar IMF, gwIMF) by summing up all individual stellar IMFs of star-forming regions is the integrated galactic IMF (IGIMF) theory (Kroupa and Weidner 2003).

In this chapter, I will first formally introduce the canonical (invariant) IMF (Section 5.1) and the observational evidence for a systematically varying (non-invariant) IMF (Section 5.2). Subsequently, I will only briefly outline the concept of the IGIMF theory (Section 5.3) for computing the gwIMF while a much more detailed mathematical description is provided in Chapter 12, which studies the implications of a varying gwIMF on the present-day main-sequence, stellar mass buildup, and gas depletion time-scale of local star-forming galaxies. Finally, I will state at the end of this chapter some potential challenges for a varying IMF (Section 5.4) which can be also considered as an outlook for upcoming projects.

5.1 The canonical stellar initial mass function

The "original" mass function proposed by Salpeter (1955) is mathematically expressed as a single power-law of the form

$$\xi_*(m) \equiv \frac{dN}{dm} = \xi_0 m^{-\alpha}\,, \tag{5.1}$$

with the normalization constant ξ_0 and a power-law index of $\alpha = 2.35$ for stellar masses between $0.4 - 10\,M_\odot$. As a historical remark, Salpeter (1955) explicitly referred to the IMF as the "original mass function" while to my knowledge the terminology "initial" appeared for the first time two years later in the study by Sandage (1957). The importance of Salpeters contribution to astrophysics has been noted in the doctoral thesis by Tereza Jerabkova:

> *"From today's perspective this scientific contribution presents an immense jump forward for astrophysics. It bridges together different scientific fields and provides a result still in use today. If Edwin Salpeter would not have written this paper, a large fraction of modern astrophysics could not have been done."* (Jerábková 2020)

In particular, Edwin Ernest Salpeter (1924–2008) managed with the stellar IMF to combine quantum physics, thermodynamics, and statistical physics with astrophysics and cosmology (Kroupa and Jerabkova 2019) as we will also see further in Section 6.2.

Since the pioneering work by Salpeter (1955), the mathematical description of the canonical IMF has been continuously updated using more recent observations (e.g. G. E. Miller and Scalo 1979; Kroupa 2001; Chabrier 2003). The analysis based on this thesis adopts the stellar IMF formulated by Kroupa (2001), upon which the next-to-identical Chabrier re-write is based, which is a multiple power-law function of the form,

$$\xi_*(m) = \begin{cases} k_1 m^{-\alpha_1} & 0.08 \leq m/M_\odot < 0.50\,, \\ k_2 m^{-\alpha_2} & 0.50 \leq m/M_\odot < 1.00\,, \\ k_3 m^{-\alpha_3} & 1.00 \leq m/M_\odot < m_{\rm max}\,, \end{cases} \tag{5.2}$$

where k_{1-3} are the normalization constants also ensuring continuity, α_{1-3} are the power-law indices, and $m_{\rm max} \approx 150\,{\rm M}_\odot$ is the maximum mass of the stars.

5.2 Towards a varying stellar initial mass function

The first observational indications for a varying stellar IMF have been reported in the 1990s by Matteucci and Brocato (1990) and Matteucci (1994) based on the metallicity distribution of Galactic bulge stars. But what does a variation of the stellar IMF actually mean? In order to address this question, the basic concept of a varying IMF is schematically illustrated in Figure 5.1. On the basis that the baseline model is the canonical IMF (solid black line), which is here represented by Kroupa (2001), we differentiate between a bottom-heavy (dotted red line), bottom-light (dotted orange), top-heavy (dotted blue), and top-light (dotted green) IMFs. A bottom-heavy IMF has an excess, while a bottom-light IMF has a deficit of low mass stars relative to the canonical IMF. The other two IMF types refer to the distribution of the high-mass end insofar as a top-heavy and a top-light IMF has an excess and a deficit of massive stars compared to the canonical IMF, respectively. A combination of these different types is also possible such that an IMF can be e.g. bottom-heavy and top-light or bottom-light and top-heavy etc..

Some further possible indications but not clear-cut evidence for a varying IMF have been reported in the late 1990s and early 2000s (Vazdekis et al. 1997; Kroupa 2001; Kroupa 2002, and references therein) such that a variation of the IMF has not been established in the astrophysical community at this time. In 2005, and therewith 50 years after the formulation of the stellar IMF, its founder Edwin

Salpeter commented on a variation in the conference proceeding entitled *The Initial Mass Function 50 years later* (2005) as follows:

> *"In particular, although I was hoping that my IMF was roughly right on the average, I expected that it would vary extremely strongly with varying conditions. For instance, I (and others) thought that massive stars would be strongly favored in regions of strong turmoil and possibly in regions of high gas column density in general and the young Galaxy in particular. These are just the controversies which we will be debating here, and there surely will be variations but just what is still not clear. This uncertain state of affairs has been good for me personally over the last 50 years - in the absence of clearcut answers, my IMF still gets quoted! However, this absence has been bad for the theorists - we need clearcut variations to decide between rival theories."* (Edwin Ernest Salpeter in *The Initial Mass Function 50 years later* 2005)

Interestingly, Salpeter concluded that "there surely will be variations but just what is still not clear" (*The Initial Mass Function 50 years later* 2005) but more observations were still required in order to understand the variation allowing to constrain different theories. In fact, more evidence for a systematically varying IMF with metallicity and star-formation rate has been discovered after 2005 (e.g. Hoversten and Glazebrook 2008; Pflamm-Altenburg and Kroupa 2008; Dabringhausen, Kroupa and Baumgardt 2009; J. C. Lee et al. 2009; Meurer et al. 2009; van Dokkum and Conroy 2010; Gunawardhana et al. 2011; Banerjee and Kroupa 2012; Conroy and van Dokkum 2012; Dabringhausen et al. 2012; Marks et al. 2012; Geha et al. 2013; Gennaro et al. 2018; Kalari et al. 2018; Parikh et al. 2018; F. R. N. Schneider et al. 2018; Watts et al. 2018; Zhang et al. 2018; Zhou et al. 2019; Martın-Navarro et al. 2019; R. J. Smith 2020; Yan, Jerabkova and Kroupa 2020; Mucciarelli et al. 2021; van Dokkum and Conroy 2021; J. Li et al. 2023, and see also Chapter 12 for further references and discussions).

5.2.1 Metallicity dependency of indices

Based on the original formulation that α_1 and α_2 might very with $[Fe/H]$ by Kroupa (2002), according to the IGIMF formulation by Yan, Jeřábková and Kroupa (2021, hereafter IGIMF-2021) the power law indices of the low and intermediate mass stars depend on the global metallicity of the galaxy via

$$\alpha_1 = 1.3 + \Delta\alpha \cdot (Z - Z_\odot) \quad \text{for} \quad 0.08 \leq m/M_\odot < 0.50\,, \tag{5.3}$$

$$\alpha_2 = 2.3 + \Delta\alpha \cdot (Z - Z_\odot) \quad \text{for} \quad 0.50 \leq m/M_\odot < 1.00\,, \tag{5.4}$$

where $\Delta\alpha = 63$ (Yan, Jeřábková and Kroupa 2021) and Z and $Z_\odot = 0.0142$ (Asplund et al. 2009) are the mean stellar metal-mass fraction of the system and the Sun, respectively. The functional dependency of the power-law indices of the previous IGIMF formulations are described and compared e.g. in Jeřábková et al. (2018).

In the IGIMF-2021 formulation, the power-law index of the more massive stars with $m > 1\,M_\odot$ is (Marks et al. 2012; Marks et al. 2014)

$$\alpha_3 = \begin{cases} 2.3 & \text{for} \quad x < -0.87\,, \\ -0.41x + 1.94 & \text{for} \quad x \geq -0.87\,, \end{cases} \tag{5.5}$$

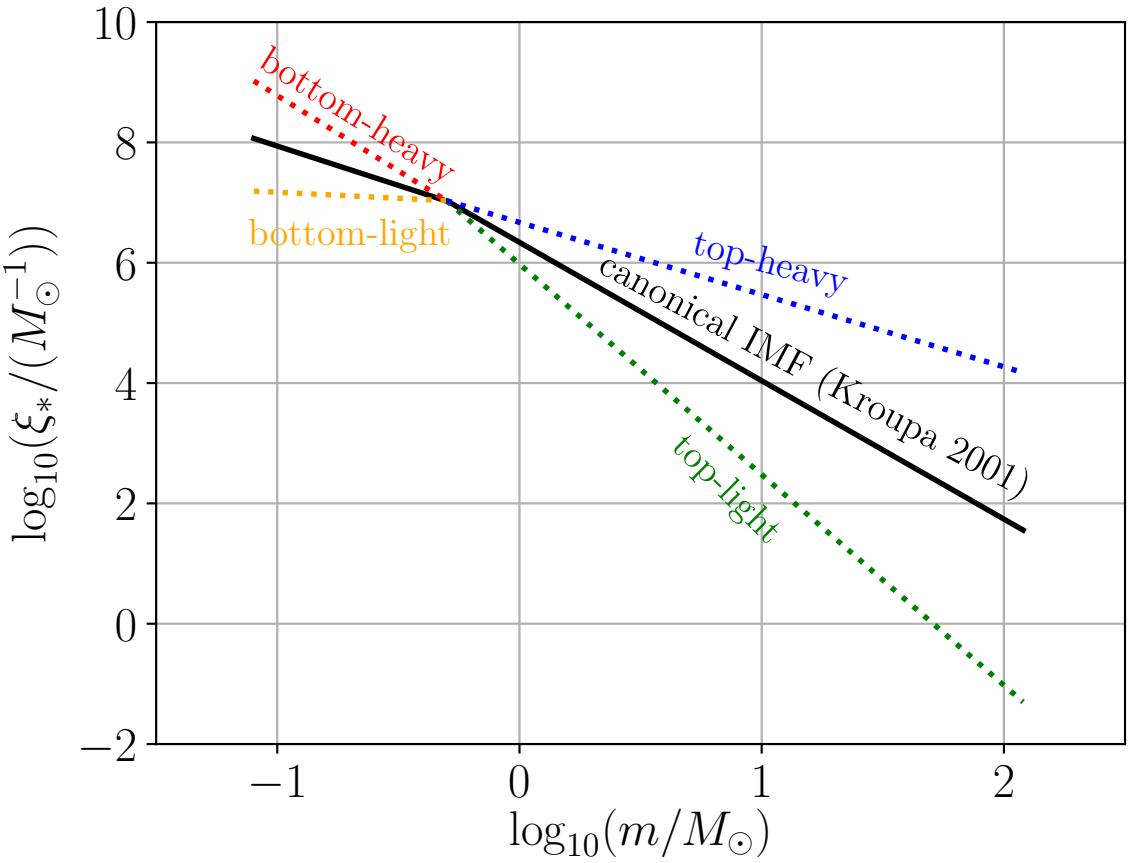

Figure 5.1: Schematic illustration of the concept of a varying IMF. The black solid line shows the canonical IMF (Equation 5.2) formulated by Kroupa (2001). A bottom-heavy IMF (red dotted) has more, while a bottom-light IMF (orange dotted) has fewer low mass stars (here at $m \lesssim 0.5\,M_\odot$) relative to the canonical IMF. A top-heavy IMF (blue dotted) has more, while a top-light IMF (green dotted) has fewer massive stars (here at $m \gtrsim 0.5\,M_\odot$) relative to the canonical IMF. Note that the y-axis shows arbitrary numbers/unit but a more quantitative analysis of the gwIMF within the IGIMF framework can be found in Figure 5.2 and in Chapter 12. Credit: figure made by the author of the thesis, but based on figure 1.2 of Kroupa and Jerabkova (2021).

with

$$x = -0.41[Z] + 0.99 \log_{10}\left(\frac{M_{\rm ecl}}{10^6 \mathrm{M}_\odot}\right), \tag{5.6}$$

where $M_{\rm ecl}$ is the mass of the embedded star cluster and $[Z] \equiv \log_{10}(Z/Z_\odot)$.

5.3 Integrated galaxy initial mass function

The IGIMF theory will be formally introduced in Chapter 12 but I will outline here the basic concepts to calculate the gwIMF. Generally speaking, the IGIMF is the computational framework to calculate the gwIMF by adding all IMFs in star-forming regions within a galaxy. The IGIMF theory was first proposed and mathematically formulated by Kroupa and Weidner (2003) and has been continuously updated over the last years taking into account new observational constraints (Marks et al. 2012; Marks et al. 2014; Yan, Jerabkova and Kroupa 2020; Yan, Jeřábková and Kroupa 2021; Yan, Jerabkova and Kroupa 2023).

The embedded cluster mass function (ECMF) can be parametrized by a single power-law (Lieberz and Kroupa 2017) of the form

$$\xi_{\rm ecl}(m,\psi) = \begin{cases} 0 & M_{\rm ecl} \leq M_{\rm ecl,min} = 5\,M_\odot\,, \\ k_{\rm ecl} M^{-\beta(\psi)} & M_{\rm ecl,min} \leq M_{\rm ecl} < M_{\rm ecl,max}(\psi)\,, \\ 0 & M_{\rm ecl,max}(\psi) \leq M_{\rm ecl,max}\,, \end{cases} \tag{5.7}$$

where k_i are normalization constants, ψ is the star formation rate (SFR), β is the power-law index which depends on ψ in such a way that the ECMF becomes top-heavy for increasing SFR. $M_{\rm ecl,min}$ and $M_{\rm ecl,max}$ are the minimum and maximum embedded cluster masses, respectively.

Assuming that the embedded clusters are the fundamental building blocks of galaxies (Kroupa 2005), the gwIMF is given by

$$\xi_{\rm IGIMF}(m,\psi,[\mathrm{Z}]) = \int_{M_{\rm ecl,min}}^{M_{\rm ecl,max}(\psi)} \xi_*(m, M_{\rm ecl}, [\mathrm{Z}])\, \xi_{\rm ecl}(M_{\rm ecl}, SFR)\, dM_{\rm ecl}\,. \tag{5.8}$$

Thus, the gwIMF constructed from the IGIMF formulation by Yan, Jeřábková and Kroupa (2021) depends on both the global metallicity and SFR of the galaxy as discussed in Figure 5.2. As the SFR and metallicity of a galaxy changes during its evolutions, its gwIMF varies over time. The time evolution of the gwIMF for a typical early-type galaxy with an increasing SFR followed by a declining SFR and a continuously metallicity enrichment is schematically illustrated by the green arrow in Figure 5.2. At the beginning of its evolution, the galaxy has a low star formation rate of $\psi = 10^{-5}\,\mathrm{M}_\odot\,\mathrm{yr}^{-1}$ and metallicity of $[Z] = -5$ which results in a bottom-light and top-light gwIMF. An increase of the SFR yields to an increase of the number of high mass stars such that the gwIMF becomes top-heavy for $\psi > 1\,\mathrm{M}_\odot\,\mathrm{yr}^{-1}$ relative to the canonical IMF. For a given SFR, the gwIMF becomes bottom-heavy and bottom-light for $[Z] > 0$ and $[Z] < 0$, respectively. Low SFRs of $\psi < 1\,\mathrm{M}_\odot\,\mathrm{yr}^{-1}$ and $[Z] > 0$ yields finally to a bottom-heavy but a top-light gwIMF.

A more detailed discussion of the IGIMF formulation is given in section 4.1 of Jeřábková et al. (2018) and Chapter 12 which investigates the effect of a varying IMF on the properties of local

star-forming galaxies. A recent review of the IGIMF theory can be found in Kroupa and Jerabkova (2021) and a historical overview of the stellar IMF in Kroupa and Jerabkova (2019).

5.4 Potential challenges for a varying IMF

As outlined in the previous sections, the IGIMF theory can be interpreted to be the operator to compute the gwIMF based on empirical scaling relations of star formation. Therefore, the IGIMF theory can be re-formulated (e.g. as already done over the last years by Marks et al. 2012; Marks et al. 2014; Yan, Jerabkova and Kroupa 2020; Yan, Jeřábková and Kroupa 2021; Yan, Jerabkova and Kroupa 2023) and adapted by taking into account new observational constraints. However, the IGIMF formulations still can be tested for internal inconsistencies. Furthermore, it has to be investigated if fundamental observed scaling relations of galaxies (see also Section 4.3) are still preserved for a varying gwIMF within the IGIMF context.

5.4.1 Baryonic Tully-Fisher relation

The baryonic Tully Fisher relation (BTFR; Tully and Fisher 1977; McGaugh et al. 2000; Lelli, McGaugh and Schombert 2016, and here discussed in the light of MOND in Section 4.1) states that the baryonic mass, $M_{\rm b}$, scales with the flat part of the rotation curve, $V_{\rm f}$, of a galaxy via

$$M_{\rm b} \propto V_{\rm f}^4 \,, \tag{5.9}$$

with

$$M_{\rm b} = M_{\rm gas} + M_* \tag{5.10}$$
$$= M_{\rm gas} + \Upsilon_{3.6\mu{\rm m}}\, L_{3.6\mu{\rm m}} \,, \tag{5.11}$$

where $M_{\rm gas}$ is the gas mass, $L_{3.6\mu{\rm m}}$ is the $3.6\,\mu$m luminosity (Spitzer photometry), and $\Upsilon_{3.6\mu{\rm m}}$ is the corresponding stellar (including remnants) mass-to-light ratio.

Lelli et al. (2019) analysed the Spitzer Photometry and Accurate Rotation Curve (SPARC) database and found

$$M_{\rm b} \propto V_{\rm f}^{3.85\pm0.09} \,, \tag{5.12}$$

with an orthogonal scatter of only $\sigma_\perp = 0.026 \pm 0.007$ by assuming a constant stellar mass-to-light-ratio of $\Upsilon_{3.6\mu{\rm m}} = 0.5\, M_\odot/L_\odot$ for a canonical IMF (right panel of Figure 4.2). Note that the power-law index is with 3.85 ± 0.09 slightly smaller than the value of 4 predicted by MOND (Section 4.3).

Importantly, the mass-to-light ratio depends on the star formation history, metallicity, and stellar IMF. Thus, if the gwIMF varies systematically with SFR and metallicity (Equation 12.12) rather than being constant, then the question arises whether the BTFR is consistent with a varying IMF (see also the discussion of section 4.3.2 in Jeřábková et al. 2018) as the mass-to-light ratio would vary. This has been noted in McGaugh and Schombert (2015) who wrote in their section 3.3:

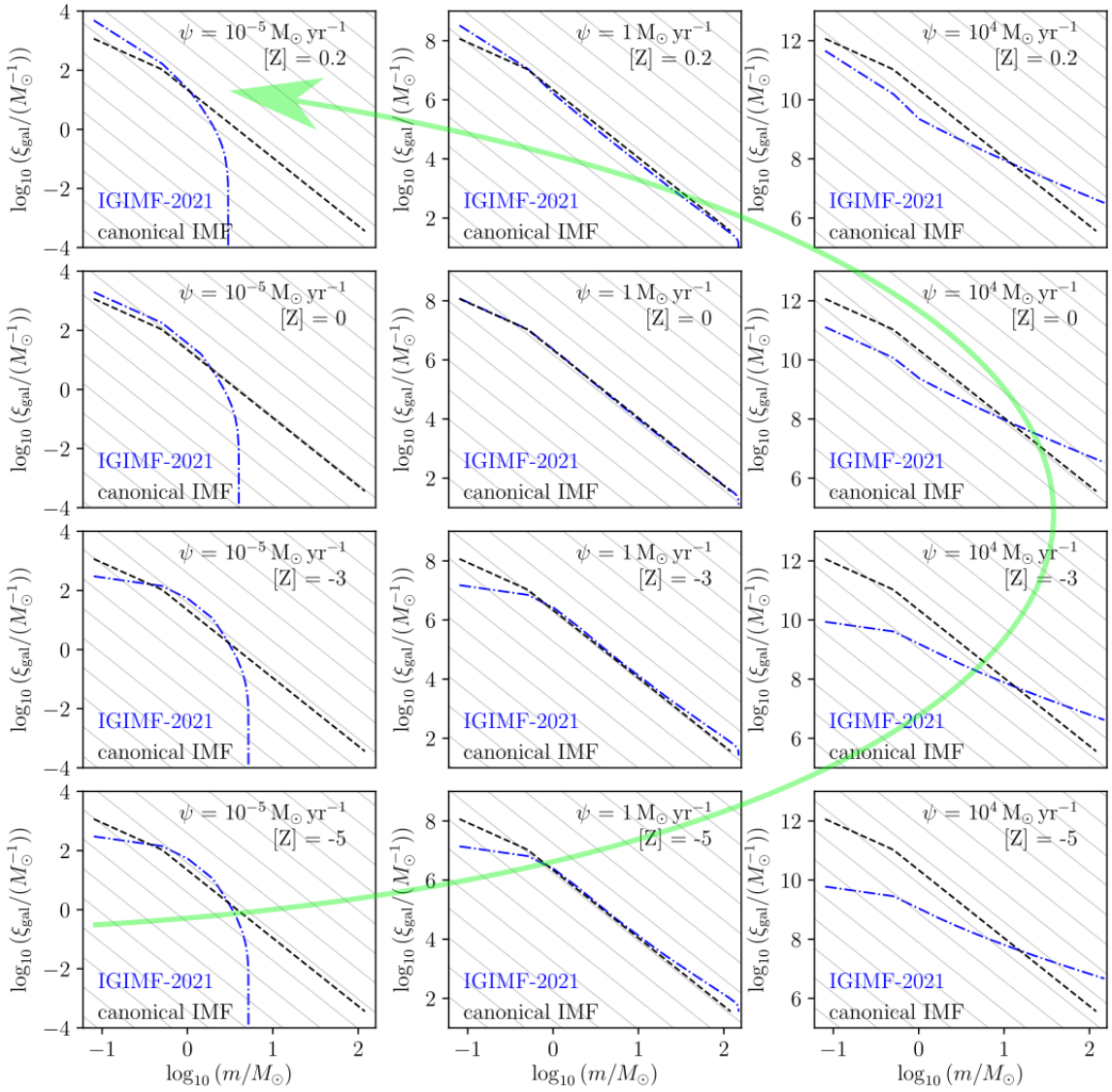

Figure 5.2: Grid of gwIMFs in dependence of the SFR (from left to right: $\psi = 10^{-5}, 1, 10^{4}$ $M_\odot\,yr^{-1}$) and metallicity (from bottom to top: [Z]= -5,-3,0,1) for the IGIMF formulation of Yan, Jeřábková and Kroupa (2021) (blue dot-dashed lines) and the canonical IMF (dashed black lines; Kroupa 2001). The gwIMFs are normalized by the mass formed over 10 Myr. The light green arrow schematically illustrates the time evolution of the gwIMF in a typical early type galaxy starting with a low SFR and metallicity (bottom left panel). A more detailed discussion of the time evolution of the gwIMF can be found in Chapter 12 and figure 2 in Jeřábková et al. (2018). Credit: figure made by the author of this thesis based on figure 2 of Jeřábková et al. (2018) and Figure 12.1 in Chapter 12 using the Python 3 module "GalIMF" developed by Yan, Jerabkova and Kroupa (2017).

> *"It thus appears that the observed scatter is entirely explained by random errors plus the expected scatter in mass-to-light ratios. The scatter in Υ_* is consistent with that expected from the inevitable variations in star formation histories. This leaves essentially no room for variations in the IMF from galaxy to galaxy. Apparently, the IMF in disk galaxies is universal, at least averaged over the many star formation events that build a galactic disk over a Hubble time."* (McGaugh and Schombert 2015)

which they affirm in their conclusion:

> *"This consistency implies that the variation in star formation history from galaxy to galaxy suffices to explain the observed scatter, leaving little room for other sources of scatter. This in turn implies that the IMF is effectively universal, at least when averaged over entire galaxies."* (McGaugh and Schombert 2015)

Studying the effect of a varying IMF on the BTFR requires the time evolution of the mass-to-light ratio at the 3.6 μm Spitzer photometry within the IGIMF context. In Chapter 12, we introduce the photometric GalIMF (photGalIMF) code which couples the GalIMF by Yan, Jerabkova and Kroupa (2017) and Yan et al. (2019) with stellar isochrones enabling to compute the photometric properties of galaxies for a canonical but also for a varying IMF. Therefore, the photGalIMF code would allow to investigate the BTFR within the IGIMF framework (Section 13.2).

CHAPTER 6

Scientific research questions addressed in this thesis

"In so far as a scientific statement speaks about reality, it must be falsifiable: and in so far as it is not falsifiable, it does not speak about reality."
(Popper 1959)

The previous Chapters 3-5 established the scientific context and theoretical background of this thesis, which is based on the following listed four peer-reviewed scientific papers and two manuscripts (submitted) led by the author of this doctoral thesis:

1. **Haslbauer M.**, Banik I., Kroupa P. (2020), *The KBC void and Hubble tension contradict ΛCDM on a Gpc scale − Milgromian dynamics as a possible solution*, Monthly Notices of the Royal Astronomical Society, 499, 2845

2. **Haslbauer M.**, Banik I., Kroupa P., Wittenburg N., Javanmardi B. (2022), *The High Fraction of Thin Disk Galaxies Continues to Challenge ΛCDM Cosmology*, The Astrophysical Journal, 925, 183

3. **Haslbauer M.**, Kroupa P., Zonoozi A. H., Haghi H. (2022) *Has JWST Already Falsified Dark-matter-driven Galaxy Formation?*, The Astrophyical Journal Letters, 939, L31

4. **Haslbauer M.**, Kroupa P., Jerabkova T. (2023), *The cosmological star formation history from the Local Cosmological Volume of galaxies and constraints on the matter homogeneity*, Monthly Notices of the Royal Astronomical Society, 524, 3252

5. **Haslbauer M.**, Banik I., Kroupa P., Zhao H., *The Magellanic Clouds are very rare in the IllustrisTNG simulations*, submitted

6. **Haslbauer M.**, Yan Z., Jerabkova T., Kroupa P., Zonoozi A. H., Gjergo E., *The effect of the environment-dependent stellar initial mass function on the properties of local star-forming galaxies*, submitted

The four published papers are attached in the Appendices A and D, and their main-scientific results are summarized in the Chapters 7-9 and Chapter 11. The two manuscripts, which are included in the Chapters 10 and 12 and Appendices E and F, have been submitted to peer-reviewed scientific journals.

In general, the thesis can be thematically divided in two parts which are, however, connected as outlined at the end of this chapter. The projects of the first part focus on testing the standard model of cosmology (ΛCDM; Chapter 3) by comparing cosmological simulations of galaxy evolution and structure formation with observations on small but also on large scales. The projects include a discussion of interpreting the observations in Milgromian dynamics (MOND; Chapter 4). The second part investigates the integrated galactic initial mass function (IGIMF; Chapter 5) theory on stellar populations of galaxies in a cosmological context which was partly conducted during a four month research visit at the European Southern Observatory (ESO) in Garching bei München (Germany). The following sections summarize the main scientific questions addressed in the research projects of this thesis (see the green boxes), which will be answered in the subsequent Chapters 7-12 followed by an outlook and conclusion in Chapter 13.

6.1 Testing ΛCDM cosmology

At the beginning of Chapter 1 we briefly discussed that the rejection of a well-established theoretical framework requires independent falsifications. Therefore, my collaborators and I tested the ΛCDM model in both the local and early Universe but also on small and large scales. The here-presented tests in combination with previous reported challenges of the ΛCDM model reviewed in Section 3.3 and their interpretation in alternative cosmological frameworks can point the way out of the current crisis of cosmology (Kroupa et al. 2010; Kroupa 2012; Kroupa 2015; Kroupa et al. 2023).

6.1.1 Local Universe

The local Universe provides access to the most-model-independent observational data and allows for precise position and proper motion measurements (e.g. by the Hubble Space Telescope or Gaia mission) of galaxies, which can be used for a comparison with cosmological and gravitational theories. An interesting local astrophysical laboratory is the configuration of the Small and Large Magellanic Clouds (SMC and LMC) which are the closest interacting (dwarf) galaxies observed from the Milky Way (MW) galaxy with a Galactocentric distance of 61.3 kpc and 50.0 kpc, respectively, and a mutual separation of only 24.5 kpc. This spatial configuration of the LMC-SMC-MW system implies that their cold dark matter haloes overlap such that dynamical friction (Section 3.3.1) causes their orbits to decay. Quantifying the efficiency of dynamical friction on galactic scales allows therefore to draw conclusions on the existence and nature of cold dark matter haloes. In the research project presented in Chapter 10, we quantified the likelihood of the spatial and kinematical configuration of the observed SMC-LMC-MW system within the ΛCDM framework using the simulation runs of the IllustrisTNG project (Section 3.2.2). The project also includes a discussion of the formation and evolution of the SMC-LMC-MW system and its connection with the DoS around the MW (Section 3.3.7) in both the ΛCDM and MOND frameworks.

Scientific research questions addressed in Haslbauer, Banik, Kroupa and Zhao (submitted):

- How likely is the observed phase-space density configuration of the LMC-SMC-MW system in the ΛCDM framework?
- How likely are the properties of the observed LMC in the ΛCDM framework?
- Can the DoS observed around the MW be explained by a group infall of LMC satellites?
- How does the LMC-SMC-MW system form in the ΛCDM framework?
- How does the LMC-SMC-MW system form in the MOND framework?

(see Chapter 10 and Appendix E)

In the research project published in Haslbauer, Banik, Kroupa, Wittenburg and Javanmardi (2022), we focused on the galaxy population in the local Universe. The dynamical and morphological properties of galaxies (Section 2.5) provide information about their evolutionary history, because (dispersion-dominated) roundish and elliptical galaxies may either have formed from a direct gas-cloud collapse (Eappen et al. 2022), or they have have undergone minor and major mergers causing a thickening of the galactic disks, while (rotation-dominated) spiral galaxies cannot have had significant merging histories in order to sustain their thin galactic disk. The ΛCDM framework is a hierarchical merger-driven galaxy evolution model in which the galaxies grow through minor and major mergers due to dynamical friction (Section 3.3.1) acting on the dark matter haloes of interacting galaxies. Therefore, comparing observed and simulated morphological distributions of galaxies can be used as a test of galaxy evolution and formation models.

Observationally, Delgado-Serrano et al. (2010) showed that the majority of galaxies in the Sloan Digital Sky Survey (SDSS; York et al. 2000; Abazajian et al. 2005) with $M_* > 1.5 \times 10^{10}\,M_\odot$ are spiral galaxies while ellipticals only account for a small fraction as visualized in Figure 6.1. It has been known for a long time that the observed galaxy population poses a challenge to cold dark matter-based simulations, which suffer from a loss of angular momentum (Section 3.3.6) producing therewith too roundish galaxies. However, Vogelsberger et al. (2014a) announced that this angular momentum problem has been now finally resolved in the Illustris-1 simulation:

> *"Simulating the formation of realistic disk galaxies, like our own Milky Way, has remained an unsolved problem for more than two decades. The culprit was an angular momentum deficit leading to too high central concentrations, overly massive bulges and unrealistic rotation curves. The fact that our calculation naturally produces a morphological mix of realistic disk galaxies coexisting with a population of ellipticals resolves this long-standing issue. It also shows that previous futile attempts to achieve this were not due to an inherent flaw of the ΛCDM paradigm, but rather due to limitations of numerical algorithms and physical modelling."* (Vogelsberger et al. 2014a)

The fact that the Illustris-1 simulation produces a mix of different morphologies of galaxies does not necessarily imply that the angular momentum problem has *indeed* been resolved in the

ΛCDM framework. Moreover, the simulations have to produce the correct distribution of spiral and elliptical galaxies rather than just forming "a morphological mix" of these galaxy types. In Haslbauer, Banik, Kroupa, Wittenburg and Javanmardi (2022), we re-addressed this problem by comparing the present-day sky-projected aspect ratio distribution of galaxies formed in the simulation runs the Illustris, IllustrisTNG (Section 3.2.2), and EAGLE projects (Section 3.2.3) with local observations.

Scientific research questions addressed in Haslbauer, Banik, Kroupa, Wittenburg and Javanmardi (2022):

- Is the present-day sky-projected aspect ratio distribution of galaxies formed in the state-of-the-art ΛCDM simulations consistent with local observations?
- How does the aspect ratio distribution of galaxies with a quiet merging history differ from those with an active merger history?
- What is the aspect ratio of a typical galaxy formed in the MONDian framework?

(see Chapter 8 and Appendix B)

6.1.2 Early Universe

Observations of astrophysical objects at high redshifts constrain the age (Section 3.1.2) and therefore the underlying expansion history of the Universe (see e.g. Melia 2023). The properties of galaxies in both the early and local (Section 6.1.1) Universe provide information about the gas and stellar mass buildup of galaxies and cosmic matter cycle.

The JWST (top left panel of Figure 2.13), which was launched in December 2021, is aimed to explore inter alia galaxy formation and evolution in the very early Universe. After the commissioning and testing phase, the JWST started the scientific programme and the "Webb's First Deep Field" (Noirot et al. 2023; Carnall et al. 2023) was presented in July 2022 showing galaxies just ≈ 600 Myr after the Big Bang according to the time evolution of the ΛCDM paradigm.[1] Subsequently, several studies reported that the JWST has discovered very luminous galaxy candidates with derived stellar masses of $M_* \gtrsim 10^9\,M_\odot$ for an invariant canonical IMF (Kroupa 2001; Chabrier 2003, and see also Chapter 5) at high photometric redshifts of $z_{\rm phot} \gtrsim 10$ (e.g. Naidu et al. 2022; Naidu et al. 2022; N. J. Adams et al. 2023; Atek et al. 2023; Harikane et al. 2023; Labbé et al. 2023). If these redshifts are spectroscopically confirmed, these objects would have accumulated their stellar mass component in just $\lesssim 500$ Myr after the Big Bang in the ΛCDM model. In the research project published in Haslbauer, Kroupa, Zonoozi and Haghi (2022), we first tested whether these luminous high-redshift galaxy candidates would be consistent with the ΛCDM model assuming that these objects are indeed located at such high redshifts and adopting an invariant canonical IMF. Secondly, we provided the first estimation of their stellar masses for a varying IMF within the IGIMF context (see also the discussion on interpreting photometric observations for a varying IMF in Section 6.2).

[1] See also the discussion of the JWST on the blog post "The James Webb Space Telescope, and the early Universe" by **Moritz Haslbauer** and Pavel Kroupa published on the science blog "The Dark Matter Crisis – The rise and fall of cosmological hypotheses"

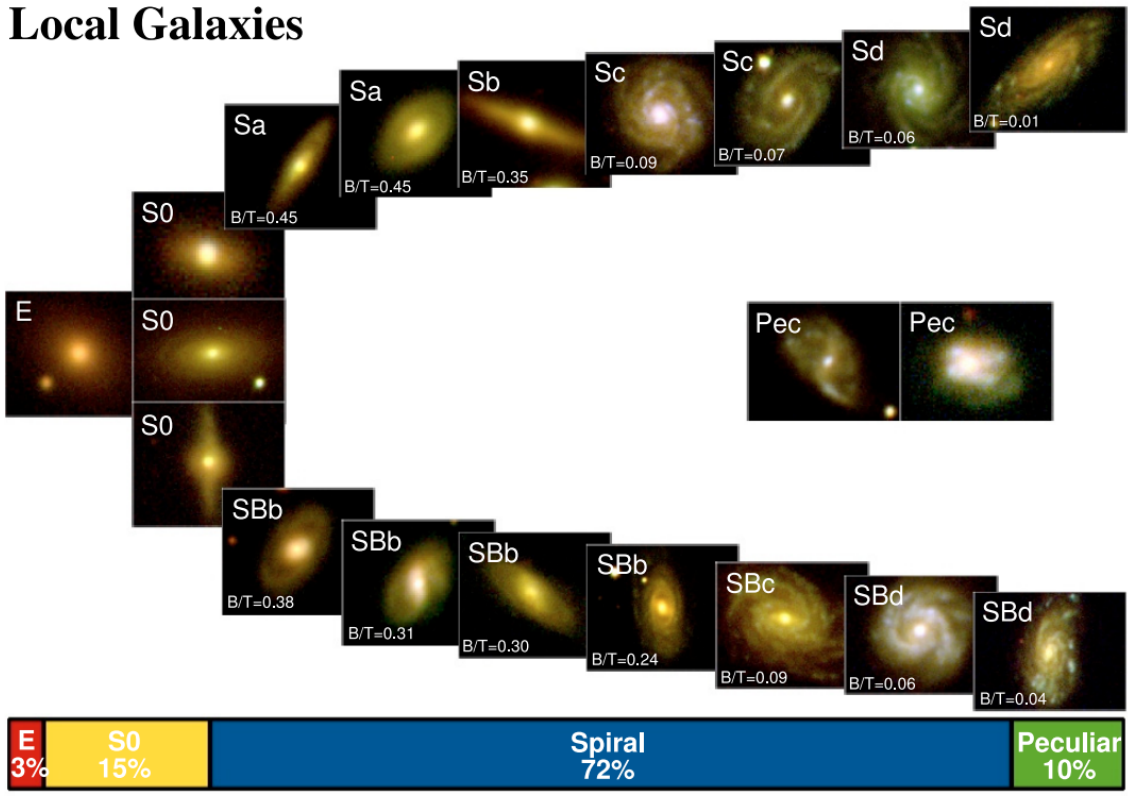

Figure 6.1: Morphological distribution of local galaxies with stellar masses $M_* > 1.5 \times 10^{10}\,M_\odot$ from the SDSS. I.e., 72 ± 8 per cent are spirals, 10 ± 3 per cent are peculiar, 15 ± 4 per cent are lentriculars (S0), and only 3 ± 1 per cent are ellipticals (table 3 of Delgado-Serrano et al. 2010). The galaxy morphological types can be used as a test of galaxy evolution models (see text). Credit: Top panel of figure 5 of Delgado-Serrano et al. (2010).

Scientific research questions addressed in Haslbauer, Kroupa, Zonoozi and Haghi (2022):

- Has JWST already falsified dark-matter-driven galaxy formation?
- Are the galaxy candidates with $M_* \gtrsim 10^9\,M_\odot$ for an invariant canonical IMF at high photometric redshift of $z_{\rm phot} \gtrsim 10$ consistent the stellar mass buildup predicted by the ΛCDM framework?
- How would the stellar masses of the galaxy candidates change if instead a varying gwIMF in the IGIMF context is applied?

(see Chapter 9 and Appendix C)

6.1.3 Large-scales

The advantage of the local Universe is that it provides the most precise and model-independent measurements of galaxy properties. However, the properties of galaxies formed in simulations are not sensitive only to the underlying cosmological framework but also to the adopted baryonic physics such that identified small-scale challenges of the ΛCDM paradigm (Weinberg et al. 2015; Bullock and Boylan-Kolchin 2017) could be potentially resolved by improved sub-grid baryonic physics prescriptions or higher sub-grid and particle resolutions.

Large-scales galaxy distributions are much less sensitive to baryonic physics but the observations at larger distances become less precise and often require model-dependent assumptions e.g. because of projection effects (see also section 5.3.1 of Haslbauer, Banik and Kroupa 2020 and section 8.2 of Banik and Zhao 2022). The advantage of large-scale structures is that they trace more accurately the cosmological and gravitational framework (see also Peebles and Nusser 2010). Moreover, the ΛCDM model reaches homogeneity on scales of $> 260\,h^{-1}$ Mpc (Yadav, Bagla and Khandai 2010, and see also Section 3.1) which functions as a benchmark for observational comparison of large-structures.

6.1.3.1 The KBC void and Hubble tension

Several observational studies reported that the local Universe is much more structured (see e.g. the Sections 3.3.7 and 3.3.9 with the references therein) by being also significantly undersense on scales up to ≈ 300 cMpc (e.g. Maddox et al. 1990; Zucca et al. 1997; Frith et al. 2003; Frith, Metcalfe and Shanks 2006; Karachentsev 2012; Keenan, Barger and Cowie 2013; Rubart and Schwarz 2013; Rubart, Bacon and Schwarz 2014; J. R. Whitbourn and Shanks 2014; Böhringer et al. 2015; Karachentsev and Telikova 2018; Shanks, Hogarth and Metcalfe 2019; Shanks et al. 2019; Böhringer, Chon and Collins 2020; J. H. W. Wong et al. 2022) as shown in Figure 6.2. In particular, Keenan, Barger and Cowie (2013) found that the Universe has a density contrast of only $\delta_{\rm obs} \equiv 1 - \rho/\rho_0 = 0.46 \pm 0.06$ in the redshift range of $0.01 < z < 0.07$ by analyzing the 2M++ catalogue (Lavaux and Hudson 2011), which covers 90 per cent of the sky. This so-called Keenan-Barger-Cowie (KBC) void has therewith a density about two times lower than the cosmic mean density on a co-moving radial distance scale of 300 cMpc (see figure 9 and table 1 of Keenan, Barger and Cowie 2013, and the light blue data point in Figure 6.2), while the σ_8 parameter (see the definition in Section 3.3.11) predicts root-mean-square density fluctuations of only 3.2 per cent on radial distance scales of 300 cMpc for the ΛCDM model.

In the first part of the research project published in Haslbauer, Banik and Kroupa (2020), we tested if the locally observed KBC void (Keenan, Barger and Cowie 2013) can arise in the ΛCDM cosmology using the MXXL simulation (Section 3.2.1). Figure 6.2 suggests that we are closely located to the centre of the KBC void causing an interesting effect potentially explaining why the locally measured Hubble constant is about 9% higher than derived from probes in the early Universe (Section 3.3.10). Galaxies within the void experience a gravitational attraction from the surrounding denser structures outside the void which causes outflows from the void centre as schematically illustrated by the red arrows in Figure 6.3. The local Universe would appear then to expand faster than on global scales because of the additional motion of the galaxies towards the void edges. Thus, we also investigate the connection between the KBC void and Hubble tension within the ΛCDM framework. In the second part, we re-address the situation in a MOND cosmology (Section 4.2). The concept of this research project is graphically outlined in Figure 6.3.

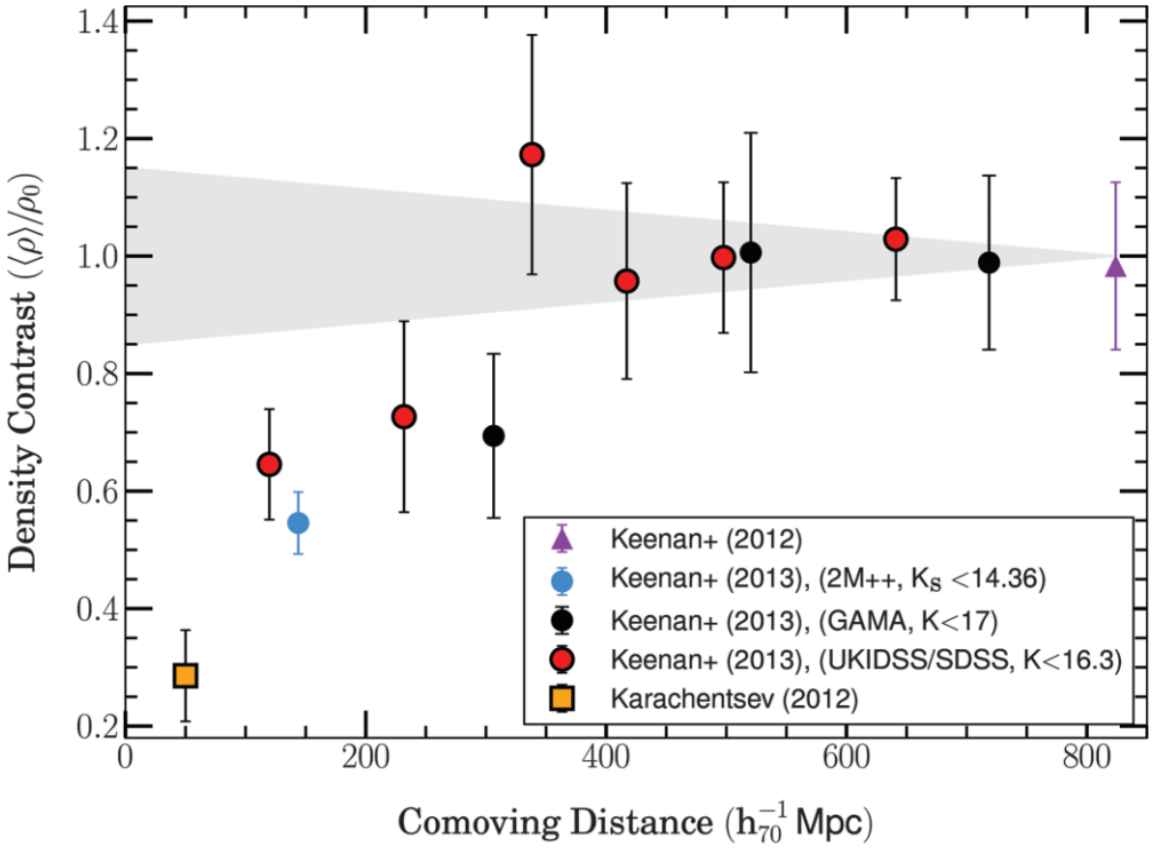

Figure 6.2: Observed density contrast, $\langle\rho\rangle/\rho_0$, in dependence of the co-moving radial distance assuming $H_0 = 70\,\mathrm{km\,s^{-1}\,Mpc^{-1}}$ and $h_{70} = 1$. The light blue data point marks $\langle\rho\rangle/\rho_0 = 0.54 \pm 0.06$, which has been derived over the redshift range of $0.01 < z < 0.07$ (corresponding to a co-moving radial distance range of 40-300 cMpc) based on the 2M++ catalogue with a limiting magnitude of $K_s < 14.36$ in the Ks-band covering 90 per cent of the sky (see figure 9 and table 1 of Keenan, Barger and Cowie 2013). The orange square refers to the measured density within a sphere with a radius of 50 Mpc (Karachentsev 2012, and see also Section 3.3.9). The black and red circles have been obtained from the GAMA survey with a limiting K-band magnitude of $K < 17$ and UKIDSS/SDSS with $K < 16.3$ (Keenan, Barger and Cowie 2013). The violet up-pointing triangle is taken from Keenan et al. (2012). The grey shaded region estimates the density fluctuations expected in the ΛCDM model but see Chapter 7 for a more sophisticated and quantitatively comparison between the observations and the ΛCDM model. Credit: figure 1 of Kroupa (2015).

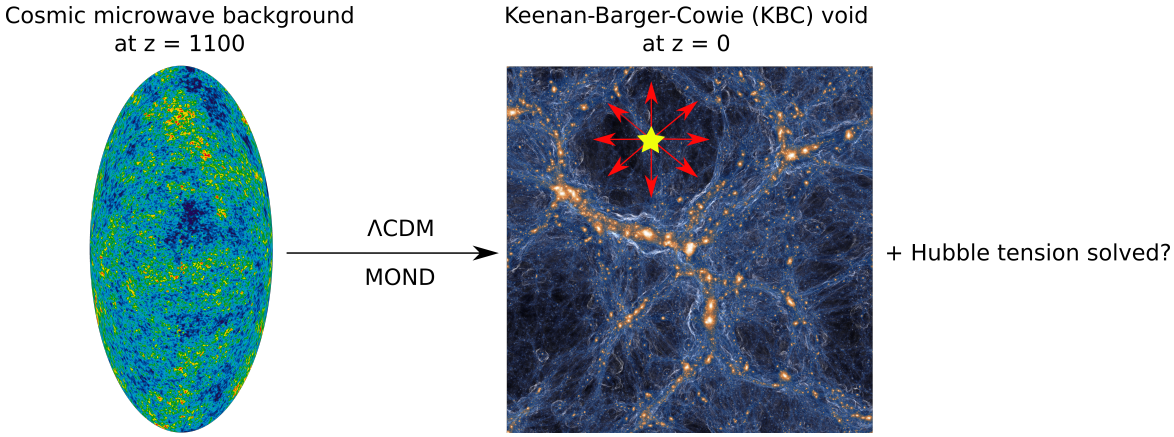

Figure 6.3: Concept outline of the research project published in Haslbauer, Banik and Kroupa (2020) in which we study the formation of the locally observed KBC void (see Figure 6.2) and its implication on the Hubble tension (Section 3.3.10) in both the ΛCDM (Section 3) and MOND (νHDM; Section 4.2) framework. Starting with the initial conditions defined by the CMB at redshift $z = 1100$, we first quantified the likelihood of the existence of KBC-void-like structures at $z = 0$ in the ΛCDM framework by mimicking the observations by Keenan, Barger and Cowie (2013) in the MXXL simulation (Section 3.2.1). We investigate if outflows (illustrated by the red arrows) from the void centre (yellow star) would explain the locally measured higher value of H_0. Secondly, we tested if both the KBC void and Hubble tension can be explained in the νHDM model. The main results of the project are summarized in the Chapter 7 and the corresponding paper is attached in Appendix A. Credit: Figure made by the author of the thesis based on figure 3 of the blog post "Solving both crises in cosmology: the KBC-void and the Hubble-Tension" published on the science blog "The Dark Matter Crisis – The rise and fall of cosmological hypotheses" using the heat map of the CMB by the 9th year WMAP (credit: NASA/WMAP Science Team (downloaded from Wikipedia on 16.09.2023), Public Domain) and the projected density map of the TNG100-1 simulation box (credit: TNG Collaboration (downloaded from the TNG project website on 30.10.2023), the red arrows and yellow star have been added by the author of the thesis).

Scientific research questions addressed in Haslbauer, Banik and Kroupa (2020):

- Is the KBC void consistent with structure formation predicted by the ΛCDM framework?
- If yes, can the KBC void explain the Hubble tension within the ΛCDM framework?
- Is the KBC void consistent with structure formation in a MOND cosmology?
- If yes, can the KBC void explain the Hubble tension in a MOND cosmology?

(see Chapter 7 and Appendix A)

6.1.3.2 The SFHs of local galaxies and the Lilly-Madau plot

The research project conducted in Haslbauer, Kroupa and Jerabkova (2023) investigates the cosmological implications of the analysis presented in Kroupa et al. (2020), who reported that galaxies located in the Local Cosmological Volume (LV; Karachentsev et al. 2004; Karachentsev, Makarov and Kaisina 2013) have an almost constant star formation history (SFH). The Lilly-Madau plot (Lilly

et al. 1996; Madau et al. 1996; Madau, Pozzetti and Dickinson 1998; Cole et al. 2001; Madau and Dickinson 2014; Madau and Fragos 2017) shows that the star-formation-rate density (SFRD) increases from redshift $z = 0$ up to the Lilly-Madau peak at $z = 1.87$ by a factor of ≈ 9 (see the figure 9 of Madau and Dickinson 2014), which is typically interpreted as the global SFH of the Universe.

Scientific research questions addressed in Haslbauer, Kroupa and Jerabkova (2023):

- Is the SFH of local galaxies consistent with the Lilly-Madau plot?
- What are the cosmological implications of the SFH of local galaxies?

(see Chapter 11 and Appendix D)

6.2 Galaxy-wide IMF in a cosmological context

Testing cosmological models by comparing simulations with observations requires to take into account that the properties of galaxies are also affected by baryonic and star formation physics. The stellar IMF is a fundamental parameter in galaxy formation and evolution as it defines the stellar population of a galaxy. The invariant canonical IMF (i.e. Chabrier 2003 which is next-to-identical to Kroupa 2001) is typically implemented in hydrodynamical cosmological simulations such as those of the Illustris, IllustrisTNG, or EAGLE project. However, as discussed in the previous Chapter 5, star-forming regions suggest that the stellar IMF systematically varies with the star formation rate and metallicity with significant implications for deriving the stellar masses or star formation rates of galaxies from photometric measurements. The linear SFR–Hα-luminosity relation given by the Kennicutt law (Kennicutt 1998) for a Salpeter (invariant) IMF becomes invalid for a varying IMF (Pflamm-Altenburg, Weidner and Kroupa 2009; Jeřábková et al. 2018, but also Chapter 12) such that galaxies with Hα luminosities of $L_{\mathrm{H}\alpha} \lesssim 10^{40}\,\mathrm{erg\,s^{-1}}$ can be 10 – 100 times higher, while galaxies with $L_{\mathrm{H}\alpha} \gtrsim 10^{43}\,\mathrm{erg\,s^{-1}}$ have up to ≈ 10 times lower SFRs within the IGIMF context. Thus, a varying IMF has significant implications for interpreting the stellar mass buildup times of galaxies or galactic and cosmic matter cycle (Kroupa and Jerabkova 2021) showing that galaxy evolution is an interplay between the gwIMF and the underlying cosmological paradigm as discussed in Figure 6.4.

The research project presented in Chapter 12 aims towards considering the stellar populations of nearby galaxies in a cosmological context by studying the main-sequence, stellar mass buildup timescale, and gas depletion timescale (star formation efficiency) of local star-forming galaxies for both an invariant canonical and varying gwIMF within the IGIMF theory. In this project, we also developed the photometric GalIMF (photGalIMF) package for the chemical evolution code GalIMF (Yan, Jerabkova and Kroupa 2017; Yan et al. 2019) which calculates photometric properties of galaxies for an invariant canonical but also for a varying gwIMF. This allows to interpret photometric measurements for different gwIMFs enabling more precise tests for cosmological galaxy evolution models. An outlook for further projects based on the photGalIMF code is presented in Section 13.2.

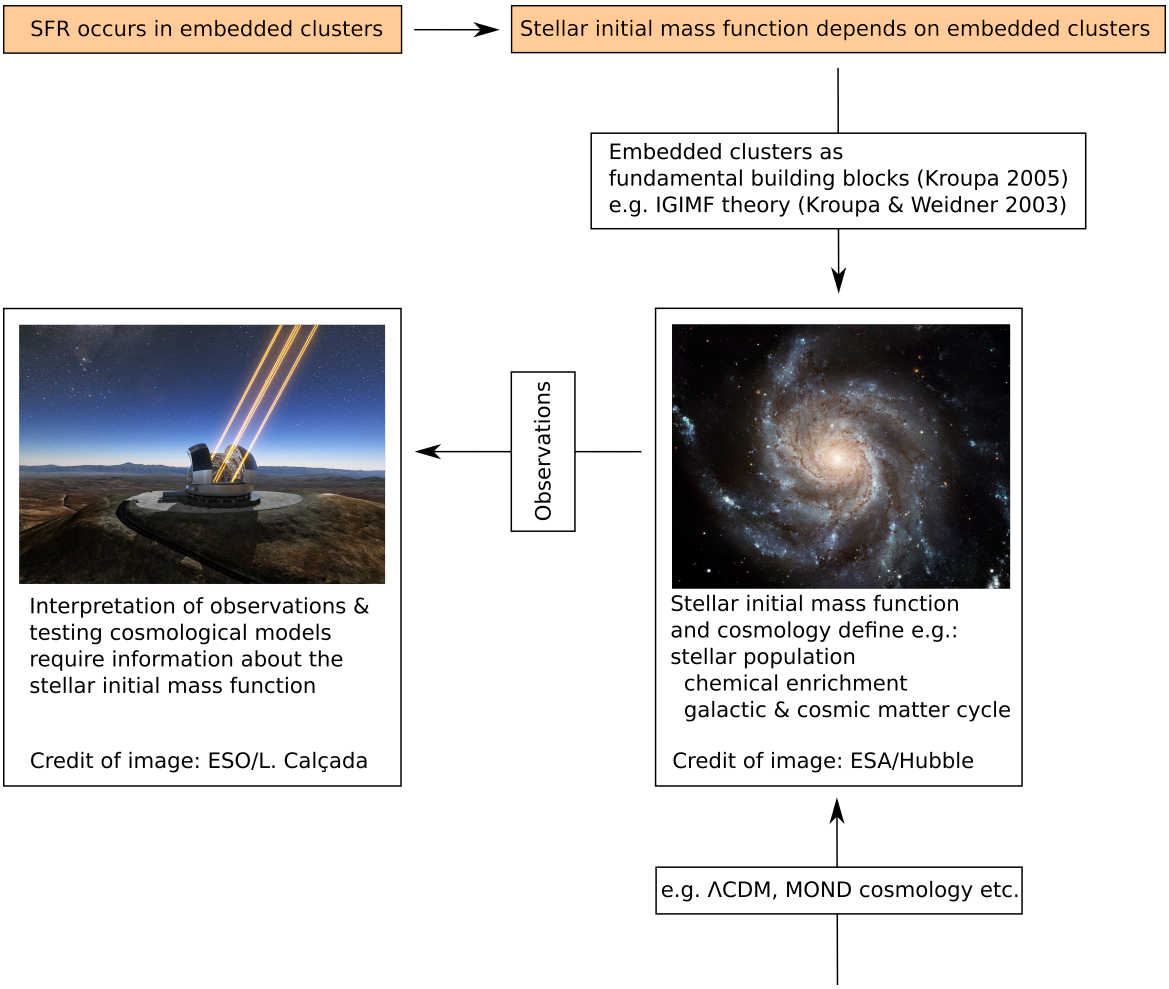

Figure 6.4: The galaxy-wide IMF (gwIMF) in a cosmology context. Star formation occurs in embedded clusters some of which evolve to young open star clusters formed out of giant molecular clouds. The stellar IMF depends on the properties of the embedded cluster (Section 5.3). Considering that the embedded clusters are the fundamental building blocks of galaxies (Kroupa 2005), the IGIMF theory allows of the calculations of the gwIMF by summing up the stellar IMFs of all embedded clusters (Kroupa and Weidner 2003). Thus, the properties of galaxies are affected by the underlying cosmological paradigm and the stellar IMF which both influence the stellar population, chemical enrichment, and galactic and cosmic matter cylce (see text). Comparing observations with galaxy formation and evolution simulations requires assumptions about the stellar IMF (see e.g. also the Chapters 9 and 12). Credits: Figure made by the author of the thesis using an illustration of the ELT (Credit: ESO/L. Calçada (downloaded from Wikipedia on 30.10.2023), CC BY 4.0) and an image of the galaxy M101/NGC 5457 taken by the HST (Credit: ESA/Hubble (downloaded from Wikipedia on 30.10.2023), CC BY 4.0 Deed).

Scientific research questions addressed in Haslbauer, Yan, Jerabkova, Kroupa, Zonoozi and Gjergo (submitted):

- How does the main-sequence of local star-forming galaxies differ for a canonical IMF and a varying IMF within the IGIMF context?
- How do the stellar mass buildup time-scales of galaxies depend on the stellar mass for a canonical IMF and a varying IMF within the IGIMF?
- How do the gas depletion time-scales (the star formation efficiencies) of galaxies depend on the gas mass for a canonical IMF and a varying IMF within the IGIMF context?

(see Chapter 12 and Appendix F)

CHAPTER 7

The KBC void and Hubble tension in the ΛCDM model and Milgromian dynamics

"Creativity is essential to particle physics, cosmology, and to mathematics, and to other fields of science, just as it is to its more widely acknowledged beneficiaries - the arts and humanities."
(Randall 2012)

This chapter summarizes the main scientific findings and author contributions of the peer-reviewed paper entitled "The KBC void and Hubble tension contradict ΛCDM on a Gpc scale – Milgromian dynamics as a possible solution" published in the journal Monthly Notices of the Royal Astronomical Society, 499, 2845, 2020 by **Moritz Haslbauer**, Indranil Banik, and Pavel Kroupa (hereafter Haslbauer, Banik and Kroupa 2020). A copy of the paper in its original form is attached in the Appendix A.

The interested reader may find a further summary of the paper aimed for the broader public in the blog post "Solving both crises in cosmology: the KBC-void and the Hubble-Tension" by **Moritz Haslbauer** published on the science blog "The Dark Matter Crisis – The rise and fall of cosmological hypotheses".

7.1 Summary

According to the Cosmological Principle (Section 3.1) the Universe becomes homogeneous and isotropic if observed on large enough scales. The ΛCDM framework is expected to reach homogeneity on scales of $\gtrsim 260\,h^{-1}$ cMpc but the local Universe appears to be much more structured (see also Section 3.3.9) by being significantly underdense on scales at least up to co-moving radial distances of ≈ 300 cMpc (see the radial density profile shown in Figure 6.2). A local underdensity is observed across the entire electromagnetic spectrum ranging from X-ray galaxy cluster observations (Böhringer et al. 2015; Böhringer, Chon and Collins 2020), via galaxy counts in the infrared (Keenan, Barger and Cowie 2013) and optical (Maddox et al. 1990; Zucca et al. 1997) and also to radio wavelengths observations (Rubart and Schwarz 2013; Rubart, Bacon and Schwarz 2014). In particular, Keenan, Barger and Cowie (2013) analyzed the local matter distribution by using the 2M++ catalogue (Lavaux and Hudson 2011) which covers 90% of the sky. They found a density contrast of $\delta_{\rm obs} \equiv 1 - \rho/\rho_0 = 0.46 \pm 0.06$ over the redshift range of $0.01 < z < 0.07$ (see the light blue data point in figure 11 and table 1 of Keenan, Barger and Cowie 2013), which corresponds to a spherical shell with an inner co-moving

radius of ≈ 40 cMpc and an outer co-moving radius of 300 cMpc. This Keenan-Barger-Cowie (hereafter KBC) void has therewith a density about two times lower than the cosmic mean density on a scale of 300 cMpc but only 3.2 per cent root-mean-square density fluctuations would be expected from structure formation theory of the ΛCDM framework. Matter-inhomogeneities such as the KBC void induces bulk matter flows from the centre towards the void edge adding an additional motion to the galaxies which are located inside the void. Consequently, the local Universe would appear to expand faster than viewed on global scales. In fact, the Hubble tension (Section 3.3.10) states that the locally measured value of the Hubble constant H_0 (see the definition in Section 3.1) is about 9 per cent higher than derived from early time probes of the Universe (see e.g. figure 2 of Di Valentino et al. 2021 and section 1.2 of Haslbauer, Banik and Kroupa 2020) which is nowadays one of the greatest problems faced in modern cosmology. Several solutions have been proposed ranging from early (e.g. Karwal and Kamionkowski 2016; Alexander and McDonough 2019; Poulin et al. 2019; Sakstein and Trodden 2020) to late (e.g. Keenan, Barger and Cowie 2013; Enea Romano 2016; Hoscheit and Barger 2018; Shanks et al. 2019) time solutions. In Haslbauer, Banik and Kroupa (2020), we considered a late time solution by investigating if the matter bulk flows from the locally observed KBC void can explain the Hubble tension in the ΛCDM (Chapter 3) and νHDM (Section 4.2) framework.

7.1.1 The Hubble tension and KBC void in the ΛCDM framework

In the first part of the project (section 2 of Haslbauer, Banik and Kroupa 2020), we quantified the likelihood of the KBC in the ΛCDM framework by determining the N-body MXXL simulation (Section 3.2.1, Angulo et al. 2012) at redshift $z = 0$. We mimicked the observations by Keenan, Barger and Cowie (2013) by calculating the density contrast within spherical shells with an inner co-moving radius of 40 cMpc and an outer radius of 300 cMpc for 10^6 vantage points as shown in the left panel of Figure 7.1. The corresponding analysis yielded that the locally observed KBC void is inconsistent with the ΛCDM framework at the 6.04σ confidence level.

The right panel of Figure 7.1 shows the effect of the apparent density contrast on H_0 for a ΛCDM cosmology revealing that even a 5σ density fluctuation would just not be able to resolve the Hubble tension at the 5σ confidence level. We quantified that the KBC void and Hubble tension together cause a 7.09σ tension demonstrating that the Hubble tension cannot be explained by large-scale matter flows from the KBC void within the ΛCDM framework.

7.1.2 The Hubble tension and KBC void in MOND

Starting with the initial conditions defined by the CMB at redshift $z = 1100$, the existence of the KBC void suggests that structure formation is more enhanced than given by Einsteinian/Newtonian gravity. Therefore, the second part of the project (sections 3 and 4 of Haslbauer, Banik and Kroupa 2020) assesses the formation of the KBC void and Hubble tension in MOND. Large enough cosmological simulations conducted within the MOND framework do not exist such that the likelihood of the KBC void cannot be quantified in the same way as presented for the ΛCDM framework. Therefore, we run semi-analytical models based on the νHDM framework (Section 4.2) in order to calculate the evolution of the density contrast starting at $z = 9$ up to present time for different initial void profiles. The models are constrained by the inner and outer density contrast of the observed KBC void (Keenan, Barger and Cowie 2013), the jointly derived present-day values of $H_0 = 75.35 \pm 1.68\,\mathrm{km\,s^{-1}\,Mpc^{-1}}$ and $q_0 = -1.08 \pm 0.29$ (see the definition of q_0 in Section 3.3.12) from the Pantheon SNe (Scolnic

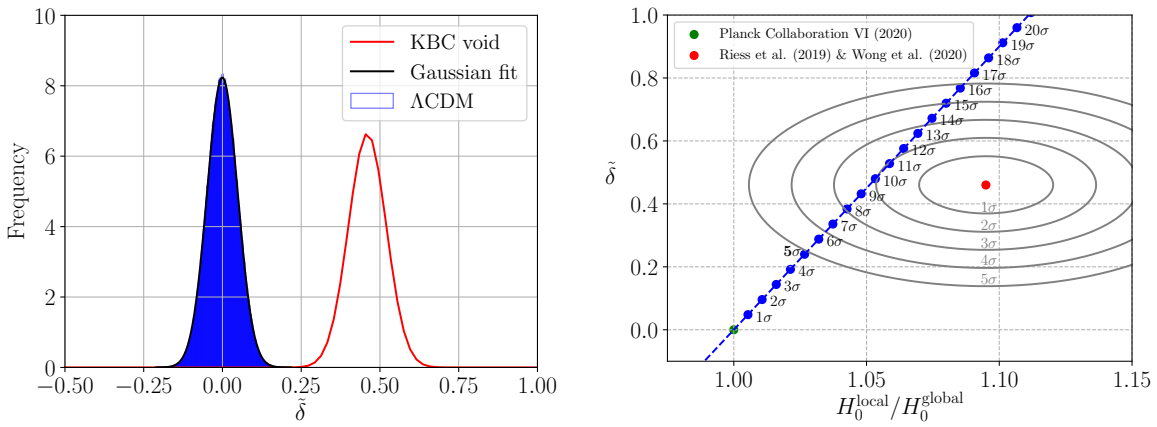

Figure 7.1: The KBC void and Hubble tension in the ΛCDM framework. *Left:* Apparent density distribution, $\tilde{\delta}$, of spherical shells with an inner radius of 40 cMpc and an outer radius of 300 cMpc for 10^6 vantage points at redshift $z = 0$ in the MXXL simulation (blue histograms) which is fitted with a Gaussian function (black solid line). The red line shows the KBC void with an observed density contrast of $\delta_{\rm obs} = 0.46$ and an observational uncertainty of $\sigma_{\rm obs} = 0.06$ (Gaussian error). Credit: figure 1 of Haslbauer, Banik and Kroupa (2020). *Right:* Relation between the apparent density contrast, $\tilde{\delta}$, and the local Hubble constant scaled by the value of the global Hubble constant, $H_0^{\rm local}/H_0^{\rm gobal}$. The green dot refers to the cosmic mean density such that $\tilde{\delta} = 0$ and to the global Hubble constant value of $H_0^{\rm global} = 67.4 \pm 0.5\,{\rm km\,s^{-1}\,Mpc^{-1}}$ (Planck Collaboration VI 2020b) while the red dot marks the locally observed KBC void with $\delta_{\rm obs} = 0.46 \pm 0.06$ (Keenan, Barger and Cowie 2013) and locally measured $H_0^{\rm local} = 73.8^{+1.1}_{-1.1}\,{\rm km\,s^{-1}\,Mpc^{-1}}$ (Riess et al. 2019; K. C. Wong et al. 2020). The grey contour lines show the corresponding confidence levels. The blue dots on the straight blue line mark the confidence levels of the expected apparent cosmic variance in the ΛCDM framework. Credit: figure 2 of Haslbauer, Banik and Kroupa (2020).

et al. 2018) in the redshift range of $0.023 < z < 0.15$ (Camarena and Marra 2020), the velocity of the LG wrt. the CMB ($627\,{\rm km\,s^{-1}}$; Kogut et al. 1993), and seven further values of H_0 derived from seven different gravitational lenses (Shajib et al. 2020; K. C. Wong et al. 2020). The left panel of Figure 7.2 compares the evolution of the density contrast in our best-fitting MOND model and the ΛCDM model demonstrating that structure formation is much more enhanced in MOND because of the stronger effective gravity. This in turn allows for the formation of KBC-like voids from which the induced matter bulk flows resolve the Hubble tension. The right panel of Figure 7.2 shows that the locally observed values of H_0 and q_0 jointly derived over the redshift range of $0.023 \leq z \leq 0.15$ agree with our best-fitting model within the 1σ confidence level. In total, our best-fitting model causes only a 2.53σ tension with the applied observational constraints providing therewith a much better description of the local Universe with the νHDM framework compared to the ΛCDM framework.

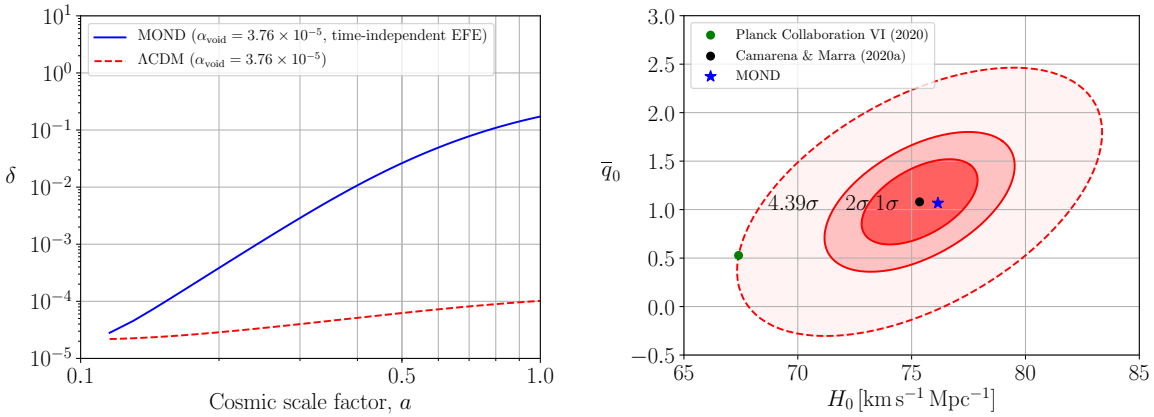

Figure 7.2: The KBC void and Hubble tension in the *ν*HDM framework. *Left:* Comparison of structure formation in the ΛCDM (red dashed line) and our best-fitting MOND (blue solid line) model by showing the true density evolution of a sphere with a co-moving radius of 300 cMpc for an initial density fluctuation of $\alpha_{\rm v} = 3.76 \times 10^{-5}$ at redshift $z = 9$ which corresponds to a cosmic scale factor of $a = 0.1$. Credit: modified version of the right panel of figure 5 of Haslbauer, Banik and Kroupa (2020) by showing only models with the same initial density fluctuation and a time-independent external field effect (EFE). *Right:* Comparison of the Hubble constant, H_0, and the acceleration parameter, $\overline{q}_0 \equiv -q_0$ (see the definition of q_0 in Section 3.3.12), jointly derived over the redshift range of $0.023 \leq z \leq 0.15$. The black dot shows the jointly derived values obtained by Camarena and Marra (2020) from the Pantheon SNe, while the blue point refers to our best-fitting MOND model. The green dot marks the global values derived from the CMB (Planck Collaboration VI 2020b), which differ with the observations by Camarena and Marra (2020) at 4.39σ. Credit: modified version of figure 6 of Haslbauer, Banik and Kroupa (2020) by showing only the best-fitting MOND model.

Scientific research questions addressed in Haslbauer, Banik and Kroupa (2020):

- **Is the KBC void consistent with structure formation predicted by the ΛCDM framework?**
  No, because the KBC void falsifies the ΛCDM model at the 6.04σ confidence level.
- **If yes, can the KBC void explain the Hubble tension within the ΛCDM framework?**
  No, the KBC void and Hubble tension both individually falsify the ΛCDM model at the $> 5\sigma$ confidence level. Combining the KBC void and Hubble tension falsifies the ΛCDM model at the 7.09σ confidence level.
- **Is the KBC void consistent with structure formation in a MOND cosmological model?**
  Yes, the enhanced structure formation allows the formation for KBC-like void in a MOND cosmological model.
- **If yes, can the KBC void explain the Hubble tension in a MOND cosmological model?**
  Yes, outflows from the KBC void explains the locally measured Hubble constant. Thus, the Hubble tension is a natural consequence of structure formation in MOND.

(see also Appendix A)

7.2 Author contributions

The authors of the corresponding publication are **Moritz Haslbauer** (MH), Indranil Banik (IB), and Pavel Kroupa (PK). PK had the idea to quantify the likelihood of the Keenan-Barger-Cowie (KBC) void in the ΛCDM framework (see e.g. the discussion in Kroupa 2015). He also proposed to investigate if the KBC void forms in Milgromian dynamics and if so whether outflows from the KBC void can in turn explain the Hubble tension. IB suggested to adopt for this project a MOND cosmology supplemented by sterile neutrinos. MH and IB wrote the codes to quantify the likelihood of the existence of the KBC void in the MXXL simulation. IB and MH developed the governing equations of the νHDM and wrote the semi-analytical simulation to calculate structure formation in the νHDM and ΛCDM framework. MH and IB wrote the codes to analyze the semi-analytical νHDM and ΛCDM model. MH wrote the manuscript with passages and comments by all co-authors. MH created the figures of the paper. All authors contributed by discussions to the interpretation of the results.

CHAPTER 8

The morphological distribution of galaxies in the ΛCDM framework

"No one trusts a model except the man who wrote it;
everyone trusts an observation, except the man who made it."
(Statement by Harlow Shapley as documented in Lorenz 2019)

This chapter summarizes the main scientific findings and author contributions of the peer-reviewed paper entitled "The High Fraction of Thin Disk Galaxies Continues to Challenge ΛCDM Cosmology?" published in the journal The Astrophysical Journal, 925, 183, 2022 by **Moritz Haslbauer**, Indranil Banik, Pavel Kroupa, Nils Wittenburg, and Behnam Javanmardi (hereafter Haslbauer, Banik, Kroupa, Wittenburg and Javanmardi 2022). A copy of the paper in its original form is attached in the Appendix B.

The interested reader may find a further summary of the paper aimed for the broader public in the blog post "The observed high fraction of thin disk galaxies is incompatible with ΛCDM cosmology: The angular momentum problem in galaxy formation is more severe than ever" by **Moritz Haslbauer** and Pavel Kroupa published on the science blog "The Dark Matter Crisis – The rise and fall of cosmological hypotheses".

8.1 Summary

Galaxies in cold dark matter-based simulations suffer from a loss of angular momentum (e.g. Navarro and Benz 1991; Navarro and White 1994; Navarro and Steinmetz 2000; van den Bosch 2001; Scannapieco et al. 2012) which causes a thickening of the galactic disk. This so-called angular momentum problem is a long-standing problem (Section 3.3.6) of galaxy evolution but Vogelsberger et al. (2014a) argued that the angular momentum problem has been resolved in the Illustris-1 simulation (see their figure 1 and see Section 6.1.1). In Haslbauer, Banik, Kroupa, Wittenburg and Javanmardi (2022), we investigated if the present-day sky-projected aspect ratio distributions of galaxies formed in the state-of-the-art hydrodynamical cosmological ΛCDM simulations are indeed consistent with local observations.

On the observational side, we assessed the updated catalogue of Neighbouring Galaxies (Karachentsev et al. 2004; Karachentsev, Makarov and Kaisina 2013) in order to study the galaxy population of

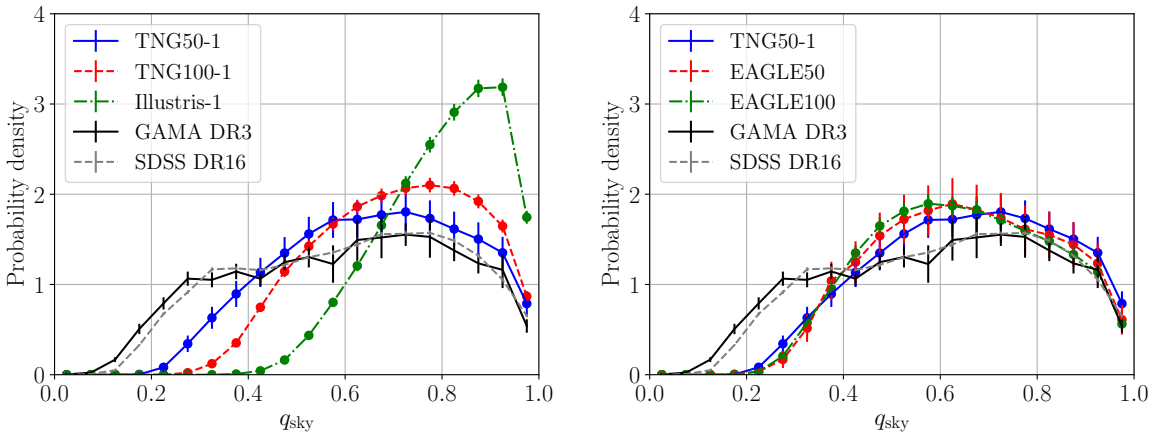

Figure 8.1: Sky-projected aspect ratio, $q_{\rm sky}$, distributions of observed and simulated galaxies with $10.0 < \log_{10}(M_*/M_\odot) \leq 11.65$ formed in the TNG50-1 (blue solid line in the left and right panels), TNG100-1 (red dashed line in the left panel), Illustris-1 (green dotted-dashed in the left panel), Ref-L0050N0752 (hereafter EAGLE50; red dashed in the right panel), and Ref-L0100N1504 (hereafter EAGLE100; green dotted-dashed in the right panel). The black solid line and grey dashed line in both panels refer to the observed sky-projected aspect ratio distributions of galaxies in the GAMA DR3 and SDSS DR16, respectively. An thin disk galaxy observed edge-on would have $q_{\rm sky} \lesssim 0.2$ and a perfect spherical galaxy has $q_{\rm sky} = 1$. Credit: figure 4 of Haslbauer et al. (2022).

the Local Cosmological Volume (see the definition in Section 3.3.9). Selecting galaxies with stellar masses of $M_* > 10^{10}\,M_\odot$, we found that 50 per cent are early-type spirals (i.e. Sa, Sab, Sb, Sbc, Sc), 23 per cent are late-type spirals (i.e. Scd, Sd, Sdm, Sm), and 27 per cent are E, S0, dSph, and S0a galaxies (see also Karachentsev, Kaisina and Makarov 2018) confirming that the majority of local massive galaxies are spirals (Delgado-Serrano et al. 2010). For our main analysis, we used the Galaxy And Mass Assembly (GAMA) DR3 (Baldry et al. 2018) and the Sloan Digital Sky Survey (SDSS York et al. 2000) DR16 (Ahumada et al. 2020) because of their larger sample sizes.

On the theoretical side, we extracted the three-dimensional intrinsic aspect ratios of the simulated galaxies from the publicly available subhalo catalogues of the IllustrisTNG (Pillepich et al. 2018a; Pillepich et al. 2018b; Pillepich et al. 2019; D. Nelson et al. 2018; D. Nelson et al. 2019; D. Nelson et al. 2019; Marinacci et al. 2018; Naiman et al. 2018; Springel et al. 2018), and EAGLE (Crain et al. 2015; Schaye et al. 2015; McAlpine et al. 2016) projects (see also Sections 3.2.2-3.2.3) projects in order to calculate the sky-projected aspect ratio distributions of the different simulation runs. Figure 8.1 shows the sky-projected aspect ratio distribution of the observed and simulated galaxies with stellar masses in the range of $10.0 < \log_{10}(M_*/M_\odot) \leq 11.65$ revealing that all assessed simulation runs significantly lack galaxies with sky-projected aspect ratios of $q_{\rm sky} \lesssim 0.3$. We quantified that the simulated sky-projected aspect ratio distributions disagree with the GAMA survey and the SDSS at the $\geq 12.52\sigma$ and $\geq 14.82\sigma$ confidence level, respectively. This implies that the angular momentum still has not been resolved in the state-of-the-art hydrodynamical cosmological ΛCDM simulations in contradiction with the conclusion of Vogelsberger et al. (2014a) based on Illustris-1. In fact, the simulations indeed manage to form some thin disk galaxies (see e.g. section 6.1 and table 4 of Haslbauer et al. 2022) but overproduce too roundish galaxies.

We discussed several possibilities which could hamper the formation of present-day thin disk

galaxies in the ΛCDM simulations. First of all, we considered if the tension arises due to insufficient numerical resolutions or an inadequate baryonic feedback description (e.g. Ludlow et al. 2021). We showed that the intrinsic aspect ratio distribution of the different resolution realizations of the EAGLE project are very consistent with each other (see figure 5 and table 4 of Haslbauer et al. 2022) suggesting that the aspect ratio distribution has been converged. Remarkably, the aspect ratio distribution of the TNG50-1 run agrees well with the EAGLE runs (see the right panel of Figure 8.1) although the IllustrisTNG and EAGLE projects rely on different computational algorithms and baryonic feedback models. Assessing the different resolution realization of the TNG50 simulation, we estimated that the above reported tensions reduce to a 5.58σ (GAMA) and 3.27σ (SDSS) tension for a 8^5 times better mass resolution than the TNG50-1 run (see figure 7 and table 5 of Haslbauer et al. 2022). Thus, it appears to be unlikely that the tension is caused by resolutions effects but this needs to be explicitly verified in higher resolution simulations than the TNG50-1 or EAGLE runs.

Secondly, the lack of thin disk galaxies cold point to a failure of the hierarchical structure formation of the ΛCDM paradigm (see the discussion of Section 6.1.1). The ΛCDM framework is a hierarchical merger-driven buildup galaxy evolution model according to which galaxies efficiently grow through mergers due to dynamical friction (Section 3.3.1) acting on the extended cold dark matter haloes. However, we showed that a sample of simulated galaxies with a quiet merging history (no major merger within the last 12 Gyr; see the definition in section 7.3) do not have a significant lower intrinsic aspect ratio distribution compared to a sample of galaxies with a more active (at least one major merger within the last 12 Gyr) merger history (figure 13 of Haslbauer et al. 2022) leaving the possibility that the thickening of the galactic disks is mainly due to minor mergers which are unavoidable in the ΛCDM framework.

Finally, we calculated that galaxies formed in the galaxy-only MOND simulations of Wittenburg, Kroupa and Famaey (2020) have three-dimensional intrinsic aspect ratios of $q_{\rm int} \approx 0.1 - 0.5$ which results in a sky-projected aspect ratio distribution as also observed for spiral galaxies (see left panel of figure 14 in Haslbauer et al. 2022). However, self-consistent cosmological hydrodynamical MOND simulations would be required for a more direct comparison between the simulated and observed sky-projected aspect ratio distribution in order to address the angular momentum problem. In fact, galaxies formed in a MOND cosmology are expected to be thinner than in a ΛCDM cosmology because of less mergers due to the absence of dynamical friction on cold dark matter haloes.

Scientific research questions addressed in Haslbauer, Banik, Kroupa, Wittenburg and Javanmardi (2022):

- **Is the present-day sky-projected aspect ratio distribution of galaxies formed in the state-of-the-art ΛCDM simulations consistent with local observations?**
  The sky-projected aspect ratio distribution of galaxies formed in the ΛCDM simulations is inconsistent with the observations at the $\geq 12.52\sigma$ confidence level.
- **How does the aspect ratio distribution of galaxies with a quiet merging history differ from those with an active merger history?**
  The intrinsic aspect ratio distribution of galaxies with a quiet merging history (no major merger within the last 12 Gyr) is slightly smaller compared to those with a more frequent merger history (at least one major merger within the last 12 Gyr). However, selecting only galaxies with a quiet merging history would not resolve the tension.
- **What is the aspect ratio of a typical galaxy formed in the MONDian framework?**
  The galaxies formed in galaxy-only MOND simulations of Wittenburg, Kroupa and Famaey (2020) have intrinsic aspect ratios of $q_{\rm int} \approx 0.1-0.5$ similar to observed galaxies.

(see also Appendix B)

8.2 Author contributions

The authors of the corresponding publication are **Moritz Haslbauer** (MH), Indranil Banik (IB), Pavel Kroupa (PK), Nils Wittenburg (NW), and Behnam Javanmardi (BJ). MH and PK had the idea to test the standard model of cosmology by comparing the morphology of simulated and observed galaxies. MH, IB, and BJ developed the method to compare the observed and simulated morphological distribution by focusing on the aspect ratio of galaxies. MH extracted the intrinsic aspect ratio of the galaxies formed in the simulations runs of the Illustris, IllustrisTNG, and EAGLE projects. IB provided the code to calculate the sky-projected aspect ratio, which MH implemented in order to compute the sky-projected aspect ratio of the simulated galaxies. MH wrote the code to calculate the level of tensions between the observed and simulated sky aspect ratio distribution for which IB provided the code to estimate the statistical significance of extreme events. MH and IB developed the method to estimate the level of tension between the observed and simulated sky-projected aspect ratio distribution for mass resolution realization higher than TNG50-1. MH wrote the code to select galaxies with an active and quiescent merger history. NW provided the intrinsic aspect ratio of galaxies formed in his MOND galaxy-only simulations (Wittenburg, Kroupa and Famaey 2020). MH analyzed the observations by extracting the sky projected aspect ratio of galaxies from the Catalogue of Neighbouring Galaxies, the GAMA Survey, the SAMI Galaxy Survey, and SDSS. BJ contributed with his expertise on observations. MH wrote the manuscript except of Section 3.1 and Appendix A which have been written by IB. All co-authors contributed to the text of the manuscript by comments and passages and interpreted the results. MH created the figures of the manuscript.

CHAPTER 9

High-redshift galaxies in the ΛCDM framework and in light of the IGIMF theory

"Die Unendlichkeit der Schöpfung ist groß genug, um eine Welt, oder eine Milchstraße von Welten, gegen sie anzusehen, wie man eine Blume oder ein Insekt, im Vergleich gegen die Erde ansieht."
(Kant 1755)

This chapter summarizes the main scientific findings and author contributions of the peer-reviewed paper entitled "Has JWST Already Falsified Dark-matter-driven Galaxy Formation?" published in the journal The Astrophysical Journal Letters, 939, L31, 2022 by **Moritz Haslbauer**, Pavel Kroupa, Akram Hasani Zonoozi, and Hosein Haghi (hereafter Haslbauer, Kroupa, Zonoozi and Haghi 2022). A copy of the paper in its original form is attached in the Appendix C.

The interested reader may find a further summary of the paper aimed for the broader public in the blog post "The James Webb Space Telescope, and the early Universe" by **Moritz Haslbauer** and Pavel Kroupa published on the science blog "The Dark Matter Crisis – The rise and fall of cosmological hypotheses".

9.1 Summary

Several studies reported the detection of luminous galaxy candidates at photometric redshifts of $z_{\rm phot} \gtrsim 10$ in early JWST observations (e.g. Naidu et al. 2022; Naidu et al. 2022; N. J. Adams et al. 2023; Atek et al. 2023; Harikane et al. 2023; Labbé et al. 2023). Remarkably, some of these objects have derived stellar masses of $M_* \gtrsim 10^9\,M_\odot$ for an invariant canonical (non-varying) IMF (Section 5.1) such that their spectroscopic confirmation would imply that they have accumulated their stellar mass content over a time span of only $\lesssim$ 500 Myr after the Big Bang in the ΛCDM framework (Planck Collaboration XIII 2016). This questions whether the stellar mass buildup of these galaxies would be consistent with the ΛCDM framework as investigated in Haslbauer, Kroupa, Zonoozi and Haghi (2022).

9.1.1 High-redshift galaxies in the ΛCDM framework

In the first part of this research project, we tested if the observed galaxy candidates are consistent with the stellar mass buildup predicted by the ΛCDM paradigm assessing the state-of-the-art

hydrodynamical simulations of the IllustrisTNG (Pillepich et al. 2018a; Pillepich et al. 2018b; Pillepich et al. 2019; D. Nelson et al. 2018; D. Nelson et al. 2019; D. Nelson et al. 2019; Marinacci et al. 2018; Naiman et al. 2018; Springel et al. 2018), and EAGLE (Crain et al. 2015; Schaye et al. 2015; McAlpine et al. 2016) projects (see also Sections 3.2.2-3.2.3) assuming the JWST calibration and measured redshifts to be correct. In particular, we analyzed the galaxy candidates ID 1514 with $\log_{10}(M_*/M_\odot) = 9.8^{+0.2}_{-0.2}$ located at the photometric redshift of $z_{\rm phot} = 9.85^{+0.18}_{-0.12}$ (N. J. Adams et al. 2023), GL-z11 with $\log_{10}(M_*/M_\odot) = 9.4^{+0.3}_{-0.3}$ at $z_{\rm phot} = 10.9^{+0.5}_{-0.4}$, GL-z13 with $\log_{10}(M_*/M_\odot) = 9.0^{+0.3}_{-0.4}$ at $z_{\rm phot} = 13.1^{+0.8}_{-0.7}$ (Naidu et al. 2022)[1], and CEERS-1749 with $\log_{10}(M_*/M_\odot) = 9.6^{+0.2}_{-0.2}$ at $z_{\rm phot} = 16.0^{+0.6}_{-0.6}$ (Naidu et al. 2022). The later has been labeled in the literature as "Schrödinger's galaxy" because this object could be either an extremely high-redshift galaxy located at $z \approx 16$ or a dust-rich galaxy with a much lower redshift of $z \approx 5$ (see table 3 Naidu et al. 2022). This example demonstrates the importance of measuring the actual spectroscopic redshifts of these objects in upcoming analysis and surveys.

The stellar mass buildup predicted by the ΛCDM simulations is presented in Figure 9.1 by plotting their most massive subhalo in terms of the stellar mass in dependence of redshift. The stellar masses of the galaxy candidates ID 14924 (Labbé et al. 2023), ID 1514 (N. J. Adams et al. 2023), GL-z11, GL-13 (Naidu et al. 2022), and CEERS-1749 (Naidu et al. 2022) are by about one order of magnitude higher than the most massive subhaloes formed in the ΛCDM simulations. The surveys of the JWST covered a co-moving volume of $\approx 10^5$ cMpc^3 at $z \approx 10 \pm 1$ (N. J. Adams et al. 2023; Boylan-Kolchin 2023) which is smaller than the simulation boxes of the TNG100-1 and RefL0100N1504 run with a co-moving volume of $\approx 10^6$ cMpc^3. Thus, the lack of massive galaxies comparable with the galaxy candidates discovered by JWST is likely not caused by a too small simulation box. Moreover, Kannan et al. (2023) reported that also the simulation with a co-moving volume of ≈ 400 cMpc^3 of the MillenniumTNG (Hernández-Aguayo et al. 2023) project underestimates the abundance of luminous galaxies at $z \gtrsim 12$.

9.1.2 JWST and varying IMF within the IGIMF theory

In the second part, we provided the first estimation of the stellar masses of these galaxy candidates for a varying (non-canonical) IMF according to the IGIMF theory (Chapter 5). The conversion of the measured luminosities to stellar masses requires the mass-to-light ratio which depends on the shape of the stellar IMF (see also the Chapters 5 and 12) such that the stellar masses could significantly change in the case of a systematic variation of the IMF (Chapter 12). According to the IGIMF-2021 formalism (Yan, Jeřábková and Kroupa 2021), the gwIMF becomes top-heavy for low metallicities of $[Z] < 0$ and star formation rates of $\psi > 1\,{\rm M}_\odot\,{\rm yr}^{-1}$ (see the Figures 5.2 and 12.1). As UV radiation is mainly produced by massive stars compared to the low mass stars, interpreting a top-heavy gwIMF wrongly as a canonical gwIMF would overestimate the stellar mass content of the objects. For simplicity, we run only IGIMF models with a constant metallicity of [Fe/H]= −2 and constant SFRs over cosmic time (see section 3.2 of Haslbauer et al. 2022, for further details). Figure 9.2 shows that the stellar masses of the galaxy candidates are about 5 – 10 times lower for a varying gwIMF based on the IGIMF theory than for an invariant canonical IMF but this would not necessarily alleviate the failure of the

[1] Note that the here listed properties of GL-z11 and GL-z13 refer to the first version of the arXiv preprint of Naidu et al. (2022) which have been slightly updated after the acceptance of our paper (see their table 3 and the discussion in the caption of Figure 9.1).

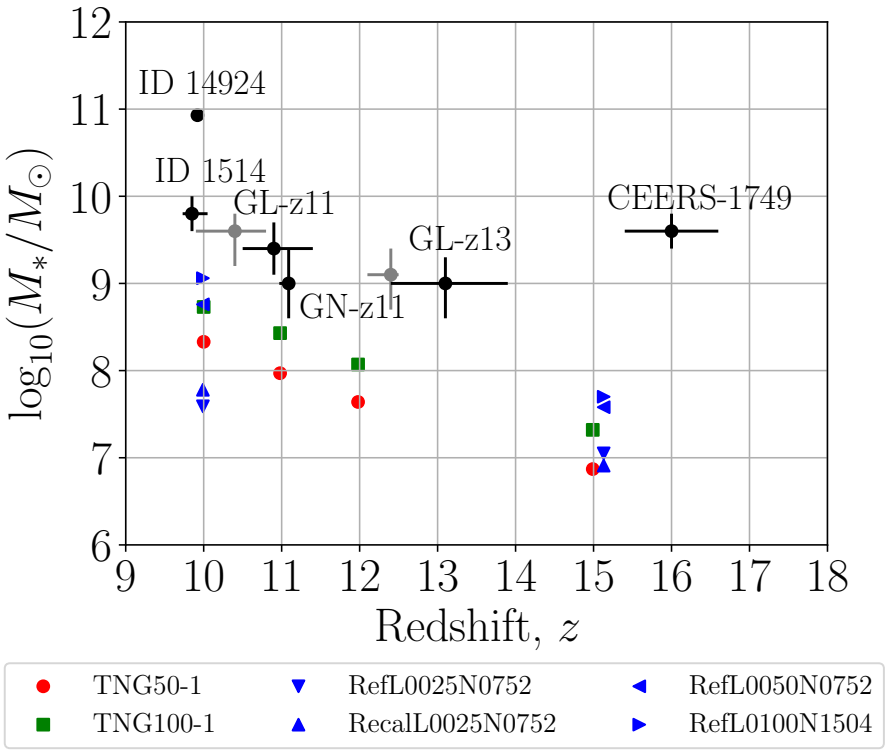

Figure 9.1: Comparison of the high-redshift galaxy candidates (grey and black errorbars) with the stellar mass buildup of the ΛCDM framework by showing the most massive subhaloes in terms of their stellar masses formed in the TNG50-1 (red circles), TNG100-1 (green squares), and different EAGLE (blue symbols) simulation runs in dependence of redshift assuming an invariant canonical IMF (Chabrier 2003). The black errorbars refer to the galaxy candidates ID 14924, ID 1514, GL-z11, GL-z13, CEERS-1749 detected by the JWST and to the spectroscopically confirmed galaxy GN-z11 (GN-z11; Oesch et al. 2016) by the HST. After the acceptance of our paper, the two galaxy candidates GL-z11 and GL-z13 have been renamed to GL-z10 and GL-z12, respectively, because of a slight revision of their physical properties by Naidu et al. (2022). In order to show these changes to the previous results, we added the two grey errorbars which refer to the updated values of $\log_{10}(M_*/M_\odot) = 9.6^{+0.2}_{-0.4}$ at $z_{\rm phot} = 10.4^{+0.4}_{-0.5}$ (GL-z10) and $\log_{10}(M_*/M_\odot) = 9.1^{+0.3}_{-0.4}$ at $z_{\rm phot} = 12.4^{+0.1}_{-0.3}$ (GL-z12; see their table 3). Credits: modified version of figure 2 of Haslbauer et al. (2022) by including the updated values of GL-z11 (now named as GL-z10 in Naidu et al. 2022) and GL-z13 (now named as GL-z12), figure 7 of Kroupa et al. (2023), and figure 3 of the blog post "The James Webb Space Telescope, and the early Universe" by **Moritz Haslbauer** and Pavel Kroupa on the science blog "The Dark Matter Crisis – The rise and fall of cosmological hypotheses".

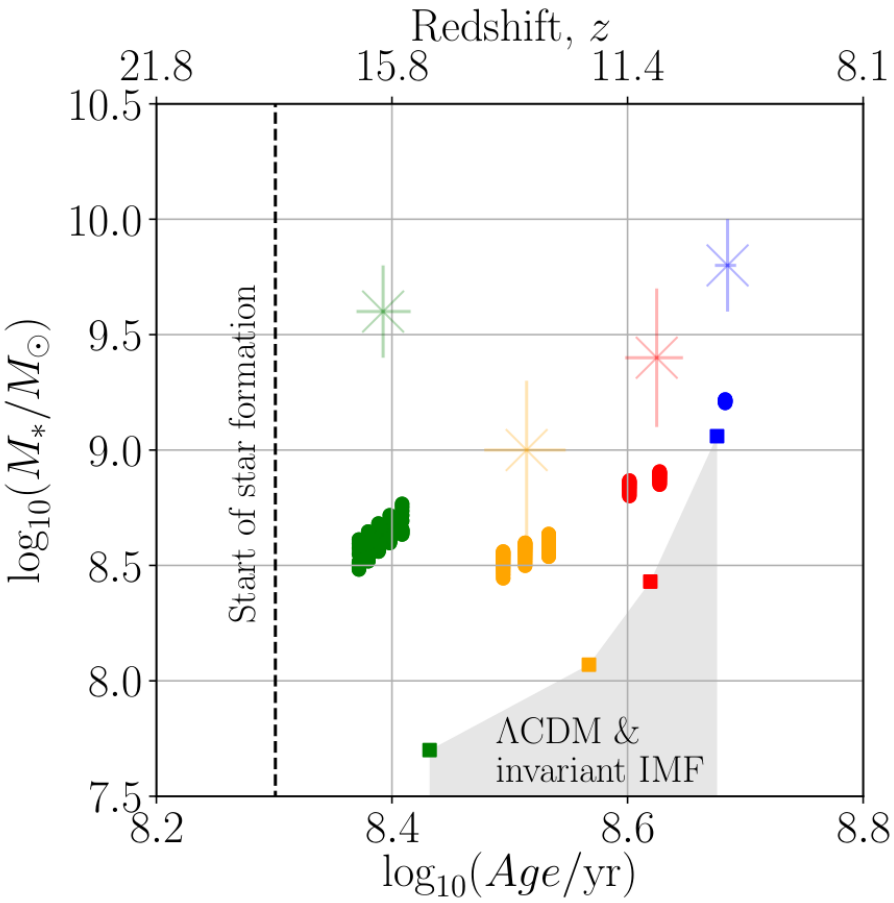

Figure 9.2: Stellar masses of the galaxy candidates ID 1514 (blue), GL-z11 (red), GL-z13 (orange), and CEERS-1749 (green) for an invariant canonical IMF (star symbols) and a systematically varying gwIMF within the IGIMF context (circles). For simplicity, the IGIMF models assume a constant metallicity of [Fe/H]= −2 and constant SFH starting 200 Myrs after the Big Bang as indicated by the dashed vertical black line. The colored squares show the most massive subhaloes in term of their stellar masses identified in the here-assessed ΛCDM simulations which adopt an invariant canonical IMF (Chabrier 2003). Galaxies with an invariant canonical IMF populate the grey shaded region in the ΛCDM simulation. Credit: right panel of figure 4 of Haslbauer et al. (2022).

ΛCDM model because the simulations analyzed here were performed with a non-varying canonical IMF (Chabrier 2003). Allowance for the variable IMF would also reduce the formed stellar masses of the simulated galaxies due to the stronger feedback.

9.1.3 Implications

We discussed possible reasons for the here-reported tension between the observations by the JWST and ΛCDM simulations (section 4 of Haslbauer et al. 2022). Firstly, the high luminosities and photometric redshifts are caused by a wrong calibration of the JWST. Secondly, the high photometric redshifts arise because of dust reddening. Thirdly, the properties of galaxies depend also on the baryonic and

star formation physics leaving the possibility that star formation could have been e.g. more efficient at high redshifts (e.g. Harikane et al. 2023; Mason, Trenti and Treu 2023; Naidu et al. 2022).

Finally, the results could imply that structure formation is more enhanced and/or that the Universe is even older (Melia 2023) than given by the ΛCDM framework (see also the Chapters 7 and 11). While structure formation is enhanced in Milgromian dynamics (e.g. Angus 2009; Malekjani, Rahvar and Haghi 2009; Famaey and McGaugh 2012; Haslbauer, Banik and Kroupa 2020), the existence of high-redshift galaxies would also challenge the νHDM framework as the power spectrum significantly lacks power at galactic scales compared to the ΛCDM model (right panel of Figure 4.1) because of the absence of the cold dark matter haloes in the early Universe (see Wittenburg et al. 2023).

Scientific research questions addressed in Haslbauer, Kroupa, Zonoozi and Haghi (2022):

- **Has JWST already falsified dark-matter-driven galaxy formation?**
  This question cannot be conclusively answered because the photometric redshifts of the galaxy candidates need be spectroscopically confirmed and their derived stellar masses depend on the stellar IMF.
- **Are the galaxy candidates with $M_* \gtrsim 10^9\,M_\odot$ for an invariant canonical IMF at high photometric redshift of $z_{\rm phot} \gtrsim 10$ consistent the stellar mass buildup predicted by the ΛCDM framework?**
  In the case for an invariant canonical IMF (and if spectroscopically confirmed), the reported stellar masses of the galaxy candidates would not be consistent with the stellar mass buildup predicted by the ΛCDM framework.
- **How would the stellar masses of the galaxy candidates change if instead a varying gwIMF in the IGIMF context is applied?**
  First estimations show that the stellar masses of the galaxy candidates would be reduced by a factor of ≈ 5 for a varying gwIMF within the IGIMF context. This would not necessarily alleviate the failure of the ΛCDM model because the simulations analyzed here were performed with a non-varying canonical IMF. Allowance for the variable IMF would reduce the formed stellar masses of the early galaxies due to the stronger feedback.

(see also Appendix C)

9.2 Author contributions

The authors of the corresponding publication are **Moritz Haslbauer** (MH), Pavel Kroupa (PK), Akram Hasani Zonoozi (AHZ), and Hosein Haghi (HH). MH had the idea to compare the derived stellar masses of luminous high-redshift galaxy candidates detected with JWST measurements with the standard model of cosmology by assessing the hydrodynamical simulation runs of the IllustrisTNG, and EAGLE project. AHZ and HH suggested to re-calculate the reported stellar masses of the galaxy candidates assuming different SFHs for an invariant canonical IMF. PK suggested to include a qualitative discussion and first estimation of the stellar masses for a variable gwIMF within the IGIMF context. MH analysed the galaxy stellar mass function and stellar mass buildup of the ΛCDM framework by determining the IllustrisTNG and EAGLE simulations. MH compared the most massive galaxies formed in the simulations with the high-redshift galaxy candidates observed by JWST. AHZ provided the stellar mass-to-light ratios of the galaxy candidates for different star formation histories assuming an invariant canonical IMF. MH run the IGIMF Fortran code developed by AHZ (see e.g. Zonoozi, Mahani and Kroupa 2019, and also the FORTRAN code GWIMFv2) in order to calculate the stellar masses of the high-redshift galaxy candidates for a varying gwIMF within the IGIMF context. MH created the figures of the paper. All authors contributed by M.H. and P.K. interpreted the results. MH wrote the manuscript except of the Section 3.1 which was mainly written by HH and AHZ. All co-authors contributed to the text of the manuscript by comments and passages.

CHAPTER 10

The Magellanic Clouds in the ΛCDM framework

"Der weiße Ochse, den er tief unter Canopus in milchigem Lichte glänzen sah, war zweifelsohne die Große Magellanische Wolke, [...]"
(Humboldt 1869)

The Small and Large Magellanic Clouds (SMC and LMC) are the two most massive satellite galaxies of our Milky Way (MW) galaxy being visible with the naked eye from the Southern hemisphere as depicted in the Figure 10.1 taken from the Paranal Observatory in Chile. The Magellanic Clouds (MCs) are named after the Portuguese explorer Ferdinand Magellan[1] (1480–1521) but because of their prominent appearance on the sky, the first documentation of the MCs goes already back to ancient times. The Iranian astronomer Abd al-Rahman al-Sūfī (903–986) described the LMC as "El-Bakar" meaning "the White Ox" (German: "weißer Ochse") as documented e.g. by Humboldt (1869). A detailed description of the historical exploration of the MCs would be beyond the scope of this chapter, but the interested reader may find further information and references e.g. in Dennefeld (2020).

This chapter and the corresponding Appendix E include the manuscript entitled "The Magellanic Clouds are very rare in the IllustrisTNG simulations" by **Moritz Haslbauer**, Indranil Banik, Pavel Kroupa, and HongSheng Zhao (hereafter Haslbauer, Banik, Kroupa and Zhao submitted), which has been submitted to a peer-reviewed scientific journal.

Summary

The MCs are of particular interest for testing cosmological models because on the one hand side they are with stellar masses of $M_* = 4.6 \times 10^8\, M_\odot$ (SMC) and $1.5 \times 10^9\, M_\odot$ (LMC; McConnachie 2012) the most massive satellites surrounding the MW galaxy and on the other hand side located at Galactocentric distances of only ≈ 55 kpc allowing for precise measurements (see also the discussion in Section 6.1.1) of their proper motions by e.g. the Hubble Space Telescope (HST; e.g. Kallivayalil et al. 2006; Kallivayalil, van der Marel and Alcock 2006; Kallivayalil et al. 2013) and more recently

[1] Recently, several astronomers have argued to rename the Magellanic Clouds because of Ferdinand Magellan's critical biography (see e.g. the article Astronomers Need to Rename the Magellanic Clouds (published on 12.09.2023) by Mia de los Reyes).

Figure 10.1: Image of the Small and Large Magellanic Clouds taken in front of the Auxiliary Telescopes of the Very Large Telescope (VLT) in Paranal (Chile). Credit: J. C. Muñoz/ESO (downloaded from the website https://www.eso.org/public/austria/images/ATs_Magellanic_Clouds_hires-CC/?lang on 16.09.2023), Creative Commons Attribution 4.0 International License.

by the Gaia mission (Gaia Collaboration 2016; Gaia Collaboration 2018b; Gaia Collaboration 2018a). This spatial configuration of the MW-MCs systems implies that the cold dark matter haloes of the three individual galaxies overlap such that dynamical friction causes a deceleration of their relative motions yielding to a decay of their orbits (Section 3.3.1). Thus, the MW-MCs system can be assessed to study the efficiency of dynamical friction as elaborated in the following attached manuscript by Haslbauer, Banik, Kroupa and Zhao (submitted). The main scientific aim of this study is to quantify the likelihood of the MW-MCs system in the ΛCDM framework by assessing different simulation runs of the IllustrisTNG project (Pillepich et al. 2018a; Pillepich et al. 2018b; Pillepich et al. 2019; D. Nelson et al. 2018; D. Nelson et al. 2019; D. Nelson et al. 2019; Marinacci et al. 2018; Naiman et al. 2018; Springel et al. 2018, and see Section 3.2.2 and Section 10.2.2).

Recent measurements by the HST and Gaia DR2 yield for the SMC and LMC Galactocentric velocities of $323.8\,\mathrm{km\,s^{-1}}$ and $245.6\,\mathrm{km\,s^{-1}}$ (tables 1 and 2 of Pawlowski and Kroupa 2020), respectively. The MCs have a mutual distance of only $d_{\mathrm{MCs}} = 24.5$ kpc and a relative velocity of only $v_{\mathrm{MCs}} = 90.8\,\mathrm{km\,s^{-1}}$, which gives an observed phase-space density of $f_{\mathrm{MCs,obs}} = (d_{\mathrm{MCs}} \cdot v_{\mathrm{MCs}})^{-3} = 9.10 \times 10^{-11}\,\mathrm{km^{-3}\,s^{3}\,kpc^{-3}}$. Using the different simulation runs of the IllustrisTNG project, we select analogues to the MCs based on their stellar masses in MW-like host haloes (see the Sections 10.2.3-10.2.4 for the details). We found that the f_{MCs} distribution of identified MW-MCs systems in the

TNG50-1 simulation run causes a 3.95σ tension with the observations. This is because the MW-MCs systems have values of $f_{\rm MCs}$ which are typically lower than $f_{\rm MCs,obs}$. Performing the analysis also in different resolution realizations of the IllustrisTNG project shows that this tension is likely not caused by numerical limitations of the TNG50-1 simulation (Section 10.3.1 and Appendix F) but this needs to be explicitly verified in upcoming higher resolution ΛCDM simulations. In total, we found only three out of 1202 analogues to the MCs with $f_{\rm MCs} \geq f_{\rm MCs,obs}$ in the flagship simulation runs TNG50-1, TNG100-1, and TNG300-1. Tracing these three objects back in cosmic time, reveals that these MW-MCs systems form according to the so-called first-infall scenario in which the MCs are accreted together towards the MW-like galaxies at late times (Section 10.3.2).

Furthermore, selected analogues to the LMC located at Galacticentric distances smaller than the observed LMC (i.e. ≤ 50.0 kpc) have total masses smaller than the observationally derived total mass of $M_{\rm LMC} = 18.8^{+3.5}_{-4.0} \times 10^{10}\,M_{\odot}$ from Galactic stellar streams close to the LMC (Shipp et al. 2021) which alone results in a $> 3.75\sigma$ tension with the ΛCDM framework (Section 10.4.4).

We discuss the MCs in the light of the observed DoS (Section 3.3.7) around the MW galaxy by demonstrating that the existence of the DoS cannot be explained by a group infall scenario. The LMC cannot bring in enough satellites to fully populate the DoS which consists of the 11 "classical satellites" arranged in a thin plane with a root-mean-square height of only 19.6 kpc (Pawlowski 2021b). We calculated that the DoS and the MCs cause a 4.11σ tension with the ΛCDM framework (Section 10.4.3).

Finally, we qualitatively discuss the formation and evolution scenarios of the MCs within the MOND framework (Section 10.4.5) in which the MCs can be either primordial or tidal dwarf galaxies (Section 3.3.8). The observed DoS around the MW and M31 galaxy strongly suggest that their satellites are TDGs formed through a past encounter between these two galaxies (Zhao et al. 2013; Banik, O'Ryan and Zhao 2018; Bílek et al. 2018; Bílek et al. 2021; Banik and Zhao 2022). However, such a scenario is ruled out in the ΛCDM paradigm because the satellite galaxies have high dynamical masses (Kroupa 2015).

We conclude that the spatial and kinematical configuration of the observed MW-MCs system suggests that Chandrasekhar dynamical friction is less efficient on galactic scales than in the state-of-the-art hydrodynamical ΛCDM simulation runs of the IllustrisTNG project because the hierarchical clustering of two massive satellites similar to the MCs in a narrow phase-space volume is an unlikely situation due to the short merger time-scales in cold dark matter-based models (Section 10.4.2 and 10.5). This is consistent with the previous conclusion reached in Chapter 8 and in other studies (e.g. Angus, Diaferio and Kroupa 2011; Oehm, Thies and Kroupa 2017; Roshan et al. 2021, and see also Section 3.3.1).

Author contributions

The authors of this manuscript are **Moritz Haslbauer** (MH), Indranil Banik (IB), Pavel Kroupa (PK), and HongSheng Zhao (HZ). PK and HZ had the idea to quantify the likelihood of the phase-space density of the Milky Way (MW)-Magellanic Clouds (MCs) system in the ΛCDM model. IB suggested to consider the MCs in the light of the disk of satellites. All authors contributed to the discussion of the formation and evolution scenario of the MCs in the ΛCDM and MOND cosmology. IB and MH modified the publicly available Fortran F90 code[2] developed by IB in Banik et al. (2021) to select

[2] https://seafile.unistra.fr/d/6b09464443da478d8926/

analogues to the MW and MCs in the simulation runs of the IllustrisTNG project. MH wrote the codes to analyze the physical and dynamical properties of the MW-MCs systems, their formation and evolution scenarios, and to quantify their likelihood in the simulation runs. MH created the figures and wrote the manuscript with comments and passages by all co-authors. All authors contributed to the interpretation of the observations and simulation data.

Scientific research questions addressed in Haslbauer, Banik, Kroupa and Zhao (submitted):

- **How likely is the observed phase-space density configuration of the LMC-SMC-MW system in the ΛCDM framework?**
  The phase-space density of the observed MCs ($f_{\mathrm{MCs,obs}} = 9.10 \times 10^{-11}\ \mathrm{km^{-3}\ s^{3}\ kpc^{-3}}$) is in a 3.95σ tension with the ΛCDM framework based on the TNG50-1 run of the IllustrisTNG project.
- **How likely are the properties of the observed LMC in the ΛCDM framework?**
  The LMC analogues at lower Galactocentric distance than the observed LMC have total masses smaller than the observationally derived mass of the LMC which alone causes a $> 3.75\sigma$ tension.
- **Can the DoS observed around the MW be explained by a group infall of LMC satellites?**
  No, a group infall of satellite of the LMC cannot populate the DoS.
- **How does the LMC-SMC-MW system form in the ΛCDM framework?**
  The first-infall scenario is the most likely formation process of the LMC-SMC-MW system within the ΛCDM framework.
- **How does the LMC-SMC-MW system form in the MOND framework?**
  In MOND, the MCs could be either primordial or tidal dwarf galaxies (see also the Dual Dwarf Theorem in Section 3.3.8). The DoS strongly suggests that the MCs are tidal dwarf galaxies which would however conflict with the ΛCDM framework because of their high dynamical masses as derived from the stellar motions within each satellite.

(see also Appendix E)

The Magellanic Clouds are very rare in the IllustrisTNG simulations

Moritz Haslbauer, Indranil Banik, Pavel Kroupa, and HongSheng Zhao (submitted)

Abstract

The Large and Small Magellanic Cloud (LMC and SMC) form the closest interacting galactic system to the Milky Way, therewith providing a laboratory to test cosmological models in the local Universe. We quantify the likelihood for the Magellanic Clouds (MCs) to be observed within the ΛCDM model using hydrodynamical simulations of the IllustrisTNG project. The orbits of the MCs are constrained by proper motion measurements taken by the Hubble Space Telescope and Gaia. The MCs have a mutual separation of $d_{\rm MCs} = 24.5\,{\rm kpc}$ and a relative velocity of $v_{\rm MCs} = 90.8\,{\rm km\,s^{-1}}$, implying a phase-space density of $f_{\rm MCs,obs} \equiv (d_{\rm MCs} \cdot v_{\rm MCs})^{-3} = 9.10 \times 10^{-11}\,{\rm km^{-3}\,s^{3}\,kpc^{-3}}$. We select analogues to the MCs based on their stellar masses and distances in MW-like haloes. None of the selected LMC analogues have a higher total mass and lower Galactocentric distance than the LMC, resulting in $> 3.75\sigma$ tension. We find that the $f_{\rm MCs}$ distribution in the TNG50-1 simulation is in 3.95σ tension with observations. Thus, a hierarchical clustering of two massive satellites like the MCs in a narrow phase-space volume is unlikely in ΛCDM, presumably because of short merger timescales due to dynamical friction between the overlapping dark matter haloes. We show that group infall led by an LMC analogue cannot populate the Galactic disc of satellites (DoS), implying that the DoS and the MCs formed in physically unrelated ways in ΛCDM. Since the 20° alignment of the LMC and DoS orbital poles has a likelihood of $P = 0.030$ (2.17σ), adding this χ^2 to that of $f_{\rm MCs}$ gives a combined likelihood of $P = 3.90 \times 10^{-5}$ (4.11σ).

10.1 Introduction

The Large Magellanic Cloud (LMC) and Small Magellanic Cloud (SMC) are the most massive and some of the closest satellite galaxies of the Milky Way (MW). The gravitational interaction between these three galaxies makes the nearby Universe an interesting laboratory to test galaxy formation and evolution models and gravitational theories. For example, the proximity of the MW, LMC, and SMC means that their dark matter haloes are strongly overlapping such that Chandrasekhar dynamical friction ought to be pronounced (Kroupa 2015). Such tests require precise proper motion measurements in order to constrain the orbits of the Magellanic Clouds (MCs). Historically, the first proper motion measurements of the MCs were reported by Kroupa, Röser and Bastian (1994) using the Positions and Proper Motions (PPM; Röser and Bastian 1993) catalogue. The High Precision Parallax Collecting Satellite (Hipparcos; Perryman et al. 1997) was the first high-precision astrometry space mission. Its proper motion measurements of the MCs were analysed in Kroupa (1997). The precision of the proper motion measurements improved further thanks to the Hubble Space Telescope (HST; e.g. Kallivayalil et al. 2006; Kallivayalil, van der Marel and Alcock 2006; Kallivayalil et al. 2013) and recently Gaia (Gaia Collaboration 2016; Gaia Collaboration 2018b; Gaia Collaboration 2018a).

In this contribution, we aim to quantify the likelihood of MW-LMC-SMC triple systems to occur in the ΛCDM cosmological model. Our analysis relies on the stellar masses and orbits of the MCs using proper motion measurements taken by the HST (Kallivayalil et al. 2013) and Gaia Data Release 2 (Gaia DR2; Gaia Collaboration 2016; Gaia Collaboration 2018b; Gaia Collaboration 2018a). The LMC and SMC have a stellar mass of $M_\star = 1.5 \times 10^9\,M_\odot$ and $M_\star = 4.6 \times 10^8\,M_\odot$, respectively (McConnachie

2012). We obtain the 3D position and velocity vectors of the MCs in Galactic coordinates from Pawlowski and Kroupa (2020), who combined proper motion data from the HST (Kallivayalil et al. 2013) with Gaia DR2 (Gaia Collaboration 2018b; Gaia Collaboration 2018a). The LMC and SMC are located at Galactocentric distances of 50.0 kpc and 61.3 kpc, respectively, with a mutual separation of only 24.5 kpc. The relative velocity of the MCs is 90.8 $\mathrm{km\,s^{-1}}$, which is quite small given that the LMC and SMC have Galactocentric velocities of 323.8 $\mathrm{km\,s^{-1}}$ and 245.6 $\mathrm{km\,s^{-1}}$, respectively, with the LMC ahead of the SMC in their orbit around the MW. Assuming as the null hypothesis that the ΛCDM paradigm is the correct description of the Universe, the rather rapid motion of the LMC combined with other observations of the MCs (discussed further below) implies that the MCs are most likely on their first pericentre passage past the MW (Besla et al. 2007). As a result, the fact that the LMC is leading the SMC is not a strong constraint – slight differences in the infall time and pre-infall trajectory can mask the $\approx 10\times$ larger expected dynamical friction on the LMC, which moreover could actually speed up if its orbit decayed more due to the so-called 'donkey effect'. The above-described geometrical and kinematic configuration of the MW-MCs system causes some interesting effects, which can be used as a test of cosmological and gravitational theories.

Besides the kinematic data, the evolutionary history of the MCs can also be accessed by studying their environment and internal properties over cosmic time. Strong evidence that the LMC and SMC interacted over at least the last 4 Gyr is provided by their star formation histories (SFHs). In particular, the SFH of the SMC has two peaks at lookback times of ≈ 9 Gyr and ≈ 4.5 Gyr (Weisz, Dolphin, Skillman, Holtzman, Dalcanton et al. 2013) and the highest star formation rate (SFR) of the LMC occurred between 4 Gyr and 0.5 Gyr ago (Mazzi et al. 2021). The SFRs of both MCs increased significantly over the last 3.5 Gyr (see, e.g., figure 5 of Weisz, Dolphin, Skillman, Holtzman, Dalcanton et al. 2013). This and the correlation between the SFHs of the LMC and SMC over the last 3.5 Gyr (see figure 2 of Massana et al. 2022) is most likely a consequence of star formation triggered by their interaction.

The MCs are surrounded by the Magellanic Stream (MS), a gaseous structure with a leading and a trailing arm that extends over about 200° on our sky (Nidever et al. 2010). The MS also aligns with the DoS: the MS normal and the DoS normal have an angular distance of 24° (Pawlowski, Pflamm-Altenburg and Kroupa 2012). Different MS formation processes have been proposed (for a review, see D'Onghia and Fox 2016). Currently, the most preferred scenario is that the MS is a tidal tail formed mostly through gravitational interactions between the MCs, though with ram-pressure stripping from hot gas surrounding the MW also playing a role in the context of a first infall scenario (Hammer et al. 2015). However, this would not explain the alignment of the MCs and the MS with the satellite plane around the MW (Sections 10.4.3).

The formation and evolution of the MCs in cosmological ΛCDM simulations was investigated in previous studies (e.g. Busha et al. 2011; Boylan-Kolchin, Besla and Hernquist 2011; Santos-Santos et al. 2021), which we discuss further in Section 10.4. We readdress the MCs in the ΛCDM context by recalculating the likelihood of MW-like galaxies hosting analogues to the MCs using the state-of-the-art hydrodynamical simulation runs of the Illustris The Next Generation (hereafter TNG) project (TNG300-1; Pillepich et al. 2018a; D. Nelson et al. 2019). In addition to this major advance on the theoretical side, we also take into account the geometrical configuration and kinematics of the MCs using proper motion measurements obtained with the HST (Kallivayalil et al. 2013) and from Gaia DR2 (Gaia Collaboration 2016; Gaia Collaboration 2018b; Gaia Collaboration 2018a).

The layout of this paper is as follows: Section 10.2 describes the TNG simulation runs and the selection criteria used to define analogues to the MW and the MCs. The likelihood of the MCs within

Object	$M_\star$ [$M_\odot$]	r_x [kpc]	r_y [kpc]	r_z [kpc]	d [kpc]	v_x [km s^{-1}]	v_y [km s^{-1}]	v_z [km s^{-1}]	$v_{\rm tot}$ [km s^{-1}]	$h/10^3$ [kpc km s^{-1}]
LMC	1.5×10^9	−0.6	−41.8	−27.5	50.0	-42 ± 6	-223 ± 4	231 ± 4	323.8	15.9
SMC	4.6×10^8	16.5	−38.5	−44.7	61.3	6 ± 8	-180 ± 7	167 ± 6	245.6	15.0

Table 10.1: Observational properties of the MCs based on tables 1 and 2 of Pawlowski and Kroupa (2020). The proper motions are a combination of data from Gaia DR2 (Gaia Collaboration 2018a) and the HST (Kallivayalil et al. 2013), as discussed further in section 2.1 of Pawlowski and Kroupa (2020). From left to right: stellar mass; position $\boldsymbol{r}$ in Galactocentric Cartesian coordinates; distance to the Galactic centre; velocity $\boldsymbol{v}$ in Galactocentric Cartesian coordinates; total velocity wrt. the MW; and absolute specific angular momentum $h \equiv |\boldsymbol{r} \times \boldsymbol{v}|$. The stellar masses of the LMC and SMC are taken from table 4 of McConnachie (2012).

the ΛCDM framework is quantified in Section 10.3. This section also includes an investigation of the formation of the MS in a cosmological context by tracing individual analogues to the MCs back through cosmic time. In Section 10.4, we compare our results with previous studies on the occurrence rate of the MCs in the ΛCDM framework and discuss the role of dynamical friction on the orbits of the MCs. We also consider the MCs in the light of the Local Group. Our concluding remarks are given in Section 10.5.

10.2 Methods

In this section, we first summarize the observational properties of the MCs. We then introduce the hydrodynamical cosmological TNG simulations and state the selection criteria for analogues to the MW and the MCs.

10.2.1 Observations

The 3D positions and velocities of the MCs in Galactocentric Cartesian coordinates are summarized in Table 10.1 and are taken from table 2 of Pawlowski and Kroupa (2020), whose results are derived by combining proper motion measurements from Gaia DR2 (Gaia Collaboration 2018a) and the HST (Kallivayalil et al. 2013). For a detailed description of these measurements, we refer the reader to section 2.1 of Pawlowski and Kroupa (2020).

The phase-space configuration of the MW-MCs system is elaborated by combining the phase-space density of the MCs with a measure of the LMC being close and moving fast wrt. the MW. The specific phase-space density of the MCs is given by

$$f_{\rm MCs} \equiv \left(d_{\rm LMC-SMC} \cdot v_{\rm LMC-SMC}\right)^{-3}, \quad \text{with} \tag{10.1}$$

$$f_{\rm MCs,obs} \approx 9.10 \times 10^{-11} \ \mathrm{km^{-3}\,s^{3}\,kpc^{-3}} \tag{10.2}$$

being the observationally inferred value.

The geometrical and kinematic configuration of the MW-LMC system is quantified by introducing the inverse kinematic timescale

$$\Omega_{\rm LMC} \equiv \frac{v_{\rm MW-LMC}}{d_{\rm MW-LMC}}, \tag{10.3}$$

which is also a measure related to the angular velocity. Observationally, $\Omega_{\mathrm{LMC,obs}} = 6.48\,\mathrm{km\,s^{-1}\,kpc^{-1}}$. The parameters $f_{\mathrm{MCs,obs}}$ and $\Omega_{\mathrm{LMC,obs}}$ contain unrelated information as the former relates to the LMC-SMC system without regard to the MW, while the latter refers to the MW-LMC system without regard to the SMC. f_{MCs} and Ω_{LMC} are thus independent. The parameters also do not include the masses of the MCs or the MW because these are already considered by the stellar mass selection criteria applied to our initial samples in Sections 10.2.3 and 10.2.4. In Section 10.4.4, we will consider if the masses of the LMC analogues are compatible with other constraints on the ΛCDM framework.

10.2.2 The TNG cosmological simulations

The IllustrisTNG project (Pillepich et al. 2018a; Pillepich et al. 2018b; Pillepich et al. 2019; D. Nelson et al. 2018; D. Nelson et al. 2019; D. Nelson et al. 2019; Marinacci et al. 2018; Naiman et al. 2018; Springel et al. 2018) is a further development of the original Illustris project (Vogelsberger et al. 2014b; D. Nelson et al. 2015), a set of hydrodynamical cosmological simulations performed within the ΛCDM framework. The different simulation runs of the TNG project are consistent with the Planck-2015 results as they use a global Hubble constant of $H_0 = 67.74\,\mathrm{km\,s^{-1}\,Mpc^{-1}}$ and a present-day baryonic matter, total matter, and dark energy density in units of the cosmic critical density of $\Omega_{\mathrm{b},0} = 0.0486$, $\Omega_{\mathrm{m},0} = 0.3089$, and $\Omega_{\Lambda,0} = 0.6911$, respectively (Planck Collaboration XIII 2016).

In order to quantify the likelihood of LMC and SMC analogues in the ΛCDM framework, we employ the TNG50-1, TNG100-1, and TNG300-1 simulation runs. These have box sides of $35\,h^{-1} = 51.7$ (TNG50-1), $75\,h^{-1} = 110.7$ (TNG100-1), and $205\,h^{-1} = 302.6$ (TNG300-1) comoving Mpc (cMpc), respectively, where h is the present Hubble constant H_0 in units of 100 km/s/Mpc. TNG300-1 has the largest simulation volume within the IllustrisTNG project, which is important to build up sufficient statistics. The TNG50-1 run has the smallest simulation volume but is the highest resolution realization, with a baryonic element mass of $m_{\mathrm{b}} = 8.5 \times 10^4\,M_\odot$ and a dark matter particle mass of $m_{\mathrm{dm}} = 4.5 \times 10^5\,M_\odot$. TNG100-1 (TNG300-1) has $m_{\mathrm{b}} = 1.4 \times 10^6\,M_\odot$ ($m_{\mathrm{b}} = 1.1 \times 10^7\,M_\odot$) and $m_{\mathrm{dm}} = 7.5 \times 10^6\,M_\odot$ ($m_{\mathrm{dm}} = 5.9 \times 10^7\,M_\odot$). We also use the lower resolution realizations of the TNG50 and TNG100 runs, i.e. TNG50-2 ($m_{\mathrm{b}} = 6.8 \times 10^5\,M_\odot$, $m_{\mathrm{dm}} = 3.6 \times 10^6\,M_\odot$), TNG50-3 ($m_{\mathrm{b}} = 5.4 \times 10^6\,M_\odot$, $m_{\mathrm{dm}} = 2.9 \times 10^7\,M_\odot$), and TNG100-2 ($m_{\mathrm{b}} = 1.1 \times 10^7\,M_\odot$, $m_{\mathrm{dm}} = 6.0 \times 10^7\,M_\odot$); to study the numerical convergence of the results presented in Section 10.3.1.

The TNG simulations self-consistently evolve the baryonic[3] components and dark matter particles from redshift $z = 127$ up to the present time, yielding 100 snapshots in the redshift range $0 \leq z \leq 20.05$. Haloes and subhaloes (substructures within haloes) were identified with a standard friends-of-friends (FoF) algorithm and the SUBFIND algorithm, respectively (Springel et al. 2001; Dolag et al. 2009). Their physical properties are listed in the FoF halo and subhalo catalogues, respectively. These can be downloaded from the IllustrisTNG website.[4] We trace galaxies through cosmic time using the Illustris SUBLINK merger tree catalogue (Rodriguez-Gomez et al. 2015). Throughout the analysis, we calculate the velocity difference between two galaxies based on their total velocities rather than the peculiar velocities listed in the online catalogues. Therefore, according to the Hubble law, the relative velocity $\boldsymbol{v}_{12}$ between two objects with relative peculiar velocity $\boldsymbol{v}_{\mathrm{pec},12}$ is

$$\boldsymbol{v}_{12} \equiv \boldsymbol{v}_{\mathrm{pec},12} + H(z)\,\boldsymbol{d}_{12}\,, \tag{10.4}$$

[3] stellar particles and gas cells

[4] https://www.tng-project.org/data/docs/specifications/ [15.03.2021]

where $H(z)$ is the Hubble parameter at redshift z, at which time $\boldsymbol{d}_{12}$ is the physical separation between the objects under consideration.

10.2.3 Selecting analogues to the MW

In order to select analogues to the MW and the MCs, we use a modified version of the publicly available searching algorithm developed by Banik et al. (2021), who used a one-level tree code to speed up the calculations.[5]

The MW has a virial mass of $M_{200} = 2.43 \times 10^{12}\,M_\odot$, with a minimum value of $0.8 \times 10^{12}\,M_\odot$ at the 95% confidence level (Y.-S. Li and White 2008). Thus, we require that a MW-like galaxy has to be within a FoF group whose total virial mass lies in the range $0.5 \times 10^{12} < M_{200}/M_\odot < 2.5 \times 10^{12}$, where M_{200} is the total mass of the group within a sphere whose mean density is 200× the cosmic critical density. The upper limit to M_{200} is designed to exclude galaxy groups and clusters.

From the so-obtained FoF halo sample, we select only those which have a central subhalo with stellar mass $M_\star > 5 \times 10^{10}\,M_\odot$. This limit is roughly the 1σ lower limit of the observed stellar mass of the MW ($M_\star = (6.08 \pm 1.14) \times 10^{10}\,M_\odot$; Licquia and Newman 2015).

In addition to its internal properties, a MW-like galaxy has to fulfil certain isolation criteria. Firstly, we select only MW-like galaxies which do not have a more massive halo (in terms of the virial mass M_{200}) within 0.5 Mpc. This is approximately the distance to M31 (McConnachie 2012), which is slightly more massive than the MW. This criterion removes especially massive interacting galaxies. Secondly, we require that there should be no further galaxy with 5× the M_{200} of the selected MW-like galaxy within 3 Mpc. This is because the nearest observed galaxy which is more massive than the MW or M31 is NGC 5128 (Centaurus A), located at a distance of ≈ 3.7 Mpc (see e.g. table 1 of Karachentsev and Telikova 2018). The M81 and IC 342 groups are also over 3 Mpc from the MW. For further discussion of the appropriate isolation criteria, we refer the reader to Banik et al. (2021).

These selection criteria give 86 (TNG50-1), 398 (TNG100-1), and 2117 (TNG300-1) MW-like galaxies at $z = 0$. To increase our final sample size, we also search for analogues to the MW and the MCs (Section 10.2.4) up to redshift $z = 0.26$, which corresponds to a lookback time of about 3.1 Gyr. This allows us to consider 20 snapshots, which together yield 1547, 7360, and 40075 MW-like galaxies with $0.0 \leq z \leq 0.26$ in the TNG50-1, TNG100-1, and TNG300-1 runs, respectively. The statistics of analogues to the MCs should be similar over this period as it is a small fraction of the Hubble time. The minimum time step between the here considered snapshots is 120 Myr, which is quite long given that we are trying to find snapshots where the MCs are at a rather short-lived phase of their orbit (close to pericentre). Thus, although a selected subhalo could in principle be a progenitor/descendent of a selected subhalo in a previous/subsequent snapshot, we treat all selected subhaloes independently from each other. We will see later that we do have one case of the same system satisfying the selection criteria at different times, but argue that this is a reasonable way to build up the statistics.

10.2.4 Selecting analogues to the MCs

In order to identify analogues to the MCs, we first extract and rank in $M_\star$ all non-central subhaloes with a non-zero SubhaloFlag parameter within 250 kpc of a MW-like galaxy (Section 10.2.3).[6] The

[5] https://seafile.unistra.fr/d/6b09464443da478d8926/ [07.11.2022]

[6] A description of the SubhaloFlag parameter can be found here: https://www.tng-project.org/data/docs/background/#subhaloflag [08.03.2022]

restriction on the SubhaloFlag parameter excludes subhaloes with a non-cosmological origin, e.g. baryonic fragments of the disc or galactic substructures.[7]

Secondly, after ranking the subhaloes according to their stellar mass, an analogue to the LMC (SMC) is defined as the most (second-most) massive satellite (in terms of $M_\star$) if it has a total-to-stellar mass ratio of $M_{\rm total}/M_\star > 5$ and $M_\star \geq 1.5 \times 10^9\, M_\odot$ ($M_\star \geq 4.6 \times 10^8\, M_\odot$) (see table 4 of McConnachie 2012). The here-used lower limit on the LMC's stellar mass is 1.8× smaller than the $2.7 \times 10^9\, M_\odot$ reported by Livio and T. M. Brown (2006), which is often quoted in the literature. The lower value is applied in order to increase the number of LMC analogues and because the study by McConnachie (2012) appeared more recently. Note that $M_{\rm total}$ is defined as the total mass of all member baryonic and dark matter particles/gas cells which are bound to the subhalo. The minimum $M_{\rm total}/M_\star$ cut removes especially substructures within the MW-like galaxy. These selection criteria give 331 (TNG50-1), 1414 (TNG100-1), and 3823 (TNG300-1) LMC analogues and 343 (TNG50-1), 766 (TNG100-1), and 1148 (TNG300-1) SMC analogues with $z \leq 0.26$. Requiring that a MW-like galaxy has to host an analogue to both the LMC and the SMC gives 147 (TNG50-1), 454 (TNG100-1), and 601 (TNG300-1) analogues. We refer to these as our initial MCs samples because only selection criteria on the total and stellar mass components are applied. A detailed comparison with the observed MCs including different physical properties is presented in the following sections.

10.3 Results

In this section, we quantify the likelihood of analogues to the MCs in the ΛCDM framework by applying different observational constraints to the initial samples that we defined in Section 10.2.4. Individual analogues to the MCs are traced back through cosmic time in order to investigate their evolution and the formation of the MS in a cosmological context.

The frequency P of analogues to the MCs around MW-like galaxies is given by the number of selected analogues divided by the number of MW-like galaxies (Section 10.2.3). This P-value is converted into an equivalent number of standard deviations for a single Gaussian variable χ by solving

$$1 - \frac{1}{\sqrt{2\pi}} \int_{-\chi}^{\chi} \exp\left(-\frac{x^2}{2}\right) dx \;\equiv\; P\,. \tag{10.5}$$

We solve this iteratively using the Newton-Raphson algorithm.

10.3.1 Phase-space density of the MCs

We select only systems with a geometrical configuration similar to the observed MW-MCs system by requiring $50\,{\rm kpc} \leq d_{\rm MW-LMC} \leq 100\,{\rm kpc}$. The lower limit is applied because the LMC is currently at pericentre with a Galactocentric distance of 50 kpc. This typically removes MW-LMC systems with rather high values of $\Omega_{\rm LMC}$, which can more easily exceed the observed $\Omega_{\rm LMC,obs} = 6.48\,{\rm km\,s^{-1}\,kpc^{-1}}$ for LMC analogues at smaller distances. The upper distance limit is set in order to select only LMC analogues reasonably close to their MW-like host galaxies. These additional criteria result in

[7] Many additional non-cosmological subhaloes are in any case removed by the $M_{\rm total}/M_\star$ cut as it excludes dark matter-deficient galaxies like tidal dwarfs (Ploeckinger et al. 2018; Haslbauer et al. 2019).

sample sizes of 46 (TNG50-1), 118 (TNG100-1), and 191 (TNG300-1), which in total gives 355 MCs analogues across all three TNG runs.

The distributions of $f_{\rm MCs}$ (Equation 10.1) and $\Omega_{\rm LMC}$ (Equation 10.3) for these systems are shown in Figure 10.2. In all three runs, none of the 355 selected MCs analogues have $f_{\rm MCs} \geq f_{\rm MCs,obs}$ and $\Omega_{\rm LMC} \geq \Omega_{\rm LMC,obs}$, as indicated by the grey region. This conclusion remains the same if we only consider the condition $f_{\rm MCs} \geq f_{\rm MCs,obs}$, indicating that the phase-space density of the MCs is the most problematic aspect of the observations. 3 out of the 355 systems satisfy $\Omega_{\rm LMC} \geq \Omega_{\rm LMC,obs}$.

In the high-resolution realization TNG50-1, the null detection of MCs analogues with $f_{\rm MCs} \geq f_{\rm MCs,obs}$ means that the frequency of MCs analogues is below $1/46$, which is equivalent to a tension of $> 2.29\sigma$ for a single Gaussian variable (Equation 10.5). In TNG100-1 and TNG300-1, the upper limit to the frequency of such MCs analogues is $1/118$ and $1/191$, corresponding to a $> 2.63\sigma$ and $> 2.79\sigma$ tension, respectively. This gives the misleading impression that the tension decreases in the higher resolution runs. However, the box size, and therefore also the sample size of MCs analogues, are smaller in the higher resolution runs. As a consequence, the lower limit to the tension becomes minimal in TNG50-1, giving the misleading impression that this simulation is in agreement with $f_{\rm MCs,obs}$.

The above analysis only sets lower limits to the tension by relying on the null detection of MCs analogues in the different TNG runs. In the following, we estimate the significance by extrapolating the cumulative $f_{\rm MCs}$ distribution (i.e. the likelihood of an even higher value) up to the observed value $f_{\rm MCs,obs}$ (see e.g. Asencio, Banik and Kroupa 2021). We fit the cumulative $f_{\rm MCs}$ distribution with a linear and a quadratic regression in $\log_{10}$-space and extrapolate the frequency of analogues up to $f_{\rm MCs,obs}$. This is visualized in Figure 10.3 for the TNG50-1 run. The extrapolated cumulative frequency at $f_{\rm MCs,obs}$ is then converted into an equivalent number of standard deviations for a single Gaussian variable (Equation 10.5). Applying the linear (quadratic) regression to the entire range of the simulated $f_{\rm MCs}$ distribution results in a 3.15σ (3.95σ), 2.47σ (3.11σ), and 2.48σ (2.82σ) tension in the TNG50-1, TNG100-1, and TNG300-1 run, respectively (see also Table 10.2). Thus, the tension becomes maximal in the highest-resolution realization TNG50-1. We will argue in Appendix E.1 that the phase-space density configuration of simulated MCs analogues is likely not affected by numerical resolution issues in this simulation.

Figure 10.3 indicates that the quadratic regression is a good fit especially for $\log_{10}\left(f_{\rm MCs,min}/\left[\mathrm{km^{-3}\,s^{3}\,kpc^{-3}}\right]\right) \lesssim -13$. The linear fit is more conservative as it underestimates the tension because it suppresses the curvature for data with $\log_{10}\left(f_{\rm MCs,min}/\left[\mathrm{km^{-3}\,s^{3}\,kpc^{-3}}\right]\right) \gtrsim -13$. But since curvature is apparent in the data, a quadratic fit should be more appropriate, so our main results refer to the quadratic extrapolation. The frequencies and tensions for different selection criteria and statistical methods are summarized in Table 10.2.

In order to assess the robustness of this method, we also derive the tension by fitting the distribution over different ranges of $f_{\rm MCs}$. For this, we fix the upper limit of the fitting range at the maximum value of $f_{\rm MCs}$ and perform different extrapolations by successively increasing the minimum limit of the fitting range, i.e. we only fit towards the upper end of the $f_{\rm MCs}$ distribution rather than using the full range. The so-estimated tensions in dependence of the minimum applied $f_{\rm MCs}$ limits are shown in Figure 10.4. In TNG100-1 and TNG300-1, the tension converges to $\approx 3.1\sigma$ and $\approx 2.8\sigma$ for $\log_{10}\left(f_{\rm MCs,min}/\left[\mathrm{km^{-3}\,s^{3}\,kpc^{-3}}\right]\right) \lesssim -15$ and $\lesssim -14$ for the quadratic fit (right panel), respectively. In TNG50-1, the tension reaches $\approx 3.9\sigma$ for $\log_{10}\left(f_{\rm MCs,min}/\left[\mathrm{km^{-3}\,s^{3}\,kpc^{-3}}\right]\right) \lesssim -14.2$. In all

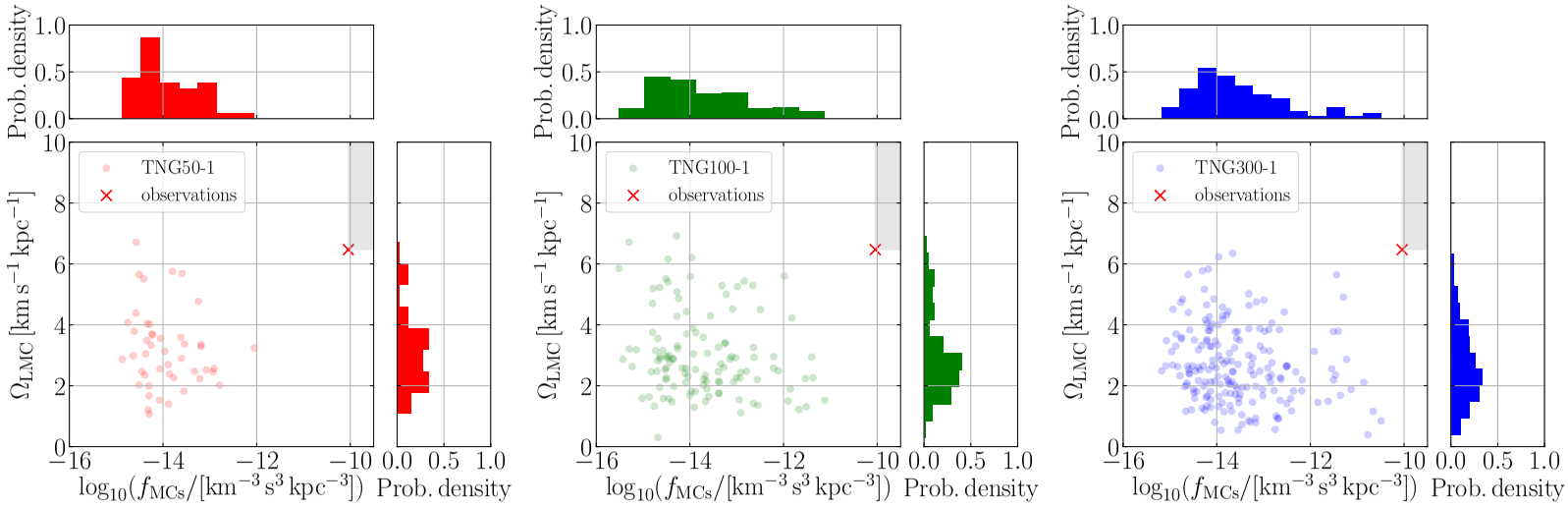

Figure 10.2: Distribution of the specific phase-space density of the MCs ($f_{\rm MCs}$; Equation 10.1) and the inverse kinematic timescale of the LMC ($\Omega_{\rm LMC}$; Equation 10.3) for systems with $50\,{\rm kpc} \leq d_{\rm MW-LMC} \leq 100\,{\rm kpc}$ in the ΛCDM cosmological simulations TNG50-1 (46 objects; left), TNG100-1 (118 objects; middle), and TNG300-1 (191 objects; right). The red cross shows the observed values, i.e. $f_{\rm MCs,obs} = 9.10 \times 10^{-11}\,{\rm km}^{-3}\,{\rm s}^3\,{\rm kpc}^{-3}$ and $\Omega_{\rm LMC,obs} = 6.48\,{\rm km\,s}^{-1}\,{\rm kpc}^{-1}$. None of the 355 analogues in the three TNG runs have $f_{\rm MCs} \geq f_{\rm MCs,obs}$ and $\Omega_{\rm LMC} \geq \Omega_{\rm LMC,obs}$, as indicated by the grey shaded region at the top right of each panel.

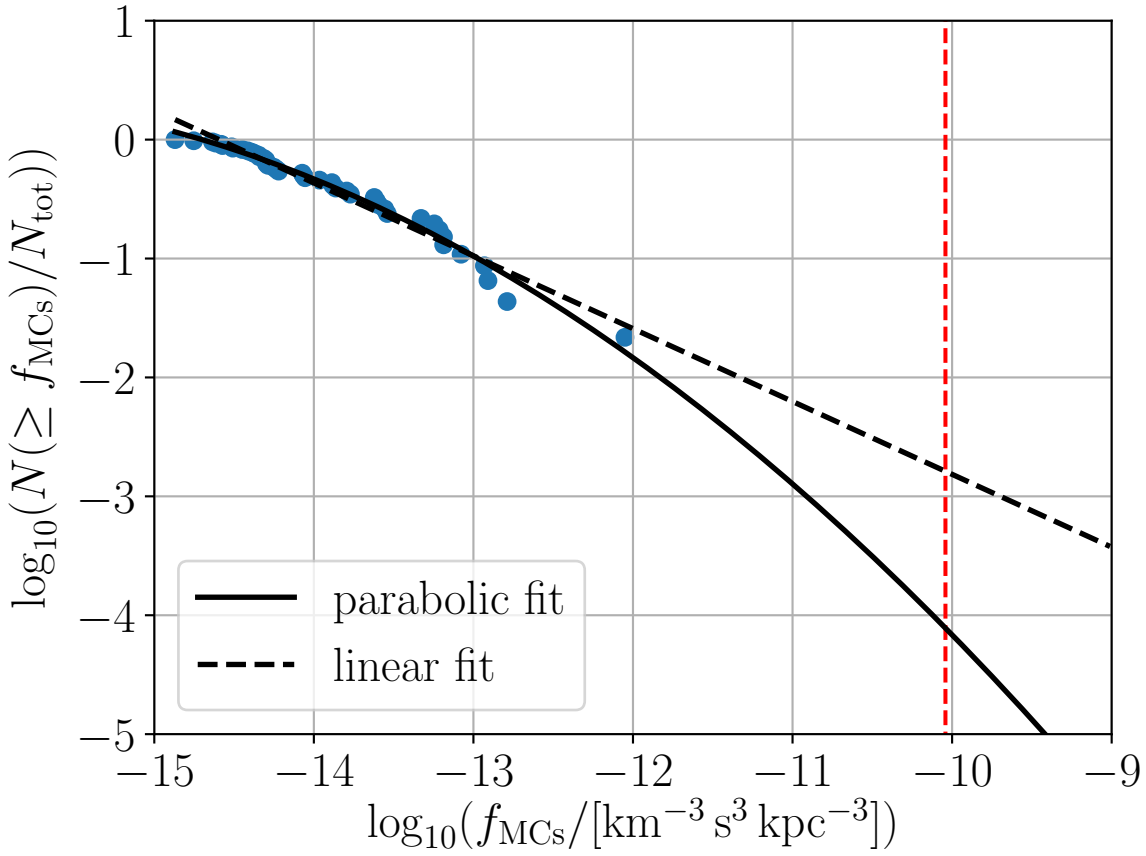

Figure 10.3: Cumulative distribution of f_{MCs} obtained from the TNG50-1 run fitted with a linear (dashed black line) and a quadratic (solid black line) function in $\log_{10}$-space. The red dashed line marks the observed value of $f_{\mathrm{MCs,obs}} = 9.10 \times 10^{-11}\,\mathrm{km}^{-3}\,\mathrm{s}^{3}\,\mathrm{kpc}^{-3}$. The intersection between the linear (quadratic) fit and the red dashed line yields a P-value of 1.62×10^{-3} (7.81×10^{-5}), which corresponds to a 3.15σ (3.95σ) tension for a single Gaussian variable (see also Table 10.2 for TNG100-1 and TNG300-1).

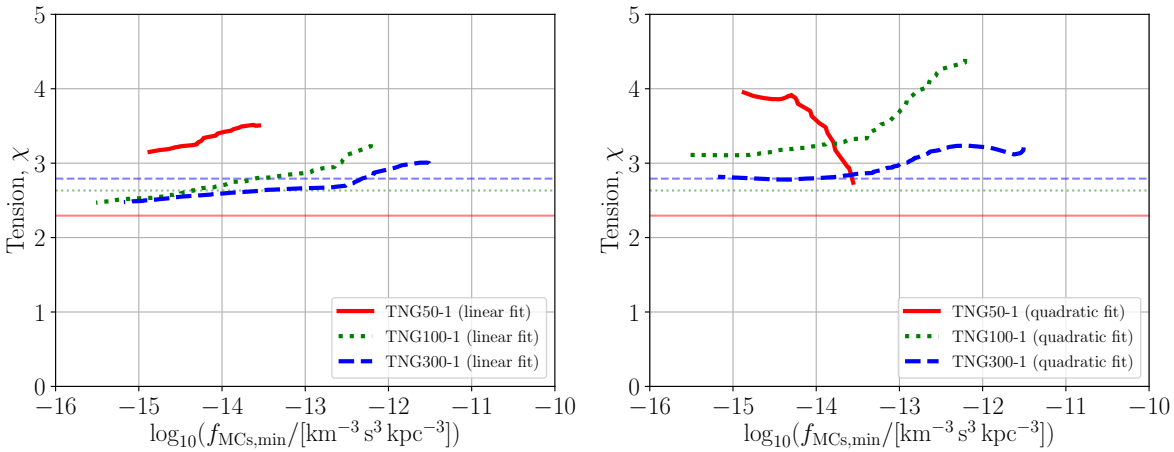

Figure 10.4: Estimated tension of the MCs' phase-space density in dependence of the minimum value of f_{MCs} beyond which the cumulative f_{MCs} distribution of the simulations is fitted with a linear (left panel) and quadratic (right panel) function. The horizontal lines correspond to the null detection of analogues as equivalent to an upper limit on the frequency of analogues.

cases, we only consider a fitting range wide enough to include at least ten points.

To assess the impact different distance criteria, Appendix E.2 discusses the f_{MCs} and Ω_{LMC} distributions for analogues to the MCs with $d_{\mathrm{MW-LMC}} \geq 50\,\mathrm{kpc}$. None of the so-selected 1193 MCs analogues in the six TNG runs have $\Omega_{\mathrm{LMC}} \geq \Omega_{\mathrm{LMC,obs}}$ and $f_{\mathrm{MCs}} \geq f_{\mathrm{MCs,obs}}$, while only one of these analogues has $f_{\mathrm{MCs}} \geq f_{\mathrm{MCs,obs}}$. Possible reasons for the discrepancy between the observed phase-space density of the MCs and the f_{MCs} distribution of the TNG simulations are discussed further in Section 10.4.2.

10.3.2 Tracing back analogues to the MCs in light of the MS

Using the initial sample of MCs analogues (Section 10.2.4), we found that 3 out of the 1202 analogues in TNG50-1, TNG100-1, and TNG300-1 combined fulfill $f_{\mathrm{MCs}} \geq f_{\mathrm{MCs,obs}}$ (Appendix E.2). In order to understand their formation and evolution in a cosmological context, we trace these analogues back through cosmic time using the SUBLINK merger tree catalogue (Rodriguez-Gomez et al. 2015). We already know that in these systems, the LMC will be either very close to the MW (within 50 kpc) or very far away (beyond 100 kpc), making them somewhat different to the observed MCs. We nevertheless consider these systems in more detail to better understand the history behind ΛCDM systems that might come close to resembling the observed MCs.

The evolution of the physical separation between the MW-LMC, MW-SMC, and LMC-SMC analogues are shown in Figure 10.5. The first of these three analogues (hereafter system 1) is identified in the TNG100-1 simulation at redshift $z = 0.26$, which corresponds to a lookback time of 3.0 Gyr. In what follows, we will assume that the time of identification of a system would be the present time if we were living in that system's MW analogue. We will therefore use 'x Gyr ago' to mean x Gyr prior to the time of identification. Both the MW-LMC and MW-SMC orbits have their first pericentre passage 0.6 Gyr ago, when $d_{\mathrm{MW-LMC}} = 157.6\,\mathrm{kpc}$ and $d_{\mathrm{MW-SMC}} = 169.0\,\mathrm{kpc}$. As mentioned above, these greatly exceed the present Galactocentric distances of the MCs. The LMC and SMC analogues

Selection criteria	Simulation	Number of analogues	Frequency	Significance
Initial sample of analogues to the MW (Section 10.2.3)	TNG50-1:	1547	–	–
	TNG100-1:	7360	–	–
	TNG300-1:	40075	–	–
	All 3 runs:	48982	–	–
Initial sample of analogues to the LMC (Section 10.2.4)	TNG50-1:	331	331/1547	1.24σ
	TNG100-1:	1414	1414/7360	1.30σ
	TNG300-1:	3823	3823/40075	1.67σ
	All 3 runs:	5568	5568/48982	1.58σ
Initial sample of analogues to the SMC (Section 10.2.4)	TNG50-1:	343	343/1547	1.22σ
	TNG100-1:	766	766/7360	1.63σ
	TNG300-1:	1148	1148/40075	2.19σ
	All 3 runs:	2257	2257/48982	1.99σ
Initial sample of analogues to the MCs (Section 10.2.4)	TNG50-1:	147	147/1547	1.67σ
	TNG100-1:	454	454/7360	1.87σ
	TNG300-1:	601	601/40075	2.43σ
	All 3 runs:	1202	1202/48982	2.25σ
Initial sample of analogues to the MCs (Section 10.2.4)	TNG50-1:	46	46/1547	2.17σ
$+50 \leq d_{\mathrm{MW-LMC}}/\mathrm{kpc} \leq 100$	TNG100-1:	118	118/7360	2.41σ
	TNG300-1:	191	191/40075	2.82σ
	All 3 runs:	355	355/48982	2.69σ
Sample of analogues to the MCs with $50 \leq d_{\mathrm{MW-LMC}}/\mathrm{kpc} \leq 100$	TNG50-1:	0	$< 1/46$	$> 2.29\sigma$
$+f_{\mathrm{MCs}} \geq f_{\mathrm{MCs,obs}}$ (Equation 10.1)	TNG100-1:	0	$< 1/118$	$> 2.63\sigma$
	TNG300-1:	0	$< 1/191$	$> 2.79\sigma$
	All 3 runs:	0	$< 1/355$	$> 2.99\sigma$
Sample of analogues to the MCs with $50 \leq d_{\mathrm{MW-LMC}}/\mathrm{kpc} \leq 100$	TNG50-1:	–	1.62×10^{-3}	3.15σ
Extrapolation of f_{MCs} distribution using a linear fit (Figure 10.4)	TNG100-1:	–	1.35×10^{-2}	2.47σ
	TNG300-1:	–	1.32×10^{-2}	2.48σ
Sample of analogues to the MCs with $50 \leq d_{\mathrm{MW-LMC}}/\mathrm{kpc} \leq 100$	TNG50-1:	–	7.81×10^{-5}	3.95σ
Extrapolation of f_{MCs} distribution using a quadratic fit (Figure 10.4)	TNG100-1:	–	1.87×10^{-3}	3.11σ
	TNG300-1:	–	4.84×10^{-3}	2.82σ
Sample of analogues to the MCs with $50 \leq d_{\mathrm{MW-LMC}}/\mathrm{kpc} \leq 100$	TNG50-1:	0	$< 6.85 \times 10^{-3}$	$> 2.70\sigma$
$+f_{\mathrm{MCs}} \geq f_{\mathrm{MCs,obs}}$	TNG100-1:	0	$< 2.98 \times 10^{-3}$	$> 2.97\sigma$
+LMC-DoS alignment	TNG300-1:	0	$< 1.93 \times 10^{-3}$	$> 3.10\sigma$
	All 3 runs:	0	$< 1.10 \times 10^{-3}$	$> 3.26\sigma$
Sample of analogues to the MCs with $50 \leq d_{\mathrm{MW-LMC}}/\mathrm{kpc} \leq 100$	TNG50-1:	–	6.65×10^{-4}	3.40σ
Extrapolation of f_{MCs} distribution using a linear fit (Figure 10.4)	TNG100-1:	–	4.52×10^{-3}	2.84σ
+LMC-DoS alignment	TNG300-1:	–	4.43×10^{-3}	2.85σ
Sample of analogues to the MCs with $50 \leq d_{\mathrm{MW-LMC}}/\mathrm{kpc} \leq 100$	TNG50-1:	–	3.90×10^{-5}	4.11σ
Extrapolation of f_{MCs} distribution using a quadratic fit (Figure 10.4)	TNG100-1:	–	7.55×10^{-4}	3.37σ
+LMC-DoS alignment	TNG300-1:	–	1.80×10^{-3}	3.12σ

Table 10.2: Analogues to the MCs (i.e., systems with satellites analogous to both the LMC and the SMC) in the redshift range $0 \leq z \leq 0.26$ in the TNG50-1, TNG100-1, and TNG300-1 simulation for different selection criteria. The table lists the number of analogues, their frequency relative to the total number of selected MW-like galaxies hosting analogues to both MCs, and the corresponding equivalent number of standard deviations for a single Gaussian variable (Equation 10.5). The first part summarizes the initial samples of analogues to the MW, LMC, SMC, and both MCs as defined in Sections 10.2.3 and 10.2.4. The other parts list the results if additional selection criteria (indicated by the plus symbol in the first column) are applied to the initial sample of analogues to the MCs. The last part of the table gives the combined likelihood of the MCs by adding up the χ^2 values of their phase-space density (Section 10.3.1) and the alignment of the LMC orbital pole with that of the DoS. The corresponding P-value is calculated for two degrees of freedom (Section 10.4.3.2). As explained in Section 10.3.1, the linear extrapolation underestimate the tension because the fit does not account for the curvature for data with $\log_{10}\left(f_{\mathrm{MCs,min}}/\left[\mathrm{km}^{-3}\,\mathrm{s}^{3}\,\mathrm{kpc}^{-3}\right]\right) \gtrsim -13$.

are accreted together towards the MW-like galaxy and have their first pericentre passage wrt. each other 0.8 Gyr ago, with $d_{\mathrm{LMC-SMC}} = 26.3\,\mathrm{kpc}$ then. At the time of identification, the MCs are at apocentre with $d_{\mathrm{LMC-SMC}} = 72.5\,\mathrm{kpc}$. The LMC has to tidally remove gas from the SMC during a past close interaction $\approx 3\,\mathrm{Gyr}$ ago to allow the stripped gas to almost circumnavigate the galaxy, which is necessary to form the MS (D'Onghia and Fox 2016). In the model of Lucchini et al. (2020), a substantial part of the MS is formed during the second close LMC-SMC interaction about 1.5 Gyr ago with a pericentre separation of about 20 kpc (see their extended data figure 2). An interaction between the MCs $\gtrsim 1$ Gyr ago could also be required to explain the northern arm of the LMC and substructures in the LMC's outskirts (Cullinane et al. 2022a; Cullinane et al. 2022b). Therefore, we consider it possible that the MS would form in our selected analogues only if the LMC and SMC have undergone a pericentre passage within 30 kpc over the time period $1 - 4$ Gyr before identification. We defined these criteria before extracting the trajectories of analogues in order to guarantee an unbiased evaluation of the situation. Such a close previous interaction between the MCs is absent in the here identified system 1, implying that it is inconsistent with the observed MS. While there is a close interaction within 30 kpc, we argue that 0.8 Gyr is too little time for the stripped gas to circumnavigate the galaxy, especially since the LMC and SMC in this system were rather widely separated at earlier times. Tracing the individual galaxies forward in cosmic time reveals that these analogue MCs merge with each other 1.3 Gyr after identification. Such short merger times are expected due to dynamical friction between the extended dark matter haloes, as discussed further in Section 10.4.2.

The second and third analogues correspond to the same system identified at different times in TNG300-1. The formation and evolution of this system are presented in the right panel of Figure 10.5. This system satisfies $f_{\mathrm{MCs}} \geq f_{\mathrm{MCs,obs}}$ at $z = 0.21$ (system 2) and $z = 0.20$ (system 3), corresponding to lookback times of 2.7 Gyr and 2.5 Gyr, respectively. Similarly to system 1 and using the $z = 0.21$ case, the LMC and SMC analogues are accreted together towards the MW-like galaxy. When the system fulfils the selection criteria at $z = 0.21$, the MW-LMC and MW-SMC have their first pericentre but the LMC-SMC system has its fourth pericentre: the first occurred 4.8 Gyr ago ($d_{\mathrm{LMC-SMC}} = 75.3\,\mathrm{kpc}$), the second was 1.4 Gyr ago ($d_{\mathrm{LMC-SMC}} = 29.9\,\mathrm{kpc}$), and the third was 0.5 Gyr ago ($d_{\mathrm{LMC-SMC}} = 13.3\,\mathrm{kpc}$). Thus, in contrast to the previous example, the close interaction of the LMC-SMC system before its detection (grey shaded region in Figure 10.5) would in principle allow the formation of a gaseous tidal stream comparable to the MS. Note that this system only marginally satisfies our MS condition because there is only one pericentre $1 - 4$ Gyr before identification and the distance then is 29.9 kpc, which only just satisfies the requirement to be within 30 kpc.

Our results support a first infall scenario in which the MCs are accreted together within the last $\lesssim 3\,\mathrm{Gyr}$, in agreement with previous studies (e.g. Boylan-Kolchin, Besla and Hernquist 2011). This causes a high relative velocity of the LMC analogue wrt. the MW-like galaxy and a high relative velocity between the MCs of $173.3\,\mathrm{km\,s^{-1}}$ at $z = 0.21$ (system 2) and $148.0\,\mathrm{km\,s^{-1}}$ at $z = 0.20$ (system 3), which significantly exceeds the observed $v_{\mathrm{LMC-SMC}} = 90.8\,\mathrm{km\,s^{-1}}$ in all cases. Furthermore, the MW-LMC and MW-SMC orbital poles are misaligned by $59^{\circ}.65$ at $z = 0.21$ (system 2) and by $115^{\circ}.67$ at $z = 0.20$ (system 3), being therewith much less aligned than observed ($\theta = 16^{\circ}.96$). Note that this MW-MCs system is again short-lived as the LMC (SMC) merges with the MW analogue 1.0 Gyr (0.7 Gyr) after identification.

The physical properties of all three MW-MCs analogues are listed in Table 10.3.

Parameter	Unit	Observed	System 1	System 2	System 3
Simulation	–	–	TNG100-1	TNG300-1	TNG300-1
Redshift	–	≈ 0	0.26	0.21	0.20
Lookback time	Gyr	≈ 0	3.1	2.7	2.5
$M^{\mathrm{MW}}_{\mathrm{total}}$	$10^{10}\,M_\odot$	–	171	232	232
$M^{\mathrm{MW}}_{\mathrm{dm}}$	$10^{10}\,M_\odot$	–	159	202	202
$M^{\mathrm{MW}}_{\star}$	$10^{10}\,M_\odot$	(6.08 ± 1.14)	5.12	5.14	5.51
$M^{\mathrm{LMC}}_{\mathrm{total}}$	$10^{10}\,M_\odot$	–	17.50	5.51	4.92
$M^{\mathrm{LMC}}_{\mathrm{dm}}$	$10^{10}\,M_\odot$	–	15.34	3.45	2.98
$M^{\mathrm{LMC}}_{\star}$	$10^{10}\,M_\odot$	0.15	0.79	0.96	0.98
$M^{\mathrm{SMC}}_{\mathrm{total}}$	$10^{10}\,M_\odot$	–	1.62	0.48	0.31
$M^{\mathrm{SMC}}_{\mathrm{dm}}$	$10^{10}\,M_\odot$	–	1.45	0.38	0.25
$M^{\mathrm{SMC}}_{\star}$	$10^{10}\,M_\odot$	0.046	0.051	0.095	0.060
$d_{\mathrm{MW-LMC}}$	kpc	50.0	187.2	23.7	47.0
$d_{\mathrm{MW-SMC}}$	kpc	61.3	235.3	28.7	55.8
$d_{\mathrm{LMC-SMC}}$	kpc	24.5	72.5	11.6	14.03
$v_{\mathrm{MW-LMC}}$	$\mathrm{km\,s^{-1}}$	323.8	213.2	381.2	92.3
$v_{\mathrm{MW-SMC}}$	$\mathrm{km\,s^{-1}}$	245.6	192.2	248.3	185.7
$v_{\mathrm{LMC-SMC}}$	$\mathrm{km\,s^{-1}}$	90.8	21.9	173.3	148.0
$h_{\mathrm{MW-LMC}}$	$10^3\,\mathrm{kpc\,km\,s^{-1}}$	15.9	36.8	5.6	2.1
$h_{\mathrm{MW-SMC}}$	$10^3\,\mathrm{kpc\,km\,s^{-1}}$	15.0	40.5	1.2	5.2
f_{MCs} (Equation 10.1)	$10^{-10}\,\mathrm{km^{-3}\,s^3\,kpc^{-3}}$	0.91	2.51	1.22	1.12
Ω_{LMC} (Equation 10.3)	$\mathrm{km\,s^{-1}\,kpc^{-1}}$	6.48	1.14	16.09	1.96
$\arccos(\widehat{\boldsymbol{h}}_{\mathrm{MW-LMC}} \cdot \widehat{\boldsymbol{h}}_{\mathrm{MW-SMC}})$	–	16°.96	15°.66	59°.65	115°.67
$\arccos(\widehat{\boldsymbol{h}}_{\mathrm{MW-LMC}} \cdot \widehat{\boldsymbol{h}}_{\mathrm{LMC-SMC}})$	–	132°.68	119°.69	87°.59	96°.43

Table 10.3: Physical properties of the observed MW, LMC, and SMC and their analogues which fulfil $f_{\mathrm{MCs}} \geq f_{\mathrm{MCs,obs}} = 9.1 \times 10^{-11}\,\mathrm{km^{-3}\,s^3\,kpc^{-3}}$ at redshift $z = 0.26$ (system 1), $z = 0.21$ (system 2), and $z = 0.20$ (system 3). Systems 2 and 3 consist of the same objects identified at different timesteps (snapshots). The last two rows list the alignment of the orbital poles, where $\widehat{\boldsymbol{h}}$ is the normalized specific angular momentum vector. The observed stellar masses of the MW and the MCs are taken from Licquia and Newman (2015) and McConnachie (2012), respectively. The distances and velocities of the MCs are taken from Pawlowski and Kroupa (2020). The dark matter and total masses of these galaxies are not listed because these parameters are very sensitive to the applied measurement method (though see Section 10.4.4).

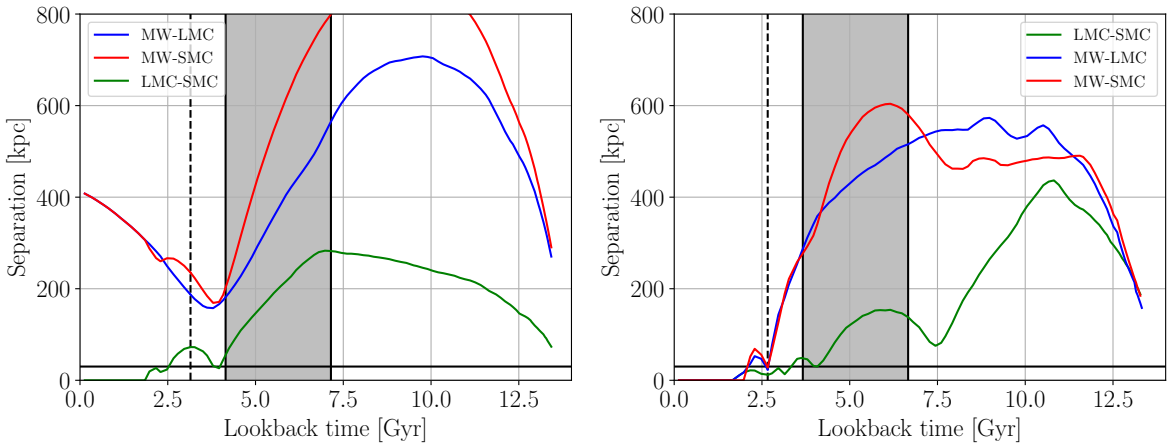

Figure 10.5: Time evolution of the physical separation between the MW-LMC (blue), MW-SMC (red), and LMC-SMC (green) in analogue system 1 (left panel) and 2 (right panel) identified at a lookback time of 3.1 Gyr ($z = 0.26$) in the TNG100-1 simulation and 2.7 Gyr ($z = 0.21$) in the TNG300-1 simulation, respectively. Systems 2 and 3 consist of the same system identified as an analogue to the MCs at slightly different times (the larger lookback time is plotted here as the former would overlap with the 2.5 Gyr gridline). The formation of the MS requires a close interaction between the MCs before identification (see the text), for which we show a solid black horizontal line at 30 kpc and shade the time period 1 – 4 Gyr before identification (dashed vertical line). *Left panel:* Since there is no close (< 30 kpc) interaction within this period, this system would not form an MS-like structure. *Right panel:* The LMC and SMC have a pericentre passage wrt. each other about 1.5 Gyr before identification with $d_{\mathrm{LMC-SMC}} = 29.9$ kpc, in principle marginally allowing the formation of an MS-like structure. The physical properties of these galaxies are listed in Table 10.3.

10.4 Discussion

In this section, we first comment on how the low P-values of our analysis compare to prior studies on the MCs in ΛCDM simulations (Section 10.4.1). Secondly, we discuss which physical processes might be responsible for the low frequencies of analogues to the MCs, paying particular attention to the effect of dynamical friction on their orbits (Section 10.4.2). We consider the relation between the MCs and the LG satellite planes (Section 10.4.3) and the dynamical mass of the LMC (Section 10.4.4). Finally, we highlight how a common origin is possible in theories beyond the current standard model of cosmology, in which the observed configuration of the MCs may be more common (Section 10.4.5).

10.4.1 Prior studies on the MCs in ΛCDM

The dynamics and occurrence rate of analogues to the MCs have been considered in several previous studies in the ΛCDM framework (e.g. Boylan-Kolchin, Besla and Hernquist 2011; Busha et al. 2011; Santos-Santos et al. 2021). In particular, Boylan-Kolchin, Besla and Hernquist (2011) examined the pure N-body simulation Millennium-II (MS-II; Boylan-Kolchin, Springel, White, Jenkins and Lemson 2009), finding that about 35% (32%) of MW-like haloes with a virial mass in the range $10^{12} < M_{\mathrm{vir}}/M_{\odot} < 3 \times 10^{12}$ host an analogue to the LMC (SMC) at $z = 0$. They defined an LMC (SMC) analogue satellite as that with the highest (second-highest) dark matter-only infall mass M_{acc}, which furthermore needs to be in the range $8 \times 10^{10} < M_{\mathrm{acc}}/M_{\odot} < 3.2 \times 10^{11}$ for the LMC and

$4 \times 10^{10} < M_{\rm acc}/M_\odot < 1.6 \times 10^{11}$ for the SMC (see section 2.3.2 of Boylan-Kolchin, Besla and Hernquist 2011). Their frequency of LMC (35%) and SMC (32%) analogues in MW-like haloes is higher than in our analysis of the TNG simulations, in which 11.4% and 4.6% of the selected MW-like galaxies host at least an LMC and SMC analogue, respectively, if we combine results from TNG50-1, TNG100-1, and TNG300-1 (Table 10.2). One reason for the difference between their result and ours could be that we select analogues based on the stellar mass and $M_{\rm total}/M_\star$ (Section 10.2.4). MS-II is a purely N-body simulation (it only considers dark matter) whereas the here-assessed IllustrisTNG runs are hydrodynamical cosmological simulations, allowing us to select satellite galaxies based on their stellar mass without the need of semi-analytic models and abundance matching techniques. Since the stellar mass is directly observed, our comparison with observations should be more direct.

Similarly to the three identified analogues to the MCs in Section 10.3.2, the LMC analogues found by Boylan-Kolchin, Besla and Hernquist (2011) were typically accreted at late times ($\lesssim 4$ Gyr ago). About 2.5% of their MW-like haloes host LMC-SMC binaries with separation $d_{\rm LMC-SMC} < 50\,h^{-1}$ kpc $\approx$ 68.5 kpc and relative velocity $v_{\rm LMC-SMC} < 150\,{\rm km\,s^{-1}}$ (see their section 5), which is comparable to the HST three-epoch proper motion measurement (Section 10.2.1) of Kallivayalil et al. (2013). These upper limits to the LMC-SMC separation and relative velocity are significantly higher than the observed values derived from the latest data ($d_{\rm LMC-SMC} = 24.5$ kpc and $v_{\rm LMC-SMC} = 90.8\,{\rm km\,s^{-1}}$). In particular, our assumed proper motions (from Pawlowski and Kroupa 2020) are based on a combination of results from Gaia DR2 (Gaia Collaboration 2018a) and the HST (Kallivayalil et al. 2013). Both of these were published after the work of Boylan-Kolchin, Besla and Hernquist (2011). Furthermore, section 5 of Boylan-Kolchin, Besla and Hernquist (2011) defined the SMC analogue of an LMC-SMC binary system as the second-ranked subhalo in the host without setting a specific mass range, which could make the SMC analogue a lot less massive than the actual SMC. We thus expect their work to overestimate the frequency of analogues to the MCs. Proper motion uncertainties generally inflate the estimated $v_{\rm LMC-SMC}$, so this may decrease further as observations improve.

In the Bolshoi simulation (Klypin, Trujillo-Gomez and Primack 2011; Trujillo-Gomez et al. 2011), about 10% of hosts with a virial mass similar to the MW have two MC-like satellites based on the maximum circular velocity (see section 2 and figure 1 of Busha et al. 2011). In contrast to our work, separation or velocity criteria between the MCs and the MW or between the MCs themselves were not applied. They subsequently used instead the r-band luminosity for a better comparison with observations (see their section 4 and table 2). Their results are very consistent with the observational findings of Liu et al. (2011), who found that 3.5% of MW-like galaxies host two satellites with luminosities comparable to the MCs within a radius of 150 kpc based on the Sloan Digital Sky Survey.

In the IllustrisTNG simulations, 9.5% (TNG50-1), 6.2% (TNG100-1), and 1.5% (TNG300-1) of MW-like galaxies host two satellites with stellar masses similar to the MCs (Table 10.2). Thus, the highest resolution realization TNG50-1 is consistent with Busha et al. (2011). The frequency of analogues to the MCs is a factor of 1.5 (6.3) higher in TNG50-1 compared to TNG100-1 (TNG300-1), which could be a resolution effect. However, this should not significantly affect our results in Section 10.3 because the phase-space density of analogues to the MCs seems to have converged in the IllustrisTNG runs: the $f_{\rm MCs}$ distribution peaks at $\log_{10}(f_{\rm MCs}/\left[{\rm km^{-3}\,s^3\,kpc^{-3}}\right]) \approx -14$ in all six analysed resolution realizations, though the dispersion is larger in the TNG100 and TNG300 runs because of the larger sample sizes (Appendix E.1).

10.4.2 First-infall scenario

The observed LMC and SMC lie at Galactocentric distances of 50.0 kpc and 61.3 kpc, respectively, with a mutual separation of only 24.5 kpc. This is much smaller than the virial radius of the MW, indicating that Chandrasekhar dynamical friction must be very efficient if the ΛCDM framework is correct because it predicts that primordial galaxies are embedded in extended CDM haloes. If a satellite galaxy moves through such a halo, it loses kinetic energy and momentum via encounters with the CDM particles.

The action of Chandrasekhar dynamical friction between dark matter haloes limits the accessible phase-space number density and mass density. For example, it would be unlikely to observe three massive galaxies in close (< 100 kpc) proximity and with small relative velocities ($< 100\,\mathrm{km\,s^{-1}}$) due to the rapid merging timescale. However, just such a scenario arises with the MCs: their mutual separation is only $d_{\mathrm{LMC-SMC}} = 24.5$ kpc, which combined with a low relative velocity of $v_{\mathrm{LMC-SMC}} = 90.8\,\mathrm{km\,s^{-1}}$ implies a high phase-space density of $f_{\mathrm{MCs,obs}} = 9.10 \times 10^{-11}\,\mathrm{km^{-3}\,s^{3}\,kpc^{-3}}$. We showed that the phase-space density of the MCs is in $\approx 3\sigma$ tension based on TNG (Section 10.3.1). The f_{MCs} distribution is similar for different resolution realizations, implying numerical robustness of our results (Appendix E.1).

The small expected phase-space density of the MCs is related to the first-infall scenario, the most likely formation process of the MCs within the ΛCDM framework (Section 10.3.2). In this scenario, the MCs have fallen into the MW from large distances, which typically yields high relative velocities between the MCs and makes it unlikely that they are very close to each other. The identified analogue system 1 in Section 10.3.2 nevertheless has $v_{\mathrm{LMC-SMC}} = 21.9\,\mathrm{km\,s^{-1}}$, being therewith much smaller than the observed value. However, the MCs in this system have large Galactocentric distances of $d_{\mathrm{MW-LMC}} = 187.2$ kpc and $d_{\mathrm{MW-SMC}} = 235.3$ kpc (Table 10.3). In contrast, systems 2 and 3 have the MCs very close to the MW analogue. In these cases, the relative velocity between the MCs is somewhat higher than observed ($173.3\,\mathrm{km\,s^{-1}}$ in system 2 and $148.0\,\mathrm{km\,s^{-1}}$ in system 3). The low LMC-SMC relative velocity and the proximity of the MCs to the MW therefore argues against a scenario where both MCs fell in from large distances and only encountered each other in the last few Gyr.

10.4.3 Relating the MCs to the DoS

The MCs are part of the DoS, a flattened and kinematically coherent plane containing 7 or 8 of the 11 classical satellite perpendicular to the Galactic disc (Kroupa, Theis and Boily 2005; Metz, Kroupa and Jerjen 2007; Pawlowski, Pflamm-Altenburg and Kroupa 2012; Pawlowski and Kroupa 2020). While it is not our intention here to assess the question of whether such a DoS is likely to arise in ΛCDM, we test the scenario that group infall of a massive galaxy like the LMC with its own retinue of satellites could explain the DoS (Section 10.4.3.1). Since we will find that this is not a viable explanation, the DoS should have formed independently of the MCs. We therefore quantify how likely it is that the LMC would fall into a pre-existing DoS, and how this further worsens the situation for ΛCDM when considered together with the high phase-space density of the MCs (Section 10.4.3.2).

10.4.3.1 Satellites of the LMC

The group infall scenario states that dwarfs orbiting the LMC become classical MW satellites and it has been argued that such an infall of satellite galaxies in groups can potentially explain the Galactic

DoS (e.g. D'Onghia and Lake 2008; Y.-S. Li and Helmi 2008; Samuel et al. 2021). To estimate the number of satellites around an infalling LMC, we select galaxies with $d_{\mathrm{MW-LMC}} > 100$ kpc from the initial LMC sample of Section 10.2.4. The distribution of the number of subhaloes with $M_\star > 10^5\,M_\odot$ within 20 kpc, 25 kpc, or 50 kpc of the infalling LMC analogue for the highest resolution realization TNG50-1 is shown in Figure 10.6. We select subhaloes with a non-zero SubhaloFlag parameter (Section 10.2.4) to include subhaloes with a non-cosmological origin, e.g. tidal dwarf galaxies, disc structures in the host galaxy, etc. This is to be more conservative by overestimating the number of satellites around an infalling LMC.

The 11 classical satellites of the MW form a plane with a root mean square (rms) height of only $\Delta_{\mathrm{rms}} = 19.6$ kpc (table 1 of Pawlowski 2021b), suggesting that 10 satellites should be distributed within a radius of 20 kpc around the infalling LMC. However, according to Figure 10.6, not a single infalling LMC analogue has more than one such satellite within 20 kpc (or even 25 kpc) even though 248 LMC analogues were considered altogether. The resolution of the TNG100-1 and TNG300-1 (Section 10.2.2) runs is too low to evaluate the group infall scenario of the MW satellite galaxies. But the TNG50-1 has an initial baryonic mass resolution of $8.5 \times 10^4\,M_\odot$, which is lower than the least massive classical satellite (Draco and Ursa Minor have $M_* = 2.9 \times 10^5\,M_\odot$; McConnachie 2012). Such galaxies would only consist of a few stellar particles in the TNG50-1 run, implying they would not be resolved – but most of the classical satellites should be resolved. It would be valuable to repeat the analysis using higher resolution realizations.

Relaxing the maximum allowed distance from the LMC to 50 kpc yields one LMC analogue with three satellites and a further one with four satellites. These satellites have stellar masses of $3.3 \times 10^5\,M_\odot$, $1.8 \times 10^6\,M_\odot$, and $2.2 \times 10^7\,M_\odot$ in the first case and $1.5 \times 10^7\,M_\odot$, $3.5 \times 10^7\,M_\odot$, $2.8 \times 10^8\,M_\odot$, and $1.4 \times 10^8\,M_\odot$ in the second case. These values are quite consistent with the stellar mass range of the 11 observed classical satellites of the MW (McConnachie 2012). However, even these two systems are unlikely to properly explain the very thin DoS because there are insufficiently many satellites around the LMC analogue and even these satellites are too far from it. More generally, it would be unusual if the LMC did bring in most of the classical satellites because this would imply that the MW had very few satellites of its own only a few Gyr ago, which seems rather unlikely in the ΛCDM paradigm because a MW-mass galaxy should have many more satellites than an LMC-mass galaxy.

Our findings are consistent with the results of Santos-Santos et al. (2021), who found that about 2 satellites with $M_\star > 10^5\,M_\odot$ have been brought in with the LMC based on the Apostle simulations. Garavito-Camargo et al. (2021) argued that the infall of an LMC-like galaxy yields orbital poles of dark matter particles aligned with the LMC orbital pole. They proposed that such an infall would similarly change the orbital poles of the other classical satellites, perhaps explaining the observed alignment of orbital poles in the DoS. However, Pawlowski et al. (2022) showed that this effect would be too small to explain the high orbital pole density of the DoS once we consider that the satellites in it have high specific angular momenta, preventing the modest tidal torques from the LMC from significantly reorienting their orbital poles (see also Correa Magnus and Vasiliev 2022).

As pointed out in section 5.1.3 of Kroupa (2015), the recent infall of a group is inconsistent with the observed low gas content of most LG satellite galaxies. Indeed, Nichols and Bland-Hawthorn (2011) estimated that the accretion of primordial satellites must have happened at much higher redshifts of $z = 3 - 10$ in order to account for most of the LG satellites being gas-depleted, therewith ruling out a recent accretion scenario. However, in order to retain the presently observed anisotropic satellite

distribution, the infall of the group must have occurred at low redshifts (Klimentowski et al. 2010; Deason et al. 2011). This is just one of many contradictory features of the DoS that make it highly problematic for ΛCDM (Pawlowski 2021a). Other proposed formation scenarios in this framework (like the accretion of galaxies along dark matter filaments; M. R. Lovell et al. 2011; Libeskind et al. 2011) are statistically highly unlikely (see, e.g., Pawlowski et al. 2014). These scenarios are in any case already included in self-consistent cosmological simulations. In particular, EAGLE has been used to show that "having most satellites accreted as a single group or along a single filament is unlikely to explain the MW DoS" (Shao et al. 2018).

10.4.3.2 Alignment of the LMC with the DoS

Eight out of the 11 satellites co-orbit within the DoS and their orbital planes align within 20° (Sculptor is counter-rotating). The orbital pole of the LMC (SMC) and the DoS normal have an angular distance of $\theta_{\rm LMC} = 19^\circ.2^{+0.4}_{-0.4}$ ($\theta_{\rm SMC} = 36^\circ.1^{+1.2}_{-1.1}$) based on combining proper motion measurements from the HST and Gaia (see table 2 of Pawlowski and Kroupa 2020). In addition, the LMC and SMC co-orbit in the DoS along with most of the other classical satellites (Pawlowski, Pflamm-Altenburg and Kroupa 2012).

As demonstrated in the previous section, the DoS is unrelated to the formation of the MCs in a first-infall scenario. Thus, we quantify the likelihood of the LMC alignment with the DoS by assuming that the LMC falls towards the MW from a random direction independently of the DoS. We approximate that the orbital pole of the LMC aligns with that of the DoS to within $\theta \approx 20^\circ$. The likelihood that the orbital pole of an infalling satellite from a random direction aligns with the DoS within an angular distance θ and orbits in the same direction as most of the other satellites is given by

$$P\,(<\theta) \;=\; \frac{1-\cos\theta}{2}\,, \tag{10.6}$$

which is about 0.030 (2.17σ) for $\theta = 20^\circ$ (see also section 4.3 of Pawlowski, Pflamm-Altenburg and Kroupa 2012).

To calculate the combined likelihood of this alignment and the high phase-space density of the MCs, we add up the corresponding χ values in quadrature.

$$\chi^2_{\rm tot} \;=\; \chi^2_{\rm MCs} + \chi^2_{\rm LMC-DoS}\,. \tag{10.7}$$

The likelihood of a higher $\chi^2_{\rm tot}$ for two degrees of freedom is

$$P \;=\; \exp\left(-\frac{\chi^2_{\rm tot}}{2}\right)\,. \tag{10.8}$$

This is $P = 3.90\times10^{-5}$ for $\chi^2_{\rm tot} = 3.95^2 + 2.17^2 = 20.30$ for the TNG50-1 simulation. Converting this P-value to an equivalent number of standard deviations for a single Gaussian variable by using Equation 10.5 results in a 4.11σ tension. Thus, the MCs alone are roughly as problematic for the ΛCDM framework as any individual DoS in the LG, as summarized in Table 10.4. The results for the other simulations are summarized in Table 10.2.

The flattened distribution and the phase-space correlation of the LG satellite galaxies strongly suggest that these are tidal dwarf galaxies (TDGs). Galaxies formed from tidal debris (e.g., Mirabel,

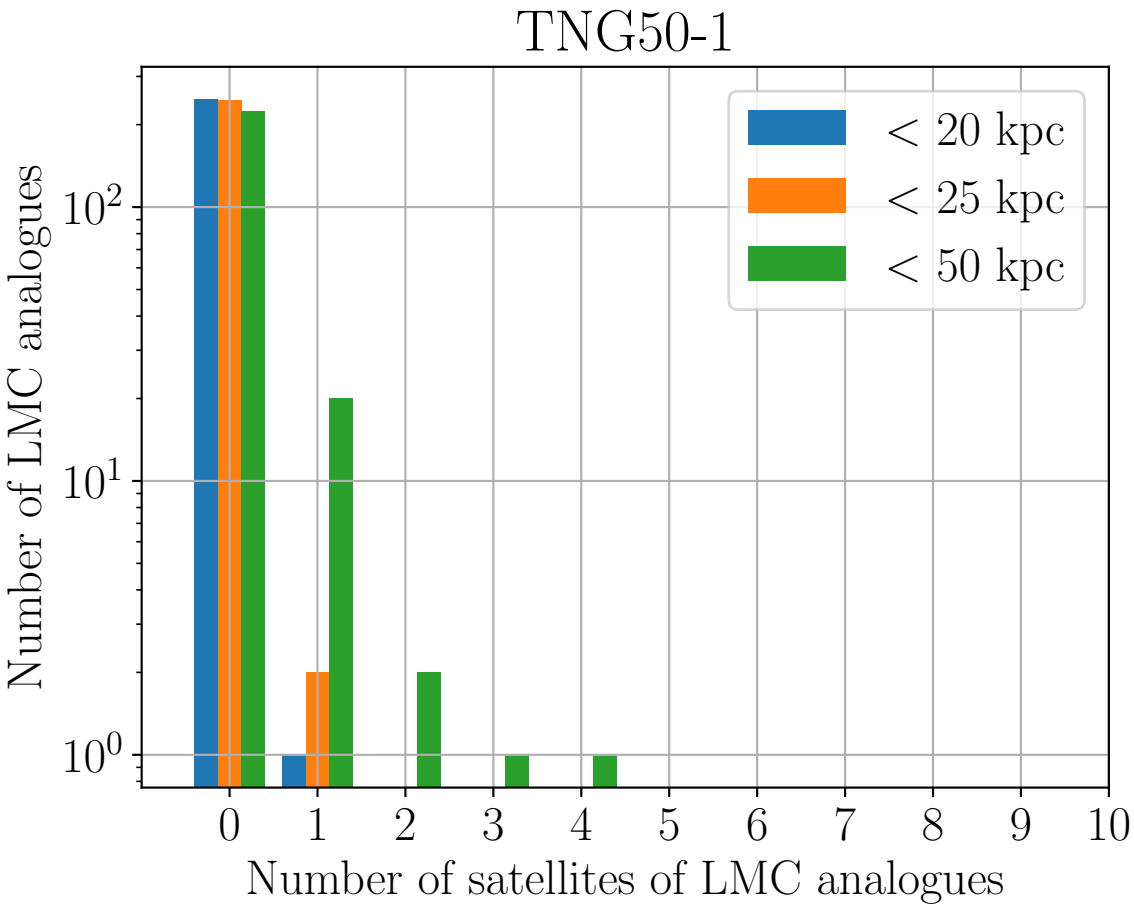

Figure 10.6: Distribution of the number of subhaloes with $M_\star > 10^5\,M_\odot$ within 20 kpc (blue), 25 kpc (orange), or 50 kpc (green) of pre-infall LMC analogues with $d_{\mathrm{MW-LMC}} > 100$ kpc in the initial LMC sample (Section 10.2.4) in the high-resolution realization TNG50-1 (248 objects).

Dottori and Lutz 1992) have to lack dark matter due to their shallow gravitational potential and the high velocity dispersion of the CDM component (Barnes and Hernquist 1992; Wetzstein, Naab and Burkert 2007; Ploeckinger et al. 2018; Haslbauer et al. 2019). However, the dwarf galaxies of the LG have high internal velocity dispersions, implying stronger self-gravity than what can be obtained from the baryonic matter alone (McGaugh and J. Wolf 2010; McGaugh and Milgrom 2013b; McGaugh and Milgrom 2013a) if Newtonian gravity is applied (e.g., Kroupa 2015).

10.4.4 Total mass of LMC analogues

Throughout the analysis of Section 10.3, we have imposed a lower limit on the stellar masses of the MCs but have not considered the total masses of analogues to them. Since the LMC is much more massive than the SMC, we focus on the LMC in the following analysis. Shipp et al. (2021) measured a total LMC mass of $M^{\mathrm{dyn}}_{\mathrm{LMC}} = 18.8^{+3.5}_{-4.0} \times 10^{10}\,M_\odot$ by using five southern hemisphere stellar streams as direct dynamical tracers of the underlying gravitational potential. Their results are

Problem for ΛCDM	Frequency	Significance
MW satellite plane	3.92×10^{-4}	3.55σ
M31 satellite plane	3.87×10^{-4}	3.55σ
NGC 3109 backsplash	$< 7.56 \times 10^{-5}$	$> 3.96\sigma$
Phase-space density of MCs	7.81×10^{-5}	3.95σ
Phase-space density of MCs + VPoS	3.90×10^{-5}	4.11σ

Table 10.4: Level of tension for different LG observations in the ΛCDM framework. The frequency of the MW DoS in ΛCDM is taken from section 4.2 of Pawlowski and Kroupa (2020), who considered 2548 MW-like galaxies and found one with a similar satellite system. We therefore assume that its likelihood in ΛCDM is $1/2548 = 3.92 \times 10^{-4}$. For M31, we use figure 2 of R. A. Ibata et al. (2014), which shows that 3 out of 7757 M31-like galaxies in the MS-II have a satellite system similar to that of M31. The likelihood of the backsplash galaxy NGC 3109 in ΛCDM has been quantified in Banik et al. (2021), who found no such analogues in 13225 galaxies similar to the MW or M31 in the TNG300-1 simulation. This implies a likelihood below $1/13225 = 7.56 \times 10^{-5}$. The last row gives the significance of the MCs as quantified using TNG50-1 in Sections 10.3.1 and 10.4.3.

compared with the distribution of the total LMC mass ($M_{\rm LMC}$)[8] in Figure 10.7, which has four panels showing results from TNG50-1, TNG100-1, TNG300-1, and the combination of all three. In each panel, results are shown for three samples depending on the imposed distance criteria. The initial LMC sample of Section 10.2.4 shows a peak at $\log_{10}\left(M_{\rm LMC}/M_\odot\right) \approx 10.8 - 10.9$ in all three runs, with the distribution going up to ≈ 11.8 in the TNG100-1 and TNG300-1 runs (see the solid blue histograms). This is consistent with the halo mass of the LMC expected from abundance matching ($\log_{10}\left(M_{\rm LMC}/M_\odot\right) \approx 11.3$; see e.g. Boylan-Kolchin et al. 2010; Moster, Naab and White 2013; Dooley et al. 2017; Shao et al. 2018).

Selecting only LMC analogues with $50\,{\rm kpc} \leq d_{\rm MW-LMC} \leq 100\,{\rm kpc}$ systematically shifts the $M_{\rm LMC}$ distribution to lower masses, with the peak now around $\log_{10}\left(M_{\rm LMC}/M_\odot\right) \approx 10.5$. Combining all three simulation runs gives that nine out of 1556 LMC analogues have a total mass equal to or larger than the 1σ lower limit of the tidal stream analysis conducted by Shipp et al. (2021). This frequency corresponds to a 2.76σ tension.

Imposing that $d_{\rm MW-LMC} \leq 50.0\,{\rm kpc}$ shifts the distribution to even lower $M_{\rm LMC}$. The maximum mass of these LMC analogues is $\log_{10}\left(M_{\rm LMC}/M_\odot\right) \approx 10.96$ (obtained in TNG300-1). This is still lower than the 1σ lower limit of the tidal stream analysis of Shipp et al. (2021), implying a null detection of sufficiently massive LMC analogues. The results for the different selection criteria and simulation runs are summarized in Table 10.5.

Our results show that LMC analogues within 50 kpc but also those with Galactocentric distances of $50 - 100$ kpc are systematically less massive compared to the initial sample in which LMC analogues could be up to 250 kpc from their MW-like host galaxy (Section 10.2.4). This distance dependence is also evident in Figure 10.8, which shows the joint distribution of the MW-LMC distance and the total LMC mass. As expected from Figure 10.7, the typical LMC mass systematically increases with its distance from the host galaxy.

The null detection of such systems is probably due to dynamical friction between CDM haloes:

[8] $M_{\rm LMC}$ here refers to the total mass of all particles and cells which are bound to this subhalo as listed in the Subfind Subhaloes catalogue (https://www.tng-project.org/data/docs/specifications/#sec2b).

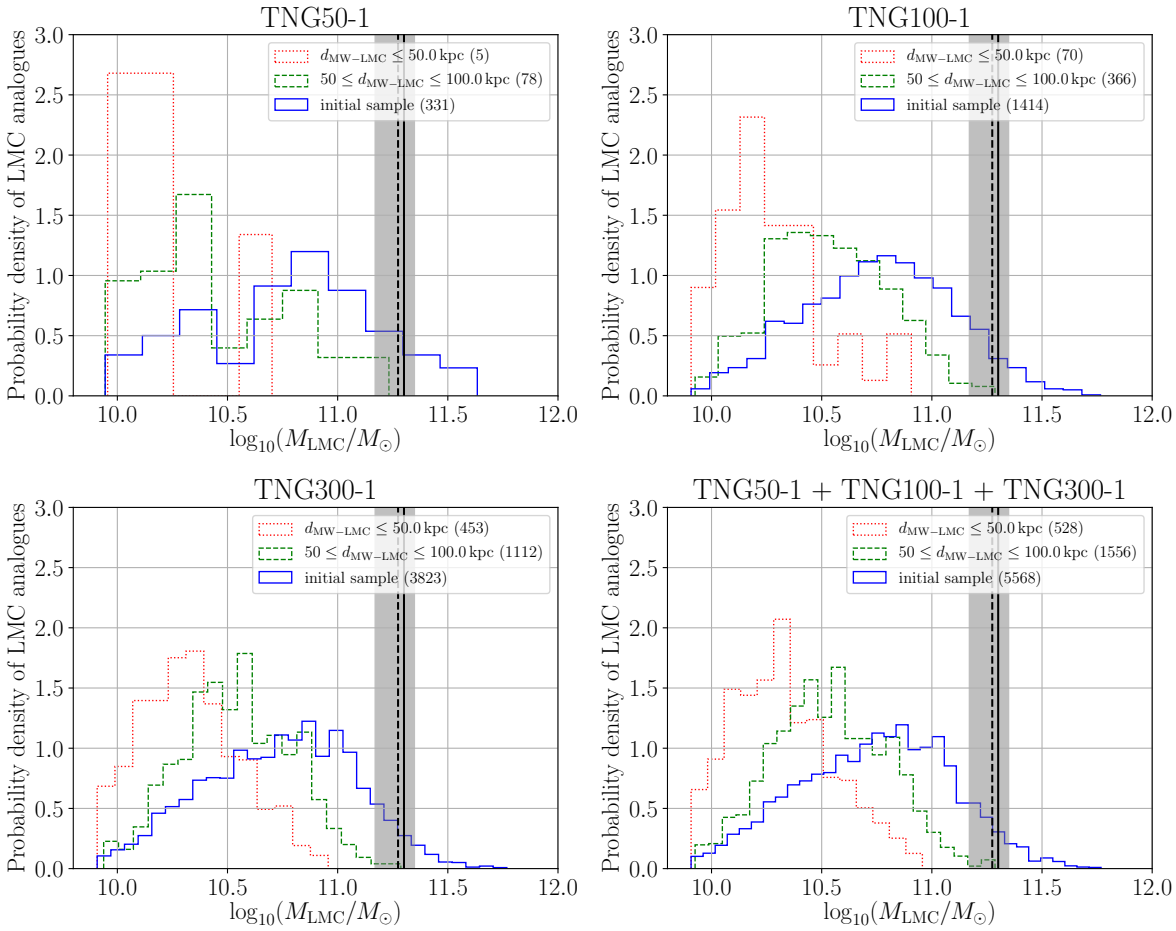

Figure 10.7: Histograms showing the total mass of LMC analogues with different distance criteria in TNG50-1 (top left), TNG100-1 (top right), and TNG300-1 (bottom left), with the combined sample shown in the bottom right panel. The solid blue histograms refer to the initial sample of analogues to the LMC. The dotted red and dashed green histograms show the results when we also require the LMC to be within 50 kpc or between 50 – 100 kpc, respectively, of the MW analogue. The sample sizes of the different distributions are given in brackets in the panel legends. The dashed vertical line and grey shaded region mark the total mass of the LMC and its uncertainty as deduced from five Galactic stellar streams near the LMC (these give $M_{\rm LMC}^{\rm dyn} = 18.8^{+3.5}_{-4.0} \times 10^{10}\,M_\odot$; Shipp et al. 2021). The solid vertical line shows the total mass of the LMC expected from abundance matching ($M_{\rm LMC} \approx 2 \times 10^{11}\,M_\odot$). Constraining the total mass of the LMC with the LG timing argument gives similar results (see the text). Table 10.5 lists the number of LMC analogues with a total mass equal to at least the 1σ lower limit of the analysis by Shipp et al. (2021).

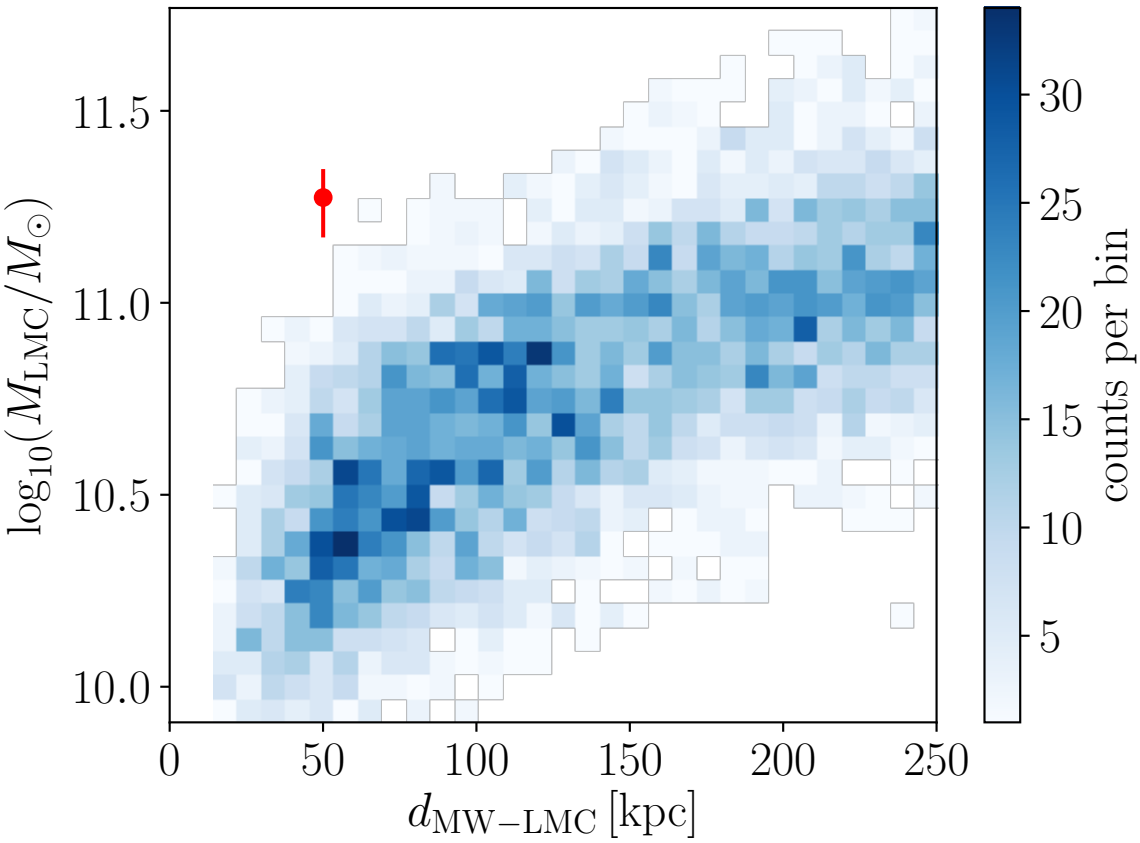

Figure 10.8: Distribution of the MW-LMC distance and the total LMC mass of analogues in the combined sample of the three TNG runs (5568 objects). The red dot with vertical error bar refers to the observed $d_{\rm MW-LMC} = 50.0\,$kpc and the total LMC mass deduced from five Galactic stellar streams near the LMC (these give $M_{\rm LMC} = 18.8^{+3.5}_{-4.0} \times 10^{10}\,M_\odot$; Shipp et al. 2021). None of the 5568 simulated objects have a lower Galactocentric distance and higher mass.

Sample	Simulation	Number of analogues	Frequency	Significance
Initial sample of analogues to the LMC (Section 10.2.4)	TNG50-1:	54	54/331	1.39σ
$+M_{\rm LMC} \geq (18.8-4.0)\times10^{10}\,M_\odot$	TNG100-1:	163	163/1414	1.57σ
	TNG300-1:	354	354/3823	1.68σ
	All runs:	571	571/5568	1.63σ
Sample of analogues to the LMC with $50\,{\rm kpc} \leq d_{\rm MW-LMC} \leq 100\,{\rm kpc}$	TNG50-1:	2	2/78	2.23σ
$+M_{\rm LMC} \geq (18.8-4.0)\times10^{10}\,M_\odot$	TNG100-1:	3	3/366	2.64σ
	TNG300-1:	4	4/1112	2.91σ
	All runs:	9	9/1556	2.76σ
Sample of analogues to the LMC with $d_{\rm MW-LMC} \leq 50\,{\rm kpc}$	TNG50-1:	0	$< 1/5$	$> 1.28\sigma$
$+M_{\rm LMC} \geq (18.8-4.0)\times10^{10}\,M_\odot$	TNG100-1:	0	$< 1/70$	$> 2.45\sigma$
	TNG300-1:	0	$< 1/453$	$> 3.06\sigma$
	All runs:	0	$< 1/528$	$> 3.11\sigma$
Initial sample of analogues to the LMC (Section 10.2.4)	All runs:	0	$< 1/5568$	$> 3.75\sigma$
$+M_{\rm LMC} \geq (18.8-4.0)\times10^{10}\,M_\odot$ & $d_{\rm MW-LMC} \leq 50\,{\rm kpc}$				
Initial sample of analogues to the LMC (Section 10.2.4)	All runs:	0	$< 3.62\times10^{-7}$	$> 5.09\sigma$
$+M_{\rm LMC} \geq (18.8-4.0)\times10^{10}\,M_\odot$ & $d_{\rm MW-LMC} \leq 50\,{\rm kpc}$				
+Extrapolation of $f_{\rm MCs}$ distribution using quadratic fit (TNG50-1)				

Table 10.5: Statistics of analogues to the LMCs (i.e., systems with a satellite analogous to the LMC) in the redshift range $0 \leq z \leq 0.26$ in the TNG50-1, TNG100-1, and TNG300-1 simulation with a total mass higher than the 1σ lower limit of the observationally inferred LMC mass ($M^{\rm dyn}_{\rm LMC} = 18.8^{+3.5}_{-4.0}\times10^{10}\,M_\odot$; Shipp et al. 2021). We show results for different distance criteria. Similarly to Table 10.2, we list the number of analogues, their frequency relative to the total number of selected MW-like analogues, and the corresponding equivalent number of standard deviations for a single Gaussian variable (Equation 10.5). The distributions of the total LMC mass for these three samples are presented in Figure 10.7. The last two parts of the table list the statistical analysis of Figure 10.8.

massive satellites rapidly merge with the host galaxy, making the MW-LMC configuration less likely for a more massive LMC (Section 10.4.2). As a result, none of the 5568 LMC analogues in our initial sample have a lower Galactocentric distance and higher total mass than estimated for the real LMC. This represents a tension of $> 3.75\sigma$, which would no doubt rise further if we simply showed the mass-distance distribution of the most massive satellite around all MW analogues without *a priori* requiring the LMC analogue to have a sufficiently high stellar mass. Since this estimate does not take into account the SMC, we can combine the tension evident in Figure 10.8 with our previously reported 3.95σ tension from the high phase-space density of the MCs (Section 10.3.1), which results in a combined highly significant $> 5.09\sigma$ tension for two degrees of freedom ($\chi^2_{\rm tot} > 3.75^2 + 3.95^2$, Equation 10.8).

10.4.5 The MCs in Milgromian dynamics (MOND)

The DoS can be explained naturally if its member satellites are TDGs (e.g., Bílek et al. 2021). The arrangement of the LG satellites (Pawlowski, Kroupa and Jerjen 2013) indeed strongly suggests that most of them formed out of tidal debris from a previous galactic encounter, perhaps between the MW and M31. The internal dynamics of the MW satellites (McGaugh and J. Wolf 2010) and those of M31 (McGaugh and Milgrom 2013b; McGaugh and Milgrom 2013a) rule out such a formation scenario in the ΛCDM framework because it would require the satellites to have much stronger self-gravity than can be obtained in Newtonian gravity (Kroupa 2012; Kroupa 2015). We therefore consider a promising modern, non-relativistic theory beyond the ΛCDM framework that was originally developed to explain galactic rotation curves without the existence of exotic CDM particles by instead enhancing

gravity at low accelerations (Milgrom 1983c; Bekenstein and Milgrom 1984).

In MOND, the MCs can either have a primordial (cosmological) origin, or they could be TDGs formed from a previous galactic interaction. We provide a qualitative discussion of this formation scenario because a cosmological MONDian simulation does not exist in which detailed cuts on the phase-space parameters can be set, as would be needed to quantify the likelihood of the MCs.

In the first scenario, the MCs are primordial dwarf galaxies that formed during the gas collapse in the early Universe (Wittenburg, Kroupa and Famaey 2020) and orbited the MW for a long time. In contrast to the ΛCDM framework, a first infall of the MCs towards the potential of the MW is inconsistent with MOND. This is firstly because the escape velocity at the Galactocentric distance to the LMC is $v_{\rm esc} = 379^{+34}_{-28}\,{\rm km\,s^{-1}}$ (Williams et al. 2017), which exceeds the Galactocentric velocity of the LMC ($v_{\rm MW-LMC} = 323.8\,{\rm km\,s^{-1}}$) and the SMC ($v_{\rm MW-SMC} = 245.6\,{\rm km\,s^{-1}}$), implying that the MCs are on a bound orbit around the MW (see also Wu et al. 2008, in which bound orbits of the LMC are discussed). Secondly, because of the absence of dynamical friction on the (not present) Galactic dark matter halo, the MCs would form a stable dynamical configuration over a much longer timescale than in ΛCDM (see, e.g., the separation of the LMC and SMC analogues in the ΛCDM simulations shown in Figure 10.5). This in turn increases the number of pericentre passages, making it more likely to detect a galactic system close to pericentre. A larger number of pericentre passages can also be achieved if the host halo mass of the MW is increased for both the ΛCDM and MOND frameworks. However, the MW has a virial mass of $2.43 \times 10^{12}\,M_\odot$ (Y.-S. Li and White 2008) such that we applied an upper limit of $M_{200} = 2.5 \times 10^{12}\,M_\odot$ on our selected MW-like galaxies in Section 10.2.3. A more massive host halo would not represent a MW-like galaxy, making this argument irrelevant for the presented analysis. Moreover, the number of past pericentre passages is not used as a selection criterion – the LMC needs to be on first infall in ΛCDM to match other constraints.

The TDG scenario ties in better with the observed DoS around the MW and M31 (Section 10.4.3). In this scenario, the MCs and most LG satellites formed in the tidal tails that developed during a galactic encounter between the MW and M31. Zhao et al. (2013) derived that they had a close encounter most likely 7 – 11 Gyr ago (see their figure 2), allowing the formation of TDGs. The stronger self-gravity in MOND implies that TDGs can be formed much more easily and are more stable against tides and baryonic feedback processes compared to the ΛCDM paradigm (Renaud, Famaey and Kroupa 2016). Using restricted N-body MOND simulations, Banik, O'Ryan and Zhao (2018) showed that an MW-M31 flyby redistributes particles from the MW disc up to radial distances of 250 kpc from the Galactic centre (see their figure 6), covering the Galactocentric distance range of the 11 classical MW satellites (figure 2 of Pawlowski, Kroupa and Jerjen 2013). Moreover, a substantial fraction of these particles have a similar orbit to the LMC (see figure 11 of Banik, O'Ryan and Zhao 2018). The flyby was explored in more detail with N-body simulations (Bílek et al. 2018) and very recently with hydrodynamical simulations, which is important as the galaxies should have been gas-rich when they interacted (Banik et al. 2022). The latter model reproduces the observed orientations of the DoS around the MW and M31 while being consistent with the proper motion of M31 and several other constraints, including the disc scale lengths and the vertical velocity dispersion at the Solar circle.

It is expected that the small velocity dispersion in the gas phase leads to some TDGs forming in a binary system. Indications for the formation of binary TDGs can be found in the hydrodynamical MOND simulations conducted by Renaud, Famaey and Kroupa (2016). In their model labelled as $\rm M_A$, one can identify two close gaseous overdensities with a projected separation of $\lesssim 10\,{\rm kpc}$ in the xy plane when the two interacting host galaxies reach their first apocentre after their first passage (see the top right corner of the panel labelled as $\rm M_A$ in figure 2 of Renaud, Famaey and Kroupa 2016).

Thus, the MCs could be binary TDGs, as could other dwarf binaries in the LG (see also section 3.1 of Pawlowski 2021b, and references therein).

A correlated formation process of the MCs is further supported by the consistency between the maximum circular velocity of the LMC ($v_c = 72 \pm 7\,\mathrm{km\,s^{-1}}$; Alves and C. A. Nelson 2000) and the relative velocity between the LMC and SMC of $v_{\mathrm{LMC-SMC}} = 84 \pm 19\,\mathrm{km\,s^{-1}}$ (based only on Gaia DR2 proper motion measurements; Gaia Collaboration 2018a) within their stated uncertainties. The uncertainty of $v_{\mathrm{LMC-SMC}}$ is calculated by using a Monte Carlo error propagation taking into account the observational uncertainties of the LMC and SMC proper motion components ($\Delta\mu_\alpha \cos\delta = 0.010\,\mathrm{mas\,yr^{-1}}$ and $\Delta\mu_\delta = 0.010\,\mathrm{mas\,yr^{-1}}$) and allowing a systematic uncertainty of $\epsilon_{\mathrm{sys}} = 0.028\,\mathrm{mas\,yr^{-1}}$ (see table 1 of Pawlowski and Kroupa 2020). For simplicity and given that the systematic uncertainties are much larger than the random uncertainties, we do not take into account the correlation coefficient between the proper motions. In reality, the values of v_c and $v_{\mathrm{LMC-SMC}}$ could potentially match even better because relative velocities are typically overestimated if they use less precise proper motion measurements.

In conclusion, the fact that the two most massive Galactic satellites are both close to pericentre is in general unlikely in every cosmological framework. The likelihood of such a configuration is raised if a theoretical framework allows for orbits with multiple pericentre passages, which applies to Milgromian dynamics because of the absence of dynamical friction on the dark matter haloes. Moreover, a past MW-M31 flyby forms a flattened and kinematically coherent plane of satellites, which would explain the DoS with an rms height of only 20 kpc based on the 11 classical satellites (Pawlowski 2021b). A chance 3-body interaction is statistically more likely in such a 2D plane than in 3D space, especially if some of the TDGs form as binary systems. High-resolution cosmological simulations in, e.g., the neutrino-Hot Dark Matter (νHDM) framework (Haslbauer, Banik and Kroupa 2020; Asencio, Banik and Kroupa 2021) would be necessary to statistically quantify the occurrence rate of the MCs in a Milgromian universe.

Objections against the formation of the MCs by a past interaction between the MW and M31 have been raised in Besla (2015)[9] as the short period and small apocentre of the MW-SMC orbit calculated by Zhao et al. (2013) seems to be in contrast with the high gas fraction and star formation history of the SMC (see their figure 2). However, the Zhao et al. (2013) MOND models assumed that the SMC is unperturbed by the LMC (see their section 3.3) and that a constant external field of $0.03\,a_0$ acts across the LG over cosmic time (see their section 3.2). Banik and Zhao (2018a) showed that the pericentre and apocentre distances could vary for a time-dependent external field strength (see their figure 20). Thus, in contrast to the model of Zhao et al. (2013), the MW-LMC, MW-SMC, and LMC-SMC orbits could all have larger pericentre distances in the past, making it not necessarily a given that the SMC becomes gas-depleted if there were only a few previous pericentres.

10.5 Conclusions

The MCs are the most massive and some of the closest satellites of the MW, making them an interesting local Universe laboratory for cosmological and gravitational theories. Our proximity to the MCs allows us to constrain their orbits to high precision (e.g. Kallivayalil et al. 2013; Gaia Collaboration

[9] the here discussed work by Besla (2015) is a conference proceeding that appears in "Lessons from the Local Group: A conference in honour of David Block and Bruce Elmegreen" (source: ArXiv), which has not been published in a peer-reviewed journal

2016; Gaia Collaboration 2018b; Gaia Collaboration 2018a). In this contribution, we quantified the likelihood of a system resembling the MW and the MCs in the standard model of cosmology (ΛCDM) as simulated in the IllustrisTNG project (Pillepich et al. 2018a; D. Nelson et al. 2019). We identified 1547, 7360, and 40075 MW-like galaxies in the redshift range $0.0 \leq z \leq 0.26$ in TNG50-1, TNG100-1, and TNG300-1, respectively (Section 10.2.3). We then selected satellites within 250 kpc and ranked them according to their stellar mass. After that, we considered the most massive satellite of a halo as a possible LMC analogue if it has $M_\star \geq 1.5 \times 10^9\, M_\odot$ and $M_{\rm total}/M_\star > 5$. For the less massive SMC, we required that the second-most massive satellite in stellar mass has $M_\star \geq 4.6 \times 10^8\, M_\odot$ and $M_{\rm total}/M_\star > 5$ (Section 10.2.4). In total, 147, 454, and 601 MW-like galaxies have analogues to both MCs in this sense, corresponding to a frequency of 9.5%, 6.2%, and 1.5% in TNG50-1, TNG100-1, and TNG300-1, respectively.

Using these galaxy samples, we investigated the formation and evolution of analogues to the MCs by applying different observational constraints. The unusual aspect of the MCs is that it is a closely interacting galactic system with a mutual separation of 24.5 kpc and a low relative velocity of 90.8 km s^{-1}, which implies a high specific phase-space density of $f_{\rm MCs,obs} = 9.10 \times 10^{-11}$ km^{-3} s^3 kpc^{-3}. In particular, 3 out of 1202 systems have $f_{\rm MCs} \geq f_{\rm MCs,obs}$. Moreover, none of the identified MCs analogues with 50 kpc $\leq d_{\rm MW-LMC} \leq$ 100 kpc in the TNG runs have $f_{\rm MCs} \geq f_{\rm MCs,obs}$. This null detection implies a frequency of $< 1/46$, $< 1/118$, and $< 1/191$, which corresponds to a $> 2.29\sigma$, $> 2.63\sigma$, and $> 2.79\sigma$ tension in the TNG50-1, TNG100-1, and TNG300-1 run, respectively. This analysis sets the lower limits to the tension by relying on the null detection of MCs analogues. Consequently, we performed an extrapolation of the cumulative $f_{\rm MCs}$ distribution in order to estimate the actual significance (Section 10.3.1). Extrapolating the simulated $f_{\rm MCs}$ distribution up to $f_{\rm MCs,obs}$ yields a tension of 3.95σ (TNG50-1), 3.11σ (TNG100-1), and 2.82σ (TNG300-1). We emphasise that this extrapolation is a usual method applied in extreme value analysis to assess likelihoods of outcomes when the numerical experiments are too costly to provide sufficient samples to cover the extreme values of interest. The discrepancy between the simulated and observed phase-space density of the MCs is likely not caused by the resolution limitations of the simulations (Appendix E.1). The number of MW-MCs systems is lower in the lower resolution runs of the TNG50 and TNG100 simulations which could be e.g. due to artificial disruption of interacting subhaloes. The statistical significance of the tension between the observed and simulated specific phase-space distribution is higher in the high-resolution run TNG50-1. Thus, a hierarchical clustering of two massive satellites in a narrow phase-space volume is an unlikely configuration within the ΛCDM framework regardless of precisely what distance range is allowed for the LMC. Testing cosmological theory using the phase-space density of the MW-LMC-SMC system is applied here for the first time. Notably, this configuration is very comparable to the similar situation observed in the nearby M81 group of galaxies (Oehm, Thies and Kroupa 2017), one of the closest galaxy groups to the LG.

By tracing the three systems with $f_{\rm MCs} \geq f_{\rm MCs,obs}$ in our initial MCs sample back through cosmic time, we found that they are accreted together towards the MW-like galaxy at late times (Section 10.3.2). This so-called 'first infall scenario' is thus the most likely formation process of the MCs in a ΛCDM universe, in agreement with previous studies (e.g., Boylan-Kolchin, Besla and Hernquist 2011). The low LMC-SMC relative velocity is unusual for a scenario where both MCs fell in from large distances and only encountered each other in the last few Gyr. This is one reason for the high observed phase-space density of the MCs compared to the analogues found in ΛCDM simulations.

The orbital pole of the LMC (SMC) and the DoS normal have an angular distance of $19^\circ.2^{+0.4}_{-0.4}$

($36^{\circ}.1^{+1.2}_{-1.1}$; Pawlowski and Kroupa 2020). As demonstrated in Section 10.4.3.1, the LMC cannot bring in enough satellites to populate the satellite plane, a finding that is consistent with previous studies (e.g. Santos-Santos et al. 2021). Thus, the DoS is physically unrelated to the proposed recent first infall of the LMC in the ΛCDM framework. We estimate that the alignment of the LMC and DoS has a likelihood of 0.030 (2.17σ) if the LMC falls towards the MW from a random direction on the sky. Adding this χ^2 value to that of the phase-space density of the MCs increases the tension to 4.11σ for two degrees of freedom in TNG50-1, assuming the DoS *a priori*. However, it was previously shown that the existence of the DoS around the MW causes a 3.55σ tension based on TNG100-1 (Pawlowski and Kroupa 2020). Consequently, although most physical properties of the MCs and the MS can be explained in non-cosmological simulations (Lucchini et al. 2020; Lucchini, D'Onghia and Fox 2021), their formation and alignment with the DoS remain a challenge in cosmological ΛCDM simulations. Looking slightly further afield, the fact that the satellite populations of the three nearest major host galaxies (the MW, M31, and Centaurus A) all reveal a DoS is in 5.27σ (Asencio et al. 2022) tension with the ΛCDM model. Similarly detailed studies are currently not possible around more distant hosts, though some progress in this regard has recently been achieved (as reviewed in Pawlowski 2021b).

Another problematic aspect of the LMC is the fact that it is only 50 kpc away but has a Newtonian dynamical mass of $M_{\rm LMC} = 18.8^{+3.5}_{-4.0} \times 10^{10}\,M_{\odot}$ according to an analysis of five tidal streams near it (Shipp et al. 2021). Timing argument analyses of the LG give similar results (see Section 10.4.4). Figure 10.8 demonstrates that the LMC is quite massive given its distance of only 50 kpc from the MW. Indeed, none of the 5568 LMC analogues in terms of stellar mass have a lower Galactocentric distance and higher total mass than the above estimates for the actual LMC, even if we adopt the 1σ lower limit on its mass. The sample size would rise further if we did not impose the condition on $M_{\star}$ a priori, indicating a tension of $> 3.75\sigma$. We attribute the lack of sufficiently massive and nearby satellites to dynamical friction (Kroupa 2015). Combining this with the 3.95σ tension form the phase-space density of the MCs results in a $> 5.09\sigma$ tension for two degrees of freedom.

The tensions caused by the phase-space density of the MCs and the alignment of the LMC with the DoS can be alleviated if dynamical friction on their CDM haloes is absent (Section 10.4.2). This evidence for a lack of dynamical friction on galactic scales is consistent with previous studies (e.g. Angus, Diaferio and Kroupa 2011; Kroupa 2015; Oehm, Thies and Kroupa 2017; Roshan et al. 2021; Roshan et al. 2021; Haslbauer et al. 2022). Dynamical friction on galactic scales would be greatly reduced in a Milgromian universe (MOND, Milgrom 1983c) due to the lack of CDM haloes. The absence of such haloes around dwarf galaxies has recently been reported in the Fornax galaxy cluster based on tidal stability arguments (Asencio et al. 2022), creating significant tension with the ΛCDM model. In MOND, the MCs can either be primordial galaxies but not on a first infall, or they could be TDGs formed by a past MW-M31 flyby (Zhao et al. 2013). The flyby scenario would also provide a natural explanation for the DoS around the MW and M31 (Banik, O'Ryan and Zhao 2018; Banik et al. 2022; Bílek et al. 2018; Bílek et al. 2021), both of which individually cause a 3.55σ tension with the ΛCDM framework (R. A. Ibata et al. 2014; Pawlowski and Kroupa 2020). Self-consistent hydrodynamical cosmological MOND simulations are needed to rigorously quantify the likelihood of the observed LG configuration in MOND, as presented in this contribution for the ΛCDM framework.

As our final remark, we mention that large galaxy surveys should be complemented by tests of cosmological models and gravitational theories in the local Universe, the only region where we have access to many types of precise yet model-independent data thanks to missions like Gaia (cf. Kroupa et al. 2022).

Acknowledgments

IB is supported by Science and Technology Facilities Council grant ST/V000861/1, which also partially supports HZ. IB acknowledges support from a "Pathways to Research" fellowship from the University of Bonn. The IllustrisTNG simulations were undertaken with computational time awarded by the Gauss Centre for Supercomputing (GCS) under GCS Large-Scale Projects GCS-ILLU and GCS-DWAR on the GCS share of the supercomputer Hazel Hen at the High Performance Computing Center Stuttgart (HLRS), as well as on the machines of the Max Planck Computing and Data Facility (MPCDF) in Garching, Germany.

CHAPTER 11

The cosmological star formation history of galaxies in the Local Cosmological Volume – evidence for a 5 Gpc-sized underdensity

"If your belief conflicts with empirically confirmed knowledge, then you are not seeking meaning; you are delusional."
(Hossenfelder 2022)

This chapter summarizes the main scientific findings and author contributions of the peer-reviewed paper entitled "The cosmological star formation history from the Local Cosmological Volume of galaxies and constraints on the matter homogeneity" published in the journal Monthly Notices of the Royal Astronomical Society, 524, 3252, 2023 by **Moritz Haslbauer**, Pavel Kroupa, and Tereza Jerabkova (hereafter Haslbauer, Kroupa and Jerabkova 2023). A copy of the paper in its original form is attached in the Appendix D. The project was partly conducted during a research visit of Moritz Haslbauer at the European Souther Observatory (ESO) in Garching bei München (Germany).

11.1 Summary

Kroupa et al. (2020) reported that the majority of galaxies located in the Local Cosmological Volume (LV), which is defined as a sphere with a radius of 11 Mpc centred around the Milky Way, has an almost constant star formation history (SFH). In Haslbauer, Kroupa and Jerabkova (2023), we supplemented their study by investigating the cosmological implications of the SFHs of nearby galaxies in the context of the Lilly-Madau plot (e.g. Lilly et al. 1996; Madau et al. 1996; Madau, Pozzetti and Dickinson 1998; Cole et al. 2001; Madau and Dickinson 2014; Madau and Fragos 2017, and references therein). Using the Updated Nearby Galaxy Catalog[1] compiled by Karachentsev et al. (2004) and Karachentsev, Makarov and Kaisina (2013), we extracted their present-day star formation rates, SFR_0, and Ks-band luminosities, $L_{\rm Ks}$, which are converted to stellar masses, M_*, by adopting a mass-to-light ratio of $0.6\,M_\odot/L_\odot$ for a canonical IMF (McGaugh and Schombert 2014). Assuming a standard ΛCDM cosmology (Planck Collaboration XIII 2016) in which all galaxies start forming

[1]The Updated Nearby Galaxy Catalog can be downloaded here: https://www.sao.ru/lv/lvgdb/introduction.php

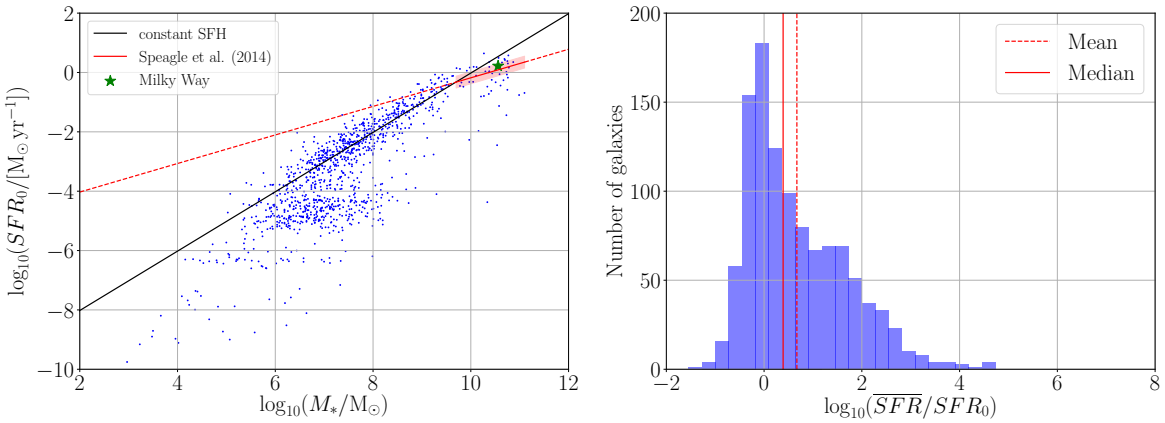

Figure 11.1: Star-formation rates of galaxies located in the Local Volume. *Left:* Present-day SFRs in dependence of the present-day stellar masses of LV galaxies. The black solid line refers to a constant SFH over a star-forming time-scale of 13.6 Gyr assuming a mass-loss factor of 1.3. The red solid line shows the present-day main-sequence of star-forming galaxies with $10^{9.7} < M_*/M_\odot < 10^{11.1}$ and an uncertainty of ±0.2 dex highlighted by the red shaded region (equation 28 of Speagle et al. 2014). The red dashed line extrapolates the main-sequence to higher and lower stellar masses. The green star shows the position of the Milky Way with $M_* = 3.6\times10^{10}\,M_\odot$ and $SFR_0 = 1.7\,\mathrm{M}_\odot\,\mathrm{yr}^{-1}$, which lies as expected on the main-sequence. *Right:* Distribution of the parameter $\log_{10}(\overline{SFR}/SFR_0)$ of LV galaxies, which has a mean and median of 0.67 (dashed line) and 0.39 (solid line), respectively. Credits: figure 3 of Haslbauer, Kroupa and Jerabkova (2023).

stars 0.2 Gyr after the Big Bang up to present time, the present-day averaged star-formation rate is given by $\overline{SFR} \equiv 1.3M_*/(13.6\,\mathrm{Gyr})$ where the prefactor 1.3 accounts for the mass-loss through stellar evolution (Baumgardt and Makino 2003; Kroupa et al. 2020).

The present-day star-formation rates of these galaxies in dependence of their present-day stellar masses is shown in the left panel of Figure 11.1. The majority of low mass galaxies with $M_* < 10^{10}\,\mathrm{M}_\odot$ and $SFR \geq 10^{-3}\,\mathrm{M}_\odot\,\mathrm{yr}^{-1}$ have a constant or increasing SFH (see also McGaugh, Schombert and Lelli 2017; Schombert, McGaugh and Lelli 2019; Kroupa et al. 2020), while more massive galaxies with $M_* > 10^{10}\,\mathrm{M}_\odot$ have decreasing SFHs as also implied by the main-sequence of star-forming galaxies (Speagle et al. 2014). The right panel of Figure 11.1 shows the distribution of $\overline{SFR}/SFR_0$ in the $\log_{10}$-space peaking at $\overline{SFR}/SFR_0 \approx 1$. Restricting the distribution only to galaxies with $SFR_0 \geq 10^{-3}\,\mathrm{M}_\odot\,\mathrm{yr}^{-1}$ yields a mean of $\overline{SFR}/SFR_0 = 0.97$ and a median of 0.83 being in agreement with the findings by Kroupa et al. (2020). Thus, a significant number of these local star-forming galaxies are consistent with an almost constant SFH over 13.6 Gyr .

However, this seems to be in contradiction with the Lilly-Madau plot according to which the co-moving star formation rate density (SFRD) increases from the present time up to a maximum at redshift $z = 1.86$ by a factor of ≈ 9 (see figure 9 and equation 15 of Madau and Dickinson 2014). In order to address this question, we reconstructed the SFHs of LV galaxies using the delayed-τ and a power-law SFH model constrained by SFR_0 and $\overline{SFR}$. This allows to derive the evolution of the SFRD and stellar mass densities (SMDs) from the LV as presented in Figure 11.2. The SMDs are calculated by integrating each SFH of the LV galaxies to the respective redshift and adding the so-obtained stellar masses and diving by the volume of the LV (for details see section 2.5 of Haslbauer, Kroupa and Jerabkova 2023). Taking into account that the majority of low-mass galaxies have an almost

constant SFH (left panel of Figure 11.1, but also McGaugh, Schombert and Lelli 2017; Schombert, McGaugh and Lelli 2019; Kroupa et al. 2020), we defined a combined SFH model by adopting the power-law model for galaxies with $M_* < 10^{10}\,M_\odot$ and the delayed-τ model for more massive galaxies with $M_* \geq 10^{10}\,M_\odot$. The so-derived cosmic SFRD evolution of the LV disagrees with the global SFH of the Universe such that the SFRD is 2.22 ± 0.33 times lower than the peak of the Lilly-Madau plot at $z = 1.86$ (Madau and Dickinson 2014). Adopting only the delayed-τ model or the power-law model underestimate the SFRD at z = 1.86 by a factor of 2.16 ± 0.32 and 5.90 ± 0.88, respectively (top right panel of Figure 11.2).

The cosmic SFRDs and SMDs are physically connected but Yu and F. Y. Wang (2016) reported that the SMDs derived from the measured SFRDs disagree with the measured SMDs in the redshift range $0.5 < z < 6$ (see also the bottom panels of Figure 11.2). The SMDs derived from the LV using the combined SFH model shows a better agreement with the observed SMDs at $z < 2$ but are systematically higher at $z > 3$ than implied from the measured SFRDs.

In Haslbauer, Kroupa and Jerabkova (2023), we discussed several reasons for the tension between the local and global SFRDs, such as e.g. observational biases or an inadequate parametrization of the SFHs. Interestingly, Carnall et al. (2019) and Leja et al. (2019) applied different parametric and non-parametric SFH models on galaxies from the Galaxy and Mass Assembly (GAMA Driver et al. 2009; Driver et al. 2016; Baldry et al. 2018) Survey, respectively, and showed that the derived SFRDs are also inconsistent with the Lilly-Madau plot making it unlikely that the tension is caused by observational biases in the Updated Nearby Galaxy Catalog (Karachentsev, Makarov and Kaisina 2013).

If the nearby galaxies are a representative sample of the global Universe, our results imply that the local SFHs are inconsistent with the global SFH suggested by the Lilly-Madau plot. Although the Lilly-Madau plot is indeed commonly interpreted as the SFH of the Universe, it is also sensitive to the underlying matter field such that Lilly-Madau peak at $z = 1.86$ could be the signature of a ≈ 5 cGpc overdensity rather than just the peak star formation activity. This new interpretation of the Lilly-Madau plot would fit into the holistic picture in which the Universe is much more structured than predicted by the ΛCDM Universe as also concluded in Chapter 7.

Deriving the SFHs of LV galaxies e.g. from color magnitude diagrams (Weisz, Dolphin, Skillman, Holtzman, Gilbert et al. 2014) and precise measurements of the matter density field over redshift would shed more light on the tension reported in this study.

11.2 Author contributions

The authors of the corresponding publication are **Moritz Haslbauer** (MH), Pavel Kroupa (PK), and Tereza Jerabkova (TJ). PK had the idea to investigate the cosmological implications of the SFH of galaxies located in the Local Cosmological Volume. MH performed the whole analysis, created the figures, and wrote the manuscript with comments by PK and TJ. All authors contributed to the interpretation of the results.

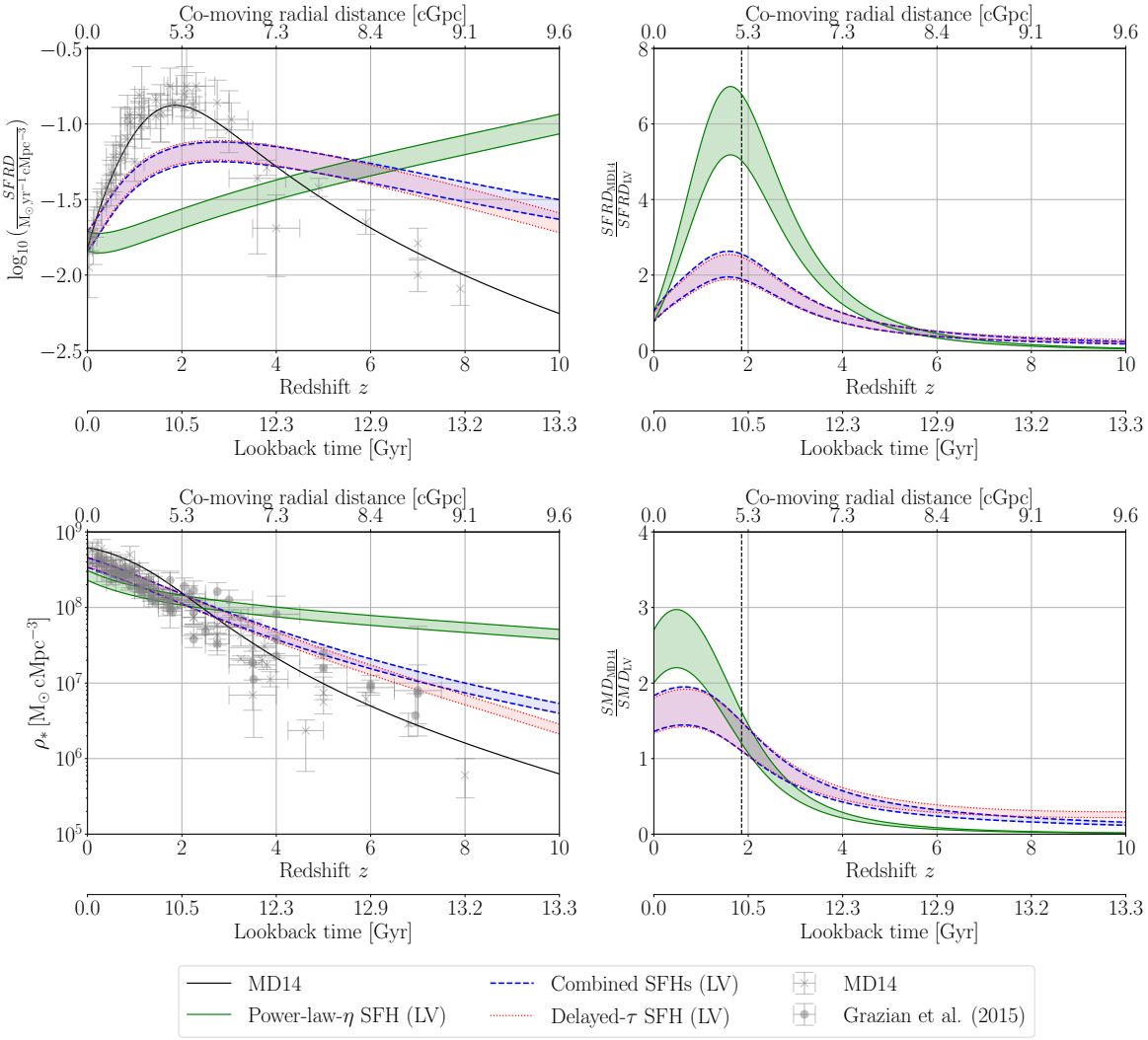

Figure 11.2: Evolution of the co-moving SFRD (*top*) and SMD (*bottom*) of the Universe assuming a standard ΛCDM cosmology (Planck Collaboration XIII 2016). The green, red, and blue shaded regions refer to the cosmic SFRDs and SMDs derived from the LV assuming the power-law, delayed-τ, and combined SFH model, respectively. *Top Left:* The "Lilly-Madau" plot. The black solid line is the best fit (equation 15 of Madau and Dickinson 2014) to the measured SFRDs marked with the grey crosses (table 2 of Madau and Dickinson 2014). *Top right:* Ratio between the SFRD of Madau and Dickinson (2014) and the SFRD derived from the LV for the thee different SFH models. The vertical dashed black line marks the peak of the Lilly-Madau plot at $z = 1.86$. *Bottom Left:* The black solid line shows the cosmic SMD implied from the best fit to the measured SFRDs (black line and grey crosses in the left panel). The grey circles and crosses are the measured SMDs taken from Madau and Dickinson (2014) and Grazian et al. (2015), respectively. Yu and F. Y. Wang (2016) reported a tension between the SMDs derived from the measured SFRDs and the measured SMDs over the redshift range of $0.5 < z < 6$ as evident also in the right panel (see the difference between the black solid line and data points). *Bottom right:* Ratio between the SMD derived from Madau and Dickinson (2014) and the SMD derived from the LV for the thee different SFH models. Credit: figure 5 of Haslbauer, Kroupa and Jerabkova (2023).

Scientific research questions addressed in Haslbauer, Kroupa and Jerabkova (2023):

- **Is the SFH of local galaxies consistent with the Lilly-Madau plot?**
  The almost constant SFHs of local galaxies are inconsistent with the Lilly-Madau plot.
- **What are the cosmological implications of the SFH of local galaxies?**
  The Lilly-Madau plot suggests that the SFRD increases from present time up to redshift $z = 1.86$ by a factor of ≈ 9 (Madau and Dickinson 2014). As the Lilly-Madau plot is commonly interpreted as the SFH of the global Universe, an almost constant SFH of local galaxies can have implications for the interpretations of the Lilly-Madau plot.
  If the LV is a representative sample of galaxies in the Universe, the peak of the Lilly-Madau plot at redshift $z = 1.86$ could be interpreted as the imprint of a large-scale density fluctuation. More precise measurements of the matter density field and derivations of the SFHs of local galaxies are required to affirm such a scenario.

(see also Appendix D)

CHAPTER 12

The effect of the environment dependent stellar initial mass function on the photometric properties of star-forming galaxies

"Est enim GALAXIA nihil aliud, quam innumerarum Stellarum coaceruatim consitarum congeries;"
(Galilei 1610)

This chapter and Appendix F contain the current version of the manuscript entitled "The effect of the environment dependent stellar initial mass function on the photometric properties of local star-forming galaxies" by **Moritz Haslbauer**, Zhiqiang Yan, Tereza Jerabkova, Pavel Kroupa, Akram Hasani Zonoozi, and Eda Gjergo (hereafter Haslbauer, Yan, Jerabkova, Kroupa, Zonoozi and Gjergo submitted), which has been submitted to a peer-reviewed scientific journal. The project was mainly developed and conducted during a research visit by Moritz Haslbauer at the European Southern Observatory (ESO) in Garching bei München (Germany).

Summary

Chapter 5 already introduced the basic concepts of the IGIMF theory (Kroupa and Weidner 2003) as a mathematical framework to compute the stellar IMF for an entire galaxy which is called the galaxy-wide stellar initial mass function (gwIMF; Section 5.3). According to the IGIMF formulation by Yan, Jeřábková and Kroupa (2021, hereafter IGIMF-2021), the gwIMF systematically varies with the global star formation rate (SFR) and metallicity of the galaxy as discussed in Figure 5.2 which has significant implications for the global properties of galaxies.

In the following manuscript by Haslbauer, Yan, Jerabkova, Kroupa, Zonoozi and Gjergo (submitted), we present the main-sequence, stellar mass buildup time-scales, and gas-depletion time-scales (i.e. the star-formation efficiencies) of local star-forming galaxies listed in the updated catalogue of Neighbouring Galaxies (Karachentsev et al. 2004; Karachentsev, Makarov and Kaisina 2013; Karachentsev and Kaisina 2013) assuming the invariant canonical but also a varying IMF within the IGIMF-2021 context. Such an analysis requires a re-calculation of the mass-to-light ratio as wells as a revised SFR–Hα-luminosity relation as the traditional (linear) Kennicutt law (Kennicutt 1998) relies on the invariant Salpeter IMF (Salpeter 1955, and see Section 5.1) being therefore not valid for

a varying IMF. In order to calculate the mass-to-light ratios of galaxies for different gwIMFs, we first introduce the photometric GalIMF (photGalIMF) code as a package to the publicly available galaxy evolution GalIMF code[1] which has been originally developed by Yan, Jerabkova and Kroupa (2017) and Yan et al. (2019). The photGalIMF code is an extension of the GalIMF code by coupling it with stellar isochrones provided by the PAdova and TRieste Stellar Evolution Code (PARSEC; Bressan et al. 2012) and COLIBRI (Marigo et al. 2013) code downloaded from the CMD 3.7 web interface[2] which enables for the first time to compute the photometric properties of galaxies in self-consistent chemical galaxy evolution models for a varying gwIMF (Section 12.2.2). Throughout the presented analysis we assume for simplicity a constant SFH, but the code also allows for more complex SFHs such as the delayed-τ model. The current version of the photGalIMF code (hereafter version 1.0) includes the K_s-band of the 2MASS sky survey (M. Cohen, Wheaton and Megeath 2003), the $K_{3.6\mu m}$-band of the Spitzer survey (Groenewegen 2006), and the V-band of the UBVRIJHK photometric system (Bessell 1990) for ten different metallicities.

Secondly, we calculate the SFR–Hα-luminosity relation for different metallicities in the IGIMF-2021 framework using the Programme d'Étude des GAlaxies par Synthèse Évolutive (PÉGASE)[3] stellar population synthesis code (Fioc and Rocca-Volmerange 1999; Fioc, Le Borgne and Rocca-Volmerange 2011) by following section 4.3 of Jeřábková et al. (2018). This shows that galaxies with H_α luminosities of $L_{H\alpha} \lesssim 10^{40}\,\mathrm{erg\,s^{-1}}$ have higher SFRs, while galaxies with $L_{H\alpha} \gtrsim 10^{43}\,\mathrm{erg\,s^{-1}}$ have lower SFRs than implied from the Kennicutt law (Section 12.2.3). In particular, galaxies with $L_{H\alpha} = 5.5 \times 10^{36}\,\mathrm{erg\,s^{-1}}$ and a low (high) metallicity of [Z]=-2.20 ([Z]=0.45) have SFRs being about 15 (about 221) times higher than derived from the Kennicutt law. In contrast, galaxies with $L_{H\alpha} = 10^{44}\,\mathrm{erg\,s^{-1}}$ and a low (high) metallicity of [Z]=-2.20 ([Z]=0.45) have about 4.4 (about 13) lower SFRs than the Kennicutt law. We provide functions to convert the observed Hα luminosity to SFRs within the IGIMF-2021 context for different metallicities.

Finally, we applied the IGIMF-corrected mass-to-light ratios and SFR–Hα luminosity relations on the sample of local star-forming galaxies in order to calculate the main-sequence, stellar mass buildup time-scales, and gas-depletion time-scales (i.e. the star-formation efficiencies). The main-sequence of star-forming galaxies defined over the stellar mass range of $10^{9.7} < M_*/M_\odot < 10^{11.1}$ (Speagle et al. 2014) becomes flatter compared for an invariant canonical IMF (Section 12.3.1 and 12.4.1) in agreement with Kroupa and Jerabkova (2021). The gas depletion time-scale decreases with the total gas mass for a canonical IMF, but increases lightly with the total gas mass in the IGIMF-2021 context, being about 4.72 Gyr (Sections 12.3.2 and 12.4.2). In the IGIMF-2021 context, the stellar mass buildup time-scale increases with stellar mass with more massive galaxies forming earlier than dwarf galaxies in contrast to the case for a canonical IMF (Section 12.3.3 and 12.4.3). We discuss how these findings agree with a previous study on local galaxies in the IGIMF context by Pflamm-Altenburg and Kroupa (2009).

This project enables the possibility for more precise tests of galaxy evolution and cosmological models because the interpretation of observed photometrics depends on the properties of the stellar IMF (Section 6.2). In future, we will make the photGalIMF code publicly available and include a finer grid of metallicities and further bands of photometric systems.

[1] https://github.com/Azeret/galIMF

[2] http://stev.oapd.inaf.it/cgi-bin/cmd_3.7

[3] https://www2.iap.fr/users/fioc/Pegase/

Scientific research questions addressed in Haslbauer, Yan, Jerabkova, Kroupa, Zonoozi and Gjergo (submitted):

- **How does the main-sequence of local star-forming galaxies differ for a canonical IMF and a varying IMF within the IGIMF context?**
  In the IGIMF-2021 context, galaxies with $L_{\mathrm{H}\alpha} \lesssim 10^{40}\,\mathrm{erg\,s^{-1}}$ have higher SFRs, while galaxies with $L_{\mathrm{H}\alpha} \gtrsim 10^{43}\,\mathrm{erg\,s^{-1}}$ have lower SFRs than obtained from the Kennicutt law. Thus, the main-sequence of star-forming galaxies with $10^{9.7} < M_*/M_\odot < 10^{11.1}$ becomes flatter compared for a canonical IMF.
- **How do the stellar mass buildup time-scales of galaxies depend on the stellar mass for a canonical IMF and a varying IMF within the IGIMF?**
  In the IGIMF-2021 context, the stellar mass buildup time-scale increases with stellar mass with more massive galaxies forming earlier than dwarf galaxies in contrast to the case for a canonical IMF
- **How do the gas depletion time-scales (the star formation efficiencies) of galaxies depend on the gas mass for a canonical IMF and a varying IMF within the IGIMF context?**
  The gas depletion time-scale decreases with the total gas mass for a canonical IMF, but increases lightly with the total gas mass in the IGIMF-2021 context, being about 4.72 Gyr.

(see also Appendix F)

Author contributions

The authors of the following manuscript entitled "The effect of the environment dependent stellar initial mass function on the photometric properties of local star-forming galaxies" (submitted) are **Moritz Haslbauer** (MH), Tereza Jerabkova (TJ), Zhiqiang Yan (ZY), Pavel Kroupa (PK), Akram Hasani Zonoozi (AHZ), and Eda Gjergo (EG). PK and TJ suggested to apply the IGIMF-2021 (Yan, Jeřábková and Kroupa 2021) formulation to a sample of local galaxies. TJ provided the code published in Jeřábková et al. (2018) to calculate the SFR–Hα luminosity relation for different IMFs using the PEGASE code. MH updated the code in order to provide new fitting functions to convert the observed Hα luminosities to SFRs for varying gwIMFs within the IGIMF-2021 context. MH suggested to calculate the mass-to-light ratio in the Ks-band in chemical evolution models in order to convert the observed luminosities to stellar masses for varying gwIMFs. MH, ZY, and TJ developed the photGalIMF code, which is an extension of the original GalIMF code by Yan, Jerabkova and Kroupa (2017) and Yan et al. (2019). MH wrote the code to convert the stellar masses to luminosities for different photometric bands using stellar isochrones of the PARSEC and COLIBRI code downloaded from the CMD 3.7 web interface[2]. ZY implemented the photometric package to his GalIMF code. MH and ZY tested the photGalIMF code. AHZ contributed with her expertise on stellar evolution tracks. EG assisted with her experience on chemical evolution models. MH applied the IGIMF corrections on a sample of nearby galaxies listed in the Catalogue of Neighbouring Galaxies (Karachentsev et al.

2004; Karachentsev, Makarov and Kaisina 2013). MH created the figures and wrote the manuscript with comments and passages by the co-authors. All authors contributed to the interpretation of the results by discussions and comments. The project was mainly conducted during a research visit by MH at the European Southern Observatory (ESO) in Garching bei München (Germany).

The effect of the environment dependent stellar initial mass function on the photometric properties of star-forming galaxies

Moritz Haslbauer, Zhiqiang Yan, Tereza Jerabkova, Pavel Kroupa, Akram Hasani Zonoozi, and Eda Gjergo (submitted)

Abstract

Context: Deriving properties of stellar systems depends on the underlying galaxy-wide initial mass function (gwIMF) which systematically varies with the global star formation rate (SFR) and metallicity according to the integrated-galactic IMF (IGIMF) theory.
Aims: We present the the stellar-mass–SFR relation, stellar mass buildup timescale, and gas depletion timescale of local star-forming galaxies in both the canonical IMF and variable gwIMF context.
Methods: In order to convert the observed luminosities to stellar masses, we develop the photometric GalIMF (photGalIMF) code which enables for the first time to compute photometric properties of galaxies in self-consistent chemical evolution models for varying gwIMFs by coupling the original GalIMF code with stellar isochrones provided by the PARSEC and COLIBRI code. Using the photGalIMF code we calculated the time evolution of the Ks-band mass-to-light ratio ($M/L_{\rm Ks}$) for the IGIMF and canonical IMF assuming constant SFRs. The SFR–Hα luminosity relation for different metallicities is computed using the PÉGASE stellar population synthesis code. We provide the corresponding fitting functions to derive the SFRs from Hα luminosities within the IGIMF context.
Results: The IGIMF-corrected $M/L_{\rm Ks}$ and SFR–Hα luminosity relation are applied to a sample of local star-forming galaxies. Galaxies with $L_{\rm Ks} \gtrsim 10^9\,L_{\rm Ks,\odot}$ have lower SFRs while less luminous galaxies have higher SFRs compared to the Kennicutt law making the present-day main sequence of local star-forming galaxies flatter for the IGIMF context. The gas depletion timescale increases with the gas mass in the IGIMF context implying that more massive galaxies have lower star formation efficiency than dwarf galaxies probably because of stronger feedback regulation. The stellar mass buildup timescale increases with stellar mass in the IGIMF context implying that dwarf disk galaxies started to form later than massive late-type galaxies.
Conclusions: The interpretation of observed photometrics requires assumptions about the IMF. The here-presented photGalIMF enables the study of the photometric properties of galaxies for varying gwIMFs.

12.1 Introduction

Galaxies in the observed distant and local Universe constrain various galaxy evolution and cosmological models, which requires precise measurements and a correct interpretation of the measured observables. The physical properties of galaxies are not only sensitive to the underlying cosmological framework (Balakrishna Subramani et al. 2019; Haslbauer et al. 2022) but also on the behavior of baryonic physics (H. Li et al. 2020, but see). A fundamental parameter in galaxy evolution is the initial stellar mass function (IMF) which describes the mass distribution of newly formed stars (A. M. Hopkins 2018). The IMF together with the star formation history (SFH) determines the stellar population of systems, the masses in living stars and remnants, and affects the matter cycle and chemical enrichment. Deducing

the SFRs of stellar systems requires measurements of SFR indicators which are available e.g. for the X-ray, ultra-violet, optical, infrared, and the radio regime (e.g. Kennicutt 1983; Donas and Deharveng 1984; Buat, Deharveng and Donas 1989; David, C. Jones and Forman 1992; Condon 1992; Kennicutt 1998; Yun, Reddy and Condon 2001; Kewley et al. 2002; Brinchmann et al. 2004; Moustakas, Kennicutt and Tremonti 2006; Rieke et al. 2009; Kennicutt and Evans 2012; Calzetti 2013; M. J. I. Brown et al. 2017; Mahajan et al. 2019, and referenes therein). Crucially, converting these tracers to a SFR depends on the shape of the IMF (Kroupa and Jerabkova 2021). Therefore, the properties and functional dependencies of the IMF are of great importance in interpreting the observations of stellar systems. While it has been commonly assumed in the past that the IMF is invariant (known as the canonical IMF) meaning that the mass distribution of stars is independent of the star-forming environment, more and more observations suggest that the IMF varies in different environments ranging from star-burst regions (Dabringhausen, Kroupa and Baumgardt 2009; Gunawardhana et al. 2011; Dabringhausen et al. 2012; Marks et al. 2012; F. R. N. Schneider et al. 2018; Zhang et al. 2018) to dwarf galaxies (Meurer et al. 2009; J. C. Lee et al. 2009; Watts et al. 2018; Yan, Jerabkova and Kroupa 2020; Mucciarelli et al. 2021) and from metal-poor stellar populations (Geha et al. 2013; Gennaro et al. 2018; Yan, Jerabkova and Kroupa 2020; J. Li et al. 2023) to galaxies with super-solar metallicities (Parikh et al. 2018; Zhou et al. 2019; Martın-Navarro et al. 2019; R. J. Smith 2020; van Dokkum and Conroy 2021, Yan et al. 2023 submitted).

The integrated galactic IMF (IGIMF) theory was introduced by Kroupa and Weidner (2003) and is a mathematical framework to calculate the galaxy-wide IMF (gwIMF) by adding up the IMFs of all embedded clusters within a galaxy. Qualitatively, the IGIMF theory relies on the empirical relation of star formation and has been constantly further developed (Kroupa et al. 2013; Jeřábková et al. 2018; Yan, Jerabkova and Kroupa 2020; Yan, Jerabkova and Kroupa 2023) with the most up-to-date formulation being provided by Yan, Jeřábková and Kroupa (2021) and Yan et al. (2023 submitted) according to which the gwIMF systematically varies with the global SFR, ψ, and averaged gas-phase metallicity of the galaxy. According to this empirically constrained IGIMF formulation, the gwIMF becomes top-heavy for $\psi \gtrsim 1\,\mathrm{M}_\odot\,\mathrm{yr}^{-1}$ meaning that the formation of more massive stars is favored compared to the canonical IMF and the gwIMF becomes top-light for $\psi \lesssim 1\,\mathrm{M}_\odot\,\mathrm{yr}^{-1}$ such that massive stars are lacking relative to the canonical IMF. The metallicity also correlates with the top slope of the IMF but only has a second-order effect. For metal-poor galaxies and metal-rich galaxies, the gwIMF becomes bottom-light (less low-mass stars) and bottom-heavy (more low-mass stars) independent of the SFR, respectively (see e.g. figure 2 of Jeřábková et al. 2018, and Section 12.2.1 for the IGIMF formulations adopted in our work). The IMF is likely to be affected by more physical parameters, such as cosmic ray density (Papadopoulos et al. 2011; Papadopoulos and Thi 2013; Fontanot et al. 2018) and temperature (Sneppen et al. 2022), but they are more difficult to measure compared to SFR and stellar metallicity.

Despite the above difficulties in constraining the empirical IMF variation and adopting the simplest formulation (linear correlations between the galactic physical parameter and the IMF power-law index), the IGIMF model successfully explained several observations over the last two decades. For example, the mass–metallicity relation (Köppen, Weidner and Kroupa 2007; Yan, Jerabkova and Kroupa 2019; Yan, Jeřábková and Kroupa 2021), the [α/Fe] relation in early-type galaxies (Recchi, Calura and Kroupa 2009; Yan, Jerabkova and Kroupa 2019; Yan, Jeřábková and Kroupa 2021), the chemical evolution of ultra-faint dwarf galaxies (Yan, Jerabkova and Kroupa 2020; Mucciarelli et al. 2021), the UV/Hα flux ratio of galaxies (J. C. Lee et al. 2009; Pflamm-Altenburg, Weidner and Kroupa 2009; Yan, Jerabkova and Kroupa 2017), the radial Hα cut-off in disk galaxies (Pflamm-Altenburg

and Kroupa 2008), the mass correlation between spheroidal galaxies and their hosted supermassive black holes (Kroupa et al. 2020).

The implications of a variable IMF for the local but also global properties of stellar systems are significant. For example, the number of ionizing photons depends on the shape of the gwIMF such that the relation between the SFR and Hα luminosity, $L_{\mathrm{H}\alpha}$, of a galaxy becomes non-linear for a varying IMF (Pflamm-Altenburg, Weidner and Kroupa 2009; Jeřábková et al. 2018) violating therewith the Kennicutt law (Kennicutt 1998). Galaxies with $L_{\mathrm{H}\alpha} > 10^{41}$ ergs/s ($L_{\mathrm{H}\alpha} < 10^{41}$ ergs/s) have SFRs lower (higher) than those given by the Kennicutt law. This affects the properties of star-forming galaxies such as the main sequence of star-forming galaxies, which is a tight correlation between the SFRs and stellar masses of galaxies (see e.g. figure 8 of Speagle et al. 2014). Applying an IGIMF-corrected SFR–Hα luminosity relation (see figure 7 of Jeřábková et al. 2018), Kroupa and Jerabkova (2021) found that the slope of the main sequence becomes flatter. However, this previous analysis does not include a correction of the galaxy stellar masses which also depends on the IMF. Another consequence of the variable IMF is on the estimation of the gas depletion timescale, $\tau_{\mathrm{gas}} = M_{\mathrm{gas}}/\psi$, and stellar-mass buildup timescale, $\tau_* = M_*/\psi$. Pflamm-Altenburg and Kroupa (2009) calculated these timescales for 200 nearby galaxies in the canonical IMF and IGIMF context. They demonstrated that in the IGIMF framework, the star formation efficiency (SFE), τ_{gas}^{-1}, remains almost constant, while massive disk galaxies have much higher τ_{gas}^{-1} than dwarf galaxies for a canonical IMF. Moreover, Pflamm-Altenburg and Kroupa (2009) find that τ_* increases with stellar mass in the IGIMF framework, implying that SFR may have been increasing slightly with time for dwarf galaxies but not for large disk galaxies. This is in agreement with observations (Fontanot et al. 2009) and in contrast with the canonical IMF expectations. A caveat of the above studies is that they only take into account the effect of IMF variation on the estimation of galactic SFR but not on the stellar mass. Therefore, not being self-consistent. This simplification is reasonable because the SFR correction is much more significant than the stellar mass correction and the tool for calculating the SFH of a galaxy with an environment-dependent IMF was developed later in Yan et al. (2019).

In this contribution, we estimate the SFRs and the stellar masses of galaxies located in the local volume (Karachentsev et al. 2004; Karachentsev, Makarov and Kaisina 2013) using the latest IGIMF formalism (Yan, Jeřábková and Kroupa 2021). To calculate the stellar mass-to-light ratio in specific photometric bands for our galaxy models, we developed the photometric GalIMF code (photGalIMF, Section 12.2.2) which couples the original variable gwIMF galaxy chemical evolution code (GalIMF, Yan, Jerabkova and Kroupa 2017; Yan et al. 2019) with stellar isochrones provided by PARSEC (Bressan et al. 2012) and COLIBRI (Marigo et al. 2013). This enables, for the first time, to study photometric properties of galaxies in self-consistent chemical evolution models with an environment-dependent gwIMF.

The paper is organized as follows: Section 12.2 introduces the IGIMF theory, the photGalIMF code to calculate the mass-to-light ratio in different photometric bands, the method to derive the SFR–Hα-luminosity relation, and describes the sample of galaxies located in the local volume (Karachentsev et al. 2004; Karachentsev, Makarov and Kaisina 2013) on which the IGIMF corrections are applied. Section 12.3 presents the the stellar-mass–SFR relation of star-forming galaxies, the gas depletion timescale, and stellar-mass buildup times of local star-forming galaxies in the canonical IMF and the IGIMF framework. The results are discussed in Section 12.4 which is followed by an outlook and a conclusion in Section 12.5.

Throughout the analysis we assume an age of the Universe of $\tau_{\mathrm{h}} = 13.8$ Gyr (table 4 of Planck

Collaboration XIII 2016).

12.2 Methods

To estimate the stellar masses and SFRs of local star-forming galaxies, we apply the empirical environment-dependent IMF variation formulation given by the IGIMF theory that has been well-developed and tested (Section 12.1). First, we state the physical assumptions and mathematical framework of the IGIMF theory by providing qualitative discussions on the functional dependence of the gwIMFs on the global SFR and the metallicity of different IGIMF formulations in Section 12.2.1. A more comprehensive description of the IGIMF theory can be found, for example, in Jeřábková et al. (2018) and Yan, Jeřábková and Kroupa (2021). In the Sections. 12.2.2 and 12.2.3, we present the methods to compute the mass-to-light ratio and the SFR of a galaxy using the photGalIMF code version 1.0 and the SFR–Hα luminosity relation, respectively. Finally, we describe in Section 12.2.4 the observational data extracted from the updated version of the Catalogue of Neighbouring Galaxies on which the IGIMF corrections are applied as described in Section 12.2.5.

12.2.1 IGIMF theory

In general, the IGIMF theory allows the calculation of the gwIMF by adding up the stellar IMFs in all embedded clusters of a galaxy (Kroupa and Weidner 2003). The stellar IMF, $\xi_*(m)$, describes the number of newly formed stars, dN, in the mass interval m to $m + dm$, and can be mathematically modeled as a three-part power law of the form

$$\xi_*(m) = \begin{cases} k_1 m^{-\alpha_1} & 0.08 \leq m/M_\odot < 0.50\,, \\ k_2 m^{-\alpha_2} & 0.50 \leq m/M_\odot < 1.00\,, \\ k_3 m^{-\alpha_3} & 1.00 \leq m/M_\odot < m_{\max}\,, \end{cases} \tag{12.1}$$

where k_i are normalization constants (ensuring continuity of the function) and α_i are the power-law indices. The canonical IMF (Kroupa 2001; Kroupa et al. 2013) has $\alpha_1 = 1.3$, $\alpha_2 = \alpha_3 = 2.3$ (the Salpeter power-law index; Salpeter 1955). The maximum mass of a star in a cluster, $m_{\max}$, is given by the $m_{\max} - M_{\rm ecl}$ relation (Weidner and Kroupa 2006; Yan, Jerabkova and Kroupa 2023), which states that $m_{\max}$ depends on the cluster mass $M_{\rm ecl}$ by solving simultaneously the following two equations

$$M_{\rm ecl} = \int_{0.08\,M_\odot}^{m_{\max}} m\xi_*(m)dm \qquad \text{and} \tag{12.2}$$

$$1 = \int_{m_{\max}}^{m_{\max,*}} k_3 m^{-\alpha_3} dm \qquad \text{when} \quad m_{\max} > 1\,M_\odot\,, \tag{12.3}$$

where $M_{\rm ecl}$ is the mass of an embedded star cluster, k_3 is the normalization constant in Equation (12.1), and $m_{\max,*} = 150\,M_\odot$ is the upper mass limit of a star (Weidner and Kroupa 2004; Figer 2005; Oey and Clarke 2005; Koen 2006; Maız Apellániz et al. 2007; Banerjee, Kroupa and Oh 2012a; Banerjee, Kroupa and Oh 2012b). We note that the stellar mass upper limit is still an open question. Changing this limit to, for example, 300 $M_\odot$ as is suggested by Crowther et al. (2010), F. R. N. Schneider et al. (2018), and Higgins et al. (2022), would not affect our study because most massive stars are extremely rare.

Based on the observation by Kroupa (2002, his Equation (3)), that the IMF may become more bottom heavy with increasing metallicity, the power-law indices of the stellar IMF for low-mass stars are

$$\begin{aligned} \alpha_1 &= 1.3 + \Delta\alpha \cdot (Z - Z_\odot) \quad \text{for} \quad 0.08 \leq m/M_\odot < 0.50\,, \\ \alpha_2 &= 2.3 + \Delta\alpha \cdot (Z - Z_\odot) \quad \text{for} \quad 0.50 \leq m/M_\odot < 1.00\,, \end{aligned} \tag{12.4}$$

where $\Delta\alpha = 63$ as revised by Yan, Jerabkova and Kroupa (2020) and Yan, Jeřábková and Kroupa (2021). Z and $Z_\odot = 0.0142$ (Asplund et al. 2009) are the mean stellar metal-mass fraction of the system and the Sun, respectively. Thus, Equation (12.1) results in the canonical (Kroupa 2001) IMF for star-forming regions when $Z = Z_\odot$. The power-law index of the high-mass stars ($1.00 \leq m/M_\odot < m_{\rm max}$) is given by (Marks et al. 2012; Marks et al. 2014)

$$\alpha_3 \;=\; \begin{cases} 2.3 & \text{for} \quad x < -0.87\,, \\ -0.41x + 1.94 & \text{for} \quad x \geq -0.87\,, \end{cases} \tag{12.5}$$

with

$$x \;=\; -0.41\,[Z] + 0.99 \log_{10}\left(\frac{M_{\rm ecl}}{10^6 M_\odot}\right), \tag{12.6}$$

where $M_{\rm ecl}$ is the initial stellar mass of the star cluster and $[Z] \equiv \log_{10}(Z/Z_\odot)$. The original IGIMF version as proposed by Kroupa and Weidner (2003) and Weidner and Kroupa (2006) adopted the canonical IMF for all embedded star clusters ($\alpha_1 = 1.3$ and $\alpha_2 = \alpha_3 = 2.3$; see e.g. the model 'IGIMF1' in Jeřábková et al. 2018).

The embedded cluster initial mass function (ECMF) is described by a single power law (C. J. Lada and E. A. Lada 2003; Lieberz and Kroupa 2017) of the form

$$\xi_{\rm ecl}(m, \psi) = k_{\rm ecl} M_{\rm ecl}^{-\beta(\psi)} \, M_{\rm ecl,min} \leq M_{\rm ecl} < M_{\rm ecl,max}(\psi)\,, \tag{12.7}$$

where $k_{\rm ecl}$ is the normalization constant, $M_{\rm ecl,min}$ and $M_{\rm ecl,max}$ are the minimum and maximum masses of an embedded cluster, respectively. The power-law index β depends on the global SFR of a galaxy as follows (Weidner, Kroupa and Larsen 2004; Yan, Jerabkova and Kroupa 2017; Jeřábková et al. 2018)

$$\beta \;=\; -0.106 \log_{10}\left(\frac{\psi}{M_\odot\,{\rm yr}^{-1}}\right) + 2\,, \tag{12.8}$$

implying that the ECMF becomes flatter with increasing SFR. The here adopted power-law index of the EMCF differs from the formulation of Pflamm-Altenburg and Kroupa (2009) in which they used a Salpeter single-power-law index of $\beta = 2.35$ for their standard IGIMF model and a two-part power-law with $\beta_1 = 1.00$ for star clusters in the mass range $5 - 50\,M_\odot$ and $\beta_2 = 2.00$ for $> 50\,M_\odot$ in their 'minimum-1' IGIMF model. The effects of this difference are discussed in Sections. 12.4.2 and 12.4.3.

The total stellar mass of the embedded cluster formed in the time-span δt is given by

$$\begin{aligned} M_{\rm tot} &= \psi \cdot \delta t \\ &= \int_{M_{\rm ecl,min}}^{M_{\rm ecl,max}(\psi)} M_{\rm ecl} \xi_{\rm ecl}(M_{\rm ecl}) dM_{\rm ecl}\,, \end{aligned} \tag{12.9}$$

where δt is set to 10 Myr (Weidner, Kroupa and Larsen 2004). Requiring that there should be one embedded cluster between $M_{\rm ecl,max}(\psi)$ and an assumed upper stellar mass limit of $10^9\,M_\odot$, implies

$$1 = \int_{M_{\rm ecl,max}(\psi)}^{10^9\,M_\odot} k_{\rm ecl} M_{\rm ecl}^{-\beta}\, dM_{\rm ecls}\,, \tag{12.10}$$

Solving these two equations defines the parameters $k_{\rm ecl}$ and $M_{\rm ecl,max}(\psi)$ of the ECMF and yields to the $M_{\rm ecl,max}$–SFR relation (Weidner, Kroupa and Larsen 2004).

Observations of the MW showed that about 70 – 90% of all stars are formed in giant molecular clouds (C. J. Lada and E. A. Lada 2003), while the other 10 – 30% may be stars formed in short-lived clusters (Recchi, Calura and Kroupa 2009; Dinnbier, Kroupa and Anderson 2022). Approximating that all stars of the galaxy are formed in embedded star clusters (Kroupa 1995; Kroupa and Weidner 2003), the gwIMF is finally given by combining the stellar IMF (Equations 12.1-12.5) and the ECMF (Equation (12.7)),

$$\xi_{\rm IGIMF}(m,\psi,[{\rm Z}]) = \tag{12.11}$$
$$= \int_0^{+\infty} \xi_*(m, M_{\rm ecl}, [{\rm Z}])\; \xi_{\rm ecl}(m, M_{\rm ecl}, \psi) dM_{\rm ecl}\,.$$

Throughout this study, we refer to the IGIMF formulation provided by Yan, Jeřábková and Kroupa (2021) as IGIMF-2021.

The effect of the environment-dependent stellar gwIMF (Equation (12.12)) is qualitatively investigated in Figure 12.1 by showing a grid of gwIMFs for different global SFRs in the range of $\psi = [10^{-5}, 10^4]\,{\rm M_\odot\,yr^{-1}}$ and metallicities in the range of $[Z] = [-5, 1]$. This grid is similar to the analysis of figure 2 by Jeřábková et al. (2018) but includes only the newer IGIMF-2021 formulation (Yan, Jeřábková and Kroupa 2021).

Generally, the gwIMF constructed from the IGIMF-2021 (red lines in Figure 12.1) systematically varies with the global SFR and metallicity but as it is constructed based on observational constraints, the gwIMF is consistent with the canonical IMF for solar metallicities and $\psi = 1\,{\rm M_\odot\,yr^{-1}}$ (dashed black line). The gwIMFs of the IGIMF-2021 formulation become bottom-heavy for $[Z] > 0$ and bottom-light for $[Z] < 0$ independent of the SFR, reproducing the observed correlation (Geha et al. 2013; Parikh et al. 2018; Zhou et al. 2019, Yan et al. 2023 submitted). The gwIMF becomes top-heavy for $\psi \gtrsim 1\,{\rm M_\odot\,yr^{-1}}$ and top-light for $\psi \lesssim 1\,{\rm M_\odot\,yr^{-1}}$. The IGIMF-2021 formulation is consistent with the previous formulations by Marks et al. (2012) and Yan, Jerabkova and Kroupa (2020) at $\gtrsim 1\,M_\odot$ but the Marks et al. (2012) underestimates the number of low-mass stars compared to the newer IGIMF formulations for non-solar metallicities. As illustrated more clearly in figure B1 of Yan, Jerabkova and Kroupa (2017) the top-heaviness of the gwIMFs for $\psi > 1\,{\rm M_\odot\,yr^{-1}}$ slightly increases with decreasing metallicity. Importantly, the IGIMF-2021 formulation yields extremely bottom-heavy gwIMFs for $[Z] \gtrsim 0.4$ independent of the SFR as discussed further in Appendix F.2.

A varying gwIMF has several implications on the global properties of galaxies (see also Section 12.1) as it affects, for example, the expected mass-to-light ratio and the relation between the SFR and Hα luminosity as outlined in the following sections.

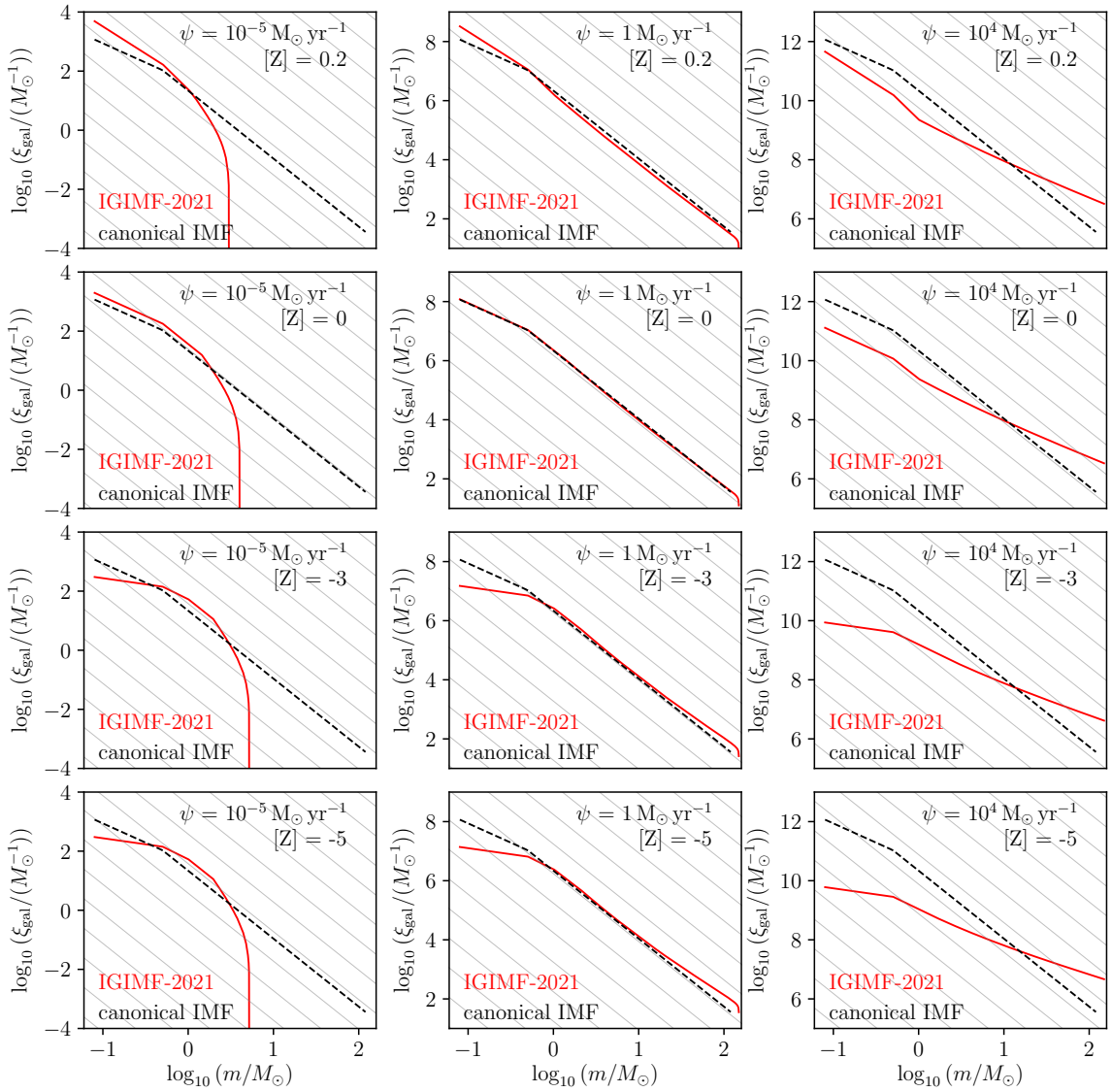

Figure 12.1: Grid of simulated gwIMFs in dependence of the SFR (from left to right: $\psi = 10^{-5}, 1, 10^{4}\ \mathrm{M}_\odot\ \mathrm{yr}^{-1}$) and metallicity (from top to bottom: [Z] = 1,0,-3,-5) for the IGIMF-2021 formulation (solid red line) by Yan, Jeřábková and Kroupa (2021) using the GalIMF code (Yan, Jerabkova and Kroupa 2017) in comparison with the canonical IMF (dashed black) with the power-law indices $\alpha = 1.3$ for stars in the mass range of $0.08 - 0.5\,M_\odot$ and $\alpha = 2.3$ for stars with $> 0.5\,M_\odot$ (Kroupa 2001). This grid is similar to figure 2 of Jeřábková et al. (2018) but includes only the IGIMF-2021 formulations which is adopted throughout the analysis presented in this study.

12.2.2 Mass-to-light ratio

Converting the observed luminosities of galaxies to stellar masses requires the stellar mass-to-light ratio, which mainly depends on the underlying stellar IMF, SFH, and chemical evolution. The mass-to-light ratio of a galaxy depends on the shape of the SFH but not on the absolute SFR values for an invariant gwIMF, while the mass-to-light ratio also depends on the SFR values for a varying gwIMF (Zonoozi, Mahani and Kroupa 2019). In order to calculate the mass-to-light ratio in different photometric bands within the canonical IMF and IGIMF framework, we developed the photometric GalIMF (photGalIMF) code (Section 12.2.2.2) by using the variable gwIMF galaxy evolution open source code (GalIMF, Yan, Jerabkova and Kroupa 2017; Yan et al. 2019; Yan, Jeřábková and Kroupa 2021) in combination with the PAdova and TRieste Stellar Evolution Code (PARSEC, Bressan et al. 2012) and COLIBRI code (Marigo et al. 2013).

12.2.2.1 Chemical evolution model

The GalIMF version 1.1 developed by Yan et al. (2019) and Yan, Jeřábková and Kroupa (2021) is a Python 3 module that couples a chemical evolution model (galevo.py) with a gwIMF generator (galimf.py). The codes are introduced and described in full detail in Yan, Jerabkova and Kroupa (2017) and Yan et al. (2019) and are publicly available on GitHub. In the following, we provide only a brief summary of the most important assumptions and model parameters.

The chemical evolution calculation assumes a monolithic collapse for galaxy formation whereby primordial gas is transformed into living stars which subsequently evolve into white dwarfs, neutron stars, and black holes over cosmic time. Throughout the study, we adopt the closed-box model in which gas infall and galactic outflows are turned off. The gas phase is modeled as a single-zone gas, which is continuously enriched by stellar evolution. The main input parameters of the galaxy evolution module are the SFH and the gas-convergence factor, $g_{\rm conv}$, which describes the mass of all formed stars divided by the initial gas mass (cf. Yan, Jeřábková and Kroupa 2021). The $g_{\rm conv}$ value affects the chemical enrichment of the simulated galaxy as a higher value of $g_{\rm conv}$ increases the metallicity, while a lower value decreases the metallicity of the galaxy. This parameter is adjusted (see figure 8 of Yan, Jeřábková and Kroupa 2021) to match the observed present-day mass–metallicity relation of galaxies (Section 12.2.2.4). For the monolithic formation of elliptical galaxies, $g_{\rm conv} = 0.2$ for present-day $M_* > 10^{10}\,M_\odot$ and $g_{\rm conv} \approx 0.2$ for $M_* \approx 10^8\,M_\odot$.

The time-step of the simulation is set to $\delta t = 10$ Myr, which corresponds to the time span for large molecular clouds to collapse and form a population of embedded star clusters that fully populates the ECMF (Yan, Jerabkova and Kroupa 2017). For each 10 Myr time step, the chemical evolution module updates the chemical abundances, the mass of stellar remnants, living stars, and gas. The code calculates the instantaneous environment-dependent (galaxy-wide SFR and gas-phase metallicity) gwIMF according to the IGIMF theory (see figure 1 of Yan et al. 2019, and Figure 12.2 in our work). The gas-convergence factor $g_{\rm conv}$ is kept constant throughout the evolution of a galaxy.

12.2.2.2 Stellar luminosity evolution

The previous GalIMF version 1.1 module only considers the zero-age-main sequence luminosity (Section 4.4 of Yan et al. 2019). To include the metallicity and age dependencies of stellar luminosities for pre-main sequences and giant stars of different photometric bands, we develop the photGalIMF code which extends the GalIMF code by coupling it with the stellar isochrones of the PARSEC and

COLIBRI code. The concept of the photGalIMF code is illustrated in Figure 12.2. This improvement is necessary as it will correctly increase the luminosity estimation of a stellar population up to a few times (Girardi et al. 2013).

The PARSEC code models the evolutionary tracks from the pre-main sequence (PMS) phase to the first thermal pulse or carbon-ignition. The COLIBRI code adds the thermally-pulsing asymptotic giant branch (TP-AGB) evolution from the 1st thermal pulse to the total loss of envelope. In particular, the current version of the photGalIMF code implements the PARSEC (Bressan et al. 2012) version 1.2s, and the COLIBRI S_37 code (Pastorelli et al. 2020) for metallicities in the range of $0.008 \leq Z \leq 0.02$, COLIBRI S_35 (Pastorelli et al. 2019) for $0.0005 \leq Z \leq 0.006$, COLIBRI PR16 (Marigo et al. 2013), and the models by Rosenfield et al. (2016) for $Z \leq 0.0002$ and $Z \geq 0.03$ (see also the description on the CMD web interface version 3.7[4]).

The Catalogue of Neighbouring Galaxies (Karachentsev et al. 2004; Karachentsev, Makarov and Kaisina 2013) lists the luminosity of galaxies in the Ks-band of the 2MASS sky survey (Jarrett et al. 2000; Jarrett et al. 2003). Therefore, we downloaded from the CMD 3.7 web interface[4] the PARSEC-COLIBRI stellar isochrone tables for the photometric systems labeled “2Mass + Spitzer (IRAC + MPIS)" (M. Cohen, Wheaton and Megeath 2003; Groenewegen 2006), which list the Ks-band magnitudes with an effective wavelength of $\lambda_{\rm eff} = 21620.75$ Å, a bandwidth of $w_{\rm eff} = 2714$ Å, and an attenuation relative to the V-band of $A_\Lambda / A_{\rm V} = 0.11675$. We apply the default options of the CMD 3.7 web interface which provide the bolometric correction “YBC+new Vega", a dust compositions of 60% Silicate and 40% AlOx for M stars and 85% AMC and 15% SiC for C stars (Groenewegen 2006), a total extinction of $A_{\rm V} = 0.0$ mag, and a long-period variability during the RGB and AGB phase as modeled by Trabucchi et al. (2021). In total, we download the isochrones for the ten diffferent metallicities [Z] = -2.17, -1.87, -1.47, -1.17, -0.57, -0.26, -0.17, 0.13, 0.31, 0.43.

The Ks-band magnitudes, $M_{\rm Ks}$, of the so-downloaded and incorporated isochrone tables are converted into luminosities via

$$\frac{L_{\rm Ks}}{L_{\rm Ks,\odot}} = 10^{0.4(M_{\rm Ks,\odot} - M_{\rm Ks})}\,, \tag{12.12}$$

where $M_{\rm Ks,\odot} = 3.27$ (table 3 of Willmer 2018) is the absolute magnitude of the Sun in the vegamag system.

The GalIMF code calculates the gwIMF for a stellar population by assuming that stars are randomly forming at different times within $\delta t = 10$ Myr (Section 12.2.2.1) without accounting for the exact formation time of the individual stars. This assumption requires us to calculate the time-averaged the luminosity of a star formed with a given initial mass, m, metallicity, Z, and age, t, by

$$\overline{L}_{\rm Ks}(m, t, Z) \quad = \quad \frac{1}{\delta t} \sum_{i=1}^{N} L_{\rm Ks}(m, t_i, Z)\ \Delta t\,, \tag{12.13}$$

where $\delta t = N \cdot \Delta t$, $t_i = t + i \cdot \Delta t$, t_i is the age of the isochrone, and N is the number of used isochrones between the time span t and $t + \delta t$ in the GalIMF code. The time-resolution of the isochrones is set to $\Delta t = 0.1$ Myr for galaxy ages of $t < 1$ Gyr and $\Delta t = 1$ Myr for $t \geq 1$ Gyr.

The photGalIMF module assigns each formed star in the GalIMF module a time-averaged luminosity value $\overline{L}_{\rm Ks}$ according to its m, Z, and t. For this, we linearly interpolate the stellar-mass-time-averaged-

[4] http://stev.oapd.inaf.it/cgi-bin/cmd

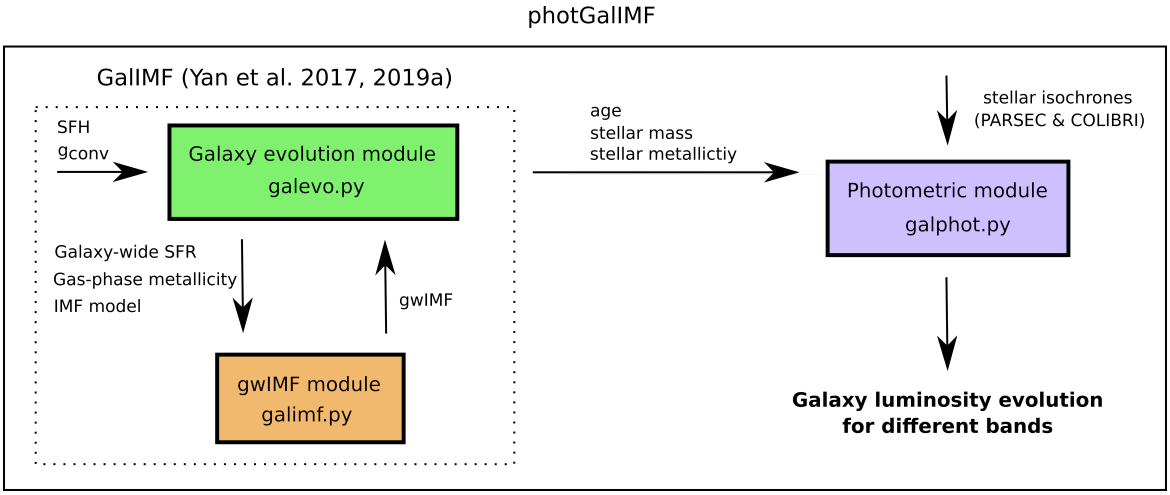

Figure 12.2: Flowchart of the photGalIMF code, which is an extension of the GalIMF code (Yan et al. 2019) by coupling it with stellar isochrones in order to calculate photometric properties of galaxies. The GalIMF code calculates the stellar population of a galaxy for a given SFH, $g_{\rm conv}$, and the gwIMF model at different times. The metallicity, masses, and ages of the living stars are then transferred to the photometric module, which calculates the luminosity for the selected photometric bands (see text) and each $\delta t = 10$ Myr time interval.

luminosity relation (MLR) for stars with $t < 10^{8.5}$ yr ensuring that the PMS is accurately described. For $t \geq 10^{8.5}$ yr, the main sequence phase of the MLR is fitted with a 10-th order polynomial in order to reduce the computational costs. The giant phase is still linearly interpolated to ensure that the TP-AGB is accurately traced. The sum of all $\overline{L}_{\rm Ks}$ values is the total luminosity of the simulated galaxy.

The Ks-band stellar (including remnants) mass-to-light ratio at a given time is then

$$\frac{M}{L_{\rm Ks}} = \frac{M_{*,\rm living} + M_{\rm rem}}{L_{\rm Ks}}\,, \tag{12.14}$$

where $M_{*,\rm living}$ and $M_{\rm rem}$ are the mass of the living stars and stellar remnants (i.e. white dwarfs, neutron stars, black holes, calculated as in Yan et al. 2019), respectively.

The current version of the photGalIMF code is freely available on Github[5] and provides the galaxy luminosity evolution in the Ks-band of the 2Mass sky survey (M. Cohen, Wheaton and Megeath 2003), the $K_{3.6\mu m}$-band of the Spitzer survey (see e.g. Groenewegen 2006), and the V-band of the UBVRIJHK photometric system (Bessell 1990; Maíz Apellániz 2006), as summarized in Appendix F.1. More bands including the GAIA and JWST photometries, as well as the hydrogen line emissions, will be added in the future.

12.2.2.3 Star formation histories

Computing the stellar population of a galaxy requires assumptions on the SFH. The real SFHs of observed galaxies are uncertain, leading to a large SFR estimation uncertainty that is hard to rectify. Main sequence galaxies are likely to include both rising and declining SFRs. Assuming a rising SFR could result in a SFR estimation that is 0.3 to 0.6 dex higher than the value when assuming a declining

[5] https://github.com/Azeret/galIMF [Author's note: photGalIMF code to be added.]

SFH (Section 3.1.4 of Speagle et al. 2014). Kroupa et al. (2020) showed that most of the star-forming galaxies in the local volume have near constant SFHs over a time-span of 12 Gyr. Therefore, it is reasonable to assume as a first approach SFH models with a constant SFR over time for star-forming galaxies. In addition, we adopt that all galaxies start forming their stars 0.2 Gyr after the Big Bang till the present time $\tau_{\rm h}$ = 13.8 Gyr (Planck Collaboration XIII 2016). Thus, throughout the analysis the present-day properties of galaxies refer to an age of 13.6 Gyr.

In total, we run a grid of galaxy evolution models with constant SFRs between $\psi = 10^{-5}\,{\rm M}_\odot\,{\rm yr}^{-1}$ and $\psi = 10^{3}\,{\rm M}_\odot\,{\rm yr}^{-1}$ in steps of 0.5 dex for two different chemical enrichment descriptions detailed in the following Section 12.2.2.4.

12.2.2.4 Mass–metallicity relation

The gwIMF of a galaxy and the mass-to-light ratio of stars depend on the metallicity. Therefore, the mass-to-light ratio of a galaxy also depends on the metallicity distribution of the stars calculated by the galaxy chemical enrichment model and it is important for the models to reproduce the observed mass–metallicity relation of the star-forming galaxies. Assuming constant SFHs over a time-span of 13.6 Gyr and no outflows, we calculate for each SFH (Section 12.2.2.3) two different chemical enrichment models with $g_{\rm conv}$ = 0.10 and $g_{\rm conv}$ = 0.25 making up in total 34 different IGIMF models. We find that with these $g_{\rm conv}$ values, the resulting galaxies reproduce the present-day stellar mass–metallicity relation (Gallazzi et al. 2005; Kirby et al. 2013) as is shown in Figure 12.3.

The galactic stellar masses estimated by Gallazzi et al. (2005) and Kirby et al. (2013) assume a canonical IMF while our calculations are based on the more realistic empirical environment-dependent gwIMF. However, the mass estimation difference is usually less than a factor of two (Yan, Jeřábková and Kroupa 2021), which is insignificant compared to the observed scatter in the mass–metallicity relation (Figure 12.3), therefore, would not affect our conclusions.

12.2.2.5 Galaxy evolution in the IMF and IGIMF framework

Figure 12.4 shows the time evolution of $M/L_{\rm Ks}$ for single stellar populations (SSPs) and constant SFR models with different metallicities ([Z] = -2.17, -0.57, 0.13, 0.43) assuming the canonical IMF (Kroupa 2001). The sharp decrease at $\approx 2\times10^{9}$ yr is due to a pronounced peak in the production rate of AGB stars as explained in Girardi and Bertelli (1998) and Girardi et al. (2013).

Figure 12.5 shows the time evolution of the gwIMF and the Ks-band mass-to-light ratio, $M/L_{\rm Ks}$, assuming constant SFRs and $g_{\rm conv}$ = 0.25, constructed from the canonical IMF and IGIMF framework. The empirical gwIMF is bottom-heavy for metal-rich star-forming galaxies. As the global metallicity of a galaxy increases over time, the present-day $M/L_{\rm Ks}$ also increases with the Ks-band luminosity for constant SFRs as demonstrated in Figure 12.6. This dependency is absent for models assuming $g_{\rm conv}$ = 0.1 and resulting in metal-poor galaxies (following the red curve in Figure 12.3) because the IMF of low-mass stars is no longer sensitive to metallicity when the metallicity is low enough.

The time evolution of the $M/L_{\rm Ks}$ constructed from the canonical IMF assuming constant metallicities and SFRs are presented and discussed in the Appendix F.1.

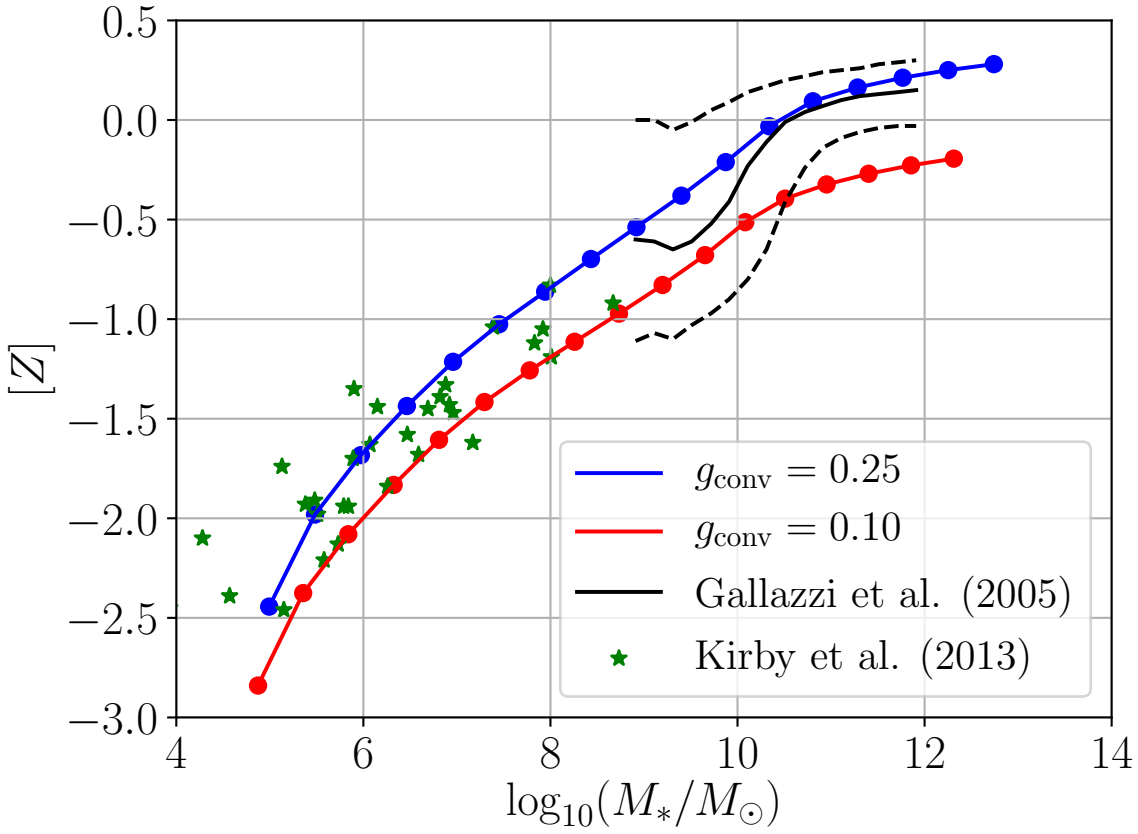

Figure 12.3: Present-day stellar (including remnants) mass–metallicity relation for galaxies with different constant SFRs over a time-span of 13.6 Gyr, adopting $g_{\rm conv} = 0.10$ (red line) and $g_{\rm conv} = 0.25$ (blue line), within the IGIMF-2021 context. The green stars refer to dwarf galaxies of the MW and M31 galaxies (table 4 of Kirby et al. 2013). The solid black line shows the median while the dashed lines the 16th and 84th percentiles of the metallicity distribution of galaxies in the Sloan Digital Sky Survey Data Release 2 (table 1 of Gallazzi et al. 2005). Note that the shown stellar masses of Kirby et al. (2013) and Gallazzi et al. (2005) are derived for the canonical gwIMF but the simulated mass–metallicity relations (red and blue lines) refers to a varying gwIMF within the IGIMF theory (see text).

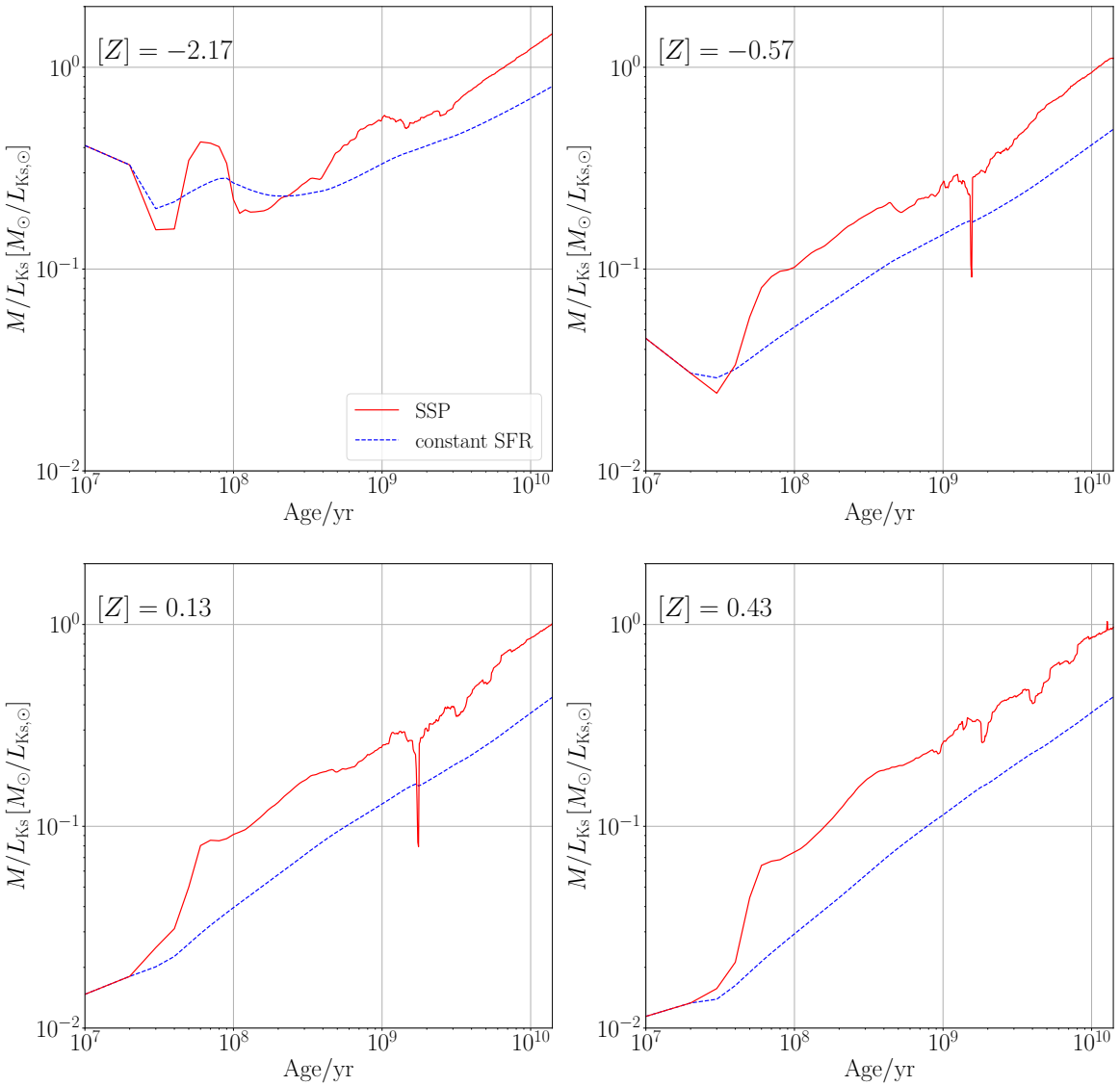

Figure 12.4: Time evolution of the Ks-band mass-to-light ratio, M/L_{Ks}, assuming constant metallicities for single stellar populations (SSP; solid red) and constant SFRs (dashed blue) for a chemical evolution model adopting $g_{\mathrm{conv}} = 0.25$. The sharp drop in the SSP models of M/L_{Ks} at $t \approx 2 \times 10^9$ yr is caused by a significant increase of the number of AGB stars.

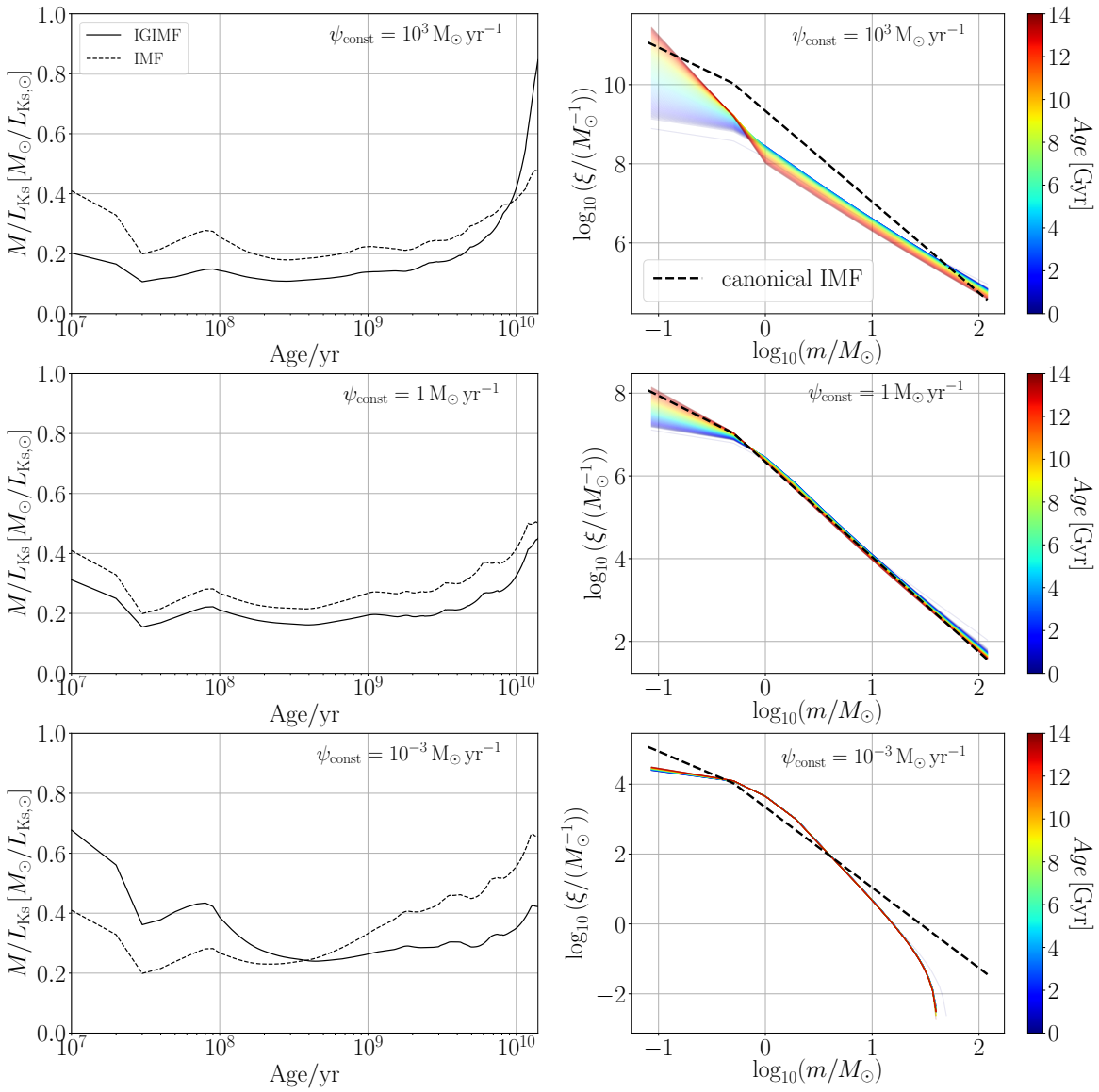

Figure 12.5: Time evolution of the gwIMF (right panels) and the mass-to-light ratio, $M/L_{\rm Ks}$, in the Ks-band (left panels) assuming a constant SFH of $\psi = 10^3\,{\rm M}_\odot\,{\rm yr}^{-1}$ (top panels), $1\,{\rm M}_\odot\,{\rm yr}^{-1}$ (middle panels), and $10^{-3}\,{\rm M}_\odot\,{\rm yr}^{-1}$ (bottom panels) over a timescale of 14 Gyr in the canonical IMF (dashed black lines in the left and right panels) and IGIMF-2021 (solid black line in the left panels and colored lines in the right panels) framework. The chemical evolution model adopts $g_{\rm conv} = 0.25$. The $M/L_{\rm Ks}$ values evaluated at an age of 13.6 Gyr are shown in Figure 12.6.

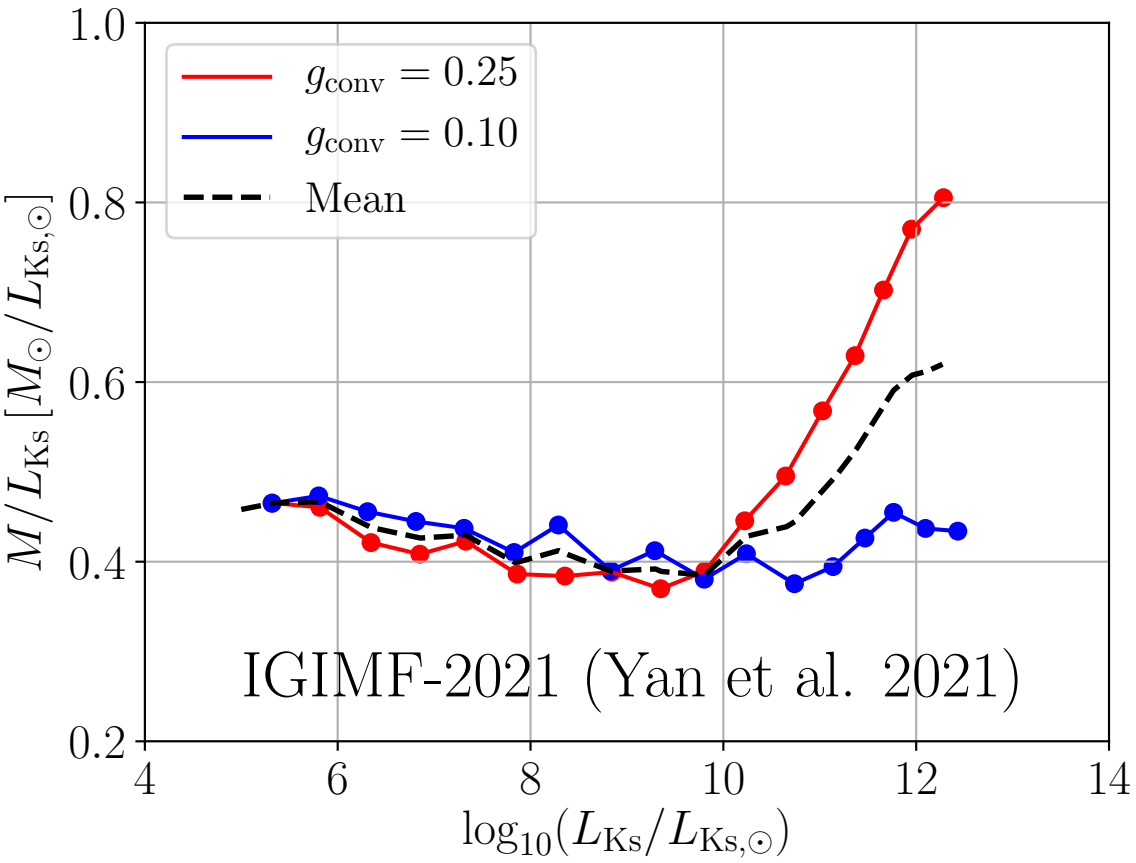

Figure 12.6: Mass-to-light ratio, $M/L_{\rm Ks}$, in the Ks-band in dependence of $L_{\rm Ks}$ for galaxies with an age of 13.6 Gyr assuming $g_{\rm conv}$ = 25% (red line) and 10% in the IGIMF-2021 context. The dashed black line shows the mean $M/L_{\rm Ks}$ of the two different chemical enrichment models (red and blue lines).

12.2.3 The SFR–Hα-luminosity relation

The Kennicutt law (Equation (2) of Kennicutt 1998) empirically relates the SFR and the Hα luminosity of a galaxy via

$$\frac{\psi_{\rm K98}}{\rm M_\odot\,yr^{-1}} = 7.9\times10^{-42}\frac{L({\rm H}\alpha)}{\rm erg\,s^{-1}}\,, \tag{12.15}$$

by assuming a Salpeter IMF (Salpeter 1955) with a power-law index of α = 2.35 in the mass range of 0.1 – 100 $M_\odot$. As the number of ionizing photons depends on the shape of the gwIMF, the Kennicutt-law is only valid for this particular invariant IMF shape (Pflamm-Altenburg, Weidner and Kroupa 2007; Pflamm-Altenburg, Weidner and Kroupa 2009; Jeřábková et al. 2018).

The current version of the photGalIMF has not included the calculation of Hα luminosity but only the three broadband filters mentioned in Section 12.2.2.2. Therefore, we apply a separate stellar population synthesis code to estimate the galactic Hα luminosity. Following Section 4.3 of Jeřábková et al. (2018), we use the second version of the Programme d'Étude des GAlaxies par Synthèse

Évolutive (PÉGASE) stellar population synthesis code (Fioc and Rocca-Volmerange 1999; Fioc, Le Borgne and Rocca-Volmerange 2011) in combination with the PyPegase python wrapper[6] to compute the SFR–Hα-luminosity relation in the IGIMF framework. The code uses the IMF as an input and calculates an average Hα flux from the ionizing photons assuming a constant SFH. However, the code only allows the implementation of a multi-power-law IMF but the gwIMFs constructed have a functional form as shown in Figure 12.1. Therefore, we adopted the same procedure developed in Jeřábková et al. (2018) who approximated the gwIMF as a four-part power law by fitting the power-law indices in the mass ranges of $0.08 - 0.5\,M_\odot$, $0.5 - 1.0\,M_\odot$, $1.0\,M_\odot - m_{\rm max}$, and $m_{\rm max} - 150\,M_\odot$. The code calculates the average Hα flux value for a timescale over 100 Myr as mostly short-lived massive stars contribute to the Hα luminosity.

The SFR–Hα-luminosity relations of the IGIMF-2021 formulation for different metallicities are presented in the left panel of Figure 12.7. In general, galaxies with $L_{\rm H\alpha} \gtrsim 10^{41}$ ergs/s ($L_{\rm H\alpha} \lesssim 10^{41}$ ergs/s) have lower (higher) SFRs compared to the SFRs derived from Kennicutt (1998), consistent with the previous IGIMF-2012 version as discussed in figure 7 of Jeřábková et al. (2018). In order to convert the observed Hα luminosities to SFRs within the IGIMF-2021 context, we provide, in the following, different fitting functions.

The SFR–Hα-luminosity relations for different metallicities are fitted in the range of $-6 < \log_{10}\left(L_{\rm H\alpha}/(10^{41}\,{\rm erg\,s^{-1}})\right) < 4$ with a fifth-order polynomial in the $\log_{10}$-space of the form

$$\log_{10}\left(\frac{\psi_{\rm IGIMF}}{\rm M_\odot\,yr^{-1}}\right) = a_\psi x^5 + b_\psi x^4 + c_\psi x^3 + d_\psi x^2 + e_\psi x + f_\psi\,, \tag{12.16}$$

where $x \equiv \log_{10}\left(L_{\rm H\alpha}/(10^{41}\,{\rm erg\,s^{-1}})\right)$. The conversion factor between the SFRs based on the linear Kennicutt law (Kennicutt 1998) and the IGIMF theory is defined as (Equation (17) of Jeřábková et al. 2018)

$$\Phi(L_{\rm H\alpha}) = \frac{\psi_{\rm IGIMF}}{\psi_{\rm K98}}\,. \tag{12.17}$$

and its $L_{\rm H\alpha}$ dependence is shown in the right panel of Figure 12.7. This relation is also in the range of $-6 < \log_{10}\left(L_{\rm H\alpha}/(10^{41}\,{\rm erg\,s^{-1}})\right) < 4$ fitted with a fifth-order polynomial

$$\log_{10}\left(\Phi(L_{\rm H\alpha})\right) = a_\phi y^5 + b_\phi y^4 + c_\phi y^3 + d_\phi y^2 + e_\phi y + f_\phi\,, \tag{12.18}$$

where $y \equiv \log_{10}\left(L_{\rm H\alpha}/(10^{41}\,{\rm erg\,s^{-1}})\right)$.

Figure 12.8 shows the relation between $\psi_{\rm K98}$ (Kennicutt 1998) and $\psi_{\rm IGIMF}$, which is fitted in the range of $-6 < \log_{10}\left(\psi_{\rm K98}/({\rm M_\odot\,yr^{-1}})\right) < 4$ with a fifth-order polynomial int the $\log_{10}$-space of the form

$$\log_{10}\left(\frac{\psi_{\rm IGIMF}}{\rm M_\odot\,yr^{-1}}\right) = a_\theta z^5 + b_\theta z^4 + c_\theta z^3 + d_\theta z^2 + e_\theta z + f_\theta\,, \tag{12.19}$$

where $z \equiv \log_{10}\left(\psi_{\rm K98}/({\rm M_\odot\,yr^{-1}})\right)$. This correction function is applied to obtain the IGIMF-corrected

[6] https://github.com/coljac/pypegase (downloaded on 03.06.2022)

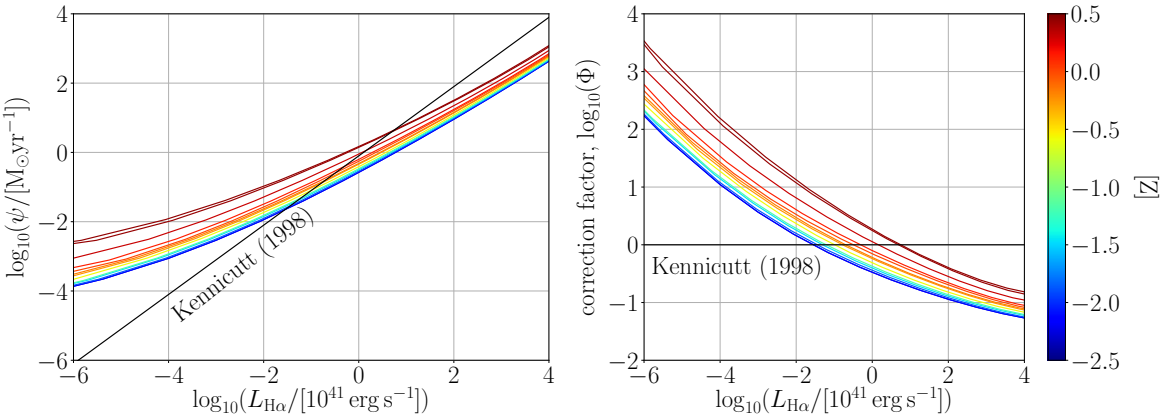

Figure 12.7: Left panel: Star formation rate in dependence of the Hα luminosity assuming a canonical IMF (solid black line; Kennicutt 1998) and the IGIMF-2021 theory (colored lines) for different metallicities calculated with the PÉGASE code (see text). Right panel: Conversion factor of the SFRs, $\Phi = \frac{\psi_{\rm IGIMF}}{\psi_{\rm K98}}$, in dependence of the H$\alpha$ luminosity. The solid black line refers to $\psi_{\rm IGIMF} = \psi_{\rm K98}$. The fitting parameters are listed in Table F.1.

SFRs of the listed SFRs in the Catalogue of Neighbouring galaxies (Section 12.2.4). For example, a galaxy traditionally thought to have $\psi_{\rm K98} = 10^{-5}\,{\rm M}_\odot\,{\rm yr}^{-1}$ would have a real (IGIMF-based) $\psi_{\rm IGIMF} \approx 10^{-3}\,{\rm M}_\odot\,{\rm yr}^{-1}$ for $[Z] \approx -0.5$.

The polynomial coefficients of the fitting functions given by the Equations (12.16), (12.18), and (12.19) are listed for different metallicities in Table F.1.

12.2.4 Observational data

The observational data are taken from the updated version (Karachentsev, Makarov and Kaisina 2013) of the Catalogue of Neighbouring Galaxies[7] (Karachentsev et al. 2004), which lists galaxies with Galactocentric distances of $D < 11\,{\rm Mpc}$ or radial velocities of $V < 600\,{\rm km\,s}^{-1}$. In order to analyse the main sequence of star-forming galaxies (Section 12.3.1) and the stellar mass buildup timescales (Section 12.3.3), we extract the Ks-band luminosity, $L_{\rm Ks}$, and the SFR based on integrated Hα assuming the Kennicutt law, $\psi_{\rm H\alpha}$ (Karachentsev and Kaisina 2013). Galaxies marked with $\psi_{\rm H\alpha}$ limit flags are excluded as only reliable SFR measurements should be included in the analysis. This gives a final sample of 603 galaxies. For calculating the gas depletion timescales (Section 12.3.2), we also select the measurements of the hydrogen mass, $M_{\rm HI}$, which reduces the sample to 544 galaxies. The total neutral gas mass of a galaxy is obtained via

$$M_{\rm gas} = 1.32 M_{\rm HI}\,, \tag{12.20}$$

where the prefactor 1.32 accounts for the amount of He (e.g. Skillman, Côté and B. W. Miller 2003; Pflamm-Altenburg and Kroupa 2009).

[7] https://www.sao.ru/lv/lvgdb/introduction.php. Here, we use the latest update from 12.04.2023.

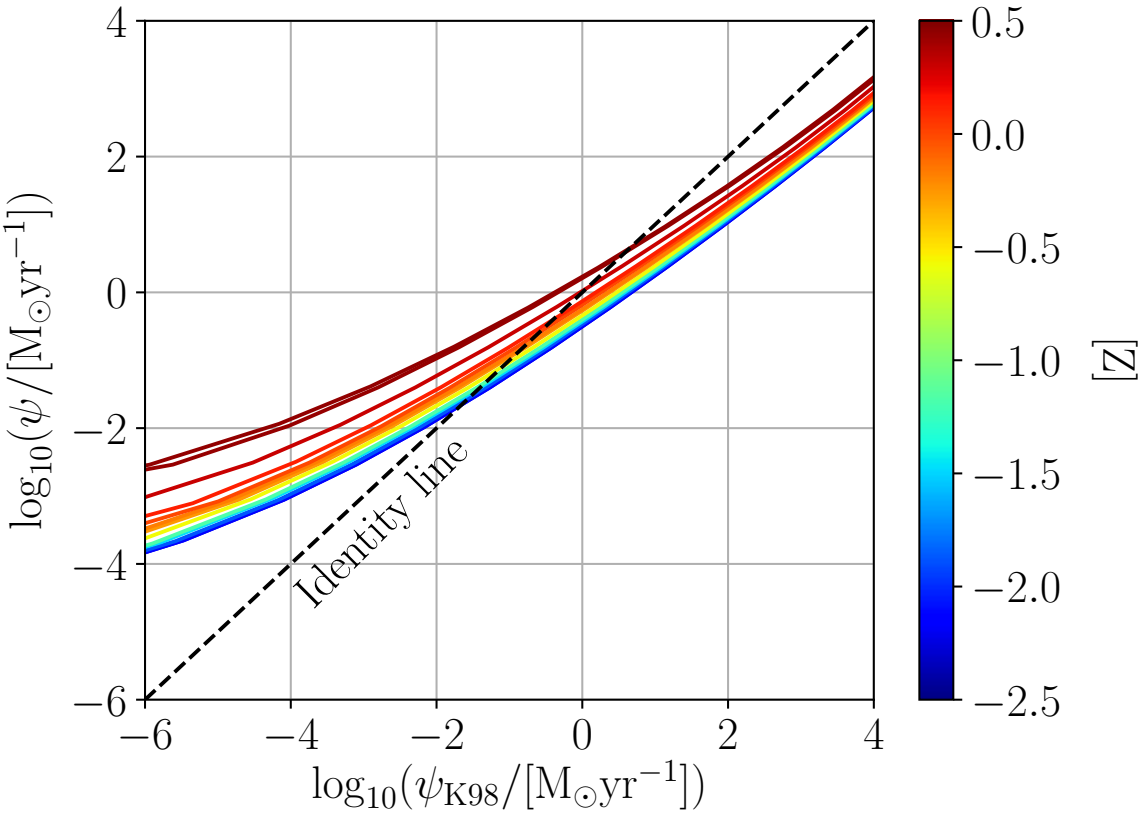

Figure 12.8: Similar to the relations presented in the panels of Figure 12.7 by showing explicitly the relation between ψ_{K98} (Kennicutt 1998) and the SFRs of the IGIMF-2021 formalism for different metallicities (colored lines). The dashed black line shows the identity line. The fitting parameters are listed in Table F.1.

12.2.5 IGIMF corrected observations

The observed Ks-band luminosities listed in the Catalogue of Neighbouring galaxies are converted to stellar masses by applying the present-day M/L_{Ks} shown in Figure 12.6. The M/L_{Ks} nominal-face-value for a given Ks-band luminosity is taken to be the mean value of the chemical enrichment models with $g_{conv} = 0.10$ and $g_{conv} = 0.25$ (Section 12.2.2.1). The upper and lower limit of M/L_{Ks} refer either to the $g_{conv} = 0.10$ or $g_{conv} = 0.25$ model depending on which yields the higher or lower M/L_{Ks} value. The IMF is affected by the metallicity more significantly in the metal-rich regime. As a consequence, the errorbar of M/L_{Ks} increases with higher L_{Ks}. Here, the resulting uncertainty denotes the possible range of M/L_{Ks} for a constant SFH (Section 12.2.2.3) and if g_{conv} is between 0.1 and 0.25. For any specific galaxy with an accurate metallicity measurement, its M/L can be estimated with a smaller uncertainty. In the Sections. 12.3.1 and 12.3.3, we adopt $M/L_{Ks} = 0.6$ for the canonical IMF (McGaugh and Schombert 2014).

The SFRs are IGIMF corrected by using the fitting function defined by Equation (12.19). The metallicities of the observed galaxies have not been estimated in the current version of the Catalogue of Neighbouring galaxies. Therefore, we apply for the nominal-face-value of the corrected SFRs Equation (12.19) for a Solar metallicity (Table F.1). The corresponding errobars are conservatively

estimated by adopting for the lower and upper limits [Z]= −2.20 and [Z]= 0.45, respectively (Figure 12.8).

12.3 Results

In this section, we calculate and compare the stellar-mass–SFR relation, stellar mass buildup timescale, and gas depletion timescale of local star-forming galaxies under two different frameworks, the canonical IMF and IGIMF-2021 (Section 12.2.1) context.

12.3.1 Stellar-mass–SFR relation of star-forming galaxies

The stellar-mass–SFR relation of star-forming galaxies in the local volume assuming the canonical IMF and IGIMF-2021 formulation is presented in Figure 12.9 by plotting the present-day star formation rates in dependence of the stellar masses derived from the Ks-band luminosities.

In the canonical IMF context, star-forming galaxies with $\psi \gtrsim 10^{-3}\,\mathrm{M_\odot\,yr^{-1}}$ and $M_* \lesssim 10^{10}\,M_\odot$ are consistent with a constant SFH over a star-forming timescale of $\approx$ 12 Gyr, while more massive galaxies typically follow the main sequence of galaxies (McGaugh, Schombert and Lelli 2017; Schombert, McGaugh and Lelli 2019; Kroupa et al. 2020; Haslbauer, Kroupa and Jerabkova 2023). That is, Speagle et al. (2014) quantified the main sequence for a given age, t, and found for star-forming galaxies with $10^{9.7} < M_*/M_\odot < 10^{11.1}$ a linear relation of the form (see their Equation (28)),

$$\begin{aligned}\log_{10}\left(\frac{\psi}{\mathrm{M_\odot\,yr^{-1}}}\right) &= (0.84 - 0.026\times t)\times\log_{10}\left(\frac{M_*}{M_\odot}\right), \\ &- (6.51 - 0.11\times t)\end{aligned} \tag{12.21}$$

which reduces, for $t = \tau_\mathrm{h}$, to

$$\log_{10}\left(\frac{\psi}{\mathrm{M_\odot\,yr^{-1}}}\right) = 0.48\,\log_{10}\left(\frac{M_*}{M_\odot}\right) - 4.99\,. \tag{12.22}$$

In the IGIMF-2021 context (right panels), galaxies with $L_\mathrm{Ks} \lesssim 10^9\,\mathrm{L_{Ks,\odot}}$ ($L_\mathrm{Ks} \gtrsim 10^9\,\mathrm{L_{Ks,\odot}}$) have higher (lower) SFRs compared to a canonical IMF as discussed in Figure 12.7. The present-day main sequence of Speagle et al. (2014) is corrected by using Equation (12.19) for $[Z] = 0$. Approximating the resulting main sequence by a linear function over $10^{9.7} < M_*/M_\odot < 10^{11.1}$ yields,

$$\log_{10}\left(\frac{\psi}{\mathrm{M_\odot\,yr^{-1}}}\right) = 0.34\,\log_{10}\left(\frac{M_*}{M_\odot}\right) - 3.70\,. \tag{12.23}$$

which indeed yields a shallower slope than Equation (12.22) (see also figure 1.8 of Kroupa and Jerabkova 2021, and the red solid line in the right panel of Figure 12.9).

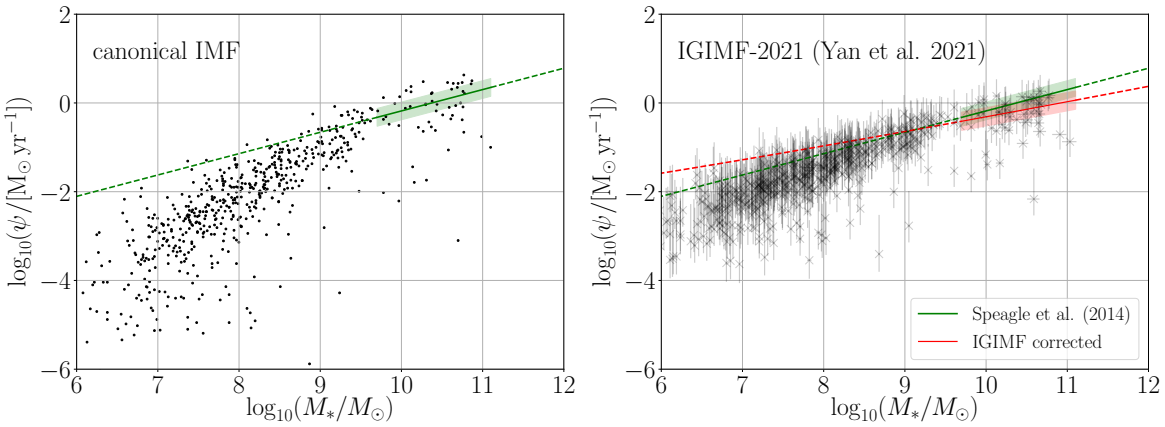

Figure 12.9: Star formation rate in dependence of the stellar mass derived from the Ks-band luminosity of local galaxies in the canonical IMF (left panels) and IGIMF-2021 (right panels) context. The observed SFR values have an estimated uncertainty of about 30% (see figure 1 of Kroupa et al. 2020) due to distance uncertainties (Karachentsev et al. 2004; Karachentsev, Makarov and Kaisina 2013). The errorbars of the IGIMF-corrected stellar mass values refer to the two different applied chemical enrichment models (Section 12.2.2.1) and the errobars of the IGIMF-corrected SFR values refer to metallicities of $[Z] = -2.20$ (lower limit) and $[Z] = 0.45$ (upper limit; see Section 12.2.5 for further details). The solid green lines show the present-day main sequence of star-forming galaxies with $10^{9.7} < M_*/M_\odot < 10^{11.1}$ and a scatter of ±0.2 dex highlighted by the red shaded area (i.e. Equation (28) of Speagle et al. 2014, and Equation (12.22)). The dashed green lines are extrapolations beyond the adopted fitted range of the stellar masses. The solid red lines show the IGIMF-corrected main sequence of star-forming galaxies (green line; Equation (12.23)) of Speagle et al. (2014) by using Equation (12.19) for $[Z] = 0$.

12.3.2 Gas depletion timescale

The present-day gas depletion timescale (c.f. Section 5 of Pflamm-Altenburg and Kroupa 2009) is defined by

$$\tau_{\rm gas} = \frac{M_{\rm gas}}{\psi}, \tag{12.24}$$

such that the inverse is a measure of the SFE of a galaxy. The gas depletion timescales in dependence of the total neutral gas mass for the canonical IMF and IGIMF-2021 for local galaxies are presented in Figure 12.10. In the canonical IMF context, the gas depletion timescale decreases with the gas mass, implying that low-mass galaxies have a lower SFE compared to more massive galaxies. The situation is just the opposite in the IGIMF-2021 context, in which low mass galaxies have a higher SFE than massive galaxies. This is probably due to massive late-type galaxies having stronger feedback associated with the forming stellar population (top-heavy gwIMF; see also Gunawardhana et al. 2011).

Following Pflamm-Altenburg and Kroupa (2009), the relation between the gas depletion timescale and total neutral gas are fitted with a function of the form

$$\tau_{\rm gas}(M_{\rm gas}) = A_{\rm g}\left(\frac{M_{\rm gas}}{M_\odot}\right)^{B_{\rm g}}, \tag{12.25}$$

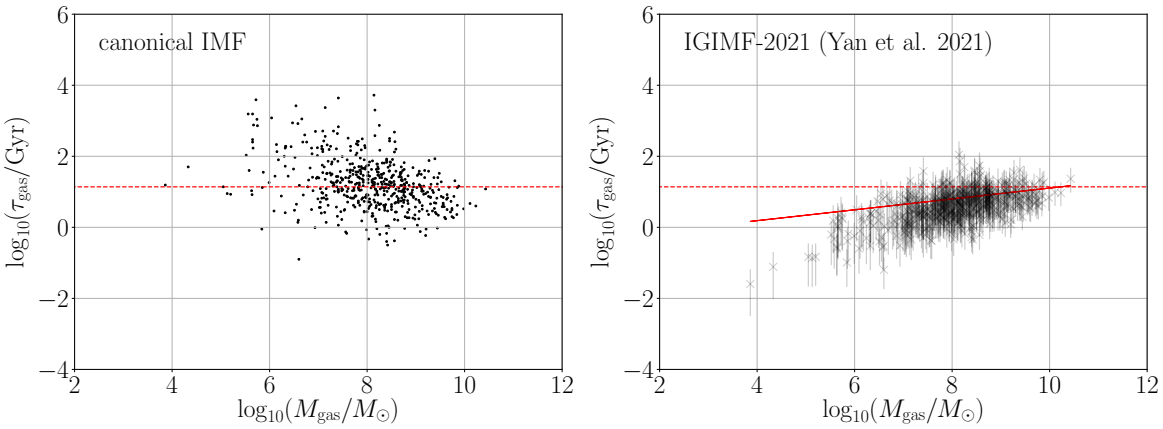

Figure 12.10: Gas depletion timescale in dependence of the gas mass of local galaxies in the canonical IMF (left panel) and IGIMF-2021 (right panel) context. The dashed red line shows the age of the Universe $\tau_{\rm gas} = \tau_{\rm h} = 13.8$ Gyr assuming the standard ΛCDM cosmology (Planck Collaboration XIII 2016). The error on the IGIMF-corrected $\tau_{\rm gas}$ values (right panel) is estimated by adopting the SFR values for $[Z] = -2.20$ (upper limit) and $[Z] = 0.45$ (lower limit). The solid red line is a fit (Equation (12.25)) to the IGIMF-2021 data in linear-space.

with $A_{\rm g} = 0.38$ Gyr and $B_{\rm g} = 0.15$ for the IGIMF-2021 case (solid red line in Figure 12.10) broadly matching the 'minimum-1' model of Pflamm-Altenburg and Kroupa (2009) with $A_{\rm g} = 0.62$ Gyr and $B_{\rm g} = 0.13$ (see their Equation (9) and figure 7) but significantly differs from their 'standard' IGIMF model with $A_{\rm g} = 2.52$ Gyr and $B_{\rm g} = 0.01$ (see their Equation (7) and figure 6) showing therewith only a weak correlation between $\tau_{\rm gas}$ and $M_{\rm gas}$.

Figure 12.11 shows the distributions of the gas depletion timescales fitted with a log-normal function of the form (following Equation (8) of Pflamm-Altenburg and Kroupa 2009)

$$\frac{dN_{\rm gal}}{d\log_{10}(\tau_{\rm gas})} = \frac{1}{\sqrt{2\pi\sigma^2}} \exp\left(\frac{(\log_{10}(\tau_{\rm gas}) - \mu)^2}{2\sigma^2}\right), \tag{12.26}$$

where μ and σ are the mean and standard deviation, respectively, being $\mu = 1.12$ (13.25 Gyr) and $\sigma = 0.60$ Gyr in the case of a canonical IMF and $\mu = 0.67$ (4.72 Gyr) and $\sigma = 0.41$ Gyr for the IGIMF-2021. The mean value but also the scatter of $\tau_{\rm gas}$ become smaller in the IGIMF framework, in agreement with figure 8 of Pflamm-Altenburg and Kroupa (2009).

12.3.3 Stellar-mass buildup times

Assuming that the SFR of a galaxy is constant over cosmic time (see also Kroupa et al. 2020), the stellar mass buildup timescale (Section 6 of Pflamm-Altenburg and Kroupa 2009) is given by

$$\tau_* = \frac{M_*}{\psi}. \tag{12.27}$$

In the canonical IMF context, a substantial number of low-mass galaxies with $M_* \lesssim 10^8\,M_\odot$ has τ_* values much larger than the age of the Universe $\tau_{\rm h} = 13.8$ Gyr while more massive galaxies up to

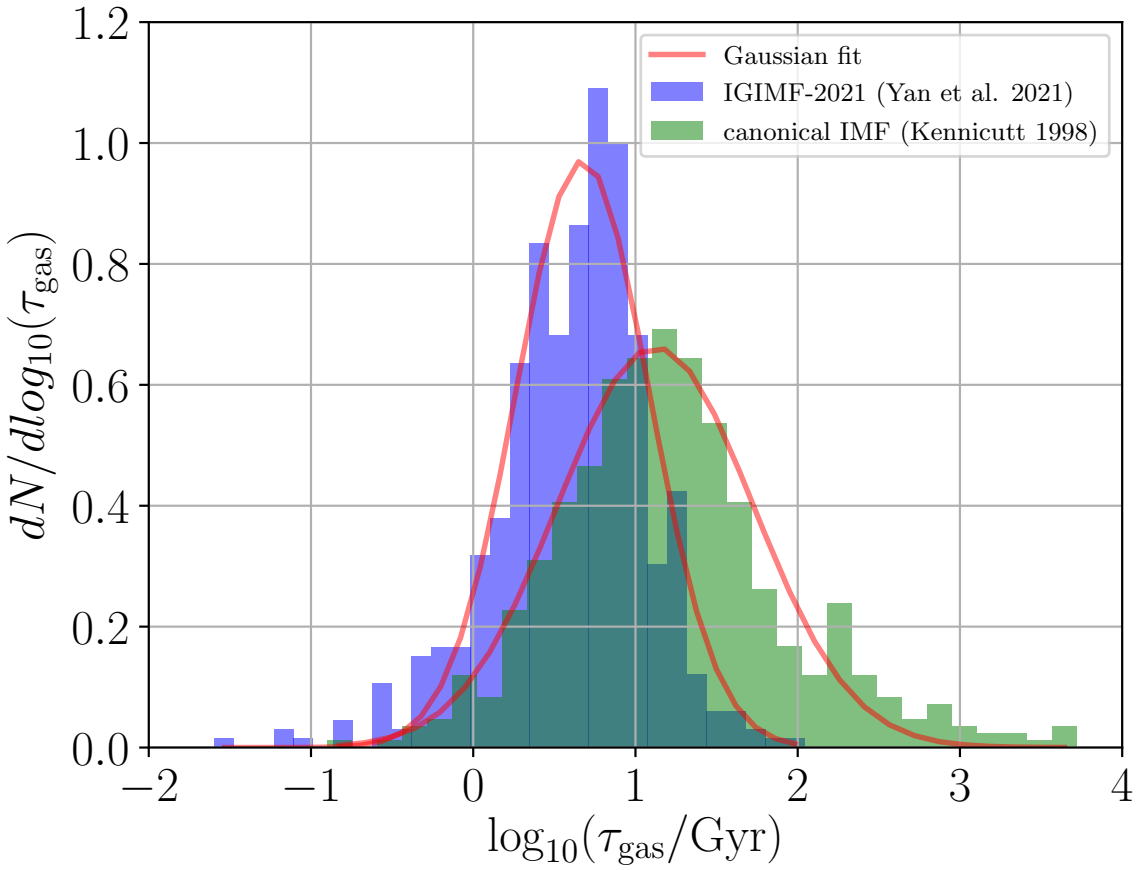

Figure 12.11: Distribution of the gas depletion timescale, $\tau_{\rm gas}$, in the canonical IMF (blue) and IGIMF-2021 (green) context in the $\log_{10}$-space. The $\tau_{\rm gas}$ are calculated by adopting the IGIMF-corrected SFR values for a Solar metallicity. The histograms are fitted with a Gaussian (solid red lines) with expected values of $\mu = \log_{10}(\tau_{\rm gas}/{\rm Gyr}) = 1.12$ (13.25 Gyr; canonical IMF) and $\mu = \log_{10}(\tau_{\rm gas}/{\rm Gyr}) = 0.67$ (4.72 Gyr; IGIMF-2021) and variances of $\sigma = 0.60$ Gyr (canonical IMF) and $\sigma = 0.41$ Gyr (IGIMF-2021).

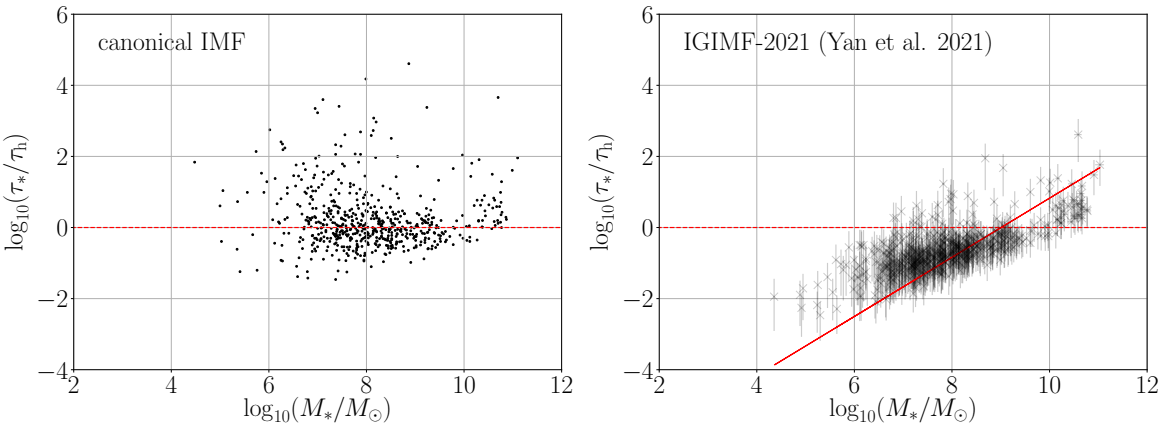

Figure 12.12: Stellar mass buildup timescale normalized by the age of the Universe of $\tau_h = 13.8$ Gyr (Planck Collaboration XIII 2016) in dependence of the stellar mass of local galaxies in the canonical IMF (left panel) and IGIMF-2021 (right panel) context. The dashed red line refers to a stellar mass buildup timescale equal to $\tau_h = 13.8$ Gyr. The upper and lower limits of the IGIMF-corrected τ_* values (right panel) are estimated by adopting $\tau_{up,*} = M_{upper,*}/\psi([Z] = -2.20)$ and $\tau_{low,*} = M_{low,*}/\psi([Z] = 0.45)$, respectively. $\psi([Z] = -2.20)$ and $\psi([Z] = 0.45)$ refer to the IGIMF-corrected SFR values for $[Z] = -2.20$ and $[Z] = 0.45$. $M_{up,*}$ and $M_{low,*}$ refer to the upper and lower IGIMF-corrected stellar masses by applying the maximum and minimum M/L_{Ks} values (Section 12.2.5). The solid (dashed) red line shows the fit of Equation (12.28) to the IGIMF-2021 data in linear-space.

$M_* \approx 10^{10}\,M_\odot$ have $\tau_* \approx \tau_h$. In contrast, the stellar mass buildup timescale increases with stellar mass in the IGIMF-2021 context as shown in Figure 12.12.

Fitting the relation between the stellar-mass buildup timescale normalized by τ_h and the stellar mass with

$$\frac{\tau_*(M_*)}{\tau_h} = A_* \left(\frac{M_*}{M_\odot}\right)^{B_*}, \tag{12.28}$$

yields $A_* = 3.2 \times 10^{-8}$ and $B_* = 0.83$ for the IGIMF-2021 case (solid red line in Figure 12.12). Most of the galaxies with $M_* \lesssim 10^{10}\,M_\odot$ have $\tau_* < \tau_h$ but more massive galaxies have $\tau_* > \tau_h$.

The results are in agreement with the 'minimum-1' IGIMF formulation in Pflamm-Altenburg and Kroupa (2009) as discussed further in Section 12.4.3, and suggest massive late-type galaxies to be older than low-mass disk galaxies. Indeed, with

$$\psi = \dot{M}_* = \psi_0\,, \tag{12.29}$$

where is ψ_0 a constant depending on the present-day M_* and τ_h, it follows that

$$M_* = \psi_0\,(t_b - \tau_h)\,, \tag{12.30}$$

where t_b is the birth time of the galaxy. Thus, from Figure 12.12 we obtain for $M_*(\tau_h) \approx 10^{10}\,M_\odot$ that $t_b \approx \tau_h$, while for $M_*(\tau_h) \approx 10^5\,M_\odot$ obtains $t_b \approx 10^{-2}\tau_h$. Deep observations of dwarfs such as Leo P (Jeřábková et al. 2018, and references therein) and DDO210 (van den Bergh 1959; M. G. Lee

et al. 1999) can verify if such late formation times are indeed correct.

12.4 Discussion

Following Section 4.1 of Jeřábková et al. (2018), we present in Section 12.2.1 a grid of gwIMFs in dependence of the averaged metallicity and global SFR constructed from the IGIMF-2021 formulation (Yan, Jeřábková and Kroupa 2021). The gwIMF systematically varies with metallicity and SFR in such a way that it becomes top-heavy for galaxies with $\psi \gtrsim 1\ \mathrm{M_\odot\,yr^{-1}}$, while being top-light for $\psi \lesssim 1\ \mathrm{M_\odot\,yr^{-1}}$ compared to the canonical IMF (Equation (12.1) with a secondary dependence on the metallicity). The gwIMF becomes bottom-heavy and bottom-light for [Z] > 0 and [Z] < 0, respectively, independent of the SFR. The gwIMF is identical to a canonical IMF when $\psi = 1\,\mathrm{M_\odot\,yr^{-1}}$ and solar metallicity (Section 12.2.1). As demonstrated in Yan et al. (2023 submitted), our modeled gwIMF variation for low-mass stars agrees quantitatively well with the observation of local metal-poor dwarf galaxies with $[Z] \approx -2.5$ (Geha et al. 2013; Gennaro et al. 2018), a metal-rich early-type galaxy (NGC3309, Lonoce, W. L. Freedman and Feldmeier-Krause 2023) with a stellar metallicity up to [Z]=0.15, and a massive lenticular galaxy FCC 167 (Martın-Navarro et al. 2019) with stellar metallicity up to [Z]=0.2. Galaxies with even higher stellar metallicities have not been compared with our model prediction in detail. This does not affect the present study which mainly focuses on dwarf galaxies with sub-Solar metallicity. The gwIMF variation for the most metal-rich galaxies will be discussed in Gjergo et al. (in preparation). The IGIMF-2021 forecasts extreme top-light and bottom-heavy gwIMFs for $[Z] \gtrsim 0.4$ (Appendix F.2) as their parameterizations have not been derived for very metal-rich galaxies. Therefore, these IGIMF formulations should only be applied for objects in the metallicities range of $-2 \lesssim [Z] < 0.4$.

12.4.1 Stellar-mass–SFR relation of star-forming galaxies for a varying IMF

As the Kennicutt-law is invalid for a varying IMF, the stellar-mass–SFR relation and therefore also the main sequence of star-forming galaxies needs to be revised within the current parameterization of the IGIMF framework. We present the SFR–Hα luminosity relation in the IGIMF-2021 formulations for different metallicities using the PÉGASE stellar population synthesis code (Section 12.2.3) and provide fitting functions in order to transform observed Hα luminosities or Kennicutt SFRs to IGIMF SFRs (Appendix F.3).

For example, less luminous Hα galaxies with $L_{\mathrm{H}\alpha} = 5.5 \times 10^{36}\,\mathrm{erg\,s^{-1}}$ (e.g. the dwarf galaxy Leo P; Jeřábková et al. 2018) have SFRs about 15 (for [Z] = -2.20) to 221 (for [Z] = 0.45) times higher than based on the Kennicutt law, while more Hα luminous galaxies with $L_{\mathrm{H}\alpha} = 10^{44}\,\mathrm{erg\,s^{-1}}$ have about 4.4 (for [Z] = -2.20) and 13 (for [Z] = 0.45) times lower SFRs. As a consequence, the IGIMF-corrected present-day main sequence defined for galaxies with $10^{9.7} < M_*/M_\odot < 10^{11.1}$ (Speagle et al. 2014) has a shallower slope (Figure 12.7).

Kroupa and Jerabkova (2021) studied the redshift evolution of the main sequence by only correcting the SFRs based on the IGIMF-2012 formulation and also found a shallower slope and a weaker redshift dependence. Thus, the IGIMF theory has also cosmological implications. Interestingly, several studies found inconsistencies between the observed and stellar mass density and SFR density over cosmic time (e.g. Grazian et al. 2015; A. M. Hopkins and Beacom 2006; A. M. Hopkins and Beacom 2008; Wilkins, Trentham and A. M. Hopkins 2008; Madau and Dickinson 2014; Leja et al. 2015;

Tomczak et al. 2016; Yu and F. Y. Wang 2016). A top-heavy or bottom-light gwIMF could alleviate this discrepancy (Yu and F. Y. Wang 2016). However, such an analysis is beyond the scope of our article, and depends on the interpretation of the Madau and Dickinson (2014) data of SFR density versus redshift z (Haslbauer, Kroupa and Jerabkova 2023).

12.4.2 Gas depletion timescales

Pflamm-Altenburg and Kroupa (2009) applied a revised SFR–Hα luminosity relation on 200 local galaxies for IGIMF versions which assume a canonical IMF and an ECMF with a single power-law index of $\beta = 2.35$ (their 'standard' IGIMF model) and a two-part power law with $\beta = 1.00$ for $5 < m/M_\odot < 50$ and $\beta = 2.00$ for $m/M_\odot > 50$ ('minimum-1' IGIMF model). Their standard model shows a stronger IGIMF effect compared to the 'minimum-1' model by yielding higher SFRs (see their figure 1).

In the canonical IMF case, the gas depletion timescale shows a decreasing trend with increasing gas mass implying that less massive galaxies have a lower SFE (Pflamm-Altenburg and Kroupa 2009). That is, galaxies with $M_{\rm gas} \lesssim 10^9\,M_\odot$ have $\tau_{\rm gas}$ up to 10^4 Gyr while more massive galaxies have $\tau_{\rm gas} < 10^2$ Gyr. In the IGIMF-2021 case, the situation differs as $\tau_{\rm gas}$ slightly increases with gas mass such that low-mass galaxies have a higher SFE. Almost all galaxies have $\tau_{\rm gas} \lesssim 10^2$ Gyr. The scatter of $\tau_{\rm gas}$ is smaller in IGIMF-2021 than for a canonical IMF.

These findings are consistent with the 'minimum-1' IGIMF formalism of Pflamm-Altenburg and Kroupa (2009) while their standard IGIMF yields an almost constant gas depletion timescale over a stellar mass range of $\approx 10^6$ to $10^{10}\,M_\odot$.

The result obtained here of a decreasing SFE with increasing gas (and thus galaxy) mass may suggest that dwarf late-type galaxies form more stars per unit gas mass per unit time because their star-formation process occurs mostly in low-mass embedded clusters that do not have cloud-destroying ionising stars.

12.4.3 Stellar-mass buildup timescales

In contrast to the canonical IMF case, the stellar mass buildup timescale increases with stellar mass in the IGIMF-2021 context. Thus, our findings confirm the results of Pflamm-Altenburg and Kroupa (2009) for a larger sample size of local galaxies.

A caveat of this analysis is that the stellar mass buildup timescale assumes that the SFR is constant over time. Speagle et al. (2014) showed that massive star-forming galaxies with $M_* \gtrsim 10^{10}\,M_\odot$ strictly evolving along the main sequence galaxies can be described by a delayed-tau SFH model with maximum SFRs when the galaxy was 3.5 – 4.5 Gyr old (see their Figs. 9 and 10). Kroupa et al. (2020) reported that most of the galaxies located in the local volume have nearly constant SFRs over a star-formation timescale of 12 Gyr. Re-addressing the analysis for more complex SFHs would be required in upcoming studies.

It would be valuable to implement the IGIMF theory in cosmological simulations. Attempts towards a varying IMF in Newtonian simulations have been made for example by Ploeckinger et al. (2014) and Ploeckinger et al. (2015), who incorporated the IGIMF theory in the FLASH code. This would allows e.g. to revisit downsizing in cosmological self-consistent simulations of structure formation and to address if a top-heavy IMF could indeed explain the JWST observations of very luminous galaxy candidates at (photometric) redshifts $z > 10$ within the standard ΛCDM paradigm (Haslbauer et al.

2022). Implementing the IGIMF theory in the Phantom of Ramses (PoR MOND patch developed by Lüghausen, Famaey and Kroupa 2015, and the corresponding user guide by) enables galaxy evolution in the IGIMF and Milgromian dynamics (MOND, Milgrom 1983c) context.

12.5 Conclusion

The IGIMF theory is a mathematical framework to compute the gwIMF by integrating over all IMFs of star-forming regions (embedded clusters) in a galaxy. The theory was originally formulated by Kroupa and Weidner (2003) and has been continuously updated by including empirical relations for example the variation of the power indices of the IMF and the ECEMF in dependence of the metallicity and global SFR, respectively (e.g. Weidner and Kroupa 2004; Weidner, Kroupa and Larsen 2004; Weidner and Kroupa 2006; Weidner, Kroupa and Bonnell 2010; Yan, Jerabkova and Kroupa 2020; Yan, Jeřábková and Kroupa 2021; Yan, Jerabkova and Kroupa 2023). Thus, the IGIMF theory can be updated by incorporating new observed relations of star formation.

A systematically varying gwIMF has fundamental implications on the global properties of the galaxy as the stellar population is constructed from the IMF. In this contribution, we supplement the studies by Jeřábková et al. (2018) and Pflamm-Altenburg and Kroupa (2009) by applying the IGIMF formulation by Yan, Jeřábková and Kroupa (2021) (hereafter IGIMF-2021) to a sample of galaxies located in the local volume (Karachentsev et al. 2004; Karachentsev, Makarov and Kaisina 2013). Our study extends their studies as Jeřábková et al. (2018) only theoretically investigated the effect of metallicity and SFR on the gwIMF using the IGIMF formulation by Marks et al. (2012). The analysis of Pflamm-Altenburg and Kroupa (2009) applied an older IGIMF-corrected SFR–Hα relation (their Section 2) and did not account the IGIMF effect on the galaxy mass estimation. Thus, we presented here for the first time the evolution of the $M/L_{\rm Ks}$ and the SFR–Hα-luminosity relation in the IGIMF-2021 context assuming constant SFHs.

In order to convert luminosities to stellar masses, we developed the photGalIMF code to calculate the evolution of the mass-to-light ratio in the Ks-band in a self-consistent chemical evolution model (Yan, Jerabkova and Kroupa 2017; Yan et al. 2019) for a systematically varying IMF in the context of the IGIMF theory. The photGalIMF code provides at its current stage the Ks-band of the 2Mass sky survey (M. Cohen, Wheaton and Megeath 2003), the $\rm K_{3.6\mu m}$-band of the Spitzer survey (see e.g. Groenewegen 2006), and the V-band of the UBVRIJHK (Bessell 1990; Maíz Apellániz 2006) photometric system (Appendix F.1). The photGalIMF code version 1.0 is freely available on GitHub. An updated version of the photGalIMF code will include further bands and photometric systems such as the GAIA and JWST photometries but in principle, all photometric systems listed on the CMD web interface[4] could be added to the photGalIMF code.

Following Jeřábková et al. (2018), we calculated the SFR–Hα-luminosity relation for different metallicities using the PÉGASE stellar population synthesis code (Fioc and Rocca-Volmerange 1999; Fioc, Le Borgne and Rocca-Volmerange 2011), based on which we provided new correcting functions for converting the measured Hα luminosity or SFRs derived from the Kennicutt-law (Kennicutt 1998) to SFRs interpreted within the IGIMF-2021 context (Section 12.2.3 and Appendix F.3). In the future, hydrogen line luminosities should be added to the photGalIMF code allowing to calculate the SFR–Hα luminosity relation self-consistently in galaxy evolution simulations for different SFHs and chemical enrichment models.

According to the IGIMF theory, galaxies with $L_{\rm Ks} \gtrsim 10^9\,{\rm L_{Ks,\odot}}$ have lower SFRs, while less

luminous galaxies have higher SFRs than given by the Kennicutt law. Therefore, the main sequence of star-forming galaxies (Speagle et al. 2014) becomes flatter in the IGIMF framework compared to the canonical IMF (Section 12.3.1). As a further consequence, the gas depletion timescale of local star-forming galaxies increases with their total gas mass in the IGIMF context while the gas depletion timescale is typically larger for low massive galaxies for a canonical IMF. Thus, massive galaxies have a lower SFE in the IGIMF context (Section 12.3.2). The stellar mass buildup of local star-forming galaxies increases with their stellar masses if these galaxies have almost constant SFRs over cosmic time (Schombert, McGaugh and Lelli 2019; Kroupa et al. 2020). In the canonical IMF context, the stellar mass buildup would be in disagreement with the age of the Universe (Section 12.3.3 and see also Pflamm-Altenburg and Kroupa 2009).

Deriving physical properties of galaxies such as the stellar masses or SFRs depends on the underlying stellar IMF. Thus, interpreting photometric observations and subsequently testing cosmological and galaxy evolution models requires assumptions about the stellar IMF. The here-presented photGalIMF code enables a more accurate comparison of photometric observations with galaxy evolution and cosmological models.

Data availability

The data underlying this article are available in the article. The Python 3 code GalIMF[5] version 1.1 developed by Yan, Jerabkova and Kroupa (2017) and Yan et al. (2019) with the package photGalIMF[5] version 1.0 (Section 12.2.2) is publicly available on GitHub. The observational data are taken from the updated version of the Catalogue of Neighbouring Galaxies (Karachentsev et al. 2004; Karachentsev, Makarov and Kaisina 2013) and have been IGIMF-corrected as described in Section 12.2.5.

Acknowledgments

MH acknowledges support from the ESO Early-Career Visitor Programme and the SPODYR group at Bonn University for a studentship. The authors thank Alice Concas for helpful discussions.

CHAPTER 13

Outlook & Conclusion

"All life is problem solving."
(Popper 1994)

This doctoral thesis covered many different astrophysical topics ranging from the stellar population of galaxies to the properties and distribution of galaxies on small but also on large scales to test cosmological models. As embedded clusters can be considered as the building blocks of galaxies (Kroupa 2005), the properties of their stellar populations and therewith the stellar IMF are of fundamental importance in order to understand galaxy formation and evolution in a cosmological context as argued in Chapter 6. The combination of both research fields, namely the study of stellar populations and of cosmology, allows to obtain a more holistic picture of the Universe. A current example is the detection of very luminous galaxies (galaxy candidates) at high-(photometric) redshifts detected by the JWST. These observations constrain the stellar mass buildup predicted by cosmological models of galaxy evolution and structure formation but the derived stellar content also depends on the applied form of the stellar IMF (Chapter 9). Thus, the interpretation of these observations in a specific cosmological paradigm must also take into account assumptions on the environmental properties of the underlying IMF.

The scientific results accumulated by this thesis are based on four peer-reviewed first author papers and two manuscripts which have been submitted to peer-reviewed scientific journals. The main scientific research questions have been outlined in Chapter 6 and the main results have been summarized and discussed in Chapters 7-12 and Appendices E- F. Copies of the corresponding four published peer-reviewed papers are attached in Appendices A-D. In the following sections, I will provide a brief summary of the main scientific findings and an outlook for upcoming research projects build on the scientific contributions presented in this thesis as well as a discussion of some open questions of the covered research fields. The chapter finally ends with concluding remarks.

13.1 Cosmology at crossroads – distinguishing between different cosmological models

A main part of the thesis is to test the standard model of cosmology (Chapter 3) on small and large scales by assessing inter alia the state-of-the-art hydrodynamical self-consistent cosmological ΛCDM

simulations of the Illustris, IllustrisTNG (Section 3.2.2), and EAGLE (Section 3.2.3) projects but also the N-body MXXL simulation (Section 3.2.1). The properties of simulated galaxies depend on the implemented sub-grid baryonic physics description and numerical resolution such that we utilized different simulations runs of the Illustris, IllustrisTNG (Section 3.2.2), and EAGLE (Section 3.2.3) projects which rely on different computational codes and baryonic physics descriptions. However, all these simulation runs adopt an invariant canonical stellar IMF (Chabrier 2003) which needs to be taken into account when comparing them with observations (see the discussions in the Sections 6.2 and Sections 13.2) and which is inappropriate (Section 5.2).

Evaluating the functioning of a cosmological framework requires independent tests on different astrophysical scales (Chapter 6). On the one hand side, large-scale distributions of galaxies are much less sensitive or even independent of the applied sub-grid baryonic physics in the simulations reflecting therewith the underlying cosmological and gravitational framework. On the other hand side, observations of the more distant Universe are less precise due to the limited resolution of telescopes or observational projection effects and small scale problems are more sub-grid model-dependent (see e.g. section 5.3.1 of Haslbauer, Banik and Kroupa 2020 and section 8.2 of Banik and Zhao 2022). The local Universe provides instead the most precise and almost model-independent measurements, but the simulated galaxy properties are then again sensitive to the adopted baryonic physics descriptions. For these reasons and to accumulate a more holistic picture of the Universe, it is important to test galaxy evolution and cosmological models on different astrophysical scales as presented in this thesis.

The performed comparisons between the observations and the simulations established a consistent picture according to which dynamical friction (Section 3.3.1) is much less effective on galactic scales (see the Chapters 8 and 10) and structure formation is much more enhanced or started even earlier (see the Chapters 7, 9, and 11) than predicted by the ΛCDM framework as discussed in the following.

13.1.1 Lack of dynamical friction on galactic scales

Observing the effect of dynamical friction on galactic scales might be the *smoking gun* for the existence of cold dark matter haloes surrounding galaxies (Kroupa 2015). This is because dynamical friction acting on the extended dark matter haloes of interacting galaxies causes a deceleration and therewith an orbital decay such that mergers become more frequent in cold dark matter-driven than in non-cold dark matter-based galaxy formation. The here-assessed hydrodynamical ΛCDM simulations self-consistently include dynamical friction, which makes them to a tool for comparing the therein occurring dynamical friction with observations.

In the research projected presented in Chapter 10, we tested the ΛCDM framework in the local Universe by investigating the formation and evolution of the Magellanic Clouds (MCs) - Milky Way (MW) system. The MCs are located at a Galactocentric distance of ≈ 55 kpc with a mutual distance separation of only 24.5 kpc which makes them to a nearby astrophysical laboratory for testing the effect of dynamical friction in their orbits around the MW. The spatial and kinematical configuration of the MW-MCs system suggest that dynamical friction is more efficient in the ΛCDM simulation than observed. We found that the phase-space density of the observed MW-MCs system is significantly higher than expected from the IllustrisTNG simulation runs causing a 3.95σ tension (TNG50-1) which increases to a 4.11σ tension if the DoS (Section 3.3.7) is taken into account. In the ΛCDM framework, the MCs are (dark matter-dominated) primordial dwarf galaxies which have fallen towards the MW at roughly the same time (similar to the interpretation of the formation of the M81 group (M81, M82, and NGC 3077) in the ΛCDM framework; see Oehm, Thies and Kroupa 2017, and Section 3.3.1). In order

to affirm our conclusions, it would be valuable to re-do the presented analysis using other ΛCDM simulations such as the simulation runs of the EAGLE project. In MOND, the MCs could be either primordial dwarfs or tidal dwarf galaxies (Section 3.3.8) formed through a past encounter between the MW and M31 galaxies which would in turn explain also the DoS (Bílek et al. 2021; Banik et al. 2022).

In Haslbauer et al. (2022), we showed that the present-day sky-projected aspect ratio distribution of galaxies formed in the simulation runs of the Illustris, IllustrisTNG, and EAGLE projects disagrees with the local observations at the $\geq 12.56\sigma$ confidence level. These simulations overproduce too roundish galaxies compared to the observations such that the angular momentum problem (Section 3.3.6) still persists in the state-of-the-art hydrodynamical simulations in contrast to the claims of Vogelsberger et al. (2014a). The thickening of the simulated galactic disks is caused by minor and major mergers which are more frequent because of dynamical friction acting on the cold dark matter haloes of interacting galaxies in the ΛCDM framework than in the real Universe. In our analysis, we only studied the galaxy population in the local Universe. Interestingly, first results by the JWST have shown that the fraction of observed disk galaxies is by a factor of ≈ 10 higher than previously observed with HST (figure 4 of Ferreira et al. 2022). Thus, it would be interesting to extend our analysis by comparing the observed morphological galaxy distributions at different redshifts (Delgado-Serrano et al. 2010; Ferreira et al. 2022; Ferreira et al. 2022) with simulations.

The lack of dynamical friction has been also reported in other studies (Angus, Diaferio and Kroupa 2011; Oehm, Thies and Kroupa 2017; Banik et al. 2021; Roshan et al. 2021, and see Section 3.3.1 for a discussion) being therewith consistent with our conclusions reached in the two research projects.

A further test for dynamical friction on galactic scales would be to study the evolution of Hickson compact groups of galaxies (HCGs; Hickson 1982) and their connection with Fossil groups (FGs; Ponman et al. 1994) in ΛCDM simulations. HCGs consist by definition of at least three similar-mass galaxy members which should merge within a few crossing time scales (about ≈ 1 Gyr) due to dynamical friction on the cold dark matter haloes in the ΛCDM model (Kroupa 2015). However, the observed number density of HCGs remains almost constant over the redshift range of $0.01 < z < 0.22$ (Sohn et al. 2015 and see also Sohn et al. 2016) corresponding to a lookback time up to about 2.6 Gyr. Hartsuiker and Ploeckinger (2020) found good agreement between the evolution of the observed and simulated number density evolution of HCGs based on the EAGLE Ref-L0100N1504 run (see their figure 1). The constant number density of HCGs formed in the ΛCDM model could be due to a replenishment effect in which the members of HCGs merge within a few crossing times but new galaxies being continuously accreted forming a new HCG. Therefore, it would be interesting to compare the environments of the observed and simulated HCGs, which could be maybe denser in the ΛCDM simulations. Furthermore, a higher merger rate of simulated HCGs could result in a higher number density of observed FGs, which could be the result of merged HCGs but the true relation between HCGs and FGs is maybe more complex (Farhang et al. 2017). Moreover, Eappen et al. (2022) quantified that the stellar age distributions of observed elliptical galaxies disagree with the ΛCDM simulations.

Small-scale cosmology is sensitive to baryonic physics. Consequently, it is often argued that many small scale challenges of the ΛCDM simulations can be resolved by adopting different sub-grid baryonic physics prescriptions (Weinberg et al. 2015; Bullock and Boylan-Kolchin 2017; Crain and van de Voort 2023). This would suggest that all small scales problems such as the core-cusp problem (Section 3.3.2), missing satellite problem (Section 3.3.3), too big to fail problem (Section 3.3.4), angular momentum problem/morphology of galaxies (Section 3.3.6 and Chapter 8), or the DoS and the MW-MCs system (Section 3.3.7 and Chapter 10) have to be resolved simultaneously by the same

baryonic physics model within the ΛCDM framework. Such a possible solution to the small-scale challenges cannot be excluded but seems to be very unlikely. Moreover, the formation of large-scale structures are less sensitive or even totally independent of the applied sub-grid baryonic physics models such that most of the large-scale challenges (see the following section) persist.

13.1.2 Enhanced structure formation

The distribution of matter in the Universe appears to be much more inhomogeneous on kpc- (e.g. Kroupa, Theis and Boily 2005; Pawlowski, Kroupa and Jerjen 2013; R. A. Ibata et al. 2013; R. A. Ibata et al. 2014; Müller et al. 2018; Pawlowski and Kroupa 2020), Mpc- (e.g. Peebles and Nusser 2010; Karachentsev 2012; Keenan, Barger and Cowie 2013; Karachentsev and Telikova 2018; Haslbauer, Banik and Kroupa 2020), and even up to Gpc- (e.g. Haslbauer, Banik and Kroupa 2020; Haslbauer, Kroupa and Jerabkova 2023) scales than predicted by structure formation of the ΛCDM framework.

On kpc up to a few Mpc scales, the ΛCDM simulations of structure formation suggest that dark matter-dominated satellite galaxies are spheroidally distributed around their host galaxies (Section 3.3.3) but the observed satellites of the Local Group are arranged in thin planes (DoS; Section 3.3.7) around the MW and M31 whereby each of these two planes individually causes a 3.55σ tension with the ΛCDM framework (Banik et al. 2021, and Chapter 10). The combination of both DoS in the Local Group yields therefore a 4.64σ discrepancy between observation and model for two degrees of freedom underpinning that the Local Group environment appears to be more structured (Pawlowski, Kroupa and Jerjen 2013) on $1-2$ Mpc scales. Moreover, DoS are also observed beyond the Local Group (Müller 2023) with the closest hosted around the Centaurus A galaxy (Müller et al. 2018) which is located at a distance of ≈ 3.7 Mpc (Karachentsev and Telikova 2018). The observed DoS around the MW, M31, and Centaurus A yield a 5.27σ tension for three degrees of freedom (Asencio et al. 2022) with the ΛCDM framework.

Signals for an enhanced growth of structure formation become evident in the distribution of galaxies on several Mpc-scales (Section 13.1.2). Peebles and Nusser (2010) showed that the galaxies located in the LV at Galactocentric distances between 1 to 8 Mpc conflicts with the ΛCDM expectations and conclude that "[...] the properties of nearby galaxies that can be observed in greatest detail suggest that a better theory would describe a mechanism by which matter is more rapidly gathered into galaxies and groups of galaxies" (see the abstract of Peebles and Nusser 2010). The LV is embedded in a local underdensity which has a density of about $3-4$ times lower than the cosmic mean density of the global Universe on co-moving radial distances scales of 50 cMpc (Karachentsev 2012; Karachentsev and Telikova 2018) which extends to even much larger scales. Indications for such an immense local underdensity have been already reported in the 1990s (e.g. Maddox et al. 1990; Zucca et al. 1997), whose existence has been confirmed in subsequent studies in the entire electromagnetic spectrum (Maddox et al. 1990; Zucca et al. 1997; Rubart and Schwarz 2013; Rubart, Bacon and Schwarz 2014; Keenan, Barger and Cowie 2013; Böhringer et al. 2015; Böhringer, Chon and Collins 2020). In particular, Keenan, Barger and Cowie (2013) calculated a density contrast which is about two times lower than the cosmic mean density on a scale of 300 cMpc assessing the 2M++ galaxy survey (Lavaux and Hudson 2011). In Haslbauer, Banik and Kroupa (2020), we quantified that this locally observed KBC void disagrees with the ΛCDM framework at the 6.04σ confidence level using the MXXL simulation. This falsification on a 300 cMpc scale further demonstrates that outflows from the KBC void cannot provide an explanation to the Hubble tension within the ΛCDM framework because both the KBC void and Hubble tension (Section 3.3.10) combined result in a 7.09σ disagreement

between observation and the ΛCDM model. If the CMB defines the initial conditions of density fluctuations, Einsteinian/Newtonian gravity is not strong enough to form structures like the local KBC void pointing to enhanced growth of structures. In the second part of Haslbauer, Banik and Kroupa (2020), we showed that the stronger effective gravity provided by MOND does not only form KBC void-like structures but yields in turn also a higher value of the local Hubble constant due to large induced bulk flows resolving therewith the Hubble tension which is considered as one of the biggest problems in modern cosmology. A local void solution to the Hubble tension predicts large matter bulk flows (see figure 8 and the discussion in section 5.3.2 of Haslbauer, Banik and Kroupa 2020) which have been indeed observed (Kashlinsky et al. 2008; Kashlinsky, Atrio-Barandela and Ebeling 2011; Migkas et al. 2020; Migkas et al. 2021; Watkins et al. 2023) on scales up to ≈ 500 cMpc. In particular, Watkins et al. (2023) measured bulk flows of $400\,\mathrm{km\,s^{-1}}$ on scales of $200\,h^{-1}$ Mpc which are in a 4.8σ tension with the ΛCDM paradigm (see also Mazurenko et al. 2023) but qualitatively agree with the peculiar velocity field predicted by the MOND models of Haslbauer, Banik and Kroupa (2020) as demonstrated recently by Mazurenko et al. (2023). Furthermore, H_0 seems to decrease with increasing redshift (e.g. Krishnan et al. 2020; K. C. Wong et al. 2020; Dainotti et al. 2021; Gómez-Valent et al. 2023) based on SNe and time-delays measurements of gravitational lensing systems which is strongly in favour with a local void scenario as a solution to the Hubble tension. Thus, the KBC void is not only evident in the number counts of galaxies but also in the motion of galaxies through a higher value of H_0 and the acceleration parameter $\overline{q}_0$ (i.e. $\overline{q}_0 \equiv -q_0$; see the definition of the deceleration parameter q_0 in Section 3.3.12) indicating a curvature in the Hubble diagram.

The enhanced growth of structure is not only apparent through underdensities but also by observed overdensities. The existence of the El Gordo interacting galaxy clusters at redshift $z = 0.89$ causes a 6.21σ tension with the ΛCDM framework (Asencio, Banik and Kroupa 2021 and see their more recent Asencio, Banik and Kroupa 2023 which confirms their previous conclusions for an updated virial mass estimation of El Gordo).

In Haslbauer, Kroupa and Jerabkova (2023), we showed that the almost constant SFH of local galaxies (Kroupa et al. 2020) is inconsistent with the Lilly-Madau plot according to which the star formation rate density increases from present time up to redshift $z \approx 1.9$ by a factor of ≈ 9. We proposed that the peak of the Lilly-Madau plot at $z \approx 1.9$ could be the imprint of a cGpc-scale overdensity rather than the cosmic noon but more precise measurements of the large-scale matter density field are required in order to underpin or discard this interpretation.

In the very early Universe, we showed in Haslbauer et al. (2022) that the galaxy candidates with stellar masses of $M_* \gtrsim 10^9\,M_\odot$ deduced for an invariant canonical IMF at photometric redshifts of $z_{\mathrm{phot}} \gtrsim 10$ (e.g. Naidu et al. 2022; Naidu et al. 2022; N. J. Adams et al. 2023; Atek et al. 2023; Harikane et al. 2023; Labbé et al. 2023) detected in the early JWST are more massive than expected from the simulation runs of the Illustris, IllustrisTNG, and EAGLE projects. Our findings have been recently confirmed in the much larger simulation run of the MillenniunTNG project (Hernández-Aguayo et al. 2023; Kannan et al. 2023), which will become publicly available in 2024 on their website[1]. A caveat of the analysis presented in the analysis of Haslbauer et al. (2022) is that the redshifts of the objects have to be spectroscopically confirmed but if these galaxies are indeed at such high redshifts, the JWST observations would underpin the above interpretation of a more rapid stellar mass buildup and/or an even older Universe (see also Melia 2023) leaving therewith more time for the growth of galaxies than in the ΛCDM framework. In future, the analysis presented in Haslbauer et al. (2022) has

[1] https://www.mtng-project.org/

to be redone for spectroscopically confirmed high-redshift galaxies. Importantly, the here-assessed ΛCDM simulations adopt only an invariant canonical IMF (Chabrier 2003) but a top-heavy IMF could reduce the derived stellar masses which shows up the importance of considering also the possibility of a varying IMF when interpreting photometric measurements (Sections 6.2 and 13.2). On the other hand, a top-heavy IMF in the simulations of the early Universe would reduce the growth of galaxies such that the tension between observations and the ΛCDM model will persist.

At first glance, our conclusion that the Universe is more inhomogeneous on kpc- up to Gpc-scales than predicted by the ΛCDM framework seems to be in contradiction with the recently emerged σ_8 problem (Section 3.3.11) according to which the Universe appears more homogeneous. However, similar as the Hubble tension and matter bulk flows, the σ_8 problem can be a consequence of the KBC void or an even more extended super void. This is because density fluctuations within an underdensity may be suppressed (Haslbauer, Kroupa and Jerabkova 2023; Kroupa et al. 2023) mimicking locally therewith a more homogeneous Universe, but the effect of a void on the σ_8 value needs to be explicitly demonstrated in structure formation simulations e.g. conducted within the framework of MOND.

Summing up, the enhanced structure formation along with the lack of dynamical friction on galactic scales (Section 13.1.1) compellingly ads to the consistent picture of an observed MONDian rather than a ΛCDM Universe.

13.1.3 Outlook for distinguishing between ΛCDM and MOND

In general, the here-presented but also previous tests of the ΛCDM framework have to be also applied in self-consistent cosmological simulations of different cosmological frameworks. The development of a self-consistent cosmology in the framework of MOND along with the corresponding hydrodynamical simulations of structure formation is a highly non-trivial task mainly because of the non-linearity of Milgrom's law of gravity (Chapter 4) increasing the computational costs. Recently, Wittenburg et al. (2023) published the first cosmological hydrodynamical νHDM simulations with a maximum box size of 600 cMpc per cubic side. Larger νHDM simulations or any other cosmological MOND simulations have to be performed in order to quantify the likelihood of KBC-void-like structures or El Gordo cluster-like objects while high-resolution realizations are required for a comparison between the therein formed morphological galaxy types with observations and investigation of the formation of Local Group-like environments (Section 3.3.7 and Chapter 10).

A problematic aspect of structure formation in the νHDM framework is a lack of power on galactic scales due to the absence of cold dark matter haloes. This lack suppresses the formation of structures in the early Universe conflicting with the observations of protoclusters at $z > 4$ and high-redshift galaxies at $z > 10$ (Section 4.4.6 and see also the discussion in Haslbauer et al. 2022; Wittenburg et al. 2023). However, this does not necessarily imply a failure of MOND but could also suggest a different implementation of MOND in a cosmological framework than proposed in the νHDM model.

Finally, the question for further tests to distinguish between Newtonian and Milgromian dynamics arises beyond those covered in the research projects of this thesis. For example, on kAU scales[2], the wide star binary (WB) test (e.g. Scarpa et al. 2017; Banik and Zhao 2018b; Pittordis and Sutherland 2018; Pittordis and Sutherland 2019; Clarke 2020; Banik, Pittordis and Sutherland 2021; Hernandez, Cookson and Cortés 2022; Hernandez 2023; Pittordis and Sutherland 2023; Chae 2023a; Chae 2023b; Banik et al. 2023) suggest that the circular velocity of binary star systems with a distance separation of

[2] An astronomical Unit (1 AU) corresponds to $\approx 150 \times 10^6$ km

> 2 kAU is increased by about 20 per cent in MOND compared to Newtonian dynamics. In fact, Chae (2023a) reported evidence for such a MOND signal in the Gaia DR3 database which has been recently confirmed by a subsequent study (Chae 2023b). Similar results have been obtained by Hernandez (2023) who found a deviation of the Newton's law at low accelerations. In contrast to these studies, Pittordis and Sutherland (2023) and Banik et al. (2023) argued that Newtonian dynamics is more consistent with the WB test.

On galactic scales, the Dual Dwarf Galaxy theorem (Section 3.3.8) should be re-addressed according to which both dark matter-free/-poor (i.e. TDGs, RPDGs) and dark matter-dominated primordial galaxies (Kroupa 2012; Haslbauer et al. 2019; Haslbauer et al. 2019) have to exist in the ΛCDM framework. Observing flat rotation curves of TDGs would be a strong indication for MOND, while a Keplerian decline of an isolated TDGs (or any other type of an isolated galaxy) would pose a major problem for MOND with at the same time favoring Newtonian dynamics. A challenging aspect of this test is that it requires securely confirmed TDGs which are settled into virial equilibrium. Interestingly, Gentile et al. (2007) studied the rotation curves of three TDGs (Bournaud et al. 2007) and found indeed a better agreement with MOND compared to Newtonian gravity (see their figure 1). A potential TDG candidate for a further test would be the galaxy NGC 5557-E1 with an age of about 4 Gyr (Duc et al. 2014).

13.2 Galaxy-wide IMF in a cosmological context

The other part of this thesis focused on the stellar population of galaxies constructed from the IGIMF theory (Chapter 5). Throughout the projects presented in this thesis, we adopted the formulation by Yan, Jeřábková and Kroupa (2021, hereafter IGIMF-2021) in which the gwIMF depends on the global metallicity and star formation rate of the galaxy as qualitatively shown in Section 5.3. The aim of the corresponding projects (Chapters 9 and 12) is to build a bridge between the gwIMF and cosmology (Section 6.2) in order to allow for more precise comparisons of cosmological and galaxy evolution models with observations.

In the research project presented in Chapter 12, we developed therefore the photometric GalIMF (photGalIMF) package of the GalIMF code by Yan, Jerabkova and Kroupa (2017) and Yan et al. (2019). The photGalIMF code couples the GalIMF code with stellar isochrones of the PARSEC and COLIBRI code which allows for the first time to compute the galaxy chemical luminosity evolution in different photometric bands for varying gwIMFs in the IGIMF context. My collaborators and I will make the photGalIMF code publicly available along with a user guide. The current realization of the photGalIMF (version 1.0) includes only the K_s-band of the 2MASS sky survey (M. Cohen, Wheaton and Megeath 2003), the $K_{3.6\mu m}$-band of the Spitzer survey (see e.g. Groenewegen 2006), and the V-band of the UBVRIJHK photometric system (Bessell 1990; Maíz Apellániz 2006) for ten different metallicities. Future versions of the photGalIMF code will provide a finer gird of metallicities but also other bands of photometric systems such as the GAIA (E)DR3 or JWST NIRCam.

A varying IMF has significant implications for the deduced SFRs of observed galaxies (Chapter 12) because e.g. the traditional Kennicutt law (Kennicutt 1998) is only valid for an invariant canonical IMF. Thus, even SFR tracers need to be re-calibrated for a varying IMF within the IGIMF framework. For example, implementing the Hα narrowband filters (e.g. the filer F658N of the HST/ACS HRC photometric system) to the photGalIMF package would allow to compute the SFR–Hα-luminosity relation for different SFH and chemical evolution models.

The development of the photGalIMF code opens the possibility for several research projects. In Haslbauer et al. (2022), which has been presented in Chapter 9, we made the first estimation of the stellar masses of identified high-redshift galaxy candidates by JWST for a varying gwIMF within the IGIMF context. This analysis calculates the luminosities of galaxies by assuming for simplicity for each a constant metallicity and SFR over cosmic time. The afterwards developed photGalIMF code allows now for a more sophisticated analysis by computing the photometric properties of galaxies for much more complex SFHs and metallicity enrichment models.

In Chapter 12, we studied the effect of a varying IMF only on the present-day main-sequence of star-forming galaxies but the entire evolution of the main-sequence over redshift should be investigated within the IGIMF framework (Kroupa and Jerabkova 2021). In this context, the Lilly-Madau plot also has to be corrected for IGIMF effects (see e.g. Chruślińska et al. 2020) in order to address if the inconsistency between the star formation rate densities and stellar mass densities over the redshift range of $0.5 \lesssim z \lesssim 6$ as reported by Yu and F. Y. Wang (2016) could be alleviated or even resolved for a varying IMF.

As discussed in Section 5.4, McGaugh and Schombert (2015) argued that the small scatter of the BTFR challenges a variation of the IMF. Analyzing the BTFR within the IGIMF framework requires the time evolution of the mass-to-light ratio in 3.6 μm Spitzer photometry which has been already implemented in the photGalIMF version 1.0. The present-day $M/L_{3.6\mu\mathrm{m}}$ ratios in dependence of $L_{3.6\mu\mathrm{m}}$ should be similar to the $\mathrm{K_s}$-band photometry for which the present-day M/L_{Ks} ratios increase within increasing L_{Ks} for constant SFRs as shown in Chapter 12. This could potentially address why a sample of massive spirals ("super spirals") deviate from the BTFR by rotating too fast for their baryonic mass content if an invariant canonical IMF is assumed (Ogle et al. 2019). However, Di Teodoro et al. (2021) argued that this tension is mainly caused because the observations did not cover the flat part of the rotation curve overestimating therewith V_{f} of Equation 5.9 such that only the two galaxies 2MFGC08638 and 2MFGC12344 might deviate from the BTFR. Furthermore, Lelli et al. (2019) reported that the observed slope of the BTFR is slightly lower than expected from MOND (Section 5.4.1). An increasing $M/L_{3.6\mu\mathrm{m}}$ with $L_{3.6\mu\mathrm{m}}$ would make the slope of the BTFR steeper which would potentially make the observed BTFR more consistent with the MOND expectations. Thus, if MOND is the correct gravitational description of galaxies, this would even favor rather than challenge the IGIMF theory. However, this all requires a more-quantitative analysis by correcting the stellar masses of the observed galaxies for different SFH models and chemical enrichment models within the IGIMF framework. If the BTFR is indeed a fundamental scaling relation attributed to MOND (Section 4.3), it can be used to constrain different IGIMF formulations and SFHs as valid solutions have to follow the BTFR.

All these projects demonstrate the importance of considering galaxy evolution in a more holistic picture by combining stellar population with cosmology. Therefore, the IGIMF theory should be implemented in hydrodynamical galaxy-only and cosmological simulations in Newtonian (see the studies by Ploeckinger et al. 2014; Ploeckinger et al. 2015) and in Milgromian dynamics.

13.3 Concluding remarks

Scientific progress is mainly driven by falsifications arising from observations and experiments in so far as shortcomings or failures of a theory can point the direction forward in which sense a correction has to be applied in order to agree with observations. Ideally, the corrected theory provides then

new *a priori* predictions which will be again tested with previous but also new observations enabled for example by advancing technologies. This scientific methodology continuously improves our knowledge of nature (Chapter 1).

The development of cosmological models has a long history (Chapter 2) with significant contributions by the ancient Greeks via the geocentric world view which has been later replaced by the heliocentric model thanks to Nicolaus Copernicus, Johannes Kepler, and Galileo Galilei. The generalization of Isaac Newton's law of gravity by Albert Einstein's General Relativity builds the foundation of the current standard model of cosmology – the ΛCDM paradigm (Chapter 3) which relies on the existence of dark energy and cold dark matter. The ΛCDM model provided over the last decades important contributions, especially in the 1990s and early 2000s by triggering the development of computational and numerical tools to perform large-scale- and high-resolution cosmological simulations. However, several observations on small but also on large scales challenge or even falsify the ΛCDM paradigm at high confidence (Sections 3.3) which has been also found in the research projects conducted within the scope of this doctoral thesis (Chapters 7-11). Consequently, modern cosmology is at crossroads or formulated more drastically: modern cosmology is in crisis.

In conclusion, the main scientific findings of the cosmological tests presented in this thesis disprove the ΛCDM framework over all probed astrophysical scales ranging from the galactic to large-scale structures of the Universe. The tests showed that Chandrasekhar dynamical friction on galactic scales is much less efficient and structure formation is more enhanced in the observed Universe than predicted by the ΛCDM framework. The results of the thesis in combination with other challenges of the ΛCDM model (Section 3.3) point to a consistent picture which disfavors the existence of cold dark matter but suggests a stronger effective gravitational force than provided by Newton's law of gravity. In fact, MOND (Chapter 4), originally proposed by Mordehai Milgrom in 1983, yields indeed a stronger self-gravity at accelerations of $\lesssim 10^{-10}\,\mathrm{m\,s^{-2}}$ without cold dark matter as an additional matter component on galactic scales. Thus, dynamical friction would be next to absent on galactic scales and structure formation more efficient potentially resolving therewith some of the here reported tensions of the ΛCDM framework. However, this has to be explicitly demonstrated in hydrodynamical cosmological MOND simulations which have been recently performed by Wittenburg et al. (2023). Implementing MOND in a full self-consistent cosmological framework still remains a challenge.

Importantly, the interpretation of photometric measurements requires knowledge about the properties of the stellar IMF (Chapter 5). Observations of star forming regions suggest that the stellar IMF systematically depends on the star formation and metallicity disfavoring stochastic star formation processes (Kroupa 2015). A deviation of the canonical IMF has significant implications for the global properties of galaxies such as their star formation rates or mass-to-light ratios as discussed in the projects of this thesis (Chapter 12). Tests of cosmological models have to take into account the possibility of a systematically varying IMF which shows therewith the link between stellar population and cosmology. The here developed photGalIMF code as a package to the GalIMF code (Yan et al. 2019) computes the photometric properties of galaxies for a canonical but also for a varying IMF based on different IGIMF formulations. This opens the possibility for more precise tests and detailed comparisons of different IGIMF formulations and cosmological models with photometric measurements.

Upcoming observations by e.g. the JWST, Gaia, or the currently constructed Extremely Large Telescope (ELT) operated by ESO will constrain and eventually falsify different cosmological models and IGIMF formulations continuously improving therewith our knowledge of nature.

APPENDIX A

Paper: The KBC void and Hubble tension contradict ΛCDM on a Gpc scale – Milgromian dynamics as a possible solution

This chapter includes a copy of the peer-reviewed paper entitled "The KBC void and Hubble tension contradict ΛCDM on a Gpc scale − Milgromian dynamics as a possible solution" published in Monthly Notices of the Royal Astronomical Society, 499, 2845, 2020 by **Moritz Haslbauer**, Indranil Banik, and Pavel Kroupa. A summary and the author contributions are provided in Chapter 7.

Monthly Notices of the ROYAL ASTRONOMICAL SOCIETY

MNRAS **499,** 2845–2883 (2020) doi:10.1093/mnras/staa2348

The KBC void and Hubble tension contradict ΛCDM on a Gpc scale – Milgromian dynamics as a possible solution

Moritz Haslbauer [1,2★] Indranil Banik [1★†] and Pavel Kroupa [1,3]

[1] *Helmholtz-Institut für Strahlen- und Kernphysik, University of Bonn, Nussallee 14-16, D-53115 Bonn, Germany*
[2] *Max-Planck-Institut für Radioastronomie, Auf dem Hügel 69, D-53121 Bonn, Germany*
[3] *Faculty of Mathematics and Physics, Astronomical Institute, Charles University, V Holešovičkách 2, CZ-180 00 Praha 8, Czech Republic*

Accepted 2020 July 31. Received 2020 July 14; in original form 2020 May 8

ABSTRACT

The KBC void is a local underdensity with the observed relative density contrast $\delta \equiv 1 - \rho/\rho_0 = 0.46 \pm 0.06$ between 40 and 300 Mpc around the Local Group. If mass is conserved in the Universe, such a void could explain the 5.3σ Hubble tension. However, the MXXL simulation shows that the KBC void causes 6.04σ tension with standard cosmology (ΛCDM). Combined with the Hubble tension, ΛCDM is ruled out at 7.09σ confidence. Consequently, the density and velocity distribution on Gpc scales suggest a long-range modification to gravity. In this context, we consider a cosmological MOND model supplemented with 11 eV/c^2 sterile neutrinos. We explain why this νHDM model has a nearly standard expansion history, primordial abundances of light elements, and cosmic microwave background (CMB) anisotropies. In MOND, structure growth is self-regulated by external fields from surrounding structures. We constrain our model parameters with the KBC void density profile, the local Hubble and deceleration parameters derived jointly from supernovae at redshifts 0.023−0.15, time delays in strong lensing systems, and the Local Group velocity relative to the CMB. Our best-fitting model simultaneously explains these observables at the 1.14 per cent confidence level (2.53σ tension) if the void is embedded in a time-independent external field of $0.055\,a_0$. Thus, we show for the first time that the KBC void can naturally resolve the Hubble tension in Milgromian dynamics. Given the many successful a priori MOND predictions on galaxy scales that are difficult to reconcile with ΛCDM, Milgromian dynamics supplemented by 11 eV/c^2 sterile neutrinos may provide a more holistic explanation for astronomical observations across all scales.

Key words: gravitation – dark matter – galaxies: abundances – large-scale structure of Universe – cosmology: theory – methods: numerical.

1 INTRODUCTION

The Cosmological Principle (CP) states that the Universe is homogeneous and isotropic on very large scales. This concept is the foundation of the current Lambda-Cold Dark Matter (ΛCDM) standard model of cosmology (Ostriker & Steinhardt 1995), which assumes that Einstein's General Relativity is valid on all astrophysical scales. Applying it to the non-relativistic outskirts of galaxies yields nearly the same result as Newtonian dynamics – the rotation curve should undergo a Keplerian decline beyond the extent of the luminous matter (de Almeida, Piattella & Rodrigues 2016). The observed flat rotation curves of galaxies (e.g. Babcock 1939; Rubin & Ford 1970; Rogstad & Shostak 1972) demonstrate that Newtonian gravity of the baryons alone is insufficient to hold them together, leading to the concept that each galaxy is surrounded by a CDM halo (Ostriker & Peebles 1973). However, no experiment has ever confirmed the existence of CDM, with stringent upper limits coming from e.g. null detection of γ-rays from DM annihilation in dwarf satellites of the Milky Way (MW; Hoof, Geringer-Sameth & Trotta 2020). In addition to the hypothetical ingredient of CDM, the ΛCDM model also requires a cosmological constant Λ in Einstein's gravitational field equations to explain the anomalous faintness of distant Type Ia supernovae (SNe Ia; Riess et al. 1998; Schmidt et al. 1998; The Supernova Cosmology Project 1999). Λ may be associated to a vacuum energy (dark energy).

This 'concordance' flat ΛCDM model explains the cosmic microwave background (CMB) as relic radiation from the Universe at redshift $z \approx 1100$ (e.g. Bennett et al. 2003; Planck Collaboration VI 2020). The temperature fluctuations within the CMB are of the order $\delta T/T \approx \delta\rho/\rho \approx 10^{-5}$ (Wright 2004). These are interpreted as tracers of density contrasts in the baryons alone, with the CDM being significantly more clustered by that time due to it not feeling radiation pressure. After recombination, baryons fell into the potential wells of the DM, starting the process of cosmic structure formation via gravitational instability.

Observations have shown that this widely used ΛCDM model faces several challenges, especially on galactic up to Mpc scales (e.g. Kroupa 2012, 2015, and references therein). One of the most serious problems is the distribution of dwarf galaxies in the Local Group (LG). The MW is surrounded by a thin co-rotating disc of satellite galaxies (Kroupa, Theis & Boily 2005), which is part of the

★ E-mail: mhaslbauer@astro.uni-bonn.de (MH); ibanik@astro.uni-bonn.de (IB)
† Alexander von Humboldt Fellow.

vast polar structure (Pawlowski, Pflamm-Altenburg & Kroupa 2012) that also includes ultrafaint galaxies, globular clusters, and gas and stellar streams. Recently, Pawlowski & Kroupa (2020) showed that its kinematic coherence has increased further with Gaia Data Release 2 (Gaia Collaboration 2018). A thin plane of co-rotating satellites is also observed around M31 (Ibata et al. 2013).

It is very difficult to understand these structures if their member satellites are primordial (Pawlowski et al. 2014). However, such phase space-correlated structures can arise during an interaction between two disc galaxies, as observed e.g. in the Antennae galaxies (Mirabel, Dottori & Lutz 1992). Due to the higher velocity dispersion of the DM, such tidal dwarf galaxies (TDGs) should be free of DM in ΛCDM, as shown with simulations of galaxy interactions (Barnes & Hernquist 1992; Wetzstein, Naab & Burkert 2007) and in cosmological simulations (Ploeckinger et al. 2018; Haslbauer et al. 2019b). This would lead to very low internal velocity dispersions, which are in conflict with observations for satellites of the MW (McGaugh & Wolf 2010) and M31 (McGaugh & Milgrom 2013).

A disc of satellites has also been observed around Centaurus A (Cen A; Müller et al. 2018), suggesting that such structures are ubiquitous and in any case not unique to the LG. Although they may well consist of TDGs, these are quite rare in ΛCDM due to their weak Newtonian self-gravity (Haslbauer et al. 2019a,b). This makes the Cen A satellite plane hard to explain even though we lack internal velocity dispersion measurements for its members (Müller et al. 2018). A review on satellite planes in the local Universe can be found in Pawlowski (2018), who suggested that the TDG hypothesis could work in an alternative gravitational framework where all galaxies are DM-free. We consider this possibility further in Section 1.3. Some evidence in favour of this scenario is the strong correlation between the bulge fractions and the number of satellite galaxies for the MW, M31, M81, Cen A, and M101 (Javanmardi & Kroupa 2020). This is unexpected in standard cosmology (Kroupa 2012, 2015; Javanmardi et al. 2019), but may indicate that bulges and satellite galaxies formed simultaneously in galactic interactions.

Although ΛCDM is widely considered a successful theory in explaining large-scale structure, the observed Universe appears to be much more structured and organized than it predicts. In particular, Peebles & Nusser (2010) reported that standard ΛCDM theory is in conflict with the distribution of galaxies within ≈ 8 Mpc of the LG. The local void contains much fewer galaxies than expected (e.g. Tikhonov & Klypin 2009), while massive galaxies are located away from the matter sheets where they ought to reside. These facts suggest a more rapid growth rate of structure (Peebles & Nusser 2010; though see Xie, Gao & Guo 2014).

Karachentsev (2012) studied the matter distribution of the Local Volume in more detail, finding that the average density of matter within ≈ 50 Mpc is only $\Omega_{\rm m,\,loc} = 0.08 \pm 0.02$, much lower than the global cosmic density at the present time ($\Omega_{\rm m,\,0} = 0.315$, Planck Collaboration VI 2020). This is consistent with a more recent work which obtained $\Omega_{\rm m,\,loc} = 0.09$–$0.14$ within a sphere of radius 40 Mpc around the LG (Karachentsev & Telikova 2018). This is striking because the Harrison–Zeldovich spectrum and the current value of $\sigma_8 = 0.811 \pm 0.006$ (Planck Collaboration VI 2020) predict root-mean-square (rms) density fluctuations of 23 per cent on this scale. Indeed, recent studies have questioned the assumption of homogeneity and isotropy (e.g. Javanmardi et al. 2015; Kroupa 2015; Javanmardi & Kroupa 2017; Bengaly et al. 2018; Colin et al. 2019; Mészáros 2019; Migkas et al. 2020).

Therefore, observations of the galaxy distribution on large scales can constrain various cosmological models and their different underlying gravitational theories. In this study, we investigate the local matter density and velocity field within 1 Gpc in ΛCDM and in a previously developed Milgromian cosmological model (Angus 2009). This allows us to assess the implications for the CP and Hubble tension.

1.1 KBC void

Several observations at different wavelengths have found evidence for a large local underdensity around the LG. The first indication for a deficiency in the galaxy luminosity density was observed in optical samples (e.g. Maddox et al. 1990). Using the ESO Slice Project galaxy survey that covers $\approx 23\,{\rm deg}^2$ on the sky, Zucca et al. (1997) found a local underdensity out to a distance of $\approx 140\,h^{-1}$ Mpc in the $b_{\rm J}$ band, where $h \approx 0.7$ is the present Hubble constant H_0 in units of $100\,{\rm km\,s^{-1}\,Mpc^{-1}}$.

Galaxy counts in the near-infrared (NIR) revealed that the local Universe is significantly underdense on a scale of 200–300 h^{-1} Mpc around the LG (e.g. Huang et al. 1997; Frith et al. 2003; Busswell et al. 2004; Frith, Shanks & Outram 2005; Frith, Metcalfe & Shanks 2006; Keenan, Barger & Cowie 2013; Whitbourn & Shanks 2014). NIR photometry accurately traces the stellar mass and is therefore a good proxy for the underlying matter distribution.

A local underdensity is also evident in the X-ray galaxy cluster surveys REFLEX II (Böhringer et al. 2015) and CLASSIX (Böhringer, Chon & Collins 2020). The latter work found a 15–30 per cent (10–20 per cent) underdensity in the matter distribution within a radius of ≈ 100 Mpc (140 Mpc).

At the opposite end of the spectrum, Rubart & Schwarz (2013) found that the cosmic radio dipole from the NRAO VLA Sky Survey is $\approx 4\times$ stronger than can be explained purely kinematically given the magnitude of the CMB dipole. Interestingly, the radio dipole points towards Galactic coordinates $(245^\circ, +43^\circ)$ which, given the uncertainty of $\approx 30^\circ$, is consistent with the direction in which the LG moves with respect to (wrt.) the CMB ($276^\circ \pm 3^\circ$, $+30^\circ \pm 3^\circ$; Kogut et al. 1993). In a subsequent study, Rubart, Bacon & Schwarz (2014) showed that the unusually strong radio dipole could be explained by a single void with a size of 11 per cent of the Hubble distance and a density contrast of $\delta \equiv 1 - \rho/\rho_0 = 1/3$, where ρ is the local density and ρ_0 is the cosmic mean.

Moreover, Bengaly et al. (2018) studied the dipole anisotropy of galaxy number counts over the redshift range $0.10 < z < 0.35$, revealing a large anisotropy for $z < 0.15$ that could be the imprint of a large local density fluctuation. Thus, a significant local underdensity is evident across the entire electromagnetic spectrum.

Here, we focus on the study by Keenan et al. (2013), who found clear evidence for a large local underdensity by measuring the *K*-band galaxy luminosity function at different distances over a large part of the sky (see their figs 9 and 10). They used the 2M++ catalogue (Lavaux & Hudson 2011), which combines photometry from the Two Micron All Sky Survey Extended Source Catalog (2MASS-XSC) with redshifts from the Sloan Digital Sky Survey (SDSS), the Two Micron Redshift Survey (2MRS), and the Six-degree Field Galaxy Redshift Survey (6DFGRS). This sample covers $37\,080\,{\rm deg}^2$ (90 per cent of the whole sky) and is ≈ 98 per cent complete to a limiting magnitude of $K_{\rm s} = 13.36$. Using this sample, Keenan et al. (2013) estimated the luminosity density and derived a relative density contrast of $\delta \approx 0.5$ in the redshift range $0.0025 < z < 0.067$ compared to larger redshifts (see the pink down-pointing triangle in their fig. 11, and their table 1). In addition, they also probed the density field to a deeper magnitude limit of $K_{\rm s} = 14.36$, but only in the SDSS and 6DFGRS regions. This yielded a slightly smaller density contrast of $\delta = 0.46 \pm 0.06$ between $z = 0.01$ (≈ 40 Mpc)

and $z = 0.07$ (≈ 300 Mpc; see the light blue dot in their fig. 11). In the following, we will show that the Keenan–Barger–Cowie (KBC) void is highly unexpected within the ΛCDM framework by virtue of its sheer size and depth. In order to minimize the tension, we assume for our analysis that $\delta = 0.46 \pm 0.06$ and refer to this as the KBC void. Calculating the *K*-band luminosity density in different regions suggests that it reaches the cosmic mean at a distance of ≈ 500 Mpc.

In the ΛCDM framework, the existence of such a deep and extended void is a puzzle given the expected Harrison–Zeldovich scale-invariant power spectrum, which states that the power $P(L)$ on some length-scale L varies as $P(L) \propto L^{-n_s}$, with $n_s = 1$ (Harrison 1970; Zeldovich 1972). Since the CMB anisotropies require a power of $\sigma_8 = 0.811 \pm 0.006$ on a scale of $8h^{-1}$ Mpc (Planck Collaboration VI 2020), we expect density fluctuations of only ≈ 3.2 per cent between spheres of radius $L = 300$ Mpc.

Combining measurement errors with cosmic variance, we can estimate that the KBC void would falsify the ΛCDM model by well over 5σ because

$$\frac{0.46}{\sqrt{0.06^2 + 0.032^2}} = 6.8\,. \tag{1}$$

In Section 2, we provide a much more sophisticated analysis of how likely the KBC void is in standard cosmology. Since the measurement uncertainty of 6 per cent is much larger than the cosmic variance of 3.2 per cent, the latter is not the main source of uncertainty in how far off ΛCDM is from matching the observations – as explicitly calculated in Section 2.2.1. Consequently, if we assume that ΛCDM is the correct model, the most likely explanation for the detection of such a deep void would be a measurement error. However, the KBC void is evident over the entire electromagnetic spectrum.

The above prediction of 3.2 per cent rests on two fundamental assumptions – that the CMB reflects baryonic density fluctuations at $z = 1100$, and that General Relativity is valid on all scales. The existence of the KBC void might indicate that either or both of these assumptions must be relaxed. In this contribution, we focus on modifying gravity because the standard approach leads to problems in galaxies (e.g. Kroupa 2012, 2015, and references therein).

A large local void should also have implications for local measurements of cosmological parameters such as the Hubble constant and deceleration parameter. If mass is conserved in the Universe and it was nearly homogeneous initially, a large fractional underdensity would show up in the velocity field. This is because the co-moving radius enclosing a fixed amount of mass must exceed its initial value, and changes in co-moving coordinates imply a peculiar velocity.

Suppose that we are living near the centre of a void whose true density relative to the cosmic mean is

$$\frac{\rho}{\rho_0} \equiv \alpha \equiv 1 - \delta\,. \tag{2}$$

This implies that the co-moving radius enclosing a fixed mass must exceed its initial value by a factor $\alpha^{-1/3}$. Depending on details of how the void grows, the impact on the locally measured Hubble parameter would be approximately the same. In other words,

$$\frac{H_0^{\rm local}}{H_0^{\rm global}} \approx \alpha^{-\frac{1}{3}}\,, \tag{3}$$

where $H_0^{\rm local}$ is the locally measured H_0, whose background (true) value is $H_0^{\rm global} \equiv \dot{a}/a$ at the present time, with a the cosmic scale factor and an overdot indicating a time derivative. The mismatch between these H_0 values would create a redshift space distortion (RSD) effect whereby the physical volume of a survey with known redshift range would be reduced by a factor α compared to the case of no void. In this way, RSD would further reduce the observed $\alpha_{\rm obs}$ by a factor α if it is not accounted for and a constant H_0 is used to convert redshifts to distances (as done in the work of Keenan et al. 2013, see their section 4.7). Thus, we expect that

$$\alpha_{\rm obs} = \alpha^2\,. \tag{4}$$

Combining equations (3) and (4), we get that

$$\frac{H_0^{\rm local}}{H_0^{\rm global}} \approx \alpha_{\rm obs}^{-\frac{1}{6}}\,. \tag{5}$$

Given that $\alpha_{\rm obs} = 0.54$, the measured $H_0^{\rm local}$ should exceed the background value $H_0^{\rm global}$ by $0.54^{-1/6}$, i.e. by 11 per cent. This would raise H_0 from the Planck-based prediction of $67.4\,{\rm km\,s^{-1}\,Mpc^{-1}}$ (Planck Collaboration VI 2020) to $74.7\,{\rm km\,s^{-1}\,Mpc^{-1}}$, which is very close to the observed value (Section 1.2). This is unlikely to be a coincidence – it is more parsimoniously explained as a consequence of the observed void under the standard assumption of matter conservation.

1.2 Hubble tension

In this context, we consider the Hubble tension, a statistically significant discrepancy between the locally measured cosmic expansion rate and the ΛCDM prediction based on the early universe properties needed to match the CMB power spectrum (e.g. Riess 2020). The local Hubble constant can be determined through the distance ladder technique. Recently, the Supernova H_0 for the Equation of State (SH0ES) team (Riess et al. 2019) calibrated the distance ladder with eclipsing binaries in the Large Magellanic Cloud, masers in NGC 4258, and parallaxes of Galactic Cepheid variables via the Leavitt law. They derived a local Hubble constant of $H_0^{\rm local} = 74.03 \pm 1.42\,{\rm km\,s^{-1}\,Mpc^{-1}}$, which results in 4.4σ tension with the Planck-based prediction ($H_0^{\rm Planck} = 67.4 \pm 0.5\,{\rm km\,s^{-1}\,Mpc^{-1}}$; Planck Collaboration VI 2020).

The systematic error of the Cepheid background subtraction is only 0.029 ± 0.037 mag, which is not sufficient to explain the ≈ 0.2 mag Hubble tension (Riess et al. 2020). Moreover, calibrating the SN Ia luminosity using instead Mira variables in the galaxy NGC 1559 with periods of 240–400 d and using NGC 4258 (the Large Magellanic Cloud) as an anchor, Huang et al. (2020) obtained $H_0^{\rm local} = 72.7 \pm 4.6\,{\rm km\,s^{-1}\,Mpc^{-1}}$ ($H_0^{\rm local} = 73.9 \pm 4.3\,{\rm km\,s^{-1}\,Mpc^{-1}}$; see also their table 6 and fig. 11). Both values are consistent with $H_0^{\rm local}$ derived from Cepheid variables within the 1σ confidence range, though the Mira-calibrated H_0 is less precise.

It is also possible to go beyond the traditional Cepheid-SN Ia route using Type II SNe as standard candles. These yield a high $H_0^{\rm local}$ of $75.8^{+5.2}_{-4.9}\,{\rm km\,s^{-1}\,Mpc^{-1}}$, which is very consistent with H_0 derived from Type Ia SNe – albeit with larger uncertainties (de Jaeger et al. 2020). Thus, systematic errors in Type Ia SNe data are likely not driving the Hubble tension.

Camarena & Marra (2020a) analysed the Pantheon SNe Ia sample without fixing the deceleration parameter ($q \equiv -a\ddot{a}/\dot{a}^2$) to the present ΛCDM prediction of $q_0 = -0.55$. They jointly derived $H_0^{\rm local} = 75.35 \pm 1.68\,{\rm km\,s^{-1}\,Mpc^{-1}}$ and $q_0 = -1.08 \pm 0.29$ from SNe in the redshift range $0.023 \leq z \leq 0.15$. This is in 4.54σ tension with ΛCDM. The unexpectedly low q_0 is robust to the choice of data set (table 5 of Camarena & Marra 2020b).

Interestingly, it is highly implausible to get such low q_0 values at the background level. Even in a pure dark energy-dominated (de Sitter) universe, it is not possible to get $q_0 < -1$. Thus, first- and second-order effects in the local Hubble diagram seem to provide

additional evidence for the KBC void. To quantify this, we compare the standard expansion rate history ($H_0 = 67.4\,\mathrm{km\,s^{-1}\,Mpc^{-1}}$, $q_0 = -0.55$) with an extrapolation of the Camarena & Marra (2020a) results. Approximating both as quadratic functions of time t with $a(t_0) \equiv 1$ at the present time t_0, we get that the reconstructed $a(t)$ parabolas coincide 4.2 Gyr ago. This provides strong evidence for a Gpc-scale void independently of the galaxy luminosity density (discussed earlier in Section 1.1).

A method of measuring H_0 independently of the cosmic distance ladder relies on time delays between multiple images of the same source, as occurs in strong gravitational lensing. Jee et al. (2019) calibrated the SNe data with angular diameter distances to two gravitational lenses, obtaining $H_0 = 82.4^{+8.4}_{-8.3}\,\mathrm{km\,s^{-1}\,Mpc^{-1}}$ for a flat ΛCDM cosmology. Although the uncertainties are quite large, their H_0 also exceeds the Planck prediction.

Shajib et al. (2020) measured $H_0 = 74.2^{+2.7}_{-3.0}\,\mathrm{km\,s^{-1}\,Mpc^{-1}}$ from the strong lens system DES J0408 − 5354, whose deflector lies at an angular diameter distance of $D_d = 1711^{+376}_{-280}\,\mathrm{Mpc}$ ($z = 0.597$). This is broadly consistent with measurements of the H_0 Lenses in COSMOGRAIL's Wellspring (H0LiCOW; Wong et al. 2020). Using a blinded analysis protocol (see their section 3.6), they obtained $H_0 = 73.3^{+1.7}_{-1.8}\,\mathrm{km\,s^{-1}\,Mpc^{-1}}$ from six lensed quasar systems in the redshift range $z = 0.295-0.745$. Combining their results with the measurement of Riess et al. (2019) leads to a 5.3σ discrepancy with ΛCDM expectations based on the CMB (Wong et al. 2020). The latter work showed for the first time that the Hubble tension exceeds the 5σ threshold typically used to judge the validity of scientific theories.

Although Kochanek (2020) suggested there might be biases in the strong lensing analysis causing ≈ 10 per cent uncertainties on the inferred H_0, Pandey, Raveri & Jain (2019) showed that the SNe and strong lensing measurements are consistent and likely have systematics much smaller than the Hubble tension, as also found by Millon et al. (2020). Indeed, the near-perfect agreement between the SNe and lensing determinations despite the blinded protocol of the latter does suggest rather small uncertainties. Moreover, Wong et al. (2020) found that H_0 measured from strong lensing decreases as a function of lens redshift at a significance of 1.9σ. Their measurements converge towards the Planck prediction for more distant lenses (see their fig. A1). This again strongly suggests that the Hubble tension is indeed driven by a local environmental effect.

Another technique to determine H_0 uses maser-derived distance and velocity measurements, as done by the Megamaser Cosmology Project (Reid et al. 2009). This method is independent of distance ladders, standard candles, and the CMB. It also faces rather different systematics to techniques that rely on gravitational lensing (Pesce et al. 2020). They used measurements for the six maser galaxies UGC 3789, NGC 6264, NGC 6323, NGC 5765b, CGCG 074-064, and NGC 4258. Except for the well-studied case of NGC 4258 (e.g. Reid, Pesce & Riess 2019), these galaxies are located at distances between $51.5^{+4.5}_{-4.0}\,\mathrm{Mpc}$ and $132.1^{+21}_{-17}\,\mathrm{Mpc}$. The resulting $H_0^{\mathrm{local}} = 73.9 \pm 3.0\,\mathrm{km\,s^{-1}\,Mpc^{-1}}$, consistent with Wong et al. (2020) and again larger than predicted by Planck.

So far, we have distinguished between the Planck prediction and H_0 measurements from the local Universe that avoid assumptions about early Universe physics. Baryon acoustic oscillation (BAO) measurements combine the two through a CMB-based prior on the sound horizon at the time of last scattering. The co-moving length of this standard ruler is assumed to remain fixed, allowing its angular size at different epochs to constrain the expansion history (Eisenstein et al. 2005). Such BAO-based H_0 measurements are available from redshift surveys at effective redshifts of $z_{\mathrm{eff}} = 0.38$, 0.51, and 0.61 (Alam et al. 2017), with the range recently extended to $z_{\mathrm{eff}} \approx 1.5$ (Zhang, Huang & Li 2019). These yield a Hubble parameter consistent with the Planck prediction.

The combination of clustering and weak lensing data, BAO, and light element abundances gives $67.4^{+1.1}_{-1.2}\,\mathrm{km\,s^{-1}\,Mpc^{-1}}$ (Dark Energy Survey & South Pole Telescope Collaborations 2018). Estimating H_0 using cosmic chronometers yields a nearly direct measure of the background cosmology. This is also consistent with Planck (Gómez-Valent & Amendola 2018). Assuming spatial flatness of the Universe, Ruan et al. (2019) combined cosmic chronometers with information on H II galaxies to show that the true value of $\dot{a}$ is much closer to the Planck value than the local value of Riess et al. (2016), with the latter discrepant at $\approx 3\sigma$.

Migkas et al. (2020) inferred H_0 from the X-ray luminosity–temperature relation of galaxy clusters, finding that it ranges from 65.20 ± 1.48 to $76.64 \pm 1.41\,\mathrm{km\,s^{-1}\,Mpc^{-1}}$ for different sky regions (see their fig. 23). This range is similar to that between H_0^{global} (Planck Collaboration VI 2020) and H_0^{local} as found using SNe (e.g. Riess et al. 2016, 2019; Camarena & Marra 2020a) or strong lensing systems (Wong et al. 2020). The apparent anisotropy of the local velocity field could potentially be caused by our off-centre location within the KBC void, a non spherical void shape, or a combination of both. However, these considerations are beyond the scope of this work.

Remarkably, all these studies reveal that only the low-redshift probes prefer a high value for the Hubble constant, with high-redshift probes yielding similar results to the Planck-based prediction (see e.g. fig. 12 in Wong et al. 2020, or fig. 1 in Verde, Treu & Riess 2019). Some recent reviews on the Hubble tension can be found in Verde et al. (2019) and Riess (2020). All these results point to the overall picture that the Hubble tension is driven by a local environmental effect like a void. In particular, the KBC void shows up not only in galaxy counts but also in the velocity field as an unexpected first and second time derivative of the apparent scale factor (as evidenced by the reported anomalies in H_0 and q_0, respectively). As discussed in Section 1.1, a large local underdensity can potentially resolve the Hubble tension if mass conservation is assumed. Therefore, this would be a natural resolution to the Hubble tension that would minimize adjustments to the ΛCDM model on cosmological scales. In particular, there would be no need to assume a novel expansion rate history driven by yet more undetected sources such as early dark energy (e.g. Karwal & Kamionkowski 2016; Alexander & McDonough 2019; Poulin et al. 2019; Sakstein & Trodden 2020).[1] Instead, the standard ΛCDM expansion rate history could be preserved. In Section 5.3, we discuss some of the objections to this approach.

The works of Enea (2018) and Shanks et al. (2019) constitute attempts to relate the Hubble tension and KBC void on the basis of mass conservation. In a next step, one has to perform more sophisticated dynamical modelling with reasonable initial conditions provided by the CMB. As we will argue, this is not possible with the standard governing equations of ΛCDM (Section 2.2). In particular, Macpherson, Lasky & Price (2018) explicitly showed that cosmic variance caused by inhomogeneities of the underlying density field cannot resolve the Hubble tension. This is because the expected cosmic variance is too low, implying the Hubble tension and KBC void must both be measurement errors. Given the very different ways in which they are measured, this is highly implausible.

[1] The work of Hill et al. (2020) argues that early dark energy cannot resolve the Hubble tension due to constraints from other data.

Thus, a large void and high $H_0^{\rm local}$ could well point to a different theory where both are explained by enhancing the long-range strength of gravity, which would promote the growth of structure. In principle, any alternative cosmological model that enhances cosmic variance through faster structure formation could explain the KBC void and Hubble tension, in so far as the model faces the Hubble tension. However, it is important for the model to explain phenomena in addition to those for which the model was explicitly designed, and to address observations on galaxy scales. Therefore, we concentrate on detailed dynamical modelling in the framework of an approach known to satisfy galaxy-scale constraints, and to promote the growth of structure on larger scales.

1.3 Milgromian dynamics

Milgrom (1983) originally developed Milgromian dynamics (MOND) to explain the flattening of galactic rotation curves without the need of massive CDM haloes. MOND is a classical potential theory of gravity with a Lagrangian formalism (Bekenstein & Milgrom 1984). It explains the dynamical effects usually attributed to CDM by an acceleration-dependent modification to Newtonian gravity. In particular, the gravity at radius r from an isolated point mass M becomes

$$g = \frac{\sqrt{GMa_0}}{r} \quad \text{for} \quad r \gg r_M \equiv \sqrt{\frac{GM}{a_0}}\,, \tag{6}$$

where G is the Newtonian gravitational constant, and a_0 is Milgrom's constant. Empirically, $a_0 = 1.2 \times 10^{-10}\,\mathrm{m\,s^{-2}}$ to match galaxy rotation curves (e.g. Begeman, Broeils & Sanders 1991; McGaugh 2011).

For a more complicated mass distribution, $\boldsymbol{g}$ follows a non-relativistic field equation (Bekenstein & Milgrom 1984). We use a more computer-friendly version known as quasilinear MOND (QUMOND; Milgrom 2010). In this approach,

$$\nabla^2\Phi \;=\; -\nabla\cdot\left[\nu\left(g_{\rm N}\right)\boldsymbol{g}_{\rm N}\right]\,, \tag{7}$$

where Φ is the gravitational potential, $\boldsymbol{g}_{\rm N}$ is the Newtonian gravitational field, and $r \equiv |\boldsymbol{r}|$ for any vector $\boldsymbol{r}$. The function $\nu\left(g_{\rm N}\right)$ interpolates between the Newtonian ($|\nabla\Phi| \gg a_0$) and deep-MOND ($|\nabla\Phi| \ll a_0$) regimes. Throughout this project, we apply the widely used 'simple' interpolating function (Famaey & Binney 2005):

$$\nu(g_{\rm N}) \;=\; \frac{1}{2} + \sqrt{\frac{1}{4} + \frac{a_0}{g_{\rm N}}}\,. \tag{8}$$

This closely approximates the empirically determined radial acceleration relation (RAR) between $\boldsymbol{g}_{\rm N}$ obtained from photometry and $\boldsymbol{g} \equiv -\nabla\Phi$ obtained from rotation curves (McGaugh 2016; Lelli et al. 2017). Our void models are not much affected by the choice of ν function as they are deep in the MOND regime. This is because any local void solution to the Hubble tension must generate peculiar velocities of $\approx 7\,\mathrm{km\,s^{-1}\,Mpc^{-1}}$ in a Hubble time. For a void with size of 300 Mpc, this implies an acceleration of only $0.04\,a_0$. Since this is $\ll a_0$, we expect MOND to have a significant effect on the void dynamics.

Equation (6) implies the baryonic Tully–Fisher relation (BTFR; McGaugh et al. 2000), namely that

$$M_{\rm b} \propto {v_{\rm f}}^{\xi}\,, \tag{9}$$

where $M_{\rm b}$ is the baryonic mass, $v_{\rm f}$ is the asymptotic rotation velocity of a disc galaxy, and the exponent $\xi = 4$. Empirically, a tight relation of this form is evident with $\xi \approx 3{-}4$ (e.g. McGaugh et al. 2000; McGaugh 2005; Stark, McGaugh & Swaters 2009; McGaugh 2011; Torres-Flores et al. 2011; Ponomareva et al. 2018). The more recent investigations put ξ very close to the MOND-predicted value of 4, which is also what we expect empirically based on the RAR. Since $v_{\rm f}$ can be measured independently of distance but $M_{\rm b}$ depends on the adopted distance, the BTFR provides another independent method to obtain $H_0^{\rm local}$. Recently, Schombert, McGaugh & Lelli (2020) calibrated the BTFR with redshift-independent distance measurements from Cepheids and/or the tip magnitude of the red giant branch for 30 galaxies in the Spitzer Photometry and Accurate Rotation Curves catalogue (SPARC; Lelli, McGaugh & Schombert 2016) and 20 galaxies from Ponomareva et al. (2018). The so-calibrated BTFR was then applied to 95 independent SPARC galaxies for which only the redshift is known. Since the SPARC catalogue contains galaxies up to distances of ≈ 130 Mpc, Schombert et al. (2020) derived H_0 of the very local Universe. They got $H_0^{\rm local} = 75.1 \pm 2.3({\rm stat}) \pm 1.5({\rm sys})\,\mathrm{km\,s^{-1}\,Mpc^{-1}}$ (see also their table 5). This is quite consistent with other measurements from the late Universe and significantly exceeds the ΛCDM prediction based on the CMB (Section 1.2). Interestingly, the dominant source of systematic uncertainty is how to correct redshifts of SPARC galaxies for peculiar velocities induced by large-scale structure. This points towards mis-modelled peculiar velocities as a possible cause for the entire Hubble tension.

According to equation (7), MOND is non-linear in the acceleration, which yields the interesting concept of the external field effect (EFE; Milgrom 1986). In contrast to Newtonian gravity, the non-linearity of Milgrom's law causes the internal gravitational forces within a MONDian subsystem to be affected by the external gravitational field from its environment *even without any tides*. This breaks the strong equivalence principle. The EFE has likely been observed in the declining rotation curves of some disc galaxies (Haghi et al. 2016) and the internal dynamics of dwarfs. For example, Crater II is a diffuse dwarf satellite galaxy of the MW at a distance of ≈ 120 kpc (Torrealba et al. 2016). Its observed velocity dispersion of $2.7 \pm 0.3\,\mathrm{km\,s^{-1}}$ (Caldwell et al. 2017) is below the isolated MOND prediction of $4\,\mathrm{km\,s^{-1}}$ (McGaugh 2016). Taking into account the Galactic EFE reduces the MOND prediction to $2.1^{+0.9}_{-0.6}\,\mathrm{km\,s^{-1}}$, matching the observed value within uncertainties. Similar examples are the ultradiffuse dwarf galaxies Dragonfly 2 (DF2) and DF4, where the MOND predictions agree with observations only if the EFE is included (Kroupa et al. 2018; Haghi et al. 2019a). For the more isolated galaxy DF44, the MOND prediction without the EFE is consistent with observations (Bílek, Müller & Famaey 2019; Haghi et al. 2019b).

The EFE is also important within the MW, whose MONDian escape velocity curve is similar to observations (Banik & Zhao 2018a). Since equation (6) yields a logarithmically divergent potential, escape from an isolated object is not possible in MOND unless the EFE is taken into account. Recently, Pittordis & Sutherland (2019) showed that MOND without an EFE is completely ruled out by the observed relative velocity distribution of wide binary stars in the Solar neighbourhood at separations of ≈10 kAU. Including the EFE leads to nearly Newtonian behaviour, though the predicted 20 per cent difference is likely detectable in a more thorough analysis (Banik & Zhao 2018c) that must include contamination by undetected close companions (Clarke 2020).

In addition to its successes with internal dynamics of galaxies (reviewed in Famaey & McGaugh 2012), MOND may also explain the discs of satellites around the MW and M31 as TDGs born out of a past MW-M31 flyby. A previous close interaction is required in MOND (Zhao et al. 2013) due to the almost radial MW-M31 orbit (van der Marel et al. 2012, 2019). In such an interaction, structures

resembling satellite planes can be formed (Bílek et al. 2018). Using restricted *N*-body models to explore a wide range of flyby geometries, Banik, O'Ryan & Zhao (2018) identified models where the tidal debris around the MW and M31 align with their observed satellite planes and have a similar radial extent. A past MW-M31 interaction would naturally explain the apparent correlation between their satellite planes, and with other structures in the LG (Pawlowski & McGaugh 2014). It may also account for the anomalous kinematics of the NGC 3109 association, which is difficult to understand in ΛCDM (Peebles 2017; Banik & Zhao 2018b).

Interestingly, there is an order of magnitude coincidence between the value of a_0 and the cosmic acceleration rate:

$$2\pi a_0 \approx cH_0 \approx c^2\sqrt{\Lambda/3}, \tag{10}$$

where c is the speed of light (Milgrom 1983). This may indicate that MOND is related to a fundamental theory of quantum gravity (e.g. Milgrom 1999; Pazy 2013; Smolin 2017; Verlinde 2017). A bigger clue would come from tighter empirical constraints on the time evolution of a_0, which at present are still weak (Milgrom 2017). Even so, his work showed that current data are sufficient to rule out the $a^{-3/2}$ scaling required by the model of Zhao (2008), which additionally would have a very significant impact on the CMB (Sections 3.1.3 and 5.2.3).

Another intriguing coincidence is that the total matter density is very nearly 2π times the baryonic density, i.e. $\Omega_{\rm m} \approx 2\pi\,\Omega_{\rm b}$ (Milgrom 2020b). This could imply that the effective gravitational constant in a MONDian Friedmann equation is a factor of 2π larger than for a system decoupled from the cosmic expansion. However, we will not follow this interpretation here.

The first relativistic version of MOND was developed by Bekenstein (2004). This was modified slightly by Skordis & Złośnik (2019) so that gravitational waves propagate at the speed of light, as required for consistency with the near-simultaneous detection of gravitational waves and their electromagnetic counterpart (Virgo & LIGO Collaborations 2017). The theory of Skordis & Złośnik (2019) allows solutions where the background cosmology follows the standard Friedmann equations to high precision (see their section 4). We discuss this further in Section 3.1, where we explain why the expansion rate history and the power spectrum of the CMB should be nearly the same as in ΛCDM. Thus, MOND would suffer from the Hubble tension in just the same way as ΛCDM if $H_0^{\rm local} = \dot{a}$ at the sub-per cent level.

Fortunately, this might not be the case − Sanders (1998) showed that due to the long-range modification to gravity, MOND produces much larger and deeper voids than predicted by ΛCDM cosmology. Thus, MOND could be a promising framework to explain both the KBC void and the Hubble tension. We therefore extrapolate Milgrom's law of gravity from sub-kpc to Gpc scales. For the first time, we study the Hubble tension and KBC void in the context of MOND. We emphasize that MOND was originally designed to address discrepancies on galactic scales (Milgrom 1983), so no new assumptions are made specifically to address the latest data on the low-z distance–redshift relation and galaxy counts − apart from the usual assumption that the background follows a standard evolution to high precision (Section 3.1.1), and that MOND applies only to density deviations from the cosmic mean (e.g. Llinares, Knebe & Zhao 2008; Angus & Diaferio 2011; Angus et al. 2013; Katz et al. 2013; Candlish 2016). In this context, we aim to provide a unified explanation for both the dynamical discrepancies on galaxy scales and the $z \lesssim 0.2$ matter density and velocity field given current constraints from the CMB.

The layout of this paper is as follows: In Section 2, we quantify the likelihood of the observed KBC void and how it might relate to the Hubble tension in a ΛCDM context. After introducing a cosmological MOND model in Section 3, we compare it to observations of the local Universe (Section 4). The implications for ΛCDM and MOND cosmologies are discussed in Section 5. We finally conclude in Section 6. Throughout this article, co-moving distances are marked with the prefix 'c' (e.g. cMpc, cGpc).

2 ΛCDM FRAMEWORK

In this section, we describe how we use a cosmological ΛCDM simulation to quantify cosmic variance and thereby determine the likelihood of finding ourselves inside the observed KBC void in standard cosmology. We also consider the implications of our results when combined with the Hubble tension.

2.1 Cosmic variance in the Millennium XXL simulation

Millennium XXL (MXXL; Angulo et al. 2012) is a standard ΛCDM cosmological simulation that evolves 6720^3 DM particles from $z = 63$ forwards to $z = 0$. Though it only considers DM, baryonic physics should have a negligible role on the 300 Mpc scale we consider. The simulation box has a length of $3h^{-1}$ cGpc, resulting in a volume that is 216× larger than that of the Millennium simulation (Springel et al. 2005). The mass of a particle is $8.456 \times 10^9\,{\rm M}_\odot$ and its Plummer-equivalent softening length is 13.7 kpc. The MXXL simulation assumes a flat ΛCDM cosmology consistent with WMAP-7 results, i.e. the present matter density parameter is $\Omega_{\rm m,\,0} = 0.25$, that of dark energy is $\Omega_{\Lambda,\,0} = 0.75$, $\sigma_8 = 0.9$, $H_0 = 73\,{\rm km\,s^{-1}\,Mpc^{-1}}$, and the power spectrum is assumed to be of the Harrison–Zeldovich form ($n_{\rm s} = 1$). The baryonic mass of each subhalo is obtained by applying the semi-analytic galaxy formation code L-GALAXIES (Springel et al. 2005) to the MXXL data (see also section 2.2 in Angulo et al. 2014).

We use MXXL to calculate the relative density contrast given by the stellar mass distribution in subhaloes with stellar mass $M_* > 10^{10}\,h^{-1}\,{\rm M}_\odot$ at $z = 0$. For this purpose, we consider 10^6 vantage points distributed on a Cartesian grid with a spacing of $30\,h^{-1}$ Mpc in each direction. To maximize the accuracy of our results, we use the nearest subhalo as our final choice for the vantage point. Our adopted minimum mass avoids an excessive computational cost but still leaves enough subhaloes to accurately determine the expected cosmic variance. Using only stellar masses makes our results more comparable to observations in the NIR.

We need to allow for the incomplete sky coverage of Keenan et al. (2013). Following their section 2.5, we adopt a sky area of $37\,080\,{\rm deg}^2$, which in dimensionless units is

$$A = 37080 \times \left(\frac{\pi}{180}\right)^2. \tag{11}$$

We assume the incompleteness is caused by observational difficulties at low Galactic latitudes. Thus, we define a mock Galactic spin axis by randomly generating a unit vector $\widehat{\boldsymbol{n}}_i$ drawn from an isotropic distribution. We can then define an angle θ_j based on the direction towards another subhalo at position $\boldsymbol{r}_j$ relative to our vantage point.

$$\cos\theta_j \equiv \frac{\boldsymbol{r}_j \cdot \widehat{\boldsymbol{n}}_i}{r_j}. \tag{12}$$

The subscript i refers to the vantage point, while j refers to another subhalo observed from there. We mimic incomplete sky coverage by requiring that

$$|\cos\theta_j| > \cos\theta_{\rm obs}, \quad \text{where} \tag{13}$$

$$\cos\theta_{\rm obs} = 1 - \frac{A}{4\pi}\,. \tag{14}$$

Since most of the sky is surveyed, $\cos\theta_{\rm obs} = 0.10$.

The observed density contrast is calculated for galaxies in the redshift range $0.01 < z < 0.07$ (table 1 in Keenan et al. 2013). Therefore, we further require selected subhaloes to satisfy

$$r_{\rm min} < r_j < r_{\rm max}\,, \tag{15}$$

where $r_{\rm min} = 40\,{\rm Mpc}$ and $r_{\rm max} = 300\,{\rm Mpc}$. The relative density contrast around vantage point i is then

$$\delta_i \equiv 1 - \frac{\sum_j M_j}{V\rho_0}\,, \quad \text{with} \tag{16}$$

$$V = \frac{4\pi}{3}\left(1-\cos\theta_{\rm obs}\right)\left(r_{\rm max}^3 - r_{\rm min}^3\right)\,. \tag{17}$$

The sum is taken over all subhaloes with $M_* > 10^{10}\,h^{-1}\,{\rm M}_\odot$ that satisfy equations (13) and (15). These conditions restrict us to a volume V. The cosmic mean density ρ_0 is found by relaxing the position-related conditions and dividing the much larger sum by the whole simulation volume.

2.2 Comparison with observations

We now compare our so-obtained list of δ_i with the observed local matter distribution. By combining our results with prior analytic work in ΛCDM, we also assess the implications for the Hubble tension and conduct a joint analysis.

2.2.1 KBC void

As discussed in Section 1.1, Keenan et al. (2013) discovered a large local underdensity with an apparent density contrast of $\delta_{\rm obs} = 0.46 \pm 0.06$ around the LG assuming a fixed distance–redshift relation with $H_0 = 70\,{\rm km\,s^{-1}\,Mpc^{-1}}$ (see their section 4.7). To compare their reported $\delta_{\rm obs}$ with ΛCDM expectations, we need to account for the fact that any underdensity δ would also affect the local Hubble parameter by

$$\frac{\Delta H}{H} \equiv f\delta\,, \tag{18}$$

where e.g. Marra et al. (2013) showed that for $\delta \ll 1$ in ΛCDM,

$$f = \frac{\Omega_{\rm m}^{0.6}}{3b}\,, \tag{19}$$

with the bias factor $b = 1$ (see also Section 5.3.1). As a result, the volume within a fixed redshift would be reduced below that assumed in Keenan et al. (2013) by a fraction

$$\frac{\Delta V}{V} = -3f\delta\,. \tag{20}$$

The apparent underdensity $\tilde{\delta}_i$ uncorrected for RSD would then be

$$1 - \tilde{\delta}_i = \frac{1-\delta_i}{1-3f\delta_i}\,. \tag{21}$$

For the small underdensities expected in ΛCDM (see next), this approximately implies

$$\tilde{\delta}_i = \delta_i\,(1+3f)\,. \tag{22}$$

In other words, the apparent (RSD-uncorrected) underdensity would be 1.5× larger than the actual value.

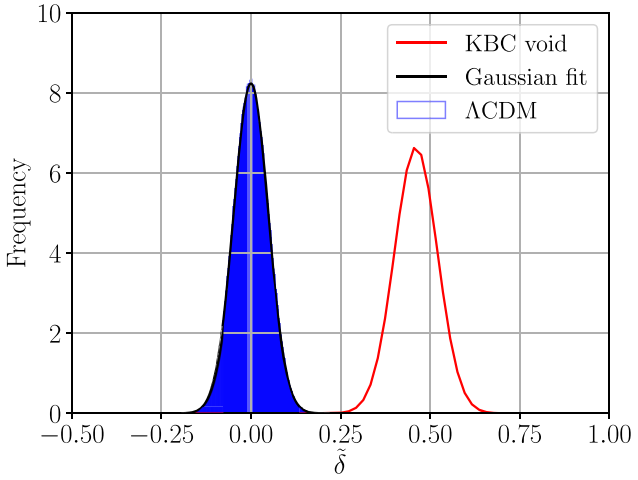

Figure 1. Distribution of the apparent relative density contrast $\tilde{\delta}$ (equation 22) of spheres with a 300 Mpc radius less an inner 40 Mpc hole in the ΛCDM MXXL simulation, calculated at redshift $z = 0$ (Section 2.1). The red solid curve shows the observed density contrast of $\delta_{\rm obs} = 0.46 \pm 0.06$ with Gaussian errors (see also fig. 11 and table 1 in Keenan et al. 2013). The $\tilde{\delta}$ values closely follow a Gaussian distribution with a dispersion of $\sigma_{\Lambda{\rm CDM}} = 0.048$ (the black curve). A more detailed Gaussianity test is performed in Appendix A. Both curves are normalized to the same area.

Fig. 1 shows the distribution of $\tilde{\delta}_i$ in the standard ΛCDM MXXL simulation. This yields true rms density fluctuations of 3.2 per cent, so observations uncorrected for RSD should exhibit fluctuations of 4.8 per cent. To a very good approximation, these should be normally distributed, as demonstrated in Appendix A. Since $46/\sqrt{6^2+4.8^2} \approx 6.0$, we expect the discrepancy to be at the $\approx 6\sigma$ level.

Comparing the density contrast predicted by standard cosmology with the observed KBC void reveals a very significant discrepancy (Fig. 1). This is usually quantified by finding the likelihood P of observing a more severe discrepancy, which we find for each vantage point and then average:

$$P = \frac{1}{N}\sum_{i=1}^{N} f_{\chi\mapsto P}\left(\left|\frac{\tilde{\delta}_i - \delta_{\rm obs}}{\sigma_{\rm obs}}\right|\right)\,, \quad \text{with} \tag{23}$$

$$f_{\chi\mapsto P}(\chi) \equiv 1 - \frac{1}{\sqrt{2\pi}}\int_{-\chi}^{\chi}\exp\left(-\frac{x^2}{2}\right){\rm d}x\,. \tag{24}$$

Here, $N = 10^6$ is the number of vantage points, $\delta_{\rm obs} = 0.46$ is the observed underdensity, and $\sigma_{\rm obs} = 0.06$ is its uncertainty. The function $f_{\chi\mapsto P}$ gives the likelihood that a 1D Gaussian is more than χ standard deviations away from its mean. We use the inverse function $f_{P\mapsto\chi}$ to convert the so-obtained P-value into a more easily understood form, as will usually be done throughout this paper. In this way, we find that the KBC void is in 6.04σ tension with ΛCDM cosmology if it is accurately represented by the MXXL simulation on a 300 Mpc scale.

2.2.2 Implications for the Hubble tension

In any matter-conserving cosmological model, we expect an underdensity to be associated with some change in the local expansion rate (equation 5). Fig. 2 illustrates the manner in which this occurs for ΛCDM. In principle, the KBC void can boost the global Hubble constant to its local value observed by the SH0ES and H0LiCOW teams ($H_0^{\rm local} = 73.8 \pm 1.1\,{\rm km\,s^{-1}\,Mpc^{-1}}$, Riess et al. 2019; Wong et al. 2020). In fact, the straight line drawn on Fig. 2 should

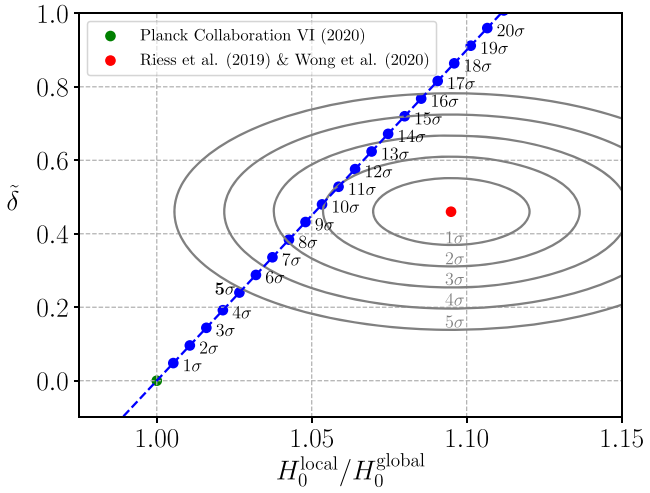

Figure 2. The local underdensity and Hubble constant in the ΛCDM framework and as found observationally. The green point shows $H_0^{\rm global} = 67.4 \pm 0.5\,{\rm km\,s^{-1}\,Mpc^{-1}}$ (Planck Collaboration VI 2020) and a local density equal to the cosmic mean ($\tilde{\delta} = 0$). The red data point is the local Hubble constant combined from the SH0ES and H0LiCOW projects ($H_0^{\rm local} = 73.8 \pm 1.1\,{\rm km\,s^{-1}\,Mpc^{-1}}$; Riess et al. 2019; Wong et al. 2020) and the locally observed $\delta_{\rm obs} = 0.46 \pm 0.06$ (Keenan et al. 2013). The grey contour lines show the indicated confidence levels assuming the measurements are independent. The blue points show the expected cosmic variance in ΛCDM corrected for RSD (equations 18 and 22) at the indicated confidence level. Notice that a 5σ fluctuation is not enough to get within 5σ of the local observations.

curve to the right for large δ because as $\delta \to 1$, we expect that $H_0^{\rm local}/H_0^{\rm global} \to \infty$ due to mass conservation (equation 5, see also fig. 1 of Marra et al. 2013). Thus, the expected relation between $H_0^{\rm local}$ and $\tilde{\delta}$ would pass rather close to the observations (red point). However, a 10σ density fluctuation would be necessary to reduce the Hubble tension to the 2σ level. Moreover, even a 5σ underdensity in ΛCDM is still not enough to get within 5σ of the local observations. This suggests that combining the KBC void and Hubble tension leads to a discrepancy with ΛCDM that slightly exceeds $5\sqrt{2}\sigma = 7.07\sigma$. We next perform a more detailed joint analysis.

2.2.3 *Combined implications for ΛCDM*

As discussed in Section 1.1, the locally measured H_0 is discrepant at the 5.3σ level with the Planck-based ΛCDM prediction (Wong et al. 2020) if we neglect the small expected impact of cosmic variance (Wojtak et al. 2014). In the previous section, we have shown that the KBC void is in 6.04σ tension with ΛCDM (Fig. 2). Therefore, both the KBC void and Hubble tension are difficult to explain within the ΛCDM framework − we can explain both simultaneously, but this would require a 10σ density fluctuation (Fig. 2). In this context, the most plausible explanation is that both are caused by measurement errors. If so, we would have to assume two independent $>5\sigma$ errors, an unlikely scenario. The combined tension would correspond to $\chi^2 = 5.30^2 + 6.04^2$ for 2 degrees of freedom. This results in a probability of $P = \exp(-\chi^2/2) = 9.4 \times 10^{-15}$, which is equivalent to 7.75σ for one variable.

Measurements of the local density and velocity fields rely on rather different techniques, justifying our assumption of independence. For instance, a miscalibration of SNe magnitudes would affect $H_0^{\rm local}$ but not $\delta_{\rm obs}$ as the latter is a relative density contrast between different redshift bins. Thus, it is extremely unlikely that both phenomena are caused purely by measurement errors. Moreover, the KBC void is evident at different wavelengths as well as independently on smaller (< 50 Mpc) scales (Karachentsev 2012), while several independent teams have measured a higher local expansion rate than the Planck-based ΛCDM prediction (Sections 1.1 and 1.2, respectively).

A more rigorous way to estimate the combined tension is to average the *P*-values across different vantage points considering their individual δ_i, how this would perturb the local expansion rate, and how the resulting RSD would lead to an enhanced apparent $\tilde{\delta}_i$. The average *P*-value is thus

$$P = \frac{1}{N}\sum_{i=1}^{N} \exp\left(-\frac{\chi_i^2}{2}\right), \quad \text{where} \tag{25}$$

$$\chi_i^2 = \left(\frac{\tilde{\delta}_i - \delta_{\rm obs}}{\sigma_\delta}\right)^2 + \left(\frac{\tilde{H}_{0,i} - H_0^{\rm local}}{\sigma_{H_0}}\right)^2 \quad \text{and} \tag{26}$$

$$\tilde{H}_{0,i} = H_0^{\rm global}(1 + f\,\delta_i) \tag{27}$$

is the apparent local Hubble constant. Here, $H_0^{\rm local} = 73.8\,{\rm km\,s^{-1}\,Mpc^{-1}}$ and $\sigma_{H_0} = 1.2\,{\rm km\,s^{-1}\,Mpc^{-1}}$, with the latter including an allowance for the $0.5\,{\rm km\,s^{-1}\,Mpc^{-1}}$ uncertainty from Planck Collaboration VI (2020). This procedure reveals that the KBC void and Hubble tension falsify the ΛCDM framework at 7.09σ, in agreement with our earlier estimate.

Our calculation of the cosmic variance in ΛCDM is derived from the stellar masses of subhaloes with $M_* > 10^{10}\,h^{-1}\,{\rm M}_\odot$, which should be more than sufficient to accurately trace the matter distribution on a 300 Mpc scale. Moreover, our results are consistent with expectations from the Harrison–Zeldovich spectrum (Harrison 1970; Zeldovich 1972) and its early Universe normalization required to match the CMB (Planck Collaboration VI 2020). In a ΛCDM context, this is parametrized using σ_8, which implies rms fluctuations of 3.2 per cent on a 300 Mpc scale at the present epoch. This agrees with our much more rigorous estimate using MXXL (Section 2.2.1).

Therefore, the KBC void is not a consequence of random measurement errors or density fluctuations expected in standard cosmology. Structure formation mainly depends on the underlying gravitational law, strongly suggesting that the observed KBC void cannot be explained by treating baryonic physics differently on galaxy scales.

Although cosmic variance in a standard context is insufficient to explain the KBC void and H_0 from low-redshift probes (e.g. Macpherson et al. 2018), Fig. 2 indicates that a large local void appears to be a promising explanation for these local observations. Consequently, we next consider a long-range modification to gravity which should enhance cosmic variance while accurately explaining observations on galactic scales with a fixed acceleration threshold (Famaey & McGaugh 2012). Section 5.3 discusses some commonly used arguments for why the KBC void cannot solve the Hubble tension.

3 MOND FRAMEWORK

As shown in the previous section, the cosmic variance expected within the ΛCDM framework is insufficient to explain the KBC void and Hubble tension. Thus, we aim to investigate structure formation and the velocity field in MOND (Milgrom 1983). In this section, we first introduce a conservative MOND cosmology that has the same expansion rate history and overall matter content as ΛCDM, but with CDM replaced by hot dark matter (HDM) to account for light element abundances, galaxy clusters, and the CMB without much affecting galaxies (Angus 2009). We then explain how we parametrize the initial void density profile and evolve it forwards to

the present time (Section 3.2). Finally, we describe how predictions for local observables are extracted from our models (Section 3.3).

3.1 The *ν*HDM cosmological model

Any viable cosmological model has to explain the angular power spectrum of the CMB and the primordial abundances of light elements. Angus (2009) provided a promising cosmological model that seeks to address the shortcomings of MOND on galaxy cluster and larger scales using an extra sterile neutrino species with a mass of $m_{\nu_s} = 11\,\mathrm{eV/c^2}$. Thermally produced neutrinos of this mass would have the same relic abundance as CDM particles in standard cosmology, but would behave as HDM in the sense of not clustering on galaxy scales.[2] However, the composition of the universe as a whole would be similar to ΛCDM – baryons would still comprise ≈ 5 per cent of the present critical density of the universe, sterile neutrinos would replace the ≈ 25 per cent contribution of CDM, and dark energy would yield the remaining ≈ 70 per cent (i.e. $\Omega_{\mathrm{m},0} = \Omega_{\mathrm{b},0} + \Omega_{\nu_s,0} \approx 0.3$ and $\Omega_{\Lambda,0} \approx 0.7$). We refer to this model as the *ν*HDM paradigm, where *ν* stands for both the interpolating function in QUMOND (equation 8) and sterile neutrinos, maximizing the chance that it is physically meaningful. The observed expansion history of the Universe seems broadly consistent with ΛCDM cosmology (e.g. Joudaki et al. 2018). As shown by Angus (2009), *ν*HDM yields the same expansion history as ΛCDM due to the same overall matter content and the same Friedmann equations at the background level (Skordis et al. 2006). This issue is discussed further in Section 3.1.1.

Although the existence of sterile neutrinos is not experimentally confirmed yet, they are theoretically consistent with standard particle physics (Merle 2017). Observationally, the *ν*HDM model is motivated mainly by galaxy clusters, where the dynamical discrepancy cannot be explained in MOND without DM (Sanders 2003). Furthermore, DM is necessary to address the offset between X-ray and lensing peaks in the Bullet Cluster (Clowe et al. 2006), since MOND acting on the baryons alone is unable to fully replace the role played by CDM in standard cosmology (Angus et al. 2007). We emphasize that these observations do not uniquely require CDM since they are on a much larger spatial scale than the hypothesized CDM haloes of individual galaxies (Ostriker & Peebles 1973).

In this context, Angus, Famaey & Diaferio (2010) analysed 30 of the most virialized galaxy groups and clusters in the *ν*HDM paradigm. They found that the required HDM density in all cases reaches the so-called Tremaine–Gunn limit (Tremaine & Gunn 1979) at the centre for sterile neutrinos with $m_{\nu_s} = 11\,\mathrm{eV/c^2}$. This is a strong indication that the DM density in galaxy cluster cores is limited by quantum degeneracy pressure (the Pauli Exclusion Principle). Note that MOND fits to galaxy rotation curves are hardly affected by sterile neutrinos with $m_{\nu_s} \lesssim 100\,\mathrm{eV/c^2}$, even if their number density reaches the Tremaine–Gunn limit (section 4.4 of Angus et al. 2010). As a result, *ν*HDM is likely to explain the internal dynamics of both galaxies and galaxy clusters. Introducing sterile neutrinos is thus well consistent with astronomical observations and almost consistent with the standard model of particle physics (unlike CDM particles), but they nevertheless require experimental verification.

[2] In ΛCDM, sterile neutrinos with $m_{\nu_s} \approx 7\,\mathrm{keV/c^2}$ are often considered as DM candidates (e.g. Bulbul et al. 2014; Boyarsky et al. 2014). Like $11\,\mathrm{eV/c^2}$ sterile neutrinos, these would also be relativistic during the nucleosynthesis era (Section 3.1.2), but would cluster in galaxies.

In the following, we address the background evolution of $a(t)$ in the *ν*HDM framework, allowing us to address the primordial abundances of light elements and the CMB. We also consider the implications for large-scale structure, where substantial differences are expected from ΛCDM. The theoretical uncertainties of the here applied MOND approach are summarized in Section 5.2.3, which focuses on how density perturbations should be treated in MOND.

3.1.1 *Background cosmology*

The background evolution $a(t)$ requires a relativistic theory that yields the appropriate MOND limit in galaxies. In this contribution, we make certain assumptions about the parent relativistic theory that gives rise to MOND. These assumptions are based on prior work, in particular with the tensor–vector–scalar (TeVeS) theory that was the first covariant framework with an appropriate MOND limit (Bekenstein 2004). His section 7 indicates that the background evolution should be very similar to General Relativity at all epochs for the same matter-energy content.

The background evolution and perturbations in TeVeS were addressed in detailed calculations done by Skordis (2006). To avoid detectable departures from the standard expansion history during the nucleosynthesis era, the free dimensionless parameter μ_0 must be rather large (Skordis et al. 2006).[3] In particular, if we allow the extra energy density contributed by the scalar field to comprise a fraction X of the critical density during the radiation-dominated era, then the contribution in the matter and Λ-dominated eras would be $X/9$. Primordial light element abundances then imply that the standard Friedmann equation would differ from the TeVeS cosmology at only the sub-per cent level (see their fig. 1). The very small contribution of the scalar field density was also demonstrated in fig. 2 of Dodelson & Liguori (2006). Therefore, we will assume that the background cosmology is identical to that of ΛCDM. Since the CMB is also expected to have similar properties in both frameworks (Section 3.1.3), they both lead to the Hubble tension in a similar manner provided that $\dot{a} = H_0^{\mathrm{local}}$, i.e. if cosmic variance in the local measurements is much smaller than the Hubble tension. Our main argument is that this assumption is valid in ΛCDM but need not be in MOND.

While the original version of TeVeS is inconsistent with gravitational waves travelling at c, a slightly modified version does have this property, even in the presence of perturbations (Skordis & Złośnik 2019). The above-mentioned results should carry over to the updated version of TeVeS, though this should be carefully demonstrated in future work. The preliminary results of Skordis & Złosnik (2020) are an important step in this direction.

Throughout this work, we assume dark energy not to be an artefact of an observer in an underdense region seeing an apparently accelerating expansion due to the developing inhomogeneities (Buchert 2000). However, we emphasize that proper time-averaging of global properties of the universe would be required to further study the present model (Wiltshire 2007).

3.1.2 *Big bang nucleosynthesis*

Big bang nucleosynthesis (BBN) occurred at a temperature of $kT \approx 1$ MeV, where k is the Boltzmann constant. A review on BBN can be found e.g. in Cyburt et al. (2016). In the *ν*HDM framework, Skordis

[3] μ_0 is related to the TeVeS parameter κ (equation 16 of Bekenstein 2004) via $\mu_0 \equiv 8\pi/\kappa$.

et al. (2006) showed that it is possible to have essentially no departure from the standard expansion history during the radiation-dominated era. However, the model would still have an effect on BBN because at $kT \approx 1\,\mathrm{MeV}$, sterile neutrinos with $m_{\nu_s} \approx 11\,\mathrm{eV/c^2}$ would be relativistic. Their weaker interactions would cause them to decouple earlier, so they would add an extra 7/8 to g_*, the number of effective relativistic degrees of freedom. Since the Hubble parameter $H \equiv \dot{a}/a$ scales as $H \propto \sqrt{g_*}$ and standard physics predicts $g_* = 10.75$, this would increase H by only 4 per cent, causing a slight impact on the primordial abundances of light elements. As shown in equation (13) of Cyburt et al. (2016), any increase in H raises the primordial *He*-4 mass fraction Y_p because free neutrons have less time to decay. Their detailed calculations have shown that this dependence can be fitted with a power law of the form

$$Y_\mathrm{p} \overset{\propto}{\sim} N_\nu^{0.163}\,. \tag{28}$$

In standard cosmology, the effective neutrino number is $N_\nu = 3.046$, which slightly exceeds 3 because neutrinos decouple only slightly before electron–positron annihilation at $kT = 511\,\mathrm{keV}$. Thus, an extra sterile neutrino species would increase Y_p by a factor of $(4.046/3.046)^{0.163} = 1.047$, implying the standard value of $Y_\mathrm{p} = 0.247$ would rise to 0.259. This is only a small effect, so observations of the primordial *He* abundance in ancient gas clouds currently do not set a strong constraint on the existence of an extra sterile neutrino. For instance, measurements of the *He* abundance of a gas cloud at $z = 1.724$ backlit by a quasar yield $Y = 0.250^{+0.033}_{-0.025}$ (Cooke & Fumagalli 2018). Using a sample of H II regions, Aver, Olive & Skillman (2012) derived $Y_\mathrm{p} = 0.2534 \pm 0.0083$. Even if their reported uncertainty is taken at face value, $Y_\mathrm{p} = 0.259$ is quite possible.

Measurements of the primordial abundances of *D* and *Li*-7 are less sensitive to N_ν (Cyburt, Fields & Olive 2002). However, primordial *D* abundances are relatively well known. Cooke, Pettini & Steidel (2018) obtained $N_\nu = 3.41 \pm 0.45$ based on $(D/H)_\mathrm{p}$ derived from a metal-poor damped Ly α system. Therefore, both *D* and *He* measurements allow an extra sterile neutrino, which was actually favoured by the earlier analysis of Steigman (2012). We do not consider the more problematic case of *Li*-7, though see Howk et al. (2012) for a gas phase measurement in the Small Magellanic Cloud that seems to resolve the lithium problem.

These considerations only hold for sterile neutrinos in thermal equilibrium during the nucleosynthesis era. However, if sterile neutrinos decoupled much earlier, their number density could be lower depending on whether any other particle subsequently became non-relativistic. If so, ΔN_ν would be lower, reducing the impact on g_* and on BBN. This scenario would require a higher sterile neutrino mass to recover the standard value of Ω_m.

3.1.3 *Radiation-dominated era and the CMB*

After BBN, the next major constraint on any cosmological model comes from the CMB. This occurred shortly after the epoch of matter-radiation equality at $z_\mathrm{eq} = 3411 \pm 48$ (Planck Collaboration VI 2020).[4] This corresponds to a photon temperature of $kT \approx 0.80\,\mathrm{eV}$, which is much less than the mass of the here considered sterile neutrinos. Consequently, they would behave just like non-relativistic CDM, causing z_eq to be the same as in the ΛCDM model.

[4] z_eq is tightly constrained by the acoustic oscillations in the CMB because during the earlier radiation-dominated era, perturbations in the sub-dominant matter component are unable to grow through gravitational instability.

The CMB was emitted at $z_\mathrm{CMB} \approx 1100$, corresponding to $kT \approx 0.26$ eV. At this time, matter dominated the energy budget of the universe. Since the background cosmology of the νHDM model is the same as for ΛCDM and the plasma physics is unchanged, the sound horizon at recombination would still have the standard value of 147.09 ± 0.26 cMpc (Planck Collaboration VI 2020). This is directly related to the angular scale of the first acoustic peak in the CMB, which should thus be unaffected in our model.

$11\,\mathrm{eV/c^2}$ sterile neutrinos would be non-relativistic at the time of last scattering. Since both T and the peculiar velocity v_pec should decline $\propto 1/a$, we expect the sterile neutrinos to typically have

$$v_\mathrm{pec} \approx \frac{0.26\,\mathrm{eV}}{11\,\mathrm{eV}} c = 0.024\,c\,. \tag{29}$$

This implies a free-streaming length of $L_\mathrm{fs} \approx 3.5\,\mathrm{cMpc}$, which is much shorter than the horizon scale. Since the first acoustic peak of the CMB occurs at a multipole moment of $\ell \approx 200$ (Jaffe et al. 2001), free-streaming becomes important only for $\ell \gtrsim 200/(0.024\sqrt{3}) = 4900$, beyond the range accessible by Planck Collaboration VI (2020). This is consistent with section 6.4.3 of Planck Collaboration XIII (2016), which explicitly states that any particles with $m > 10\,\mathrm{eV/c^2}$ 'are so massive that their effect on the CMB spectra is identical to that of CDM.'

The νHDM paradigm does more than simply replace CDM with HDM. Because of the Milgromian force law, the paradigms differ with regards to the evolution of sub-horizon perturbations. In the following, we estimate the gravitational field from inhomogeneities around t_CMB, the time of recombination.

The peculiar velocities are of order $v_\mathrm{pec} \approx c\delta$ and were built up over a duration of $t_\mathrm{CMB} = 380\,\mathrm{kyr}$. Assuming rms density fluctuations of $\delta_\mathrm{CMB} = 10^{-5}$ as observed in the baryons, we can obtain a lower bound on the peculiar acceleration g_CMB sourced by inhomogeneities.

$$g_\mathrm{CMB} \geq \frac{c\delta_\mathrm{CMB}}{t_\mathrm{CMB}} \approx 2.1\,a_0\,. \tag{30}$$

This already exceeds Milgrom's constant a_0. However, the gravity must have been significantly stronger to compensate for resistance from radiation pressure. In order to estimate the density fluctuations in the HDM component at t_CMB, we consider the value of $\sigma_8 = 0.811 \pm 0.006$ on a scale of $8\,h^{-1} \approx 12\,\mathrm{cMpc}$ that is required to fit the CMB anisotropies (Planck Collaboration VI 2020). For a scale-invariant power spectrum, the density fluctuations on the 147 cMpc scale of the first acoustic peak in the CMB are $12\sigma_8/147 \approx 0.065$ at the present epoch, as can also be seen by scaling our results of Section 2.2 for fluctuations on a 300 cMpc scale.[5] Since ΛCDM predicts that $\delta \propto a$ in the matter-dominated era and neglecting the effect of dark energy, we would expect density fluctuations of $\delta_\mathrm{CMB} \approx 5.9 \times 10^{-5}$ at t_CMB. Taking into account that structure formation slowed down when the Universe became dark energy-dominated at $z \leq 0.7$ and was slower around the time of recombination due to the still significant amount of radiation, we estimate that

$$\delta_\mathrm{CMB} \approx 10^{-4}\,. \tag{31}$$

Thus, the typical gravitational field at recombination was

$$g_\mathrm{CMB} \approx 21 a_0\,, \tag{32}$$

implying MOND had only a minor impact at that time.

[5] The here used MXXL simulation is calibrated to the CMB data gathered by WMAP-1 (Angulo et al. 2012).

In the matter-dominated era ($a \gg a_{\rm eq}$), the density perturbations grow $\propto a$ after their mode enters the horizon. Therefore, the Harrison–Zeldovich power spectrum predicts that the power of the density perturbations scales inversely with their length L (Harrison 1970; Zeldovich 1972), i.e.

$$P(L) \propto L^{-1}. \tag{33}$$

Since the mass enclosed by the mode is $M \propto L^3$, the mass perturbation must scale as

$$\Delta M \propto L^2. \tag{34}$$

Therefore, the perturbation's Newtonian gravity is independent of L, i.e.

$$g_{\rm N} = \text{const.} \tag{35}$$

The Harrison–Zeldovich power spectrum breaks down for length-scales that enter the horizon before $a_{\rm eq}$. Since no modes would be able to grow during the radiation-dominated era, these short-wavelength modes would have much less power than predicted by a $1/L$ scaling relation. Thus, $g_{\rm N}$ would be smaller. However, in MOND, these short-wavelength modes would be embedded in the EFE generated especially by long-range modes (Section 1.3). This would severely limit the MOND boost to the internal gravity of shorter modes, since their total $g_{\rm N}$ depends on both their internal gravity and any external field. For this reason, we expect that modes of any L were unaffected by MOND around the epoch of recombination.

We next consider how this picture changes with time. Since Newtonian density perturbations are expected to grow as $\delta \propto a$ in the matter-dominated era, the mass perturbation should also scale as

$$\Delta M \propto a. \tag{36}$$

For linear ($\delta \ll 1$) perturbations whose co-moving size hardly changes, the Newtonian gravity should scale as

$$g_{\rm N} \propto a^{-1}. \tag{37}$$

Our previous estimation showed that the gravitational field sourced by inhomogeneities is $g \gg a_0$ at $t_{\rm CMB}$ (equation 32). We now see that even larger gravitational fields are expected at earlier times, further justifying our assumption that MOND would have little effect then.[6]

We can combine equations (32) and (37) to deduce that MOND does not play a significant role in structure formation until $z \lesssim z_{\rm MOND} = 50$. This underpins the commonly used assumption that MOND does not play a role in the very early universe but would promote the formation of the first galaxies (Sanders 1998).

The high accelerations around the time of recombination strongly suggest that the MOND gravity law would not by itself affect the acoustic oscillations in the CMB. This issue was investigated further by Skordis et al. (2006), who considered a covariant formulation of MOND. Their fig. 2 confirms our conclusion that the modification to gravity has by itself only a very small effect for plausible choices of the model parameters consistent with BBN. However, their use of three ordinary neutrino species with a much lower mass of $2\,{\rm eV/c^2}$ led to significant free streaming effects that are totally inconsistent with the latest observations (Planck Collaboration XXVII 2014). If instead a single $11\,{\rm eV/c^2}$ sterile neutrino is used, a very good fit can be obtained to the CMB power spectrum for the reasons just discussed (fig. 1 of Angus 2009). Note also that with a standard $a(t)$, the angular diameter distance to the CMB would be the same as in ΛCDM, placing the acoustic peaks at the correct angular scales. Indeed, fig. 1 of Angus & Diaferio (2011) shows that the CMB power spectra in the νHDM and ΛCDM models agree quite closely, so both paradigms are consistent with observations taken by WMAP-7, the Atacama Cosmology Telescope (ACT), and the Arcminute Cosmology Bolometer Array Receiver up to $\ell = 2500$.

3.1.4 *Evolution of perturbations and large-scale structure*

Even if the CMB power spectrum is correct in our framework, the observed CMB is also influenced by foreground structures. Section 5.3.3 discusses the gravitational redshift of the entire last scattering surface due to the rather high MOND potential of the KBC void. Foreground lensing of the CMB by large-scale structures and the integrated Sachs–Wolfe (ISW) effect would also be stronger in MOND. There are some observational hints that these effects are stronger than expected in ΛCDM (Section 5.3.1). These tensions could be eased in a theory where structure formation is more efficient. However, it is possible that νHDM overcorrects the problem and produces too much foreground lensing and/or a Sachs–Wolfe effect in disagreement with observations. These issues are beyond the scope of our work, but should be addressed before the νHDM framework can be considered to fully account for all observed aspects of the CMB. This would almost certainly require numerical simulations of structure formation. In addition, photon propagation through such a simulation would need to be handled with care, taking account of inhomogeneities and their time evolution (e.g. Wiltshire 2007).

Nusser (2002) considered the growth of density perturbations in a Milgromian framework. Their section 2 introduced the basic principle used in all subsequent MOND cosmological simulations (Llinares et al. 2008; Angus & Diaferio 2011; Angus et al. 2013; Katz et al. 2013; Candlish 2016). These simulations make the ansatz that a MONDified Poisson equation (usually equation 7) is applied only to the density perturbations about the mean background value, as evident in e.g. equation (2) of Candlish (2016).[7] This 'Jeans swindle' (Binney & Tremaine 1987) approach to MOND was justified using the earlier work of Sanders (2001), who showed its validity in a non-relativistic Lagrangian formulation of MOND (see his section 2). The approach is certainly valid for systems such as galaxies that are much denser than the cosmic mean. The use of non-relativistic gravitational equations should be sufficient when dealing with structures such as the KBC void that are much smaller than the cosmic horizon, since gravity traveltime effects would not be too significant.

Falco et al. (2013) showed that the Jeans swindle is formally correct in Newtonian gravity – including the background would simply add on the force required to maintain the time-dependent Hubble flow velocity. However, it still needs to be rigorously demonstrated that the swindle remains mathematically valid in a MONDian model with a non-linear gravity law. Therefore, although this ansatz is commonly used by the MOND community, it is one of the strongest assumptions in the here presented cosmological model.

[6] MOND effects can be further reduced at early times if a_0 was smaller, or if density perturbations couple to the background in a non-trivial way (Section 5.2.3).

[7] Equation (4) of Nusser (2002) assumes the deep-MOND limit, but we generalize it to an arbitrary acceleration using an interpolating function (equation 8). Note that the deep-MOND limit is a reasonable assumption for the KBC void (Section 5.2.3).

One of the few works that does not make this assumption is Sanders (2001), whose model is a non-relativistic two-field Lagrangian-based theory of MOND. The coupling between these two fields is described by an adjustable parameter β in his modified Poisson equation (8). Setting $\beta = 0$ is equivalent to applying the Jeans swindle approach. However, if $\beta \neq 0$, there exists a coupling between the peculiar acceleration sourced by inhomogeneities and the zeroth-order Hubble flow acceleration $\boldsymbol{g}_{\rm Hubble}$ (equation 38). Sanders (2001) adopted $\beta = 3.5$ for his main analysis. As discussed in the cosmology section of Sanders & McGaugh (2002), $\boldsymbol{g}_{\rm Hubble}$ essentially contributes an extra source of gravity to the total entering the ν calculation in equation (7), limiting the MOND boost to gravity. We call this the 'Hubble field effect' (HFE), since it is similar to but distinct from the usual EFE in MOND − both make the behaviour more Newtonian. In Section 5.2.3, we address theoretical uncertainties arising from the HFE, which is neglected in our main analysis. A non-zero HFE would substantially affect large-scale structures especially at scales $\gtrsim 100$ cMpc, which could be used to constrain it in future studies (Section 5.2.3). However, we argue there that even with a strong HFE, cosmic variance would still be enhanced 3× compared to ΛCDM expectations on a 300 Mpc scale under conservative assumptions, enough to reproduce the KBC void.

Nusser (2002) built on the model of Sanders (2001) but assumed instead that $\beta = 0$ because he could not find any physical justification for coupling both fields, i.e. for the HFE. This uncoupled (Jeans swindle) approach is generally the one adopted in MOND cosmological simulations (e.g. Llinares et al. 2008; Angus et al. 2013; Katz et al. 2013; Candlish 2016). In particular, Angus et al. (2013) used it in a cosmological *N*-body simulation designed to address the formation of large-scale structure in MOND supplemented by sterile neutrinos. Although their work was novel and very advanced for its time, it faces some conceptual and numerical problems. In particular, they concluded that their model with $11\,{\rm eV/c^2}$ sterile neutrinos significantly underestimates the number of low-mass galaxy clusters and slightly overestimates the number of very massive clusters (see e.g. their fig. 4). This inconsistency between the model and observational data could arise for several reasons. Their conclusion is based on a simulation with a box size of $256\,h^{-1}$ cMpc and a particle resolution of only $\approx 3.78 \times 10^{10}\,{\rm M}_\odot$. The underproduction of low-mass galaxy clusters could be explained by the low particle resolution and therewith by an absence of low-mass particles needed to form such systems. In addition, they do not use a grid with adaptive mesh refinement (AMR), which causes that the potential wells especially of the smaller clusters may not be resolved properly, making them difficult to form. Therefore, it would be highly valuable to revisit their cosmological simulations with an AMR grid code such as PHANTOM of RAMSES (Lüghausen, Famaey & Kroupa 2015), which adapts the potential solver of the widely used RAMSES algorithm (Teyssier 2002).

In general, small simulation boxes lack large-scale modes. Since the EFE is mainly sourced by very massive objects, a too small simulation box would potentially underestimate the EFE on MONDian subsystems. Thus, the internal gravitational field would be too strong, which could also explain the efficient formation of massive galaxy clusters in Angus et al. (2013).

As already discussed at the beginning of this section, Angus et al. (2010) demonstrated that the required neutrino density in 30 virialized galaxy groups and clusters reaches the Tremaine–Gunn limit at the centre, which supports the νHDM model. However, the neutrino degeneracy pressure in the cores of galaxy clusters has not been included in the simulations of Angus et al. (2013). If one would account for this effect, it would be more difficult to form massive galaxy clusters because gravity is resisted by neutrino degeneracy pressure.

Finally, Angus et al. (2013) compared their simulated halo mass functions with cluster mass functions derived from observations at $z \leq 0.3$ (Reiprich & Böhringer 2002) and $z \leq 0.1$ (Rines, Diaferio & Natarajan 2008). As we have seen in Section 1.1, the KBC void has a similar extent. It is evident in X-ray galaxy cluster surveys (e.g. Böhringer et al. 2015, 2020). Therefore, local observations are biased against high-mass clusters, e.g. the massive merging galaxy cluster El Gordo (ACT-CL J0102-4915, Marriage et al. 2011) with a mass of $3 \times 10^{15}\,{\rm M}_\odot$ (Jee et al. 2014) at $z = 0.87$ (Menanteau et al. 2012) would almost certainly not be evident in local observations from within a deep void. Thus, local observations do not provide a representative cluster mass function of the whole Universe, so cannot be compared with the entire simulated halo population.

Consequently, the Angus et al. (2013) cosmological model has never been tested in full detail on large scales. An object similar to El Gordo was identified in the νHDM simulation of Katz et al. (2013), so initial results seem promising. It would be highly valuable to revisit their analysis in more physically and numerically advanced large-scale simulations. This is because the νHDM framework provides a viable explanation for BBN and the CMB, but also works on galaxy cluster scales while recovering the successes of MOND in galaxies. At present, there is no *N*-body or hydrodynamical simulation with a large enough box size to study the KBC void in a MONDian framework. Therefore, we develop a semi-analytic simulation for this purpose. In the following, we introduce the governing equations and parameters of the here discussed νHDM cosmological model.

3.2 Governing equations

We develop a simplified simulation in which the trajectories of particles are integrated up to the present time from $z = 9$, which corresponds to ≈ 0.5 Gyr after the big bang (equation 45). As derived from General Relativity in section 2.2 of Banik & Zhao (2016), the particle's trajectory is described by the background cosmological acceleration term and any additional gravity sourced by inhomogeneities:

$$\ddot{\boldsymbol{r}} = \boldsymbol{g}_{\rm void} + \overbrace{\frac{\ddot{a}}{a}\boldsymbol{r}}^{\boldsymbol{g}_{\rm Hubble}}\,, \tag{38}$$

$$\dot{\boldsymbol{r}}_i = H_i \boldsymbol{r}_i\,, \tag{39}$$

where $\boldsymbol{r}$ is the particle's position relative to the void centre, $\boldsymbol{g}_{\rm void}$ is the local gravitational acceleration sourced only by density deviations from the cosmic mean, $\boldsymbol{g}_{\rm Hubble}$ is the acceleration in a homogeneously expanding spacetime, and i subscripts denote initial values when $a = 0.1$. At that time, particles are assumed to be on the Hubble flow. However, the initial matter distribution is assumed to be inhomogeneous. A spherically symmetric underdensity causes a Newtonian gravitational force of

$$g_{\rm N} \equiv \frac{G\Delta M}{r^2}\,, \qquad \text{with} \tag{40}$$

$$\Delta M \equiv \frac{4\pi}{3}\rho_0 \left(\frac{r}{a}\right)^3 - M_{\rm enc}\,, \tag{41}$$

where ΔM is the mass deficit within radius r, ρ_0 is the present cosmic mean density of matter, and $M_{\rm enc}$ is the enclosed mass. Since we assume mass conservation and no shell crossing, $M_{\rm enc}$ remains

constant for an individual particle. In the case of no void, $g_N = 0$ since $\Delta M = 0$. The exact set-up of the initial void profile is described in Section 3.2.1 and Appendix B.

Applying the Jeans swindle approach to MOND (Section 3.1.4), the gravitational force g is calculated with the 'simple' interpolation function (equation 8) between the Newtonian and deep-MOND regimes (Famaey & Binney 2005). The EFE is included by quadrature summing g_N and the Newtonian-equivalent external field $g_{N,ext}$ (Famaey, Bruneton & Zhao 2007):

$$g = g_N \left(\frac{1}{2} + \sqrt{\frac{1}{4} + a_0 \left(g_N^2 + g_{N,ext}^2 \right)^{-\frac{1}{2}}} \right) . \quad (42)$$

The EFE and its impact on the void will be described in more detail in Sections 3.2.2 and 3.3.6, respectively. Milgrom's constant $a_0 = 1.2 \times 10^{-10}\,\mathrm{m\,s^{-2}}$ is taken to be constant over cosmic time. Substantially higher values in the past may conflict with the CMB (Section 3.1.3) and high-redshift rotation curves (Milgrom 2017).

Solving equation (38) requires knowledge of the background cosmology. As argued in Section 3.1.1, assuming this follows a standard Friedmann equation should be accurate at the sub-per cent level. We therefore apply the second Friedmann equation and assume a standard flat background cosmology ($\Omega_{m,0} + \Omega_{\Lambda,0} = 1$), yielding

$$\frac{\ddot{a}}{a} = -\frac{4\pi G}{3}(\rho_m - 2\rho_\Lambda) \quad (43)$$

$$= H_0^2 \left(-\frac{1}{2}\Omega_{m,0} a^{-3} + \Omega_{\Lambda,0} \right) , \quad (44)$$

where ρ_m and ρ_Λ are the cosmic mean densities of matter and dark energy, respectively. We assume that $\rho_m \propto a^{-3}$ while $\rho_\Lambda = \mathrm{const}$. The parameters $\Omega_{m,0}$ and $\Omega_{\Lambda,0}$ are the present-day matter and the dark energy densities in units of the critical density $\rho_c = 3H_0^2/(8\pi G)$. We set $\Omega_{m,0} = 0.315$, $\Omega_{\Lambda,0} = 0.685$, and choose a global Hubble constant of $H_0 = 67.4\,\mathrm{km\,s^{-1}\,Mpc^{-1}}$, consistently with the latest Planck data (Planck Collaboration VI 2020). Imposing the boundary conditions $a = 0$ when $t = 0$ and $\dot{a} = H_0$ at $a = 1$, we get that

$$a(t) = \left(\frac{\Omega_{m,0}}{\Omega_{\Lambda,0}} \right)^{\frac{1}{3}} \sinh^{\frac{2}{3}} \left(\frac{3}{2} \sqrt{\Omega_{\Lambda,0}} H_0 t \right) . \quad (45)$$

3.2.1 *Initial void profile*

The implemented void in the fiducial simulation run is initialized with a Maxwell–Boltzmann radial density profile. This is motivated by the observed Local Volume, where the density increases inwards for distances $\lesssim 40\,\mathrm{Mpc}$ (see e.g. fig. 3 in Karachentsev & Telikova 2018). The enclosed mass within co-moving radius r_{com} from the void centre is thus given by

$$M_{enc} = 4\pi\rho_0 r_{void}^3 \left(\frac{x^3}{3} - \alpha_{void}\epsilon \right) , \text{ where} \quad (46)$$

$$\epsilon = \int_0^x x'^4 \exp\left(-\frac{x'^2}{2} \right) \mathrm{d}x' \quad (47)$$

$$= 3\sqrt{\frac{\pi}{2}}\,\mathrm{erf}\left(\frac{x}{\sqrt{2}} \right) - x\left(x^2 + 3 \right) \exp\left(-\frac{x^2}{2} \right) . \quad (48)$$

The dimensionless radius $x \equiv r_{com}/r_{void}$, while α_{void} is the initial void strength and r_{void} is the parameter determining its co-moving size at $z = 9$. The first term in equation (46) is the mass within a sphere of co-moving radius r_{com} if the density were equal to the cosmic mean, with the void arising from the mass deficit imposed by the second term.

We run different simulations with α_{void} ranging from 10^{-5} to 10^{-2} and r_{void} ranging from (50–1030) cMpc. The parameter range of the initial void strength is motivated by the expected density fluctuations at $z = 9$ based on CMB data. In addition, we also run simulations in which the void is modelled with a Gaussian or an exponential initial density profile (Appendices B and C).

3.2.2 *External field history*

As stated in Section 1.3, the EFE is a consequence of the non-linearity of Milgrom's law of gravity (Milgrom 1986). Thus, we allow for the possibility that the void as a whole is embedded in an EF from even larger scales. We follow the usual approach of assuming the EF is sourced by a distant point-like object. This allows us to obtain the present-day Newtonian-equivalent external field using the simple interpolation function (Famaey & Binney 2005):

$$\frac{g_{N,ext}}{a_0} = \frac{\tilde{g}_{ext}^2}{1 + \tilde{g}_{ext}} , \quad (49)$$

where $\tilde{g}_{ext}$ is the external field in units of a_0.

The evolution of the EFE over cosmic time is unknown due to the lack of a fully self-consistent MONDian framework. Since the EFE depends on the environment in which the MONDian system is embedded and thus on the formation of structure, we assume that the external field has a power-law dependence on the cosmic scale factor:

$$g_{N,ext}(t) = g_{N,ext}(t_0) a^{n_{EFE}}(t) , \quad (50)$$

where $t_0 = 13.8\,\mathrm{Gyr}$ is the present time, and n_{EFE} is a free parameter ranging from -2 to $+2$ in steps of 0.5 for different models. For our fiducial simulation run, we adopt a time-independent external field ($n_{EFE} = 0$). The results for different external field histories are discussed in Section 5.2.2. Table 1 summarizes the fixed and free parameters of our models.

3.3 Extracting mock observables

Our cosmological MOND models are constrained by the observed density contrast of the KBC void (Keenan et al. 2013), the local Hubble constant and deceleration parameter derived jointly from SNe data (Camarena & Marra 2020a), the Hubble constant from strong lensing (Shajib et al. 2020; Wong et al. 2020), and the motion of the LG wrt. the CMB (Kogut et al. 1993). In the following, we explain how we obtain the corresponding simulated quantities.

Our approach involves comparing the void models described in Section 3.2 with a control simulation of a void-free standard cosmology. The control trajectories have a fixed co-moving radius:

$$r(t) = r(t_0)\, a(t) . \quad (51)$$

Since the lookback time can be derived from SNe luminosities or angular diameter distances in a standard background cosmology, we fix this variable between the void and control models, allowing us to analyse the difference in other variables. The main advantage of this approach is that in the absence of a local void, our calculated late-time cosmological parameters (e.g. H_0 and q_0) would revert to their values in standard cosmology.

Local observations imply that we are located close to the void centre (Keenan et al. 2013; Karachentsev & Telikova 2018). Therefore, as a simplification we assume in our analysis that we are at

Table 1. Constants and parameters of the here used cosmological MOND models. Our fiducial model assumes a Maxwell–Boltzmann initial density profile for the void (Section 3.2.1) and a time-independent external field ($n_{\rm EFE} = 0$ in equation 50).

Constants	Description	Value
$H_0^{\rm global}$	Present-day global Hubble constant	$67.4\,{\rm km\,s^{-1}\,Mpc^{-1}}$
$\Omega_{\rm m,\,0}$	Present-day matter density in units of $\rho_{\rm c}$	0.315
$\Omega_{\Lambda,\,0}$	Present-day dark energy density in units of $\rho_{\rm c}$	0.685
a_i	Cosmic scale factor at the start of the simulation	0.1
a_0	Milgrom's constant	$1.2\times10^{-10}\,{\rm m\,s^{-2}}$
External field parameters		Parameter range
$\tilde{g}_{\rm ext}$	Present-day external field in units of a_0	(0, 0.5)
$n_{\rm EFE}$	Time dependence of the external field (equation 50)	(−2, +2)
Void parameters		
$\alpha_{\rm void}$	Initial void strength at $z = 9$	$(10^{-5}, 10^{-2})$
$r_{\rm void}$	Initial void size at $z = 9$	(50 cMpc, 1030 cMpc)

the void centre (Sections 3.3.2–3.3.5), except when calculating the likelihood of the observed LG peculiar velocity (Section 3.3.6). It is beyond the scope of our work to analyse the Hubble diagram and density field that might be seen by a substantially off-centre observer.

3.3.1 Apparent scale factor

The main quantity we extract is the redshift experienced by a photon as it travels from a particle to the void centre. This is given by

$$\frac{\lambda_{\rm obs}}{\lambda_{\rm emit}} = \frac{1}{a(t)}\overbrace{\sqrt{\frac{c+v_{\rm int}}{c-v_{\rm int}}}}^{\rm Doppler}\overbrace{\exp\left(\frac{1}{c^2}\int g_{\rm void}\,{\rm d}r\right)}^{\rm GR}, \tag{52}$$

where $\lambda_{\rm obs}$ and $\lambda_{\rm emit}$ are the wavelengths of the light as measured by the observer and at the source of emission, respectively, $v_{\rm int}$ is the peculiar velocity of the particle relative to the void centre, and $g_{\rm void}$ is the gravity in the radially outwards direction. The factor of a^{-1} arises from expansion of the universe while light from the particle is travelling towards us. This is the only factor that needs to be considered even without the void. The term marked 'Doppler' is the special relativistic Doppler effect, while the exponential factor (marked 'GR') is the gravitational redshift that arises because photons must climb up the void potential to reach its centre. As discussed in Section 3.3.5, relativistic lensing in MOND should yield similar results to General Relativity for the same g.

To limit the complexity of our algorithm and because we are dealing with a void at low z, we approximate the GR contribution by assuming the final density profile of the void is also applicable at earlier times. This leads to a time-independent gravitational field $g_{\rm void}(r)$. We use this to calculate the integral in equation (52) out to the co-moving distance where our past lightcone intersects the particle's trajectory (Section 3.3.3).

Since the observed SNe and lensing Hubble diagrams reported by observers are not corrected for the large peculiar velocities we expect in our model, the apparent scale factor is simply

$$a_{\rm app} \equiv \frac{\lambda_{\rm emit}}{\lambda_{\rm obs}}\,. \tag{53}$$

We compare the behaviour of this $a_{\rm app}$ with the corresponding values in our control simulations, which are governed by equation (51). Since we run a finite number of trajectories for each model, we interpolate between them to ensure the comparison is done at fixed lookback time.

3.3.2 Density contrast and redshift space distortion

In our models, the fractional underdensity inside a shell between radii $r_{\rm min,\,now}$ and $r_{\rm max,\,now}$ at the present time is

$$1-\delta_{\rm model} = \left[1-3\alpha_{\rm void}\left(\frac{I_{\rm max}-I_{\rm min}}{x_{\rm max}^3-x_{\rm min}^3}\right)\right] \times\left(\frac{r_{\rm max,initial}^3-r_{\rm min,initial}^3}{r_{\rm max,now}^3-r_{\rm min,now}^3}\right), \text{ with} \tag{54}$$

$$I_{\rm min} = \int_0^{x_{\rm min}} x^4\exp\left(-\frac{x^2}{2}\right){\rm d}x\,. \tag{55}$$

Here, $r_{\rm min,\,initial}$ and $r_{\rm max,\,initial}$ are the initial co-moving distances of particles that are currently at $r_{\rm min,\,now}$ and $r_{\rm max,\,now}$, respectively, and $x_{\rm min} \equiv r_{\rm min,initial}/r_{\rm void}$. Similar procedures are used to calculate $x_{\rm max}$ and $I_{\rm max}$. The first term represents the initial density contrast, while the second accounts for expansion of the co-moving volume enclosed by the two shells.

As discussed in Section 1.1, the analysis of Keenan et al. (2013) used a distance–redshift relation based on the assumption of no void (see their section 4.7). Therefore, we apply an RSD correction to the observed relative density contrast in order to estimate the true value:

$$\left(1-\delta_{\rm obs,corr}\right) = \left(1-\delta_{\rm obs}\right)f_{\rm model}\,, \quad \text{with} \tag{56}$$

$$f_{\rm model} = \left(\frac{r_{\rm control,out}^3-r_{\rm control,in}^3}{r_{\rm void,out}^3-r_{\rm void,in}^3}\right). \tag{57}$$

Here, $\delta_{\rm obs}$ is the observed relative density contrast between the distances $r_{\rm void,\,in}$ and $r_{\rm void,\,out}$ at the present time. However, observations uncorrected for RSD are reported as if the known redshift range of the survey covers the distance range $r_{\rm control,\,in} - r_{\rm control,\,out}$, which are the corresponding distances to the same z in a void-free universe. The number of galaxies counted by the observers thus corresponds to a different δ than what they report, which is the RSD effect. Note that its magnitude will depend on the void model, so it is not possible to know the true density contrast in a model-independent way. This is because it is not possible to convert redshifts to distances without a dynamical model of the void. As a result, the uncertainty $\sigma_{\rm obs,\,corr}$ is also model-dependent.

We can compare the so-corrected observed δ to the model prediction (equation 54). This leads to a χ^2 contribution of

$$\chi_\delta^2 = \left(\frac{\delta_{\rm model}-\delta_{\rm obs,corr}}{\sigma_{\rm obs,corr}}\right)^2, \tag{58}$$

which is calculated for the relative density contrasts in the redshift range $0.01 < z < 0.07$ and between distances of 600 Mpc and 800 Mpc at the present time. According to Keenan et al. (2013), we estimate that $\delta_{\rm obs,\,in} = 0.46 \pm 0.06$ in the inner part of the void, while $\delta_{\rm obs,\,out} = 0.0 \pm 0.1$ in its outer part (see their table 1 and fig. 11).

3.3.3 Lightcone analysis

To determine exactly when we would observe a test particle, we need to determine the intersection between its trajectory and our past lightcone. This occurs when the co-moving distance travelled by a light ray emitted from a particle equals the time-dependent co-moving distance to the particle. In other words,

$$c\int_{t_{\rm LC}}^{t_0}\frac{{\rm d}t}{a\left(t\right)} \;=\; \frac{r(t_{\rm LC})}{a(t_{\rm LC})}\,, \tag{59}$$

where $t_{\rm LC}$ is the cosmic time when our past lightcone intersects a particle's trajectory. This is obtained by solving equation (59) using the Newton–Raphson algorithm. We can then calculate relevant quantities at that time, which is used in our analyses related to the Hubble diagram (Section 3.3.4).

However, when comparing the simulated $v_{\rm pec}$ with the observed LG peculiar velocity (Section 3.3.6), we need to extract $v_{\rm pec}$ at the present epoch since the measurement relates to the LG motion today. To limit the complexity of our analysis, we also use the present positions of particles when determining the density field of the void (Section 3.3.2). This should be valid if the void has not appreciably changed in the time needed for light to cross it, which is reasonable for a void much smaller than the Hubble distance $c/H_0 = 4.4\,$Gpc.

3.3.4 Hubble constant and deceleration parameter from SNe

We constrain our models with the results of Camarena & Marra (2020a), who derived the local Hubble constant and deceleration parameter jointly from Pantheon SNe in the redshift range $0.023 \leq z \leq 0.15$. As discussed earlier, we first find the difference in the apparent scale factor between our void model and a control void-free model.

$$\Delta a\left(t\right) \;\equiv\; a_{\rm app} - a_{\rm control}\,, \tag{60}$$

where $a_{\rm app}$ is the apparent scale factor (equation 53), and $a_{\rm control}$ is the scale factor at the same cosmic time in the control model of a void-free standard cosmology. Expanding equation (60) as a Taylor series in the vicinity of the present time t_0, we get that

$$\Delta a\left(t\right) = \Delta\dot{a}\left(t_0\right)\left(t-t_0\right) + \frac{1}{2}\Delta\ddot{a}\left(t_0\right)\left(t-t_0\right)^2 + \mathcal{O}\left(t-t_0\right)^3\,. \tag{61}$$

Dividing the above equation by $a\left(t_0\right) \equiv 1$ and using the definitions of the Hubble parameter ($H \equiv \dot{a}/a$) and deceleration parameter ($q \equiv -a\ddot{a}/\dot{a}^2$), we obtain that

$$\begin{aligned}\frac{\Delta a\left(t\right)}{a\left(t_0\right)} &= \frac{\Delta\dot{a}\left(t_0\right)}{a(t_0)}\left(t-t_0\right) + \frac{\Delta\ddot{a}\left(t_0\right)}{2a\left(t_0\right)}\left(t-t_0\right)^2 + \mathcal{O}\left(t-t_0\right)^3\\ &= \Delta H_0\left(t-t_0\right) - \frac{\Delta\left(q_0H_0^2\right)}{2}\left(t-t_0\right)^2 + \mathcal{O}\left(t-t_0\right)^3\,,\end{aligned} \tag{62}$$

where ΔH_0 and $\Delta\left(q_0H_0^2\right)$ are the boosts to these parameters due to the void, and the $_0$ subscripts denote present-day quantities. We find these by fitting $\Delta a(t)$ using a parabola forced to pass through $\Delta a = 0$ at $t = t_0$. The local Hubble and deceleration parameters are thus

$$H_0^{\rm local} \;=\; H_0^{\rm global} + \Delta H_0\,, \tag{63}$$

$$q_0^{\rm local} \;=\; \frac{\left(H_0^{\rm global}\right)^2\left(\frac{\Omega_{\rm m,0}}{2} - \Omega_{\Lambda,0}\right) + \Delta\left(q_0H_0^2\right)}{\left(H_0^{\rm local}\right)^2}\,. \tag{64}$$

Because of a historical accident where it was assumed that the expansion of the Universe should decelerate, q_0 was defined as the present deceleration parameter $-a\ddot{a}/\dot{a}^2$. It was subsequently shown that the Universe accelerates, implying $q_0 < 0$ (Riess et al. 1998; Schmidt et al. 1998; The Supernova Cosmology Project 1999). In order to minimize confusion from unnecessary use of $-$ signs, we introduce from now on the acceleration parameter:

$$\overline{q}_0 \;\equiv\; -\,q_0 \;\equiv\; \frac{a\ddot{a}}{\dot{a}^2}\left(t=t_0\right)\,. \tag{65}$$

The ΛCDM theory with the parameters obtained from Planck Collaboration VI (2020) predicts $\overline{q}_0 = \Omega_{\Lambda,0} - \frac{1}{2}\Omega_{\rm m,0} = 0.53$. In the absence of a void, $H_0^{\rm local}$ and $\overline{q}_0^{\rm local}$ become identical to the Planck values since we use those for the background cosmology (equation 45).

The combined χ^2 contribution from H_0 and $\overline{q}_0$ is

$$\chi^2_{H_0,\overline{q}_0} \;=\; \frac{1}{2}\left[\frac{(A+B)^2}{1+C} + \frac{(A-B)^2}{1-C}\right]\,, \quad \text{where} \tag{66}$$

$$A \;\equiv\; \frac{H_0 - H_0^{\rm local}}{\sigma_{H_0}} \quad \text{and} \tag{67}$$

$$B \;\equiv\; \frac{\overline{q}_0 - \overline{q}_0^{\rm local}}{\sigma_{\overline{q}_0}}\,. \tag{68}$$

Observationally, $\overline{q}_0^{\rm local} = 1.08 \pm 0.29$ and $H_0^{\rm local} = 75.35 \pm 1.68\,{\rm km\,s^{-1}\,Mpc^{-1}}$, with a mutual correlation coefficient of $C = 0.515$ (Camarena & Marra 2020a). Their section 4 mentions that their posterior inference is very close to Gaussian, justifying our χ^2 approach.

3.3.5 Hubble constant from strong lensing

Empirically, it has been shown that light deflection in strong lenses works similar to General Relativity for the same non-relativistic $\boldsymbol{g}$ (Collett et al. 2018). In the H0LiCOW lenses, $\boldsymbol{g}$ is constrained using the positions and time delays between images and also with velocity dispersion data. Their analysis should remain valid even in a MOND context, since the results of Collett et al. (2018) can be reproduced in relativistic versions of MOND (Milgrom 2013). The latter work showed that this approach works well empirically even in the deep-MOND regime, which can only be probed using weak lensing. This is because strong lensing always occurs in the Newtonian regime due to MOND's cosmological coincidence (equation 10), as explained in Sanders (1999). Hence, strong lensing is little affected by MOND. None the less, we discuss in Section 5.2.1 how H_0 measurements from strong lensing impact our analysis, and consider the effect of excluding these measurements.

In our main analysis, we constrain our MOND models with H_0 measured from seven strong-lens systems with the deflector at redshift z_d. Our data set is derived from Shajib et al. (2020) and Wong et al. (2020). In our models, the Hubble constant at redshift z_d is estimated as

$$H_{0,\rm lensing}^{\rm model} \;=\; H_0^{\rm global} + \frac{\Delta a_d}{t_d - t_0}\,, \tag{69}$$

Table 2. Measurements of H_0 from lensed quasars with the deflector at redshift z_d, as reported by Wong et al. (2020) and Shajib et al. (2020) for a flat ΛCDM cosmology. Their data are used to constrain the MOND models in Section 4, where low and high error bars are averaged to get a single Gaussian uncertainty for each lens.

Lens system	z_d	H_0 (km s^{-1} Mpc^{-1})	Reference
B1608 + 656	0.6304	$71.0^{+2.9}_{-3.3}$	Wong et al. (2020)
RXJ1131 − 1231	0.295	$78.2^{+3.4}_{-3.4}$	”
HE 0435 − 1223	0.4546	$71.7^{+4.8}_{-4.5}$	”
SDSS 1206 + 4332	0.745	$68.9^{+5.4}_{-5.1}$	”
WFI2033 − 4723	0.6575	$71.6^{+3.8}_{-4.9}$	”
PG 1115 + 080	0.311	$81.1^{+8.0}_{-7.1}$	”
DES J0408 − 5354	0.597	$74.2^{+2.7}_{-3.0}$	Shajib et al. (2020)

where Δa_d is the difference in $a_{\rm app}$ between the void and control models, and t_d is the cosmic age at redshift z_d. The χ^2 contribution from all seven lenses is

$$\chi^2_{H_0,\rm lensing} = \sum_{i=1}^{7}\left(\frac{H^{\rm model}_{0,{\rm lensing},i} - H^{\rm obs}_{0,{\rm lensing},i}}{\sigma^{\rm lensing}_{{\rm obs},i}}\right)^2, \quad (70)$$

where $H^{\rm obs}_{0,{\rm lensing},i}$ and $\sigma^{\rm lensing}_{{\rm obs},i}$ are the derived Hubble constant and corresponding uncertainty for lens system i as reported by Shajib et al. (2020) or Wong et al. (2020), which we summarize in Table 2.

3.3.6 *Local Group peculiar velocity*

An important constraint on our model is the observed motion of the LG relative to the surface of last scattering. The observed CMB dipole indicates that the LG moves with a peculiar velocity of $v_{\rm LG} = 627 \pm 22\,{\rm km\,s^{-1}}$ towards Galactic coordinates $(l, b) = (276^\circ \pm 3^\circ, 30^\circ \pm 3^\circ)$ (Kogut et al. 1993).

To calculate the expected peculiar velocity in different parts of the void, we first need to consider the motion of the void as a whole. The void peculiar velocity $\boldsymbol{v}_{\rm void}$ arises from the time-integrated EFE. Using the approach stated in section 2.2 of Banik et al. (2018), we get that

$$a\left(t_0\right)\boldsymbol{v}_{\rm void} = \int_{t_i}^{t_0} \boldsymbol{g}_{\rm ext}\left(t\right) a\left(t\right) {\rm d}t\,, \quad (71)$$

where $\boldsymbol{g}_{\rm ext}$ is the external field, and the integrating factor a accounts for Hubble drag. The total velocity of a particle wrt. the CMB is

$$v^2_{\rm tot} = v^2_{\rm int} + v^2_{\rm void} + 2v_{\rm int}v_{\rm void}\cos\theta\,, \quad (72)$$

where $\boldsymbol{v}_{\rm int}$ is the ‘internal’ velocity of the particle relative to the void centre, and θ is the angle between $\boldsymbol{v}_{\rm void}$ and the void-centric position of the particle. A schematic representation of this situation is depicted in Fig. 3.

For numerical purposes, the simulated void is divided into cells. The volume of cell i is

$$V_i = \frac{\Delta\left(r^3\right)}{3} \times 2\pi\,\Delta\left(\cos\theta\right), \quad (73)$$

where Δr and $\Delta\theta$ are the radial and angular bin size, respectively. V_i is determined by the change in r^3 and $\cos\theta$ across the cell.

In order to quantify how the observed $v_{\rm LG} = 627\,{\rm km\,s^{-1}}$ affects the relative probability of a model, we define $f_{\rm motion}$ as the proportion of cells that satisfy

$$v_{\rm LG} - \epsilon \leq v_{\rm tot} < v_{\rm LG} + \epsilon\,, \quad (74)$$

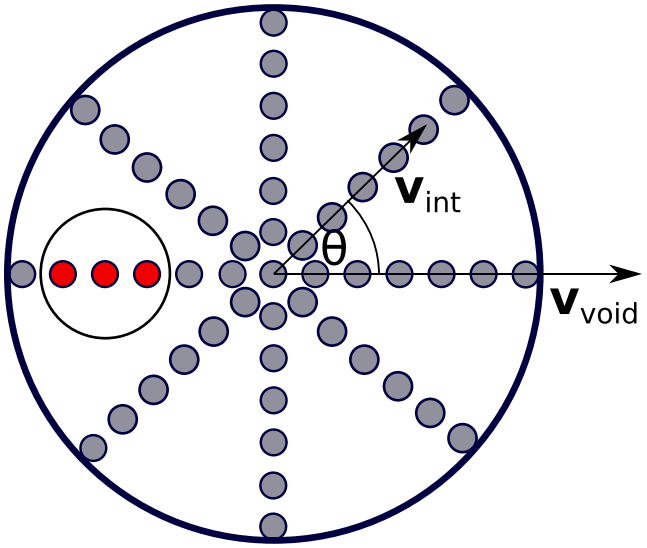

Figure 3. Schematic of the KBC void, which as a whole moves with velocity $v_{\rm void}$ due to the time-integrated EFE accounting for Hubble drag (equation 71, see also section 2.2 in Banik et al. 2018). The total peculiar velocity of a particle wrt. the CMB, $v_{\rm tot}$, is calculated by combining $v_{\rm void}$ with the internal velocity $v_{\rm int}$ of a particle relative to the void centre (equation 72). The inner circle illustrates the region in which $v_{\rm tot} \leq v_{\rm LG} = 627\,{\rm km\,s^{-1}}$. We estimate its volume by adding the volumes of the red cells.

where ϵ is a numerical parameter whose choice should have no bearing on our final results. To get a good balance between reducing numerical noise and increasing the accuracy, we choose $\epsilon = 50\,{\rm km\,s^{-1}}$. The resulting error should be of order $(50/630)^2$, which is acceptable given other uncertainties. On the other hand, $50\,{\rm km\,s^{-1}}$ is much larger than the change in $v_{\rm tot}$ between adjacent cells. We obtain similar results if $\epsilon = 30\,{\rm km\,s^{-1}}$ is used instead. Using this discretized scheme, we get that

$$f_{\rm motion} \equiv \sum_i V_i \div \frac{4\pi\left(nr^{\rm rms}_{\rm void}\right)^3}{3}\,, \quad (75)$$

where $r^{\rm rms}_{\rm void}$ is the rms size of the void, and n is a dimensionless factor of order unity that sets our prior expectation for how close we are to the void centre (we must be within a distance of $nr^{\rm rms}_{\rm void}$). Since observations suggest that we are located quite close to the centre (e.g. Keenan et al. 2013; Karachentsev & Telikova 2018), we adopt $n = 0.5$ for our probability calculations. We estimate the void size as

$$r^{\rm rms}_{\rm void} \equiv \sqrt{\frac{\int_0^\infty r^2\delta\left(r\right){\rm d}r}{\int_0^\infty \delta\left(r\right){\rm d}r}}\,, \quad (76)$$

with the void profile $\delta(r)$ found using equation (54). In practice, we cut off the integrals at a very large distance much beyond the possible extent of the void. Since $\delta \to 0$ at large r, this is sufficient to accurately estimate the limiting values of both integrals.

In Section 4.2, we apply a less sophisticated probability calculation where we assume that $v_{\rm tot}$ follows a Gaussian distribution. The extent to which the observed $v_{\rm LG}$ is an outlier to the simulated $v_{\rm tot}$ distribution is given by the proportion of the void volume with $v_{\rm tot} \leq v_{\rm LG}$. This allows an easier comparison with the other constraints.

Table 3 summarizes the here presented observational constraints, which are used to test our cosmological MOND model in the following section.

Table 3. Parameters used to quantify the tension of different MOND models with observations, along with a brief description. More information can be found in the indicated section.

Parameter	Description	Section
$\chi^2_{\delta_{\rm in}}$	Density contrast of the void in the redshift range $0.01 < z < 0.07$	Section 3.3.2
$\chi^2_{\delta_{\rm out}}$	Density contrast of the void between 600 Mpc and 800 Mpc	Section 3.3.2
$\chi^2_{H_0,\bar{q}_0}$	Hubble constant and acceleration parameter derived jointly from SNe with $0.023 \leq z \leq 0.15$	Section 3.3.4
$\chi^2_{H_0,\rm lensing}$	Hubble constant using time delays from seven strong lenses	Section 3.3.5
$f_{\rm motion}$	Fraction of void volume whose velocity wrt. the CMB is similar to that of the LG	Section 3.3.6

4 RESULTS OF MOND SIMULATIONS

In this section, we perform a detailed parameter study of our cosmological MOND models. This includes an estimation of the tension between our best-fitting model and observations of the local Universe. We focus on a void initialized with a Maxwell–Boltzmann profile (Section 3.2.1). Results for Gaussian and exponential starting profiles are presented in Appendix C. We first quantify the relative probabilities of different models (Section 4.1), and then check how well our best-fitting model agrees with observations (Section 4.2).

4.1 Relative probabilities of different models

The observational constraints can mostly be assumed to have a Gaussian distribution, allowing a standard χ^2-based analysis. This is due to the central limit theorem and the fact that e.g. many SNe are used in the study of Camarena & Marra (2020a). However, the expected distribution of $v_{\rm tot}$ (equation 72) is based on just one void, so we cannot assume Gaussianity. This constraint requires a more careful treatment, as explained in Section 3.3.6.

Combining the different constraints, we get that the joint probability of each model is

$$P(\text{Model} \mid \text{Observations}) \propto \left(\prod_i \frac{1}{\sigma_{\text{obs},i}}\right) \exp\left(-\frac{\chi^2}{2}\right) \times f_{\rm motion}\,, \quad \text{with} \tag{77}$$

$$\chi^2 = \chi^2_{\delta_{\rm in}} + \chi^2_{\delta_{\rm out}} + \chi^2_{H_0,\bar{q}_0} + \chi^2_{H_0,\rm lensing}\,. \tag{78}$$

We use i to label different observational constraints, each of which has uncertainty $\sigma_{\text{obs},\,i}$. The only model-dependent uncertainties are the density contrasts of the inner and outer parts of the KBC void, a consequence of the applied RSD correction (equation 57).

Fig. 4 shows the marginalized posterior distributions of the model parameters and parameter pairs based on 10^6 MOND models. The assumed external field strength has a significant impact on individual models. On the one hand, increasing the EFE typically makes the MONDian subsystem more Newtonian, suppressing the growth of structures. This results in less pronounced voids at the present time, and consequently a local Hubble constant and acceleration parameter closer to the Planck predictions. On the other hand, some EFE is required because otherwise structure formation would be too efficient, causing a very high local Hubble constant and acceleration parameter. These considerations restrict $g_{\rm ext}$ to the range $(0.024\text{–}0.076)\,a_0$ at 2σ confidence, with the most likely value being $0.04\,a_0$.

In contrast, the initial void size and strength are not strongly constrained – our analysis merely yields 2σ limits of $\alpha_{\rm void} = 10^{-5} - 2.91 \times 10^{-4}$ and $r_{\rm void} = (173.4\text{–}818.6)$ cMpc. This is because the local Hubble constant and acceleration parameter are estimated only for SNe in the redshift range $0.023 \leq z \leq 0.15$, which does not constrain the outer part of the void. Although some constraints are available at higher z from lensed quasars, the uncertainties of H_0 measured in this way are relatively large, allowing for a wide range of possible model parameters (Table 2).

The best-fitting model is that for which the joint probability (equation 78) becomes maximal. We mark this as a red dot in Fig. 4 and consider it our fiducial model. It has an initial void strength of $\alpha_{\rm void} = 3.76 \times 10^{-5}$ at $z = 9$, an initial void size of $r_{\rm void} = 228.2$ cMpc, and an external field strength of $g_{\rm ext} = 0.055\,a_0$, causing the void as a whole to move with $v_{\rm void} = 1586\,{\rm km\,s^{-1}}$. We analyse this particular model in more detail in the subsequent section.

The marginalized posterior distributions for MOND models with Gaussian and exponential initial profiles are shown in Appendix C. Those models still assume a time-independent EFE. In Section 5.2.2, we present and discuss an analysis demonstrating that allowing time-dependence of the EFE reveals no strong preference for a time-varying EFE, though some variation is expected on theoretical grounds.

4.2 The fiducial model

In the following, we discuss the results of our best-fitting (fiducial) model.

4.2.1 Density profile

We begin by studying the density contrast of the fiducial model at different times. This is plotted in the left-hand panel of Fig. 5. The void starts with an initial size of $r_{\rm void} = 228.2$ cMpc and a very small initial strength of $\alpha_{\rm void} = 3.76 \times 10^{-5}$ at $z = 9$. Equation (76) implies that $r^{\rm rms}_{\rm void} = r_{\rm void}\sqrt{3} = 395.2$ cMpc at that time. At present, the void has grown to a size of $r^{\rm rms}_{\rm void} = 528.7$ Mpc and has a density contrast of $\delta_{\rm in} = 0.172$ in the redshift range $0.01 < z < 0.07$. Correcting the corresponding observed density contrast from Keenan et al. (2013) by the model-dependent RSD correction factor $f^{\rm in}_{\rm model} = 1.38$ yields $\delta^{\rm in}_{\rm obs,corr} = 0.254 \pm 0.083$. This agrees with the simulated value at the 0.99σ level. The calculated density contrast between 600 and 800 Mpc is $\delta_{\rm out} = 0.050$, which also compares favourably with the RSD-corrected observed density contrast $\delta^{\rm out}_{\rm obs,corr} = -0.052 \pm 0.105$ ($f^{\rm out}_{\rm model} = 1.05$). The tension in this case is only 0.97σ.

The long-range modification to gravity in MOND causes structure formation to be much more efficient than in ΛCDM cosmology (e.g. Sanders 1999; Famaey & McGaugh 2012, and references therein). This can be seen in the right-hand panel of Fig. 5, which shows the density contrast of a 300 cMpc sphere for the best-fitting MOND model (the blue solid line) and two Newtonian models (the red lines, with shaded grey region between them) over cosmic time. The solid red and blue lines correspond to the same initial conditions, but end up with very different δ at the present time. As expected, Newtonian models with different initial δ show a similar pattern of structure growth since they are all in the linear regime. The density contrast

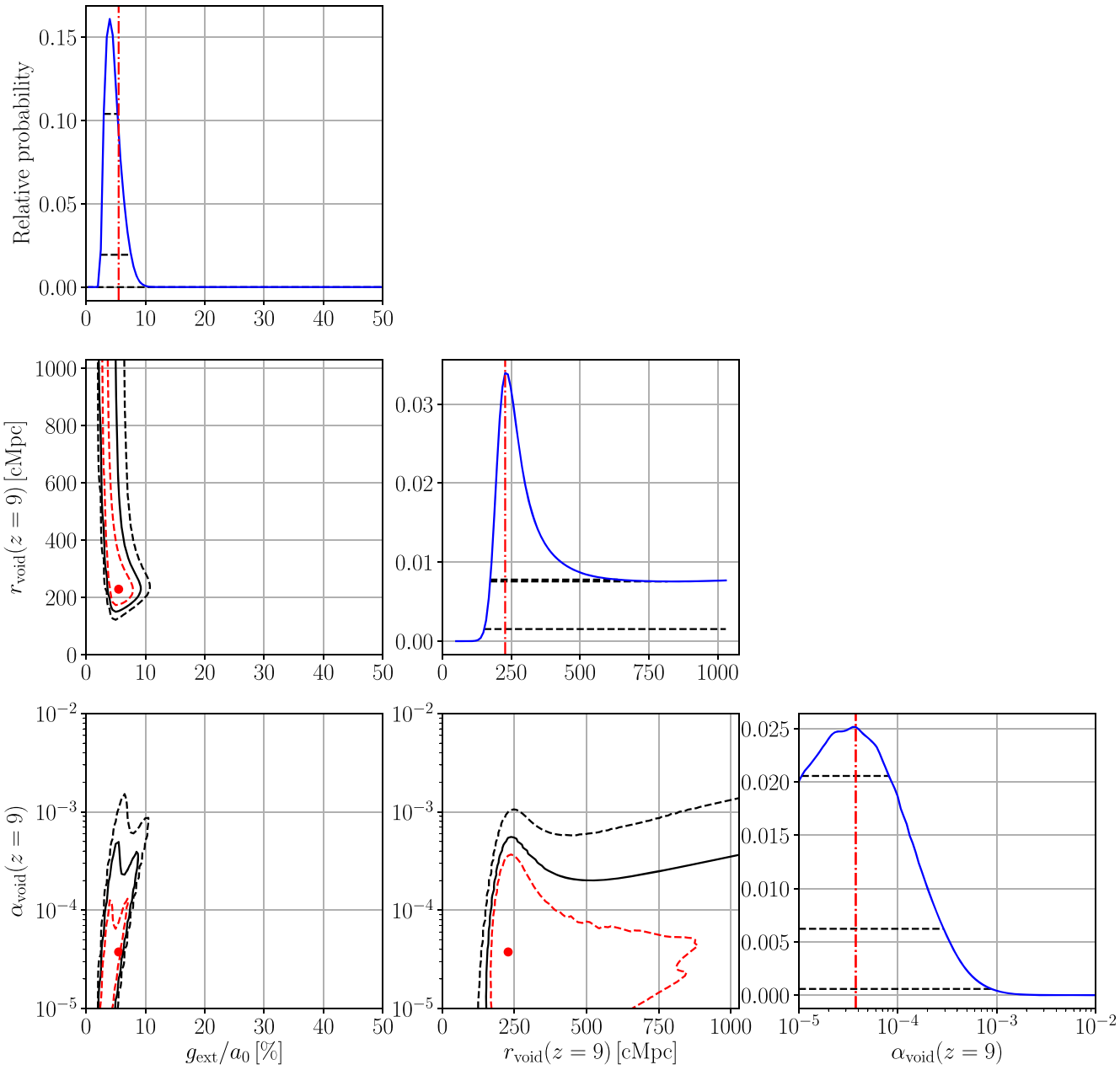

Figure 4. Marginalized posterior distribution of the indicated model parameters based on 10^6 Maxwell–Boltzmann MOND void models. The red dashed, black solid, and black dashed contours mark the 1σ, 2σ, and 3σ confidence levels, respectively. For 1D posteriors, these are shown using the horizontal black lines. The 1σ and 2σ lines are at almost the same level for $r_{\rm void}$. The red dot or vertical line marks the best-fitting model with an external field strength of $g_{\rm ext} = 0.055\,a_0$, and an initial void size and strength of $r_{\rm void} = 228.2$ cMpc and $\alpha_{\rm void} = 3.76 \times 10^{-5}$, respectively, at $z = 9$. This model is analysed in more detail in Section 4.2.

scales as $\delta \overset{\propto}{\sim} a^{3.8}$ and $\delta \overset{\propto}{\sim} a^{0.8}$ over the interval $0.3 \leq a \leq 0.7$ in our best-fitting MONDian model and equivalent Newtonian model, respectively. The ΛCDM scaling is slightly <1 because dark energy slows down the growth of structure at late times. The very rapid structure growth in our MOND model can be reduced by applying a higher EFE in the past. In the case of a time-dependent EFE with $n_{\rm EFE} = -1$ in equation (50), the growth rate reduces to $\delta \overset{\propto}{\sim} a^{3.3}$. The initial void strength must then be $13\times$ larger ($\alpha_{\rm void} = 4.98 \times 10^{-4}$) to compensate for the higher EFE in the past (the blue dot–dashed line in the right-hand panel of Fig. 5). Models with a time-dependent EFE are discussed further in Section 5.2.2.

4.2.2 *Hubble diagram*

Our fiducial model yields $H_0^{\rm model} = 76.15\,{\rm km\,s^{-1}\,Mpc^{-1}}$ and $\overline{q}_0^{\rm model} = 1.07$. This is consistent with the observations of Camarena & Marra (2020a) at the 84.20 per cent confidence level (only 0.20σ tension). The combined inference on both parameters is shown in Fig. 6, which demonstrates that the best-fitting models with Maxwell–Boltzmann, Gaussian, and exponential initial profiles are all consistent with these observations within 1σ. Thus, we show for the first time that the Hubble tension can be resolved in MOND. Note that the Planck parameters (the green dot) are in $\approx 4.39\sigma$ tension with these local observations.

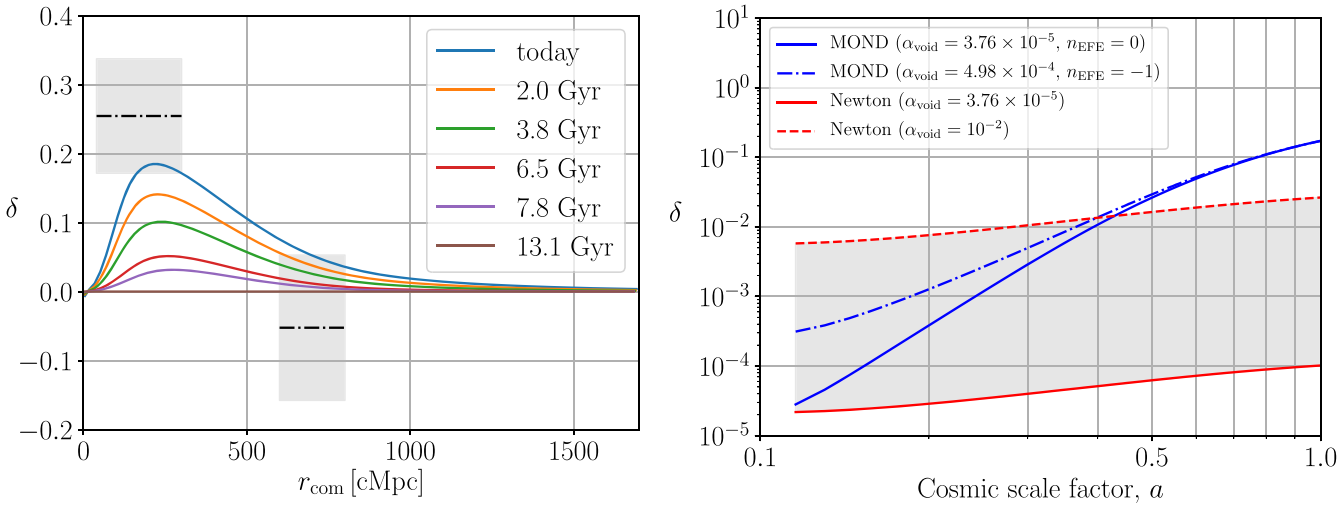

Figure 5. *Left*: Time evolution of the radial density profile of the fiducial MOND model ($g_{\rm ext} = 0.055\,a_0$, $r_{\rm void} = 228.2$ cMpc, $\alpha_{\rm void} = 3.76 \times 10^{-5}$). Different line colours refer to different lookback times, as indicated in the legend. The two black dot–dashed lines and the grey-shaded areas mark the RSD corrected observed density contrast of the KBC void, i.e. $\delta^{\rm in}_{\rm obs,corr} = 0.254 \pm 0.083$ between 40 and 300 Mpc, and $\delta^{\rm out}_{\rm obs,corr} = -0.052 \pm 0.105$ between 600 and 800 Mpc. *Right*: Evolution of the density contrast within a sphere of radius 300 cMpc for the fiducial MOND model (the blue solid line, $\delta \overset{\propto}{\sim} a^{3.8}$ for $0.3 \leq a \leq 0.7$), a MOND model with approximately the same δ and EFE today but with higher EFE in the past according to $n_{\rm EFE} = -1$ in equation (50) (the blue dot–dashed line, $\delta \overset{\propto}{\sim} a^{3.3}$ for $0.3 \leq a \leq 0.7$), and Newtonian models (the red lines, $\delta \overset{\propto}{\sim} a^{0.8}$ for $0.3 \leq a \leq 0.7$). The red solid line shows the Newtonian model with the same initial void parameters as the fiducial MOND model, while the red dashed line refers to another Newtonian model with the same $r_{\rm void}$ but where $\alpha_{\rm void} = 10^{-2}$.

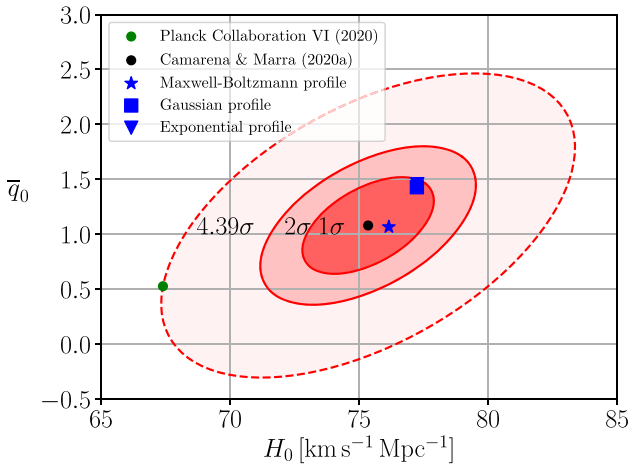

Figure 6. Combined inference on H_0 and $\overline{q}_0$ (the black dot and red error ellipses) derived jointly from Pantheon SNe in the redshift range $0.023 \leq z \leq 0.15$ (Camarena & Marra 2020a). The blue points show the results for the best-fitting MOND models with a Maxwell–Boltzmann (star), Gaussian (square), and exponential (triangle) void profiles. All three models are consistent with the observations at the 1σ confidence level. H_0 and $\overline{q}_0$ derived from a Gaussian and an exponential void profile are in both models almost the same and cannot be distinguished in the plot (the triangle and the square coincide). Note that the indicated tension with Planck results (the green dot) differs from the 4.54σ reported by Camarena & Marra (2020a) because we have not included the correlation coefficient between H_0 and $\overline{q}_0$ for Planck.

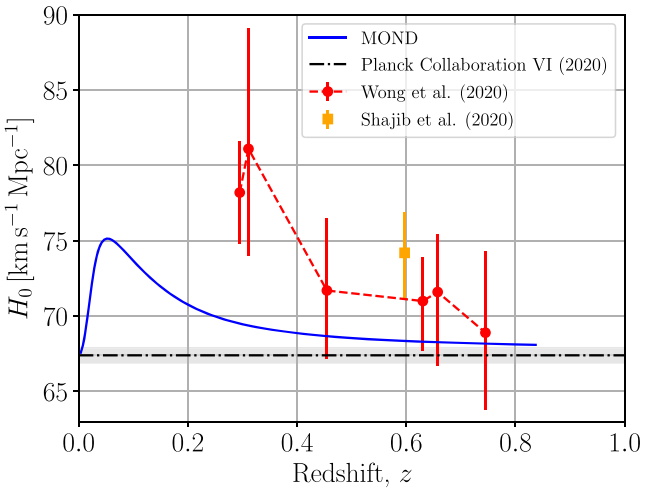

Figure 7. Hubble constant in dependence of redshift for the fiducial MOND model. The red data points are measurements of H_0 from lensed quasars by Wong et al. (2020) and Shajib et al. (2020) assuming a flat ΛCDM cosmology (see also our Table 2 and fig. A1 in Wong et al. 2020). The black horizontal dot–dashed line and its surrounding grey band marks $H_0^{\rm global} = 67.4 \pm 0.5$ km s^{-1} Mpc^{-1} (Planck Collaboration VI 2020).

Time delays from strong gravitational lenses also provide an important constraint on our model. We use Fig. 7 to show $H^{\rm lensing}_{0,\rm model}$ in dependence of redshift, allowing a comparison with measurements from seven lens systems (Section 3.3.5). Interestingly, our model systematically underestimates H_0 especially at low redshifts, causing a 2.05σ tension with the observations of Wong et al. (2020) and Shajib et al. (2020). We expect that this discrepancy is partly caused by void motion due to the EFE, though there is also some internal inconsistency between the void profile of Keenan et al. (2013) and the lensing Hubble data. In general, the latter are difficult to produce in any void model if the background $H_0^{\rm global} = 67.4$ km s^{-1} Mpc^{-1}, since it is difficult to imagine a local void having substantial effects at $z = 0.5$. We discuss these issues in more detail in Section 5.2. Although it is expected that strong lensing in MOND occurs similarly to standard cosmology (Section 3.3.5), we redo our analysis without constraints from lensing-based H_0 measurements in Section 5.2.1.

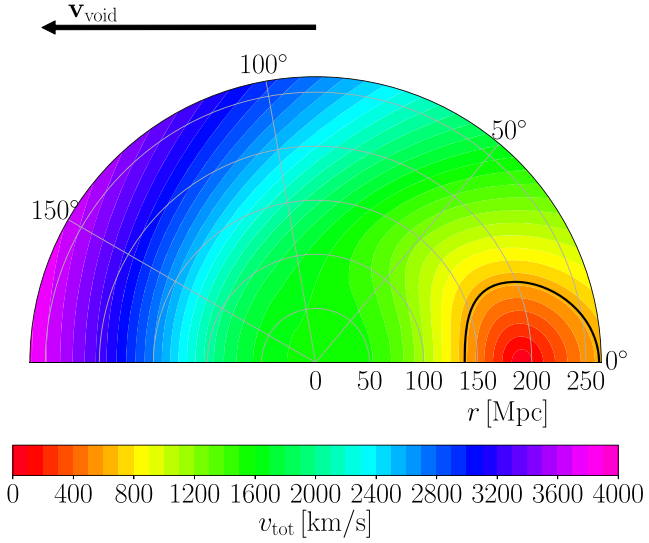

Figure 8. Total peculiar velocity (equation 72) map wrt. the CMB for the fiducial MOND model. The black arrow indicates the direction of the void motion $v_{\rm void}$. The black solid curve marks the region within which $v_{\rm tot} \leq 627\,{\rm km\,s^{-1}}$. The LG is probably near the right end of this curve because the observed radio dipole (Section 1.1) indicates that we are currently moving away from the void centre in the CMB frame. We show only half of the velocity map because $v_{\rm tot}$ is axisymmetric about $v_{\rm void}$. The here shown total peculiar velocities are $v_{\rm tot} \lesssim 0.01c$, justifying the use of non-relativistic equations for the void gravitational field (Section 3.2).

4.2.3 *LG peculiar velocity*

Our model yields the total peculiar velocity wrt. the CMB in different parts of the void, as mapped in Fig. 8. The entire void moves in the direction indicated by the arrow, which arises from the EFE (Section 3.2.2). Interestingly, the model allows for very high total and internal peculiar velocities, especially towards the void edge. We can also get partial or total cancellation between internal motions within the void and that of the void as a whole, creating a rather large region in which $v_{\rm tot} \leq v_{\rm LG} = 627\,{\rm km\,s^{-1}}$ (Kogut et al. 1993). This region is at a distance of $\approx$ (150–270) Mpc from the void centre, implying that the LG must be slightly off-centre. Applying equation (75) to find the fraction this region represents of the whole void, we estimate that the observed $v_{\rm LG}$ represents a 2.34σ outlier to the simulated $v_{\rm tot}$ distribution, which causes therewith the highest tension amongst the here used observational constraints.

4.2.4 *Overall agreement with observations*

Finally, we quantify the combined tension of our fiducial MOND model with local observations. As discussed earlier, most observables can be treated using a standard χ^2 approach, but additional care is needed for $v_{\rm LG}$. Thus, we quantify the likelihood of different (χ^2, $v_{\rm tot}$) combinations according to our fiducial model, with χ^2 found using equation (78). We can then quantify the extent to which the actually observed combination is unlikely.

In our model universe, the joint probability that the observables can be summarized by some (χ^2, $v_{\rm tot}$) combination is

$$P\,(\text{Observations}|\text{Best-fitting model}) = P\left(\chi^2\right) \cdot P_{\rm motion}\left(v_{\rm tot}\right)\,, \quad (79)$$

where $P(\chi^2)$ is the probability density function for a χ^2 distribution

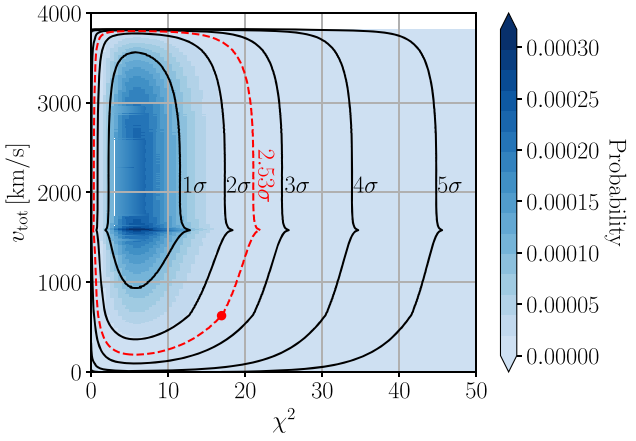

Figure 9. Joint probability of χ^2 and $v_{\rm tot}$, the total peculiar velocity wrt. the CMB, in the fiducial MOND model obtained in Section 4.1. The black contours show the indicated confidence levels. The red dot marks the total χ^2 of the fiducial model and $v_{\rm tot} = v_{\rm LG} = 627\,{\rm km\,s^{-1}}$. This is consistent with the model at the 1.14 per cent confidence level (the red dashed line), representing a 2.53σ tension. The sharp feature in each contour occurs when $v_{\rm tot} = v_{\rm void} = 1586\,{\rm km\,s^{-1}}$ (Section 3.3.6).

with 8 degrees of freedom (i.e. 11 observational constraints and three model parameters). $P_{\rm motion}(v_{\rm tot})$ is estimated from our simulation by splitting the volume into cells (Section 3.3.6) and assigning the volume in each cell to different bins in $v_{\rm tot}$, thereby building up a discretized picture of its distribution. This procedure does not assume that $v_{\rm tot}$ follows a Gaussian.

If our fiducial model is correct, χ^2 must arise solely from measurement errors, while the observed $v_{\rm LG}$ reflects our position within the void. This causes that χ^2 and $v_{\rm tot}$ have independent distributions, allowing them to be multiplied. We neglect the $22\,{\rm km\,s^{-1}}$ uncertainty in $v_{\rm LG}$ (Kogut et al. 1993) because this is much smaller than the $\approx 4000\,{\rm km\,s^{-1}}$ range in $v_{\rm tot}$ allowed by our model (Fig. 8).

We use Fig. 9 to show the joint (χ^2, $v_{\rm tot}$) distribution based on our fiducial model. This explains the local observations at the 1.14 per cent confidence level (2.53σ tension). Individual observational constraints are summarized and compared with observations in Table 4.

The χ^2 contributions from different constraints are visualized in Fig. 10 as a pie chart, which also shows the number of data points each constraint represents, and the corresponding level of tension. To facilitate a comparison with the other constraints, we use our previous estimate that $v_{\rm LG}$ is a 2.34σ outlier to the simulated $v_{\rm tot}$ distribution (Section 4.2.3). Therefore, we assign a χ^2 contribution of 2.34^2 to this constraint.

The best-fitting MOND models with a Gaussian and an exponential void profile agree with the local observations at the 0.45 per cent (2.84σ) and 0.34 per cent (2.93σ) confidence level, respectively (see also Appendix C). Thus, our best-fitting void model with a constant EFE cannot be rejected regardless of the initial density profile. The implications of our results are discussed in Section 5.2, which also looks at the overall picture of the νHDM model and the theoretical uncertainties of the here applied MOND approach (Section 5.2.3).

5 DISCUSSION

We discuss what our results in Sections 2 and 4 imply for ΛCDM and MOND cosmologies. This is followed by a consideration of

Table 4. Comparison of individual local Universe observables with our fiducial MOND model (Maxwell–Boltzmann profile, $g_{\rm ext} = 0.055\,a_0$, $r_{\rm void} = 228.2$ cMpc, $\alpha_{\rm void} = 3.76 \times 10^{-5}$, $v_{\rm void} = 1586\,{\rm km\,s^{-1}}$, $r_{\rm void}^{\rm rms} = 528.7$ Mpc, $n_{\rm EFE} = 0$). The last row shows the probability of a higher χ^2 given the number of degrees of freedom. We express this as the equivalent number of standard deviations for a 1D Gaussian (inverting equation 24). For $v_{\rm LG}$, we show the proportion of the void volume where $v_{\rm tot} \leq v_{\rm LG}$. Results for other void profiles are shown in Appendix C.

Parameter	$H_0^{\rm local}$ (km s^{-1} Mpc^{-1})	$\overline{q}_0^{\rm local}$	$H_0^{\rm lensing}$ (km s^{-1} Mpc^{-1})	$v_{\rm LG}$ (km s^{-1})	$\delta_{\rm in}$	$\delta_{\rm out}$
Observations	75.35 ± 1.68	1.08 ± 0.29	–	627	0.254 ± 0.083	-0.052 ± 0.105
MOND model	76.15	1.07	See Fig. 7	See Fig. 8	0.172	0.050
χ^2	0.34		14.66	–	0.99	0.94
Degrees of freedom	2		7	–	1	1
χ (1D Gaussian equivalent)	0.20		2.05	2.34	0.99	0.97

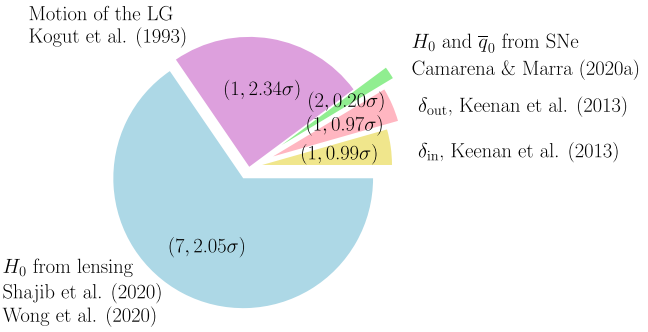

Figure 10. Pie chart showing the χ^2 contributions from different constraints (Table 4). The bracketed numbers show the number of degrees of freedom and corresponding level of tension for each constraint. The value for the motion of the LG is estimated based on the fraction of the void volume for which $v_{\rm tot} \leq v_{\rm LG} = 627\,{\rm km\,s^{-1}}$.

commonly proposed arguments claiming that a local underdensity cannot solve the Hubble tension (Section 5.3).

5.1 Assessing the tension for ΛCDM

Keenan et al. (2013) measured the *K*-band luminosity density as a function of redshift and found evidence for an underdensity around the LG with a radial extent of ≈ 300 Mpc (see their figs 9 and 10). They used the 2M++ catalogue (Lavaux & Hudson 2011), which covers ≈ 90 per cent of the sky based on photometric data from the 2MASS-XSC catalogue and redshift data from the 2MRS, 6DFGRS, and SDSS catalogues. From the $K_s < 13.36$ luminosity density, Keenan et al. (2013) estimated a relative density contrast of $\delta \equiv 1 - \rho/\rho_0 \approx 0.5$ in the redshift range $0.0025 < z < 0.067$ (pink down-pointing triangle in their fig. 11). Probing the luminosity density slightly deeper ($K_s < 14.36$) but only in the SDSS and 6DFGRS regions, they derived a slightly lower density contrast of $\delta = 0.46 \pm 0.06$ in the redshift range $0.01 < z < 0.07$ (the light blue dot in fig. 11 of Keenan et al. 2013). We used this value for the inner density contrast of the KBC void in order to minimize tension with the ΛCDM framework.

Using the MXXL simulation (Angulo et al. 2012), we calculated the density contrast for spheres with an outer radius of 300 Mpc and an inner hole of radius 40 Mpc around 10^6 vantage points at $z = 0$. We also took into account the sky coverage of the 2M++ survey by generating at each vantage point a random observing direction from which 90 per cent of the mock sky is covered (Section 2.1). The so-selected density fluctuations have an rms amplitude of 3.2 per cent. This is consistent with the prediction of the Harrison–Zeldovich spectrum (Harrison 1970; Zeldovich 1972) in combination with the early universe normalization of $\sigma_8 = 0.811 \pm 0.006$ (Planck Collaboration VI 2020). Since Keenan et al. (2013) used a fixed distance–redshift relation (see their section 4.7), we applied an RSD correction to the simulated density fluctuations. The rms fluctuation then became 4.8 per cent, with the individual values closely following a Gaussian of this width (Appendix A). Thus, the observational uncertainty of 6 per cent is larger than the expected cosmic variance.

Based on our analysis, the observed KBC void is in 6.04σ tension with standard ΛCDM cosmology and cannot be explained with cosmic variance (Section 2.2.1). This contrasts with Sahlén, Zubeldía & Silk (2016), who concluded that supervoids such as the KBC void are consistent with standard theory. However, for this they used a top-hat galaxy density radius of $210\,h^{-1}$ Mpc and a DM density contrast of $\delta = 0.15-0.2$. Their assumed δ describes a much less pronounced void than the observed density contrast derived from the 2M++ survey (Keenan et al. 2013).[8] Moreover, even a 15 per cent true underdensity on a 300 Mpc scale is very difficult to reconcile with ΛCDM due to the expected variance being only 3.2 per cent (Section 2.2.1). While it may be possible for such large voids to exist somewhere in the Universe, it would be unlikely for us to live inside one – unless they are more common.

5.1.1 *Hubble tension*

Several studies have already discussed a potential connection between the local void and the Hubble tension (e.g. Keenan et al. 2013; Enea 2018; Shanks et al. 2019; Kenworthy, Scolnic & Riess 2019). Indeed, if mass conservation is assumed, a large underdensity in the local number density of galaxies should also show up in the velocity field. However, given the expected cosmic variance in ΛCDM, Fig. 2 indicates that a $\approx 10\sigma$ density fluctuation would be necessary to explain the locally observed expansion rate within its 2σ confidence region ($H_0^{\rm local} = 73.8 \pm 1.1\,{\rm km\,s^{-1}\,Mpc^{-1}}$, Riess et al. 2019; Wong et al. 2020). The maximum plausible 5σ density fluctuation is still not enough to explain $H_0^{\rm local}$ at the 5σ level.

These findings are broadly consistent with Wu & Huterer (2017), who concluded that a void with $\delta = 0.8$ and a radius of $120\,h^{-1}$ Mpc could resolve the Hubble tension. Such a void would be in $\approx 20\sigma$ tension with ΛCDM (Kenworthy et al. 2019). While this by itself does not constitute an argument against such a large local underdensity, Wu & Huterer (2017) stated that observations disfavour it. Section 5.3 of our work contains a more detailed discussion of claimed problems with a local void solution to the Hubble tension.

Combining the mutually consistent SH0ES and H0LiCOW results, Wong et al. (2020) showed that the Hubble tension has now reached

[8] In ΛCDM, the RSD effect implies $\delta \approx \frac{2}{3}\delta_{\rm obs}$ (equation 22). Thus, $\delta_{\rm obs} = 0.46$ does not correspond to a true underdensity of $\delta = 0.2$.

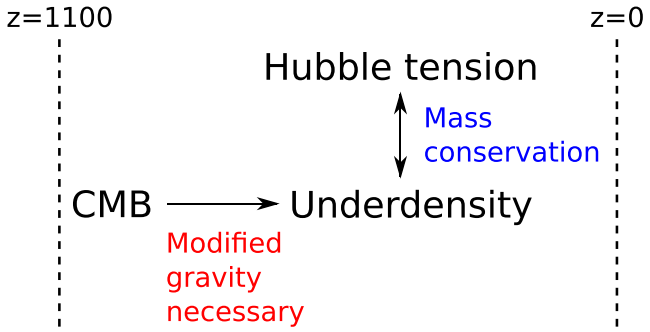

Figure 11. The KBC void in context. This large local underdensity and the Hubble tension can both be reconciled if mass is conserved in the Universe. However, such a large void cannot form out of the initial conditions of the CMB if the initial scale-invariant power spectrum (Harrison 1970; Zeldovich 1972) is preserved. In particular, the existence of the KBC void within the ΛCDM framework is ruled out at 6.04σ, as demonstrated in Section 2.2. Thus, modified gravity is required to explain low redshift observables (Section 4.2) if the initial conditions at $z = 1100$ are indeed set by the CMB (Section 5.3.8). Importantly, *any* solution must simultaneously solve both the Hubble and underdensity tensions in order to conserve mass.

the 5.3σ level. Thus, both the KBC void and the Hubble tension falsify ΛCDM at $>5\sigma$ significance. The most likely explanation in the context of standard theory is that both are caused purely by measurement errors, since there is less cosmic variance than observational uncertainty in both the KBC data and the H_0 measurement. This is especially true for the latter – equation (18) shows that density fluctuations of 3.2 per cent would impact $H_0^{\rm local}$ by only $0.4\,{\rm km\,s^{-1}\,Mpc^{-1}}$ (see also Wojtak et al. 2014). Since galaxy counting and measurements of the local Hubble constant face rather different observational challenges, the measurement errors would be independent, yielding a combined tension of 7.75σ. Using a more rigorous estimation that allows for cosmic variance results in a 7.09σ falsification of the ΛCDM paradigm (Section 2.2.3).

Importantly, *any* cosmological model which solves the Hubble tension without addressing the void (or vice versa) would violate the assumption of mass conservation in the Universe. Thus, early dark energy models (e.g. Hill et al. 2020; Khoraminezhad et al. 2020) which simply increase H_0 at the background level by ≈ 10 per cent would overestimate the local H_0 by about this much once the observed KBC void is taken into account (Section 1.1). Perhaps the most important implication of the KBC void is that the Planck value of H_0 is probably correct at the background level, since any attempt to substantially change it would likely cause the void-corrected local value to disagree with local observations if mass is conserved in the Universe.

Therefore, the KBC void is a plausible explanation for the Hubble tension if we can preserve a Planck background cosmology but enhance the cosmic variance. A schematic that considers the KBC void in a broader context is presented in Fig. 11. Starting from the initial conditions of the CMB at $z = 1100$ and assuming the scale-invariant Harrison–Zeldovich power spectrum to be valid at that time, we have shown that the existence of a KBC-like void at present is virtually impossible in a standard context. This indicates that a scale-invariant power spectrum is violated today – order unity fluctuations on a 10 Mpc scale (e.g. Mantz et al. 2015) do not give way to 3 per cent fluctuations on a 300 Mpc scale. *This is a very strong hint that the gravitational inverse square law has to break down.* Thus, the spatial distribution of matter on both an 8 Mpc scale (Peebles & Nusser 2010) and on an ≈ 1 Gpc scale (this work) suggest a long-range enhancement to gravity.

5.2 Assessing the tension for MOND

MOND (Milgrom 1983) is a low-acceleration modification to gravity originally designed to explain galaxy rotation curves without CDM. It has enjoyed a great deal of predictive success in this regard (Section 1.3). Therefore, extrapolating MOND from kpc to Gpc scales could be a promising way to address large-scale challenges for standard cosmology such as massive high-redshift galaxy clusters (e.g. El Gordo, Katz et al. 2013) and supervoids.

In this context, we study the possible origin of the KBC void from small initial density fluctuations, and its impact on the local Hubble constant. Unfortunately, we do not presently have a large enough cosmological *N*-body or hydrodynamical MOND simulation to quantify the likelihood of the KBC void, as done for the ΛCDM framework with the MXXL simulation (Section 2).

We therefore used the νHDM framework (Section 3.1) to develop a semi-analytical MOND simulation in which the expansion history is a standard flat background cosmology consistent with the latest Planck data (Planck Collaboration VI 2020) – which should be a good approximation also in MOND (Section 3.1.1). We applied MOND only to the density deviations from the cosmic mean (Section 3.1.4). In Section 5.2.3, we discuss the possibility of a non-trivial coupling between density perturbations and the background.

Our main MOND models assume an initial Maxwell–Boltzmann density profile motivated by the radial density distribution of the Local Volume. Karachentsev & Telikova (2018) showed that the matter density within a sphere of $r = 40$ Mpc ($r = 135$ Mpc) around the LG is only $\Omega_{\rm m,\,loc} = 0.09{-}0.14$ ($\Omega_{\rm m,\,loc} = 0.05{-}0.16$). This is $\approx 2{-}3\times$ lower than the cosmic mean density measured by Planck Collaboration VI (2020), confirming the existence of a large local underdensity (Section 1.1). Karachentsev & Telikova (2018) also showed that the density increases inwards for heliocentric distances $\lesssim 40$ Mpc (see their fig. 3), justifying our choice of a Maxwell–Boltzmann void profile (Section 3.2.1). In addition, we also run void models initialized with a Gaussian and an exponential profile (Appendix B). In all cases, the void profiles are parametrized by an initial void size and strength at $z = 9$. The initial void strengths range from $\alpha_{\rm void} = 10^{-5}{-}10^{-2}$, with the lower limit based on the observed density fluctuations in the CMB. By the time that $z = 9$, we expect significantly larger perturbations. Our upper limit on $\alpha_{\rm void}$ is sufficient to capture the range of models preferred by our analysis (Section 5.2.2).

The EFE is strongly constrained in our models because it affects the formation of cosmic structure and thus internal velocities within the void, in addition to the void's motion as a whole (Section 3.3.6). Models with a very small EFE create extremely deep and extended voids, which disagrees with the density contrast of the KBC void – especially for its outer region. This also results in a much larger local Hubble constant than observed. Increasing the EFE leads to $v_{\rm void} \gg v_{\rm LG}$, so the observed $v_{\rm LG}$ can only be explained by nearly complete cancellation with a large $v_{\rm int}$. However, a strong EFE makes the MONDian system more Newtonian and suppresses therewith the growth of structure. Consequently, models with a very high EFE produce very shallow voids and a local Hubble constant similar to its global value, causing that $v_{\rm int}$ is not large enough to cancel $v_{\rm void}$.

Our analysis for the Maxwell–Boltzmann profile restricts $g_{\rm ext}$ to the range $(0.030{-}0.053)a_0$ at the 1σ confidence level. Models with a Gaussian and an exponential void profile prefer a slightly larger EFE, i.e. $(0.054{-}0.094)a_0$ (Fig. C1) and $(0.054{-}0.092)a_0$ (Fig. C2) at

the 1σ confidence level, respectively. This is because the Maxwell–Boltzmann profile reduces δ near the void centre and therewith slows down the internal peculiar velocities of individual particles within the void. Thus, a lower EFE is required to achieve $v_{\rm tot} \leq v_{\rm LG} = 627\,{\rm km\,s^{-1}}$ over a large part of the void.

Our analysis rules out models without an EFE, which is in any case a logical consequence of the non-linearity inherent to Milgrom's law of gravity (Milgrom 1986). Observationally, MOND without the EFE is strongly disfavoured by the velocity distribution of wide binary stars in the Solar neighbourhood (Pittordis & Sutherland 2019). The EFE is also necessary to explain the internal velocity dispersions of dwarf galaxies (Section 1.3). We discuss the time dependence of the EFE in more detail in Section 5.2.2.

In contrast to the EFE, Fig. 4 indicates that the initial void size and strength are not strongly constrained by observations. Thus, other initial void parameters could in principle also yield reasonable results at the present time. In particular, our analysis of Maxwell–Boltzmann voids yields 1σ confidence intervals on $r_{\rm void}$ and $\alpha_{\rm void}$ of (173.9–636.9) cMpc and $(1.07-8.12)\times10^{-5}$, respectively. Models with Gaussian or exponential initial profiles allow for larger voids, but with a similar void strength (Appendix C). There are two main reasons why both void parameters are only weakly constrained by local observations. First of all, H_0 and $\overline{q}_0$ are derived from data in the redshift range $0.023 \leq z \leq 0.15$ and constrain therewith only the inner and not the outer part of the void. Secondly, the uncertainties of H_0 measured from strong lens systems are relatively large, which allows for a wide range of possible void behaviours in the outskirts.

We found that our best-fitting Maxwell–Boltzmann MOND model requires an EFE of $g_{\rm ext} = 0.055\,a_0$, an initial void size of $r_{\rm void} = 228.2\,{\rm cMpc}$, and an initial void strength of $\alpha_{\rm void} = 3.76\times10^{-5}$ at $z = 9$. The EFE causes a bulk flow of $v_{\rm void} = 1586\,{\rm km\,s^{-1}}$ at $z = 0$. Our fiducial model explains the local observations listed in Table 3 at the 1.14 per cent confidence level (2.53σ tension). Fig. 4 shows that models with somewhat different initial conditions also provide reasonable results.

The rms density fluctuation in the total matter field at the CMB ($z = 1100$) is $\delta_{\rm rms} \approx 10^{-4}$ (Section 3.1.3), which implies $\delta_{\rm rms} \approx 10^{-2}$ at $z = 9$ for a ΛCDM cosmology. Thus, $\alpha_{\rm void}$ of our best-fitting model is much lower than the expected cosmic variance in ΛCDM. This could make KBC-like voids very common in the universe, potentially conflicting with the observed foreground lensing of the CMB (Section 5.3.1). This problem could be alleviated if the EFE was stronger in the past (Section 5.2.2), or if the peculiar accelerations and the Hubble flow are coupled (Section 5.2.3) – both would slow down the growth of structure. It would be highly interesting to quantify the existence of KBC-like voids in a large cosmological MONDian *N*-body simulation, especially if it accounts for the HFE in some way.

As already shown in several previous studies (e.g. Sanders 1998; Famaey & McGaugh 2012, and references therein), we affirm that structure formation is much more efficient in MOND compared to the Newtonian case (right-hand panel of Fig. 5). Applying an RSD correction based on the best-fitting model, the observed underdensity is 25.4 ± 8.3 per cent (-5.2 ± 10.5 per cent) in the inner (outer) part of the KBC void. The enhanced growth of structure allows our fiducial model to match these constraints at the 0.99σ (0.97σ) confidence level. In contrast, the KBC void rules out the ΛCDM framework at 6.04σ (Section 2.2.1).

In MOND, the long-range modification to gravity causes a very shallow decrease of the density contrast with distance, causing our model to systematically underestimate the density at the outer part of the KBC void as derived from the *K*-band luminosity data of Keenan et al. (2013). However, observational uncertainties on the density contrast there are still relatively large. Future surveys would be necessary to more precisely measure the density profile beyond ≈ 400 Mpc. This may provide an important test of our model because the radial density profile should be sensitive to the underlying growth rate.

Interestingly, Angus & Diaferio (2011) found some evidence for large voids with a diameter of $250\,h^{-1}$ Mpc in their $512\,h^{-1}$ cMpc *N*-body cosmological MOND simulation with massive neutrinos. Although both large voids and massive galaxy clusters are expected in a MOND cosmology (e.g. Sanders 1998), it is not fully clear if those were formed artificially due to the low particle resolution (Angus et al. 2013). Their simulations also assume no coupling between peculiar accelerations and the Hubble flow (i.e. $\beta = 0$ in equation 8 of Sanders 2001). As discussed further in Section 5.2.3, a coupling to the Hubble flow would suppress the formation of massive voids and clusters on scales $\gtrsim 100$ Mpc. Therefore, it would be very valuable to revisit their cosmological simulations with a higher particle resolution and an AMR grid code such as PHANTOM of RAMSES (Teyssier 2002; Lüghausen et al. 2015). Such MOND simulations would require very large box sizes in order to include large-scale modes and the resulting EFE on smaller regions (Section 3.1.4). For very long modes, light traveltime effects could be important such that a relativistic code is required. This could be based on the model of Skordis & Złośnik (2019).

A unique characteristic of our void model is the prediction of very high total peculiar velocities, especially towards the void edge in the direction parallel to $\boldsymbol{g}_{\rm ext}$. In the best-fitting model, the void as a whole moves with a peculiar velocity of $v_{\rm void} = 1586\,{\rm km\,s^{-1}}$ due to the EFE from source(s) beyond the void (i.e. at $z \gtrsim 0.15$). Thus, our model predicts a sphere centred on the LG should have a large bulk flow of $\approx 1000\,{\rm km\,s^{-1}}$ in a similar direction to $\boldsymbol{g}_{\rm ext}$. This is qualitatively similar to the results of previous νHDM simulations (Katz et al. 2013). Interestingly, some evidence for a large bulk flow has been found (Kashlinsky et al. 2008; Kashlinsky, Atrio-Barandela & Ebeling 2011). We discuss this further in Section 5.3.2.

Partial cancellation between the void's motion and internal motions within it leads to a region $\approx$ (150–270) Mpc from the void centre in which $v_{\rm tot} \leq v_{\rm LG} = 627\,{\rm km\,s^{-1}}$. The fraction that this volume represents of the whole void corresponds to a 2.34σ event, implying that the LG is statistically not at a special position in the void. Note that the LG motion causes the highest tension amongst our constraints (Table 4 and Fig. 10).

Our fiducial model gives an apparent expansion history very close to ΛCDM (Fig. 12), but with local Hubble constant $H_0^{\rm model} = 76.15\,{\rm km\,s^{-1}\,Mpc^{-1}}$ and acceleration parameter $\overline{q}_0^{\rm model} = 1.07$ in the redshift range $0.023 \leq z \leq 0.15$. This agrees with the observations of Camarena & Marra (2020a) at the 84.20 per cent confidence level (0.20σ tension). The best-fitting models with a Gaussian and an exponential void profile agree at the 0.83σ and 0.89σ level, respectively (Fig. 6). *Thus, we showed for the first time that the KBC void can arise in MOND and solve therewith the Hubble tension.*

The locally observed acceleration parameter $\overline{q}_0 = 1.08\pm0.29$ (Camarena & Marra 2020a) disagrees with the ΛCDM expectation of $\overline{q}_{0,\Lambda{\rm CDM}} = 0.53$ (Planck Collaboration VI 2020) at the 1.9σ level. In combination with the H_0 discrepancy between these studies, this would falsify ΛCDM at 4.54σ confidence (see also Fig. 6). Interestingly, $\overline{q}_0 > 1$ is not possible for a standard background cosmology. The locally observed high Hubble constant and acceleration parameter provide compelling evidence that the Hubble tension is caused by a local effect like the KBC void. This addresses the concern of Kenworthy et al. (2019) that the KBC void is not evident in the SNe distance–redshift relation (Section 5.3.6) – both the first and

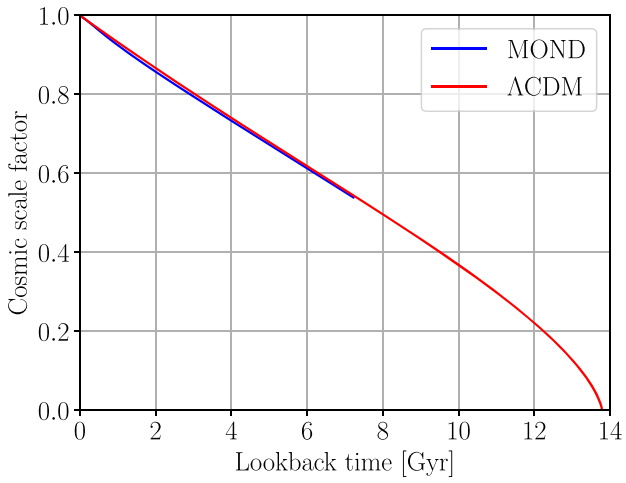

Figure 12. Time dependence of the cosmic scale factor in ΛCDM (red) and the apparent scale factor in our fiducial MOND model (blue). This model has a Maxwell–Boltzmann initial profile with $r_{\rm void} = 228.2\,{\rm cMpc}$ and $\alpha_{\rm void} = 3.76 \times 10^{-5}$ embedded in a constant ($n_{\rm EFE} = 0$) external field of strength $g_{\rm ext} = 0.055\,a_0$.

second derivatives of the distance–redshift relation very much point to a local void. Observationally, a discrepancy could also appear as a third order effect in the jerk parameter $j \equiv a^2\dddot{a}/\dot{a}^3$, but given the already large uncertainty of $\overline{q}_0$, it would be difficult to measure j_0 precisely.

As discussed in Section 3.3.5, strong lensing does not occur in the MOND regime and so should be similar to in ΛCDM cosmology (Sanders 1999). Thus, our main analysis includes H_0 constraints from seven strongly lensed quasars as obtained by Shajib et al. (2020) and Wong et al. (2020). The latter work applied a blinded analysis (described in their section 3.6) and found that H_0 decreases as a function of lens redshift at 1.9σ significance (see their appendix A). H_0 becomes consistent with Planck expectations at $z \gtrsim 0.5$, well beyond the void. This is again a very strong indication that the Hubble tension is driven by a local environmental effect such as the KBC void. A decrease of the inferred H_0 with redshift is also apparent in our MOND model (Fig. 7) and is a generic consequence of any local resolution to the Hubble tension. The redshift dependence of $H_{0,\rm lensing}^{\rm model}$ depends mainly on the density profile of the void. For our fiducial model, the combined tension with all seven lensing-based H_0 measurements is $\chi^2 = 14.66$, which represents 2.05σ tension for 7 degrees of freedom. In the case of a Gaussian and an exponential void profile, this would reduce to 1.76σ and 1.83σ, respectively, because the best-fitting models have a larger void (Appendix C). This discrepancy with the lensing data is mainly caused by a systematic underestimation of H_0 by our models, especially for the two lowest redshift lenses RXJ1131 − 1231 at $z = 0.295$ and PG 1115 + 080 at $z = 0.311$ (Section 5.2.1).

The high values of H_0 at $z \gtrsim 0.4$ are also conspicuous because according to Keenan et al. (2013) the density should have reached the cosmic mean already at $z \approx 0.2$ (see their fig. 11). Consequently, we would expect that H_0 obtained from lenses located at $z \gtrsim 0.4$ must be very similar to the Planck prediction. The H_0 values from the four highest redshift lenses of Wong et al. (2020) give a median (mean) of $71.3\,{\rm km\,s^{-1}\,Mpc^{-1}}$ ($70.8\,{\rm km\,s^{-1}\,Mpc^{-1}}$), which is $3.9\,{\rm km\,s^{-1}\,Mpc^{-1}}$ ($3.4\,{\rm km\,s^{-1}\,Mpc^{-1}}$) higher than the Planck prediction. This systematic offset can be reduced if the background H_0 is underestimated due to errors in the Planck measurements caused by intergalactic dust (Yershov et al. 2020; see also Vavryčuk 2018, 2019). We discuss this issue further in Section 5.3.8. It is also possible that there is some systematic offset in H_0 measurements using strong lensing time delays (Kochanek 2020). Since we assume mass conservation in our models, this discrepancy cannot be fully resolved in our analysis − the algorithm searches for a compromise between the KBC and lensing data. It seems that there is some internal inconsistency between them. A strong test of our model would be to infer H_0 very accurately from nearby and high-redshift lens systems. The model predicts that H_0 should be almost identical to the Planck prediction at $z \gtrsim 0.9$. However, a substantial anomaly is expected for a lens at $z = 0.1$. A measurement here would nicely complement the SNe results of Camarena & Marra (2020a), which go out to $z = 0.15$.

5.2.1 *Excluding strong lensing time delays*

Although strong lensing in MOND should be similar to the ΛCDM framework (Sanders 1999), the H_0 measurements from strong lensing could be affected by the EFE on the void. This requires a better understanding of its origin. We have assumed that the EFE in our simulations affects the void as a whole, implying that it must be sourced by something beyond the void, i.e. at $z \gtrsim 0.15$. This approach would be valid for deriving H_0 and $\overline{q}_0$ from SNe data in the range $0.023 \leq z \leq 0.15$ since the EFE would similarly move everything in this region. However, this may not be true for even the lowest redshift lens as its $z = 0.295$ (Table 2). If the EFE is sourced by something at lower z, it would move the void − but not the lens.

In this context, we consider in more detail the geometry of the void and the sky positions of the lenses. The observed CMB dipole shows that the LG moves with a velocity of $627\,{\rm km\,s^{-1}}$ wrt. the CMB towards Galactic coordinates ($276^\circ \pm 3^\circ$, $30^\circ \pm 3^\circ$), which roughly matches the direction of the radio dipole (Section 1.1). Thus, the LG motion wrt. the CMB frame is probably directed away from the void centre (see also Fig. 8). Interestingly, the two lowest redshift lens systems (RXJ1131 − 1231 and PG 1115 + 080) are located at Galactic coordinates (274.4°, $+45.9^\circ$) and (249.9°, $+60.6^\circ$), respectively, which roughly coincides with the directions of the CMB and radio dipoles. Thus, both lenses are also most likely located on the opposite side to the void centre. Assuming these lenses are not affected by the EFE on the void, this would cause an extra redshift. Consequently, a larger Hubble anomaly would be expected than calculated thus far.

Relative to the CMB dipole, the direction to each lens subtends an angle θ, where $\cos\theta = 0.96$ and $\cos\theta = 0.82$ for RXJ1131 − 1231 and PG 1115 + 080, respectively. The impact on the measured H_0 from these two low-z lenses can be estimated as

$$\Delta H_0 = \frac{\Delta a}{\Delta t}\,, \quad \text{with} \tag{80}$$

$$\Delta a = \frac{a\,v_{\rm void,r}}{c}\,, \tag{81}$$

$$v_{\rm void,r} \equiv v_{\rm void}\cos\theta\,, \tag{82}$$

where a is the scale factor at which the lens is observed, and Δt is the corresponding lookback time. Thus, assuming the lenses are unaffected by the EFE, H_0 derived from the lens systems RXJ1131 − 1231 and PG 1115 + 080 would be overestimated by 1.10 and $0.88\,{\rm km\,s^{-1}\,Mpc^{-1}}$, respectively. This would only slightly reduce the tension with our best-fitting models. Therefore, the sharp rise in H_0 values for the two lowest redshift lenses cannot be fully accounted for with the EFE and is still hard to explain. Additional lenses are needed to confirm this feature.

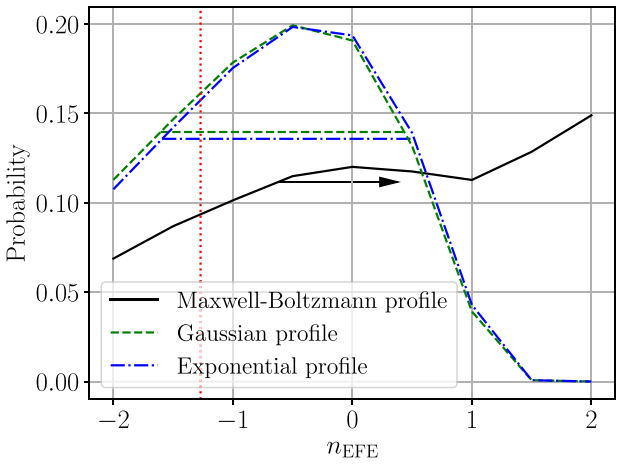

Figure 13. Marginalized posterior distribution of the time dependence of the external field ($n_{\rm EFE}$ in equation 50), based on 9×10^6 MOND models where the initial void profile is Maxwell–Boltzmann (solid black), Gaussian (dashed green), or exponential (dot–dashed blue). The black arrow and the horizontal lines indicate the 1σ confidence interval for each profile. The red-dotted vertical line marks the expected $n_{\rm EFE} = -1.27$ (equation 83), which we derive from the $g_{\rm ext}$ of our fiducial model and the expected gravitational acceleration at recombination.

We address the possible impact of the EFE on the lensing-based H_0 measurements by redoing the analysis for our Maxwell–Boltzmann model without the constraints from strong lensing time delays. In this case, the best-fitting model has $g_{\rm ext} = 0.050\,a_0$ causing $v_{\rm void} = 1442\,{\rm km\,s^{-1}}$, $r_{\rm void} = 208.4\,{\rm cMpc}$, and $\alpha_{\rm void} = 2.15 \times 10^{-5}$. This model yields $H_0^{\rm model} = 76.47\,{\rm km\,s^{-1}\,Mpc^{-1}}$ and $\overline{q}_0^{\rm model} = 1.21$ (0.26σ combined tension), $\delta_{\rm in} = 0.167$ ($\delta^{\rm in}_{\rm obs,corr} = 0.258 \pm 0.082$; 1.11σ), and $\delta_{\rm out} = 0.037$ ($\delta^{\rm out}_{\rm obs,corr} = -0.038 \pm 0.104$; 0.73σ). The fraction of the void with $v_{\rm tot} \leq v_{\rm LG}$ represents a 2.25σ tension. The model explains all these local observations at the 1.96σ (5.0 per cent) confidence level. Thus, excluding the lensing data allows for a somewhat better overall fit, but has little effect on the preferred model parameters.

5.2.2 Structure formation and external field history in MOND

Since the EFE acting on a MONDian subsystem depends on surrounding structure and therewith on the scale factor, we made in Section 3.2.2 the ansatz $g_{\rm N,ext}(t) = g_{\rm N,ext}(t_0)\, a^{n_{\rm EFE}}(t)$. So far, we have restricted attention to the case $n_{\rm EFE} = 0$. Letting $n_{\rm EFE}$ vary in the range $(-2, 2)$, Fig. 13 shows its marginalized posterior based on 9×10^6 different models. In the case of a Maxwell–Boltzmann profile, the analysis yields $n_{\rm EFE} > -0.62$ at the 1σ confidence level. Gaussian and exponential initial profiles allow for $(-1.60, +0.43)$ and $(-1.59, +0.52)$ at the 1σ level, respectively. Thus, only the Maxwell–Boltzmann profile prefers a weaker EFE in the past, while the other profiles prefer the opposite. A time-independent EFE ($n_{\rm EFE} = 0$) – assumed for all our models thus far – lies within the 1σ range for all three considered void profiles. This justifies our assumption of a time-independent EFE in our main analysis.

The marginalized posterior distributions for $n_{\rm EFE}$ and the initial $\alpha_{\rm void}$ are shown in Fig. 14. As expected, a stronger EFE in the past ($n_{\rm EFE} < 0$) requires a deeper initial void. In particular, values of $\alpha_{\rm void}$ up to $\approx 10^{-3}$ are now allowed, contrary to the case where we fix $n_{\rm EFE} = 0$ (Fig. 4). This would be closer to the expected density fluctuations in ΛCDM when $a = 0.1$, since the $\approx 10^{-5}$ density fluctuations in the CMB should have grown $\approx 100\times$. This is only mildly disfavoured by our analysis.

We can estimate the external field history based on the parameters of our fiducial model and the gravitational acceleration at recombination:

$$n_{\rm EFE} \approx \frac{\ln g_{\rm N}(t_0) - \ln g_{\rm N}\left(t_{\rm CMB}\right)}{\ln a(t_0) - \ln a\left(t_{\rm CMB}\right)}, \tag{83}$$

where $t_{\rm CMB} = 380\,{\rm kyr}$, and $t_0 = 13.8\,{\rm Gyr}$. As explained in Section 3.1.3, $g_{\rm N}\left(t_{\rm CMB}\right) \approx 21\,a_0$, causing MOND to have only a very small effect before recombination. Since our fiducial model prefers an external field of $0.055\,a_0$, we use this as our estimate of $g(t_0)$, which via equation (8) yields $g_{\rm N}(t_0) = 0.0029\,a_0$. Comparing the expected large-scale Newtonian gravitational fields at these times gives $n_{\rm EFE} = -1.27$ (the red vertical line in Fig. 13). This is consistent with the marginalized posterior distribution for the Gaussian and exponential profile models at the 1σ level and for the Maxwell–Boltzmann models at the 2σ level. The Gaussian and exponential models prefer $n_{\rm EFE} \approx -0.5$.

Equation (83) implies $n_{\rm EFE} = -1.27$, which is a faster decline than the $n_{\rm EFE} = -1$ suggested by equation (37) for linear perturbations in the matter-dominated era (Section 3.1.3). This could be due to the effect of dark energy, which is not taken into account in equation (37) as it only dominates at $z \lesssim 0.8$. Since dark energy slows down the growth of structure, $n_{\rm EFE}$ would be shifted to more negative values – if the fractional density perturbations are frozen in co-moving coordinates, we would get $n_{\rm EFE} = -2$.

Though it is beyond the scope of our semi-analytic study, we mention briefly that as structure grows in a MONDian universe, it imposes an external field on surrounding structures, thereby hampering their growth. This leads to structure formation in different regions becoming mutually correlated. In particular, since MOND gravity declines as $1/r$ whereas Newtonian tides scale as $1/r^3$ (there being no EFE), any structure in a Milgromian universe is affected by much more distant structures compared to the Newtonian case. This makes it difficult to conduct a MOND simulation with sufficiently large volume to satisfy the CP.

5.2.3 Theoretical uncertainties in the MOND approach & outlook for further studies

At present, it is not known if MOND is related to a fundamental (quantum) theory (i.e. 'FUNDAMOND', Milgrom 2020a,b). As a result, we do not have a completely secure understanding of cosmology and structure formation in MOND. In fact, it is likely that the implications on these scales are not uniquely derivable from the RAR in disc galaxies. Although the relativistic MOND theory of Skordis & Złośnik (2019) seems quite promising, its consequences for cosmology are not yet established. Therefore, the here applied cosmological model required us to make some ansatzes, whose uncertainties will be summarized and discussed in the following (see also Section 3.1).

Motivated by previous theoretical studies, we assumed that the background cosmology in a Milgromian universe obeys the same Friedmann equation as in ΛCDM (Section 3.1.1). While this is not necessarily true in MOND, the observations of Joudaki et al. (2018) suggest that this works well empirically. Moreover, constraints from BBN imply rather small deviations from the standard $a(t)$ during the radiation-dominated era. In a MOND context, this forces the expansion history to obey the standard Friedmann equation to sub-per cent precision in the matter and Λ-dominated eras (Skordis et al.

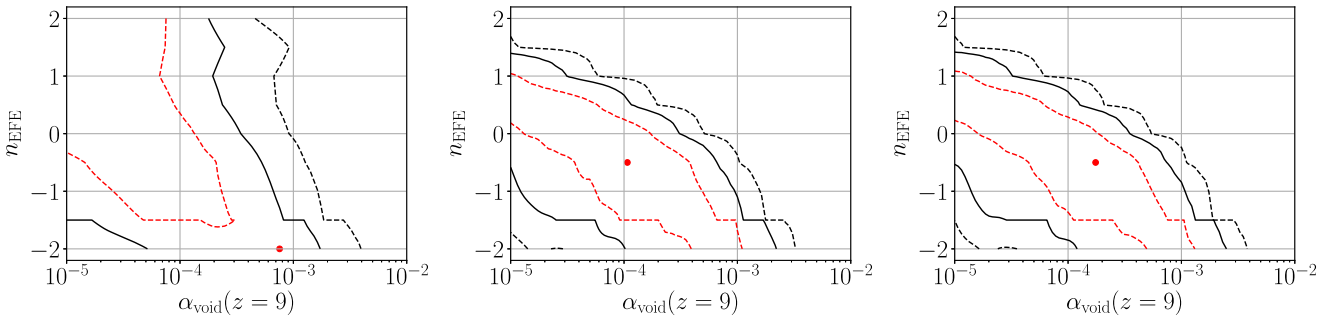

Figure 14. Marginalized posterior distribution of the indicated model parameters based on 9×10^6 MOND models for a Maxwell–Boltzmann (left), Gaussian (middle), and exponential (right) initial profile. The red dashed, black solid, and black dashed lines mark the 1σ, 2σ, and 3σ confidence levels, respectively. A stronger EFE in the past ($n_{\rm EFE} < 0$) requires a stronger initial void strength at $z = 9$. The red dots mark the best-fitting models: $g_{\rm ext} = 0.030\,a_0$, $r_{\rm void} = 218.3$ cMpc, $\alpha_{\rm void} = 7.56 \times 10^{-4}$, $n_{\rm EFE} = -2$ (Maxwell–Boltzmann profile, left-hand panel); $g_{\rm ext} = 0.065\,a_0$, $r_{\rm void} = 1030.0$ cMpc, $\alpha_{\rm void} = 1.07 \times 10^{-4}$, $n_{\rm EFE} = -0.5$ (Gaussian profile, middle panel); and $g_{\rm ext} = 0.070\,a_0$, $r_{\rm void} = 1030.0$ cMpc, $\alpha_{\rm void} = 1.75 \times 10^{-4}$, $n_{\rm EFE} = -0.5$ (exponential profile, right-hand panel).

2006). Moreover, the source term for the Friedmann equation remains the same if CDM is replaced with the same density in sterile neutrinos with $m_{\nu_s} = 11\,{\rm eV/c^2}$ since both would be non-relativistic up to very high $z \gg z_{\rm eq}$. Consequently, there is very good reason to suppose that the background $a(t)$ is very nearly the same as in ΛCDM.

Sterile neutrinos would only slightly affect primordial nucleosynthesis and plasma physics prior to recombination (Sections 3.1.2 and 3.1.3, respectively, see also fig. 1 in Angus 2009). Given also a very nearly standard expansion history and high peculiar gravitational accelerations at that time, we expect the νHDM framework to yield the same CMB power spectrum as ΛCDM. The angular diameter distance to the CMB would also be the same in both frameworks, causing both to suffer from the Hubble tension if $H_0^{\rm local}$ is little affected by cosmic variance. Our main argument is that this last assumption holds in ΛCDM but not MOND.

To simulate structure formation in MOND, we made the usual ansatz that MOND should be applied only to the density deviations from the cosmic mean (e.g. Llinares et al. 2008; Angus & Diaferio 2011; Angus et al. 2013; Katz et al. 2013; Candlish 2016). We justified this in Section 3.1.4 based on the fact that Sanders (2001) showed in his section 2 that this approach (elaborated further in Sanders & McGaugh 2002) is valid in a non-relativistic Lagrangian that has the MOND behaviour. This so-called Jeans Swindle (Binney & Tremaine 1987) is one of the strongest assumptions of current cosmological MOND models. Falco et al. (2013) has formally shown that it can be justified in an expanding General Relativistic universe, but this needs to be mathematically demonstrated for a MONDian framework in which the Poisson equation is non-linear. Despite this uncertainty, it seems inevitable that structure formation would be significantly faster in MOND compared to ΛCDM on a 100 Mpc scale. This is because 100 Mpc is much larger than the free streaming length of both sterile neutrinos and CDM, so the only major difference between the ΛCDM and νHDM frameworks is a different gravity law. Since the accelerations are much smaller than a_0 (Section 1.3), we expect any MOND theory to yield a significant enhancement to the gravity generated by density perturbations. As a result, we argue that MOND models naturally possess the ability to explain the KBC void and Hubble tension.

We now discuss whether this conclusion remains valid if the Jeans swindle approach is not applicable because of the HFE, a coupling between the background cosmology and structures within it. As mentioned in Section 3.1.4, Sanders (2001) developed a non-relativistic two-field Lagrangian-based theory of MOND that couples the Hubble flow and the peculiar accelerations from inhomogeneities.

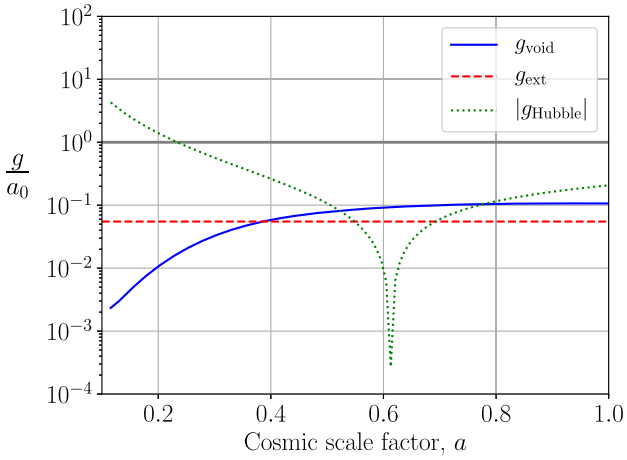

Figure 15. Accelerations along the trajectory of a particle ending up 300 Mpc from the void centre in our best-fitting model. We show the time evolution of $g_{\rm void}$ (the blue solid line), $g_{\rm ext} = 0.055\,a_0$ (the red horizontal dashed line), and $|g_{\rm Hubble}|$ for a standard background cosmology (the green dotted line). The thick horizontal grey line refers to a_0. Note that $g_{\rm Hubble}$ changes sign when $a = 0.61$ ($z = 0.63$) – it is positive at later times and negative earlier on. At present, $g_{\rm void} \approx 0.1\,a_0$ and $g_{\rm Hubble} \approx 0.2\,a_0$, so the latter would limit the MOND boost to gravity at the void edge in case of a strong HFE.

This coupling is described by the adjustable parameter β in his equation (8), and is elaborated further in Sanders & McGaugh (2002). If $\beta = 0$, the coupling between these fields vanishes, which is equivalent to the above-mentioned Jeans swindle. In the case $\beta \neq 0$, the background cosmology would remain intact, but the Hubble flow acceleration ($\boldsymbol{g}_{\rm Hubble}$ in equation 38) would appear as an additional source of gravity that suppresses the ν factor in equation (7).

As argued in Section 2.2.2, the existence of the KBC void and the Hubble tension can be simultaneously reconciled in the ΛCDM framework due to mass conservation, but only for a 10σ density fluctuation (Fig. 2). We demonstrated that in the absence of any HFE, our best-fitting model can explain both the KBC void and the Hubble tension because of an enhanced cosmic variance compared to ΛCDM (Section 4.2). A coupling to $g_{\rm Hubble}$ would reduce the cosmic variance in our MOND model, and therewith also the frequency of KBC-like voids. To estimate the possible impact, we use Fig. 15 to plot the various accelerations entering equation (38) over time for the same test particle presently 300 Mpc from the void centre.

MOND should boost structure formation somewhat at all epochs with $a \gtrsim 0.2$ since $|g_{\rm Hubble}| < a_0$ and the other acceleration terms are even smaller. However, in order to obtain a lower limit on the cosmic variance expected in the MOND framework, we assume the most conservative scenario in which structures grow only as fast as in the ΛCDM framework $\left(\delta \overset{\propto}{\sim} a^{0.8}\right)$ at all epochs when $g_{\rm Hubble}$ is dominant – it is after all unclear exactly what would happen then. As shown in the right-hand panel of Fig. 5, density fluctuations in our best-fitting model grow as $\delta \overset{\propto}{\sim} a^{3.0}$ for the period $0.5 \leq a \leq 0.8$. During this period, our previous approach should be valid because $|g_{\rm Hubble}| < g_{\rm void}$ (Fig. 15). Thus, the 3.2 per cent standard ΛCDM cosmic variance is increased by a factor of at least $(0.8/0.5)^{3.0-0.8} \approx 2.8$, implying a 9.0 per cent cosmic variance. Since our best-fitting MOND model yields a present underdensity of $\delta_{\rm in} = 0.172$ on a 300 Mpc scale,[9] it requires an $\approx 1.9\sigma$ fluctuation. In a MONDian model with $n_{\rm EFE} = -1$ (equation 50), density fluctuations grow slower as $\delta \overset{\propto}{\sim} a^{2.8}$ for $0.5 \leq a \leq 0.8$, implying an 8.2 per cent cosmic variance and thus a 2.1σ fluctuation. The latter scenario may be more realistic in light of our discussion in Section 5.2.2. Since the present value of δ is essentially fixed by the observations of Keenan et al. (2013), the slower structure growth in such a model implies a deeper void in the past, increasing $g_{\rm void}$ relative to our fiducial model. This would increase the timespan during which $g_{\rm Hubble}$ is sub-dominant, thereby allowing MOND to enhance structure growth to a greater extent. We conclude that even in the case of a strong HFE and making very conservative assumptions, our MOND approach still succeeds in explaining the KBC void, which by mass conservation also resolves the Hubble tension.

This is mainly because $g_{\rm Hubble}$ was much smaller a few Gyr ago – it is $\propto \ddot{a}$ (equation 38), which crossed zero at a lookback time of ≈ 6 Gyr (Fig. 15). r was also smaller in the past if we consider the same co-moving scale. While $g_{\rm Hubble}$ can undoubtedly suppress the growth of structure, it was sub-dominant for an extended period – during which it should be appropriate to neglect the HFE. Indeed, a much more rapid growth of perturbations around the time $\ddot{a} = 0$ is also evident in fig. 1 of Sanders (2001), who considered MOND with a strong HFE. Thus, the presence of dark energy can actually promote the growth of structure in a MOND context by reducing $|g_{\rm Hubble}|$. Observations of structure growth on a $\gtrsim$ 100 Mpc scale at $a \approx 0.61$ might reveal evidence for this growth spurt, which would occur at a redshift beyond the extent of the KBC void.

Sanders & McGaugh (2002) showed that since $g_{\rm Hubble}$ scales directly with the size of a system, perturbations on smaller length-scales would be shielded from the HFE, allowing them to grow much faster in case of a strong coupling (see their fig. 12). For instance, $g_{\rm Hubble} \approx 7 \times 10^{-3} a_0$ for a particle at a scale of 10 Mpc, so $g_{\rm Hubble}$ would be very sub-dominant compared to typical external fields of a few per cent of a_0 (e.g. Famaey et al. 2007). This justifies the Jeans swindle approach used in numerical simulations if the goal is to address problems on this scale.

The initial $\alpha_{\rm void}$ required by our fiducial model is lower than the expected rms density fluctuations at $z = 9$ for a ΛCDM cosmology, which we can estimate by scaling the present value of 0.032 by $0.1^{0.8}$ to obtain ≈ 0.005. Our results in Fig. 14 show that this remains true even with a stronger EFE in the past ($n_{\rm EFE} < 0$), implying that KBC-like voids would be quite common in MOND. Such a void could explain the Cold Spot in the CMB, which is often interpreted as a huge underdensity (Nadathur et al. 2014). However, such structures are quite rare, suggesting that large voids are not very frequent in the Universe (Section 5.2). Moreover, a high frequency of KBC-like voids could cause too much foreground lensing of the CMB – though this is far from clear (Section 5.3.1).

In principle, the implications of MOND on large scales depend on an adjustable parameter analogous to β in equation (8) of Sanders (2001), which can be used to alter the frequency of KBC-like voids or massive galaxy clusters such as El Gordo at high redshift. A strong HFE would reduce the frequency of such structures. We apply Occam's Razor and assume $\beta = 0$ since there is no compelling observational or theoretical evidence for $\beta \neq 0$. In particular, it is not yet clear if covariant theories (such as that proposed recently by Skordis & Złośnik 2019) have any flexibility in the coupling between peculiar and Hubble flow accelerations, at least when we impose other constraints, e.g. that gravitational waves travel at c. Since $g_{\rm Hubble}$ acts to suppress the void gravity and increases with distance, the outer density profile of the KBC void could empirically constrain the coupling. Our best-fitting model implies that at present, $g_{\rm ext} \ll g_{\rm void} \ll a_0$ at 300 Mpc, implying that $g_{\rm void} \overset{\propto}{\sim} r^{-1}$ in the outer part of the void. Since $g_{\rm Hubble} > g_{\rm void}$, a strong background coupling would make the system more Newtonian, causing therewith a steeper decline of gravity with distance. However, current measurements of the KBC void's outer density profile are not sufficiently precise to strongly constrain the HFE.

If a particular cosmological MOND model predicts that structure formation on 300 cMpc scales is very similar to standard cosmology, such a model would not be able to account for the KBC void – and would have to be rejected for similar reasons to ΛCDM (Section 2). Any viable covariant formalism of MOND has to describe the density and velocity field of the local Universe. Interestingly, the here applied approach can reproduce the KBC void, which solves therewith the Hubble tension due to mass conservation. Therefore, our model can serve to guide further theoretical development of MOND in a cosmological context.

The $g_{\rm Hubble}$ term would be much larger in the CMB era. For the sound horizon scale at recombination (147.09 ± 0.26 cMpc, Planck Collaboration VI 2020), $|g_{\rm Hubble}| \approx 35000\, a_0$. Thus, even a slight background-perturbation coupling would completely eliminate any MOND effects, making the pre-CMB universe purely Newtonian. This is also true in the absence of any such coupling, since the gravity from inhomogeneities is $\approx 21\, a_0$ (Section 3.1.3). Thus, our conclusions regarding the CMB are not affected by a possible HFE.

This is also true for the model of Zhao (2008), which implies that the MOND acceleration scale $a_\dagger$ is time-dependent, with

$$a_\dagger = a_0 a^{-3/2}\,. \tag{84}$$

At the time of recombination, $a_\dagger = 36500\, a_0$, which exceeds $|g_{\rm Hubble}|$ at that epoch. Thus, even in the presence of a very strong coupling of perturbations to $g_{\rm Hubble}$, his model implies significant MOND effects in the CMB, making it very difficult to fit its power spectrum. Furthermore, Milgrom (2017) showed that the model of Zhao (2008) is in tension with the rotation curves of galaxies at high redshift.

In this contribution, we assumed that Milgrom's constant a_0 is constant in space and cosmic time. While the former is expected in a fundamental theory, a time-varying a_0 is in principle quite possible. Although this is observationally not supported at the moment (e.g. Milgrom 2017), $a_0 \approx c H_0/(2\pi)$, which could be a hint that MOND is fundamentally related to cosmology. If this relation is true, a_0 would decrease over cosmic time, implying that the early universe was more MONDian than assumed in our models. Thus, postulating that $a_0 \propto$

[9] This is consistent with the observed 0.46 ± 0.06 (Keenan et al. 2013) due to the RSD correction (Table 4).

H would cause strong MOND effects in the CMB, arguing against the idea (Section 3.1.3). On the other hand, a much lower a_0 in the past would significantly raise the MOND timing argument mass of the LG, which for a constant a_0 ends up rather similar to its baryonic mass (Banik et al. 2018). Since HDM should not significantly cluster on such a small scale to avoid disrupting MOND fits to galaxy rotation curves, it appears that very strong time evolution of a_0 in either sense is ruled out empirically if not theoretically.

MOND as currently understood cannot explain the CMB power spectrum and the dynamics of galaxy clusters without an extra matter component. Therefore, we follow Angus (2009) in postulating the existence of HDM. This is another strong assumption of our model – but not more hypothetical than the existence of CDM. If anything, sterile neutrinos have been described as 'almost part of the standard model' of particle physics (Merle 2017), while CDM particles are generally thought to require supersymmetry. In future, it will be very important to directly search for sterile neutrinos in terrestrial experiments.

In addition, precise measurements of the CMB power spectrum at $\ell > 4900$ could put strong constraints on our model. This is because small shifts to the CMB power spectrum may arise when applying MOND supplemented with sterile neutrinos rather than Newtonian gravity with CDM. We have assumed that the effects are either not detectable or can be compensated through small adjustments to the cosmological parameters.

Furthermore, we modelled the gravitational field of the void using non-relativistic equations. This should be quite accurate because the total peculiar velocities are $v_{\rm tot} \lesssim 0.01c$ within ≈ 250 Mpc of the void centre (Fig. 8). Moreover, the void is much smaller than the cosmic horizon. Gravity traveltime effects should thus not be too significant if gravitational waves travel at c, as occurs in the model of Skordis & Złośnik (2019).

The exact density profile of the KBC void is not fully known, so further assumptions are required when modelling it. Motivated by observations of an increasing density as one goes inwards for distances $\lesssim 40$ Mpc (Karachentsev & Telikova 2018), we assumed an initial Maxwell–Boltzmann profile (Section 4). We demonstrated the robustness of our results by also implementing Gaussian and exponential void profiles (Appendix C). The best-fitting models with those profiles yield a slightly larger overall tension compared to our main analysis, with the best parameters shifting to a stronger EF and larger initial void with comparable depth (Table C1). Thus, other void profiles could yield reasonable results with adjusted EF and void parameters. This issue could be constrained with better knowledge regarding the exact density profile of the KBC void.

Although the here presented MOND approach suffers from theoretical uncertainties especially with regards to the HFE, the encouraging results of our best-fitting models (Section 4.2 and Appendix C) suggest that our assumptions are reasonable. Furthermore, our models allow a wide range of possible void parameters (Figs 4, C1, and C2), so adjusting these could in principle compensate theoretical uncertainties. In particular, a stronger HFE would require an initially deeper void – though we argued that the required depth would be reasonable even under conservative assumptions.

Once it is clear which covariant MONDian framework should be applied, the role of the HFE (if any) would become apparent. It would then be valuable to statistically quantify the existence of the KBC void within a large numerical MONDian cosmological simulation, enabling a comparison with our analysis of its likelihood in ΛCDM (Section 2). Such a simulation would also deliver a better understanding of void profiles at low redshift, and on how the growth of structure is regulated by the EFE from surrounding structures (Section 5.2.2).

5.3 Claimed problems for a local void solution to the Hubble tension

In the following, we address some commonly used arguments for why a void model cannot resolve the Hubble tension.

5.3.1 Other anomalies in large-scale structure

If the growth of structure is much more rapid than predicted by standard theory, large underdensities such as the KBC void should also exist at higher redshift. Large voids are not evident in the galaxy two-point correlation function, suggesting that large-scale structure seems to be consistent with the ΛCDM paradigm. However, it must be borne in mind that the underlying matter density field is not measured directly – it is estimated from the distribution of galaxies. At large distances, only the brightest galaxies can be observed, so one has to assume the so-called bias factor:

$$b \equiv \frac{\delta_{\rm galaxy}}{\delta}, \tag{85}$$

which relates the galaxy density contrast $\delta_{\rm galaxy}$ to that of the underlying matter distribution. This bias factor is typically chosen to match the ΛCDM expectation for cosmic variance at the relevant scale. Thus, an accurate model-independent estimation of the density contrast can only be achieved for low-mass galaxies observed in the NIR, for which $b \approx 1$ on 100 Mpc scales in any cosmological model. This makes it very difficult to perform a similarly detailed analysis to Keenan et al. (2013) for $z \gtrsim 0.5$. Even the 2MASS survey they used only covers 57–75 per cent of the luminosity function (see their fig. 9). This fraction would be much lower for higher redshift galaxy samples.

We are also faced with the problem that galaxy positions are in general unknown – in the distant Universe, only redshifts are available. Even the redshifts are often not measured directly but are estimated photometrically. This leads to a significant smearing effect along the line of sight, making it rather difficult to identify distant supervoids (DES Collaboration 2019). The situation is reminiscent of the LG satellite planes – due to distance uncertainties, it is difficult to know if the satellites of a distant galaxy are distributed anisotropically. In both cases, if similar anomalies had not been reported at larger distances, this would not tell us whether such anomalies exist.[10]

However, supervoids identified in the Dark Energy Survey do seem to show an enhanced ISW effect (DES Collaboration 2019). Their stacked analysis of 87 supervoids found that the effect has an amplitude of 5.2 ± 1.6 times the conventional expectation when combined with the earlier results of Kovács (2018).

Another possibly related anomaly is that the lensing amplitude implied by the CMB power spectrum is stronger than predicted (Di Valentino, Melchiorri & Silk 2020a). They suggested that this problem could instead be an indication that the Universe has a positive curvature. This would have serious implications for our entire understanding of the Universe and require a completely different cosmological model. For instance, a closed universe would imply a very low H_0 of $54^{+3.3}_{-4.0}$ km s^{-1} Mpc^{-1}, which is completely inconsistent with local measurements (see their fig. 7). However, the enhanced lensing amplitude – evident also in Di Valentino, Melchiorri & Silk (2020b) – could be the imprint of unexpectedly large density fluctuations caused by more rapid growth of structure. In this scenario, a supervoid would be a more likely explanation for

[10] A satellite plane has recently been discovered around Cen A (Müller et al. 2018).

the CMB Cold Spot (Nadathur et al. 2014). Indeed, their suggested void profile has a central underdensity of 0.25 and characteristic size of 280 Mpc, rather similar to the KBC void (see their equation 1). They concluded that such a void is highly unlikely in ΛCDM, as also implied by our results in Fig. 1. It would be very valuable to empirically determine the actual frequency of such voids.

5.3.2 High peculiar velocities

Our fiducial model implies the existence of void regions with total peculiar velocity $v_{\rm tot} \leq v_{\rm LG} = 627\,{\rm km\,s^{-1}}$ relative to the surface of last scattering. Such low velocities are unlikely but allowed at the 2.34σ level.

Interestingly, our model predicts $v_{\rm tot}$ of up to $\approx 4000\,{\rm km\,s^{-1}}$ for objects ≈ 250 Mpc from the void centre in the direction of its motion (Fig. 8). Such high peculiar velocities are potentially detectable with the kinematic Sunyaev–Zeldovich (kSZ) effect of galaxy clusters (Sunyaev & Zeldovich 1980). However, this is difficult to disentangle from the thermal Sunyaev–Zeldovich (tSZ) effect because our model predicts similar peculiar velocities to the internal velocity dispersions of galaxy clusters. A large local underdensity also reduces the number of clusters available for kSZ studies, increasing the uncertainty.

Hoscheit & Barger (2018) concluded that the KBC void is consistent with the linear kSZ effect (see their fig. 6). Similar results were obtained by Ding, Nakama & Wang (2020). Some evidence for a bulk flow of $\approx 1000\,{\rm km\,s^{-1}}$ has been found (Kashlinsky et al. 2008, 2011). This is broadly consistent with the expected motion of the whole void due to the EFE ($v_{\rm void} = 1586\,{\rm km\,s^{-1}}$), though the bulk flow of a smaller region will depend on our exact location within the void and the survey volume. Bulk flows of $\approx 1000\,{\rm km\,s^{-1}}$ are not possible on a 100 Mpc scale in a ΛCDM universe, but would be expected in MOND (Katz et al. 2013).

5.3.3 Gravitational redshifting of the CMB monopole

A large local underdensity like the KBC void should also affect the mean temperature (monopole) of the CMB. This is because the height of the potential at our location causes a gravitational redshift. Using equation (52), the general relativistic redshift for a photon travelling uphill from distance r to the centre becomes

$$1 + z_{\rm GR} \;=\; \exp\left(\frac{1}{c^2}\int g\,{\rm d}r\right)\,. \tag{86}$$

In the best-fitting MOND model, we obtain $z_{\rm GR} = 8.4 \times 10^{-3}$ for the most distant test particle, which is 700× larger than the 1σ rms fluctuations of $z_{\rm GR} = 1.2 \times 10^{-5}$ assumed in the study of Yoo et al. (2019). Their fig. 2 shows that the impact of such a gravitational redshift on the inferred cosmological parameters is very small, even with an extra factor of 700. Moreover, we expect that the actual gravitational redshift at our position in the void should be much smaller. This is because we are not exactly at the centre of the void, and thus not at the highest part of its gravitational potential hill (Fig. 8). Redshifting from the void's gravity would also be partially counteracted by the EFE, which is required in order to explain the rather slow motion of the LG wrt. the CMB (Section 4.2.3).

None the less, it is possible that gravitational redshifting of the CMB would change the best-fitting HDM and baryon fractions by a few times their official uncertainties. Since these are nowadays rather small (Planck Collaboration VI 2020), we conclude that this effect has only a small impact on the CMB power spectrum, which moreover could probably be compensated through slight adjustments to the cosmological parameters. Of particular relevance for the Hubble tension is that gravitational redshifting of the CMB has a negligible impact on the precisely measured angular scale of the first acoustic peak (fig. 2 of Yoo et al. 2019).

5.3.4 Assumption of Newtonian gravity for the void dynamics

Applying Newtonian gravity to the dynamics of any void would lead to sharp gradients in the predicted density and velocity profiles due to the steep inverse square law. Kenworthy et al. (2019) found no evidence for such a sharp edge in the SN luminosity−distance relation, which would − according to them − rule out the existence of a large local void with $\delta > 0.2$ at the $4\sigma-5\sigma$ confidence level. Also, Hoscheit & Barger (2018) applied the large scale void radial profile of Keenan et al. (2013) to show that H_0 is $1.27 \pm 0.59\,{\rm km\,s^{-1}\,Mpc^{-1}}$ higher in the redshift range $0.0233 < z < 0.07$ compared to $0.07 < z < 0.15$. This only modestly reduces the Hubble tension, e.g. with the SNe data of Riess et al. (2016).

However, as shown in Section 2.2, an inverse square law is too weak to produce a deep and extended underdensity like the KBC void. Therefore, the assumption of Newtonian gravity for the void dynamics is not sustainable. In MOND, the long-range modification to gravity would cause a much more gradual return from the void-induced peculiar velocities to the background cosmology, as demonstrated in Fig. 12. Therefore, sharp features in the density profile and Hubble diagram are not expected in a MONDian model. This holds especially for H_0 derived from SNe data because in order to constrain the cosmological model, one has to consider many individual SNe. Consequently, the inferred H_0 only gradually declines towards the Planck prediction as SNe beyond the void are included in the analysis (as e.g. done by Colgáin 2019).

5.3.5 Restrictive upper limit on the void size

The present void size can be treated as a model parameter independently of the applied gravity theory. Adopting a very low upper limit on the allowed void size would unavoidably cause sharp features in the density and velocity profiles in any framework. Moreover, the Hubble tension cannot be resolved by a small void unless we postulate that it is extremely deep. This issue affected the analysis of Wu & Huterer (2017), who assumed a void size of 180 Mpc. They noticed that since the SNe data go out much further, it is difficult for such a small void to resolve the Hubble tension. None the less, they did not consider a larger void, opting instead for a very large density contrast of $\delta = 0.8$. This led to poor agreement with direct measurements of the density field. However, a larger and shallower void would have provided much better agreement with observations, as shown in this work.

Using the high-resolution ΛCDM N-body cosmological simulation called Millennium-II, Xie et al. (2014) obtained that ≈14 per cent of LG-like systems are located in a region that resembles the observed local void. Thus, they concluded that 'the emptiness of the Local Void is indeed a success of the standard ΛCDM theory.' However, by 'Local Void', they meant a sphere of radius ≈8 Mpc, which is much smaller than the KBC void. Thus, their work cannot be used as an argument that the local void observed by Keenan et al. (2013) is consistent with ΛCDM cosmology, as is done in section 5 of Sahlén et al. (2016).

5.3.6 Fixing the acceleration parameter

The acceleration parameter $\overline{q}_0$ describes the second time derivative of the scale factor (equation 65). It is therefore a measure of the void's gravity. As discussed in Section 5.3.4, Kenworthy et al. (2019)

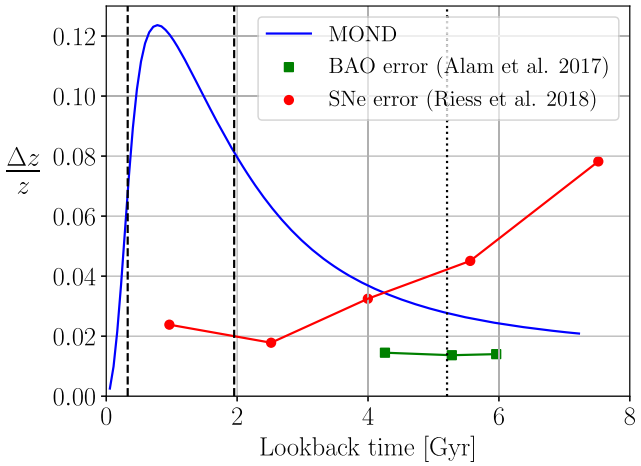

Figure 16. Difference in the redshift between our best-fitting model and a standard void-free cosmology (latter subtracted), shown as a function of lookback time. The first two dashed vertical lines show the range $0.023 \leq z \leq 0.15$ covered by Camarena & Marra (2020a). The dotted vertical line marks $z = 0.5$. For comparison, the red points and green squares show fractional distance uncertainties using SNe (table 6 of Riess et al. 2018) and BAO (table 8 of Alam et al. 2017), respectively. Since fractional redshift errors are generally rather small, this gives an estimate of the uncertainty in the inferred Hubble constant, which has similar sensitivity to redshift and distance.

concluded that the KBC void is not evident in the SN luminosity–distance relation. In addition to assuming Newtonian gravity, they fixed the acceleration parameter to the ΛCDM prediction of $\overline{q}_0 = 0.55$. In general, $\overline{q}_0$ would have a higher value if there is a large local void. To allow for this possibility, $\overline{q}_0$ must be treated as a free parameter when using the apparent expansion rate history to constrain the properties of a local void.

Fortunately, Camarena & Marra (2020a) address this shortcoming by deriving $\overline{q}_0$ and $H_0^{\rm local}$ jointly from SNe data without a restrictive choice of prior. Their analysis yields $\overline{q}_0 = 1.08 \pm 0.29$, much higher than in the Planck cosmology. A high $\overline{q}_0$ is also evident when using BAO data or treating the SNe Ia absolute magnitude as a free parameter (Camarena & Marra 2020b). This is a strong hint for the existence of a local void independently of the galaxy luminosity density (e.g. Keenan et al. 2013). Indeed, Colgáin (2019) inferred a local underdensity at $z \lesssim 0.15$ using SNe data alone. Both the local Hubble constant and acceleration parameter can be explained in our best-fitting MOND models (Fig. 6).

5.3.7 *Effect of the void at high redshift*

The apparent expansion rate history in our fiducial MOND model is very similar to the Planck cosmology (Fig. 12). None the less, the fractional difference in z between void and void-free cosmologies (i.e. $\Delta z/z$) reaches the 12 per cent level and is sufficient to solve the Hubble tension (Fig. 16). Observations at higher z could distinguish our void model from other possible solutions, e.g. miscalibrated SNe, early dark energy, etc. This is because a local void predicts that the inferred H_0 decreases with the redshift of the data set used, and asymptotically approaches the Planck prediction (Fig. 7).

Unfortunately, Fig. 16 shows that high-redshift SNe currently do not pose strong constraints on our model. This is because the simulated $\Delta z/z$ decreases with redshift, while the uncertainty of binned SNe distance measurements to fixed z increases for $z \gtrsim 0.2$. It crosses the simulated $\Delta z/z$ curve at $z \approx 0.38$, corresponding to a lookback time of ≈ 4.2 Gyr. At $z \approx 0.5$ (the dotted vertical line in Fig. 16), the predicted $\Delta z/z \approx 3$ per cent, but the observational uncertainty is much larger (see also Cuceu et al. 2019; Macaulay et al. 2019). As a result, even the 9 per cent Hubble tension could not be reliably detected in SNe at these redshifts, which is reasonable given that the uncertainty of H_0 derived from SNe at $0.023 \leq z \leq 0.15$ is already ≈ 2 per cent (Camarena & Marra 2020a). Moreover, there are much fewer observed SNe at high redshifts, which could increase systematic errors.

In contrast to high-redshift SNe, the current BAO precision (Alam et al. 2017) lies slightly below the predicted $\Delta z/z$. However, the uncertainties are still too large to distinguish our model from a void-free Planck cosmology at high significance. We note that BAO-based H_0 measurements (Alam et al. 2017; Zhang et al. 2019) are very close to the Planck prediction (Section 1.2), which is consistent with our void model. The small excess it predicts can only be confirmed or ruled out with more precise observations.

In conclusion, it is currently difficult to distinguish void and void-free models with data only at $z \gtrsim 0.5$. Data at lower z are more useful in this regard. In particular, the redshift range $0.023 \leq z \leq 0.15$ covered by Camarena & Marra (2020a) brackets the peak of the simulated $\Delta z/z$ curve and poses therewith a strong test of our model. In this redshift range, our void model differs from ΛCDM by $\Delta z/z = 7 - 12$ per cent, which is quite consistent with the 9.5 per cent difference between local and early universe measures of H_0. Note that the position of the peak in $\Delta z/z$ depends on the underlying void profile – it would occur at the void centre for a Gaussian or an exponential profile.

5.3.8 *CMB contamination by intergalactic dust*

Finally, we consider the possibility that the CMB is contaminated by intergalactic dust, which in turn would affect the $H_0^{\rm global}$ required by Planck Collaboration VI (2020). Some distant foreground emission can increase $H_0^{\rm global}$ (Yershov et al. 2020), which would slightly reduce the mild tension between our model and the strong lensing data (Fig. 7). This is because the $z > 0.4$ lenses all give H_0 systematically above the Planck prediction by a similar extent. But changing the Planck H_0 would not explain the high inferred H_0 from the two lowest z lenses, which would continue to hint at a local void.

It is also possible that the CMB is more substantially affected by dust. In contrast to the ΛCDM model in which the CMB is explained as relic radiation from the early Universe at $z \approx 1100$ (e.g. Bennett et al. 2003; Planck Collaboration VI 2020), an alternative model is that the entire CMB is thermal radiation from intergalactic dust particles heated up by starlight (Vavryčuk 2018). Assuming the observed intergalactic dust is in thermal equilibrium with the radiation field from galaxies, the model of Vavryčuk (2018) implies a dust temperature of $T_{\rm D} = 2.776$ K. This is only slightly higher than the measured $T_{\rm CMB} = 2.72548 \pm 0.00057$ K (Fixsen 2009). The exact value of $T_{\rm D}$ depends on the amount of intergalactic dust and the intergalactic opacity ratios, which are both poorly known observationally. In future, it would be important to study which dust parameters are necessary to match the observed $T_{\rm CMB}$. In other words, it would be important to quantify the uncertainty on $T_{\rm D}$, which was not explicitly addressed by Vavryčuk (2018). Furthermore, it needs to be demonstrated that the model can yield the observed perfect blackbody spectrum within rather small uncertainties (Planck Collaboration XXVII 2014), and also yield nearly Gaussian temperature fluctuations (Planck Collaboration XXIII 2014). It is therefore possible that intergalactic dust significantly affects the CMB, but a detailed consideration of such a scenario is beyond the scope of our work. Interestingly, Vavryčuk (2019) showed in a subsequent study

that the anomalous dimming of SNe Ia can in principle be explained by light extinction due to intergalactic dust.

In addition to heating by starlight, dust grains would also be heated by the primordial CMB, especially at high z. This may have caused rethermalization of the CMB by dust from the first stars at $z \approx 15$. In this scenario, the angular scale evident in BAO measurements corresponds to a different co-moving length than the sound horizon at the time of last scattering. However, agreement can be recovered if we assume a non-standard background cosmology where $a \propto t$ (Melia 2020). In fact, it is not possible that $a \propto t$ without such a late rethermalization of the primordial CMB (Fujii 2020). While the late-time expansion history is indeed approximately of this form (Fig. 12), the model does not yet explain the nature of the acoustic oscillations in the CMB power spectrum. Moreover, BBN would be modified to a very substantial extent, making it difficult to explain the observed light element abundances (Lewis, Barnes & Kaushik 2016).

6 CONCLUSIONS

Cosmic structure – and therewith the distribution of galaxies – provide strong constraints on the underlying cosmological model. In this context, we used the framework of the standard ΛCDM theory and MOND (Milgrom 1983) to investigate the KBC void, a large underdensity with a relative density contrast of $\delta \equiv 1 - \rho/\rho_0 = 0.46 \pm 0.06$ between $z = 0.01$ and $z = 0.07$ (Keenan et al. 2013). A large local underdensity is evident throughout the whole electromagnetic spectrum (Section 1.1).

Using the MXXL simulation (Angulo et al. 2012), we showed that the KBC void is in 6.04σ tension with standard cosmology (Section 2.2.1). In principle, if mass conservation is assumed, such an immense void should also show up in the velocity field, and would approximately solve the Hubble tension (equation 5). This tension nowadays exceeds the 5σ threshold based on numerous independent techniques (Section 1.2). However, we demonstrated that a 10σ density fluctuation would be necessary to solve the Hubble tension at the 2σ level (Fig. 2). This is due to the very small expected cosmic variance in ΛCDM (e.g. Macpherson et al. 2018). The most likely explanation in this framework is that both the KBC void and Hubble tension are caused by measurement errors. However, the measurements rely on very different observational techniques. For instance, a zero-point error in SNe Ia fluxes would change the inferred H_0 but would not affect the KBC void. Thus, both phenomena would independently falsify ΛCDM at more than 5σ confidence, yielding a combined tension of 7.75σ. Taking into account the cosmic variance expected in ΛCDM, both tensions are not completely independent, reducing the combined tension with standard cosmology to 7.09σ (Section 2.2.3). The ΛCDM model (or any dark-matter-based Einsteinian/Newtonian cosmological model) is thus rigorously ruled out by the data on kpc, Mpc, and Gpc scales (see also Kroupa 2012, 2015).

As discussed in Section 5.1.1, an early change in the expansion history is unlikely to solve the Hubble tension, and would in any case not explain the KBC void. Importantly, we argued that the locally measured Hubble constant is very similar to the Planck prediction in ΛCDM once the KBC void is accounted for (equation 5). Our results thus support the Planck cosmology at the background level and in the early Universe.

However, a deep and large void such as the KBC void implies that the growth of structure must be more rapid than predicted by standard theory. This would also fit into the picture obtained by Peebles & Nusser (2010), who concluded that the structure of the Local Volume with its void and sheet on an 8 Mpc scale points to a faster growth rate of cosmic structure. Since gravity is the dominant force on these scales, it is very likely that gravity has to be enhanced at long range (Fig. 11).

Consequently, we aimed to study the KBC void and its velocity field in MOND, an acceleration-dependent modification of Newtonian gravity. MOND was originally designed to explain the dynamical discrepancies in galaxies without the need of CDM (Milgrom 1983). Unfortunately, there is currently no N-body or hydrodynamical cosmological MOND simulation large enough to quantify the likelihood of a KBC void, as done for the ΛCDM framework. Therefore, we developed a semi-analytic approach based on the Angus (2009) cosmological model, which relies on MOND supplemented by sterile neutrinos with a mass of $m_{\nu_s} = 11\,\mathrm{eV/c^2}$. We call this the νHDM framework, where ν refers to both the interpolating function in QUMOND (Milgrom 2010) and sterile neutrinos as an HDM component. The energy budget would be similar to the ΛCDM cosmology, with a baryonic matter density of $\Omega_{\mathrm{b},0} \approx 0.05$, a sterile neutrino density of $\Omega_{\nu_s,0} \approx 0.25$, and a dark energy density of $\Omega_{\Lambda,0} \approx 0.7$ at the present time (Section 3.1).

This paradigm is mainly motivated by a sample of 30 virialized galaxy groups and clusters which all reach the Tremaine–Gunn limit for sterile neutrinos with $m_{\nu_s} = 11\,\mathrm{eV/c^2}$ (Angus et al. 2010). Moreover, the model provides a viable explanation of the thermal history of the Universe. As discussed in Section 3.1.3, an extra sterile neutrino species is consistent with the standard model of particle physics (which accommodates neutrino oscillations) and only slightly affects the nucleosynthesis era – it would raise the primordial helium abundance from $Y_\mathrm{p} = 0.247$ to $Y_\mathrm{p} = 0.259$. Measurements of high-redshift metal-poor gas clouds backlit by quasars do not rule this out (Aver et al. 2012; Cooke & Fumagalli 2018). At $z = 1100$, sterile neutrinos with $m_{\nu_s} = 11\,\mathrm{eV/c^2}$ have a free-streaming length of ≈ 3.5 cMpc, implying that they would only affect multipoles $\ell \gtrsim 4900$ in the CMB power spectrum, beyond the range of Planck. This is confirmed in section 6.4.3 of Planck Collaboration XIII (2016), which states that sterile neutrinos with $m_{\nu_s} > 10\,\mathrm{eV/c^2}$ are indistinguishable from CDM in Planck measurements of the power spectrum. Importantly, typical accelerations at the CMB would exceed a_0, causing structure formation to be little affected by MOND until $z \lesssim 50$ (equation 32). Furthermore, the νHDM model closely recovers the standard expansion history (Angus 2009), which is currently favoured by observations (e.g. Joudaki et al. 2018). This is because not only the overall matter content but also the Friedmann equation should be very similar to ΛCDM (Dodelson & Liguori 2006; Skordis et al. 2006).

Within this framework, we developed a semi-analytical model with the usual ansatz that density perturbations obey Milgrom's law of gravity (e.g. Angus et al. 2013; Katz et al. 2013; Candlish 2016), but a standard background cosmology applies (Section 3.1). In particular, we adopted a background Hubble constant of $H_0^{\mathrm{global}} = 67.4\,\mathrm{km\,s^{-1}\,Mpc^{-1}}$, $\Omega_{\mathrm{m},0} = 0.315$, and $\Omega_{\Lambda,0} = 0.685$ (Planck Collaboration VI 2020). In this way, we extrapolated Milgrom's gravitational theory from sub-kpc to Gpc scales without further theoretical assumptions to specifically address the local density and velocity field (Section 3.2).

Our simulation starts at $z = 9$ with a void profile parametrized by an initial void size r_void ranging from 50–1030 cMpc and an initial void strength α_void ranging from 10^{-5} to 10^{-2}. In our fiducial model, the void is described by a Maxwell–Boltzmann profile (Section 3.2.1) motivated by the density profile of the Local Volume (Karachentsev & Telikova 2018). We also run models with a Gaussian and an exponential initial profile (Appendices B and C). Furthermore, we vary the present EFE from $g_\mathrm{ext} = 0$ up to $0.5\,a_0$. For our main

analysis, we assume that the EFE is constant over cosmic time, but models with different power-law dependencies on the scale factor are also considered (Section 5.2.2). In total, we run 10^6 MOND models for our main analysis (Maxwell–Boltzmann initial profile with time-independent $g_{\rm ext}$).

We constrain our models with observations of the local Universe, i.e. the inner ($0.01 < z < 0.07$) and outer (600–800 Mpc) density contrast of the KBC void (see also fig. 11 and table 1 in Keenan et al. 2013), the local Hubble constant and acceleration parameter derived jointly from SNe in the redshift range $0.023 \leq z \leq 0.15$ (Camarena & Marra 2020a), H_0 measured from seven strong lenses (Wong et al. 2020; Shajib et al. 2020), and the motion of the LG wrt. the CMB (Kogut et al. 1993).

Our fiducial MOND model has $g_{\rm ext} = 0.055\,a_0$ causing a bulk flow of $v_{\rm void} = 1586\,{\rm km\,s^{-1}}$ at $z = 0$, $r_{\rm void} = 228.2\,{\rm cMpc}$ at $z = 9$, and $\alpha_{\rm void} = 3.76 \times 10^{-5}$ then. In this model, the density contrast in a 300 cMpc sphere grows as $\delta \overset{\propto}{\sim} a^{3.8}$, which is much faster than in ΛCDM where $\delta \overset{\propto}{\sim} a^{0.8}$ (Fig. 5). At the present epoch, our model yields $\delta_{\rm in} = 0.172$ and $\delta_{\rm out} = 0.050$, which explains the observed density contrasts after an RSD correction (Section 3.3.2) at 0.99σ and 0.97σ, respectively. The model yields a local Hubble constant of $H_0^{\rm model} = 76.15\,{\rm km\,s^{-1}\,Mpc^{-1}}$ and an acceleration parameter of $\overline{q}_0^{\rm model} = 1.07$ in the redshift range $0.023 \leq z \leq 0.15$, consistent with the observations of Camarena & Marra (2020a) at the 84.20 per cent confidence level (0.20σ tension, Section 4.2). Similar results are obtained for models initialized with a Gaussian or an exponential profile (Appendix B). Thus, we have shown for the first time that the Hubble tension can be solved in MOND. Several other tensions are also simultaneously resolved, notably the KBC void and that in $\overline{q}_0$ (see also Camarena & Marra 2020b).

While all our best-fitting models generally imply larger peculiar velocities than the observed $v_{\rm LG}$ of only $627\,{\rm km\,s^{-1}}$, the possibility that $v_{\rm tot} \leq v_{\rm LG}$ cannot be excluded at the 99 per cent confidence level (Section 4.2 and Appendix C). Thus, we do not require the LG to be at a special position within the KBC void in a statistically significant sense. Our results indicate that we should be 150−270 Mpc from the void centre in roughly the opposite direction to the external field on the void (Fig. 8).

As we go beyond the void, all our models predict that the inferred H_0 decreases with redshift. Indeed, observations of strongly lensed quasars taken by the H0LICOW team have shown that H_0 decreases with the lens redshift at a significance level of 1.9σ (Wong et al. 2020). However, our best-fitting model systematically underestimates the lensing-inferred H_0, which may be related to the EFE sourced by a massive object beyond the void at $z \gtrsim 0.15$ but closer than the lenses at $z > 0.3$ (Section 5.2.1). It could also be a sign of systematic errors (Kochanek 2020), but the sharp rise for the two nearest lenses is suggestive of a void-induced effect.

Taking into account all observational constraints (Section 3.3), our fiducial MOND model explains these local observations at the 1.14 per cent confidence level, representing 2.53σ tension (Section 4.2). The best-fitting MOND models with a Gaussian and an exponential void profile are consistent with observations at 0.45 per cent (2.84σ) and 0.34 per cent (2.93σ), respectively (Appendix C).

Although strong lensing does not occur in the MOND regime (Sanders 1999) and works similarly to standard cosmology (Section 3.3.5), we also redo our analysis without the H_0 constraints from this method. Our best-fitting model is then consistent with observations at the 5.0 per cent (1.96σ) confidence level, with only small changes to the best-fitting parameters (Section 5.2.1).

Our analysis strongly disfavours models without an EFE, consistent with results from wide binaries (Pittordis & Sutherland 2019). Furthermore, we showed that allowing time variation of the EFE has only a minor impact on our results because a constant EFE is well within uncertainties (Section 5.2.2). The main effect of allowing a stronger EFE in the past is to raise the required void strength at $z = 9$, with values up to $\approx 10^{-3}$ becoming allowed at 1σ (Fig. 14). This is more in line with the expected cosmic variance at that epoch.

We also discussed structure formation and the implications for the KBC void in MOND if peculiar accelerations are coupled to the Hubble flow acceleration $\boldsymbol{g}_{\rm Hubble}$, as proposed by Sanders (2001). Such a coupling (or HFE) would effectively add $g_{\rm Hubble}$ as an extra source of gravity when calculating the MOND boost to gravity, making the behaviour more nearly Newtonian (Sections 3.1.4 and 5.2.3). However, even a strong HFE implies a significant enhancement to gravity and the formation of voids compared to the Newtonian case. This is because $g_{\rm Hubble} \approx 0.2\,a_0$ on a 300 Mpc scale, and completely vanished 6 Gyr ago (Fig. 15). As a result, we conservatively estimated that even with a strong HFE, the cosmic variance in MOND would still be at least 2.8× that in standard ΛCDM on a 300 Mpc scale (≈9.0 per cent instead of 3.2 per cent). This would mean that whereas ΛCDM needs a 10σ density fluctuation to simultaneously explain the KBC void and Hubble tension (Fig. 2), a MOND cosmology would only need an $\approx 2\sigma$ fluctuation (Section 5.2.3). Thus, MOND can successfully describe the density and velocity field on a Gpc scale under a wide range of plausible theoretical assumptions on how density perturbations couple to the background cosmology. In principle, the strength of the coupling introduces additional degrees of freedom that could be used to match the observed frequency of KBC-like voids, the observed lensing of the CMB, and the ISW effect. However, it is not clear if a covariant version of MOND has this flexibility when other constraints are imposed, e.g. that gravitational waves should travel at c. These theoretical uncertainties should be addressed in future work.

While the MONDian framework provides a reasonable fit to the locally observed density and velocity field, we emphasize that other alternative cosmologies might do so as well. Our results suggest that a successful model should have an expansion history similar to ΛCDM, but yield significantly more cosmic variance on a 300 Mpc scale. Additionally, the model must also accurately describe the dynamics of galaxies in order to provide a holistic explanation of the observed Universe. In this regard, a modification to gravity at length-scales beyond e.g. 10 Mpc would not be sufficient as it would face the same issues as ΛCDM on galaxy scales.

There are still considerable theoretical uncertainties in the here developed cosmological MOND simulation (Sections 3.1 and 5.2.3) because we lack an understanding of the fundamental theory behind MOND (i.e. FUNDAMOND, Milgrom 2020a,b). Nevertheless, a promising relativistic MOND version was recently developed in which gravitational waves travel at the speed of light (Skordis & Złośnik 2019). Its implications for cosmology should be explored, though a rather large box size would be required to reach the scale at which the CP holds in a Milgromian universe. This is because in MOND the EFE suppresses the growth of structure, causing structure formation in different regions to become correlated (Section 5.2.2). Without such simulations and/or further analytic work, we cannot draw any strong conclusions on the expected time evolution of the EFE. We none the less expect our results to hold because a wide range of possible EFE histories yield reasonable results, and because other void parameters such as its initial size and strength could be adjusted to optimize the fit (Fig. 14).

Any viable cosmological model has to explain both the local and global Universe. The KBC void is virtually impossible within the ΛCDM framework (Section 2.2). Consequently, the ΛCDM model faces serious challenges on Gpc scales, as shown in this contribution – the KBC void and Hubble tension falsify the ΛCDM paradigm at the 7.09σ level, and point towards much more rapid growth of structure than predicted by standard cosmology. Moreover, Di Valentino et al. (2020a) reported 'a possible crisis for cosmology' based on the Planck power spectra, while Di Valentino, Melchiorri & Silk (2020c) concluded that the ΛCDM paradigm has to be replaced. These large-scale issues should be addressed together with the severe problems faced by ΛCDM on galactic scales (e.g. the satellite planes and the RAR, see also Kroupa 2015, and references therein).

Previous studies have shown that MOND is successful on several astrophysical scales ranging from the equilibrium dynamics of galaxies (Famaey & McGaugh 2012) and their formation out of gas clouds (Wittenburg, Kroupa & Famaey 2020), to the equilibrium dynamics of virialized galaxy clusters (Angus et al. 2013), and the formation of extreme clusters like El Gordo (e.g. Katz et al. 2013). The cluster-scale successes require the assumption of sterile neutrinos as HDM, which allows MOND to produce a standard expansion history and have very little effect on BBN and the high-acceleration CMB (Section 3.1). Consequently, there exist only very few (if any) scales at which the ΛCDM framework provides a unique explanation for the observations. Rather, observations of the local and global Universe strongly suggest that we should replace ΛCDM with the νHDM framework, which relies on MOND and sterile neutrinos.

The encouraging results we obtained using this approach should be put on a more secure theoretical footing using a covariant framework such as that of Skordis & Złośnik (2019). In particular, it is important to rigorously demonstrate that the background cosmology behaves like in ΛCDM at the sub-per cent level. A covariant framework would also clarify if there is any coupling between the Hubble flow acceleration and that sourced by inhomgeneities. If there is and if its strength is adjustable, the value could be found empirically using numerical simulations of large-scale structure. Calculating photon propagation through the resulting time-varying inhomogeneous gravitational field would then allow comparison with the observed lensing of the CMB by intervening structures, and the resulting ISW effect (Buchert 2000; Wiltshire 2007). Although these both appear to be underestimated in the ΛCDM framework (Section 5.3.1), they may be overestimated in νHDM. In this context, it is worth mentioning that the CMB Cold Spot could be caused by a KBC-like void (Nadathur et al. 2014). The expected frequency of such voids should be quantified using numerical simulations, which would also account for more complicated effects such as non-sphericity of the void. This may lead to predictions for angular dependence of the apparent expansion rate, which could be contrasted with observations (e.g. those of Migkas et al. 2020).

We conclude that unlike ΛCDM as presently understood, MOND supplemented by HDM appears to be a promising way to explain observations across all astrophysical scales. In particular, we expect this νHDM model to yield an almost standard expansion history but with enhanced cosmic variance on a 300 Mpc scale, allowing it to explain the observed KBC void and therewith the Hubble tension. This scenario has to be investigated in an open-minded manner in future studies.

ACKNOWLEDGEMENTS

IB is supported by an Alexander von Humboldt Foundation post-doctoral research fellowship. We are grateful to Karl Menten for his support and helpful suggestions. We would also like to thank Raul Angulo for providing data from the MXXL simulation, and David Camarena for providing the observational correlation coefficient between their inferred H_0 and $\overline{q}_0$. We thank the referee for her/his useful comments to improve especially the theoretical aspects of this publication.

DATA AVAILABILITY

The data underlying this article are available in the article.

REFERENCES

Alam S. et al., 2017, MNRAS, 470, 2617
Alexander S., McDonough E., 2019, Phys. Lett. B, 797, 134830
Angulo R. E., Springel V., White S. D. M., Jenkins A., Baugh C. M., Frenk C. S., 2012, MNRAS, 426, 2046
Angulo R. E., White S. D. M., Springel V., Henriques B., 2014, MNRAS, 442, 2131
Angus G. W., 2009, MNRAS, 394, 527
Angus G. W., Diaferio A., 2011, MNRAS, 417, 941
Angus G. W., Shan H. Y., Zhao H. S., Famaey B., 2007, ApJ, 654, L13
Angus G. W., Famaey B., Diaferio A., 2010, MNRAS, 402, 395
Angus G. W., Diaferio A., Famaey B., van der Heyden K. J., 2013, MNRAS, 436, 202
Aver E., Olive K. A., Skillman E. D., 2012, J. Cosmol. Astropart. Phys., 2012, 004
Babcock H. W., 1939, Lick Obs. Bull., 498, 41
Banik I., Zhao H., 2016, MNRAS, 459, 2237
Banik I., Zhao H., 2018a, MNRAS, 473, 419
Banik I., Zhao H., 2018b, MNRAS, 473, 4033
Banik I., Zhao H., 2018c, MNRAS, 480, 2660
Banik I., O'Ryan D., Zhao H., 2018, MNRAS, 477, 4768
Barnes J. E., Hernquist L., 1992, Nature, 360, 715
Begeman K. G., Broeils A. H., Sanders R. H., 1991, MNRAS, 249, 523
Bekenstein J., Milgrom M., 1984, ApJ, 286, 7
Bekenstein J. D., 2004, Phys. Rev. D, 70, 083509
Bengaly C. A. P., Novaes C. P., Xavier H. S., Bilicki M., Bernui A., Alcaniz J. S., 2018, MNRAS, 475, L106
Bennett C. L. et al., 2003, ApJS, 148, 1
Binney J., Tremaine S., 1987, Galactic Dynamics. Princeton Univ. Press, Princeton, NJ
Boyarsky A., Ruchayskiy O., Iakubovskyi D., Franse J., 2014, Phys. Rev. Lett., 113, 251301
Buchert T., 2000, General Relativ. Gravit., 32, 105
Bulbul E., Markevitch M., Foster A., Smith R. K., Loewenstein M., Randall S. W., 2014, ApJ, 789, 13
Busswell G. S., Shanks T., Frith W. J., Outram P. J., Metcalfe N., Fong R., 2004, MNRAS, 354, 991
Bílek M., Müller O., Famaey B., 2019, A&A, 627, L1
Bílek M., Thies I., Kroupa P., Famaey B., 2018, A&A, 614, A59
Böhringer H., Chon G., Bristow M., Collins C. A., 2015, A&A, 574, A26
Böhringer H., Chon G., Collins C. A., 2020, A&A, 633, A19
Caldwell N. et al., 2017, ApJ, 839, 20
Camarena D., Marra V., 2020a, Phys. Rev. Res., 2, 013028
Camarena D., Marra V., 2020b, MNRAS, 495, 2630
Candlish G. N., 2016, MNRAS, 460, 2571
Clarke C. J., 2020, MNRAS, 491, L72
Clowe D., Bradač M., Gonzalez A. H., Markevitch M., Randall S. W., Jones C., Zaritsky D., 2006, ApJ, 648, L109
Colgáin E. Ó., 2019, J. Cosmol. Astropart. Phys., 2019, 006
Colin J., Mohayaee R., Rameez M., Sarkar S., 2019, A&A, 631, L13
Collett T. E. et al., 2018, Science, 360, 1342
Cooke R. J., Fumagalli M., 2018, Nat. Astron., 2, 957
Cooke R. J., Pettini M., Steidel C. C., 2018, ApJ, 855, 102
Cuceu A., Farr J., Lemos P., Font-Ribera A., 2019, J. Cosmol. Astropart. Phys., 2019, 044

Cyburt R. H., Fields B. D., Olive K. A., 2002, Astropart. Phys., 17, 87
Cyburt R. H., Fields B. D., Olive K. A., Yeh T.-H., 2016, Rev. Mod. Phys., 88, 015004
Dark Energy Survey, South Pole Telescope Collaborations, 2018, MNRAS, 480, 3879
de Almeida Á. O. F., Piattella O. F., Rodrigues D. C., 2016, MNRAS, 462, 2706
de Jaeger T., Stahl B. E., Zheng W., Filippenko A. V., Riess A. G., Galbany L., 2020, MNRAS, 496, 3402
DES Collaboration, 2019, MNRAS, 484, 5267
Ding Q., Nakama T., Wang Y., 2020, Sci. China Phys. Mech. Astron., 63, 290403
Di Valentino E., Melchiorri A., Silk J., 2020a, Nat. Astron., 4, 196
Di Valentino E., Melchiorri A., Silk J., 2020b, J. Cosmol. Astropart. Phys., 2020, 013
Di Valentino E., Melchiorri A., Silk J., 2020c, preprint (arXiv:2003.04935v1)
Dodelson S., Liguori M., 2006, Phys. Rev. Lett., 97, 231301
Eisenstein D. J. et al., 2005, ApJ, 633, 560
Enea A. R., 2018, IJMPD, 27, 1850102
Falco M., Hansen S. H., Wojtak R., Mamon G. A., 2013, MNRAS, 431, L6
Famaey B., Binney J., 2005, MNRAS, 363, 603
Famaey B., McGaugh S. S., 2012, Living Rev. Relativ., 15, 10
Famaey B., Bruneton J.-P., Zhao H., 2007, MNRAS, 377, L79
Fixsen D. J., 2009, ApJ, 707, 916
Frith W. J., Busswell G. S., Fong R., Metcalfe N., Shanks T., 2003, MNRAS, 345, 1049
Frith W. J., Shanks T., Outram P. J., 2005, MNRAS, 361, 701
Frith W. J., Metcalfe N., Shanks T., 2006, MNRAS, 371, 1601
Fujii H., 2020, Res. Notes Am. Astron. Soc., 4, 72
Gaia Collaboration, 2018, A&A, 616, A1
Gómez-Valent A., Amendola L., 2018, J. Cosmol. Astropart. Phys., 2018, 051
Haghi H., Bazkiaei A. E., Zonoozi A. H., Kroupa P., 2016, MNRAS, 458, 4172
Haghi H. et al., 2019a, MNRAS, 487, 2441
Haghi H., Amiri V., Hasani Zonoozi A., Banik I., Kroupa P., Haslbauer M., 2019b, ApJ, 884, L25
Harrison E. R., 1970, Phys. Rev. D, 1, 2726
Haslbauer M., Banik I., Kroupa P., Grishunin K., 2019a, MNRAS, 489, 2634
Haslbauer M., Dabringhausen J., Kroupa P., Javanmardi B., Banik I., 2019b, A&A, 626, A47
Hill J. C., McDonough E., Toomey M. W., Alexander S., 2020, Phys. Rev. D, 102, 043507
Hoof S., Geringer-Sameth A., Trotta R., 2020, J. Cosmol. Astropart. Phys., 2020, 012
Hoscheit B. L., Barger A. J., 2018, ApJ, 854, 46
Howk J. C., Lehner N., Fields B. D., Mathews G. J., 2012, Nature, 489, 121
Huang C. D. et al., 2020, ApJ, 889, 5
Huang J. S., Cowie L. L., Gardner J. P., Hu E. M., Songaila A., Wainscoat R. J., 1997, ApJ, 476, 12
Ibata R. A. et al., 2013, Nature, 493, 62
Jaffe A. H. et al., 2001, Phys. Rev. Lett., 86, 3475
Javanmardi B., Kroupa P., 2017, A&A, 597, A120
Javanmardi B., Kroupa P., 2020, MNRAS, 493, L44
Javanmardi B., Porciani C., Kroupa P., Pflamm-Altenburg J., 2015, ApJ, 810, 47
Javanmardi B., Raouf M., Khosroshahi H. G., Tavasoli S., Müller O., Molaeinezhad A., 2019, ApJ, 870, 50
Jee I., Suyu S. H., Komatsu E., Fassnacht C. D., Hilbert S., Koopmans L. V. E., 2019, Science, 365, 1134
Jee M. J., Hughes J. P., Menanteau F., Sifón C., Mandelbaum R., Barrientos L. F., Infante L., Ng K. Y., 2014, ApJ, 785, 20
Joudaki S., Kaplinghat M., Keeley R., Kirkby D., 2018, Phys. Rev. D, 97, 123501
Karachentsev I. D., 2012, Astrophys. Bull., 67, 123
Karachentsev I. D., Telikova K. N., 2018, Astron. Nachr., 339, 615
Karwal T., Kamionkowski M., 2016, Phys. Rev. D, 94, 103523
Kashlinsky A., Atrio-Barandela F., Kocevski D., Ebeling H., 2008, ApJ, 686, L49
Kashlinsky A., Atrio-Barandela F., Ebeling H., 2011, ApJ, 732, 1
Katz H., McGaugh S., Teuben P., Angus G. W., 2013, ApJ, 772, 10
Keenan R. C., Barger A. J., Cowie L. L., 2013, ApJ, 775, 62
Kenworthy W. D., Scolnic D., Riess A., 2019, ApJ, 875, 145
Khoraminezhad H., Viel M., Baccigalupi C., Archidiacono M., 2020, J. Cosmol. Astropart. Phys., 2020, 039
Kochanek C. S., 2020, MNRAS, 493, 1725
Kogut A. et al., 1993, ApJ, 419, 1
Kovács A., 2018, MNRAS, 475, 1777
Kroupa P., 2012, Publ. Astron. Soc. Aust., 29, 395
Kroupa P., 2015, Can. J. Phys., 93, 169
Kroupa P., Theis C., Boily C. M., 2005, A&A, 431, 517
Kroupa P. et al., 2018, Nature, 561, E4
Lavaux G., Hudson M. J., 2011, MNRAS, 416, 2840
Lelli F., McGaugh S. S., Schombert J. M., 2016, AJ, 152, 157
Lelli F., McGaugh S. S., Schombert J. M., Pawlowski M. S., 2017, ApJ, 836, 152
Lewis G. F., Barnes L. A., Kaushik R., 2016, MNRAS, 460, 291
Llinares C., Knebe A., Zhao H., 2008, MNRAS, 391, 1778
Lüghausen F., Famaey B., Kroupa P., 2015, Can. J. Phys., 93, 232
Macaulay E. et al., 2019, MNRAS, 486, 2184
Macpherson H. J., Lasky P. D., Price D. J., 2018, ApJ, 865, L4
Maddox S. J., Sutherland W. J., Efstathiou G., Loveday J., Peterson B. A., 1990, MNRAS, 247, 1P
Mantz A. B. et al., 2015, MNRAS, 446, 2205
Marra V., Amendola L., Sawicki I., Valkenburg W., 2013, Phys. Rev. Lett., 110, 241305
Marriage T. A. et al., 2011, ApJ, 737, 61
McGaugh S. S., 2005, ApJ, 632, 859
McGaugh S. S., 2011, Phys. Rev. Lett., 106, 121303
McGaugh S. S., 2016, ApJ, 832, L8
McGaugh S. S., Wolf J., 2010, ApJ, 722, 248
McGaugh S. S., Schombert J. M., Bothun G. D., de Blok W. J. G., 2000, ApJ, 533, L99
McGaugh S., Milgrom M., 2013, ApJ, 775, 139
Melia F., 2020, Eur. Phys. J. Plus, 135, 511
Menanteau F. et al., 2012, ApJ, 748, 7
Merle A., 2017, Sterile Neutrino Dark Matter. Morgan & Claypool Publishers, California
Migkas K., Schellenberger G., Reiprich T. H., Pacaud F., Ramos-Ceja M. E., Lovisari L., 2020, A&A, 636, A15
Milgrom M., 1983, ApJ, 270, 365
Milgrom M., 1986, ApJ, 302, 617
Milgrom M., 1999, Phys. Lett. A, 253, 273
Milgrom M., 2010, MNRAS, 403, 886
Milgrom M., 2013, Phys. Rev. Lett., 111, 041105
Milgrom M., 2017, preprint (arXiv:1703.06110v3)
Milgrom M., 2020a, preprint (arXiv:2001.09729v1)
Milgrom M., 2020b, Science Direct, 71, 170
Millon M. et al., 2020, A&A, 639, A101
Mirabel I. F., Dottori H., Lutz D., 1992, A&A, 256, L19
Mészáros A., 2019, Astron. Nachr., 340, 564
Müller O., Pawlowski M. S., Jerjen H., Lelli F., 2018, Science, 359, 534
Nadathur S., Lavinto M., Hotchkiss S., Räsänen S., 2014, Phys. Rev. D, 90, 103510
Nusser A., 2002, MNRAS, 331, 909
Ostriker J. P., Peebles P. J. E., 1973, ApJ, 186, 467
Ostriker J. P., Steinhardt P. J., 1995, Nature, 377, 600
Pandey S., Raveri M., Jain B., 2019, Phys. Rev. D, 102, 023505
Pawlowski M. S., 2018, Mod. Phys. Lett. A, 33, 1830004
Pawlowski M. S., Kroupa P., 2020, MNRAS, 491, 3042
Pawlowski M. S., McGaugh S. S., 2014, MNRAS, 440, 908
Pawlowski M. S., Pflamm-Altenburg J., Kroupa P., 2012, MNRAS, 423, 1109
Pawlowski M. S. et al., 2014, MNRAS, 442, 2362
Pazy E., 2013, Phys. Rev. D, 87, 084063
Peebles P. J. E., 2017, preprint (arXiv:1705.10683v1)
Peebles P. J. E., Nusser A., 2010, Nature, 465, 565
Pesce D. W. et al., 2020, ApJ, 891, L1
Pittordis C., Sutherland W., 2019, MNRAS, 488, 4740

Planck Collaboration VI, 2020, A&A, 641, A6
Planck Collaboration XIII, 2016, A&A, 594, A13
Planck Collaboration XXIII, 2014, A&A, 571, A23
Planck Collaboration XXVII, 2014, A&A, 571, A27
Ploeckinger S., Sharma K., Schaye J., Crain R. A., Schaller M., Barber C., 2018, MNRAS, 474, 580
Ponomareva A. A., Verheijen M. A. W., Papastergis E., Bosma A., Peletier R. F., 2018, MNRAS, 474, 4366
Poulin V., Smith T. L., Karwal T., Kamionkowski M., 2019, Phys. Rev. Lett., 122, 221301
Reid M. J., Braatz J. A., Condon J. J., Greenhill L. J., Henkel C., Lo K. Y., 2009, ApJ, 695, 287
Reid M. J., Pesce D. W., Riess A. G., 2019, ApJ, 886, L27
Reiprich T. H., Böhringer H., 2002, ApJ, 567, 716
Riess A. G., 2020, Nat. Rev. Phys., 2, 10
Riess A. G. et al., 1998, AJ, 116, 1009
Riess A. G. et al., 2016, ApJ, 826, 56
Riess A. G. et al., 2018, ApJ, 853, 126
Riess A. G., Casertano S., Yuan W., Macri L. M., Scolnic D., 2019, ApJ, 876, 85
Riess A. G., Yuan W., Casertano S., Macri L. M., Scolnic D., 2020, ApJ, 896, L43
Rines K., Diaferio A., Natarajan P., 2008, ApJ, 679, L1
Rogstad D. H., Shostak G. S., 1972, ApJ, 176, 315
Ruan C.-Z., Melia F., Chen Y., Zhang T.-J., 2019, ApJ, 881, 137
Rubart M., Schwarz D. J., 2013, A&A, 555, A117
Rubart M., Bacon D., Schwarz D. J., 2014, A&A, 565, A111
Rubin V. C., Ford W. Kent J., 1970, ApJ, 159, 379
Sahlén M., Zubeldía Í., Silk J., 2016, ApJ, 820, L7
Sakstein J., Trodden M., 2020, Phys. Rev. Lett., 124, 161301
Sanders R. H., 1998, MNRAS, 296, 1009
Sanders R. H., 1999, ApJ, 512, L23
Sanders R. H., 2001, ApJ, 560, 1
Sanders R. H., 2003, MNRAS, 342, 901
Sanders R. H., McGaugh S. S., 2002, ARA&A, 40, 263
Schmidt B. P. et al., 1998, ApJ, 507, 46
Schombert J., McGaugh S., Lelli F., 2020, AJ, 160, 71
Shajib A. J. et al., 2020, MNRAS, 494, 6072
Shanks T., Hogarth L. M., Metcalfe N., Whitbourn J., 2019, MNRAS, 490, 4715
Skordis C., 2006, Phys. Rev. D, 74, 103513
Skordis C., Mota D. F., Ferreira P. G., Bœhm C., 2006, Phys. Rev. Lett., 96, 011301
Skordis C., Złośnik T., 2019, Phys. Rev. D, 100, 104013
Skordis C., Złosnik T., 2020, preprint (arXiv:2007.00082v1)
Smolin L., 2017, Phys. Rev. D, 96, 104042
Springel V. et al., 2005, Nature, 435, 629
Stark D. V., McGaugh S. S., Swaters R. A., 2009, AJ, 138, 392
Steigman G., 2012, Adv. High Energy Phys., 2012, 268321
Sunyaev R. A., Zeldovich I. B., 1980, MNRAS, 190, 413
Teyssier R., 2002, A&A, 385, 337
The Supernova Cosmology Project, 1999, ApJ, 517, 565
Tikhonov A. V., Klypin A., 2009, MNRAS, 395, 1915
Torrealba G., Koposov S. E., Belokurov V., Irwin M., 2016, MNRAS, 459, 2370
Torres-Flores S., Epinat B., Amram P., Plana H., Mendes de Oliveira C., 2011, MNRAS, 416, 1936
Tremaine S., Gunn J. E., 1979, Phys. Rev. Lett., 42, 407
van der Marel R. P., Besla G., Cox T. J., Sohn S. T., Anderson J., 2012, ApJ, 753, 9
van der Marel R. P., Fardal M. A., Sohn S. T., Patel E., Besla G., del Pino A., Sahlmann J., Watkins L. L., 2019, ApJ, 872, 24
Vavryčuk V., 2018, MNRAS, 478, 283
Vavryčuk V., 2019, MNRAS, 489, L63
Verde L., Treu T., Riess A. G., 2019, Nat. Astron., 3, 891
Verlinde E., 2017, SciPost Phys., 2, 016
Virgo, LIGO Collaborations, 2017, Phys. Rev. Lett., 119, 161101
Wetzstein M., Naab T., Burkert A., 2007, MNRAS, 375, 805
Whitbourn J. R., Shanks T., 2014, MNRAS, 437, 2146
Wiltshire D. L., 2007, New J. Phys., 9, 377
Wittenburg N., Kroupa P., Famaey B., 2020, ApJ, 890, 173
Wojtak R., Knebe A., Watson W. A., Iliev I. T., Heß S., Rapetti D., Yepes G., Gottlöber S., 2014, MNRAS, 438, 1805
Wong K. C. et al., 2020, MNRAS, 498, 1420
Wright E. L., 2004, in Freedman W. L., ed., Measuring and Modeling the Universe. Cambridge Univ. Press, Cambridge, p. 291
Wu H.-Y., Huterer D., 2017, MNRAS, 471, 4946
Xie L., Gao L., Guo Q., 2014, MNRAS, 441, 933
Yershov V. N., Raikov A. A., Lovyagin N. Y., Kuin N. P. M., Popova E. A., 2020, MNRAS, 492, 5052
Yoo J., Mitsou E., Dirian Y., Durrer R., 2019, Phys. Rev. D, 100, 063510
Zeldovich Y. B., 1972, MNRAS, 160, 1P
Zhang X., Huang Q.-G., Li X.-D., 2019, MNRAS, 483, 1655
Zhao H., 2008, preprint (arXiv:0805.4046v2)
Zhao H., Famaey B., Lüghausen F., Kroupa P., 2013, A&A, 557, L3
Zucca E. et al., 1997, A&A, 326, 477

APPENDIX A: GAUSSIANITY OF THE ΛCDM DENSITY FLUCTUATIONS

We perform a Gaussianity test to determine if the density fluctuations calculated in the MXXL simulation (Section 2) follow a normal distribution. For this, we run 10^4 Monte Carlo trials in which each time we select the three lowest values out of 10^6 randomly generated

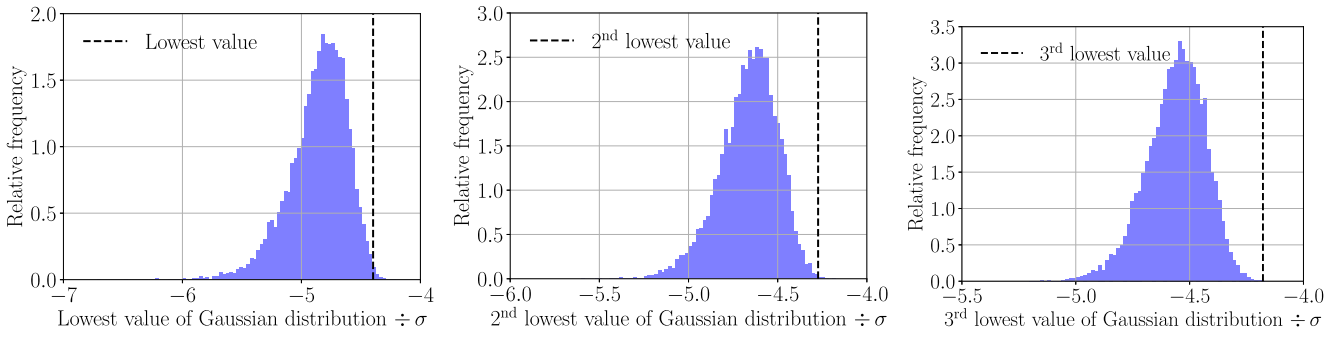

Figure A1. Normality tests on the density fluctuations in the ΛCDM MXXL simulation within a spherical shell with an inner radius of 40 Mpc and an outer radius of 300 Mpc at redshift $z = 0$. The distributions (blue) show the lowest (left-hand panel), second (middle panel), and third (right-hand panel) lowest values generated using 10^4 Monte Carlo trials, with each value shown based on 10^6 Gaussian random numbers to mimic the number of vantage points used in MXXL. The dashed lines mark the lowest, second, and third lowest relative density contrast scaled by the rms fluctuations of the MXXL simulation (Section 2.1).

Gaussian numbers. The left-hand panel of Fig. A1 shows the distribution of the lowest value of each Monte Carlo trial compared with the lowest relative density contrast in MXXL scaled by the rms fluctuation. The same procedure is applied for the second and third lowest values in the middle and right-hand panels of Fig. A1, respectively. As expected, the lowest, second and third lowest values generated by the Monte Carlo trials cluster in a narrow region around -5σ. The three most underdense regions in the MXXL simulation match roughly with the expected values from the Monte Carlo distributions, indicating that the MXXL density fluctuations closely follow a normal distribution.

APPENDIX B: KBC VOID MASS PROFILES

In addition to our fiducial MOND simulation based on a Maxwell–Boltzmann void density profile (Section 3.2.1), we also model the void with a Gaussian and an exponential profile. The enclosed mass of the void within co-moving radius $r_{\rm com}$ for a Gaussian profile is

$$M_{\rm enc} = 4\pi\rho_0 r_{\rm void}^3 \left(\frac{x^3}{3} - \alpha_{\rm void}\left[\sqrt{\frac{\pi}{2}}{\rm erf}\left(\frac{x}{\sqrt{2}}\right) - x\exp\left(-\frac{x^2}{2}\right)\right]\right). \tag{B1}$$

As before, $x \equiv r_{\rm com}/r_{\rm void}$, $\alpha_{\rm void}$ is the initial void strength, and $r_{\rm void}$ is the initial co-moving void size at $z = 9$.

The corresponding result for an exponential profile is

$$M_{\rm enc} = 4\pi\rho_0 r_{\rm void}^3 \left(\frac{x^3}{3} - \alpha_{\rm void}\left[2 - \left(x^2 + 2x + 2\right)\exp\left(-x\right)\right]\right). \tag{B2}$$

In both cases, $\alpha_{\rm void}$ is the initial underdensity at the void centre. The results of using these void profiles are presented and compared with local observations in Appendix C.

APPENDIX C: RESULTS FOR DIFFERENT VOID PROFILES

The marginalized posterior distribution of the model parameters based on 10^6 MOND models for a Gaussian and an exponential initial void profile are shown in Figs C1 and C2, respectively. All these models assume a time-independent EFE (i.e. $n_{\rm EFE} = 0$ in equation 50). As with the Maxwell–Boltzmann profile, models with a very weak or a very strong EFE are ruled out, but the initial void parameters are only weakly constrained by local observations. In particular, models with a Gaussian and an exponential profile restrict $g_{\rm ext}$ to the range $(0.045 - 0.127)\,a_0$ and $(0.045 - 0.117)\,a_0$ at the 3σ level, respectively.

The best-fitting model for a Gaussian void profile has an external field strength of $g_{\rm ext} = 0.070\,a_0$, an initial void size of $r_{\rm void} = 1030.0$ cMpc (the upper limit of the allowed parameter range), and an initial void strength of $\alpha_{\rm void} = 3.76 \times 10^{-5}$. This model is in 2.84σ (0.45 per cent) tension with local observations (Section 3.3).

For an exponential void profile, the best-fitting model has $g_{\rm ext} = 0.080\,a_0$, $r_{\rm void} = 1030.0$ cMpc, and $\alpha_{\rm void} = 7.56 \times 10^{-5}$. The overall tension with observations is 2.93σ (0.34 per cent).

The results for both models are listed and compared with observations in Table C1. A time-dependent EFE and its implications for structure formation are studied in Section 5.2.2 for all three considered profiles.

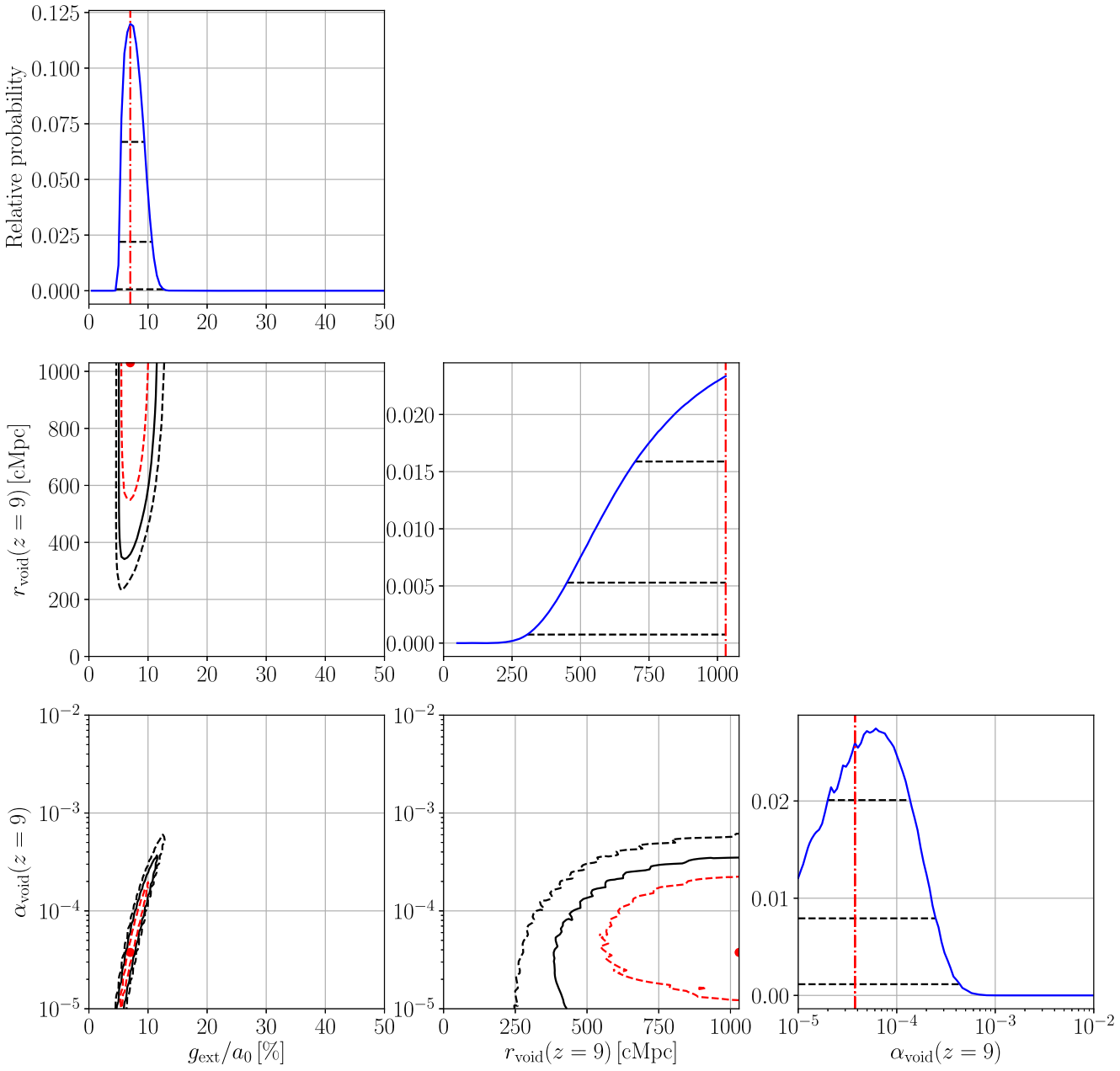

Figure C1. Similar to Fig. 4, but for a void modelled with a Gaussian profile (equation B1). The red dashed, black solid, and black dashed lines mark the 1σ, 2σ, and 3σ confidence levels, respectively. For 1D posteriors, these are shown using horizontal black lines. The red dot or vertical line marks the best-fitting model with an external field strength of $g_{\rm ext} = 0.070\,a_0$, an initial void size of $r_{\rm void} = 1030$ cMpc (the upper limit of the allowed parameter range), and an initial void strength of $\alpha_{\rm void} = 3.76 \times 10^{-5}$ at $z = 9$.

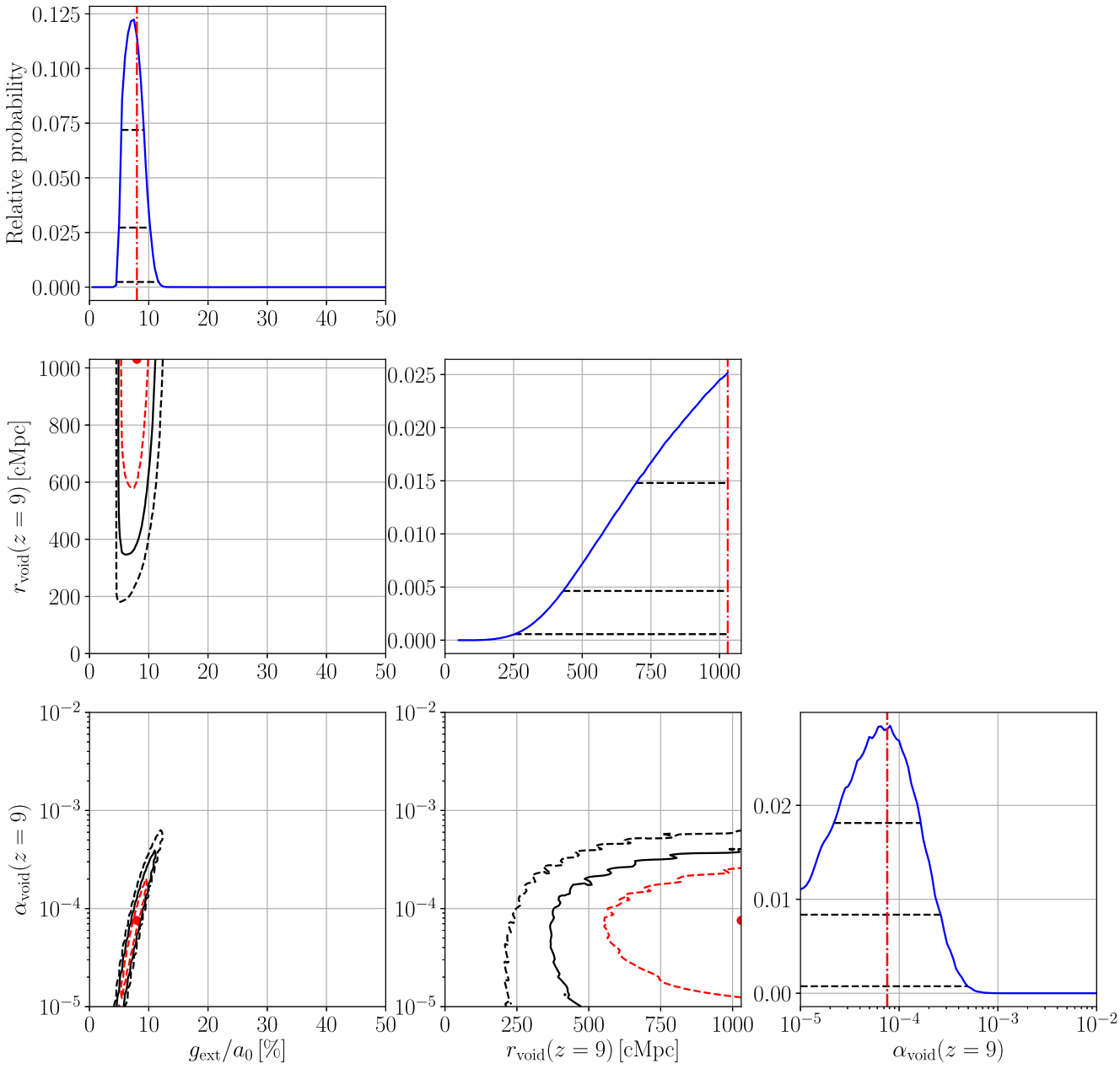

Figure C2. Similar to Fig. 4, but for a void modelled with an exponential profile (equation B2). The red dashed, black solid, and black dashed lines mark the 1σ, 2σ, and 3σ confidence levels, respectively. For 1D posteriors, these are shown using horizontal black lines. The red dot or vertical line marks the best-fitting model with an external field strength of $g_{\rm ext} = 0.080\,a_0$, an initial void size of $r_{\rm void} = 1030$ cMpc (the upper limit of the allowed range), and an initial void strength of $\alpha_{\rm void} = 7.56 \times 10^{-5}$ at $z = 9$.

Table C1. Similar to Table 4, but now showing results for different void profiles. In all cases, we fix $n_{\rm EFE} = 0$.

Maxwell–Boltzmann density profile, $g_{\rm ext} = 0.055\,a_0$, $r_{\rm void} = 228.2\,$cMpc, $\alpha_{\rm void} = 3.76 \times 10^{-5}$, $v_{\rm void} = 1586\,{\rm km\,s^{-1}}$, $r_{\rm void}^{\rm rms} = 528.7\,$Mpc, $n_{\rm EFE} = 0$						
Parameter	$H_0^{\rm local}$ (km s^{-1} Mpc^{-1})	$\bar{q}_0^{\rm local}$	$H_0^{\rm lensing}$ (km s^{-1} Mpc^{-1})	$v_{\rm LG}$ (km s^{-1})	$\delta_{\rm in}$	$\delta_{\rm out}$
Observations	75.35 ± 1.68	1.08 ± 0.29	–	627	0.254 ± 0.083	-0.052 ± 0.105
MOND model	76.15	1.07	See Fig. 7	See Fig. 8	0.172	0.050
χ^2	0.34		14.66	–	0.99	0.94
Degrees of freedom	2		7	–	1	1
χ (1D Gaussian equivalent)	0.20		2.05	2.34	0.99	0.97
Gaussian density profile, $g_{\rm ext} = 0.070\,a_0$, $r_{\rm void} = 1030.0\,$cMpc, $\alpha_{\rm void} = 3.76 \times 10^{-5}$, $v_{\rm void} = 2018\,{\rm km\,s^{-1}}$, $r_{\rm void}^{\rm rms} = 744.7\,$Mpc, $n_{\rm EFE} = 0$						
Parameter	$H_0^{\rm local}$ (km s^{-1} Mpc^{-1})	$\bar{q}_0^{\rm local}$	$H_0^{\rm lensing}$ (km s^{-1} Mpc^{-1})	$v_{\rm LG}$ (km s^{-1})	$\delta_{\rm in}$	$\delta_{\rm out}$
Observations	75.35 ± 1.68	1.08 ± 0.29	–	627	0.274 ± 0.081	-0.085 ± 0.108
MOND model	77.24	1.43	–	–	0.155	0.078
χ^2	1.79		12.74	–	2.19	2.26
Degrees of freedom	2		7	–	1	1
χ (1D Gaussian equivalent)	0.83		1.76	2.35	1.48	1.50
Exponential density profile, $g_{\rm ext} = 0.080\,a_0$, $r_{\rm void} = 1030.0\,$cMpc, $\alpha_{\rm void} = 7.56 \times 10^{-5}$, $v_{\rm void} = 2307\,{\rm km\,s^{-1}}$, $r_{\rm void}^{\rm rms} = 730.4\,$Mpc, $n_{\rm EFE} = 0$						
Parameter	$H_0^{\rm local}$ (km s^{-1} Mpc^{-1})	$\bar{q}_0^{\rm local}$	$H_0^{\rm lensing}$ (km s^{-1} Mpc^{-1})	$v_{\rm LG}$ (km s^{-1})	$\delta_{\rm in}$	$\delta_{\rm out}$
Observations	75.35 ± 1.68	1.08 ± 0.29	–	627	0.276 ± 0.080	-0.078 ± 0.108
MOND model	77.25	1.46	–	–	0.158	0.073
χ^2	1.98		13.19	–	2.17	1.97
Degrees of freedom	2		7	–	1	1
χ (1D Gaussian equivalent)	0.89		1.83	2.47	1.47	1.40

This paper has been typeset from a TEX/LATEX file prepared by the author.

APPENDIX B

Paper: The High Fraction of Thin Disk Galaxies Continues to Challenge ΛCDM cosmology

This chapter includes a copy of the peer-reviewed paper entitled "The High Fraction of Thin Disk Galaxies Continues to Challenge ΛCDM cosmology" published in The Astrophysical Journal, 925, 183, 2022 by **Moritz Haslbauer**, Indranil Banik, Pavel Kroupa, Nils Wittenburg, and Behnam Javanmardi. A summary and the author contributions are provided in Chapter 8.

The Astrophysical Journal, 925:183 (20pp), 2022 February 1 https://doi.org/10.3847/1538-4357/ac46ac

The High Fraction of Thin Disk Galaxies Continues to Challenge ΛCDM Cosmology

Moritz Haslbauer[1,2], Indranil Banik[1,3], Pavel Kroupa[1,4], Nils Wittenburg[1], and Behnam Javanmardi[5]
[1] Helmholtz-Institut für Strahlen- und Kernphysik (HISKP), University of Bonn, Nussallee 14−16, D-53115 Bonn, Germany; mhaslbauer@astro.uni-bonn.de
[2] Max-Planck-Institut für Radioastronomie, Auf dem Hügel 69, D-53121 Bonn, Germany
[3] Scottish Universities Physics Alliance, University of Saint Andrews, North Haugh, Saint Andrews, Fife, KY16 9SS, UK; ib45@st-andrews.ac.uk
[4] Charles University in Prague, Faculty of Mathematics and Physics, Astronomical Institute, V Holešovičkách 2, CZ-180 00 Praha 8, Czech Republic
[5] Institute for Genomic Statistics and Bioinformatics, University of Bonn, Venusberg-Campus 1, D-53127 Bonn, Germany
Received 2021 June 23; revised 2021 December 22; accepted 2021 December 24; published 2022 February 4

Abstract

Any viable cosmological framework has to match the observed proportion of early- and late-type galaxies. In this contribution, we focus on the distribution of galaxy morphological types in the standard model of cosmology (Lambda cold dark matter, ΛCDM). Using the latest state-of-the-art cosmological ΛCDM simulations known as Illustris, IllustrisTNG, and EAGLE, we calculate the intrinsic and sky-projected aspect ratio distribution of the stars in subhalos with stellar mass $M_* > 10^{10}\,M_\odot$ at redshift $z = 0$. There is a significant deficit of intrinsically thin disk galaxies, which however comprise most of the locally observed galaxy population. Consequently, the sky-projected aspect ratio distribution produced by these ΛCDM simulations disagrees with the Galaxy And Mass Assembly (GAMA) survey and Sloan Digital Sky Survey at $\geqslant 12.52\sigma$ (TNG50-1) and $\geqslant 14.82\sigma$ (EAGLE50) confidence. The deficit of intrinsically thin galaxies could be due to a much less hierarchical merger-driven build-up of observed galaxies than is given by the ΛCDM framework. It might also arise from the implemented sub-grid models, or from the limited resolution of the above-mentioned hydrodynamical simulations. We estimate that an 8^5 times better mass resolution realization than TNG50-1 would reduce the tension with GAMA to the 5.58σ level. Finally, we show that galaxies with fewer major mergers have a somewhat thinner aspect ratio distribution. Given also the high expected frequency of minor mergers in ΛCDM, the problem may be due to minor mergers. In this case, the angular momentum problem could be alleviated in Milgromian dynamics because of a reduced merger frequency arising from the absence of dynamical friction between extended dark matter halos.

Unified Astronomy Thesaurus concepts: Galaxies (573); Galaxy properties (615); Galaxy structure (622); Galaxy evolution (594); Galaxy mergers (608); Disk galaxies (391); Elliptical galaxies (456); Cosmology (343); Cold dark matter (265); Modified Newtonian dynamics (1069)

1. Introduction

Observed galaxies show a wide spectrum of structural and dynamical properties. According to the morphological classification scheme, early-type galaxies typically have a smooth ellipsoidal shape whereas late-type galaxies have a flattened disk that often contains spiral features. A dynamical characterization divides galaxies into dispersion- and rotation-dominated systems. These classifications are not identical, e.g., most early-type galaxies in the ATLAS^{3D} sample are rotation-supported (Emsellem et al. 2011).

The vast majority of nearby galaxies with stellar mass $M_* > 10^{10}\,M_\odot$ are of late type (e.g., Kautsch et al. 2006; Delgado-Serrano et al. 2010; Kormendy et al. 2010). In particular, Delgado-Serrano et al. (2010) analyzed local galaxies with an absolute magnitude $J < -20.3$ ($M_* \gtrsim 1.5 \times 10^{10}\,M_\odot$) from the Sloan Digital Sky Survey (SDSS; SDSS Collaboration 2000) and found that only $3\% \pm 1\%$ of galaxies are elliptical, $15\% \pm 4\%$ are lenticular, $72\% \pm 8\%$ are spiral, and $10\% \pm 3\%$ are peculiar. Interestingly, they also showed that the relative fraction of ellipticals and lenticulars has hardly evolved over the last 6 Gyr (see Table 3 and Figure 5 of Delgado-Serrano et al. 2010), which is consistent with their early and rapid formation (Kroupa et al. 2020, and references therein). Moreover, the relative fraction of non-spheroidals (70%–80%; i.e., spirals, irregulars, and interacting galaxies) and early types (20%–30%; i.e., ellipticals and transition E/S0 galaxies) with an apparent K_s magnitude brighter than 22 selected from the GOODS-MUSIC catalog (Grazian et al. 2006; Santini et al. 2009) of the Great Observatory Origins Deep Survey (Giavalisco et al. 2004) remains constant over the redshift range $0.6 \leqslant z \leqslant 2.5$ (see Figure 8 of Tamburri et al. 2014).

The morphology of a galaxy is closely related to internal physical processes (e.g., rapid monolithic collapse of post–Big Bang gas clouds, star formation, feedback from supernovae and active galactic nuclei), its dynamical history (interactions and mergers with other galaxies), and its environment (e.g., tidal and ram pressure effects). Thus, the observed distribution of galaxy morphological types constrains models of galaxy formation and evolution. Indeed, Disney et al. (2008) emphasized that the observed population of galaxies shows a significantly smaller variation of individual properties than expected in a hierarchical formation model where galaxies undergo mergers stochastically. Several simulations in the standard cosmological model known as Lambda cold dark matter (ΛCDM; Efstathiou et al. 1990; Ostriker & Steinhardt 1995) show an excessive loss of angular momentum (e.g., Katz & Gunn 1991; Navarro & Benz 1991; Navarro & White 1994; Navarro & Steinmetz 2000; van den Bosch 2001; Piontek & Steinmetz 2011; Scannapieco et al. 2012). This hampers the formation of bulgeless disk galaxies. Due to dynamical friction on the extended dark matter halos (Kroupa 2015), galactic mergers are common in ΛCDM. Indeed, *N*-body simulations yield that ≈ 95% of galaxies with dark matter halo

mass $M_{\rm halo} \approx 10^{12}\,h^{-1}\,M_{\odot}$ accreted at least one galaxy with $M_{\rm halo} > 5 \times 10^{10}\,h^{-1}\,M_{\odot}$ within the last 10 Gyr, where h is the present Hubble constant H_0 in units of $100\,{\rm km\,s^{-1}\,Mpc^{-1}}$ (Stewart et al. 2008). In the Millennium-II simulation (Springel et al. 2005), 69% of galaxies with a similar halo mass have had a major merger since $z = 3$ (Fakhouri et al. 2010). Galaxy mergers thicken the stellar disk and grow the bulge component, making it difficult for ΛCDM to account for the observed large population of bulgeless disk galaxies (Graham & Worley 2008; Kormendy et al. 2010). Trayford et al. (2017) showed that disk galaxies in the Evolution and Assembly of GaLaxies and their Environments (EAGLE) simulation are thicker than those observed (see their Figure 3), but concluded that this is because of the underlying subgrid physics (we discuss this further in Section 7).

Although the formation of such galaxies is generally known to be a challenge for the ΛCDM paradigm, some works claimed that the angular momentum problem has been resolved in the latest self-consistent ΛCDM simulations. For example, Vogelsberger et al. (2014) argued that the loss of angular momentum was caused by numerical and physical modeling limitations rather than a failure of the ΛCDM paradigm, because the Illustris-1 simulation produces a mix of disk galaxies and ellipticals (but see our Section 6.2, which comes to a different conclusion). Indeed, it is possible to form a Milky Way–like galaxy with a small bulge in the ΛCDM framework, but only under very special conditions of a quiescent merger history and rapid star formation, which removes low angular momentum gas from the inner part of the galaxy (Guedes et al. 2011). However, in the observed universe, such late-type galaxies are frequent, with ≈ 50% of them having no classical merger-built bulge (Kormendy et al. 2010). The same problem was identified by Graham & Worley (2008) two years earlier, who found that most real lenticular galaxies have bulge/total fractions $\lesssim 1/3$. A recent attempt to quantify the tension (Rodriguez-Gomez et al. 2019) showed that the median of the sky-projected ellipticity distribution of galaxies in the "Illustris The Next Generation" simulation (IllustrisTNG; Pillepich et al. 2018; Nelson et al. 2019) lies within the 16th–84th percentile range of the Panoramic Survey Telescope And Rapid Response System (Pan-STARRS) observational sample (Chambers et al. 2016). However, this is only a very crude test. In order to rigorously assess the angular momentum problem in a cosmological framework, one has to consider the overall distribution of galaxy morphology, as addressed by this contribution.

The present-day morphological distribution of galaxies has already been studied in the Illustris-1 simulation using mock photometry. Based on dust-free synthetic images of simulated galaxies with $M_* > 10^{10}\,M_{\odot}$ at $z = 0$, Bottrell et al. (2017a) derived photometric bulge/total fractions $(B/T)_{\rm phot}$ by performing a 2D parametric surface brightness decomposition with a fixed Sérsic index of $n_{\rm d} = 1$ for the disk component and $n_{\rm b} = 4$ for the bulge. This was done in the SDSS g and r bands at four different camera angles. In a subsequent study (Bottrell et al. 2017b), those authors applied the same decomposition analysis to observed galaxies from the SDSS. By comparing the simulated and observed galaxy samples in the space of M_* and $(B/T)_{\rm phot}$, they surprisingly found a significant deficit of bulge-dominated subhalos in the Illustris-1 simulation at $10^{10} \leqslant M_*/M_{\odot} \leqslant 10^{11}$ (see also their Figures 4 and 6). This would imply that the angular momentum problem has been resolved in ΛCDM cosmology despite mergers being very common. However, we will argue in Section 7.2 that their derived $(B/T)_{\rm phot}$ is not an appropriate measure to quantify the morphology of a galaxy in the Illustris-1 simulation. Instead of a deficit of bulge-dominated subhalos, the simulation in fact overproduces these and lacks disk-dominated galaxies, contrary to the claims of Bottrell et al. (2017b).

In this contribution, we statistically compare the observed sky-projected aspect ratio ($q_{\rm sky}$) distribution with that provided by the ΛCDM framework based on the latest state-of-the-art hydrodynamical cosmological ΛCDM simulations from the projects known as EAGLE (Schaye et al. 2015; McAlpine et al. 2016), Illustris (Vogelsberger et al. 2014; Nelson et al. 2015), and IllustrisTNG (Pillepich et al. 2018; Nelson et al. 2019). Our analysis focuses on the stellar distribution in a galaxy without regards to individual structural components like its thin or thick disk. The main aim of our work is to test whether state-of-the-art ΛCDM simulations form galaxies with a realistic distribution of morphologies.

The layout of this paper is as follows: Section 2 describes the here assessed hydrodynamical cosmological ΛCDM simulations. The methods to calculate the intrinsic and sky-projected aspect ratio of a galaxy are given in Section 3. In Section 4, we introduce the observational galaxy samples from which we extract the aspect ratio distribution. The statistical method to quantify the tension between the simulated and observed galaxy populations is explained in Section 5. The present-day intrinsic and sky-projected aspect ratio distributions yielded by the ΛCDM framework are presented and the latter are compared with observations in Section 6. In Section 7, we test the numerical convergence of the TNG50 and EAGLE runs, seek to understand the mismatch between the photometric parameters (Bottrell et al. 2017a, 2017b) and intrinsic aspect ratios in the Illustris-1 simulation, and investigate the effect of different merger histories on galaxy shapes. We also qualitatively compare the $q_{\rm sky}$ distribution of SDSS spirals with that of disk galaxies formed in hydrodynamical Milgromian dynamics (MOND; Milgrom 1983) simulations. Our conclusions are given in Section 8.

2. Cosmological ΛCDM Simulations

We investigate the aspect ratio distribution provided by different simulation runs of the projects known as EAGLE (Schaye et al. 2015; McAlpine et al. 2016), Illustris (Vogelsberger et al. 2014; Nelson et al. 2015), and TNG (Pillepich et al. 2018; Nelson et al. 2019).[6] These state-of-the-art simulations self-consistently evolve dark matter and baryons from shortly after the Big Bang up to the present time in a ΛCDM cosmology consistent with the WMAP-9 (Hinshaw et al. 2013), Planck 2015 (Planck Collaboration XIII 2016), and Planck 2013 (Planck Collaboration I 2014) measurements of the cosmic microwave background for Illustris, TNG, and EAGLE, respectively. These simulations differ in the implemented baryonic feedback models and underlying grid solvers. Both the Illustris and TNG simulations were performed with the moving-mesh code AREPO (Springel 2010), whereas the EAGLE simulations employed the GADGET-3 (Springel 2005) smoothed particle hydrodynamics (SPH) code. Here, we use the TNG50-1, TNG100-1, Illustris-1, EAGLE Ref-L050N0752 (hereafter EAGLE50), and EAGLE Ref-L100N1504 (EAGLE100) simulations, with TNG50-1 having the highest resolution. In

[6] IllustrisTNG (abbreviated as TNG hereafter) is a further development of the Illustris project with an improved galaxy formation and evolutionary model (Nelson et al. 2019).

Table 1
Numerical and Cosmological Parameters of the Here Analyzed ΛCDM Simulations

Simulation	L (cMpc)	N ⋯	H_0 (km s^{-1} Mpc^{-1})	$\Omega_{\mathrm{b},0}$ ⋯	$\Omega_{\mathrm{m},0}$ –	$\Omega_{\Lambda,0}$ ⋯	m_{b} ($M_\odot$)	m_{dm} ($M_\odot$)
EAGLE100	100	2×1504^3	67.77	0.04825	0.307	0.693	1.81×10^6	9.70×10^6
EAGLE50	50	2×752^3	67.77	0.04825	0.307	0.693	1.81×10^6	9.70×10^6
EAGLE25	25	2×752^3	67.77	0.04825	0.307	0.693	2.26×10^5	1.21×10^6
Illustris-1	106.5	2×1820^3	70.4	0.0456	0.2726	0.7274	1.3×10^6	6.3×10^6
TNG50-1	51.7	2×2160^3	67.74	0.0486	0.3089	0.6911	8.5×10^4	4.5×10^5
TNG50-2	51.7	2×1080^3	67.74	0.0486	0.3089	0.6911	6.8×10^5	3.6×10^6
TNG50-3	51.7	2×540^3	67.74	0.0486	0.3089	0.6911	5.4×10^6	2.9×10^7
TNG50-4	51.7	2×270^3	67.74	0.0486	0.3089	0.6911	4.3×10^7	2.3×10^8
TNG100-1	110.7	2×1820^3	67.74	0.0486	0.3089	0.6911	1.4×10^6	7.5×10^6

Note. From left to right: simulation name; co-moving box size (cubic side length); number of dark matter particles plus the initial number of gas cells/particles (hence the factor of two); present-day Hubble constant; present baryonic density in units of the cosmic critical density; same for the total matter density; the dark energy density; the baryonic mass resolution; and the dark matter mass resolution. The highest-resolution realization TNG50-1 has a Plummer-equivalent gravitational softening length for the collisionless component of 288 pc and a minimum adaptive gas gravitational softening length of 72 pc at redshift $z = 0$ (for more information, see Table 1 of Pillepich et al. 2019). EAGLE25 refers to the EAGLE Recal-L0025N0752 simulation. Additional parameters for the EAGLE set can be found in Table 1 of McAlpine et al. (2016), for Illustris-1 in Table 1 of Nelson et al. (2015), and for TNG100-1 in Table 1 of Nelson et al. (2018).

Section 7.1, we also employ the lower-resolution realizations TNG50-2, TNG50-3, and TNG50-4 of the TNG50 sets and the higher-resolution realization EAGLE Recal-L0025N0752 (hereafter EAGLE25) in order to study the effect of resolution on the shapes of simulated galaxies. The numerical and cosmological parameters of these simulations are listed in Table 1.[7]

3. Quantifying the Shape of a Galaxy

The shape of a galaxy can be quantified by the 3D intrinsic aspect ratio of its mass distribution as defined by $q_{\mathrm{int}} \equiv \lambda_1/\sqrt{\lambda_2 \lambda_3}$, where λ_1, λ_2, and λ_3 (sorted so $\lambda_1 < \lambda_2 < \lambda_3$) are the square roots of the eigenvalues of the mass distribution tensor (MDT, sometimes also called the moment of inertia tensor) divided by the total mass (see, e.g., Equation D.39 in Appendix D of Binney & Tremaine 2008). In this contribution, we consider only the stellar MDT because we are interested in the appearance of a galaxy in optical images. This analysis does not distinguish different structural components of the galaxy like its thin or thick disk. A completely intrinsically thin disk galaxy has $q_{\mathrm{int}} = 0$, whereas a perfectly spherical galaxy has $q_{\mathrm{int}} = 1$. Spiral galaxies account for the bulk of galaxies in the locally observed universe (Delgado-Serrano et al. 2010), with typical $q_{\mathrm{int}} \approx 0.2$ (see, e.g., Figure 1 of Mosenkov et al. 2010 and Figure 1 of Hoffmann et al. 2020). About 57% (79%) of all galaxies in the the Sydney–AAO Multi-object Integral field spectrograph (SAMI) Galaxy Survey (Croom et al. 2012; Bryant et al. 2015) have $q_{\mathrm{int}} < 0.4$ (<0.6) (see Figure 15 of Oh et al. 2020). The Galactic thin disk has an exponential scale length of $l = 2.6 \pm 0.5$ kpc and an exponential scale height of $h = 220$–450 pc (Bland-Hawthorn & Gerhard 2016), which results in an aspect ratio of $h/l \approx 0.07$–0.21. The Andromeda galaxy (M31) has a thin disk with $1 - \epsilon \equiv b/a \equiv q_{\mathrm{sky}} = 0.27 \pm 0.03$, where ϵ and b/a are the sky-projected ellipticity and axis ratio, respectively (Courteau et al. 2011). Because M31 is not viewed exactly edge-on, it must be intrinsically thinner than it appears on the sky (Section 2.1 of Banik & Zhao 2018).

We extract the eigenvalues of the stellar MDT from supplementary data catalogs provided by the Illustris, TNG, and EAGLE teams (Thob et al. 2019).[8] The MDTs of subhalos in the Illustris and TNG simulations are calculated from the stellar particles within twice the stellar half-mass–radius $r_{0.5,*}$ (Genel et al. 2015). This slightly differs from the EAGLE simulations in which an iterative form of the reduced MDT is used, with the initial selection being all stellar particles inside a spherical aperture of physical radius 30 kpc (Section 2.3 of Thob et al. 2019). As demonstrated in Section 7.5, this method provides a secure division into spirals and ellipticals, whereas other bulge-disk decomposition methods face problems when applied to ΛCDM simulations (Section 7.2).

3.1. Projecting an Ellipsoid onto the Sky

In order to compare simulations with observations, we have to determine q_{sky} for a galaxy with λ_i, where $i = 1$–3 (Section 3). Only the ratios of the λ_i are relevant for our analysis, but it will be helpful to think of them as actual lengths. We approximate that the galaxy is an ellipsoid and find what this looks like when viewed by a distant observer. We work in Cartesian coordinates in a reference frame centered on the galaxy and aligned with the eigenvectors of its inertia tensor. Thus, the "edge" of the galaxy is given by

$$\frac{x^2}{{\lambda_1}^2} + \frac{y^2}{{\lambda_2}^2} + \frac{z^2}{{\lambda_3}^2} = 1. \quad (1)$$

Suppose a distant observer is located toward the direction $\hat{\boldsymbol{n}}$, where we use hats to denote unit vectors. Our approach is to find the extent of the image along the direction $\hat{\boldsymbol{n}}_3$, which lies entirely within the sky plane (i.e., $\hat{\boldsymbol{n}} \cdot \hat{\boldsymbol{n}}_3 = 0$). Our main goal is to find the position vector $\boldsymbol{r}$ of the point corresponding to the edge of the galaxy image along the direction $\hat{\boldsymbol{n}}_3$. For this purpose, it will be useful to define the unit vector within the sky plane in the orthogonal direction, which we call $\hat{\boldsymbol{n}}_2$ (orthogonal to both $\hat{\boldsymbol{n}}$ and $\hat{\boldsymbol{n}}_3$).

We know that $\boldsymbol{r} \cdot \hat{\boldsymbol{n}}_2 = 0$, or else the point would not appear to be in the direction $\hat{\boldsymbol{n}}_3$ from the galaxy's center. To get an

[7] In the Illustris and TNG simulations, the initial speed of a baryonic wind particle has an unphysical dependence on the local 1D dark matter velocity dispersion (see Equation (1) in Pillepich et al. 2018).

[8] The eigenvalues of the stellar MDT for Illustris and TNG subhalos can be downloaded from https://www.tng-project.org/data/docs/specifications/#sec5c [21.07.2020].

additional constraint, we note that the tangent plane to the galaxy at the point $\boldsymbol{r}$ must not contain $\hat{\boldsymbol{n}}_3$, or else it would be possible to move along the galaxy's boundary and reach a larger apparent separation along $\hat{\boldsymbol{n}}_3$. The plane normal must therefore be $\pm\hat{\boldsymbol{n}}_3$, but for our analysis, it is sufficient to know that the plane normal is orthogonal to $\hat{\boldsymbol{n}}$.

These two constraints are sufficient to determine the direction of $\boldsymbol{r}$. Its magnitude is found through Equation (1). Thus, the extent of the image along $\hat{\boldsymbol{n}}_3$ is d, which we find through the following procedure involving the intermediate vectors $\boldsymbol{q}$ and $\boldsymbol{v}$:

$$\boldsymbol{q}_i \equiv \frac{\hat{\boldsymbol{n}}_i}{{\lambda_i}^2}, \tag{2}$$

$$\boldsymbol{v} \equiv \hat{\boldsymbol{n}}_2 \times \boldsymbol{q}, \tag{3}$$

$$d = \frac{\boldsymbol{v} \cdot \hat{\boldsymbol{n}}_3}{\sqrt{\sum_{i=1}^{3}\left(\frac{v_i}{\lambda_i}\right)^2}}. \tag{4}$$

We repeat this for a low-resolution grid of $\hat{\boldsymbol{n}}_3$, whose direction we parameterize using the so-called position angle. Starting from the $\hat{\boldsymbol{n}}_3$ in this grid which gives the lowest d, we apply the gradient descent algorithm (Fletcher & Powell 1963) to find the minimum value of d to high precision. We then rotate $\hat{\boldsymbol{n}}_3$ through a right angle, and start a gradient ascent stage to search for the maximum extent of the image. The ratio of these d values is the sky-projected aspect ratio $q_{\rm sky} \leqslant 1$, which forms the heart of our analysis.

To build up the $q_{\rm sky}$ distribution, we repeat this procedure for a 2D grid of viewing angles $\hat{\boldsymbol{n}}$, with each result weighted according to the solid angle it represents. The observer is thus assumed to be in a random direction relative to the galaxy.

4. Observational Galaxy Samples

The sky-projected aspect ratio distributions of the following observational galaxy samples are statistically compared with the simulations discussed in Section 2.

4.1. GAMA Survey

The Galaxy And Mass Assembly survey (GAMA; Driver et al. 2009, 2011) is a multiwavelength photometric and spectroscopic survey. An overview of the survey regions and their corresponding magnitude limits is given in Table 1 of Baldry et al. (2018). Here, we download the stellar masses, redshifts, and ellipticities by submitting an SQL query to the GAMA DR3 database (Baldry et al. 2018).[9] In detail, we extract the GALFIT (Peng et al. 2002, 2010) r-band ellipticity $(1-b/a)$ from the SérsicPhotometry (v09) - SérsicCatSDSS catalog (Kelvin et al. 2012). We use the stellar mass labeled as "logmstar" from the StellarMasses (v20) catalog (Taylor et al. 2011), which is derived from matched aperture photometry in the r band, missing therewith flux beyond the AUTO aperture.[10] Consequently, the stellar masses $M_{*,\rm AUTO}$ within the photometric aperture ("logmstar") are corrected by

$$\log_{10}\left(\frac{M_*}{M_\odot}\right) = \log_{10}\left(\frac{M_{*,\rm AUTO}}{M_\odot}\right) + \log_{10}\left(\frac{f_{\rm Sérsic}}{f_{\rm AUTO}}\right),$$

where $f_{\rm Sérsic}/f_{\rm AUTO}$ is the so-called "fluxscale" parameter, i.e., the linear ratio between the total r-band flux from a Sérsic profile fit cut at 10 effective radii and the r-band AUTO aperture flux (see also, e.g., Taylor et al. 2011; Kelvin et al. 2014; Lange et al. 2016; Vázquez-Mata et al. 2020). The stellar masses are calculated by assuming concordance cosmology with the cosmological parameters being $\Omega_{\rm m,0}=0.3$, $\Omega_{\Lambda,0}=0.7$, and h=0.7 (Taylor et al. 2011).

For our analysis, we only consider galaxies with a fluxscale correction of $0.5 < \text{fluxscale} < 2$ and a spectral energy distribution (SED) fit with a posterior predictive P-value $PPP > 0$, which removes failed SED fits. In addition, we exclude objects with a heliocentric redshift $z < 0.005$ to remove stars.[11] Also requiring $M_* > 10^{10}\,M_\odot$ and $z < 0.1$ yields a final sample of 5304 galaxies that pass the above quality cuts.

4.2. GAMA and Cluster Input Catalogs for the SAMI Galaxy Survey

The SAMI Galaxy Survey Data Release 3 (DR3) includes 3068 galaxies in the redshift range $0.004 < z < 0.095$. The ellipticity distribution of a subsample of the SAMI Galaxy Survey consisting of 826 galaxies is shown in the third panel of Figure 6 in Oh et al. (2020).

In order to increase the sample size, we analyze the aspect ratio distribution of galaxies listed in the input catalogs of the three equatorial regions of the GAMA survey (i.e., G09, G12, and G15; Bryant et al. 2015) and the eight cluster regions (i.e., APMCC0917, A168, A4038, EDCC442, A3880, A2399, A119, and A85; Owers et al. 2017) for the SAMI DR3 Galaxy Survey. For this, we download the stellar masses, redshifts, and projected ellipticities by using an SQL/Astronomical Data Query Language (ADQL) query to the Data Central database servers[12] of the InputCatGAMADR3 and InputCatClustersDR3 catalogs (for more details, see also Table 1 of Croom et al. 2021). The ellipticities are derived from Sérsic fits in the r band (Bryant et al. 2015; Owers et al. 2019).

Requiring $M_* > 10^{10}\,M_\odot$ gives a sample of 4252 galaxies, of which 3238 are from GAMA and 1014 are from the cluster regions. As we show in Section 5, the aspect ratio distributions of the GAMA survey and the here described sample disagree only at the 0.013σ confidence level. Although the ellipticity values of the same galaxy listed in the InputCatGAMADR3 and the GAMA survey are slightly different, these catalogs are not fully independent of each other. Because of these reasons and since the GAMA survey contains more galaxies (5304), we do not use the input catalogs of the GAMA and cluster regions for SAMI DR3 in our statistical comparison with simulations (Section 5).

4.3. SDSS

The SDSS is a flux-limited galaxy survey including galaxies with a Petrosian r magnitude brighter than 17.77 (SDSS Collaboration 2000). Here, we download the stellar masses, redshifts, and photometric parameters from its DR16[13] (Ahumada et al. 2020) using an SQL query to the SDSS database server.[14]

[9] http://www.gama-survey.org/dr3/query/ [11.11.2021].

[10] For further information on the stellar masses, see also http://www.gama-survey.org/dr3/schema/dmu.php?id=9 [11.11.2021].

[11] Private communication with Edward Taylor.

[12] https://datacentral.org.au/services/query/ [04.11.2021].

[13] https://www.sdss.org/dr16/

[14] http://skyserver.sdss.org/dr16/en/home.aspx [11.11.2021].

We selected galaxies listed in the PhotoPrimary catalog, which also contains the aspect ratios of galaxies derived from an exponential and a de Vaucouleurs profile (de Vaucouleurs 1948) for the SDSS r, i, u, z, and g filters. Throughout this analysis, we use the aspect ratio parameters based on the SDSS r-band magnitude. In order to distinguish between spiral and elliptical galaxies, we access the fracDeV parameter, the weight of the de Vaucouleurs component in a linear combination of the exponential and de Vaucouleurs profiles (for a more detailed description, see Section 3.1 of Abazajian et al. 2004). Following Padilla & Strauss (2008), we use the aspect ratio derived from the exponential fit if fracDeV < 0.8 and from the de Vaucouleurs fit if fracDeV $\geqslant 0.8$.

The here used stellar masses from the galSpecExtra table correspond to the median of the estimated logarithmic stellar mass probability density function using model photometry (Kauffmann et al. 2003; Salim et al. 2007). The redshifts are extracted from the SpecObj table.[15]

Selecting galaxies with $z < 0.1$ and $M_* > 10^{10}\,M_\odot$ gives a sample of 232,315 galaxies. The so-obtained and here analyzed $q_{\rm sky}$ distribution is consistent with Padilla & Strauss (2008), as shown in Section 5. They obtained a volume-limited sample by weighting each galaxy in the SDSS DR6 (Adelman-McCarthy et al. 2008) by $1/V_{\rm max}$, where $V_{\rm max}$ is the volume corresponding to the maximum distance at which we can observe a galaxy with its absolute magnitude (see Section 3.1 of Padilla & Strauss 2008). In total, their sample contains 303,290 "spirals" (fracDeV < 0.8) and 282,203 "ellipticals" (fracDeV $\geqslant 0.8$). Here, we extract the $1/V_{\rm max}$ weighted $q_{\rm sky}$ distributions of the spiral and elliptical samples from their Figure 1 (bottom panels), and combine these in order to obtain the $q_{\rm sky}$ distribution of the total galaxy sample.

4.4. The Catalog of Neighboring Galaxies

As a consistency check, we also investigate the $q_{\rm sky}$ distribution of galaxies within the Local Volume (LV), a sphere of radius 11 Mpc centered on the Sun. The stellar masses are calculated from K-band luminosities using a mass-to-light ratio of 0.6 (e.g., McGaugh & Schombert 2014). We select 52 galaxies with $10.0 < \log_{10}(M_*/M_\odot) \leqslant 11.65$ from the Updated Nearby Galaxy Catalog (Karachentsev et al. 2013), a renewed version of The Catalog of Neighboring Galaxies[16] (Karachentsev et al. 2004). These galaxies cover a wide range of $q_{\rm sky}$ (0.13–0.94), as shown in the right panel of Figure 1. Due to the small sample size and high resulting Poisson uncertainties, we do not calculate its tension with the simulated $q_{\rm sky}$ distributions.

These are nearby galaxies with well-established morphological types, allowing direct well-resolved images to inform us of which galaxies are thin disks. Therefore, we show the distribution of the morphological T-types of our LV galaxy sample in the left panel of Figure 1. The T-types of these galaxies are listed in the Updated Nearby Galaxy Catalog and discussed and analyzed in detail in Karachentsev et al. (2018). Of the 52 galaxies, 50% are early-type spirals (Sa, Sab, Sb, Sbc, Sc; morphological type $T = 1$–5), 23% are late-type spirals (Scd, Sd, Sdm, Sm; $T = 6$–8), and the remaining 27% are E, S0, dSph, or S0a galaxies ($T < 1$). Thus, the morphological classification scheme used by Karachentsev et al. (2013, 2018) is slightly different to the de Vaucouleurs system.

It is not in general possible to disentangle the contributions to $q_{\rm sky}$ from inclination and intrinsic thickness. The inclination i between disk and sky planes listed in the Updated Nearby Galaxy Catalog is derived with Equation (5) of Karachentsev et al. (2013):

$$\sin^2 i \;=\; \frac{1 - q_{\rm sky}^2}{1 - \widetilde{q}_{\rm int}^2}, \tag{5}$$

where the assumed intrinsic aspect ratio $\widetilde{q}_{\rm int}$ is assigned a value depending on the morphological T-type (T) of the considered galaxy as given by their Equation (6):[17]

$$\log_{10}\widetilde{q}_{\rm int} \;=\; \begin{cases} -0.43 \;-\; 0.053T & (T \leqslant 8), \\ -0.38 & (T = 9,\ 10), \end{cases} \tag{6}$$

where according to Karachentsev et al. (2018) $T = 9$ and $T = 10$ refer to Im/BCD and Ir galaxies, respectively. Thus, the so-obtained intrinsic aspect ratios are a best guess based on the observed morphology. As an example, the M31 galaxy with $T = 3$ has with this approach $\widetilde{q}_{\rm int} = 0.26$ ($q_{\rm sky} = 0.33$).

Applying Equation (6) to the 52 selected LV galaxies shows that their intrinsic aspect ratio distribution covers the range $\widetilde{q}_{\rm int} = 0.07$–$0.55$ with a global peak at $\widetilde{q}_{\rm int} \approx 0.23$, as presented in the right panel of Figure 1. Converting $q_{\rm sky}$ to $q_{\rm int}$ depends on the relation between $\widetilde{q}_{\rm int}$ and the morphological T-type, so the intrinsic aspect ratio distribution of our LV sample is mainly considered for illustrative purposes. However, it helps to demonstrate that the LV galaxies seem to be mostly thin disks. According to this, if the LV were to be representative of the universe, then $81\% \pm 13\%$ (42/52) of all galaxies heavier than $M_* = 10^{10}\,M_\odot$ are thin disk galaxies with $\widetilde{q}_{\rm int} < 0.4$. For completeness, we quantify the tension between the here obtained intrinsic aspect ratio distribution of LV galaxies and the ΛCDM models in Section 6.1.

In order to avoid any bias on the shapes of galaxies introduced by model assumptions when converting $q_{\rm sky}$ to $q_{\rm int}$, we only consider the former when statistically comparing observations to simulations in our main analysis. As explained in Section 3.1, this requires us to generate the $q_{\rm sky}$ distribution given the intrinsic shapes of simulated galaxies. We can then directly compare the resulting distribution with the observed $q_{\rm sky}$ distribution (Section 6.2).

5. Quantifying the Tension between Simulations and Observations

The stellar mass distributions of the GAMA survey and SDSS are compared with that of the TNG50-1 run in the left panel of Figure 2. Galaxies with $10.30 \lesssim \log_{10}(M_*/M_\odot) \lesssim 11.05$ are more abundant in the

[15] Although the SpecObj catalog does not contain duplicate observations, there is the rare situation that the catalog lists more than one redshift measurement for the same object. In this case, the R.A. and decl. values of the fibers are different during the spectroscopic observation. We take this into account by checking if our downloaded catalog lists more than one redshift measurement for the same object ID. If so, we remove the measurement with the lower signal-to-noise ratio. Of our 232,315 selected galaxies, a duplicate happened only once for the object with ID 1237663782590021834.

[16] https://www.sao.ru/lv/lvgdb/tables.php [22.11.2021].

[17] There seems to be a typo in Equation (6) of Karachentsev et al. (2013). The relation between the assumed intrinsic aspect ratio and the T-type parameter for galaxies with $T \leqslant 8$ should be $\log_{10}(a/b)_0 = -\log_{10}\widetilde{q}_{\rm int} = 0.43 \;+\; 0.053\,T$ (see also Equation (14) of Paturel et al. 1997) rather than $0.43 + 0.53\,T$, which would make late-type galaxies far too thin.

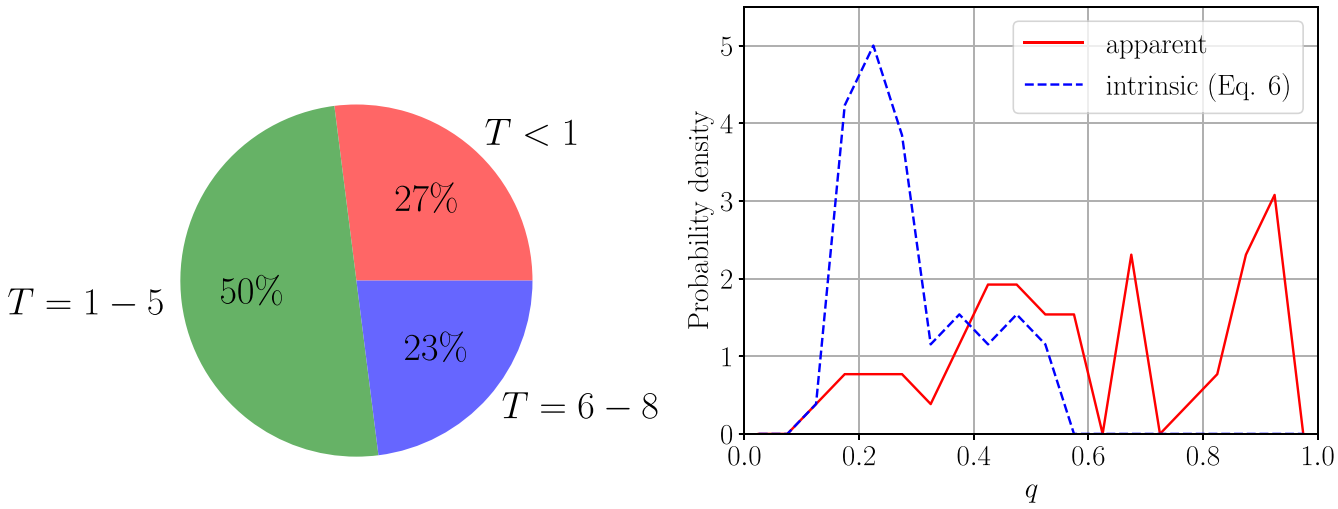

Figure 1. Left: distribution of the morphological T-types of galaxies with $M_* > 10^{10}\,M_\odot$ in the Local Volume (LV). The red slice refers to E, S0, dSph, and S0a galaxies ($T < 1$), the green slice to early-type spirals (Sa, Sab, Sb, Sbc, Sc; $T = 1$–5), and the blue slice to late-type spirals (Scd, Sd, Sdm, Sm; $T = 6$–8). Right: the sky-projected (solid red) and intrinsic (dashed blue) aspect ratio distribution of galaxies with $M_* > 10^{10}\,M_\odot$ in the LV. The bin width is $\Delta q_{\rm sky} = \Delta \tilde{q}_{\rm int} = 0.05$. The intrinsic aspect ratios are derived using Equation (6), which is a best guess based on the morphological T-type (see the text). It is statistically compared with the TNG50-1 simulation run in Section 6.1, but the model dependence of the $\tilde{q}_{\rm int}$ values means this is not our main result.

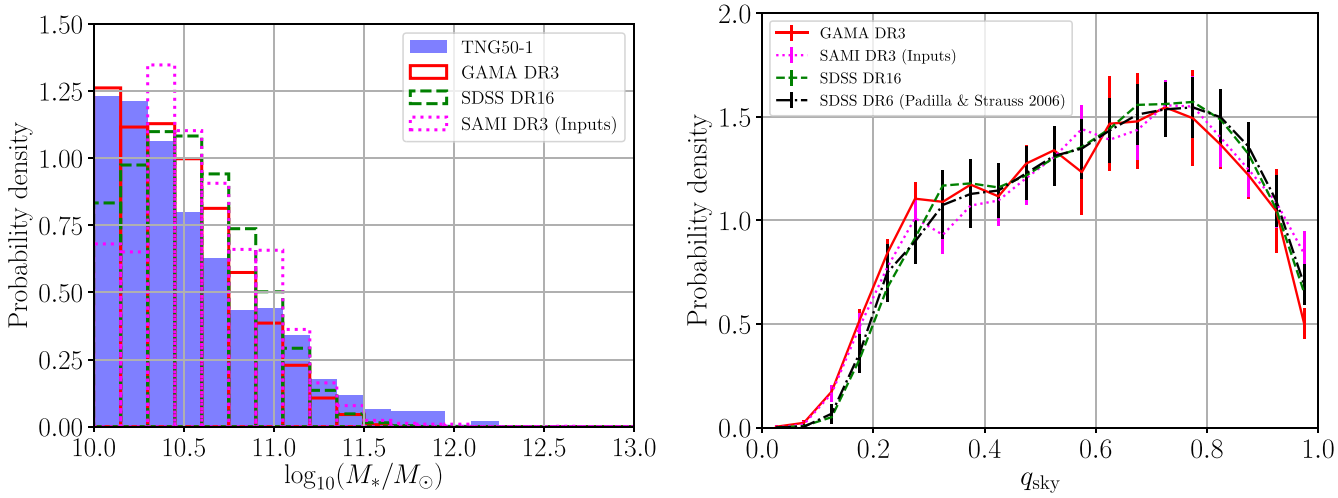

Figure 2. Left: stellar mass distribution of the TNG50-1 simulation run (filled blue) and on the observational side GAMA DR3 (open solid red, Section 4.1), the input catalogs of the GAMA and cluster regions for SAMI DR3 (open dotted magenta, Section 4.2), and SDSS DR16 (open dashed green, Section 4.3). We use a bin width of $\Delta \log_{10}(M_*/M_\odot) = 0.15$. Right: sky-projected aspect ratio distribution of GAMA DR3 (solid red), the input catalogs of the GAMA and cluster regions for the SAMI DR3 (dotted magenta), and SDSS DR16 (dashed green) after weighting the galaxies in order to match the stellar mass distribution of the TNG50-1 run. Invisible error bars (Equation (8)) are smaller than the data point symbol. The black dotted–dashed line refers to the volume-weighted SDSS DR6 sample (Padilla & Strauss 2008) with $N_{\rm spirals} = 303{,}290$ and $N_{\rm ellipticals} = 282{,}203$ (see the bottom panels of their Figure 1). The error bars of the spiral and elliptical aspect ratio distributions have been obtained from the jackknife technique and were here weighted by the above-mentioned proportion of spirals and ellipticals. The bin width is $\Delta q_{\rm sky} = 0.05$.

observational samples than in the simulation, while the opposite is true at higher mass. This is most likely because the used stellar masses in the Subfind catalog of the TNG50-1 simulation refer to the mass of all stellar particles bound to each considered subhalo, not to the stellar mass within a certain aperture size.

The different M_* distributions would bias the comparison between the observed and simulated $q_{\rm sky}$ distributions. Thus, we apply an M_*-weighting scheme to each observed galaxy in order to match the simulated M_* distribution, as explained in the following. The total χ^2 between the simulated and observed sky-projected aspect ratio distributions is

$$\chi^2 = \sum_{i=1}^{N_{\rm bins}} \frac{\left(\frac{w_{{\rm tot},i}}{w_{\rm tot}} - \frac{N_{{\rm model},i}}{N_{\rm model,tot}}\right)^2}{\sigma^2_{{\rm obs},i} + \sigma^2_{{\rm model},i}}, \tag{7}$$

$$\sigma_{{\rm obs},i} = \begin{cases} \frac{w_{{\rm max},i}}{w_{\rm tot}} \sqrt{\frac{w_{{\rm tot},i}}{w_{{\rm max},i}} + 1} & (w_{{\rm obs},i} \neq 0), \\ \frac{w_{\rm max}}{w_{\rm tot}} & (w_{{\rm obs},i} = 0), \end{cases} \tag{8}$$

$$\sigma_{{\rm model},i} = \frac{\sqrt{N_{{\rm model},i} + 1}}{N_{\rm model,tot}}, \tag{9}$$

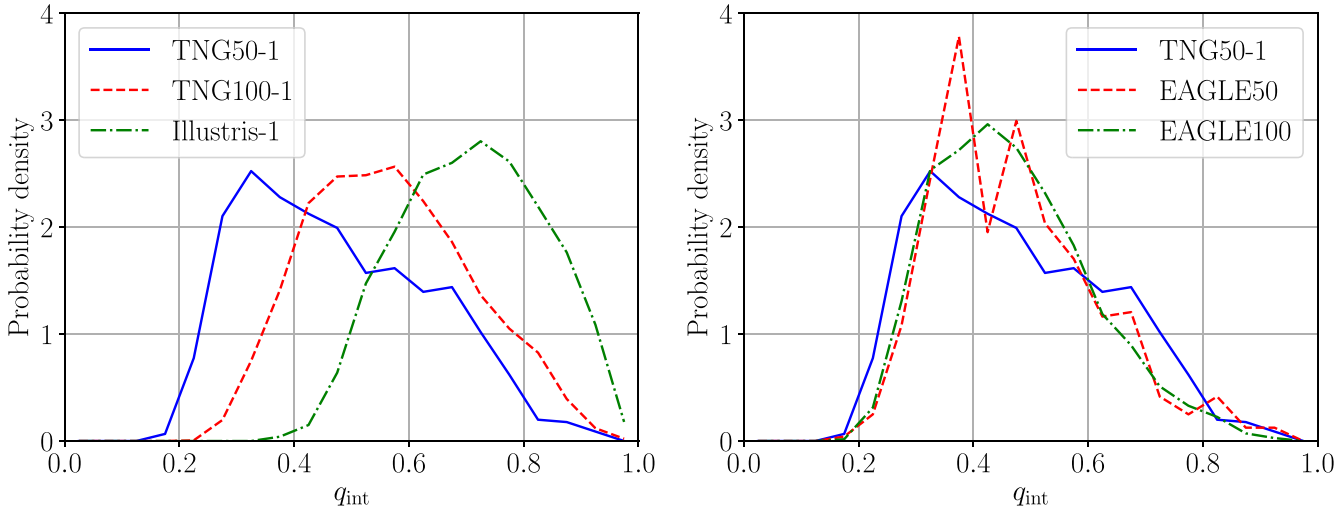

Figure 3. Distribution of the intrinsic aspect ratio $q_{\rm int}$ for galaxies with $M_* > 10^{10}\,M_\odot$ in the Illustris and TNG (left) and EAGLE (right) simulations, with the TNG50-1 result shown in both panels as a solid blue line for clarity. The bin width is $\Delta q_{\rm int} = 0.05$ throughout this work.

where $N_{{\rm model},i}$ is the number of simulated galaxies in bin i, $N_{\rm bins} = 20$ is the number of bins in $q_{\rm sky}$, and $N_{\rm model,tot}$ is the total number of simulated galaxies. In order to avoid the bias caused by the different M_* distributions of the simulations and observations, we group simulated and observed galaxies in M_* bins of width 0.15 dex over the range $10.0 < \log_{10}(M_*/M_\odot) \leqslant 11.65$. Each observed galaxy is weighted by $w_{\rm obs} = N_{\rm sim}/N_{\rm obs}$, where $N_{\rm sim}$ ($N_{\rm obs}$) is the number of simulated (observed) galaxies in the M_* bin of the considered galaxy. The lower limit on M_* is set to guarantee that only well-resolved simulated galaxies are analyzed. The maximum limit is applied because the GAMA DR3 sample runs out of galaxies at higher stellar mass, leading to an undefined $w_{\rm obs}$. These criteria give final GAMA, SAMI DR3 inputs, and SDSS sample sizes of 5304, 4229, and 232,128, respectively. $w_{{\rm tot},i}$ is then the weighted number of galaxies in $q_{\rm sky}$ bin i, while $w_{{\rm max},i}$ is the weight of the galaxy in this $q_{\rm sky}$ bin with the maximum weight, $w_{\rm max}$ is the maximum weight of all considered observed galaxies (regardless of $q_{\rm sky}$), and $w_{\rm tot}$ is the total weight of all observed galaxies, which by definition must match the number of simulated galaxies used for the comparison. This approach is invariant to a uniform scaling of the weights. $\sigma_{{\rm obs},i}$ and $\sigma_{{\rm model},i}$ are Poisson uncertainties. The use of Poisson statistics is valid because we choose a bin width of $\Delta q_{\rm sky} = 0.05$, so each bin contains only a small fraction of the full sample.

This M_*-weighting scheme is not applied when the aspect ratio distributions are being compared between simulations. The total χ^2 between any two models is

$$\chi^2 = \sum_{i=1}^{N_{\rm bins}} \frac{\left(\frac{N_{{\rm model\ 1},i}}{N_{\rm model\ 1,tot}} - \frac{N_{{\rm model\ 2},i}}{N_{\rm model\ 2,tot}}\right)^2}{\sigma^2_{{\rm model\ 1},i} + \sigma^2_{{\rm model\ 2},i}}. \quad (10)$$

The uncertainties $\sigma_{\rm model\ 1}$ and $\sigma_{\rm model\ 2}$ can be thought of as given by Equation (8) with all galaxies equally weighted.

The total χ^2 between any model and observations (Equation (7)) or between two models (Equation (10)) is converted to a probability or P-value of a more extreme outlier using the χ^2 distribution for the appropriate number of degrees of freedom, which we call n. For convenience, we then express the P-value as an equivalent number of standard deviations for a single Gaussian variable. We denote this x, which we find by iteratively solving

$$1 - \frac{1}{\sqrt{2\pi}} \int_{-x}^{x} \exp\left(-\frac{x^2}{2}\right) dx \equiv P. \quad (11)$$

A protocol to convert particularly large χ^2 values is given in the Appendix, which provides a way to solve this equation despite numerical difficulties that arise for very high χ^2.

The right panel of Figure 2 shows the $q_{\rm sky}$ distributions of the GAMA Galaxy Survey and SDSS, weighted based on the TNG50-1 run for galaxies with $10.0 < \log_{10}(M_*/M_\odot) \leqslant 11.65$. The GAMA DR3 and SDSS DR16 results disagree at 3.25σ confidence, indicating good agreement considering the large sample sizes. The aspect ratio distributions of GAMA DR3 and the input catalogs of the GAMA and cluster regions for the SAMI DR3 differ only at 0.013σ confidence. Because of this and the larger sample size of the GAMA survey, we only use the GAMA survey and SDSS for the following analysis.

6. Results

In this section, we present both the intrinsic and the sky-projected aspect ratio distribution at $z = 0$ as produced by the ΛCDM paradigm. We then statistically compare the simulated $q_{\rm sky}$ distribution with local observations from the GAMA survey and SDSS.

6.1. Intrinsic Aspect Ratio Distribution

Figure 3 shows the $q_{\rm int}$ distribution of galaxies in central and noncentral subhalos with $M_* > 10^{10}\,M_\odot$ in the TNG50-1, TNG100-1, Illustris-1, EAGLE50, and EAGLE100 simulations. These all show a unimodal distribution with different peak positions. We show later that increasing the resolution broadens the peak and shifts it to smaller $q_{\rm int}$ (Section 7.1). Galaxies in the EAGLE and TNG50-1 runs are typically thinner than in the Illustris-1 and TNG100-1 runs. The TNG50-1 run contains 133 galaxies with $q_{\rm int} < 0.3$ and $M_* > 10^{10}\,M_\odot$, with the thinnest galaxy of this sample having $q_{\rm int} \approx 0.19$. Clearly, the resolution and the adopted temperature floor of about 10^4 K (10 kK; see Trayford et al. 2017 for EAGLE and

Nelson et al. 2019 for TNG) allow for the formation of massive thin disk galaxies. This is consistent with the work of Sellwood et al. (2019), who managed to maintain a thin disk in a hydrodynamical CDM-based simulation of M33 with a slightly higher temperature floor of 12 kK.

The EAGLE runs have a very similar $q_{\rm int}$ distribution—the peak position is similar to TNG50, and EAGLE forms galaxies as thin as $q_{\rm int} = 0.18$ (the thinnest galaxies in each run are $q_{\rm int} = 0.20$ for EAGLE25, $q_{\rm int} = 0.19$ for EAGLE50, and $q_{\rm int} = 0.18$ for EAGLE100). This is in agreement with TNG50-1 (right panel of Figure 3). By using different resolution realizations of the TNG50 and EAGLE simulations, we test the numerical convergence of the aspect ratio distribution in Section 7.1. While there is no evidence that the TNG50 simulation has numerically converged, the aspect ratio distributions of different EAGLE runs closely agree with each other, possibly because they have the same resolution. The similarity between EAGLE runs is consistent with Lagos et al. (2018), who showed that higher-resolution realizations of the EAGLE project yield galaxies with a similar ellipticity distribution (see their Figures A2 and A3). Moreover, the $q_{\rm int}$ distributions of EAGLE and TNG50-1 are very similar despite differences in resolution and other details of the models.

In the LV, $81\% \pm 13\%$ of galaxies with $M_* > 10^{10}\,M_\odot$ have $\widetilde{q}_{\rm int} < 0.4$ (Section 4.4). In contrast, the fractions of galaxies with such masses that have $q_{\rm int} < 0.4$ in the highest-resolution simulations analyzed here (TNG50-1, EAGLE25) are only $39\% \pm 2\%$ and $46\% \pm 8\%$, respectively. The stated Poisson uncertainties are estimated as $\sigma = \sqrt{N_{<0.4} + 1}\,/N_{\rm tot}$, where $N_{<0.4}$ and $N_{\rm tot}$ are the number of galaxies with $q_{\rm int} < 0.4$ and the total number of galaxies, respectively. The overall intrinsic aspect ratio distribution of the LV galaxies (blue dashed line in the left panel of Figure 1) is in 5.42σ tension with the TNG50-1 run. We emphasize again that the intrinsic aspect ratios of LV galaxies are based on the morphological T-type (Equation (6)). Therefore, we provide in the following section another test of the ΛCDM framework in which we compare the sky-projected aspect ratio distributions of the ΛCDM simulations with the GAMA survey and SDSS.

6.2. Sky-projected Aspect Ratio Distribution and Comparison with Observations

In order to compare these simulation results with observations from the GAMA survey and SDSS (Section 4), the simulated galaxies are projected onto the sky from a grid of viewing angles to find the distribution of $q_{\rm sky}$ (Section 3.1). The resulting $q_{\rm sky}$ distribution of each simulation is compared with the GAMA survey and SDSS in Figure 4. This reveals that the simulations significantly underproduce the fraction of galaxies with a low $q_{\rm sky}$. In particular, only about 10% of simulated galaxies with $10.0 < \log_{10}(M_*/M_\odot) \leqslant 11.65$ have $q_{\rm sky} < 0.4$, while these galaxies make up about 22%–25% of locally observed galaxies (Table 2).

The tension between the simulated and observed $q_{\rm sky}$ distributions is quantified using a standard χ^2 statistic (Section 5). All simulations significantly disagree with local observations. The smallest tension is 12.52σ, which arises from comparing the GAMA survey with TNG50-1. The smallest tension for the SDSS is 14.82σ, corresponding to a comparison with EAGLE50 (we do not consider results from the EAGLE25 run as it only has 81 galaxies within the analyzed M_* range, but see Section 7.1). The total χ^2 values and the corresponding levels of tension are listed in Table 3 for different simulations.

7. Discussion

Although state-of-the-art cosmological ΛCDM simulations produce a variety of galaxy types (Vogelsberger et al. 2014; Schaye et al. 2015), we showed that the overall morphological distribution produced by the ΛCDM framework significantly disagrees with local observations. The $q_{\rm sky}$ distribution is similar between different observational samples, with the GAMA survey and SDSS being in 3.25σ tension with each other despite the large sample size of both (Figure 2). Here the important result has been documented that the different ΛCDM simulations disagree with the observed galaxy population. Galaxies formed in cosmological ΛCDM simulations are typically intrinsically thick rather than intrinsically thin (Section 6.2), making it challenging to explain the observed common formation of galaxies like the Milky Way or M31. This contrasts with the conclusion of Vogelsberger et al. (2014) based on the Illustris-1 simulation, who claimed that the angular momentum problem of ΛCDM has been resolved. Although the simulations can produce *some* disk galaxies, the fraction of such galaxies is far too small compared with observations (Table 2). The lack of such thin disk galaxies in simulations underlies the significant discrepancy between the observed and simulated distributions of galaxy shapes.

Our results broadly agree with those of van de Sande et al. (2019), who showed that the intrinsic (see their Figure 10) and sky-projected aspect ratio distributions (their Figures 4 and 8) of the EAGLE (Crain et al. 2015; Schaye et al. 2015; McAlpine et al. 2016), HYDRANGEA (Bahé et al. 2017; Barnes et al. 2017), HORIZON-AGN (Dubois et al. 2014), and MAGNETICUM (Hirschmann et al. 2014; Dolag et al. 2016, 2017) simulations all disagree with observational data from the ATLAS^{3D}, Calar Alto Legacy Integral Field Area Survey (CALIFA), and MASSIVE surveys, and also with the SAMI Galaxy Survey (MAGNETICUM produced too few very round galaxies). Similar results were obtained by Peebles (2020), who recently showed that stellar particles in ΛCDM subhalos have kinematics different to stars in local galaxies. However, the very small sample size made a statistical comparison difficult.

7.1. The Effect of Numerical Resolution

The fact that zoomed-in ΛCDM simulations can produce thin disk galaxies (e.g., Wetzel et al. 2016) suggests that further increasing the numerical resolution may solve the discrepancy reported in Section 6.2. For example, Ludlow et al. (2021) recently argued that the coarse-grained implementation of dark matter halos causes an artificial heating of the stellar particles, which increases the vertical velocity dispersion of the galaxies. This yields thicker disks than better resolved galaxies, which could be the reason for the here reported tension. According to their Table 3, the vertical velocity dispersion σ_z of TNG50-1 galaxies embedded in a dark matter halo of $M_{200} < 7.9 \times 10^{11}\,M_\odot$ is numerically increased by $\Delta\sigma_z > 0.1\,V_{200}$, where V_{200} is the virial velocity of the halo, and M_{200} is its virial mass.

In this section, we analyze the effect of numerical resolution on the distribution of galaxy shapes using the TNG50 simulation. The flagship of the TNG project is called TNG50-1, which has the highest resolution among the here analyzed simulation runs. In addition, the TNG50 simulation suite includes the runs TNG50-2, TNG50-3, and TNG50-4, where a higher suffixed number indicates a lower-resolution realization as summarized in Table 1. The particle mass differs by a factor of eight between any TNG50 run and the next higher-resolution realization.

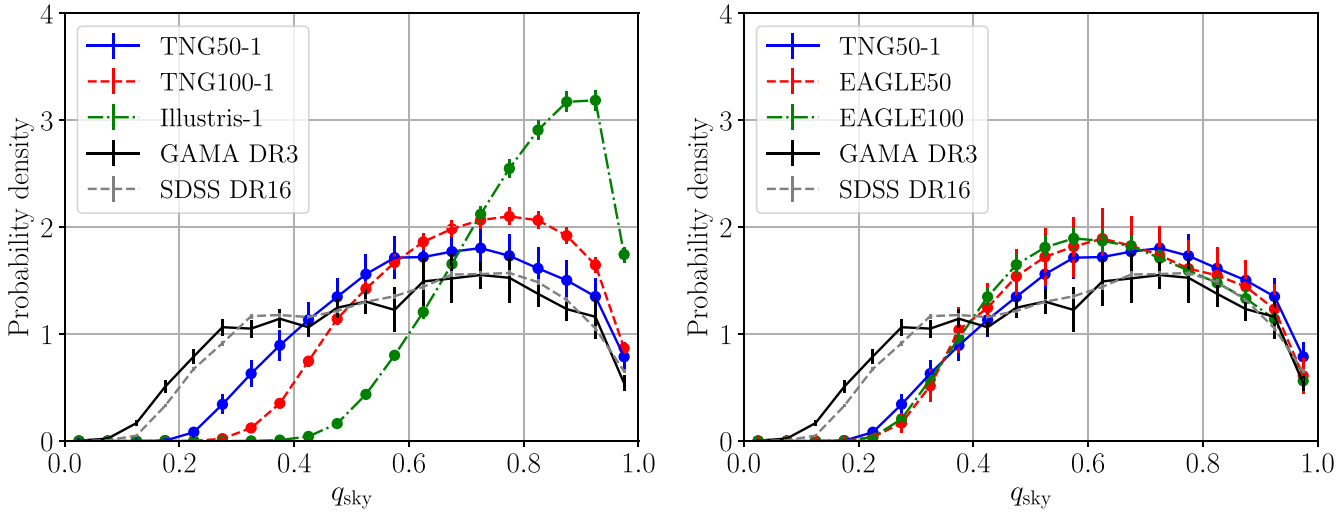

Figure 4. Comparison between the observed distribution of $q_{\rm sky}$ and that produced by different cosmological ΛCDM simulations for galaxies with $10.0 < \log_{10}(M_*/M_\odot) \leqslant 11.65$. The observed $q_{\rm sky}$ distributions (black and gray points with error bars) have been weighted based on the stellar mass distribution of the TNG50-1 run (shown in Figure 2). Invisible error bars (Equation (8)) are smaller than the data point symbol. The total χ^2 values between the observed and simulated distributions (Equation (7)) and the corresponding levels of tension are reported in Table 3. The TNG50-1, TNG100-1, Illustris-1, EAGLE50, and EAGLE100 computations shown here use 882, 6424, 6842, 480, and 3613 subhalos, respectively.

Table 2
Fraction of Galaxies with $q_{\rm sky} < 0.4$ in the Stellar Mass Range $10.0 < \log_{10}(M_*/M_\odot) \leqslant 11.65$ in Different Simulation Runs (Left Columns) and Observational Surveys (Right Columns)

Simulations		Observations	
EAGLE100	0.089 ± 0.005	Local 11 Mpc[a]	0.212 ± 0.067
EAGLE50	0.088 ± 0.014	GAMA DR3[a]	0.246 ± 0.007
EAGLE25	0.106 ± 0.038	GAMA DR3[b]	0.238 ± 0.009
Illustris-1	0.0005 ± 0.0003	SDSS DR16[a]	0.220 ± 0.001
TNG100-1	0.025 ± 0.002	SDSS DR16[b]	0.216 ± 0.002
TNG50-1	0.098 ± 0.011		

Notes. The stated Poisson uncertainties are estimated as $\sigma = \sqrt{N_{<0.4} + 1}/N_{\rm tot}$, where $N_{<0.4}$ and $N_{\rm tot}$ are the number of galaxies with $q_{\rm sky} < 0.4$ and the total number of galaxies, respectively. The Poisson uncertainties for M_*-weighted distributions are given by Equation (8), where $w_{\rm tot,i}$ is the sum of weights of galaxies with $q_{\rm sky} < 0.4$, and $w_{\rm max,i}$ is the maximum weight of such galaxies.
[a] No M_*-weighting applied.
[b] M_*-weighting applied based on the TNG50-1 stellar mass distribution.

Table 3
Statistical Comparison of the Observed Sky-projected Aspect Ratio Distribution from GAMA DR3 and SDSS DR16 with the Results of Different Cosmological ΛCDM Simulations

Simulation	GAMA DR3	SDSS DR16
EAGLE100	551.20 (21.68σ)	2679.88 (50.68σ)
EAGLE50	252.89 (13.65σ)	288.51 (14.82σ)
Illustris-1	1768.16 (40.80σ)	14689.73 (120.61σ)
TNG100-1	964.54 (29.54σ)	7421.62 (85.39σ)
TNG50-1	220.69 (12.52σ)	358.36 (16.89σ)

Note. The numbers show the total χ^2 calculated from 20 bins (Equation (7)). The bracketed numbers correspond to the level of tension for 20 degrees of freedom. The method for calculating the statistical significance of such extreme events is presented in the Appendix.

The left panel of Figure 5 shows the intrinsic aspect ratio distribution for different resolution realizations of the TNG50 simulation. The formation of thin galaxies and the peak position of the $q_{\rm int}$ distribution strongly depend on the resolution: the mode shifts from $q_{\rm int} = 0.88$ for TNG50-4 to $q_{\rm int} = 0.33$ for TNG50-1.

The convergence of different simulation runs is statistically quantified in Table 4. The $q_{\rm int}$ distributions of the TNG50-1 and TNG50-2 runs disagree with each other at 7.60σ. Although this is still a high tension, it is much lower compared to that between TNG50-2(-3) and TNG50-3(-4), which differ at the 13.75σ (14.17σ) confidence level. Based on the $q_{\rm sky}$ distribution, the TNG50-1 and TNG50-2 runs disagree at only 0.83σ.

The right panel of Figure 5 compares the $q_{\rm int}$ distribution of TNG50-1 with EAGLE100, EAGLE50, and the higher-resolution realization EAGLE25 (Recal-L0025N0752). The similarity of the EAGLE results (Table 4) implies that the EAGLE simulations have numerically converged, so the deficit of intrinsically thin galaxies cannot be explained by resolution effects—as also concluded by Lagos et al. (2018) and apparent in their Figures A2 and A3. Although the $q_{\rm int}$ distribution of the EAGLE25 run is very similar to EAGLE50 or EAGLE100, the tension between the sky-projected aspect ratio distribution of EAGLE25 and GAMA DR3 (SDSS) is only 1.44σ (0.37σ). This is because EAGLE25 only has 81 galaxies in the stellar mass range $10.0 < \log_{10}(M_*/M_\odot) \leqslant 11.65$, which results in large Poisson uncertainties that decrease therewith the total χ^2.

Importantly, the $q_{\rm sky}$ distributions of galaxies in TNG50-1 and EAGLE50 (EAGLE100) are consistent with each other at $1.4 \times 10^{-3}\sigma$ (0.58σ) confidence (Table 4). Thus, we demonstrate for the first time that ΛCDM simulations with SPH-based (EAGLE) and adaptive grid (Illustris/TNG) methods produce the same sky-projected aspect ratio distribution. The baryonic algorithms are also quite different between these simulations.

In order to quantify the thickening of simulated galaxies due to limited numerical resolution (e.g., Ludlow et al. 2021), we apply as an ansatz a parametric correction to the intrinsic shape distribution. The short axis λ_1 of each galaxy is scaled down by the factor x such that its $q_{\rm int}$ is corrected by

$$q_{\rm int,\ corr} = x q_{\rm int}, \quad x = \alpha + (1 - \alpha) q_{\rm int}. \tag{12}$$

α is a variable ranging from 0–1 in steps of $\Delta\alpha = 0.01$. Applying this correction to the $q_{\rm int}$ of simulated galaxies keeps

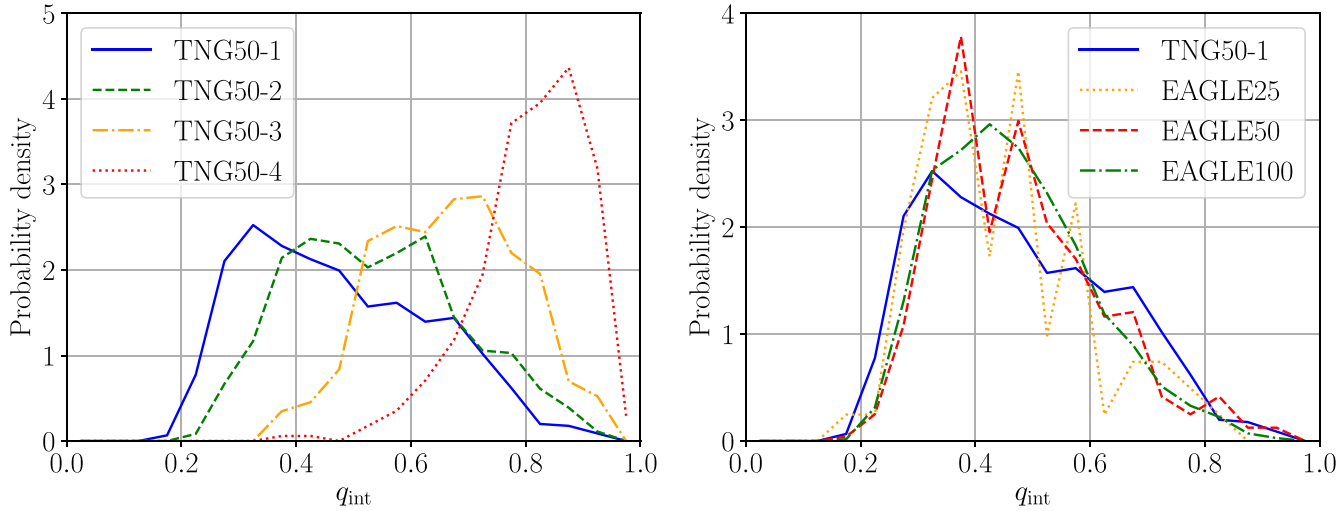

Figure 5. Intrinsic aspect ratio distribution of subhalos with $M_* > 10^{10}\,M_\odot$ for different resolution realizations of the simulation TNG50 (left) and EAGLE (right). A higher suffixed number for the TNG50 runs indicates a lower-resolution realization (i.e., TNG50-1 has the highest resolution). The simulated distributions are statistically compared in Table 4. EAGLE100 and EAGLE50 have the same resolution, while EAGLE25 has a higher resolution (Table 1).

Table 4

Testing the Numerical Convergence of Different Simulation Runs (Column 1) for Subhalos with $M_* > 10^{10}\,M_\odot$ by Showing the Total χ^2 (Equation (10)) between Their Distributions of $q_{\rm int}$ (Column 2) and $q_{\rm sky}$ (Column 3), along with the Corresponding Level of Tension (Bracketed Numbers)

Simulations	$\chi^2_{\rm int}$ between Them (Tension)	$\chi^2_{\rm sky}$ between Them (Tension)
TNG50-3 versus TNG50-4	268.26 (14.17σ)	91.80 (6.69σ)
TNG50-2 versus TNG50-3	255.73 (13.75σ)	105.10 (7.45σ)
TNG50-1 versus TNG50-2	107.85 (7.60σ)	20.82 (0.83σ)
TNG50-1 versus EAGLE100	87.83 (6.35σ)	18.35 (0.58σ)
TNG50-1 versus EAGLE50	56.78 (4.24σ)	6.04 (0.0014σ)
TNG50-1 versus EAGLE25	19.70 (0.71σ)	2.98 ($4.83 \times 10^{-6}\sigma$)
EAGLE100 versus EAGLE25	19.23 (0.66σ)	0.50 ($2.80 \times 10^{-13}\sigma$)
EAGLE50 versus EAGLE25	12.87 (0.15σ)	0.95 ($1.26 \times 10^{-10}\sigma$)

Note. We use 20 bins in $q_{\rm int}$ and $q_{\rm sky}$, giving 20 degrees of freedom. EAGLE50 and EAGLE100 use the same resolution, so the similarity between their results (χ^2 not shown) is not a strong test of numerical convergence. Note that the higher-resolution realization EAGLE25 only has 81 galaxies with $M_* > 10^{10}\,M_\odot$, which reduces the total χ^2 because of the higher Poisson uncertainties. The intrinsic aspect ratio distributions underlying these comparisons are plotted in Figure 5.

a galaxy with a high $q_{\rm int}$ round, but makes a thin disk galaxy even thinner. $\alpha = 1$ does not change the $q_{\rm int}$ of a galaxy, while $\alpha = 0$ yields a corrected $q_{\rm int,\,corr} = q_{\rm int}^2$, therewith causing the most substantial thinning of the galaxy population in our parameterization.

The tension between the observed and rescaled simulated $q_{\rm sky}$ distributions is shown in Figure 6 for different resolution realizations of the TNG50 simulation. As expected from our previous analysis, the tension systematically decreases with higher resolution. The tension between TNG50-1 and the GAMA survey (SDSS) reaches the 5σ confidence level if galaxies in the TNG50-1 run are corrected by $\alpha = 0.668$ ($\alpha = 0.738$). The tension between TNG50-1 and GAMA (SDSS) is minimized for a correction factor of $\alpha = 0.32$ ($\alpha = 0.47$), the tension in this case being only $4.6 \times 10^{-3}\sigma$ ($1.2 \times 10^{-2}\sigma$). This demonstrates that our simple parametric correction with a single parameter α (Equation (12)) can make the simulations agree very well with observations.

We can use this procedure to quantify how improving the resolution affects the simulated aspect ratio distribution, which then allows us to quantify if the simulations are numerically converged. To do this, we first find which α value must be applied to a TNG50 run to minimize the tension with the uncorrected $q_{\rm int}$ distribution of the next higher-resolution realization with an eight-times-higher mass resolution. We find that the tensions between the $q_{\rm int}$ distributions of the rescaled TNG50-4 and TNG50-3, rescaled TNG50-3 and TNG50-2, and rescaled TNG50-2 and TNG50-1 runs become minimal for α values of 0.03 (0.85σ), 0.44 ($5.9 \times 10^{-3}\sigma$), and 0.69 (0.80σ) applied to the TNG50-4, TNG50-3, and TNG50-2 runs, respectively. The true $q_{\rm int}$ distribution of each TNG50 run and the so-corrected distribution of the next lower-resolution TNG50 run is compared in the left panel of Figure 7, demonstrating that our parametric correction to, e.g., TNG50-2 galaxy shapes reproduces quite well the actual $q_{\rm int}$ distribution of TNG50-1. The required α value increases with higher resolution, but we cannot confirm that the TNG50 simulations have numerically converged, as that would be achieved if $\alpha = 1$.

In a second step, we extrapolate the α values by plotting $\ln(1 - \alpha)$ against the logarithmic dark matter particle mass of the corresponding TNG50 run (right panel of Figure 7). The α value required for galaxies in the TNG50-1 run to mimic the result of an eight-times-lower dark matter particle mass simulation is estimated using a parabolic and a linear fit in the $\log_{10}(m_{\rm dm}/M_\odot)$ versus $\ln(1 - \alpha)$ diagram of Figure 7. This predicts $\alpha = 0.824$ (0.834) for a linear (parabolic) fit. Being more conservative, we apply the linearly extrapolated result

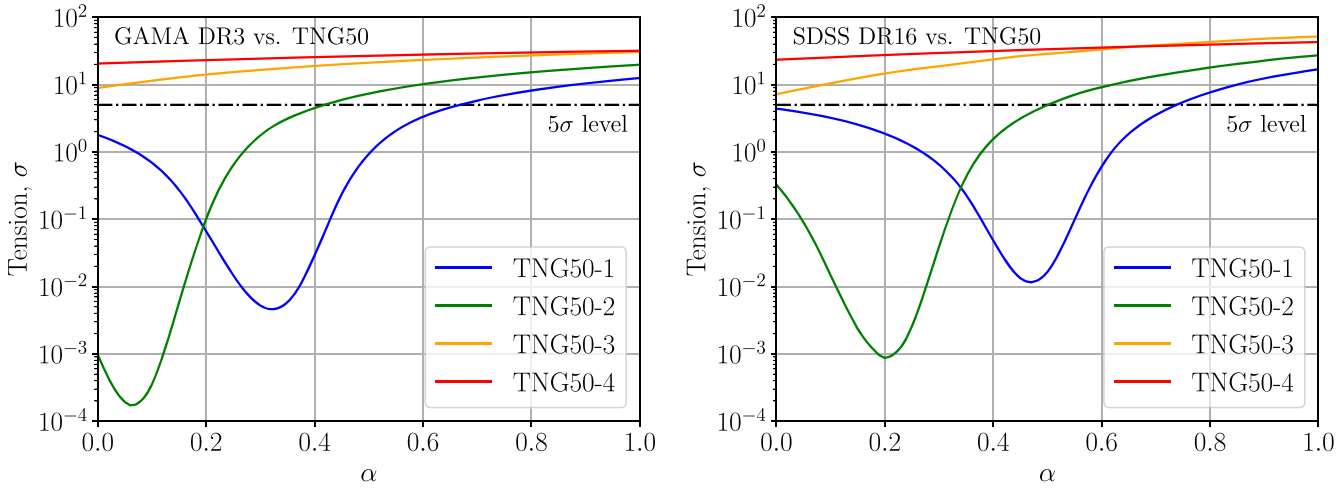

Figure 6. Level of tension between the observed and simulated $q_{\rm sky}$ distribution of galaxies with $10.0 < \log_{10}(M_*/M_\odot) \leqslant 11.65$ in dependence of α (Equation (12)) for different resolution realizations of the TNG50 simulation, which we show with different colored lines (see the legend). The left panel considers GAMA as the observational sample, while the right panel uses SDSS. The tension between TNG50-1 and GAMA DR3 (SDSS DR16) reaches the 5σ confidence level (dashed horizontal line) if $\alpha = 0.668$ ($\alpha = 0.738$), with the tension becoming minimal if instead $\alpha = 0.32$ ($\alpha = 0.47$), the tension in this case being only $4.6 \times 10^{-3}\sigma$ ($1.2 \times 10^{-2}\sigma$).

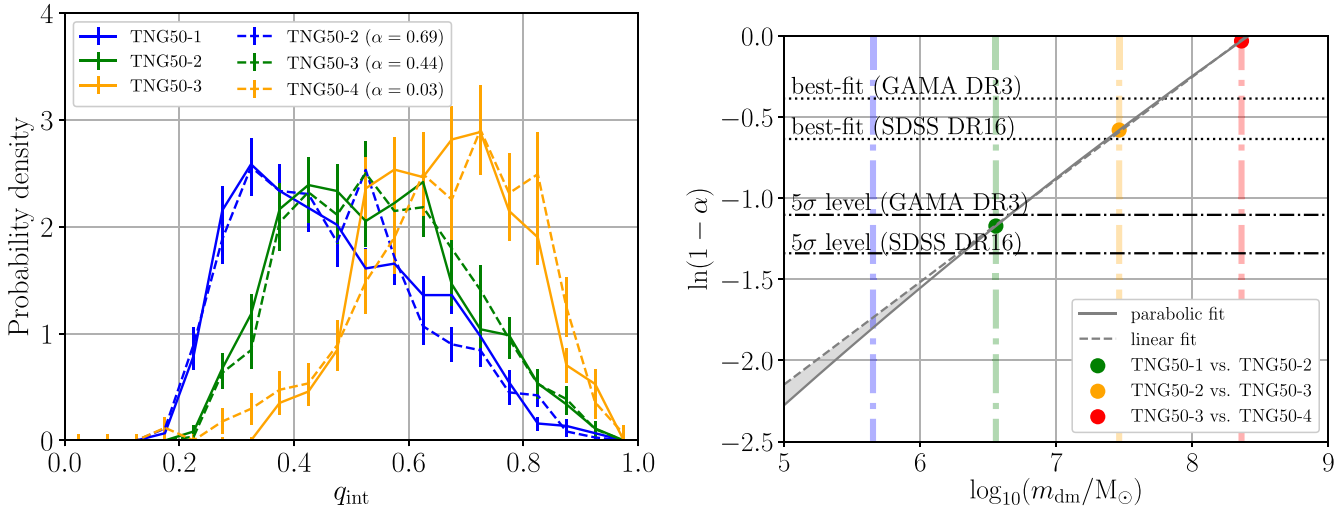

Figure 7. Left: the $q_{\rm int}$ distribution of subhalos with $10.0 < \log_{10}(M_*/M_\odot) \leqslant 11.65$ in each TNG50 simulation (solid lines) is compared with the corrected distribution for subhalos in the next lower-resolution simulation, which we show using a dashed line of the same color. The applied correction factors and resulting levels of tension are $\alpha = 0.69$ (0.80σ), $\alpha = 0.44$ ($5.9 \times 10^{-3}\sigma$), and $\alpha = 0.03$ (0.85σ) for subhalos in TNG50-2, TNG50-3, and TNG50-4, respectively. These corrections minimize the tension with the uncorrected $q_{\rm int}$ distribution of the next higher-resolution simulation. Right: checking for convergence of the TNG50 $q_{\rm int}$ distribution with respect to the dark matter mass resolution $m_{\rm dm}$ for galaxies with $10.0 < \log_{10}(M_*/M_\odot) \leqslant 11.65$. The above-mentioned α values are plotted in terms of $\ln(1-\alpha)$ against $\log_{10}(m_{\rm dm}/M_\odot)$. The vertical lines mark the mass of a dark matter particle in the TNG50 runs as listed in Table 1. The dotted–dashed horizontal lines mark $\alpha = 0.668$ and $\alpha = 0.738$, which are required for the $q_{\rm sky}$ distribution of the TNG50-1 run to match that of GAMA DR3 and SDSS DR16, respectively, at the 5σ confidence level. The dotted lines represent $\alpha = 0.32$ and 0.47 because these values would minimize the tension of TNG50-1 with GAMA and SDSS, respectively. The dashed (solid) gray line is a linear (parabolic) fit. The gray shaded region indicates how much the $q_{\rm int}$ distribution could differ in an even higher-resolution run than TNG50-1. We estimate that using an eight-times lower dark matter particle mass than TNG50-1 (dotted–dashed blue vertical line) is equivalent to scaling galaxies in it by α in the range between 0.834 (parabolic fit) and 0.824 (linear fit).

that $\alpha = 0.824$ to the TNG50-1 run, which yields an 8.68σ (8.71σ) tension with GAMA (SDSS). Thus, an eight-times higher-resolution realization of the TNG50-1 run would almost certainly not reduce the here reported tension below the 5σ confidence level.

In the third and final step, we estimate the tension with observations by extrapolating the data further to five more refinement levels than in the TNG50-1 run. Therefore, we extract the α values not only for an eight-times-lower $m_{\rm dm}$ but also for an $8^2\times$, $8^3\times$, $8^4\times$, and $8^5\times$ lower $m_{\rm dm}$ than in the TNG50-1 run. These so-obtained α values for the five different resolution levels are listed in Table 5 for the parabolic and linear extrapolations. The α values are then successively applied to estimate the intrinsic aspect ratio of each subhalo in an $8^5\times$ higher-resolution realization than TNG50-1. In other words, the aspect ratio distribution for an $8^2\times$ higher-resolution run than TNG50-1 is obtained by correcting the aspect ratios of subhalos in the eight-times higher-resolution run by applying Equation (12) with $\alpha = 0.915$ (parabolic fit) or $\alpha = 0.900$ (linear fit). This procedure is repeated until we reach an $8^5\times$ higher refinement level, which on the last step requires applying $\alpha = 0.991$ (parabolic fit) or $\alpha = 0.982$ (linear fit) to the $q_{\rm int}$ distribution of the $8^4\times$ higher-resolution realization than TNG50-1. Since α is now close to unity, this almost

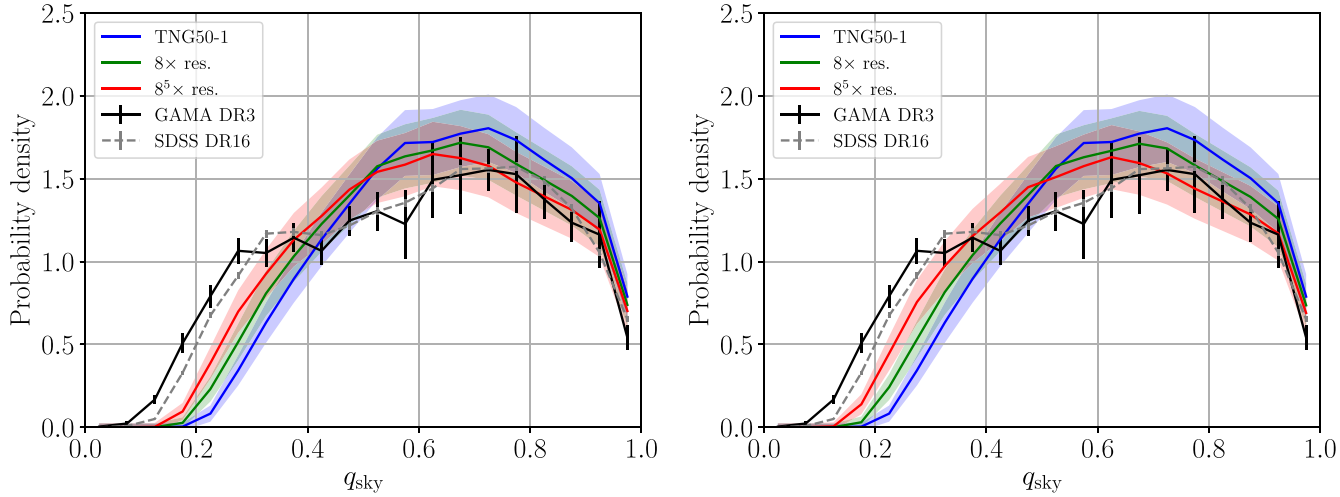

Figure 8. Similar to Figure 4, but for an eight-times-higher (green line) and $8^5\times$ higher (red line) resolution run than TNG50-1 (blue line). The colored shaded regions highlight the uncertainties given by Equation (8). The simulated $q_{\rm sky}$ distributions for a higher-resolution run than TNG50-1 have been estimated with a parabolic (left panel) or linear (right panel) extrapolation in the $\log_{10}(m_{\rm dm}/M_\odot)$ vs. $\ln(1-\alpha)$ diagram as shown in the right panel of Figure 7 (see the text). The total χ^2 (Equation (7)) between the observed and simulated distribution for different refinement levels is reported in Table 5 along with the corresponding level of tension.

Table 5
Statistical Comparison of the Observed Sky-projected Aspect Ratio Distributions from GAMA DR3 (Fourth and Fifth Columns) and SDSS DR16 (Sixth and Seventh Columns) with the Results of Five More Refinement Levels (First Column) Than in the TNG50-1 Run

	α (Equation (12))		χ^2 and Tension with GAMA DR3		χ^2 and Tension with SDSS DR16	
Resolution	Parabolic Fit	Linear Fit	Parabolic Fit	Linear Fit	Parabolic Fit	Linear Fit
TNG50-1	...	...	220.69 (12.52σ)	220.69 (12.52σ)	358.36 (16.89σ)	358.36 (16.89σ)
$8\times$	0.834	0.824	134.17 (8.94σ)	128.96 (8.68σ)	140.34 (9.23σ)	129.60 (8.71σ)
$8^2\times$	0.915	0.900	99.29 (7.12σ)	90.08 (6.59σ)	77.38 (5.72σ)	63.95 (4.78σ)
$8^3\times$	0.958	0.944	84.94 (6.18σ)	71.83 (5.34σ)	57.06 (4.26σ)	41.14 (2.91σ)
$8^4\times$	0.980	0.968	78.27 (5.77σ)	63.12 (4.72σ)	48.57 (3.57σ)	32.31 (2.05σ)
$8^5\times$	0.991	0.982	75.37 (5.58σ)	58.36 (4.36σ)	45.12 (3.27σ)	28.06 (1.61σ)

Note. The second and third columns list the α values obtained by extrapolating the TNG50 runs to an $8\times$, $8^2\times$, $8^3\times$, $8^4\times$, and $8^5\times$ lower dark matter particle mass than in TNG50-1 using a parabolic or a linear fit in the $\log_{10}(m_{\rm dm}/M_\odot)$ versus $\ln(1-\alpha)$ diagram (right panel of Figure 7). These so-obtained α values have been successively applied to the intrinsic aspect ratios of subhalos in TNG50-1 (see the text).

reaches full convergence in $q_{\rm int}$. Further improvements to the resolution can be expected to have sub-percent level effects on the intrinsic aspect ratios.

The $q_{\rm sky}$ distributions for an $8\times$ and $8^5\times$ higher dark matter mass resolution than the TNG50-1 run derived from a parabolic (linear) extrapolation are presented in the left (right) panel of Figure 8. Raising the resolution of the dark matter mass in TNG50-1 by a factor of 8^5 yields an estimated tension of 5.58σ (parabolic fit) and 4.36σ (linear fit) with GAMA. In contrast, the discrepancy is significantly alleviated with respect to the older SDSS data set—we estimate a tension of 3.27σ with a parabolic fit and only a 1.61σ tension with a linear fit. The difference between the two observational samples is mainly because the fraction of galaxies with $q_{\rm sky}\lesssim 0.3$ is higher in the GAMA survey compared to SDSS (Figure 8). The total χ^2 values and corresponding levels of tension with the GAMA and SDSS surveys for different resolution realizations and extrapolation methods are summarized in Table 5.

Since the parabolic fit considers more information than the linear fit and exactly matches the data, we consider it as the nominal case in our main analysis. The linear fit is still shown in order to illustrate the effect of uncertainties in the extrapolation procedure. Therefore, our estimate is that increasing the mass resolution of TNG50-1 by $8^5\times$ still leaves a significant tension of 5.58σ with GAMA, exceeding the 5σ plausibility threshold. The SDSS data set is then in 3.27σ tension, which still points to an underestimated fraction of very thin galaxies in the ΛCDM simulations (see Figure 8).

Finally, we note that our approach is very conservative with respect to the ΛCDM framework. First of all, the extrapolation to five more refinement levels than TNG50-1 is based only on the four resolution realizations of the TNG50 simulation. For example, the TNG50-4 simulation has $m_{\rm dm}=2.3\times10^8\,M_\odot$, which is a factor of $8^8=1.7\times10^7$ more massive than dark matter particles in an $8^5\times$ higher-resolution realization than the TNG50-1 run. The parabolic and linear fits have been derived from simulations with $4.5\times10^5\,({\rm TNG50}-1)\leqslant m_{\rm dm}/M_\odot\leqslant 2.3\times10^8\,({\rm TNG50}-4)$. This introduces additional uncertainties because the shape of the relation between $\log_{10}(m_{\rm dm}/M_\odot)$ and $\ln(1-\alpha)$ may deviate significantly from the derived polynomial fits at lower $m_{\rm dm}$. Second, we performed the extrapolation to very high-resolution realizations without assuming that numerical convergence is reached between two different refinement levels. It is not impossible that numerical convergence ($\alpha=1$) is already attained before reaching the $8^5\times$ higher-resolution level. Consequently, higher-resolution runs of self-consistent ΛCDM simulations are still required to test when numerical convergence is reached and if the tension with observations is then alleviated.

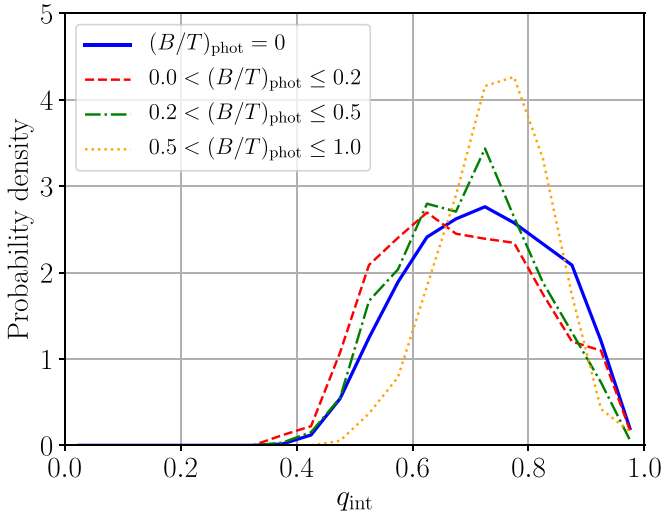

Figure 9. The $q_{\rm int}$ distribution of subhalos with $M_* > 10^{10}\,M_\odot$ in different photometric $(B/T)_{\rm phot}$ bins in the Illustris-1 simulation as derived by Bottrell et al. (2017a) for camera angle 0. The solid blue, dashed red, dotted–dashed green, and dotted yellow lines refer to galaxy subsamples with $(B/T)_{\rm phot} = 0$ (3999 subhalos), $0 < (B/T)_{\rm phot} \leqslant 0.2$ (1715 subhalos), $0.2 < (B/T)_{\rm phot} \leqslant 0.5$ (658 subhalos), and $0.5 < (B/T)_{\rm phot} \leqslant 1.0$ (380 subhalos), respectively.

7.2. Photometric Bulge/Total Ratios of Illustris-1 Subhalos

In contrast to our findings, Bottrell et al. (2017b) found a significant deficit of bulge-dominated galaxies based on the photometric bulge/total ratios of subhalos in the Illustris-1 simulation compared to SDSS. In particular, Bottrell et al. (2017a) photometrically derived $(B/T)_{\rm phot}$ ratios of subhalos with $M_* > 10^{10}\,M_\odot$ at $z = 0$ in the Illustris-1 simulation by performing a bulge-disk decomposition of the surface brightness profile with fixed Sérsic indices $n_{\rm b} = 4$ for the bulge and $n_{\rm d} = 1$ for the disk. By applying the same decomposition analysis to observed SDSS galaxies, they found a significant deficit of bulge-dominated galaxies with $M_*/M_\odot = 10^{10}$–10^{11} in the Illustris-1 simulation (see Figures 4 and 6 in Bottrell et al. 2017b).

If the Illustris-1 simulation indeed lacks bulge-dominated galaxies, this deficit should also be evident in the $q_{\rm int}$ parameter (Section 6.1). To test if $(B/T)_{\rm phot}$ reflects the shapes of simulated galaxies as quantified by $q_{\rm int}$, we show in Figure 9 its distribution for four simulated galaxy subsamples of Bottrell et al. (2017a) with different photometric morphologies, i.e., $(B/T)_{\rm phot}$: 0, (0,0.2], (0.2,0.5], and (0.5,1].[18] Throughout this work, we use the $(B/T)_{\rm phot}$ ratio derived for the r band from camera angle 0. Remarkably, all four galaxy subsamples have a very similar aspect ratio distribution, with the peak between $q_{\rm int} = 0.6$–0.8. The distributions have very few galaxies with $q_{\rm int} < 0.5$: the proportions for the above-mentioned $(B/T)_{\rm phot}$ bins are only 3.4%, 7.1%, 3.6%, and 0.26%, respectively, implying that the sample of Bottrell et al. (2017a) is actually bulge-dominated.

In order to understand this mismatch between $(B/T)_{\rm phot}$ and $q_{\rm int}$, we begin by presenting color images[19] generated from the Friends-of-Friends (FoF) halo finder. Subhalos with low $0 < (B/T)_{\rm phot} < 0.2$ and $q_{\rm int} < 0.4$ indeed have spiral structures and a disk (Figure 10). The $\kappa_{\rm rot}$ morphological parameter (Equation (2) in Rodriguez-Gomez et al. 2015) indicates that these subhalos are rotation-dominated ($\kappa_{\rm rot} > 0.5$).

The mismatch between the morphological parameters becomes evident in Figure 11, which shows the significant fraction of subhalos (13.1%) with low $0 < (B/T)_{\rm phot} < 0.2$ but high $q_{\rm int} > 0.8$ for their stellar component.[20] These are featureless-looking dispersion-dominated ($\kappa_{\rm rot} < 0.5$) galaxies without a pronounced disk or spiral structures. Based on these images and given that the intrinsic aspect ratio is a very robust parameter to quantify the actual shape of a galaxy, we conclude that the 2D parametric surface brightness decomposition applied by Bottrell et al. (2017a) is inadequate if applied to simulated galaxies.

In addition to a bulge-disk decomposition, Bottrell et al. (2017a) also applied a pure Sérsic model to the galaxies in subhalos by varying the Sérsic index between 0.5 and 8. Figure 12 shows a significant correlation between $(B/T)_{\rm phot}$ and the Sérsic index, highlighting the inevitable confusion between an elliptical galaxy with $n_s \approx 1$ and a thin exponential disk if only considering the surface brightness profile. Choosing a different camera angle leads to the same results. In combination with Figure 9, this shows that neither $n_{\rm s}$ nor $(B/T)_{\rm phot}$ correlates with $q_{\rm int}$.

This might be due to the resolution of the Illustris-1 simulation not being sufficient to apply a photometric decomposition. Importantly, we have shown in this contribution that the observed and simulated galaxy morphology distributions differ significantly (Table 3). The vast majority of observed galaxies are spirals (e.g., Loveday 1996; Delgado-Serrano et al. 2010), while the ΛCDM simulations form a far-too-large fraction of bulge-dominated galaxies (Figures 3 and 4). Thus, assuming that all galaxies with low $(B/T)_{\rm phot}$ are intrinsically thin is quite accurate in the real universe where spirals are quite common, but not in a ΛCDM universe where they are rare (Section 6.2). In the Illustris-1 simulation, there are so few disk galaxies that galaxies with low $(B/T)_{\rm phot}$ are nearly always ellipticals with an exponential-like surface brightness profile (Sérsic index close to 1).

These problems with the $(B/T)_{\rm phot}$ parameter are avoided by using the sky-projected aspect ratio (Figure 4), which is closely linked to the intrinsic aspect ratio and thus yields a more robust measurement of the galaxy morphology. Since $q_{\rm sky}$ is observable, it allows for a much more direct test of the model, provided the sample size is sufficient to statistically sample over projection effects. This is true in our case because the TNG50-1, GAMA DR3, and SDSS DR16 samples contain 882, 5304, and 232,128 galaxies, respectively, in the range $10.0 < \log_{10}(M_*/M_\odot) \leqslant 11.65$ used for our comparisons.

7.3. Impact of the Merger History

The ΛCDM theory strictly implies a hierarchical merger-driven build-up of the galaxy population. Galaxy mergers are driven by dynamical friction on the extended dark matter halos of interacting galaxies (e.g., Kroupa 2015). Mergers grow the bulge component and thicken the stellar disk. By studying galaxy–galaxy interactions in N-body/hydrodynamical simulations, Hwang et al. (2021) showed that the disk angular

[18] We use their DISTINCT catalog, which contains the galaxy sample analyzed by Torrey et al. (2015).

[19] Downloaded [26.06.2020] from the Illustris-1 webpage using the Illustris Galaxy Observatory tool: https://www.illustris-project.org/galaxy_obs.

[20] Subhalos with $(B/T)_{\rm phot} = 0$ are probably erroneous (Bottrell et al. 2017a) and are excluded from our analysis except in Figure 9.

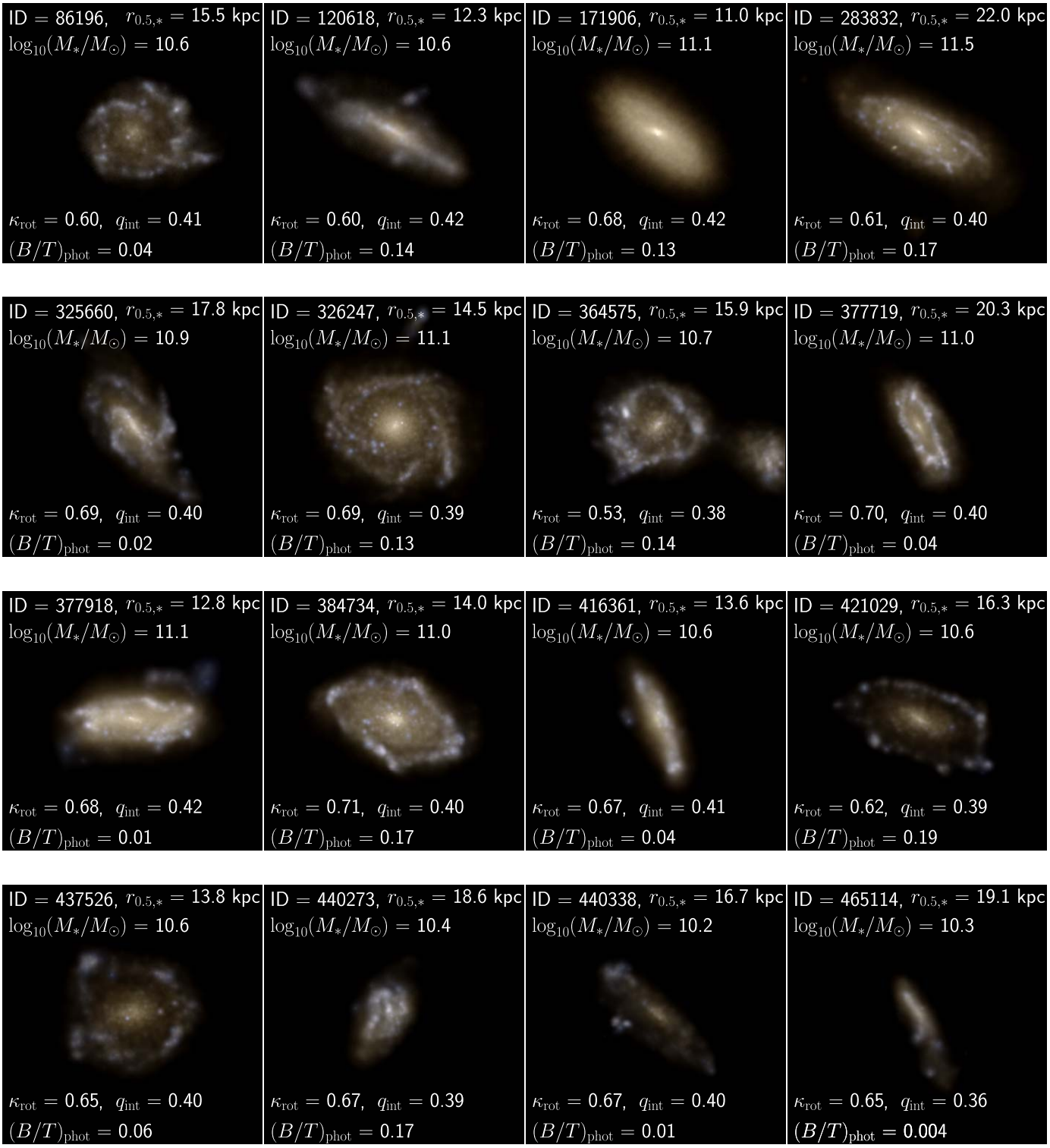

Figure 10. Images of Illustris-1 galaxies in subhalos with $0 < (B/T)_{\rm phot} < 0.2$ from camera angle 0 that have the lowest $q_{\rm int}$ values in the sample of Bottrell et al. (2017a). These galaxies are rotation-dominated ($\kappa_{\rm rot} > 0.5$) and have spiral features, with $q_{\rm int} \approx 0.4$. The FoF images were downloaded from the Illustris Galaxy Observatory tool: https://www.illustris-project.org/galaxy_obs. The field of view is ten stellar half-mass radii of the shown subhalo. These are genuinely disk-dominated galaxies.

momentum of the late-type galaxy decreases by about 15%–20% after a prograde collision. Thus, galaxies with a quiescent merger history are expected to have lower bulge fractions than galaxies that have undergone a major merger (see also, e.g., Bournaud et al. 2005; D'Onghia et al. 2006). Since most observed galaxies are late types (e.g., Delgado-Serrano et al. 2010) and ≈50% of these have no classical bulge (Graham & Worley 2008; Kormendy et al. 2010), we might expect that galactic mergers are less frequent in the universe than in ΛCDM simulations (Disney et al. 2008; Stewart et al. 2008;

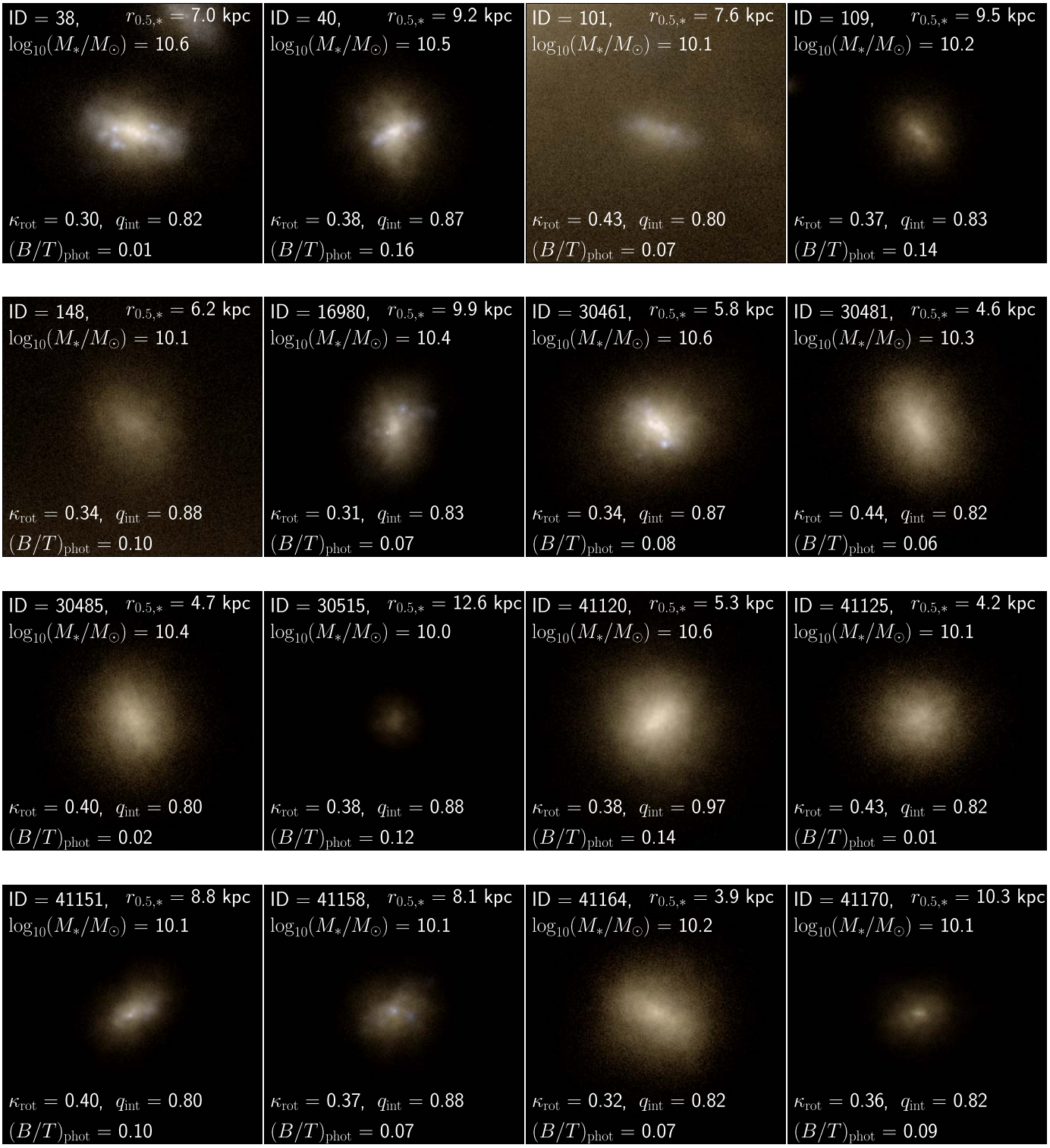

Figure 11. Similar to Figure 10, but for galaxies with high $q_{\rm int} > 0.8$ despite a low $(B/T)_{\rm phot} < 0.2$. These are dispersion-dominated ($\kappa_{\rm rot} < 0.5$) featureless-looking galaxies. They are best understood as early-type galaxies where the photometric classification failed by assigning a low $(B/T)_{\rm phot}$.

Fakhouri et al. 2010; Kroupa 2015; Wu & Kroupa 2015). This may underlie the tension between the observed and simulated sky-projected aspect ratio distributions (Figure 4).

We therefore investigate if galaxies with a quiescent merger history in the ΛCDM framework are typically much thinner. We focus on the TNG50-1 run, as it has the highest resolution (Table 1) and yields the lowest tension in the here analyzed simulations (Table 3). The merger trees of the Illustris and TNG projects can be downloaded from their webpages,[21] with a detailed description available in Rodriguez-Gomez et al. (2015). We quantify the merger history of a galaxy by

[21] https://www.illustris-project.org [21.07.2020] and https://www.tng-project.org [21.07.2020].

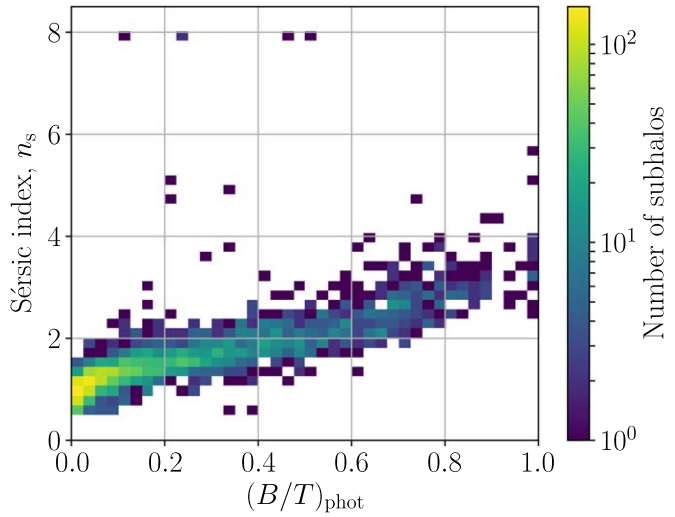

Figure 12. Correlation between the photometric $(B/T)_{\rm phot}$ ratio and the Sérsic index n_s for the Illustris-1 simulated subhalo sample analyzed by Bottrell et al. (2017a). The parameters shown here are from catalogs provided in their Tables A1 and A2 for camera angle 0, with different camera orientations leading to the same results (not shown). Notice the tight correlation between $(B/T)_{\rm phot}$ and n_s but a lack of correlation between $(B/T)_{\rm phot}$ and $q_{\rm int}$ (see Figure 9).

considering the total mass ratio $\mu \leqslant 1$ of the two progenitors and the maximum lookback time $t_{\rm max}$ during which we consider mergers. If there are multiple mergers in this timeframe, we use the most major merger, i.e., that with the highest μ. This μ value is used to construct two galaxy samples that differ according to whether the galaxy had at least one major merger with $\mu \geqslant 1/12$ within a lookback time of $t_{\rm max} = 12$ Gyr ($z = 3.7$). We restrict ourselves to galaxies with $M_* > 10^{10}\,M_\odot$ and $M_{\rm dm}/M_* > 1$ at $z = 0$. The constraint on the $M_{\rm dm}/M_*$ ratio is applied to exclude dark matter–poor galaxies, which cannot be traced back accurately. This excludes 26 galaxies from the original sample. About 89% of all subhalos at $z = 0$ have undergone at least one major merger, which is broadly consistent with other ΛCDM simulations (Stewart et al. 2008; Fakhouri et al. 2010). The remaining 11% of all subhalos had at most only minor merger(s) with $\mu \leqslant 1/12$ during the past 12 Gyr.

As expected from zoomed-in simulations of galaxies in underdense environments, intrinsically thin galaxies are more frequent in the sample of galaxies with a quiescent merger history compared to that with an active merger history (see the left panel of Figure 13). In particular, $39\% \pm 2\%$ of galaxies with an active merger history have $q_{\rm int} < 0.4$, but this rises to $50\% \pm 7\%$ for galaxies with a quiescent merger history. The aspect ratio of the thinnest such galaxy ($q_{\rm int} = 0.22$) is similar to that in the sample with an active merger history ($q_{\rm int} = 0.19$). Additionally, $9.5\% \pm 1.1\%$ of galaxies with an active merger history have $q_{\rm sky} < 0.4$, but this rises to $12.5\% \pm 3.7\%$ for the galaxies with a quiescent merger history (right panel of Figure 13).

Thus, the lack of intrinsically thin galaxies in ΛCDM could be partly due to major mergers. More likely, it is due to a combination of major and minor mergers, which are unavoidable in ΛCDM, as galaxies grow their mass through mergers. We emphasize that minor mergers are expected to be much less frequent in an alternative framework where galaxies lack extended dark matter halos, as occurs in MOND (Milgrom 1983). In addition, secular processes like disk-halo angular momentum exchange could also drive the formation of significant bars and bulges in ΛCDM (Athanassoula 2002; Sellwood et al. 2019), but perhaps not in the real universe (Banik et al. 2020; Roshan et al. 2021a) where the fraction of bars differs substantially from ΛCDM expectations (Reddish et al. 2021). There is also a highly significant discrepancy between the pattern speeds of bars in observations and in ΛCDM simulations, where the results seem to have converged with respect to the ratio of bar length to corotation radius (Roshan et al. 2021b). The tension is caused by the fact that bars are expected to be slowed down by dynamical friction with the dark matter halo, but observed bars are fast. This is another indication against dynamical friction from massive dark matter halos.

7.4. Feedback

In the previous section, we discussed that the disagreement between the observed and ΛCDM simulated galaxy shapes could be partly due to the frequency of mergers being too high in this framework. Another possibility is that the tension is caused by the feedback description used in the simulations. In particular, Lagos et al. (2018) discussed the link between loss/gain of angular momentum and dry/wet mergers. Using the EAGLE and HYDRANGEA (Bahé et al. 2017; Barnes et al. 2017) hydrodynamical simulations, they showed that dry mergers typically decrease the stellar spin parameter while wet mergers increase it. Therefore, galaxies that further accrete cold gas are able to reform their disks. This process is sensitive to the implemented feedback description.

As shown in Sections 6.1 and 7.1, the TNG50-1 and EAGLE simulations produce very similar aspect ratio distributions despite relying on different sub-grid models. This is a strong indication that the tension is likely not caused by the implemented sub-grid feedback models. Even so, improved models might yet alleviate or resolve the tension. For example, the feedback recipe in both the TNG and EAGLE projects could be too strong to allow the (re)formation of disks. In this case, the shape of the galaxies would be set by the merger rate independently of whether the mergers are dry or wet. However, a weaker feedback description could potentially increase the efficiency of disk formation. We note that strong feedback is required in ΛCDM simulations for them to explain why the Newtonian dynamical mass of a galaxy or galaxy group often greatly exceeds $6.4\times$ its baryonic mass (e.g., Müller et al. 2021), even though ΛCDM needs this to be the cosmic ratio between baryonic and total mass (Planck Collaboration VI 2020). A strong feedback prescription is also needed to solve the missing satellite galaxy problem (e.g., Brooks et al. 2013).

7.5. Disk Galaxies in MOND

The difficulties faced by ΛCDM with regards to the high fraction of thin disk galaxies motivate us to consider MOND one of the main alternative frameworks that is generally considered to perform better on galaxy scales (for reviews, see, e.g., Famaey & McGaugh 2012; Kroupa 2015; Banik & Zhao 2022). For illustrative purposes, we show in the left panel of Figure 14 the present-day $q_{\rm int}$ distribution of six disk galaxies with $10^{10} < M_*/M_\odot \leqslant 9.56 \times 10^{10}$ formed in hydrodynamical MOND simulations of collapsing gas clouds conducted by Wittenburg et al. (2020) using the PHANTOM

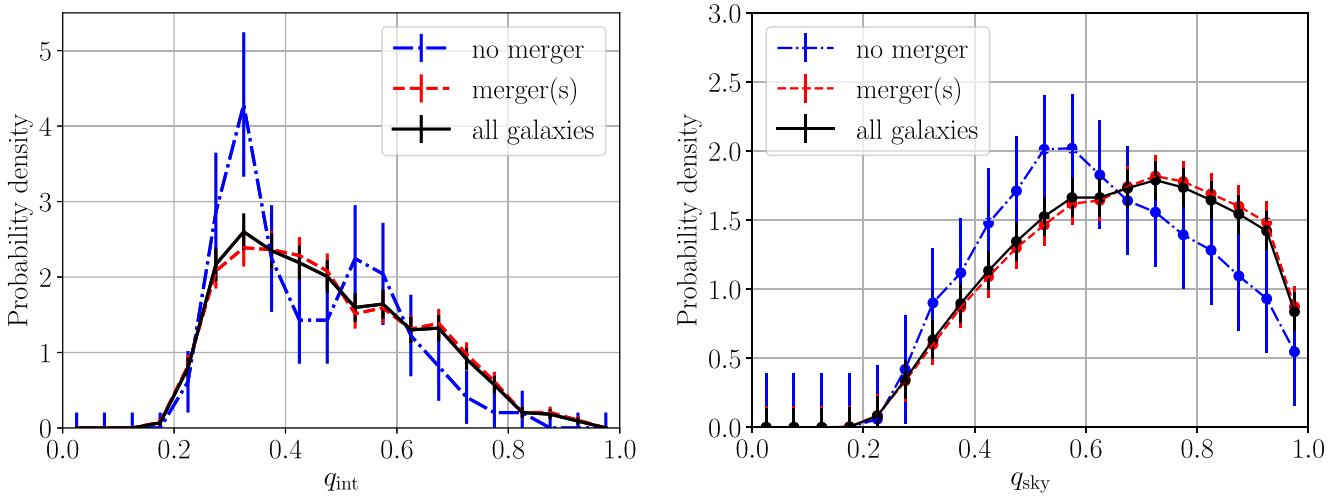

Figure 13. Intrinsic (left) and sky-projected (right) aspect ratio distribution of subhalos in the TNG50-1 simulation with $M_* > 10^{10}\,M_\odot$ and $M_{\rm dm}/M_* > 1$ with an active (dashed red) and quiescent (dotted–dashed blue) merger history, defined according to whether the galaxy had at least one major merger with total mass ratio $\mu \geqslant 1/12$ within the last 12 Gyr. The intrinsic aspect ratio distribution of the active (quiescent) sample, which contains 779 (98) galaxies, has a median of $q_{\rm int} = 0.40$ (0.45). Results for all 877 galaxies (regardless of merger history) are shown by the solid black lines. The proportion of galaxies with $q_{\rm int} < 0.4$ is $39\% \pm 2\%$ and $50\% \pm 7\%$ in the sample with an active and a quiescent merger history, respectively. If instead we require $q_{\rm sky} < 0.4$, these proportions become $9.5\% \pm 1.1\%$ (active) and $12.5\% \pm 3.7\%$ (quiescent).

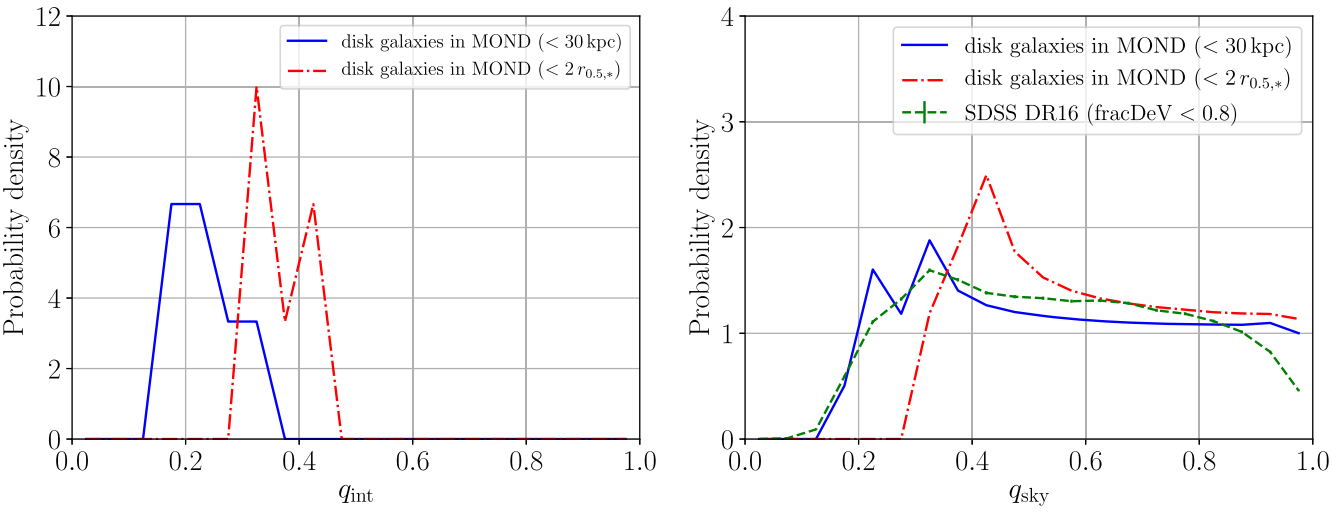

Figure 14. Distribution of the intrinsic (left) and sky-projected (right) aspect ratio for six disk galaxies with $10^{10} < M_*/M_\odot \leqslant 9.56 \times 10^{10}$ formed in MOND simulations conducted by Wittenburg et al. (2020). The solid blue (dotted–dashed red) line refers to the aspect ratio derived from the mass tensor of particles within a sphere of radius 30 kpc (2 $r_{0.5,*}$). These MOND results are shown for illustrative purposes only—they are not directly comparable to the ΛCDM simulations because the Milgromian galaxies are not formed in a self-consistent cosmological simulation. The dashed green line in the right panel shows the $q_{\rm sky}$ distribution derived from an exponential fit to SDSS galaxies with fracDeV < 0.8 and $10^{10} < M_*/M_\odot \leqslant 9.56 \times 10^{10}$. We do not apply an M_*-weighting to the observed sample as we only have a small number of simulated MONDian galaxies.

of RAMSES code (Lüghausen et al. 2015), an adaptation of the *N*-body and hydrodynamics solver RAMSES (Teyssier 2002) for MOND gravity (for a user guide, see Nagesh et al. 2021). These non-cosmological simulations have a box size of 960 kpc per side, a minimum stellar mass of $M_* \approx 3 \times 10^4\,M_\odot$, and depending on the run a maximum grid cell resolution of 117.19 pc, 234.38 pc, or 468.75 pc. The temperature floor for the gas is set to 10 kK (for further information on the initial conditions and numerical parameters of the individual simulations, see Table 1 of Wittenburg et al. 2020). The Milgromian disk galaxies are systematically thinner than in the here analyzed ΛCDM simulations, as evidenced by their $q_{\rm int} = 0.18$–0.30 (0.31–0.54) for $r < 30$ kpc ($r < 2\,r_{0.5,*}$), with the global peak at $q_{\rm int} \approx 0.2$ (0.3). While these isolated MOND results cannot yet be directly compared with self-consistent cosmological ΛCDM simulations that allow for galaxy interactions and mergers, we note that neglecting mergers may be a good approximation in MOND as mergers are expected to be rare due to the absence of dynamical friction with the dark matter halo (Renaud et al. 2016).

Interestingly, the right panel of Figure 14 shows that the sky-projected aspect ratio distribution of these MONDian disk galaxies is very consistent with that of SDSS spiral galaxies (fracDeV <0.8; see Section 4.3). This also demonstrates that the distinction of spiral from elliptical galaxies based on the linear combination of the exponential and de Vaucouleurs models (Abazajian et al. 2004) succeeds in SDSS, in contrast to the bulge-disk decomposition applied to the Illustris-1 simulation (possible reasons were discussed in Section 7.2). In the future, whether a self-consistent cosmological MOND simulation would

be able to reproduce the observed fraction of spiral and elliptical galaxies needs to be explicitly shown. Such MOND simulations are not available at the moment, but are underway in the Bonn-Prague group based on the promising cosmological MOND framework detailed in Haslbauer et al. (2020). Given the problems in reproducing the observed distribution of galactic morphologies with ΛCDM simulations, it is often argued that these simulations depend sensitively on the implemented feedback model and that the problem is likely to be alleviated once the correct feedback implementation has been found. Hydrodynamical MOND simulations of galaxy formation out of post–Big Bang gas clouds, on the other hand, naturally lead to realistic galaxies similar to the observed ones with the available feedback implementations (Wittenburg et al. 2020, Eappen et al. 2022, submitted).

8. Conclusions

In this contribution, we considered the distribution of galaxy morphologies in state-of-the-art cosmological ΛCDM simulations. The present-day sky-projected aspect ratio distribution of galaxies in the TNG50-1 (EAGLE50) simulation disagrees with the GAMA survey and SDSS at $\geqslant 12.52\sigma$ ($\geqslant 14.82\sigma$) confidence (Section 6.2). The lowest tension is obtained when comparing GAMA with the TNG50-1 simulation run, which has the highest resolution of the TNG project. The main reason for this mismatch is that the ΛCDM simulations significantly underproduce galaxies with $q_{\rm sky} < 0.4$ (Table 2), making it difficult for the latest ΛCDM simulations to form thin disk galaxies like the Milky Way (with a ratio of scale height to scale length of $h/l \approx 0.07$–0.21; Bland-Hawthorn & Gerhard 2016) or M31 (with a sky-projected aspect ratio of 0.27 ± 0.03; Courteau et al. 2011). The intrinsic aspect ratio distribution of the highest-resolution models conflicts with the best-observed local galaxy sample at 5.42σ significance if we use the recently released TNG50-1 run (Section 6.1), confirming this discrepancy independently of the GAMA and SDSS data sets. The advantage of the LV sample is the higher spatial resolution of the galaxy images compared to SAMI, GAMA, and SDSS.

Our results agree with other recent studies (e.g., Lagos et al. 2018; van de Sande et al. 2019; Peebles 2020). We therefore disagree that the angular momentum problem has been resolved in the Illustris-1 simulation as concluded by Vogelsberger et al. (2014). The loss of angular momentum remains a significant problem in the latest cosmological ΛCDM simulations, as quantified in the present work.

The aspect ratio distribution has numerically converged in the EAGLE simulations (Section 7.1; see also Lagos et al. 2018). However, convergence cannot be confirmed for the TNG50 simulation, where the tension reported here could be related to numerical heating of the stellar particles by the coarse-grained implementation of dark matter halos (Ludlow et al. 2021). Therefore, we apply a parametric correction to the $q_{\rm int}$ of each simulated galaxy in TNG50 (Equation (12)). Depending on the extrapolation, we estimate that galaxies in an eight-times-higher particle resolution realization compared to the TNG50-1 run would be thinned by a factor in the range $0.824 \leqslant \alpha \leqslant 0.834$, where $\alpha = 1.0$ would imply numerical convergence in $q_{\rm int}$. Applying the lower limit and being therewith more conservative with respect to the ΛCDM framework, the here reported tension would decrease to the 8.68σ (8.71σ) confidence level for GAMA DR3 (SDSS DR16). Extrapolating the TNG50 results to $8^5\times$ better dark matter mass resolution than TNG50-1, the tension with GAMA DR3 (SDSS DR16) becomes 5.58σ (3.27σ) for the parabolic extrapolation, which better fits the available data (the tension is slightly lower with a linear extrapolation; see Table 5). However, such an extrapolation to much higher resolution than the TNG50 runs introduces additional uncertainties, so it is not yet clear if an arbitrarily higher-resolution realization than TNG50-1 can indeed resolve the here reported tension.

Thus, additional self-consistent cosmological ΛCDM simulations are useful to test if higher-resolution realizations and further improved sub-grid models for the interstellar medium can resolve the tension (e.g., Trayford et al. 2017; Lagos et al. 2018; van de Sande et al. 2019). This long-standing problem is likely not caused by limitations of the sub-grid model because the latest EAGLE and TNG simulations that are based on very different computational algorithms and baryonic feedback coding lead to galaxy populations whose sky-projected aspect ratio distributions agree with each other (Table 4). Moreover, isolated CDM simulations with a similar temperature floor of about 10 kK in the gas are able to produce thin disk galaxies (Sellwood et al. 2019)—as indeed are EAGLE and TNG50.

An uncertainty that has not been elaborated on in our work is how observed aspect ratios could be affected by the difference in stellar ages between the typically older bulges in spiral galaxies and their typically younger disks, which thus end up with a lower mass-to-light ratio. This could cause a difference between the mass-weighted aspect ratios obtained from simulations and the luminosity-weighted aspect ratios obtained from observations. However, the high fraction of bulgeless disk galaxies locally (Kormendy et al. 2010) suggests that this issue is not by itself sufficient to reconcile ΛCDM with the observed galaxy population. Observational systematics can be expected to differ between, e.g., GAMA and the high-resolution LV observations (Section 4.4), but even here there is still a significant 5.42σ tension with TNG50.

It appears to be impossible to form as many thin disk galaxies as observed. Consequently, the angular momentum problem persists in the hierarchical cosmological ΛCDM framework and is unlikely to be solved by improving the resolution. This conclusion can also be reached independently through observed galaxy bars being fast with no sign of slowdown through Chandrasekhar dynamical friction on the hypothetical dark matter halo (Roshan et al. 2021b). ΛCDM also faces many problems on other scales (Kroupa 2012, 2015; Pawlowski 2021; Banik & Zhao 2022). Almost 50 yr after dark matter halos were first postulated to surround galaxies (Ostriker & Peebles 1973), numerical implementations of this model still cannot explain the observed fraction of early- and late-type galaxies, so the observed galaxy population continues to pose a severe challenge to this framework.

If better resolved and/or improved sub-grid models of the interstellar medium in self-consistent ΛCDM cosmological simulations cannot resolve this tension, the loss of angular momentum would question the hierarchical merger-driven build-up of galaxies in this paradigm. We showed that intrinsically thin galaxies are more frequent in a ΛCDM galaxy sample selected to have a very quiescent merger history compared to one with an active merger history. However, a sample with a quiescent merger history cannot resolve the tension.

This leaves open the possibility that the tension we reported here is due to minor mergers and/or disk-halo angular momentum exchange (see also Sellwood et al. 2019; Banik et al. 2020; Roshan et al. 2021a, 2021b). If so, the angular momentum problem might be alleviated in a cosmological MOND framework (Milgrom 1983) due to the absence of dynamical friction on extended dark matter halos reducing the merger rate (Kroupa 2015; Renaud et al. 2016). In MOND, cluster-scale and early-universe observables can be explained within the neutrino hot dark matter (νHDM) model (Angus 2009; Haslbauer et al. 2020; Asencio et al. 2021). In particular, we emphasize that the statistically significant Hubble tension does not appear in this model (Haslbauer et al. 2020) but does exist in the standard ΛCDM model, independently showing ΛCDM to be invalid (Riess et al. 2021). Thus, the Hubble tension is naturally solved by using the standard MOND cosmological model without tuning any theoretical parameter. The sky-projected aspect ratio distribution of disk galaxies formed in hydrodynamical MOND simulations of collapsing post–Big Bang gas clouds (Wittenburg et al. 2020) is very consistent with observed SDSS spiral galaxies (Section 7.5). Self-consistent cosmological MOND simulations underway in Bonn and in Prague will allow us to determine the entire galactic morphological distribution for comparison with observations, enabling the same tests as documented here for ΛCDM.

I.B. is supported by Science and Technology Facilities Council grant ST/V000861/1. He acknowledges support from an Alexander von Humboldt Foundation postdoctoral research fellowship (2018–2020) and the University of Bonn "Pathways to Research" program. The authors are grateful to Veselina Kalinova for valuable comments, Karl Menten for his support, Sylvia Plöckinger for assistance with the EAGLE database, Sree Oh for explanations on the Data Central platform (https://datacentral.org.au/), and Edward Taylor for clarifications on the stellar masses of GAMA DR3 galaxies. The authors are very grateful to the anonymous referee for helpful suggestions that significantly improved this publication. They also thank the GAMA and SDSS teams for providing their data and useful related discussions.

GAMA is a joint European-Australasian project based around a spectroscopic campaign using the Anglo-Australian Telescope. The GAMA input catalog is based on data taken from the Sloan Digital Sky Survey and the UKIRT Infrared Deep Sky Survey. Complementary imaging of the GAMA regions is being obtained by a number of independent survey programs including GALEX MIS, VST KiDS, VISTA VIKING, WISE, Herschel-ATLAS, GMRT, and ASKAP, providing UV to radio coverage. GAMA is funded by the STFC (UK), the ARC (Australia), the AAO, and the participating institutions. The GAMA website is http://www.gama-survey.org/.

The SAMI Galaxy Survey is based on observations made at the Anglo-Australian Telescope. The Sydney-AAO Multi-object Integral field spectrograph (SAMI) was developed jointly by the University of Sydney and the Australian Astronomical Observatory. The SAMI input catalog is based on data taken from the Sloan Digital Sky Survey, the GAMA Survey, and the VST ATLAS Survey. The SAMI Galaxy Survey is funded by the Australian Research Council Centre of Excellence for All-sky Astrophysics (CAASTRO), through project No. CE110001020, and other participating institutions. The SAMI Galaxy Survey website is http://sami-survey.org/.

Funding for the SDSS and SDSS-II has been provided by the Alfred P. Sloan Foundation, the Participating Institutions, the National Science Foundation, the U.S. Department of Energy, the National Aeronautics and Space Administration, the Japanese Monbukagakusho, the Max Planck Society, and the Higher Education Funding Council for England. The SDSS is managed by the Astrophysical Research Consortium for the Participating Institutions. The Participating Institutions are the American Museum of Natural History, Astrophysical Institute Potsdam, University of Basel, University of Cambridge, Case Western Reserve University, University of Chicago, Drexel University, Fermilab, the Institute for Advanced Study, the Japan Participation Group, Johns Hopkins University, the Joint Institute for Nuclear Astrophysics, the Kavli Institute for Particle Astrophysics and Cosmology, the Korean Scientist Group, the Chinese Academy of Sciences (LAMOST), Los Alamos National Laboratory, the Max-Planck-Institute for Astronomy (MPIA), the Max-Planck-Institute for Astrophysics (MPA), New Mexico State University, Ohio State University, University of Pittsburgh, University of Portsmouth, Princeton University, the United States Naval Observatory, and the University of Washington. The SDSS website is http://www.sdss.org/.

Appendix
Statistical Significance of Extreme Events

If the χ^2 value is particularly large, the P-value is too low for a finite element computer to handle. We therefore make an analytic approximation for the integrals of the χ^2 and Gaussian distributions. In both cases, as the integrand declines very rapidly, we locally approximate it as declining exponentially. This allows us to approximate the integral out to infinity. Using this approach, we need to solve for x based on the known value of χ^2 using

$$\sqrt{\frac{2}{\pi}}\frac{\exp(-x^2)}{x} = \frac{(\chi^2)^{\frac{n}{2}-1}\exp\left(-\frac{\chi^2}{2}\right)}{2^{\frac{n}{2}}\left(\frac{n}{2}-1\right)!\left(\frac{1}{2}-\frac{\frac{n}{2}-1}{\chi^2}\right)}. \quad \text{(A1)}$$

Factorials of non-integer numbers are defined using the Γ function.

To minimize numerical errors, we set up Equation (A1) as an equality between the logarithms of both sides. We then solve for x using the Newton-Raphson algorithm. The statistical significance of the result is approximately x standard deviations, with the approximation becoming very accurate for $x > 7$. This is fortunate, as lower values of x allow Equation (11) to be solved directly without the approximation of Equation (A1). We checked that both methods give similar results for $x = 5$–7, but numerical difficulties mean that Equation (A1) is necessary for higher x.

ORCID iDs

Moritz Haslbauer https://orcid.org/0000-0002-5101-6366
Indranil Banik https://orcid.org/0000-0002-4123-7325
Pavel Kroupa https://orcid.org/0000-0002-7301-3377
Nils Wittenburg https://orcid.org/0000-0001-9332-0000
Behnam Javanmardi https://orcid.org/0000-0002-9317-6114

References

Abazajian, K., Adelman-McCarthy, J. K., Agüeros, M. A., et al. 2004, AJ, 128, 502
Adelman-McCarthy, J. K., Agüeros, M. A., Allam, S. S., et al. 2008, ApJS, 175, 297
Ahumada, R., Prieto, C. A., Almeida, A., et al. 2020, ApJS, 249, 3
Angus, G. W. 2009, MNRAS, 394, 527
Asencio, E., Banik, I., & Kroupa, P. 2021, MNRAS, 500, 5249
Athanassoula, E. 2002, ApJL, 569, L83
Bahé, Y. M., Barnes, D. J., Dalla Vecchia, C., et al. 2017, MNRAS, 470, 4186
Baldry, I. K., Liske, J., Brown, M. J. I., et al. 2018, MNRAS, 474, 3875
Banik, I., Thies, I., Candlish, G., et al. 2020, ApJ, 905, 135
Banik, I., & Zhao, H. 2018, MNRAS, 473, 4033
Banik, I., & Zhao, H. 2022, arXiv:2110.06936
Barnes, D. J., Kay, S. T., Bahé, Y. M., et al. 2017, MNRAS, 471, 1088
Binney, J., & Tremaine, S. 2008, Galactic Dynamics (2nd ed.; Princeton, NJ: Princeton Univ. Press)
Bland-Hawthorn, J., & Gerhard, O. 2016, ARA&A, 54, 529
Bottrell, C., Torrey, P., Simard, L., & Ellison, S. L. 2017a, MNRAS, 467, 1033
Bottrell, C., Torrey, P., Simard, L., & Ellison, S. L. 2017b, MNRAS, 467, 2879
Bournaud, F., Jog, C. J., & Combes, F. 2005, A&A, 437, 69
Brooks, A. M., Kuhlen, M., Zolotov, A., & Hooper, D. 2013, ApJ, 765, 22
Bryant, J. J., Owers, M. S., Robotham, A. S. G., et al. 2015, MNRAS, 447, 2857
Chambers, K. C., Magnier, E. A., Metcalfe, N., et al. 2016, arXiv:1612.05560
Courteau, S., Widrow, L. M., McDonald, M., et al. 2011, ApJ, 739, 20
Crain, R. A., Schaye, J., Bower, R. G., et al. 2015, MNRAS, 450, 1937
Croom, S. M., Lawrence, J. S., Bland-Hawthorn, J., et al. 2012, MNRAS, 421, 872
Croom, S. M., Owers, M. S., Scott, N., et al. 2021, MNRAS, 505, 991
de Vaucouleurs, G. 1948, AnAp, 11, 247
Delgado-Serrano, R., Hammer, F., Yang, Y. B., et al. 2010, A&A, 509, A78
Disney, M. J., Romano, J. D., Garcia-Appadoo, D. A., et al. 2008, Natur, 455, 1082
Dolag, K., Komatsu, E., & Sunyaev, R. 2016, MNRAS, 463, 1797
Dolag, K., Mevius, E., & Remus, R.-S. 2017, Galax, 5, 35
D'Onghia, E., Burkert, A., Murante, G., & Khochfar, S. 2006, MNRAS, 372, 1525
Driver, S. P., Hill, D. T., Kelvin, L. S., et al. 2011, MNRAS, 413, 971
Driver, S. P., Norberg, P., Baldry, I. K., et al. 2009, A&G, 50, 5.12
Dubois, Y., Pichon, C., Welker, C., et al. 2014, MNRAS, 444, 1453
Efstathiou, G., Sutherland, W. J., & Maddox, S. J. 1990, Natur, 348, 705
Emsellem, E., Cappellari, M., Krajnović, D., et al. 2011, MNRAS, 414, 888
Fakhouri, O., Ma, C.-P., & Boylan-Kolchin, M. 2010, MNRAS, 406, 2267
Famaey, B., & McGaugh, S. S. 2012, LRR, 15, 10
Fletcher, R., & Powell, M. J. D. 1963, CompJ, 6, 163
Genel, S., Fall, S. M., Hernquist, L., et al. 2015, ApJL, 804, L40
Giavalisco, M., Ferguson, H. C., Koekemoer, A. M., et al. 2004, ApJ, 600, L93
Graham, A. W., & Worley, C. C. 2008, MNRAS, 388, 1708
Grazian, A., Fontana, A., de Santis, C., et al. 2006, A&A, 449, 951
Guedes, J., Callegari, S., Madau, P., & Mayer, L. 2011, ApJ, 742, 76
Haslbauer, M., Banik, I., & Kroupa, P. 2020, MNRAS, 499, 2845
Hinshaw, G., Larson, D., Komatsu, E., et al. 2013, ApJS, 208, 19
Hirschmann, M., Dolag, K., Saro, A., et al. 2014, MNRAS, 442, 2304
Hoffmann, K., Laigle, C., Chisari, N. E., et al. 2020, arXiv:2010.13845
Hwang, J.-S., Park, C., Nam, S.-h., & Chung, H. 2021, JKAS, 54, 71
Karachentsev, I. D., Kaisina, E. I., & Makarov, D. I. 2018, MNRAS, 479, 4136
Karachentsev, I. D., Karachentseva, V. E., Huchtmeier, W. K., & Makarov, D. I. 2004, AJ, 127, 2031
Karachentsev, I. D., Makarov, D. I., & Kaisina, E. I. 2013, AJ, 145, 101
Katz, N., & Gunn, J. E. 1991, ApJ, 377, 365
Kauffmann, G., Heckman, T. M., White, S. D. M., et al. 2003, MNRAS, 341, 33
Kautsch, S. J., Grebel, E. K., Barazza, F. D., & Gallagher, J. S. I. 2006, A&A, 445, 765
Kelvin, L. S., Driver, S. P., Robotham, A. S. G., et al. 2012, MNRAS, 421, 1007
Kelvin, L. S., Driver, S. P., Robotham, A. S. G., et al. 2014, MNRAS, 444, 1647
Kormendy, J., Drory, N., Bender, R., & Cornell, M. E. 2010, ApJ, 723, 54
Kroupa, P. 2012, PASA, 29, 395
Kroupa, P. 2015, CaJPh, 93, 169
Kroupa, P., Subr, L., Jerabkova, T., & Wang, L. 2020, MNRAS, 498, 5652
Lagos, C. D. P., Schaye, J., Bahé, Y., et al. 2018, MNRAS, 476, 4327
Lange, R., Moffett, A. J., Driver, S. P., et al. 2016, MNRAS, 462, 1470
Loveday, J. 1996, MNRAS, 278, 1025
Ludlow, A. D., Fall, S. M., Schaye, J., & Obreschkow, D. 2021, MNRAS, 508, 5114
Lüghausen, F., Famaey, B., & Kroupa, P. 2015, CaJPh, 93, 232
McAlpine, S., Helly, J. C., Schaller, M., et al. 2016, A&C, 15, 72
McGaugh, S. S., & Schombert, J. M. 2014, AJ, 148, 77
Milgrom, M. 1983, ApJ, 270, 365
Mosenkov, A. V., Sotnikova, N. Y., & Reshetnikov, V. P. 2010, MNRAS, 401, 559
Müller, O., Lelli, F., Famaey, B., et al. 2021, A&A, in press (arXiv:2111.10306)
Nagesh, S. T., Banik, I., Thies, I., et al. 2021, CaJPh, 99, 607
Navarro, J. F., & Benz, W. 1991, ApJ, 380, 320
Navarro, J. F., & Steinmetz, M. 2000, ApJ, 538, 477
Navarro, J. F., & White, S. D. M. 1994, MNRAS, 267, 401
Nelson, D., Pillepich, A., Genel, S., et al. 2015, A&C, 13, 12
Nelson, D., Pillepich, A., Springel, V., et al. 2018, MNRAS, 475, 624
Nelson, D., Springel, V., Pillepich, A., et al. 2019, ComAC, 6, 2
Oh, S., Colless, M., Barsanti, S., et al. 2020, MNRAS, 495, 4638
Ostriker, J. P., & Peebles, P. J. E. 1973, ApJ, 186, 467
Ostriker, J. P., & Steinhardt, P. J. 1995, Natur, 377, 600
Owers, M. S., Allen, J. T., Baldry, I., et al. 2017, MNRAS, 468, 1824
Owers, M. S., Hudson, M. J., Oman, K. A., et al. 2019, ApJ, 873, 52
Padilla, N. D., & Strauss, M. A. 2008, MNRAS, 388, 1321
Paturel, G., Andernach, H., Bottinelli, L., et al. 1997, A&AS, 124, 109
Pawlowski, M. S. 2021, NatAs, 5, 1185
Peebles, P. J. E. 2020, MNRAS, 498, 4386
Peng, C. Y., Ho, L. C., Impey, C. D., & Rix, H.-W. 2002, AJ, 124, 266
Peng, C. Y., Ho, L. C., Impey, C. D., & Rix, H.-W. 2010, AJ, 139, 2097
Pillepich, A., Nelson, D., Springel, V., et al. 2019, MNRAS, 490, 3196
Pillepich, A., Springel, V., Nelson, D., et al. 2018, MNRAS, 473, 4077
Piontek, F., & Steinmetz, M. 2011, MNRAS, 410, 2625
Planck Collaboration I 2014, A&A, 571, A1
Planck Collaboration VI 2020, A&A, 641, A6
Planck Collaboration XIII 2016, A&A, 594, A13
Reddish, J., Kraljic, K., Petersen, M. S., et al. 2021, arXiv:2106.02622
Renaud, F., Famaey, B., & Kroupa, P. 2016, MNRAS, 463, 3637
Riess, A. G., Yuan, W., Macri, L. M., et al. 2021, arXiv:2112.04510
Rodriguez-Gomez, V., Genel, S., Vogelsberger, M., et al. 2015, MNRAS, 449, 49
Rodriguez-Gomez, V., Snyder, G. F., Lotz, J. M., et al. 2019, MNRAS, 483, 4140
Roshan, M., Banik, I., Ghafourian, N., et al. 2021a, MNRAS, 503, 2833
Roshan, M., Ghafourian, N., Kashfi, T., et al. 2021b, MNRAS, 508, 926
Salim, S., Rich, R. M., Charlot, S., et al. 2007, ApJS, 173, 267
Santini, P., Fontana, A., Grazian, A., et al. 2009, A&A, 504, 751
Scannapieco, C., Wadepuhl, M., Parry, O. H., et al. 2012, MNRAS, 423, 1726
Schaye, J., Crain, R. A., Bower, R. G., et al. 2015, MNRAS, 446, 521
SDSS Collaboration 2000, AJ, 120, 1579
Sellwood, J. A., Shen, J., & Li, Z. 2019, MNRAS, 486, 4710
Springel, V. 2005, MNRAS, 364, 1105
Springel, V. 2010, MNRAS, 401, 791
Springel, V., White, S. D. M., Jenkins, A., et al. 2005, Natur, 435, 629
Stewart, K. R., Bullock, J. S., Wechsler, R. H., Maller, A. H., & Zentner, A. R. 2008, ApJ, 683, 597
Tamburri, S., Saracco, P., Longhetti, M., et al. 2014, A&A, 570, A102
Taylor, E. N., Hopkins, A. M., Baldry, I. K., et al. 2011, MNRAS, 418, 1587
Teyssier, R. 2002, A&A, 385, 337
Thob, A. C. R., Crain, R. A., McCarthy, I. G., et al. 2019, MNRAS, 485, 972
Torrey, P., Snyder, G. F., Vogelsberger, M., et al. 2015, MNRAS, 447, 2753
Trayford, J. W., Camps, P., Theuns, T., et al. 2017, MNRAS, 470, 771
van de Sande, J., Lagos, C. D. P., Welker, C., et al. 2019, MNRAS, 484, 869
van den Bosch, F. C. 2001, MNRAS, 327, 1334
Vázquez-Mata, J. A., Loveday, J., Riggs, S. D., et al. 2020, MNRAS, 499, 631
Vogelsberger, M., Genel, S., Springel, V., et al. 2014, Natur, 509, 177
Wetzel, A. R., Hopkins, P. F., Kim, J.-H., et al. 2016, ApJL, 827, L23
Wittenburg, N., Kroupa, P., & Famaey, B. 2020, ApJ, 890, 173
Wu, X., & Kroupa, P. 2015, MNRAS, 446, 330

APPENDIX C

Paper: Has JWST already falsified dark-matter-driven galaxy formation?

This chapter includes a copy of the peer-reviewed paper entitled "Has JWST Already Falsified Dark-matter-driven Galaxy Formation?" published in The Astrophysical Journal Letters, 939, L31, 2020 by **Moritz Haslbauer**, Pavel Kroupa, Akram Hasani Zonoozi, and Hosein Haghi. A summary and the author contributions are provided in Chapter 9.

The Astrophysical Journal Letters, 939:L31 (7pp), 2022 November 10 https://doi.org/10.3847/2041-8213/ac9a50

Has JWST Already Falsified Dark-matter-driven Galaxy Formation?

Moritz Haslbauer[1,2], Pavel Kroupa[1,3], Akram Hasani Zonoozi[4], and Hosein Haghi[4]
[1] Helmholtz-Institut für Strahlen- und Kernphysik (HISKP), University of Bonn, Nussallee 14−16, D-53115 Bonn, Germany; mhaslbauer@astro.uni-bonn.de
[2] Max-Planck-Institut für Radioastronomie, Auf dem Hügel 69, D-53121 Bonn, Germany
[3] Astronomical Institute, Faculty of Mathematics and Physics, Charles University, V Holešovičkách 2, CZ-180 00 Praha 8, Czech Republic
[4] Department of Physics, Institute for Advanced Studies in Basic Sciences (IASBS), Zanjan 45137-66731, Iran
Received 2022 July 28; revised 2022 October 13; accepted 2022 October 13; published 2022 November 10

Abstract

The James Webb Space Telescope (JWST) discovered several luminous high-redshift galaxy candidates with stellar masses of $M_* \gtrsim 10^9\,M_\odot$ at photometric redshifts $z_{\rm phot} \gtrsim 10$, which allows to constrain galaxy and structure formation models. For example, Adams et al. identified the candidate ID 1514 with $\log_{10}(M_*/M_\odot) = 9.8^{+0.2}_{-0.2}$ located at $z_{\rm phot} = 9.85^{+0.18}_{-0.12}$ and Naidu et al. found even more distant candidates labeled as GL-z11 and GL-z13 with $\log_{10}(M_*/M_\odot) = 9.4^{+0.3}_{-0.3}$ at $z_{\rm phot} = 10.9^{+0.5}_{-0.4}$ and $\log_{10}(M_*/M_\odot) = 9.0^{+0.3}_{-0.4}$ at $z_{\rm phot} = 13.1^{+0.8}_{-0.7}$, respectively. Assessing the computations of the IllustrisTNG (TNG50-1 and TNG100-1) and EAGLE projects, we investigate if the stellar mass buildup as predicted by the ΛCDM paradigm is consistent with these observations assuming that the early JWST calibration is correct and that the candidates are indeed located at $z \gtrsim 10$. Galaxies formed in the ΛCDM paradigm are by more than an order of magnitude less massive in stars than the observed galaxy candidates implying that the stellar mass buildup is more efficient in the early universe than predicted by the ΛCDM models. This in turn would suggest that structure formation is more enhanced at $z \gtrsim 10$ than predicted by the ΛCDM framework. We show that different star formation histories could reduce the stellar masses of the galaxy candidates alleviating the tension. Finally, we calculate the galaxy-wide initial mass function (gwIMF) of the galaxy candidates assuming the integrated galaxy IMF theory. The gwIMF becomes top-heavy for metal-poor star-forming galaxies decreasing therewith the stellar masses compared to an invariant canonical IMF.

Unified Astronomy Thesaurus concepts: Cold dark matter (265); Initial mass function (796); Stellar mass functions (1612); Stellar masses (1614); Galaxy evolution (594); Galaxy formation (595); Galaxy mass distribution (606); Galaxy properties (615); High-redshift galaxies (734); Early universe (435); Cosmology (343); James Webb Space Telescope (2291)

1. Introduction

The formation of the first galaxies in the observed universe is a key question in modern astrophysics and one of the most important science goals of the recently launched James Webb Space Telescope (JWST). The Near Infrared Camera instrument (NIRCam; Rieke et al. 2005) of JWST observes the universe in the ≈0.6–5 μm regime. This allows the detection of objects at redshifts $z \gtrsim 12$, thus, revealing the evolutionary stage of galaxies in the early universe just ≈400 Myr after the Big Bang. The most distant confirmed galaxy is GN-z11 with a stellar mass of $M_* \approx 10^9\,M_\odot$ at a spectroscopic redshift of $z_{\rm spec} = 11.09^{+0.08}_{-0.12}$ detected with the Hubble Space Telescope (Oesch et al. 2016). Recently, Naidu et al. (2022b) reported the discovery of two luminous galaxy candidates labeled as GLASS-z11 (hereafter GL-z11) and GLASS-z13 (GL-z13) with $\log_{10}(M_*/M_\odot) = 9.4^{+0.3}_{-0.3}$ and $9.0^{+0.3}_{-0.4}$ located at photometric redshifts of $z_{\rm phot} = 10.9^{+0.5}_{-0.4}$ and $z_{\rm phot} = 13.1^{+0.8}_{-0.7}$, respectively (see their Table 3). In a subsequent publication, Naidu et al. (2022a) presented the galaxy candidate CEERS-1749 with $\log_{10}(M_*/M_\odot) = 9.6^{+0.2}_{-0.2}$ most likely located at $z_{\rm phot} = 16.0^{+0.6}_{-0.6}$ but a secondary redshift solution of $z \approx 5$ cannot be excluded (see their Figure 1 and Table 3).

Further luminous high-redshift galaxy candidates have been discovered by JWST (e.g., Adams et al. 2022; Atek et al. 2022; Furtak et al. 2022; Harikane et al. 2022; Yan et al. 2022; Labbe et al. 2022). For example, Adams et al. (2022) studied the properties of candidates over a redshift range of $9 < z_{\rm phot} < 12$ and the source with ID 1514 has $\log_{10}(M_*/M_\odot) = 9.8^{+0.2}_{-0.2}$ at $z_{\rm phot} = 9.85^{+0.18}_{-0.12}$ (see their Tables 3 and 5). Labbe et al. (2022) identified candidates with $M_* > 10^{10}\,M_\odot$ over $7 < z_{\rm phot} < 11$ from which the two most massive are ID 14924 with $\log_{10}(M_*/M_\odot) = 10.93$ at $z_{\rm phot} = 9.92$ and ID 38094 with $\log_{10}(M_*/M_\odot) = 11.16$ at $z_{\rm phot} = 7.56$ (see their Figure 3). The spectroscopical confirmation of these objects is still outstanding because the high photometric redshifts of these galaxy candidates can, e.g., artificially emerge due to dust attenuation (Naidu et al. 2022a, 2022b; Zavala et al. 2022).

In this contribution, we aim to investigate if ID 1514, ID 14924, GL-z11, GL-z13, and CEERS-1749 are consistent with the hierarchical buildup of stellar mass as predicted by the ΛCDM paradigm (Efstathiou et al. 1990; Ostriker & Steinhardt 1995) using the Illustris The Next Generation (TNG; Pillepich et al. 2018a; Nelson et al. 2019b; Pillepich et al. 2019) and Evolution and Assembly of GaLaxies and their Environments (EAGLE; Crain et al. 2015; Schaye et al. 2015; McAlpine et al. 2016) projects.

2. Method

The IllustrisTNG (Pillepich et al. 2018a, 2018b; Marinacci et al. 2018; Naiman et al. 2018; Nelson et al. 2018, 2019a, 2019b;

Springel et al. 2018; Pillepich et al. 2019) and EAGLE (Crain et al. 2015; Schaye et al. 2015; McAlpine et al. 2016) projects consist of a suite of hydrodynamical cosmological simulation runs conducted in the ΛCDM framework.

The IllustrisTNG project assumes a Planck-2015 (Planck Collaboration XIII 2016) cosmology with the cosmological parameters being $H_0 = 67.74\,\mathrm{km\,s^{-1}\,Mpc^{-1}}$, $\Omega_{\mathrm{b},0} = 0.0486$, $\Omega_{\mathrm{m},0} = 0.3089$, $\Omega_{\Lambda,0} = 0.6911$, $\sigma_8 = 0.8159$, and $n_\mathrm{s} = 0.9667$. The simulation runs are based on the moving-mesh code AREPO (Springel 2010) and self-consistently evolve the gas cells, stellar, black hole, and dark matter particles from redshift $z = 127$ up to present time. The Subfind Subhalos[5] and Group[6] catalogs are available for 100 different time steps (snapshots) in the redshift range of $0 \leqslant z \leqslant 20.05$. Here, we analyze the snapshot at redshift $z = 14.99$ (corresponding to an age of the universe of $t = 0.271$ Gyr and a snapshot number of snapnum = 1), at $z = 11.98$ ($t = 0.370$ Gyr, snapnum = 2), at $z = 10.98$ ($t = 0.418$ Gyr, snapnum = 3), and at $z = 10.00$ ($t = 0.475$ Gyr, snapnum = 4) of the high-resolution realization TNG50-1 and TNG100-1. The former has a box side of $35\,h^{-1} = 51.7$ comoving Mpc (cMpc), respectively, where h is the present Hubble constant H_0 in units of $100\,\mathrm{km\,s^{-1}\,Mpc^{-1}}$, a baryonic element mass of $m_\mathrm{b} = 8.5 \times 10^4\,M_\odot$, and a dark matter particle mass of $m_\mathrm{dm} = 4.5 \times 10^5\,M_\odot$. TNG100-1 has, with $75\,h^{-1} = 110.7$ cMpc, a larger box size and with $m_\mathrm{b} = 1.4 \times 10^6\,M_\odot$, and $m_\mathrm{dm} = 7.5 \times 10^6\,M_\odot$, a lower resolution than TNG50-1 (see, e.g., also Table 1 of Nelson et al. 2019b).

The EAGLE project is consistent with the Planck-2013 (Planck Collaboration I 2014) cosmology being $H_0 = 67.77\,\mathrm{km\,s^{-1}\,Mpc^{-1}}$, $\Omega_{\mathrm{b},0} = 0.04825$, $\Omega_{\mathrm{m},0} = 0.307$, $\Omega_{\Lambda,0} = 0.693$, $\sigma_8 = 0.8288$, and $n_\mathrm{s} = 0.9611$ (see also Table 1 of Schaye et al. 2015). Its simulations run with a modification of the GADGET-3 smoothed particle hydrodynamics code (e.g., Springel 2005) starting also at $z = 127$ and self-consistently evolving the baryonic and dark matter particles up to the present day. The publicly available subhalo catalogs (Table B.1 of McAlpine et al. 2016) are recorded for 29 snapshots in the redshift range of $0 \leqslant z \leqslant 20.00$ (see Table C.1 of McAlpine et al. 2016). We use the two high-resolution realization runs RefL0025N0752 and RecalL0025N0752, and the two lower resolution runs RefL0050N0752 and RefL0100N1504 at $z = 15.13$ (snapnum = 1) and $z = 9.99$ (snapnum = 2). The two high-resolution runs have a box size of 25 cMpc with an initial baryonic particle mass of $m_\mathrm{b} = 2.26 \times 10^5\,M_\odot$, and a dark matter particle mass of $m_\mathrm{dm} = 1.21 \times 10^6\,M_\odot$. RefL0050N0752 and RefL0100N1504 have a size of 50 cMpc and 100 cMpc, respectively, and both have an initial baryonic particle mass of $m_\mathrm{b} = 1.81 \times 10^6\,M_\odot$ and a dark matter particle mass of $m_\mathrm{dm} = 9.70 \times 10^6\,M_\odot$ (Table 2 of Schaye et al. 2015).

3. Results

The galaxy stellar mass function (GSMF) at redshifts $z = 14.99$, 11.98, 10.98, and 10.00 in the TNG runs and at $z = 15.13$ and 9.99 in the EAGLE runs are presented in Figure 1. The global peak of the distribution depends on the resolution and/or box size of the simulation runs such that the formation of low massive galaxies depends on the particle resolution but also because small simulation boxes lack large-scale density fluctuations. As a consequence, not-large-enough simulation boxes would not allow the formation of large galaxy clusters, therefore hampering the growth of central (but also noncentral) galaxies. Thus, we mainly focus on the larger simulation boxes TNG100-1 and RefL0100N1504.

In the following, we compare the stellar mass buildup as predicted by the ΛCDM simulations with the masses of the observed high-redshift galaxy candidates ID 1514 (Adams et al. 2022), ID 14924 (Labbe et al. 2022)[7], GL-z11, GL-z13 (Naidu et al. 2022b), and CEERS-1749 (Naidu et al. 2022a). For the TNG runs, ID 1514 located at $z_\mathrm{phot} = 9.85^{+0.18}_{-0.12}$ and ID 14924 at $z_\mathrm{phot} = 9.92$ are compared with simulated galaxies at $z = 10.00$. GL-z11 at $10.9^{+0.5}_{-0.4}$, GL-z13 at $13.1^{+0.8}_{-0.7}$, and CEERS-1749 at $16.0^{+0.6}_{-0.6}$ are compared with the simulations at $z = 10.98$, 11.98, and 14.99, respectively. The comparison with GL-z13 and CEERS-1749 is therewith more conservative because snapshots corresponding to lower redshifts than observed are addressed allowing the galaxies to grow in stars for a longer time span than in the observed cases.

In TNG100-1, the GSMF at $z = 14.99$ reaches a maximum value of $\log_{10}(M_*/M_\odot) = 7.32$ being therewith ≈ 191 times lower than the stellar mass of CEERS-1749 with $\log_{10}(M_*/M_\odot) = 9.6^{+0.2}_{-0.2}$. At $z = 11.98$ and $z = 10.98$, the maximum stellar masses of subhalos are $\log_{10}(M_*/M_\odot) = 8.07$ and 8.43, respectively, which is less massive than GL-z13 with $\log_{10}(M_*/M_\odot) = 9.0^{+0.3}_{-0.4}$ and GL-z11 with $\log_{10}(M_*/M_\odot) = 9.4^{+0.3}_{-0.3}$. The maximum value of $\log_{10}(M_*/M_\odot) = 8.73$ at $z = 10.00$ is significantly lower than the stellar mass of ID 1514, which has $\log_{10}(M_*/M_\odot) = 9.8^{+0.2}_{-0.2}$. The discrepancy becomes even more significant for ID 14924, which has $\log_{10}(M_*/M_\odot) = 10.93$ at $z_\mathrm{phot} = 9.92$. The above stellar masses refer to all stellar particles bound to the considered subhalo depending therewith on the subhalo-finding algorithm. The identification of subhalos can be disturbed, e.g., by merger events, which frequently occur especially at high redshifts. Therefore, we also assess the maximum stellar masses of halos, which accounts for both the fact that the subhalo finder can split a galaxy in clumps underestimating the total mass of the galaxy, and for the inclusion of observationally unresolved satellite galaxies. The maximum stellar masses of halos are $\log_{10}(M_*/M_\odot) = 7.32$ (7.05), 8.10 (7.88), 8.43 (8.24), and 8.78 (8.59) at $z = 14.99$, 11.98, 10.98, and 10.00, in the TNG100-1 (TNG50-1) run, respectively. Thus, using the most massive halo instead of the most massive subhalo in terms of its stellar mass does not significantly effect the results of the TNG runs.

In the EAGLE runs, ID 1514/ID 14924 and CEERS-1749 are compared with the GSMF at $z = 9.99$ and 15.13, respectively. Unfortunately, the EAGLE database does not list snapshots that match the observed redshifts of GL-z11 and GLz-13. Thus, the EAGLE analysis only focuses on ID 1514, ID 14924, and CEERS-1749.

The RefL0050N0752 and RefL0100N1504 snapshots contain galaxies reaching up to $\log_{10}(M_*/M_\odot) \approx 7.70$ at $z = 15.13$ and $\log_{10}(M_*/M_\odot) \approx 9.06$ at $z = 9.99$, which is ≈ 79 and ≈ 5.5 times lower than the observed stellar mass of CEERS-1749 and ID 1514, respectively. The stellar mass of ID 14924 is 74 times higher than the most massive simulated galaxy at $z = 9.99$.

The evolution of the stellar mass growth is summarized in Figure 2 and Table 1 by showing the maximum stellar mass of a subhalo in dependence of redshift for different simulation runs.

[5] https://www.tng-project.org/data/docs/specifications/#sec2b (23.07.2022).

[6] https://www.tng-project.org/data/docs/specifications/#sec2a (12.09.2022).

[7] We only show ID 1514 and not the more massive candidate ID 14924 in the bottom right panel of Figure 1 in order to be more conservative.

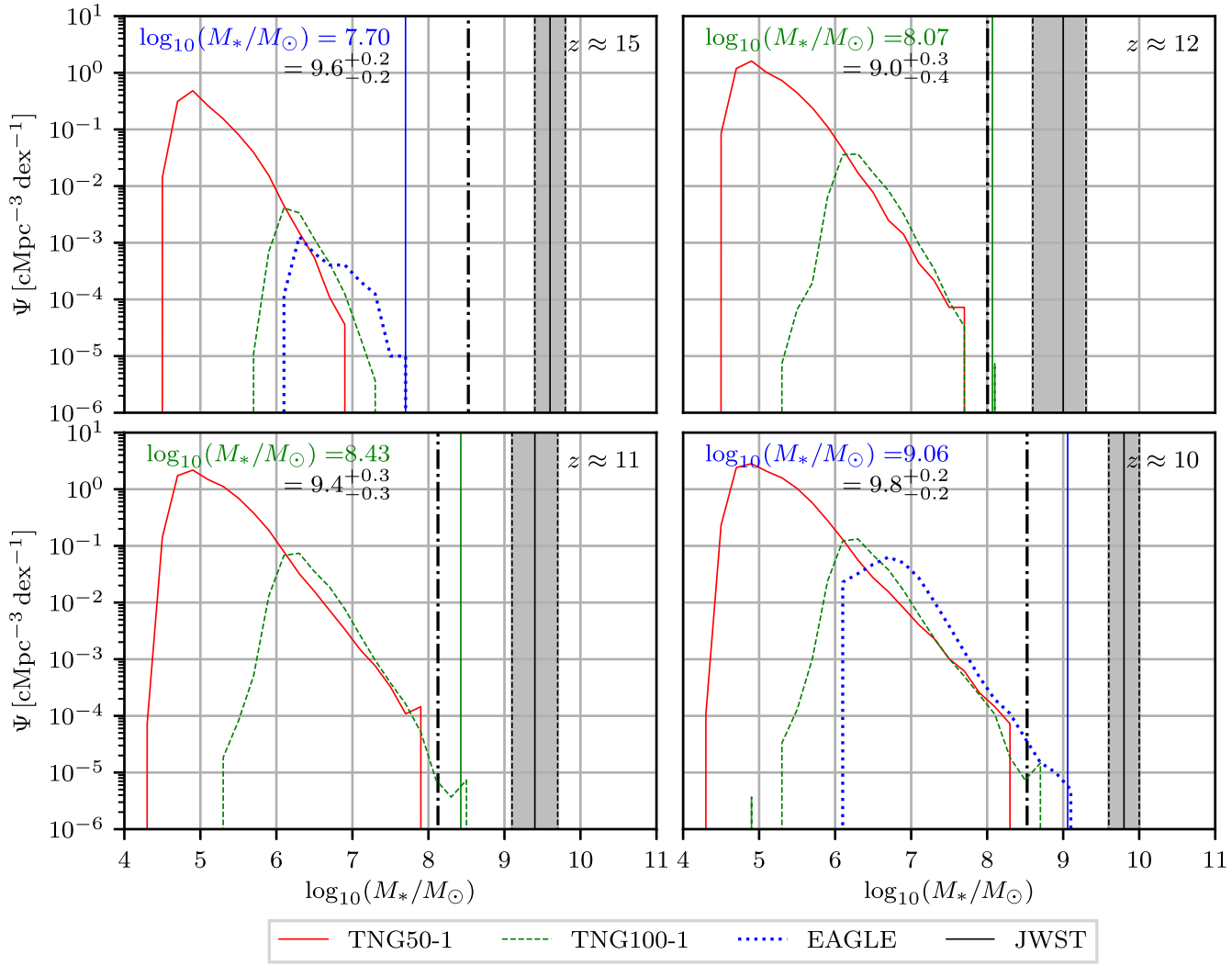

Figure 1. The GSMF at redshifts $z \approx 15$ (top left), 12 (top right), 11 (bottom left), 10 (bottom right) in the TNG50-1 (solid red), TNG100-1 (dashed green), and RefL0100N1504 (dotted blue) simulation. The colored vertical solid line marks the most massive subhalo in terms of the stellar mass in the simulations. The vertical black solid lines refer to the reported galaxy candidates CEERS-1749 (top left), GL-z13 (top right), GL-z11 (bottom left), and ID 1514 (bottom right), where the black dashed lines correspond to the measurement uncertainties. The vertical dashed–dotted lines mark the lowest possible value as inferred for different star formation histories (SFHs) in Section 3.1. The histograms are normalized by their bin width of $\Delta \log_{10}(M_*/M_\odot) = 0.2$ and volume of the simulation box.

The observed high-redshift galaxy candidates are, by more than 1 order of magnitude, more massive than the most massive simulated galaxies in the ΛCDM framework.

The inferred stellar mass of observed galaxies is sensitive to the adopted SFH and initial mass function (IMF). In the following sections, we first investigate if the tension reported here of the stellar mass buildup in the early universe can be resolved if different SFHs of the observed galaxy candidates are assumed. Second, the effect of a varying IMF on the observed stellar masses is discussed.

3.1. The Minimum Inferred Galaxy Masses for Different Star Formation Histories

In order to calculate the minimum possible mass that the observed high-redshift galaxy candidates CEERS-1749, GL-z11, GL-z13, and ID 1514 can have for an invariant IMF, different sets of models of galaxies with different star formation histories (SFHs) are constructed. Using stellar population synthesis models, we let the age of the modeled galaxies vary in the range of [≈4, 400 Myr] to investigate their UV-band (1500 Å) stellar mass (including remnants)-to-light ratio, $M_*/L_{\rm UV}$, for an invariant canonical IMF (Kroupa 2001; Kroupa et al. 2013). The lower limit is set by the implemented stellar evolution tracks of the Padova group (Marigo & Girardi 2007; Marigo et al. 2008; see also Zonoozi et al. 2019) and is roughly comparable to the mean stellar age (≈1–20 Myr) of observed high-redshift galaxies ($5 \lesssim z_{\rm spec} \lesssim 8$) as found by Carnall et al. (2022).

Since the spectral energy distribution fitting analysis of high-redshift star-forming galaxies shows more consistency with increasing SFHs, here we adopt the delayed-τ model (e.g., Kroupa et al. 2020a)

$$\psi_{\rm del}(t) = \psi_0 t \exp(-t/\tau), \quad (1)$$

and an exponentially increasing SFH

$$\psi_{\rm exp}(t) = \psi_0 \exp(t/\tau), \quad (2)$$

where $\psi(t)$ is the star formation rate (SFR), t is the age since star formation started, ψ_0 is the normalization parameter, and τ is the e-folding timescale. The mass and light of a galaxy are calculated by an integral over the SFR. Note that, using the

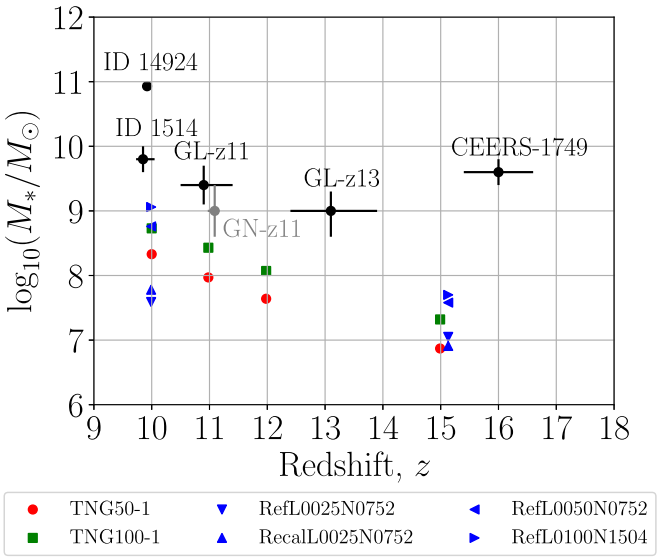

Figure 2. The most massive subhalo in terms of the stellar mass in dependence of redshift in the TNG50-1 (red), TNG100-1 (green), and EAGLE (blue) runs. The black error bars are the observed galaxy candidates by JWST as listed in Table 1. The gray error bar shows GN-z11 (Oesch et al. 2016).

Table 1
Comparison of Several Observed Galaxy Candidates with ΛCDM Simulations

	Redshift (z)	Stellar Mass $\log_{10}(M_*/M_\odot)$
CEERS-1749	$16.0^{+0.6}_{-0.6}$	$9.6^{+0.2}_{-0.2}$ (8.53)[a]
GL-z13	$13.1^{+0.8}_{-0.7}$	$9.0^{+0.3}_{-0.4}$ (8.01)[a]
GL-z11	$10.9^{+0.5}_{-0.4}$	$9.4^{+0.3}_{-0.3}$ (8.13)[a]
ID 1514	$9.85^{+0.18}_{-0.12}$	$9.8^{+0.2}_{-0.2}$ (8.53)[a]
TNG50-1	14.99	6.87
TNG50-1	11.98	7.64
TNG50-1	10.98	7.97
TNG50-1	10.00	8.33
TNG100-1	14.99	7.32
TNG100-1	11.98	8.07
TNG100-1	10.98	8.43
TNG100-1	10.00	8.73
RefL0025N0752	15.13	7.05
RefL0025N0752	9.99	7.59
RecalL0025N0752	15.13	6.91
RecalL0025N0752	9.99	7.78
RefL0050N0752	15.13	7.58
RefL0050N0752	9.99	8.76
RefL0100N1504	15.13	7.70
RefL0100N1504	9.99	9.06

Notes. The first four rows show the photometric redshifts and stellar masses of the observed galaxy candidates ID 1514 (see Tables 3 and 5 of Adams et al. 2022), GL-z11, GL-z13 (see Table 3 of Naidu et al. 2022b), and CEERS-1749 (see Table 3 of Naidu et al. 2022a). The other rows list the maximum stellar mass of a subhalo at a given redshift for the TNG and EAGLE runs.
[a] Lowest possible stellar mass value for an invariant canonical IMF as quantified in Section 3.1.

invariant IMF, at a given t, the mass-to-light ratio is independent of the total mass that is converted into stars. This is because of cancellation of the normalization parameter, ψ_0.

The effect of the SFHs on the $M_*/L_{\rm UV}$ ratio of galaxies by adopting different values of τ is shown in the left panels of Figure 3. We set that galaxies start forming stars 200 Myr after the Big Bang, with an averaged metallicity of [Fe/H] = −2, and we assume that the mass loss from galaxies is only through stellar evolution in the form of ejected gas. Since the stellar loss due to dynamical evolution is significant only for systems with initial stellar mass less than $M_* = 10^6\ M_\odot$, no stars are lost by the dynamical evolution of galaxies. As can be seen, the minimum mass-to-light ratio that can be considered for these galaxies assuming different SFHs is $M_*/L_{\rm UV} \approx 3.2 \times 10^{-8}\ M_\odot/L_\odot$.

According to the estimated UV absolute magnitude of these objects, $M_{\rm UV,CEERS-1749} = -22.0$, $M_{\rm UV,GL-z13} = -20.7$, $M_{\rm UV,GL-z11} = -21.0$, and $M_{\rm UV,ID\ 1514} = -22.0$ mag, we obtain the lowest possible stellar masses of $\log_{10}(M_*/M_\odot) =$ 8.53, 8.01, 8.13, and 8.53 for CEERS-1749, GL-z13, GL-z11, and ID 1514 in the case of an exponential SFH, respectively, as visualized in the right panels of Figure 3.

These lower stellar mass limits just resolve the discrepancy for GL-z11, GL-z13, and ID 1514 (see the vertical dashed–dotted lines in Figure 1). In the case of CEERS-1749, the maximum stellar mass obtained in the ΛCDM simulation is ≈6.8 lower than its inferred lower limit.

3.2. Galaxy Masses for a Varying IMF

In the previous section we applied an invariant IMF but recent observations (e.g., Schneider et al. 2018; Zhang et al. 2018; Senchyna et al. 2021) suggest that the mass distribution of a stellar population may depend on its local star-forming environment. Especially metal-poor Population III stars are expected to follow a top-heavy IMF.

A theoretical framework to describe the stellar population of an entire galaxy is the integrated galactic initial mass function (IGIMF) theory, which adds up all the IMFs of star-forming regions (embedded clusters) within a galaxy (Kroupa & Weidner 2003; Weidner & Kroupa 2006). The resulting galaxy-wide IMF (gwIMF) systematically varies with the global SFR and averaged metallicity of the galaxy, i.e., the gwIMF becomes top-heavy for galaxies with SFR $\gtrsim 1\ M_\odot\ {\rm yr}^{-1}$ and metallicities [Fe/H] < 0 (see Figure 2 of Jeřábková et al. 2018) compared to the canonical IMF. In order to study the effect of a varying IMF on the high-redshift galaxy candidates, we calculate the stellar population of galaxies assuming the latest IGIMF formalism by Yan et al. (2021) and using an IGIMF Fortran code developed by Akram Hasani Zonoozi. For simplification, we assume that all galaxies start to form stars 200 Myr after the Big Bang, with a constant SFR over time, and an average metallicity of [Fe/H] = −2. Since the gwIMF is time dependent, we require that realistic IGIMF models have to match the observed $M_{\rm UV}$ within ±1 mag in the 1σ interval of the observed redshift of the corresponding galaxy candidate. The left panel of Figure 4 shows the time evolution of the absolute UV-band magnitude for IGIMF models that fulfill these constraints for observed galaxy candidates CEERS-1749, GL-z13, GL-z11, and ID 1514. These models have constant SFRs in the range of ≈2–30 $M_\odot\ {\rm yr}^{-1}$ and thus a top-heavy IMF. The stellar masses at the observed redshifts of the galaxy candidates are shown in the right panel of Figure 4 and are systematically lower than the derived stellar masses of Adams et al. (2022), Naidu et al. (2022b), and Naidu et al. (2022a) because of the top-heavy gwIMF compared to the canonical IMF.

4. Discussion and Conclusion

While the redshifts of the galaxy candidates need to be spectroscopically verified, we use these JWST observations to

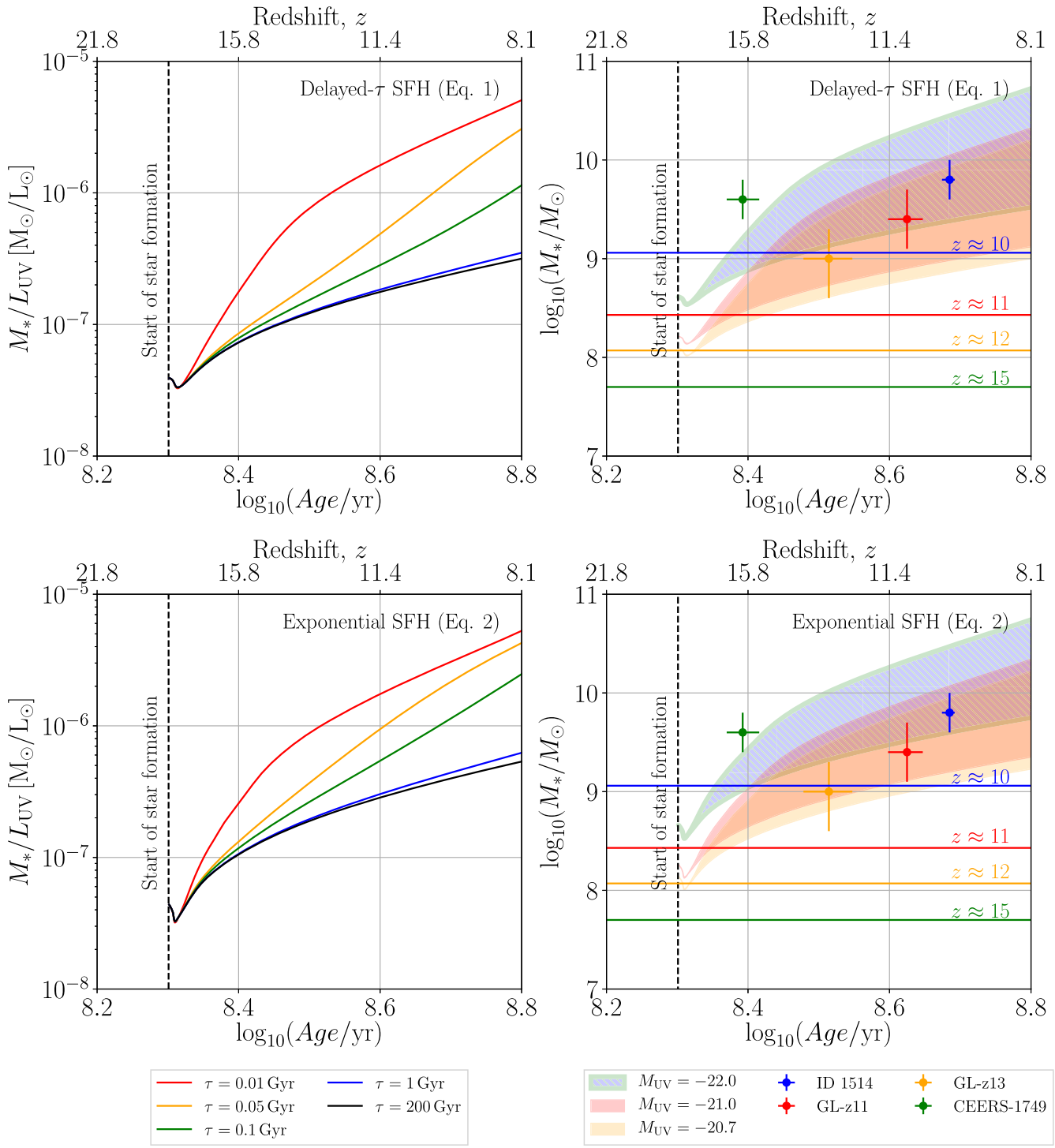

Figure 3. Left panels: cosmic time evolution of the stellar M_*/L_{UV} ratio for stellar populations constructed assuming an invariant canonical IMF and using a delayed-τ (Equation (1); top panels) and an exponentially increasing SFH (Equation (2); bottom panels). We assume that star formation starts 200 Myr after the Big Bang (dashed vertical line). The minimum mass-to-light ratio for these galaxies assuming different SFHs is $M_*/L_{UV} \approx 3.2 \times 10^{-8}\, M_\odot/L_\odot$. Right panels: cosmic time evolution of the total stellar mass of the galaxy candidates CEERS-1749 (green hatched area), GL-z13 (orange area), GL-z11 (red area), and ID 1514 (blue area) calculated based on the inferred mass-to-light ratios of the left panels. The colored areas cover the stellar mass range for SFHs with τ values between 0.01 Gyr (upper limit) and 200 Gyr (lower limit; see the left panels). The filled circles with error bars show the observed values as quantified by Adams et al. (2022), Naidu et al. (2022b), Naidu et al. (2022a). The most massive subhalos in terms of stellar mass in the ΛCDM simulations are shown as horizontal lines.

quantify how quickly galaxies form in the currently most advanced cosmological simulations. Using state-of-the-art ΛCDM simulations of the IllustrisTNG and EAGLE project, we showed that the stellar mass buildup is much more efficient in the early universe than predicted by these ΛCDM models (see also, e.g., Boylan-Kolchin 2022; Lovell et al. 2022). In particular, the stellar masses of ID 1514 (Adams et al. 2022), ID 14924 (Labbe et al. 2022), GL-z11, GL-z13 (Naidu et al. 2022b), and CEERS-1749 (Naidu et al. 2022a) analyzed in Section 3 are higher by about 1 order of magnitude than the most massive galaxies formed in these simulations. In particular, massive high-redshift candidates appear more

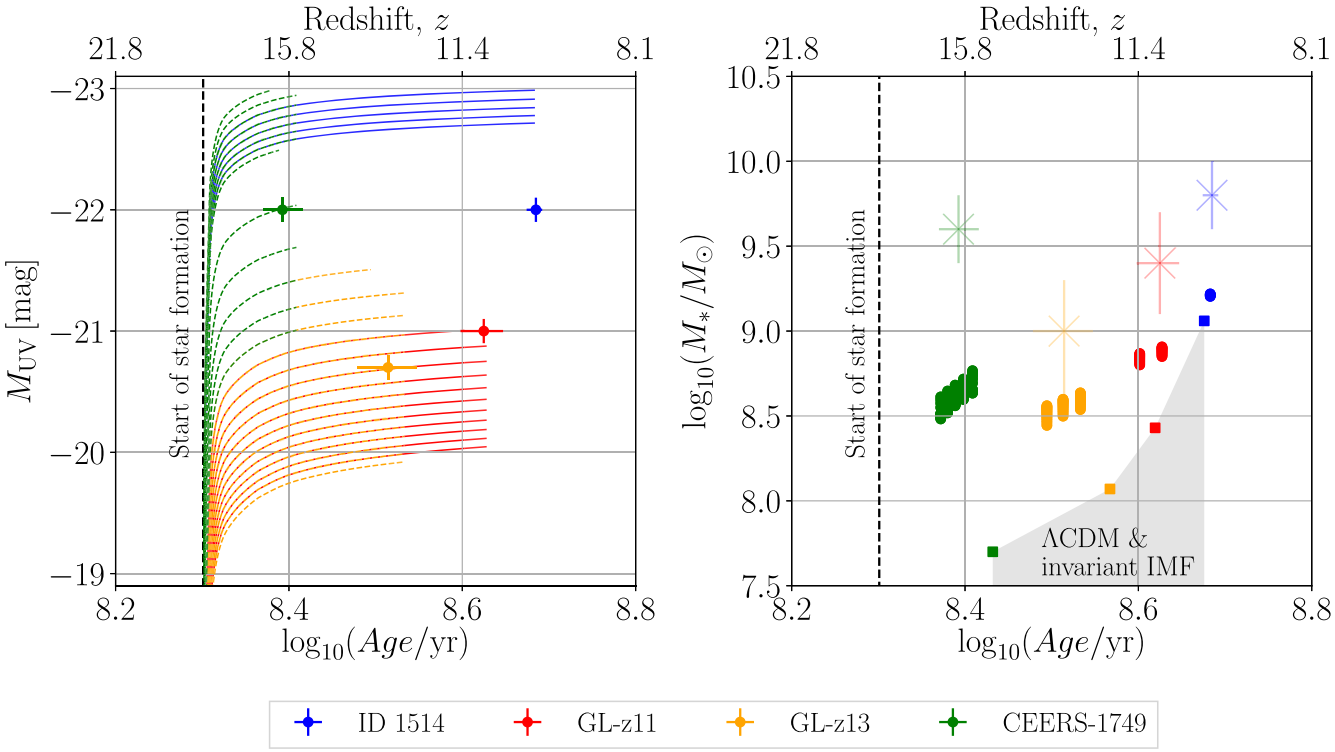

Figure 4. Left panel: cosmic time evolution of the absolute UV-band magnitude for stellar populations constructed using constant SFRs and assuming the IGIMF theory and that star formation starts 200 Myr after the Big Bang (dashed vertical line). The shown green, orange, red, and blue models match the observed magnitudes within ± 1 mag at the 1σ redshift interval of the galaxy candidates CEERS-1749, GL-z13, GL-z11, and ID 1514, respectively. The error bars show the observed absolute magnitudes of these four galaxy candidates. Right panel: the filled circles show the stellar masses of the galaxy candidates (of same color as the corresponding filled circles) assuming the M_*/L_{UV} ratios of the IGIMF models presented in the left panel. The faded error bars refer to the reported stellar masses as derived by Adams et al. (2022), Naidu et al. (2022b), Naidu et al. (2022a) based on an invariant canonical IMF. The squares mark the upper stellar mass limit found in the ΛCDM simulations assuming an invariant canonical IMF, and would be smaller for stronger-feedback regulation through an early top-heavy gwIMF.

frequent at $z \gtrsim 10$ than expected in the ΛCDM framework. For example, Boylan-Kolchin (2022) argued that a volume of $\approx 10^8$ cMpc^3 is required to explain ID 14924 with $\log_{10}(M/M_\odot) = 10.93$ at $z = 9.92$ (Labbe et al. 2022). However, the survey covers $\approx 10^5$ cMpc^3 at $z = 10 \pm 1$ (see Section 3 of Boylan-Kolchin 2022). The TNG100-1 and RefL 0100N1504 simulations have a box volume of $\approx 10^6$ cMpc^3 suggesting that the absence of massive galaxies in these runs is not because of a too small simulation volume.

The discrepancy between the observed and simulated stellar mass buildup could be caused by several reasons. First of all, high photometric redshifts can emerge due to dust reddening. For example, Zavala et al. (2022) demonstrated that Lyman-break galaxy candidates at $z_{phot} \gtrsim 12$ can resemble dusty star-forming galaxies at $z \lesssim 6$–7. Second, it could be that the high observed stellar masses are caused by an erroneous calibration of JWST.

Furthermore, it has been argued that star formation could be much more efficient in the early universe (e.g., Naidu et al. 2022b; Harikane et al. 2022; Mason et al. 2022). Assuming that the ΛCDM model is the correct description of the universe, this would mean that the underlying galaxy formation and evolution interstellar medium models of the EAGLE and IllustrisTNG runs must be improved in order to reproduce such galaxies. For example, these simulations assume that gas above a given density threshold (e.g., Schaye et al. 2015; Nelson et al. 2019b) is able to form stars, which is likely a too simplified implementation especially for describing high-redshift galaxies. Boylan-Kolchin (2022) showed that even a 100% star formation efficiency in ΛCDM would not be enough to explain the stellar mass density measured by Labbe et al. (2022).

Another possibility is that the IMF systematically varies with the galactic properties. The IllustrisTNG and EAGLE simulations and the analysis of the Sections 3 and 3.1 assume an invariant IMF, but it is expected that metal-poor star-forming stellar populations follow a top-heavy IMF. Using the IGIMF theory we calculated the gwIMF of the observed galaxy candidates in dependence of the metallicity and SFR of forming galaxies resulting in lower stellar masses compared to an invariant canonical IMF. For this, the IGIMF theory has to be included in cosmological simulations (see, e.g., Ploeckinger et al. 2014) in order to make a firm conclusion if a top-heavy IMF can resolve the reported tension.

Finally, the present findings can also imply that structure formation is much more efficient and/or that the observed universe is even older than predicted by ΛCDM. The existence of these massive galaxies ≈300–400 Myr after the Big Bang also questions the hierarchical (bottom-up) structure formation suggesting that late-type galaxies begin to form early through the initial monolithic collapse of rotating post-Big-Bang gas clouds (Wittenburg et al. 2020) while early-type massive galaxies and associated formation of supermassive black halos form by the monolithic collapse of post-Big-Bang gas clouds with little net rotation (e.g., Kroupa et al. 2020b; Wittenburg et al. 2020; Yan et al. 2021; Eappen et al. 2022).

Evidence for an enhanced growth of structures has been reported at different astrophysical scales and redshift ranges in the observed universe. For example, Steinhardt et al. (2016) showed that the observed number density of luminous galaxies

at $5 \lesssim z \lesssim 10$ is much higher than predicted by the ΛCDM model (see their Figure 1). However, their analysis relies on the stellar-to-halo mass relation from Leauthaud et al. (2012) measured only at $z = 0.2 - 1$, while, e.g., Behroozi et al. (2019) suggest that there is a strong evolution at $z \gtrsim 5$. Furthermore, the existence of the massive interacting galaxy cluster El Gordo (ACT-CL J0102-4915; Marriage et al. 2011) at $z = 0.87$ and the Keenan–Barger–Cowie void (Keenan et al. 2013) at $z \lesssim 0.07$ both individually falsify the hierarchical ΛCDM structure formation with more than 5σ (Haslbauer et al. 2020; Asencio et al. 2021).

An enhanced growth of structure compared to the ΛCDM paradigm is expected in Milgromian dynamics (Milgrom 1983; Angus 2009; Malekjani et al. 2009; Famaey & McGaugh 2012; Kroupa et al. 2012; Haslbauer et al. 2020; Banik & Zhao 2022). Assuming the cosmic microwave background as the $z = 1100$ boundary condition and because of the reduced power on <1 Mpc scales compared to ΛCDM (Angus & Diaferio 2011) due to the missing cold dark matter (CDM) component, it may be impossible to form galaxies in the early universe.

This work indicates that the currently available most advanced ΛCDM simulations cannot form galaxies as massive as observed at $z_{\rm phot} \gtrsim 10$. This tension needs to be readdressed for extreme SFHs and/or if the gwIMF was top-heavy, which would reduce the stellar mass buildup through more intense feedback.

Upcoming ultradeep and wider-area JWST observations will reveal more light on the number density of such luminous high-redshift galaxies over redshift required to evaluate the significance of the here-reported tension of the stellar mass buildup of high-redshift galaxies in more detail.

We thank an anonymous referee for helpful comments that significantly improved the manuscript. This project was largely conducted at the Charles University in Prague and we acknowledge the "DAAD-Eastern-European" exchange program for financing visits at the Charles University in Prague during which we discussed several aspects of the formation and evolution of high-redshift galaxy candidates in the ΛCDM and Milgromian frameworks. We are also grateful to Nils Wittenburg, Nick Samaras, Ingo Thies, and Elena Asencio for helpful discussions on structure formation in Milgromian dynamics.

ORCID iDs

Moritz Haslbauer https://orcid.org/0000-0002-5101-6366
Pavel Kroupa https://orcid.org/0000-0002-7301-3377
Akram Hasani Zonoozi https://orcid.org/0000-0002-0322-9957
Hosein Haghi https://orcid.org/0000-0002-9058-9677

References

Adams, N. J., Conselice, C. J., Ferreira, L., et al. 2022, arXiv:2207.11217v2
Angus, G. W. 2009, MNRAS, 394, 527
Angus, G. W., & Diaferio, A. 2011, MNRAS, 417, 941
Asencio, E., Banik, I., & Kroupa, P. 2021, MNRAS, 500, 5249
Atek, H., Shuntov, M., Furtak, L. J., et al. 2022, arXiv:2207.12338v1
Banik, I., & Zhao, H. 2022, Symm, 14, 1331
Behroozi, P., Wechsler, R. H., Hearin, A. P., & Conroy, C. 2019, MNRAS, 488, 3143
Boylan-Kolchin, M. 2022, arXiv:2208.01611v1
Carnall, A. C., Begley, R., McLeod, D. J., et al. 2022, MNRAS, Adance Access
Crain, R. A., Schaye, J., Bower, R. G., et al. 2015, MNRAS, 450, 1937
Eappen, R., Kroupa, P., Wittenburg, N., Haslbauer, M., & Famaey, B. 2022, MNRAS, 516, 1081
Efstathiou, G., Sutherland, W. J., & Maddox, S. J. 1990, Natur, 348, 705
Famaey, B., & McGaugh, S. S. 2012, LRR, 15, 10
Furtak, L. J., Shuntov, M., Atek, H., et al. 2022, arXiv:2208.05473v1
Harikane, Y., Ouchi, M., Oguri, M., et al. 2022, arXiv:2208.01612v1
Haslbauer, M., Banik, I., & Kroupa, P. 2020, MNRAS, 499, 2845
Jeřábková, T., Hasani Zonoozi, A., Kroupa, P., et al. 2018, A&A, 620, A39
Keenan, R. C., Barger, A. J., & Cowie, L. L. 2013, ApJ, 775, 62
Kroupa, P. 2001, MNRAS, 322, 231
Kroupa, P., Haslbauer, M., Banik, I., Nagesh, S. T., & Pflamm-Altenburg, J. 2020a, MNRAS, 497, 37
Kroupa, P., Pawlowski, M., & Milgrom, M. 2012, IJMPD, 21, 1230003
Kroupa, P., Subr, L., Jerabkova, T., & Wang, L. 2020b, MNRAS, 498, 5652
Kroupa, P., & Weidner, C. 2003, ApJ, 598, 1076
Kroupa, P., Weidner, C., Pflamm-Altenburg, J., et al. 2013, in Planets, Stars and Stellar Systems. Volume 5: Galactic Structure and Stellar Populations, ed. T. D. Oswalt & G. Gilmore, Vol. 5 (Dordrecht: Springer), 115
Labbe, I., van Dokkum, P., Nelson, E., et al. 2022, arXiv:2207.12446v2
Leauthaud, A., Tinker, J., Bundy, K., et al. 2012, ApJ, 744, 159
Lovell, C. C., Harrison, I., Harikane, Y., Tacchella, S., & Wilkins, S. M. 2022, arXiv:2208.10479v1
Malekjani, M., Rahvar, S., & Haghi, H. 2009, ApJ, 694, 1220
Marigo, P., & Girardi, L. 2007, A&A, 469, 239
Marigo, P., Girardi, L., Bressan, A., et al. 2008, A&A, 482, 883
Marinacci, F., Vogelsberger, M., Pakmor, R., et al. 2018, MNRAS, 480, 5113
Marriage, T. A., Acquaviva, V., Ade, P. A. R., et al. 2011, ApJ, 737, 61
Mason, C. A., Trenti, M., & Treu, T. 2022, arXiv:2207.14808v2
McAlpine, S., Helly, J. C., Schaller, M., et al. 2016, A&C, 15, 72
Milgrom, M. 1983, ApJ, 270, 365
Naidu, R. P., Oesch, P. A., Setton, D. J., et al. 2022a, arXiv:2208.02794v1
Naidu, R. P., Oesch, P. A., van Dokkum, P., et al. 2022b, arXiv:2207.09434v1
Naiman, J. P., Pillepich, A., Springel, V., et al. 2018, MNRAS, 477, 1206
Nelson, D., Pillepich, A., Springel, V., et al. 2018, MNRAS, 475, 624
Nelson, D., Pillepich, A., Springel, V., et al. 2019a, MNRAS, 490, 3234
Nelson, D., Springel, V., Pillepich, A., et al. 2019b, ComAC, 6, 2
Oesch, P. A., Brammer, G., van Dokkum, P. G., et al. 2016, ApJ, 819, 129
Ostriker, J. P., & Steinhardt, P. J. 1995, Natur, 377, 600
Pillepich, A., Nelson, D., Hernquist, L., et al. 2018a, MNRAS, 475, 648
Pillepich, A., Nelson, D., Springel, V., et al. 2019, MNRAS, 490, 3196
Pillepich, A., Springel, V., Nelson, D., et al. 2018b, MNRAS, 473, 4077
Planck Collaboration I. 2014, A&A, 571, A1
Planck Collaboration XIII. 2016, A&A, 594, A13
Ploeckinger, S., Hensler, G., Recchi, S., Mitchell, N., & Kroupa, P. 2014, MNRAS, 437, 3980
Rieke, M. J., Kelly, D., & Horner, S. 2005, Proc. SPIE, 5904, 1
Schaye, J., Crain, R. A., Bower, R. G., et al. 2015, MNRAS, 446, 521
Schneider, F. R. N., Sana, H., Evans, C. J., et al. 2018, Sci, 359, 69
Senchyna, P., Stark, D. P., Charlot, S., et al. 2021, MNRAS, 503, 6112
Springel, V. 2005, MNRAS, 364, 1105
Springel, V. 2010, MNRAS, 401, 791
Springel, V., Pakmor, R., Pillepich, A., et al. 2018, MNRAS, 475, 676
Steinhardt, C. L., Capak, P., Masters, D., & Speagle, J. S. 2016, ApJ, 824, 21
Weidner, C., & Kroupa, P. 2006, MNRAS, 365, 1333
Wittenburg, N., Kroupa, P., & Famaey, B. 2020, ApJ, 890, 173
Yan, H., Ma, Z., Ling, C., et al. 2022, arXiv:2207.11558v1
Yan, Z., Jeřábková, T., & Kroupa, P. 2021, A&A, 655, A19
Zavala, J. A., Buat, V., Casey, C. M., et al. 2022, arXiv:2208.01816v1
Zhang, Z.-Y., Romano, D., Ivison, R. J., Papadopoulos, P. P., & Matteucci, F. 2018, Natur, 558, 260
Zonoozi, A. H., Mahani, H., & Kroupa, P. 2019, MNRAS, 483, 46

APPENDIX D

Paper: The cosmological star formation history from the Local Cosmological Volume of galaxies and constraints on the matter homogeneity

This chapter includes a copy of the peer-reviewed paper entitled "The cosmological star formation history from the Local Cosmological Volume of galaxies and constraints on the matter homogeneity" published in Monthly Notices of the Royal Astronomical Society, 524, 3252, 2023 by **Moritz Haslbauer**, Pavel Kroupa, and Tereza Jerabkova. A summary and the author contributions are provided in Chapter 11.

Monthly Notices of the ROYAL ASTRONOMICAL SOCIETY

MNRAS **524,** 3252–3262 (2023)
Advance Access publication 2023 July 4

https://doi.org/10.1093/mnras/stad1986

The cosmological star formation history from the Local Cosmological Volume of galaxies and constraints on the matter homogeneity

Moritz Haslbauer [1]★ Pavel Kroupa [1,2] and Tereza Jerabkova [3]

[1] *Helmholtz-Institut für Strahlen- und Kernphysik (HISKP), University of Bonn, Nussallee 14–16, D-53115 Bonn, Germany*
[2] *Astronomical Institute, Faculty of Mathematics and Physics, Charles University, V Holešovičkách 2, CZ-180 00 Praha 8, Czech Republic*
[3] *European Southern Observatory, Karl-Schwarzschild-Straße 2, D-85748 Garching bei München, Germany*

Accepted 2023 June 27. Received 2023 June 23; in original form 2023 April 27

ABSTRACT

The Lilly–Madau plot is commonly interpreted as the history of the cosmic star formation of the Universe by showing the co-moving star formation rate density (SFRD) over cosmic time. Therefore, the Lilly–Madau plot is sensitive not only to the star formation history (SFH) but also to the number density of galaxies. Assessing the Catalogue of Neighbouring Galaxies, we reconstruct the SFHs of galaxies located in the Local Cosmological Volume (LV) based on delayed-τ and power-law SFH models. Galaxies with stellar masses of $M_* \gtrsim 10^{10}\,\mathrm{M}_\odot$ typically evolve according to the delayed-τ model by having first increasing followed by exponentially declining SFRs, while the majority of less massive star-forming galaxies have an almost constant or increasing SFH. Deducing the cosmic SFRD evolution of the LV reveals that the SFHs of local galaxies are inconsistent with the Lilly–Madau plot. The SFRDs of the LV are significantly lower at redshifts of $z \lesssim 3$ underestimating the Lilly–Madau peak at $z = 1.86$ by a factor of 2.16 ± 0.32 (delayed-τ model) and 5.90 ± 0.88 (power-law model). Assuming the delayed-τ model for galaxies with $M_* \geq 10^{10}\,\mathrm{M}_\odot$ and a power-law model for less massive galaxies, the SFRD is 2.22 ± 0.33 lower than measured at $z = 1.86$. This inconsistency between the evolution of the local and global SFRD has cosmological implications. Since the Lilly–Madau plot also constrains the cosmological matter field, the near-constancy of SFHs of LV galaxies could imply that the peak of the Lilly–Madau plot at $z = 1.86$ is the imprint of an ≈5 co-moving Gpc-scale inhomogeneity.

Key words: galaxies: abundances – galaxies: evolution – galaxies: formation – galaxies: star formation – galaxies: stellar content – large-scale structure of Universe.

1 INTRODUCTION

The observed history of cosmic star formation of the Universe constrains cosmological models of galaxy evolution and structure formation. Determining the stellar masses and star formation rates (SFRs) of galaxies over cosmic time is therewith of particular importance as the stellar mass growth reflects also the matter cycle and mass budget of the Universe (e.g. Kroupa et al. 2020).

Over the last three decades, several studies measured the SFR per co-moving volume of the Universe over cosmic time (e.g. Lilly et al. 1996; Madau et al. 1996; Madau, Pozzetti & Dickinson 1998; Cole et al. 2001; Madau & Dickinson 2014; Madau & Fragos 2017) from which the following picture qualitatively emerged: The first stars and galaxies form during the epoch of the 'cosmic dawn' at redshifts of $z \gtrsim 9$ (Laporte et al. 2021). This is followed by a phase in which galaxies rapidly grow in stellar mass such that the co-moving star formation rate density (SFRD) of the Universe increases from redshift $z \approx 8$ up to $z \approx 2$ by about one order of magnitude. During the so-called high cosmic noon at $2 \lesssim z \lesssim 3$, the SFRD becomes maximal, which is widely interpreted as an active phase of the Universe where galaxies show high star formation activities. After that, the 'cosmic afternoon' occurs during which the cosmic SFRD declines to the present time by again about one order of magnitude. This evolution of the SFRD is the so-called Madau or Lilly–Madau plot and is understood as the history of the cosmic star formation of the Universe.

In a review, Madau & Dickinson (2014, hereafter MD14) show the evolution of the cosmic SFRD over redshift by measuring the SFRs in the rest-frame far-ultraviolet (FUV) and infrared (IR) continuum (see their figs 8 and 9) and assuming SFR–luminosity conversion factors for the Salpeter initial mass function (IMF; Salpeter 1955). Their best fit to the cosmic co-moving SFRD (see equation 15 of MD14) has the form

$$\mathrm{SFRD}_{\mathrm{MD14}}(z) = \frac{0.015\,(1+z)^{2.7}}{1+[(1+z)/2.9]^{5.6}}\,\mathrm{M}_\odot\,\mathrm{yr}^{-1}\,\mathrm{cMpc}^{-3}, \qquad (1)$$

which yields an SFRD of $\approx 0.015\,\mathrm{M}_\odot\,\mathrm{yr}^{-1}\,\mathrm{cMpc}^{-3}$ at $z = 0$ and a global maximum of $\approx 0.13\,\mathrm{M}_\odot\,\mathrm{yr}^{-1}\,\mathrm{cMpc}^{-3}$ at $z = 1.86$ corresponding to an age of the Universe of 3.5 Gyr (see their fig. 9 and also our Section 3.2). Thus, the SFRD increases by a factor of ≈8.9 from the present time up to $z = 1.86$. The star formation history (SFH) and stellar mass growth of galaxies are physically linked such that the cosmic stellar mass density (SMD) can be deduced from the cosmic SFRD or vice versa.

The Lilly–Madau plot as parametrized by equation (1) states the SFR per co-moving volume over cosmic time and therefore

★ E-mail: mhaslbauer@astro.uni-bonn.de

not only reflects the history of cosmic star formation but is also sensitive to the number density of the galaxies over cosmic time. Consequently, the Lilly–Madau plot also sets constraints on the matter homogeneity of the Universe. Galaxies in the local Universe provide the cosmological boundary conditions that have to be fulfilled by any viable model of structure formation and galaxy evolution (Kroupa et al. 2020; Kroupa & Jerabkova 2021). The sample of galaxies located in the Local Cosmological Volume (Karachentsev et al. 2004; Karachentsev, Makarov & Kaisina 2013), which is defined as a sphere with a radius of 11 Mpc centred around the Milky Way (MW), should have reliable well-observed quantities that can be assessed to constrain the cosmic SFH and matter density of the local Universe. While massive star-forming galaxies with stellar masses of $M_* \gtrsim 10^{10}\,\mathrm{M}_\odot$ typically follow the main sequence of star-forming galaxies (Speagle et al. 2014), less massive galaxies show evidence for an almost constant SFR (McGaugh, Schombert & Lelli 2017; Schombert, McGaugh & Lelli 2019; Kroupa et al. 2020) meaning that their present-day SFR, SFR_0, is comparable to the present-day averaged SFR, $\overline{\mathrm{SFR}} \approx M_*/(12\,\mathrm{Gyr})$. Galaxies evolving according to the main sequence of star-forming galaxies (Speagle et al. 2014) have $\mathrm{SFR}_0 < \overline{\mathrm{SFR}}$ and are described by the so-called delayed-τ SFH model in which the SFRs first increase and subsequently decline to present time (see their figs 9 and 10).

Analysing the Catalogue of Neighbouring Galaxies (Karachentsev et al. 2004, 2013), Kroupa et al. (2020) reported that the sample of galaxies in the Local Cosmological Volume (LV) with $\mathrm{SFR}_0 \geq 10^{-3}\,\mathrm{M}_\odot\,\mathrm{yr}^{-1}$ has a mean value of $\overline{\mathrm{SFR}}/\mathrm{SFR}_0 = 0.85$ (see their figs 3–5) implying that most of the local galaxies have nearly constant SFRs over cosmic time. The SFH of these galaxies can be parametrized by a power-law of the form $\mathrm{SFR}(t) \propto (t - t_{\mathrm{start}})^{\eta}$ for $t_{\mathrm{start}} = 1.8\,\mathrm{Gyr}$ and $\eta = 0.18 \pm 0.03$. As discussed by Kroupa et al. (2020), such an SFH is inconsistent with the evolutionary track of galaxies that strictly evolve along the main sequence of star-forming galaxies by Speagle et al. (2014). Galaxies on the main sequence typically have $\overline{\mathrm{SFR}}/\mathrm{SFR}_0 \approx 2$ (Kroupa et al. 2020). Similar results have been found by Schombert et al. (2019), who showed that galaxies of the Cook et al. (2014) and LSB + SPARC (McGaugh et al. 2017) sample with $M_* \lesssim 10^{10}\,\mathrm{M}_\odot$ are consistent with a constant SFH over a time-scale of 13 Gyr (see their fig. 1).

Given that the majority of galaxies located in the LV have almost constant SFRs over cosmic time (Kroupa et al. 2020), the question arises whether the SFHs of local galaxies are consistent with the global history of cosmic star formation as implied by the Lilly–Madau plot. In this contribution, we supplement the work by Kroupa et al. (2020) by investigating the SFRs and stellar masses of galaxies located in the LV (Karachentsev et al. 2004, 2013) in the context of the Lilly–Madau plot. The paper is organized as follows: Section 2 describes the observational data extracted from the updated version of the Catalogue of Neighbouring Galaxies as compiled by Karachentsev et al. (2004, 2013) and introduces the parametrization of different SFH models. The SFHs, SFRD, and SMD of the LV are presented and compared with the Lilly–Madau plot in Section 3. A discussion on the SFRD and matter homogeneity and concluding remarks are provided, respectively, in Sections 4 and 5. Throughout the analysis, we assume a standard Lambda cold dark matter (ΛCDM) cosmology with a global Hubble constant of $H_0 = 67.74\,\mathrm{km\,s^{-1}\,Mpc^{-1}}$, and a present-day total matter density and dark energy density in units of the cosmic critical density of $\Omega_{\mathrm{m},0} = 0.3089$ and $\Omega_{\Lambda,0} = 0.6911$, respectively (Planck Collaboration XIII 2016).

2 METHODS

This section introduces the observational parameters of the sample of neighbouring galaxies and the SFH models used to calculate the cosmic SFRD and SMD of the LV.

2.1 The Local Cosmological Volume

The Local Cosmological Volume (hereafter LV) is defined as a sphere with a radius of 11 Mpc centred around the MW. The observational data of galaxies located inside the LV are extracted from the updated version (Karachentsev et al. 2013) of the Catalogue of Neighbouring Galaxies (Karachentsev et al. 2004),[1] which lists galaxies with a Galactic-centric distance of $D < 11\,\mathrm{Mpc}$ or radial velocities of $V < 600\,\mathrm{km\,s^{-1}}$ (see section 2 of Karachentsev et al. 2013). We extract the *Ks*-band luminosities, L_{Ks}, the Galactocentric distances, D, and the SFRs based on the integrated H α and FUV measurements (Karachentsev & Kaisina 2013), $\mathrm{SFR}_{\mathrm{H}\,\alpha}$ and $\mathrm{SFR}_{\mathrm{FUV}}$, respectively (including flagged SFRs). Selecting galaxies with $D < 11\,\mathrm{Mpc}$ results in a total sample of 1102 galaxies from which 115 have only the $\mathrm{SFR}_{\mathrm{H}\,\alpha}$, 447 only the $\mathrm{SFR}_{\mathrm{FUV}}$, and 540 both SFR measurements.

2.1.1 *Present-day SFR*

The present-day SFR of galaxies with both SFR measurements is calculated by

$$\mathrm{SFR}_0 = \frac{\mathrm{SFR}_{\mathrm{H}\alpha} + \mathrm{SFR}_{\mathrm{FUV}}}{2}, \tag{2}$$

and $\mathrm{SFR}_0 = \mathrm{SFR}_{\mathrm{H}\,\alpha}$ or $\mathrm{SFR}_0 = \mathrm{SFR}_{\mathrm{FUV}}$ is adopted if only H α- or FUV-based measurements are available, respectively (see also section 2 of Kroupa et al. 2020).

2.1.2 *Present-day SFRD and SMD*

The present-day SFRD of the LV is

$$\mathrm{SFRD}(D \leq 11\,\mathrm{Mpc}) \equiv \frac{1}{V}\sum_{i=1}^{N} \mathrm{SFR}_{0,i}, \tag{3}$$

where N is the number of galaxies located in a co-moving volume V. The estimated lower limit of the SFRD is simply given for the volume of a sphere with a radius of 11 Mpc

$$V = \frac{4\pi\,(11\,\mathrm{Mpc})^3}{3} \approx 5575.3\,\mathrm{Mpc}^3, \tag{4}$$

while the upper limit corresponds to a volume of

$$V = \frac{4\pi\,(11\,\mathrm{Mpc})^3}{3}\left(1 - \sin(15^\circ)\right) \approx 4132.3\,\mathrm{Mpc}^3, \tag{5}$$

by taking into account potentially missed galaxies due to dust obscuration at Galactic latitudes of $b < |15^\circ|$ (e.g. section 2 of Karachentsev & Telikova 2018). This gives an SFRD of $0.014 - 0.019\,\mathrm{M}_\odot\,\mathrm{yr}^{-1}\,\mathrm{Mpc}^{-3}$ for the LV, which is consistent with the present-day SFRD of $0.015\,\mathrm{M}_\odot\,\mathrm{yr}^{-1}\,\mathrm{Mpc}^{-3}$ as found by MD14.

The present-day SMD in the LV is

$$\mathrm{SMD}(D \leq 11\,\mathrm{Mpc}) \equiv \frac{1}{V}\sum_{i=1}^{N} M_{*,i}, \tag{6}$$

[1]The catalogues of galaxies in the LV can be downloaded using the following link: https://www.sao.ru/lv/lvgdb/introduction.php. Here, we use the latest update from 2023 April 12.

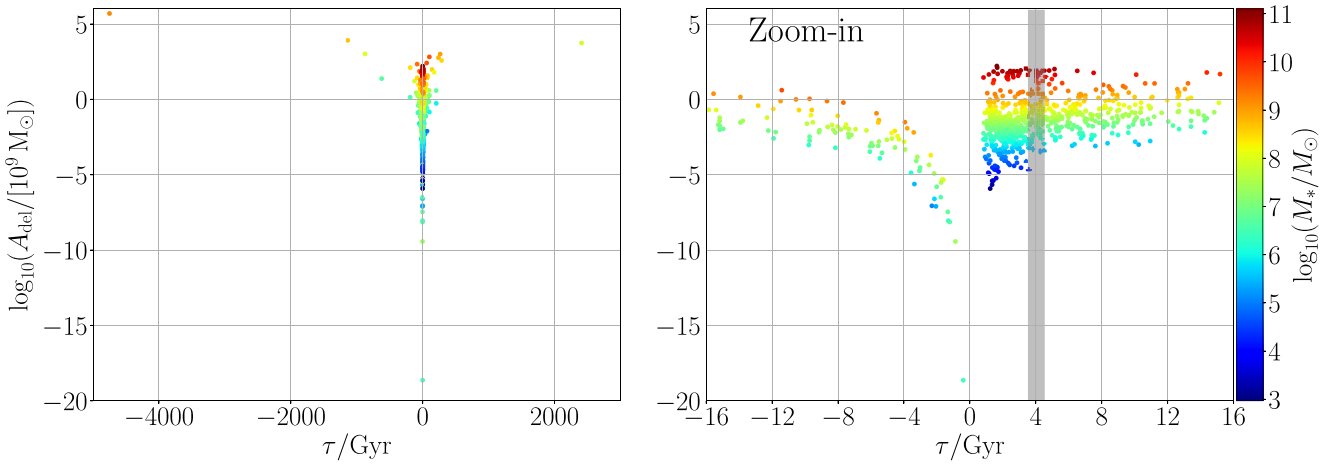

Figure 1. Parameter distribution of the delayed-τ SFH models for galaxies located in the LV. The colourbar represents the present-day stellar mass of the galaxies. The left-hand panel shows the parameter range of the LV galaxies (apart from one galaxy with an extreme negative value of τ), while the right-hand panel is a zoom-in on galaxies with $-16 \leq \tau/{\rm Gyr} \leq 16$. Galaxies on the main sequence have $3.5 \lesssim \tau/{\rm Gyr} \lesssim 4.5$ (Speagle et al. 2014; Kroupa et al. 2020) as highlighted by the grey area. Galaxies with $\tau < 0$ have slowly risings SFRs.

where $M_{*,i}$ is the present-day stellar mass of the i-th galaxy assuming a mass-to-light ratio of $0.6\,{\rm M}_\odot/{\rm L}_\odot$ in the *Ks* band (e.g. McGaugh & Schombert 2014). The LV has an SMD of $(3.45 - 4.65) \times 10^8\,{\rm M}_\odot\,{\rm Mpc}^{-3}$.

2.1.3 *Present-day averaged SFR*

Throughout the analysis, we assume that all galaxies start forming stars 0.2 Gyr after the big bang,[2] which corresponds to a redshift of $z = 18$ in standard ΛCDM cosmology (Planck Collaboration XIII 2016). The observed present-day averaged SFR over the onset of SFR at time $t_{\rm start} = 0.2$ Gyr and present-day $t_{\rm end} = 13.8$ Gyr is then defined by

$$\overline{\rm SFR} \equiv \frac{\zeta\, M_*}{t_{\rm end} - t_{\rm start}} = \frac{\zeta\, M_*}{t_{\rm sf}}, \tag{7}$$

where ζ takes into account the mass-loss through stellar evolution. Simulations conducted by Baumgardt & Makino (2003) suggested a stellar mass-loss from bound stars of about 30 per cent implying $\zeta = 1.3$ for the canonical two-part power-law IMF (Kroupa 2001). Throughout this study, we also set $\zeta = 1.3$ in order to be consistent with the analysis of Kroupa et al. (2020).

2.2 Delayed-τ SFH model

The delayed-τ model describes the SFH of a galaxy assuming that the SFRs typically rise in the early phase of galaxy evolution and gradually decline to the present time (e.g. Reddy et al. 2012; Carnall et al. 2019). In fact, Speagle et al. (2014) showed in their figs 9 and 10 that the SFH of galaxies following the main sequence of star-forming galaxies can be accurately parametrized by the delayed-τ model of the form

$$\begin{aligned}&{\rm SFR}_{\rm del}(t) = \\ &= \begin{cases} \frac{A_{\rm del}}{\tau^2}(t - t_{\rm start}) \exp\left(-\frac{t-t_{\rm start}}{\tau}\right) & \text{if } t > t_{\rm start}, \\ 0 & \text{if } t \leq t_{\rm start}, \end{cases}\end{aligned} \tag{8}$$

[2]We note that this differs from the analysis by Kroupa et al. (2020) in which $t_{\rm start} = 1.8$ Gyr.

where t is the age of the Universe, $A_{\rm del}$ is the normalization constant, and τ is the star formation time-scale. The model yields a declining SFH for $t/\tau \gg 1$ and a linear rising SFH for $t/\tau \ll 1$ (see also e.g. section 3.1.4 of Speagle et al. 2014). Empirically, galaxies on the main sequence have $3.5 \lesssim \tau/{\rm Gyr} \lesssim 4.5$ (Speagle et al. 2014; Kroupa et al. 2020). We also allow solutions with $\tau < 0$ in order to describe galaxies with a gradually increasing SFH.

The present-day SFR is given by adopting $t = t_{\rm end} = 13.8$ Gyr, such that $t_{\rm sf} = 13.6$ Gyr is the total star-forming lifetime,

$${\rm SFR}_{0,\rm del} \equiv {\rm SFR}_{\rm del}(t = t_{\rm end}) = \frac{A_{\rm del} t_{\rm sf}}{\tau^2} \exp\left(-\frac{t_{\rm sf}}{\tau}\right). \tag{9}$$

The present-day averaged SFR is

$$\begin{aligned}\overline{\rm SFR}_{\rm del} &\equiv \frac{1}{t_{\rm sf}} \int_{t_{\rm start}}^{t_{\rm end}} {\rm SFR}_{\rm del}(t)\,{\rm d}t \\ &= \frac{A_{\rm del}}{t_{\rm sf}} \left[1 - \left(1 + \frac{t_{\rm sf}}{\tau}\right) \exp\left(-\frac{t_{\rm sf}}{\tau}\right)\right].\end{aligned} \tag{10}$$

Solving these two equations for the observed present-day (Section 2.1.1) and present-day averaged (Section 2.1.3) SFRs of the LV galaxies, determines the parameters $A_{\rm del}$ and τ. This allows to reconstruct the SFH of each LV galaxy as illustrated for some selected galaxies in Section 3.1. Fig. 1 shows the distribution of the parameters $A_{\rm del}$ and τ of all LV galaxies.

Reconstructing the SFHs of individual LV galaxies enables to calculate the evolution of the SFRD over cosmic time. The SFRD of the LV based on the delayed-τ model is therefore

$${\rm SFRD}_{\rm del}(t) = \frac{1}{V} \sum_{i=1}^{N} {\rm SFR}_{{\rm del},i}(t), \tag{11}$$

where ${\rm SFR}_{{\rm del},\,i}(t)$ is the SFR at time t for the i-th galaxy. The so-calculated time evolution of the SFRD is presented in Section 3.2.

2.3 Power-law SFH model

Following section 3.3 of Kroupa et al. (2020), the SFHs of LV galaxies can be parametrized by a power-law (hereafter power-law-η

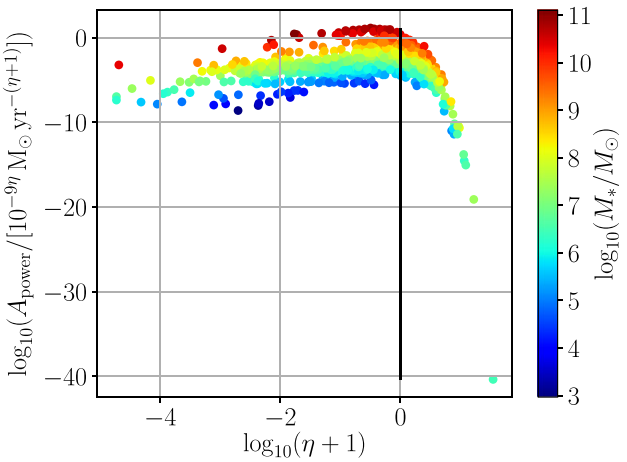

Figure 2. Parameter distribution of the power-law-η SFH model for galaxies located in the LV. The colourbar represents the present-day stellar mass of the shown galaxies. The black solid line separates galaxies with an rising (i.e. $\eta > 0$) and a falling (i.e. $\eta < 0$) SFH.

SFH model) of the form

$$\mathrm{SFR}_{\rm power}(t) = \begin{cases} A_{\rm power}(t - t_{\rm start})^\eta & \text{if} \quad t > t_{\rm start}, \\ 0 & \text{if} \quad t \leq t_{\rm start}, \end{cases} \tag{12}$$

where $A_{\rm power}$ is the normalization constant and $\eta \neq -1$ is the power-law index such that $\eta = 0, > 0$, and < 0 implies a constant, increasing, and decreasing SFH, respectively. The present-day SFR is given by

$$\mathrm{SFR}_{0,\rm power} \equiv \mathrm{SFR}_{\rm power}(t = t_{\rm end}) = A_{\rm power}(t_{\rm sf})^\eta, \tag{13}$$

and the present-day averaged SFR is

$$\overline{\mathrm{SFR}}_{\rm power} \equiv \frac{1}{t_{\rm sf}} \int_{t_{\rm start}}^{t_{\rm end}} \mathrm{SFR}_{\rm power}(t)\mathrm{d}t = \frac{A_{\rm power}}{1+\eta} t_{\rm sf}^\eta \,. \tag{14}$$

It follows that the power-law index depends on the present-day and present-day averaged SFR via

$$\eta = \frac{\mathrm{SFR}_{0,\rm power}}{\overline{\mathrm{SFR}}_{\rm power}} - 1 \,. \tag{15}$$

Solving the equations (13) and (14) for the present-day and present-day averaged SFRs of the LV sample, yields their parametrization of the power-law-η SFH model as defined by equation (12). The distribution of the parameters $A_{\rm power}$ and η of the LV galaxies is depicted in Fig. 2.

As elaborated in the previous section, the cosmic SFRD of the LV based on the power-law-η SFH model is

$$\mathrm{SFRD}_{\rm power}(t) = \frac{1}{V} \sum_{i=1}^{N} \mathrm{SFR}_{\rm power,i}(t) \,. \tag{16}$$

2.4 Combined SFH model

Star-forming galaxies with $M_* \gtrsim 10^{10}\,\mathrm{M_\odot}$ typically follow the main sequence of Speagle et al. (2014) while most galaxies with $M_* \lesssim 10^{10}\,\mathrm{M_\odot}$ have an almost constant SFH (McGaugh et al. 2017; Schombert et al. 2019; Kroupa et al. 2020). Therefore, we also apply a combination of the delayed-τ and power-law-η SFH model by adopting

$$\mathrm{SFR}_{\rm combined}(t) = \begin{cases} \mathrm{SFR}_{\rm del}(t) & \text{if } M_* \geq 10^{10}\,\mathrm{M_\odot}, \\ \mathrm{SFR}_{\rm power}(t) & \text{if } M_* < 10^{10}\,\mathrm{M_\odot}, \end{cases} \tag{17}$$

and

$$\mathrm{SFRD}_{\rm combined}(t) = \frac{1}{V} \sum_{i=1}^{N} \mathrm{SFR}_{\rm combined,i}(t) \,. \tag{18}$$

Throughout the study, we refer to this as the combined SFH model.

2.5 Stellar mass density

The cosmic evolution of the co-moving SFRD and SMD are physically connected via

$$\mathrm{SMD}(t) = (1-R) \int_0^t \mathrm{SFRD}(t')\mathrm{d}t', \tag{19}$$

which rewrites in terms of redshifts to

$$\mathrm{SMD}(z) = (1-R) \int_z^\infty \mathrm{SFRD}(z') \frac{\mathrm{d}z'}{H(z')(1+z')}, \tag{20}$$

where $H(z) = H_0\sqrt{\Omega_{\rm m,0}(1+z)^3 + (1-\Omega_{\rm m,0})}$ is the Hubble parameter in a standard ΛCDM cosmology (Planck Collaboration XIII 2016) and $R = 1 - 1/\zeta$ (e.g. section 4.1 of Pipino, Lilly & Carollo 2014) is the recycling fraction (see also section 4 of Yu & Wang 2016).

3 RESULTS

The present-day SFR (Section 2.1.1) in dependence of the stellar mass of galaxies located in the LV is presented in the left-hand panel of Fig. 3. Low-mass galaxies with $M_* \lesssim 10^{10}\,\mathrm{M_\odot}$ and $\mathrm{SFR}_0 \gtrsim 10^{-3}\,\mathrm{M_\odot\,yr^{-1}}$ typically have a constant SFH (black line), while galaxies with $M_* \gtrsim 10^{10}\,\mathrm{M_\odot}$ have $\mathrm{SFR}_0 < \overline{\mathrm{SFR}}$ following the main sequence of star-forming galaxies (solid red line). The right-hand panel shows the distribution of the values $\overline{\mathrm{SFR}}/\mathrm{SFR}_0$ in the $\log_{10}$-space, which peaks at $\overline{\mathrm{SFR}}/\mathrm{SFR}_0 \approx 1$ and has mean (median) of 4.69 (2.45). Galaxies on the main sequence are expected to have $\overline{\mathrm{SFR}}/\mathrm{SFR}_0 \approx 2$ (Speagle et al. 2014; Kroupa et al. 2020).

For a comparison with Kroupa et al. (2020), we select only galaxies with $\mathrm{SFR}_0 \geq 10^{-3}\,\mathrm{M_\odot\,yr^{-1}}$, which gives a sample size of 511. These galaxies have a mean (median) value of $\overline{\mathrm{SFR}}/\mathrm{SFR}_0 = 0.97$ (0.83) being broadly consistent with Kroupa et al. (2020)[3] who obtained a mean (median) of 1.11 (0.96) for $t_{\rm end} = 1.8$ Gyr.

3.1 SFHs of galaxies in the LV

The SFHs of selected galaxies in the LV parametrized by the delayed-τ (Section 2.2) and the power-law-η (Section 2.3) SFH models are presented in Fig. 4. In the delayed-τ model, the massive galaxies (i.e. $M_* > 10^{10}\,\mathrm{M_\odot}$) MW, M31, NGC 5128/Cen A, M81, and IC 342 have first a phase of increasing SFRs, which is followed by a decreasing SFH over cosmic time. For example, the SFR of the MW globally peaks at a lookback time of ≈9.5 Gyr with a value of $5\,\mathrm{M_\odot\,yr^{-1}}$ and subsequently decreases to a present-day value of $1.7\,\mathrm{M_\odot\,yr^{-1}}$. The less massive Small Magellanic Cloud (SMC) and M32 galaxy with a stellar mass of 4.2×10^8 and $7.4 \times 10^8\,\mathrm{M_\odot}$, respectively, have also first an increasing and later on a decreasing SFH. The SMC has a maximal SFR of $0.05\,\mathrm{M_\odot\,yr^{-1}}$ at a lookback time of ≈4.7 Gyr, which is about 1.1 times higher than the present-day value. M32 has an SFR

[3]We note that Kroupa et al. (2020) used the Catalogue of Neighbouring Galaxies from 2020 May 8.

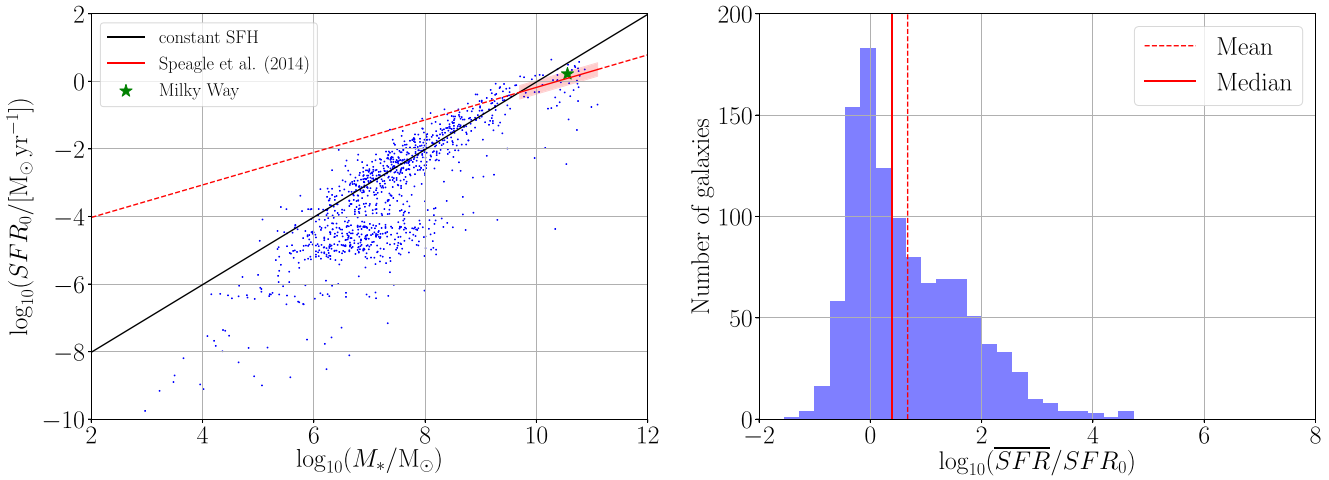

Figure 3. Left: Present-day SFR, SFR_0, in dependence of the stellar mass of galaxies located in the LV. The black line marks a constant SFH by assuming $\zeta = 1.3$ and $t_{\mathrm{sf}} = 13.6$ Gyr (equation 7). The red solid line shows the present-day main sequence of star-forming galaxies with $10^{9.7} \leq M_*/M_\odot \leq 10^{11.1}$ (equation 28 and fig. 8 of Speagle et al. 2014) and an uncertainty of ± 0.2 dex (red shaded region). The red dashed line extrapolates the main sequence beyond the adopted fitting range by Speagle et al. (2014). The green star marks the MW with $M_* = 3.6 \times 10^{10}\,\mathrm{M}_\odot$ and $\mathrm{SFR}_0 = 1.7\,\mathrm{M}_\odot\,\mathrm{yr}^{-1}$ (Karachentsev et al. 2013). Right: Distribution of $\overline{\mathrm{SFR}}/\mathrm{SFR}_0$ values of galaxies in the LV with a median and mean value of 0.39 (solid line) and 0.67 (dashed line) in the $\log_{10}$-space, respectively.

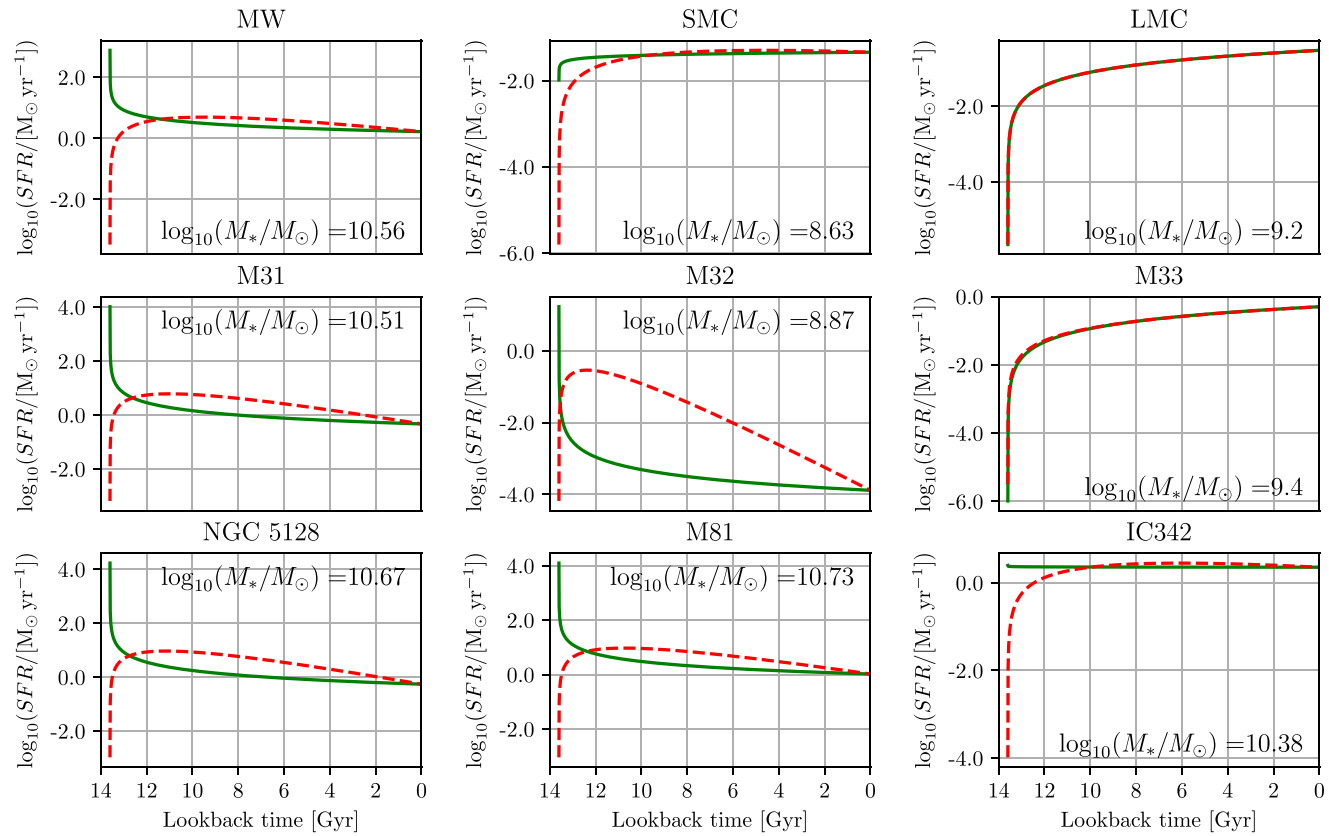

Figure 4. Reconstructed SFHs of the LV galaxies MW, SMC, LMC, M31, M32, M33, NGC 5128/Cen A, M81, and IC 342 assuming the delayed-τ (dashed red) and power-law-η (solid green) SFH model. The panels state the present-day stellar masses of the galaxies. Note that the delayed-τ and power-law-η SFH model give basically the same SFH for the LMC (top right) and M33 (middle right) galaxy.

peak of $0.3\,M_\odot\,yr^{-1}$ at a lookback time of 12.4 Gyr and a present-day SFR of only $1.3 \times 10^{-4}\,M_\odot\,yr^{-1}$. The Large Magellanic Cloud (LMC) with $M_* = 1.6 \times 10^9\,M_\odot$ and M33 with $M_* = 2.5 \times 10^9\,M_\odot$ have continuously rising SFHs in both the delayed-τ and power-law-η SFH model.

In the power-law-η SFH model, the massive galaxies MW, M31, NGC 5128/Cen A, M81, IC 342, but also M32 have a decreasing, while the low-mass galaxies SMC, LMC, and M33 have an increasing SFH over cosmic time in agreement with e.g. McGaugh et al. (2017), Schombert et al. (2019), and Kroupa et al. (2020).

3.2 Cosmic SFRD and SMD of the LV

The evolution of the cosmic SFRD and SMD derived from the LV is presented in Fig. 5. The LV has an SFRD of $0.014 - 0.019\,M_\odot\,yr^{-1}\,Mpc^{-3}$ (Section 2.1.2) which is fully consistent with the measured value of $0.015\,M_\odot\,yr^{-1}\,Mpc^{-3}$ at $z = 0$ by MD14. However, the evolution of the cosmic SFRD of the LV significantly differs from MD14 by being systematically lower at $z \lesssim 3$ but higher at $z \gtrsim 5.5$ (top left panel). The delayed-τ and the combined SFH model peak globally with a value of $0.058 - 0.078\,M_\odot\,yr^{-1}\,cMpc^{-3}$ at $z = 2.73$ and $0.056 - 0.076\,M_\odot\,yr^{-1}\,cMpc^{-3}$ at $z = 2.78$, respectively, while the MD14 plot reaches a much higher maximum of $0.13\,M_\odot\,yr^{-1}\,cMpc^{-3}$ at $z = 1.86$. The SFRD of the power-law-η SFH model peaks with $1.00 - 1.35\,M_\odot\,yr^{-1}\,cMpc^{-3}$ at $z = 18$, which corresponds to an age of the Universe of 0.2 Gyr (Planck Collaboration XIII 2016) and the assumed onset of star formation (Section 2.1.3). The SFRD derived from the LV is 2.16 ± 0.32 (delayed-τ SFH model), 2.22 ± 0.33 (combined SFH model), and 5.90 ± 0.88 (power-law-η SFH model) times lower than measured by MD14 (their equation 15) at the peak of the Lilly–Madau plot located at $z = 1.86$ (top right panel). Comparing the ratio between the global and local SFRD at $z < 8$ (top left panel) yields a maximum at $z \approx 1.6$ where the SFRD derived from the LV is by a factor 2.22 ± 0.33 (delayed-τ SFH model), 2.29 ± 0.34 (combined SFH model), and 6.09 ± 0.90 (power-law-η SFH model) times lower.

As the SFH and the stellar mass growth of galaxies are physically connected (Section 2.5), the discrepancy is also evident in the evolution of the local and global SMDs as shown in the bottom panels of Fig. 5. The SMD derived from the LV is systematically lower at $z \lesssim 2$ and higher at $z \gtrsim 3$ than implied by the global cosmic SFH of MD14 (bottom left panel), i.e. the ratio between the cosmic SMD deduced from MD14 and the LV peaks with 1.67 ± 0.25 at $z = 0.67$ (delayed-τ SFH model), 1.70 ± 0.25 at $z = 0.64$ (combined SFH model), and 2.59 ± 0.38 at $z = 0.48$ (power-law-η SFH model; bottom right panel).

The derived SMDs are compared with the observed SMD by MD14 and Grazian et al. (2015) in the bottom left panel of Fig. 5. As already reported by Yu & Wang (2016), the observed SMD is inconsistent with the SFRD measured by MD14 at $0.5 \lesssim z \lesssim 6$ (see also the figs 2–4 of Yu & Wang 2016). The delayed-τ and combined SFH models agree much better with the SMD measured by MD14 and Grazian et al. (2015) at $z \lesssim 2$ but systematically overstimate this measured SMD at higher redshifts. The power-law-η SFH model disagrees with the observations by MD14 and Grazian et al. (2015) over the entire redshift range.

The implications and possible interpretations of the discrepancy between the local and global SFRD and SMD are discussed in the following section.

4 DISCUSSION

The physical properties of local galaxies provide the cosmological boundary conditions for galaxy evolution and structure formation models. Galaxies located in the Local Cosmological Volume (Karachentsev et al. 2004; Karachentsev et al. 2013) ought to have well-observed physical parameters like the present-day SFRs and stellar masses (Karachentsev & Kaisina 2013; Kroupa et al. 2020), which can be assessed to constrain their SFHs (Sections 2.2–2.4). Assessing the updated version of the Catalogue of Neighbouring Galaxies as compiled by Karachentsev et al. (2004, 2013), Kroupa et al. (2020) reported that the SFH of galaxies with $SFR_0 \geq 10^{-3}\,M_\odot\,yr^{-1}$ in the LV can be parametrized by a power-law of the form of $SFR(t) \propto (t - t_{start})^\eta$ for $t_{start} = 1.8$ Gyr with a power-law index of $\eta = 0.18 \pm 0.03$. This implies that the majority of LV galaxies has almost constant SFRs over time being in tension with the evolution of the SFH as implied by the main sequence of star-forming galaxies (figs 9 and 10 in Speagle et al. 2014). The cosmological implications are investigated in this contribution.

4.1 SFHs of galaxies in the LV

We reconstructed the SFHs of galaxies in the LV based on their present-day and present-day averaged SFRs assuming the delayed-τ (Sections 2.2) and a power-law (Section 2.3) SFH models. For the galaxies in the LV, we found that those with $M_* \gtrsim 10^{10}\,M_\odot$ typically have decreasing SFHs over the last $\gtrsim 5$ Gyr, while less mass galaxies with $SFR_0 \gtrsim 10^{-3}\,M_\odot\,yr^{-1}$ have almost constant or even increasing SFHs. A substantial number of objects with $SFR_0 \lesssim 10^{-4}\,M_\odot\,yr^{-1}$ have $SFR_0 < \overline{SFR}$ suggesting a decreasing SFH (Fig. 3). These findings are consistent with the studies by Speagle et al. (2014), McGaugh et al. (2017), Schombert et al. (2019), and Kroupa et al. (2020) according to which galaxies with $M_* \gtrsim 10^{10}\,M_\odot$ follow the main sequence of star-forming galaxies and less massive galaxies with $M_* \gtrsim 10^{10}\,M_\odot$ have a constant SFH.

For example, the MW with $M_* = 3.6 \times 10^{10}\,M_\odot$ has $SFR_0 = 1.7\,M_\odot\,yr^{-1}$ and $\overline{SFR} = 3.5\,M_\odot\,yr^{-1}$ resulting in a power-law index of $\eta = -0.52$ and therewith a gradually decreasing SFH over time in the power-law-η model. The delayed-τ model yields a star formation time-scale of $\tau = 4.1$ Gyr. Thus, the MW is consistent with galaxies on the main sequence of star-forming galaxies by Speagle et al. (2014) which have star formation time-scales in the range of $3.5 \lesssim \tau/\mathrm{Gyr} \lesssim 4.5$ (Kroupa et al. 2020).

The LMC and M33 (Triangulum) galaxy have $M_* = 1.6 \times 10^9\,M_\odot$ and $2.5 \times 10^9\,M_\odot$ and $SFR_0 = 0.3\,M_\odot\,yr^{-1}$ and $0.5\,M_\odot\,yr^{-1}$, respectively. Therefore, both galaxies have a very similar increasing SFH in the delayed-τ and power-law-η SFH model (Fig. 4). Indeed, Javadi et al. (2017) measured the SFH across the entire disc of M33 and found that the SFR increased from $\approx 0.04\,M_\odot\,yr^{-1}$ up to $\approx 0.5\,M_\odot\,yr^{-1}$ over the last 10 Gyr with a local minimum of $\approx 0.06\,M_\odot\,yr^{-1}$ at a lookback time of ≈ 2.4 Gyr (see their fig. 6). We derived an SFR of $0.12\,M_\odot\,yr^{-1}$ (delayed-τ) and $0.11\,M_\odot\,yr^{-1}$ (power-law-η) at a lookback time of 10 Gyr, which is about three times higher than measured by Javadi et al. (2017). A possible explanation for these differences could be that the SFH of M33 is likely affected by interactions with M31. Such dynamical effects have not been taking account by our SFH models. Similarly, the MCs have an SFH which is influenced by their mutual gravitational interaction (Weisz et al. 2013) and encounters with the MW. In particular, the SFH of the MCs increased over the last 3.5 Gyr (fig. 5 of Weisz et al. 2013 and fig. 2 of Massana et al.

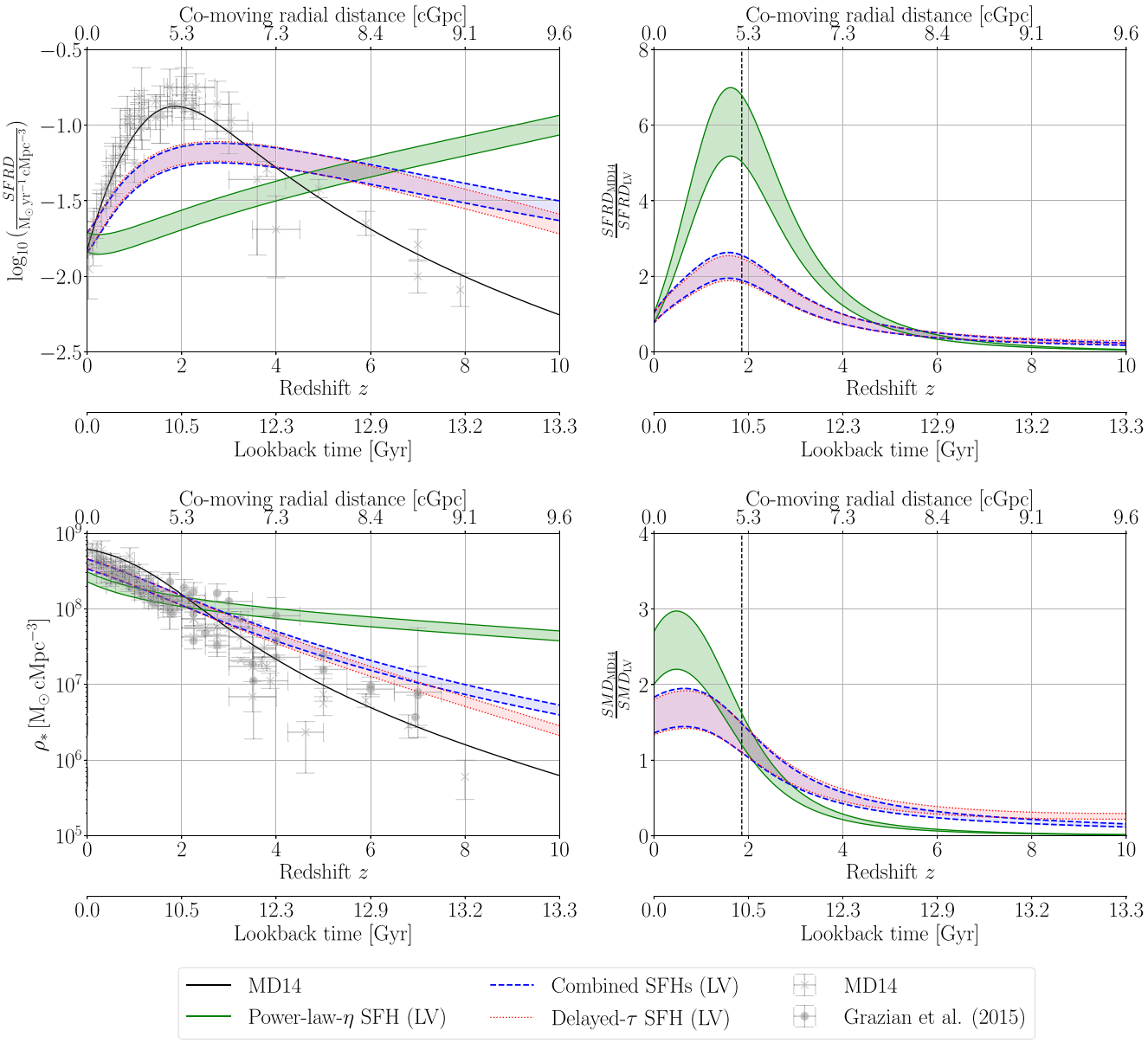

Figure 5. The SFRD (top panels) and SMD (bottom panels) over redshift and lookback time (bottom x-axis) and co-moving radial distance (top x-axis). Top left: The black solid curve shows the best-fitting function of MD14 (see their equation 15 and equation 1 in Section 1) to the FUV and IR measurements (grey crosses) as shown in their fig. 9 and listed in their table 1. The red dotted and green solid curves show the cosmic SFRDs as deduced from the LV galaxies assuming the delayed-τ and power-law-η SFH model, respectively. The blue dashed line is the combined SFH model, which adopts the delayed-τ for galaxies with $M_* \geq 10^{10}\,M_\odot$ and power-law-η SFH model for galaxies with $M_* < 10^{10}\,M_\odot$. The lower and upper limits of the SFRDs are given by equations (4) and (5), respectively. Top right: Ratio between the cosmic SFRD measured by MD14 (their equation 15) and the SFRD of the LV. The black dashed vertical line marks the peak of the Lilly–Madau plot at $z = 1.86$. Bottom left: SMD deduced from the measured SFRD by MD14 and the SFH of the LV assuming the delayed-τ (red dotted), power-law-η (green solid), and our combined (blue dashed) SFH models. The grey crosses and circles are observations by MD14 and Grazian et al. (2015), who assume a recycling factor of $R = 0.27$ and $R = 0.28$, respectively. These data are taken from table 2 of MD14 and table 2 of Yu & Wang (2016). The derivation of the SMDs assumes $R = 0.23$ (Section 2.5) in order to be consistent with the analysis of Kroupa et al. (2020) but this difference with the observations is negligible without changing the interpretation of the results. Bottom right: Ratio between the cosmic SMD deduced from MD14 and the LV.

2022), which is likely caused by star formation triggering during interactions between the MCs–MW system.

4.2 Caveats of the adopted SFH parametrization and outlooks

The parametrization of the galactic SFHs by the delayed-τ (Section 2.2) and power-law (Section 2.3) model come along with some caveats as discussed in the following. The SFRs given by the power-law SFH model diverge to infinity at $t = t_{\rm start}$ for a power-law index of $\eta < 0$ which fails in describing the rising part of the SFH at early galaxy evolution (Reddy et al. 2012; Carnall et al. 2019). This in turn affects the general slope of the SFHs (Fig. 4) and yields too high SFRDs and SMDs at redshifts $z \gtrsim 6$ (see the left-hand panels of Fig. 5) being in disagreement with the observations.

The delayed-τ SFH model accounts for rising star formation during early stages of galaxy formation but also allows for the description of gradually increasing SFHs by allowing negative values of τ (equation 8) providing therewith a better description of galaxy evolution. Consequently, this parametrization yields to lower cosmic SFRDs and SMDs compared to the power-law model. According to Fig. 3, the majority of star-forming LV galaxies with $\mathrm{SFR}_0 \geq 10^{-3}\,\mathrm{M}_\odot\,\mathrm{yr}^{-1}$ and $M_* \lesssim 10^{10}\,\mathrm{M}_\odot$ have an almost constant SFH over a time-scale of 13.6 Gyr (see also Kroupa et al. 2020 for a more extended discussion). The combined SFH model (Section 2.4) broadly accounts for that by adopting the delayed-τ model for galaxies with $M_* \geq 10^{10}\,\mathrm{M}_\odot$ and power-law-η model for galaxies with $M_* < 10^{10}\,\mathrm{M}_\odot$. The cosmic SFRDs and SMDs derived from the combined model only slightly differs from the delayed-τ model as the low-mass galaxies make only a small contribution to the SFRDs. More observables e.g. metallicity and chemical composition to fit the model parameters would be required. Unfortunately, the metallicities of the LV galaxies are not listed in the Catalogue of Neighbouring Galaxies (Karachentsev et al. 2004, 2013). Chemical galaxy evolution models (e.g. Yan, Jerabkova & Kroupa 2019; Gjergo et al. 2023) along with metallicity measurements would pin down further the SFH of LV galaxies.

Another method to reconstruct the evolution of the local SFRD would be to derive the SFHs of LV galaxies using colour magnitude diagrams as performed e.g. by Weisz et al. (2014) for Local Group (LG) dwarfs. Such analysis would be required to affirm the tension between the local and global cosmic SFRDs.

Some studies argued that the cosmic SFRD can be described by a lognormal SFH (e.g. Behroozi, Wechsler & Conroy 2013; Gladders et al. 2013; Abramson et al. 2016) which is typically parametrized by a normalization constant, the logarithmic delay time, and the star formation time-scale. Because of these three unknown parameters, the lognormal SFH of LV galaxies cannot be just reconstructed by their present-day SFRs and stellar masses as presented in this study. In fact, Carnall et al. (2019) parametrized the SFHs of galaxies in the spectroscopic redshift range $0.05 < z < 0.08$ of the Galaxy and Mass Assembly (GAMA) Survey (Driver et al. 2009, 2016) of DR3 (Baldry et al. 2018). Interestingly, they showed that the derived SFRDs assuming the exponentially declining and delayed-τ but also the lognormal and double power-law SFH models (see their section 2) are inconsistent with the Lilly–Madau plot of MD14. We discuss this further in the following section.

4.3 Constraints on the matter homogeneity

The LV has an SFRD of $0.014 - 0.019\,\mathrm{M}_\odot\,\mathrm{yr}^{-1}\,\mathrm{Mpc}^{-3}$ (Section 2.1.2) being therewith in agreement with the measurements by MD14. Calculating the SFRD of the LG environment by selecting only galaxies with $D < 1.5\,\mathrm{Mpc}$ gives a much higher value of $0.22 - 0.29\,\mathrm{M}_\odot\,\mathrm{yr}^{-1}\,\mathrm{Mpc}^{-3}$. This is because the LG (i.e. the MW and M31 galaxies with their surrounding dwarf galaxies) forms an overdensity within the LV as evident e.g. in the figs 1 and 2 of Karachentsev & Telikova (2018).

Kroupa et al. (2020) reported that the majority of galaxies located in the LV has a constant SFH over a time-scale of $t_{\mathrm{sf}} = 12$ Gyr. As the global co-moving SFRD increases from the present time up to the Lilly–Madau peak at $z = 1.86$ by a factor of 8.9 (MD14), the findings by Kroupa et al. (2020) raise the question if the SFH of the LV is consistent with the global SFH of the Universe. Supplementing their analysis, we deduce the evolution of the SFRD by reconstructing the cosmic SFH of LV galaxies. We found that the SFHs implied from the LV galaxies systematically underestimate the SFRDs at $z \lesssim 3$ and overestimates the SFRDs at $z \gtrsim 6$ as in comparison to those of MD14. In particular, the SFRD at the peak of the Lilly–Madau plot is 2.16 ± 0.32 and 5.90 ± 0.88 times lower in the case of the delayed-τ and power-law-η SFH model, respectively. The combined SFH model underestimates the SFRD by a factor of 2.22 ± 0.33 at $z = 1.86$. Thus, the SFHs of galaxies located in the LV disagree with the expectations from the Lilly–Madau plot.

Similar conclusions have been reached by Carnall et al. (2019) who parametrized the SFH of galaxies in the redshift range of $0.05 < z < 0.08$ from the GAMA Survey (Section 4.2). They derived a peak of the SFRD with a value of $\approx 0.05\,\mathrm{M}_\odot\,\mathrm{yr}^{-1}\,\mathrm{cMpc}^{-3}$ at $z \approx 0.4$ (see their fig. 10). While the maximum value is similar to our results, the peak appeared at much later times. In a companion study, Leja et al. (2019) applied non-parametric SFH models, which disagrees with the shape of the cosmic SFRD evolution suggested by MD14 (left-hand panel of fig. 13).

The SFH and the stellar mass growth are physically connected (Section 2.5) such that the disagreement between the local and global SFHs is also evident in the cosmic SMDs deduced from the SFRDs. The SMD derived from the local SFHs is up to 1.67 ± 0.25 (delayed-τ SFH model), 1.70 ± 0.25 (combined SFH model), and 2.59 ± 0.39 (power-law-η SFH model) times lower at $z \lesssim 2$ and systematically higher at $z \gtrsim 3$ than implied by MD14. Interestingly, several studies reported an inconsistency between the observed SMD and SFRD over cosmic time (e.g. Hopkins & Beacom 2006, 2008; Wilkins, Trentham & Hopkins 2008; Madau & Dickinson 2014; Grazian et al. 2015; Leja et al. 2015; Tomczak et al. 2016; Yu & Wang 2016). For example, Yu & Wang (2016) found that the observed SFRD by MD14 is by a factor of about 2 higher than the SFH derived from the observed SMD (Madau & Dickinson 2014; Grazian et al. 2015). The reason is not understood yet but it has been proposed that a top-heavy or bottom-light IMF could alleviate or even resolve the discrepancy (Yu & Wang 2016). The affect of a varying IMF on the Lilly–Madau plot in the context of the integrated-galactic IMF (IGIMF, Kroupa & Weidner 2003) has been studied by Chruślińska et al. (2020) but also a correction of the SMD would be required for a direct comparison. Investigating the effect of a varying IMF on the present-day and present-day averaged SFR would be valuable but is beyond the scope of this work.

The SMD derived from the LV assuming the delayed-τ and combined SFH model agrees much better with the observed SMD at $z \lesssim 2$ compared with the power-law model but is still systematically higher at $z \gtrsim 2$. Upcoming observations of high-redshift galaxies by the *JWST* could potentially increase the observed SMD at $z \gtrsim 5$ alleviating therewith this discrepancy.

The tension between the local and global SFHs could be caused by several reasons. First of all, the measurements of the LV could have a systematic error by overestimating the present-day SFRs or underestimating the stellar masses (see also section 4 of Kroupa et al. 2020). This seems to be unlikely because the spatial proximity of the LV to the MW should provide access to reliable and model-independent galaxy data and Carnall et al. (2019) also derived lower SFRDs than MD14 based on the GAMA Survey. Alternatively, the SFRD given by Madau & Dickinson (2014) could be systematically overestimated. However, the measured SFRDs especially at high redshifts of $z \gtrsim 1$ should rather be treated as lower instead of upper limits because of the potential non-detection of low-surface-brightness galaxies (Kim et al. 2022) and high-redshift galaxies (e.g. Castellano et al. 2023; Helton et al. 2023).

Secondly, the assumed parametrization of the applied SFH models may be inadequate to describe galaxy evolution. Speagle et al. (2014)

showed that the delayed-τ model provides an accurate description of the SFHs of galaxies, which strictly follow the main sequence of star-forming galaxies (see their figs 9 and 10). Kroupa et al. (2020) argued that the power-law-η model parametrizes the SFH of LV galaxies (see their section 3.3). Therefore, the combined SFH model should provide a reasonable parametrization of galaxy evolution. Modelling the SFH of all galaxies with the power-law-η model conflicts with the observed SMD (see the bottom left panel of 5).

Thirdly, the LV is not a representative sample of the observed Universe as discussed in section 4 of Kroupa et al. (2020). As pointed out by Peebles & Nusser (2010), the spatial arrangement of major galaxies in a sphere with $D < 8$ Mpc disagrees with the hierarchical structure formation of the ΛCDM framework. Furthermore, the LV is embedded in a local void, which is evident across the entire electromagnetic spectrum ranging from the radio to the X-ray regime (e.g. Maddox et al. 1990; Zucca et al. 1997; Karachentsev 2012; Keenan, Barger & Cowie 2013; Rubart & Schwarz 2013; Rubart, Bacon & Schwarz 2014; Böhringer et al. 2015; Karachentsev & Telikova 2018; Böhringer, Chon & Collins 2020; Wong et al. 2022). For example, Karachentsev (2012) measured an average total matter density of $\Omega_{\rm m,loc} = 0.08 \pm 0.02$ for a sphere with 50 Mpc centred around the MW, which is about four times lower than the global value given by Planck Collaboration XIII (2016). The local Universe is underdense on even much larger scales. Keenan et al. (2013) found that the matter density is about two times lower than the cosmic mean density on a 300 cMpc radial scale. The density contrast increases between 300 and 600–800 cMpc by a factor of about 2 (see their fig. 11). This so-called KBC void contradicts the ΛCDM model at more than 5σ confidence (Haslbauer, Banik & Kroupa 2020), which predicts root-mean-square (rms) density fluctuations of only 3.2 per cent on a 300 Mpc scale. The evolution of galaxies located in underdense regions like the LV may be retarded compared to galaxies in overdensities (Douglass & Vogeley 2017).

Finally, the Lilly–Madau plot as quantitatively described by equation (1) is sensitive not only to SFRs but also to the number density of galaxies. Thus, the here reported tension could imply that the peak of the Lilly–Madau plot is mainly caused by an overdensity at $z \approx 1.86$, which corresponds to a co-moving radius distance of ≈ 5.1 cGpc. Interestingly, the evolution of the co-moving mass density of molecular gas in galaxies partially follows the shape of the Lilly–Madau plot (e.g. Decarli et al. 2016; Riechers et al. 2019; Walter et al. 2020). As star formation is mainly driven by molecular gas, the Lilly–Madau plot could be therefore the consequence of the underlying molecular gas density. This would be consistent with an overdensity at $z \approx 2$ since the matter field should also be evident in the gas component.

Although this leads to an entirely new interpretation of the Lilly–Madau peak, indications of a significant overdensity on very large scales have been reported by several studies (e.g. Horváth, Hakkila & Bagoly 2014; Horváth et al. 2015, 2020; Migkas et al. 2021; Secrest et al. 2022). Inhomogeneities in the matter field affect the measurements of cosmological parameters as they change the motion of galaxies (Haslbauer et al. 2020). Remarkably, there is observationally evidence that H_0 decreases up to $z \approx 1.7$ in the SN data (figs 2 and 3 of Jia, Hu & Wang 2023, but see also Krishnan et al. 2020 and Dainotti et al. 2021). Measuring H_0 from six gravitationally lensed quasars with lens redshifts between $z = 0.295$ and 0.745, Wong et al. (2020) obtained that H_0 decreases with an increasing lens redshift but only with a significance of 1.9σ (see their fig. A1). In this scenario, the Hubble tension is not only caused by the 300 cMpc scale KBC void (Haslbauer et al. 2020) but is rather the consequence of an $\approx$5.1 cGpc scale inhomogeneity.

Further evidence for large-scale matter flows and inhomogeneities comes from Migkas et al. (2021), who reported bulk flows with velocities of $\approx 900\,{\rm km\,s^{-1}}$ to at least 500 cMpc scales from galaxy cluster data. Secrest et al. (2022) found that the dipole amplitude and direction of distant radio galaxies and quasars significantly differ from the cosmic microwave background (CMB) dipole violating the cosmological principle with a significance of 5.1σ. The authors argue that this favours the existence of an overdensity on large scales at Galactic coordinates of $(l, b) = (217^\circ \pm 10^\circ, +20^\circ \pm 7^\circ)$. Interestingly, the Hercules–Corona Borealis Great Wall as observed by an excess of gamma-ray bursts (GRBs) between $z = 1.6$ and 2.1 (Horváth et al. 2014, 2015, 2020) coincides with the Lilly–Madau peak at $z = 1.86$. However, these GRBs are observed at the second, third, and fourth Galactic quadrants and not towards $(l, b) = (217^\circ \pm 10^\circ, +20^\circ \pm 7^\circ)$.

Large-scale anisotropies in the morphological distribution of galaxies have been studied by Javanmardi & Kroupa (2017) who showed that the Northern hemisphere has more late-type galaxies, while the Southern hemisphere has more early-type galaxies. Notably, the Southern ecliptic hemisphere has also more power in the CMB than the Northern ecliptic hemisphere (Eriksen et al. 2004; Schwarz et al. 2016).

A large-scale density variation could potentially resolve the so-called σ_8 problem, which states that the present rms matter fluctuation averaged over a sphere with a radius of $8\,h^{-1}$ Mpc is locally lower ($\sigma_8 = 0.785 \pm 0.029$; Abbott et al. 2023) than on global scales ($\sigma_8 = 0.8159 \pm 0.0086$; Planck Collaboration XIII 2016). This is because density fluctuations within a larger scale underdensity could be suppressed making the Universe to appear locally 'less clumpy' than predicted by the ΛCDM model.

The accelerated expansion of the Universe could also be an apparent effect due to large-scale inhomogeneities that grow with cosmic time (Wiltshire 2007a, b, 2009, 2019).

More precise observations of the matter distribution are required to test the here proposed hypothesis that the peak of the Lilly–Madau peak could be the imprint of a large-scale density variation. Directional anisotropies in the Lilly–Madau plot could be caused by different density contrasts at different sky directions. Gpc-large-scale matter inhomogeneities would violate the cosmological principle of the ΛCDM model, which predicts an upper limit to the scale of homogeneity of about $260\,h^{-1}$ Mpc, being homogeneous on larger scales (Yadav, Bagla & Khandai 2010). However, several observations indeed question the scale of homogeneity of the ΛCDM model as outlined above (e.g. Gott et al. 2005; Clowes et al. 2012; Keenan et al. 2013; Horváth et al. 2014; Javanmardi et al. 2015; Javanmardi & Kroupa 2017; Colin et al. 2019; Haslbauer et al. 2020; Migkas et al. 2020, 2021; Secrest et al. 2021, 2022; Aluri et al. 2023). Interestingly, Milgromian (MOND; Milgrom 1983) cosmological models with a non-zero cosmological constant also predict large-scale homogeneity on a scale of several hundred Mpc (Sanders 1998).

5 CONCLUSION

Supplementing the analysis of Kroupa et al. (2020), we investigated the cosmological implications of the SFHs of galaxies located in the LV. We reconstructed the SFHs with the delayed-τ (Section 2.2) and power-law-η (Section 2.3) models in order to calculate the SFRD of the LV over cosmic time. The near-constancy of the SFH of LV galaxies as reported by Kroupa et al. (2020) has implications for the Lilly–Madau plot, which shows that the SFRD increases from present time up to redshift $z = 1.86$ by a factor of about

9. While the local SFRD is consistent with MD14, the derived SFHs parametrized by the delayed-τ and power-law-η SFH models underestimate the cosmic SFRD at $z \lesssim 3$ and overestimate the SFRD at $z \gtrsim 6$. In particular, the SFRD is 2.16 ± 0.32 and 5.90 ± 0.88 times lower than measured at the peak of the Lilly–Madau plot at $z = 1.86$ if the delayed-τ and power-law-η SFH models are assumed, respectively. Combining both SFH models by adopting the delayed-τ model for galaxies with $M_* \geq 10^{10}\,\mathrm{M}_\odot$ and the power-law-η model for galaxies with $M_* < 10^{10}\,\mathrm{M}_\odot$ (Section 2.4) underestimates the SFRD by a factor of 2.22 ± 0.33 at $z = 1.86$. Several reasons for the disagreement between the local and global cosmic SFRDs such as measurement biases or parametrization of the SFHs have been discussed in Section 4.

In conclusion, we found that the derived SFHs of LV galaxies are in disagreement with the Lilly–Madau plot (see also Carnall et al. 2019; Leja et al. 2019 for the GAMA survey). As the cosmological SFH of the local Universe sets constraints on the matter homogeneity, the discrepancy could be caused by the local underdensity (Karachentsev 2012; Karachentsev & Telikova 2018) and/or the peak of the Lilly–Madau plot is the imprint of ≈5 cGpc-scale density variations at $z \approx 1.86$. Independent evidence of significant inhomogeneity on >100 Mpc scales is discussed in Section 4.3. Precise measurements of the SFH and the number counts of galaxies would be required to affirm such an interpretation of the Lilly–Madau peak.

ACKNOWLEDGEMENTS

The authors thank an anonymous referee for helpful suggestions improving the manuscript. Moritz Haslbauer acknowledges support from the European Southern Observatory (ESO) Early-Career Visitor Programme. The project has been discussed during the 'Jindřichův Hradec-meeting on stellar populations, gravitational dynamics and Milgromian-based cosmology' held at the Florian Palace in Jindřichův Hradec (Czech Republic). The authors acknowledge the Deutscher Akademischer Austauschdienst (DAAD) Eastern-European exchange programme for financial support and the Florian Palace for hosting this meeting.

DATA AVAILABILITY

The data underlying this article are available in the article. The physical parameters of galaxies located in the LV are taken from the updated version of the Catalogue of Neighbouring Galaxies (Karachentsev et al. 2004, 2013) as explained in Section 2.1.

REFERENCES

Abbott T. M. C. et al., 2023, Phys. Rev. D, 107, 023531
Abramson L. E., Gladders M. D., Dressler A., Oemler A., Jr, Poggianti B., Vulcani B., 2016, ApJ, 832, 7
Aluri P. K. et al., 2023, Classical and Quantum Gravity, 40, 094001
Baldry I. K. et al., 2018, MNRAS, 474, 3875
Baumgardt H., Makino J., 2003, MNRAS, 340, 227
Behroozi P. S., Wechsler R. H., Conroy C., 2013, ApJ, 770, 57
Böhringer H., Chon G., Bristow M., Collins C. A., 2015, A&A, 574, A26
Böhringer H., Chon G., Collins C. A., 2020, A&A, 633, A19
Carnall A. C., Leja J., Johnson B. D., McLure R. J., Dunlop J. S., Conroy C., 2019, ApJ, 873, 44
Castellano M. et al., 2023, ApJ, 948, L14
Chruślińska M., Jeřábková T., Nelemans G., Yan Z., 2020, A&A, 636, A10
Clowes R. G., Campusano L. E., Graham M. J., Söchting I. K., 2012, MNRAS, 419, 556
Cole S. et al., 2001, MNRAS, 326, 255
Colin J., Mohayaee R., Rameez M., Sarkar S., 2019, A&A, 631, L13
Cook D. O. et al., 2014, MNRAS, 445, 899
Dainotti M. G., De Simone B., Schiavone T., Montani G., Rinaldi E., Lambiase G., 2021, ApJ, 912, 150
Decarli R. et al., 2016, ApJ, 833, 69
Douglass K. A., Vogeley M. S., 2017, ApJ, 837, 42
Driver S. P. et al., 2009, Astron. Geophys., 50, 5.12
Driver S. P. et al., 2016, MNRAS, 455, 3911
Eriksen H. K., Hansen F. K., Banday A. J., Górski K. M., Lilje P. B., 2004, ApJ, 605, 14
Gjergo E. et al., 2023, ApJS, 264, 44
Gladders M. D., Oemler A., Dressler A., Poggianti B., Vulcani B., Abramson L., 2013, ApJ, 770, 64
Gott J. R. III, Jurić M., Schlegel D., Hoyle F., Vogeley M., Tegmark M., Bahcall N., Brinkmann J., 2005, ApJ, 624, 463
Grazian A. et al., 2015, A&A, 575, A96
Haslbauer M., Banik I., Kroupa P., 2020, MNRAS, 499, 2845
Helton J. M. et al., 2023, preprint (arXiv:2302.10217v1)
Hopkins A. M., Beacom J. F., 2006, ApJ, 651, 142
Hopkins A. M., Beacom J. F., 2008, ApJ, 682, 1486
Horvath I. et al., 2020, MNRAS, 498, 2544
Horváth I., Bagoly Z., Hakkila J., Tóth L. V., 2015, A&A, 584, A48
Horváth I., Hakkila J., Bagoly Z., 2014, A&A, 561, L12
Javadi A., van Loon J. T., Khosroshahi H. G., Tabatabaei F., Hamedani Golshan R., Rashidi M., 2017, MNRAS, 464, 2103
Javanmardi B., Kroupa P., 2017, A&A, 597, A120
Javanmardi B., Porciani C., Kroupa P., Pflamm-Altenburg J., 2015, ApJ, 810, 47
Jia X. D., Hu J. P., Wang F. Y., 2023, A&A, 674, A45
Karachentsev I. D., 2012, Astrophys. Bull., 67, 123
Karachentsev I. D., Kaisina E. I., 2013, AJ, 146, 46
Karachentsev I. D., Karachentseva V. E., Huchtmeier W. K., Makarov D. I., 2004, AJ, 127, 2031
Karachentsev I. D., Makarov D. I., Kaisina E. I., 2013, AJ, 145, 101
Karachentsev I. D., Telikova K. N., 2018, Astron. Nachr., 339, 615
Keenan R. C., Barger A. J., Cowie L. L., 2013, ApJ, 775, 62
Kim J. et al., 2022, preprint (arXiv:2212.14539v2)
Krishnan C. et al., 2020, Phys. Rev. D, 102, 103525
Kroupa P., 2001, MNRAS, 322, 231
Kroupa P., Haslbauer M., Banik I., Nagesh S. T., Pflamm-Altenburg J., 2020, MNRAS, 497, 37
Kroupa P., Jerabkova T., 2021, preprint (arXiv:2112.10788v1)
Kroupa P., Weidner C., 2003, ApJ, 598, 1076
Laporte N., Meyer R. A., Ellis R. S., Robertson B. E., Chisholm J., Roberts-Borsani G. W., 2021, MNRAS, 505, 3336
Leja J., Carnall A. C., Johnson B. D., Conroy C., Speagle J. S., 2019, ApJ, 876, 3
Leja J., van Dokkum P. G., Franx M., Whitaker K. E., 2015, ApJ, 798, 115
Lilly S. J., Le Fevre O., Hammer F., Crampton D., 1996, ApJ, 460, L1
Madau P., Dickinson M., 2014, ARA&A, 52, 415 (MD14)
Madau P., Ferguson H. C., Dickinson M. E., Giavalisco M., Steidel C. C., Fruchter A., 1996, MNRAS, 283, 1388
Madau P., Fragos T., 2017, ApJ, 840, 39
Madau P., Pozzetti L., Dickinson M., 1998, ApJ, 498, 106
Maddox S. J., Sutherland W. J., Efstathiou G., Loveday J., Peterson B. A., 1990, MNRAS, 247, 1P
Massana P. et al., 2022, MNRAS, 513, L40
McGaugh S. S., Schombert J. M., 2014, AJ, 148, 77
McGaugh S. S., Schombert J. M., Lelli F., 2017, ApJ, 851, 22
Migkas K., Pacaud F., Schellenberger G., Erler J., Nguyen-Dang N. T., Reiprich T. H., Ramos-Ceja M. E., Lovisari L., 2021, A&A, 649, A151
Migkas K., Schellenberger G., Reiprich T. H., Pacaud F., Ramos-Ceja M. E., Lovisari L., 2020, A&A, 636, A15
Milgrom M., 1983, ApJ, 270, 365
Peebles P. J. E., Nusser A., 2010, Nature, 465, 565
Pipino A., Lilly S. J., Carollo C. M., 2014, MNRAS, 441, 1444
Planck Collaboration XIII, 2016, A&A, 594, A13

Reddy N. A., Pettini M., Steidel C. C., Shapley A. E., Erb D. K., Law D. R., 2012, ApJ, 754, 25
Riechers D. A. et al., 2019, ApJ, 872, 7
Rubart M., Bacon D., Schwarz D. J., 2014, A&A, 565, A111
Rubart M., Schwarz D. J., 2013, A&A, 555, A117
Salpeter E. E., 1955, ApJ, 121, 161
Sanders R. H., 1998, MNRAS, 296, 1009
Schombert J., McGaugh S., Lelli F., 2019, MNRAS, 483, 1496
Schwarz D. J., Copi C. J., Huterer D., Starkman G. D., 2016, Class. Quantum Gravity, 33, 184001
Secrest N. J., von Hausegger S., Rameez M., Mohayaee R., Sarkar S., 2022, ApJ, 937, L31
Secrest N. J., von Hausegger S., Rameez M., Mohayaee R., Sarkar S., Colin J., 2021, ApJ, 908, L51
Speagle J. S., Steinhardt C. L., Capak P. L., Silverman J. D., 2014, ApJS, 214, 15
Tomczak A. R. et al., 2016, ApJ, 817, 118
Walter F. et al., 2020, ApJ, 902, 111
Weisz D. R., Dolphin A. E., Skillman E. D., Holtzman J., Dalcanton J. J., Cole A. A., Neary K., 2013, MNRAS, 431, 364
Weisz D. R., Dolphin A. E., Skillman E. D., Holtzman J., Gilbert K. M., Dalcanton J. J., Williams B. F., 2014, ApJ, 789, 148
Wilkins S. M., Trentham N., Hopkins A. M., 2008, MNRAS, 385, 687
Wiltshire D. L., 2007a, New J. Phys., 9, 377
Wiltshire D. L., 2007b, Phys. Rev. Lett., 99, 251101
Wiltshire D. L., 2009, Phys. Rev. D, 80, 123512
Wiltshire D. L., 2019, A&A, 624, A12
Wong J. H. W., Shanks T., Metcalfe N., Whitbourn J. R., 2022, MNRAS, 511, 5742
Wong K. C. et al., 2020, MNRAS, 498, 1420
Yadav J. K., Bagla J. S., Khandai N., 2010, MNRAS, 405, 2009
Yan Z., Jerabkova T., Kroupa P., 2019, A&A, 632, A110
Yu H., Wang F. Y., 2016, ApJ, 820, 114
Zucca E. et al., 1997, A&A, 326, 477

This paper has been typeset from a TEX/LATEX file prepared by the author.

APPENDIX E

Appendix: The Magellanic Clouds are very rare in the IllustrisTNG simulations

This chapter contains the appendix of the manuscript entitled "The Magellanic Clouds are very rare in the IllustrisTNG simulation" (Chapter 10) by **Moritz Haslbauer**, Indranil Banik, Pavel Kroupa, and HongSheng Zhao.

E.1 Effect of resolution

The distributions of $f_{\rm MCs}$ (Equation 10.1) and $\Omega_{\rm LMC}$ (Equation 10.3) of MCs analogues with $50\,{\rm kpc} \leq d_{\rm MW-LMC} \leq 100\,{\rm kpc}$ in the three low-resolution runs TNG50-2, TNG50-3, and TNG100-2 are shown in Figure E.1. The observed phase-space density of the MCs ($\log_{10}\left(f_{\rm MCs,obs}/\left[{\rm km^{-3}\,s^{3}\,kpc^{-3}}\right]\right) \approx -10.04$) is significantly higher than expected from the TNG simulations, which have $f_{\rm MCs}$ distributions with medians of $\log_{10}\left(f_{\rm MCs}/\left[{\rm km^{-3}\,s^{3}\,kpc^{-3}}\right]\right) = -14.07$ (TNG50-1), -12.83 (TNG50-2), -15.30 (TNG50-3; but this refers to only one data point), -13.92 (TNG100-1), -13.95 (TNG100-2), and -13.75 (TNG300-1), as visualized in the left panel of Figure E.2. Thus, TNG50-1, TNG100-1, TNG100-2, and TNG300-1 all have medians that cluster within the same region: $\log_{10}\left(f_{\rm MCs}/\left[{\rm km^{-3}\,s^{3}\,kpc^{-3}}\right]\right) \approx -14$ and $\Omega_{\rm LMC} \approx 2.7\,{\rm km\,s^{-1}\,kpc^{-1}}$. The highest resolution run TNG50-1 has an even lower median than the lower resolution run TNG50-2, implying that increasing the resolution does not increase the phase-space density of MCs analogues in the simulations. This conclusion is supported by the right panel of Figure E.2, which shows that the cumulative $f_{\rm MCs}$ distribution is very similar between different TNG runs. Moreover, the cumulative distribution of TNG50-1 is shifted to even lower values than in the lower resolution runs TNG100-1 and TNG300-1, which increases therewith the tension in TNG50-1. Consequently, we conclude that the discrepancy between the observed and simulated phase-space configuration of the MCs is likely not caused by the numerical limitations of the assessed TNG50-1 run – if anything, improving the resolution worsens the problem.

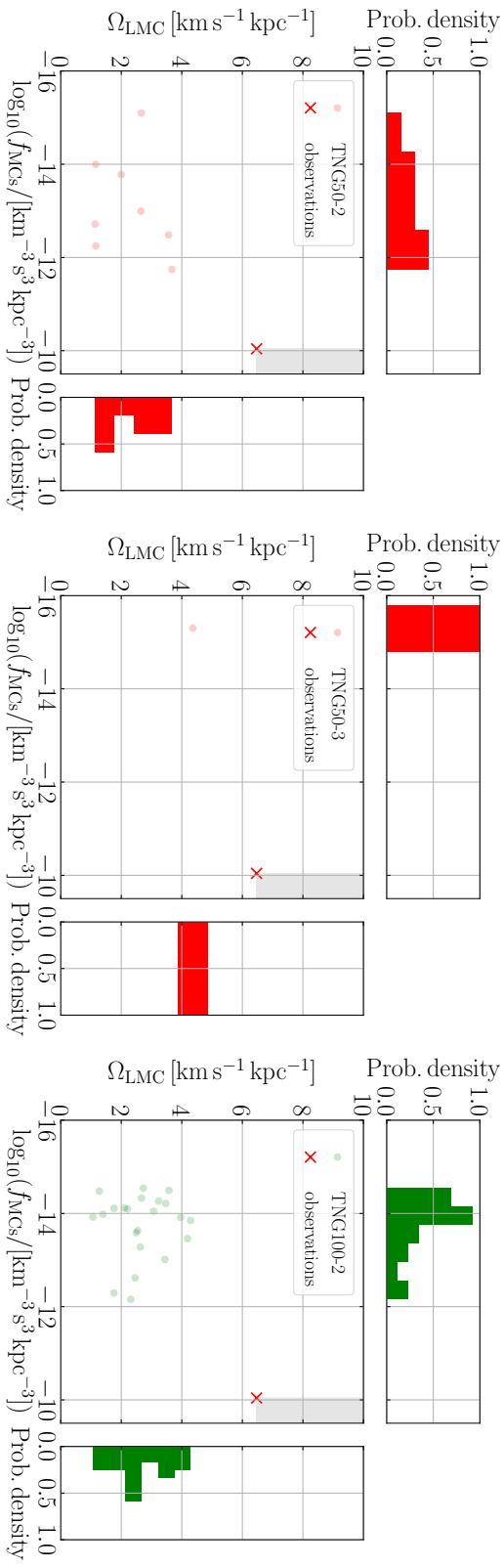

Figure E.1: Same as Figure 10.2 but for the low-resolution runs TNG50-2 (8 objects; left), TNG50-3 (1 object; middle), and TNG100-2 (22 objects; right).

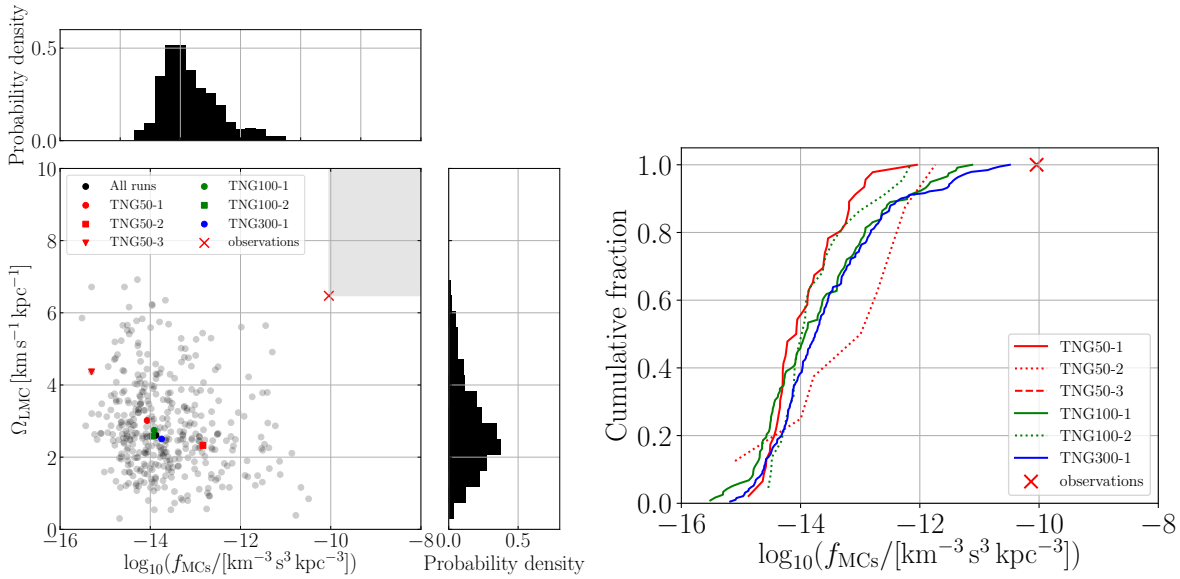

Figure E.2: *Left panel*: Similar to Figure 10.2, but here the black dots show the results of TNG50-1 (46 objects), TNG50-2 (8 objects), TNG50-3 (one object), TNG100-1 (118 objects), TNG100-2 (22 objects), and TNG300-1 (191 objects). The colored symbols mark the medians of the different resolution runs: $\log_{10}\left(f_{\rm MCs}/\left[{\rm km}^{-3}\,{\rm s}^3\,{\rm kpc}^{-3}\right]\right) = -14.07$ (TNG50-1), -12.83 (TNG50-2), -15.30 (TNG50-3), -13.92 (TNG100-1), -13.95 (TNG100-2), and -13.75 (TNG300-1). *Right panel:* Cumulative distribution of the specific phase-space density of the MCs ($f_{\rm MCs}$; Equation 10.1). In both panels, the red cross shows the observed value of $f_{\rm MCs,obs} = 9.10 \times 10^{-11}$ km^{-3} s^3 kpc^{-3}.

E.2 Different selection criteria

In Section 10.3.1 and Appendix E.1, we focused only on MCs analogues with 50 kpc $\leq d_{\rm MW-LMC} \leq$ 100 kpc. Including also MW-MCs systems with $d_{\rm MW-LMC} > 100$ kpc and thus requiring only that 50 kpc $\leq d_{\rm MW-LMC} \leq 250$ kpc yields a total sample of 1193 systems in the six TNG runs, as visualized in Figure E.3. Only one out of these analogues has $f_{\rm MCs} \geq f_{\rm MCs,obs}$ – this system is found in the TNG100-1 run. Taking into account that TNG100-1 has 431 systems with $d_{\rm MW-LMC} \geq 50$ kpc, this would correspond to a 3.05σ tension. The null detection in the TNG50-1 (143 systems) and TNG300-1 (521 systems) runs implies $> 2.27\sigma$ and $> 3.10\sigma$ tension, respectively. Combining the simulations yields a frequency of 1/1095 (3.32σ).

Using the initial sample of MCs analogues in which we require merely that $d_{\rm MW-LMC} \leq 250$ kpc, we find that 3 out of 1312 analogues in the six TNG runs fulfill the phase-space density criterion (3.37σ). One of these analogues is found in TNG100-1 (out of 454 systems) and two in TNG300-1 (out of 601 systems), implying a 3.06σ and 3.14σ tension, respectively. The null detection in TNG50-1 (147 systems) gives a lower limit of 2.71σ.

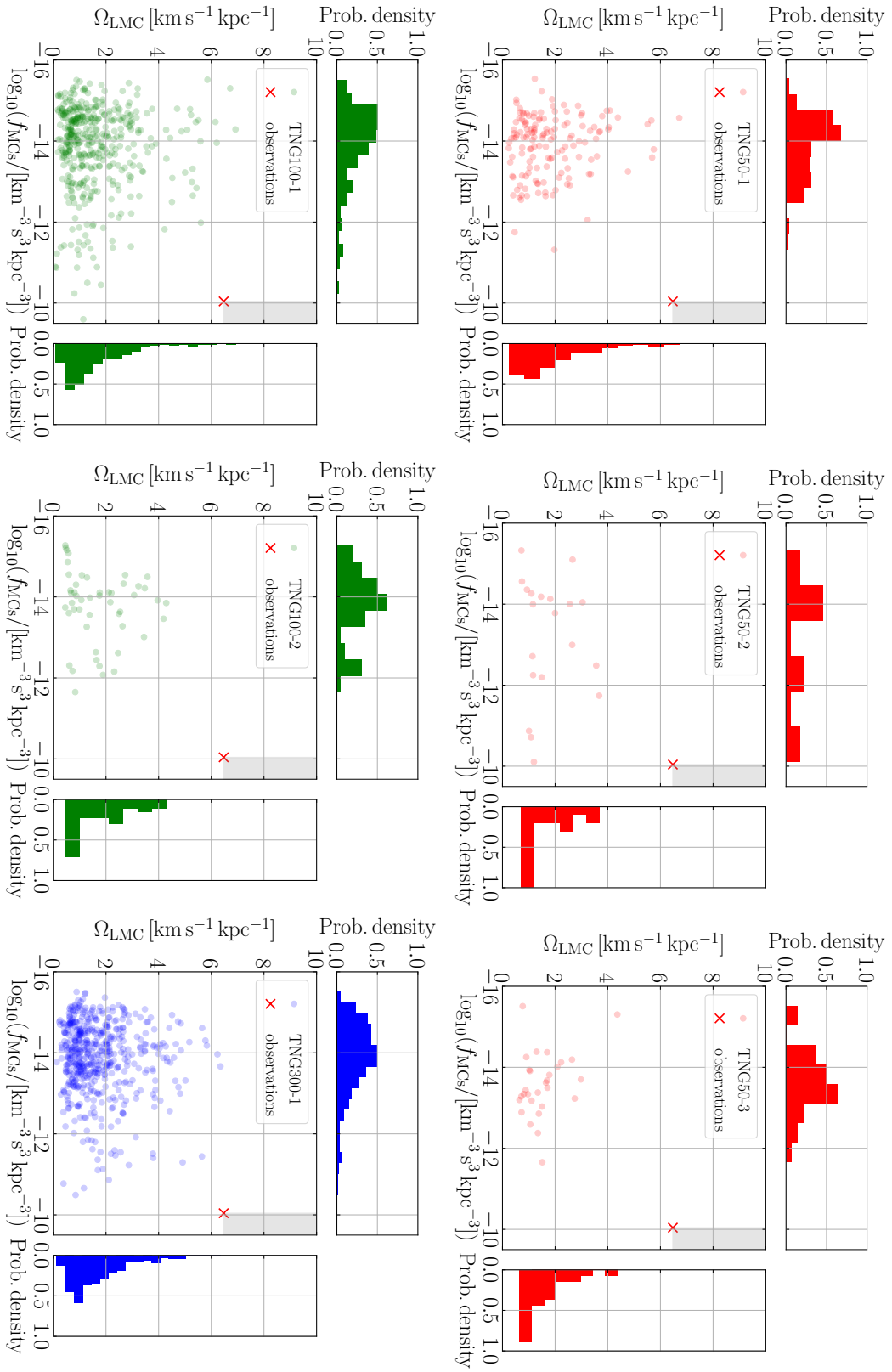

Figure E.3: Similar to Figure 10.2, but for analogues to the MCs with $d_{\rm MW-LMC} \geq 50\,$kpc. None of the 143 (TNG50-1), 20 (TNG50-2), 29 (TNG50-3), 431 (TNG100-1), 49 (TNG100-2), or 521 (TNG300-1) analogues have $f_{\rm MCs} \geq f_{\rm MCs,obs}$ and $\boldsymbol{\Omega}_{\rm LMC} \geq \boldsymbol{\Omega}_{\rm LMC,obs}$. One of the 1193 analogues has $f_{\rm MCs} \geq f_{\rm MCs,obs}$.

APPENDIX F

Appendix: The effect of the environment-dependent stellar initial mass function on the photometric properties of star-forming galaxies

This chapter contains the appendix of the manuscript entitled "The effect of the environment-dependent stellar initial mass function on the photometric properties of local star-forming galaxies" (Chapter 12) by **Moritz Haslbauer**, Zhiqiang Yan, Tereza Jerabkova, Pavel Kroupa, Akram Hasani Zonoozi, and Eda Gjergo.

F.1 Mass-to-light ratios in different photometrics bands for a canonical IMF

The current version of the photGalIMF code only includes the Ks-band of the 2Mass sky survey M. Cohen, Wheaton and Megeath (2003), the $K_{3.6\mu m}$-band of the Spitzer survey (see e.g. Groenewegen 2006), and the V-band of the UBVRIJHK photometric system (Bessell 1990; Maíz Apellániz 2006) as summarized in Figure F.1 by showing the present-day M/L in dependence of the metallicty for a canonical IMF. The present-day Ks- and $K_{3.6\mu m}$-band M/L values decrease with higher metallicity while the V-band M/L values show the opposite behaviour by increasing with higher metallicity. This is because of the luminosity during the TP-AGB (McQuinn et al. 2019).

F.2 gwIMF for high metallicities

The gwIMFs of metal-rich galaxies with [Z]$\geq$ 0.4 are presented in Figure F.2. The IGIMF-2021 formulation produces very top-light and bottom-heavy gwIMFs for [Z]$\geq$ 0.8. This is mainly because of the extrapolated the variation of the power-law indices α_1 and α_2 (Equation (12.4); these have not been constrained by very metal-rich galaxies).

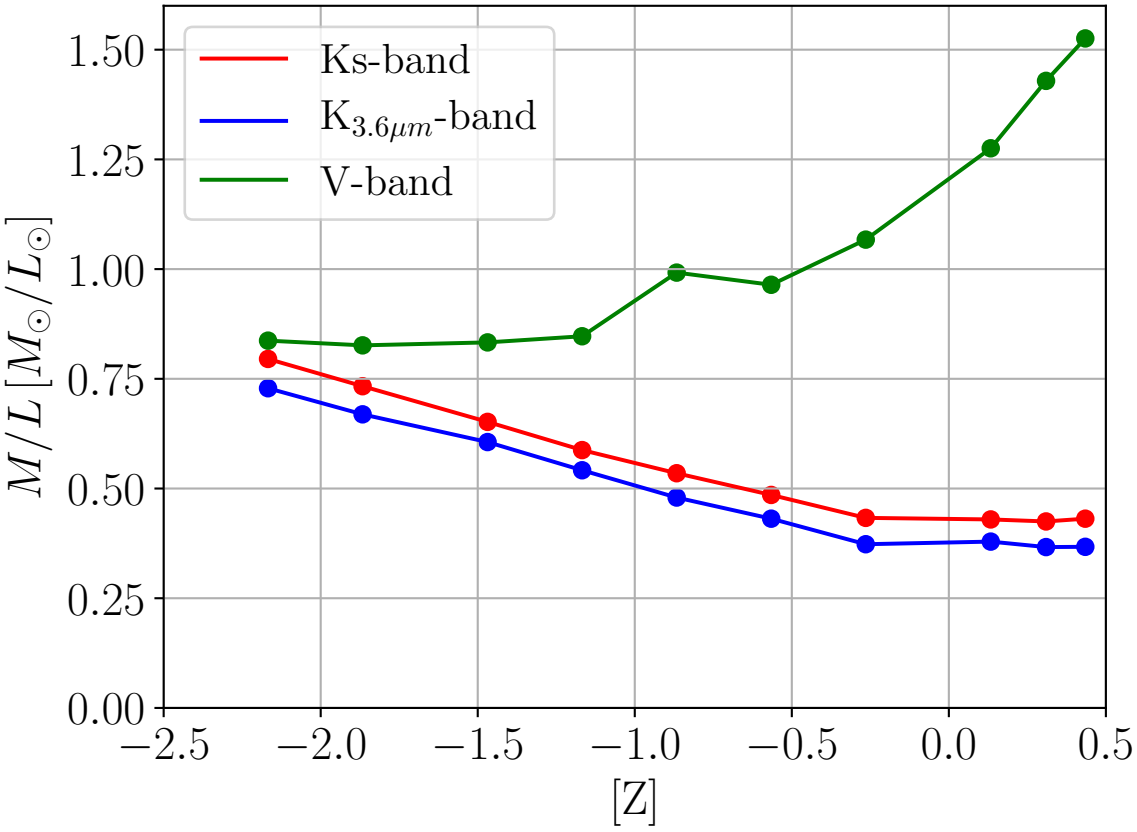

Figure F.1: Mass-to-light ratios in the Ks- (blue), $K_{3.6\mu m}$- (red), and V- (green) band evaluated at 13.6 Gyr in dependence of the metallicity assuming constant SFRs and metallicities for a canonical IMF (Kroupa 2001).

F.3 Fitting parameters

Table F.1 lists the polynomial coefficients for different metallicities of the fitting functions presented in Sect. 12.2.3.

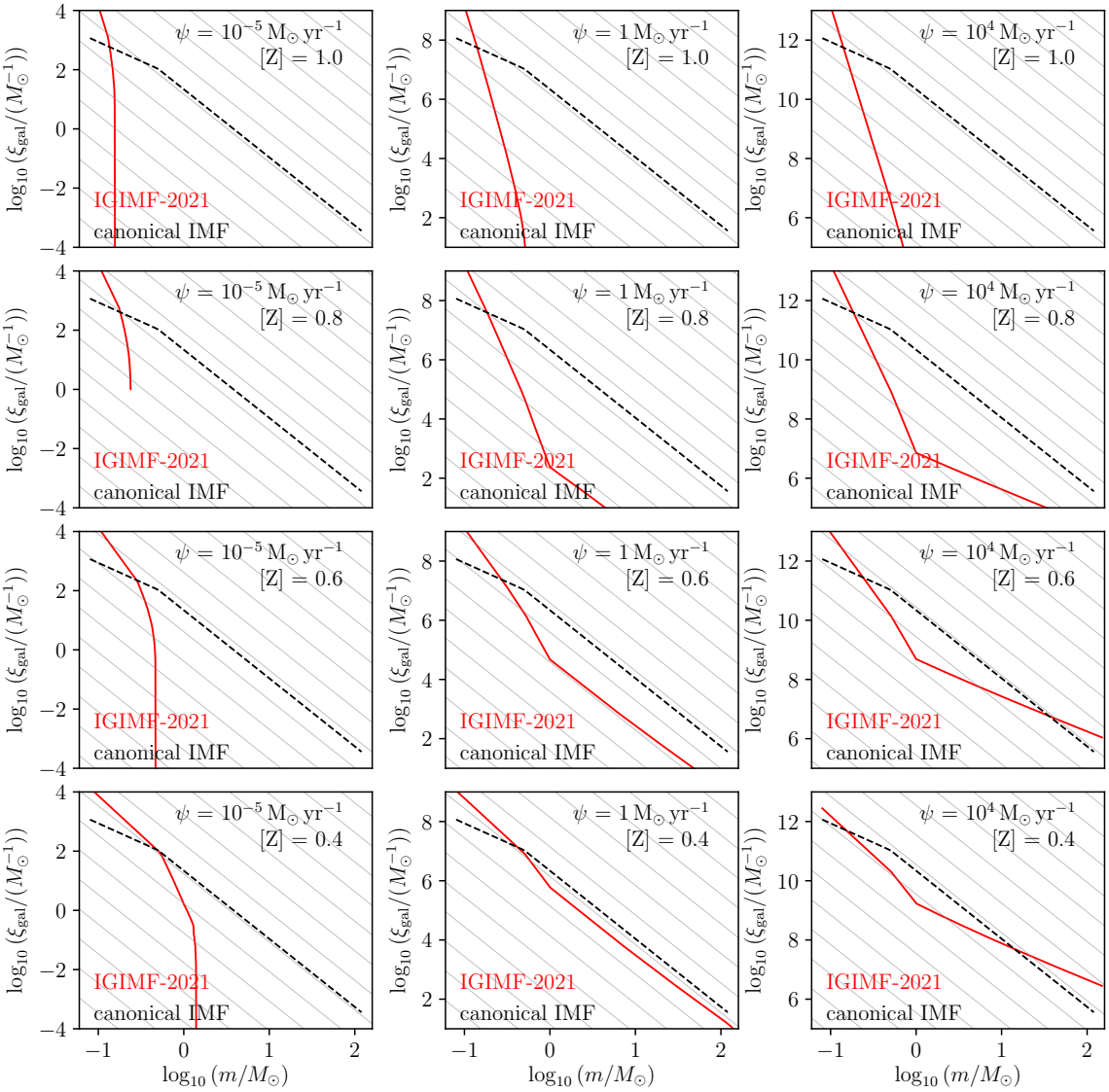

Figure F.2: Same as Figure 12.1 but showing gwIMFs for high metallicities of [Z]≥ 0.4.

Relation	IGIMF	Z	[Z]*	a	b	c	d	e	f
SFR–Hα	2021	9.0×10^{-5}	−2.20	2.2238×10^{-5}	1.2128×10^{-4}	-1.5783×10^{-3}	2.0957×10^{-2}	7.3060×10^{-1}	-5.7930×10^{-1}
(Equation (12.16))	2021	9.6×10^{-5}	−2.17	2.2364×10^{-5}	1.2240×10^{-4}	-1.5890×10^{-3}	2.0895×10^{-2}	7.3092×10^{-1}	-5.7876×10^{-1}
	2021	0.00019	−1.87	2.2504×10^{-5}	1.3788×10^{-4}	-1.5479×10^{-3}	2.0022×10^{-2}	7.2795×10^{-1}	-5.4425×10^{-1}
	2021	0.00048	−1.47	1.8490×10^{-5}	1.1702×10^{-4}	-1.2605×10^{-3}	2.0782×10^{-2}	7.2005×10^{-1}	-5.0532×10^{-1}
	2021	0.00096	−1.17	1.9246×10^{-5}	1.3371×10^{-4}	-1.2517×10^{-3}	1.9954×10^{-2}	7.1826×10^{-1}	-4.7476×10^{-1}
	2021	0.0038	−0.57	1.5919×10^{-5}	1.2457×10^{-4}	-9.7997×10^{-4}	2.0551×10^{-2}	7.0787×10^{-1}	-4.1389×10^{-1}
	2021	0.0078	−0.26	1.9228×10^{-5}	1.8041×10^{-4}	-1.1073×10^{-3}	1.8449×10^{-2}	7.0538×10^{-1}	-3.4245×10^{-1}
	2021	0.0096	−0.17	1.7296×10^{-5}	1.6136×10^{-4}	-9.4291×10^{-4}	1.9413×10^{-2}	7.0002×10^{-1}	-3.2063×10^{-1}
	2021	0.0142	0.0	2.3876×10^{-5}	2.4911×10^{-4}	-1.2368×10^{-3}	1.6128×10^{-2}	7.0077×10^{-1}	-2.5619×10^{-1}
	2021	0.019	0.13	2.0135×10^{-5}	2.3304×10^{-4}	-8.7799×10^{-4}	1.7239×10^{-2}	6.8696×10^{-1}	-2.0074×10^{-1}
	2021	0.029	0.31	1.8947×10^{-5}	2.4694×10^{-4}	-5.3669×10^{-4}	1.8314×10^{-2}	6.6154×10^{-1}	-4.9672×10^{-2}
	2021	0.038	0.43	2.1314×10^{-5}	2.7855×10^{-4}	-3.6256×10^{-4}	1.9320×10^{-2}	6.3030×10^{-1}	1.4218×10^{-1}
	2021	0.040	0.45	1.5181×10^{-5}	1.9780×10^{-4}	-6.5759×10^{-5}	2.2975×10^{-2}	6.2133×10^{-1}	1.6575×10^{-1}
$\Phi - L_{\mathrm{H}\alpha}$	2021	9.0×10^{-5}	−2.20	2.2238×10^{-5}	1.2128×10^{-4}	-1.5783×10^{-3}	2.0957×10^{-2}	-2.6940×10^{-1}	-4.7893×10^{-1}
(Equation (12.18))	2021	9.6×10^{-5}	−2.17	2.2364×10^{-5}	1.2240×10^{-4}	-1.5890×10^{-3}	2.0895×10^{-2}	-2.6908×10^{-1}	-4.7839×10^{-1}
	2021	0.00019	−1.87	2.2504×10^{-5}	1.3788×10^{-4}	-1.5479×10^{-3}	2.0022×10^{-2}	-2.7205×10^{-1}	-4.4388×10^{-1}
	2021	0.00048	−1.47	1.8490×10^{-5}	1.1702×10^{-4}	-1.2605×10^{-3}	2.0782×10^{-2}	-2.7995×10^{-1}	-4.0495×10^{-1}
	2021	0.00096	−1.17	1.9246×10^{-5}	1.3371×10^{-4}	-1.2517×10^{-3}	1.9954×10^{-2}	-2.8174×10^{-1}	-3.7439×10^{-1}
	2021	0.0038	−0.57	1.5919×10^{-5}	1.2457×10^{-4}	-9.7997×10^{-4}	2.0551×10^{-2}	-2.9213×10^{-1}	-3.1351×10^{-1}
	2021	0.0078	−0.26	1.9228×10^{-5}	1.8041×10^{-4}	-1.1073×10^{-3}	1.8449×10^{-2}	-2.9462×10^{-1}	-2.4208×10^{-1}
	2021	0.0096	−0.17	1.7296×10^{-5}	1.6136×10^{-4}	-9.4291×10^{-4}	1.9413×10^{-2}	-2.9998×10^{-1}	-2.2026×10^{-1}
	2021	0.0142	0.0	2.3876×10^{-5}	2.4911×10^{-4}	-1.2368×10^{-3}	1.6128×10^{-2}	-2.9923×10^{-1}	-1.5582×10^{-1}
	2021	0.019	0.13	2.0135×10^{-5}	2.3304×10^{-4}	-8.7799×10^{-4}	1.7239×10^{-2}	-3.1304×10^{-1}	-1.0037×10^{-1}
	2021	0.029	0.31	1.8947×10^{-5}	2.4694×10^{-4}	-5.3669×10^{-4}	1.8314×10^{-2}	-3.3846×10^{-1}	5.0707×10^{-2}
	2021	0.038	0.43	2.1314×10^{-5}	2.7855×10^{-4}	-3.6256×10^{-4}	1.9320×10^{-2}	-3.6970×10^{-1}	2.4256×10^{-1}
	2021	0.040	0.45	1.5181×10^{-5}	1.9780×10^{-4}	-6.5760×10^{-5}	2.2975×10^{-2}	-3.7867×10^{-1}	2.6612×10^{-1}
$SFR_{\mathrm{K98}} - SFR_{\mathrm{IGIMF}}$	2021	9.0×10^{-5}	−2.20	2.2238×10^{-5}	1.3244×10^{-4}	-1.5273×10^{-3}	2.0489×10^{-2}	7.3476×10^{-1}	-5.0576×10^{-1}
(Equation (12.19))	2021	9.6×10^{-5}	−2.17	2.2364×10^{-5}	1.3362×10^{-4}	-1.5376×10^{-3}	2.0424×10^{-2}	7.3506×10^{-1}	-5.0519×10^{-1}
	2021	0.00019	−1.87	2.2504×10^{-5}	1.4917×10^{-4}	-1.4903×10^{-3}	1.9564×10^{-2}	7.3192×10^{-1}	-4.7098×10^{-1}
	2021	0.00048	−1.47	1.8490×10^{-5}	1.2630×10^{-4}	-1.2116×10^{-3}	2.0410×10^{-2}	7.2418×10^{-1}	-4.3284×10^{-1}
	2021	0.00096	−1.17	1.9246×10^{-5}	1.4337×10^{-4}	-1.1961×10^{-3}	1.9585×10^{-2}	7.2223×10^{-1}	-4.0246×10^{-1}
	2021	0.0038	−0.57	1.5919×10^{-5}	1.3256×10^{-4}	-9.2835×10^{-4}	2.0264×10^{-2}	7.1196×10^{-1}	-3.4263×10^{-1}
	2021	0.0078	−0.26	1.9228×10^{-5}	1.9005×10^{-4}	-1.0329×10^{-3}	1.8126×10^{-2}	7.0905×10^{-1}	-2.7146×10^{-1}
	2021	0.0096	−0.17	1.7296×10^{-5}	1.7004×10^{-4}	-8.7638×10^{-4}	1.9139×10^{-2}	7.0389×10^{-1}	-2.5017×10^{-1}
	2021	0.0142	0.0	2.3876×10^{-5}	2.61089×10^{-4}	-1.1344×10^{-3}	1.5771×10^{-2}	7.0397×10^{-1}	-1.8569×10^{-1}
	2021	0.019	0.13	2.0135×10^{-5}	2.4314×10^{-4}	-7.8240×10^{-4}	1.6989×10^{-2}	6.9040×10^{-1}	-1.3162×10^{-1}
	2021	0.029	0.31	1.8947×10^{-5}	2.5645×10^{-4}	-4.3564×10^{-4}	1.8167×10^{-2}	6.6520×10^{-1}	1.6910×10^{-2}
	2021	0.038	0.43	2.1314×10^{-5}	2.8925×10^{-4}	-2.4858×10^{-4}	1.9228×10^{-2}	6.3417×10^{-1}	2.0564×10^{-1}
	2021	0.040	0.45	1.5181×10^{-5}	2.0542×10^{-4}	1.5184×10^{-5}	2.2968×10^{-2}	0.6259×10^{-1}	2.2834×10^{-1}

Table F.1: Polynomial coefficients of the fitting functions Equations (12.16), (12.18), and (12.19) to the SFR–Hα and $\Phi - L_{\mathrm{H}\alpha}$, $SFR_{\mathrm{K98}} - SFR_{\mathrm{IGIMF}}$ relations, respectively, for different metallicities. The fitting relations of the SFR–Hα and $\Phi - L_{\mathrm{H}\alpha}$ are defined for the Hα luminosity range of $-6 < \log_{10}\left(L_{\mathrm{H}\alpha}/(10^{41}\,\mathrm{erg\,s^{-1}})\right) < 4$ and $SFR_{\mathrm{K98}} - SFR_{\mathrm{IGIMF}}$ relations for SFRs derived from the Kennicutt law in the range of $-6 < \log_{10}\left(\psi_{\mathrm{K98}}/(\mathrm{M_\odot\,yr^{-1}})\right) < 4$ (Sect. 12.2.3).
*Using the relation $[Z] = \log_{10}(Z/Z_\odot)$, where $Z_\odot = 0.0142$ (Sect. 12.2.1).

Bibliography

Aarseth, S. J. and S. M. Fall (1980), *Cosmological N-body simulations of galaxy merging*, ApJ **236** 43 (cit. on p. 34).

Aarseth, S. J., I. Gott J. R. and E. L. Turner (1979), *N-body simulations of galaxy clustering. I. Initial conditions and galaxy collapse times.*, ApJ **228** 664 (cit. on p. 34).

Abazajian, K. et al. (2005), *The Third Data Release of the Sloan Digital Sky Survey*, AJ **129** 1755, arXiv: astro-ph/0410239 [astro-ph] (cit. on p. 75).

Abbott, B. P. et al. (2016), *Observation of Gravitational Waves from a Binary Black Hole Merger*, Phys. Rev. Lett. **116**, 061102 061102, arXiv: 1602.03837 [gr-qc] (cit. on pp. 26, 59).

Abbott, B. P. et al. (2017), *Gravitational Waves and Gamma-Rays from a Binary Neutron Star Merger: GW170817 and GRB 170817A*, ApJL **848**, L13 L13, arXiv: 1710.05834 [astro-ph.HE] (cit. on pp. 26, 32).

Abbott, T. M. C. et al. (2023), *Joint analysis of Dark Energy Survey Year 3 data and CMB lensing from SPT and Planck. III. Combined cosmological constraints*, Phys. Rev. D **107**, 023531 023531, arXiv: 2206.10824 [astro-ph.CO] (cit. on p. 54).

Adams, N. J. et al. (2023), *Discovery and properties of ultra-high redshift galaxies ($9 < z < 12$) in the JWST ERO SMACS 0723 Field*, MNRAS **518** 4755, arXiv: 2207.11217 [astro-ph.GA] (cit. on pp. 76, 95, 96, 175).

Aguirre, A., J. Schaye and E. Quataert (2001), *Problems for Modified Newtonian Dynamics in Clusters and the Lyα Forest?*, ApJ **561** 550, arXiv: astro-ph/0105184 [astro-ph] (cit. on pp. 63, 64).

Ahumada, R. et al. (2020), *The 16th Data Release of the Sloan Digital Sky Surveys: First Release from the APOGEE-2 Southern Survey and Full Release of eBOSS Spectra*, ApJS **249**, 3 3, arXiv: 1912.02905 [astro-ph.GA] (cit. on p. 92).

Aker, M. et al. (2019), *Improved Upper Limit on the Neutrino Mass from a Direct Kinematic Method by KATRIN*, PhRvL **123**, 221802 221802, arXiv: 1909.06048 [hep-ex] (cit. on p. 59).

Alberts, S. and A. Noble (2022), *From Clusters to Proto-Clusters: The Infrared Perspective on Environmental Galaxy Evolution*, Universe **8** 554, arXiv: 2209.02781 [astro-ph.GA] (cit. on p. 64).

Albrecht, A. and P. J. Steinhardt (1982), *Cosmology for Grand Unified Theories with Radiatively Induced Symmetry Breaking*, Phys. Rev. Lett. **48** 1220 (cit. on p. 32).

Alexander, S. and E. McDonough (2019), *Axion-dilaton destabilization and the Hubble tension*, Physics Letters B **797**, 134830 134830, arXiv: 1904.08912 [astro-ph.CO] (cit. on p. 86).

Alpher, R. A. and R. Herman (1948), *Evolution of the Universe*, Nature **162** 774 (cit. on p. 32).

Aluri, P. K. et al. (2023), *Is the observable Universe consistent with the cosmological principle?*, Classical and Quantum Gravity **40**, 094001 094001, arXiv: 2207.05765 [astro-ph.CO] (cit. on p. 54).

Alves, D. R. and C. A. Nelson (2000), *The Rotation Curve of the Large Magellanic Cloud and the Implications for Microlensing*, ApJ **542** 789, arXiv: astro-ph/0006018 [astro-ph] (cit. on p. 129).

Andernach, H. and F. Zwicky (2017), *English and Spanish Translation of Zwicky's (1933) The Redshift of Extragalactic Nebulae*, arXiv e-prints, arXiv:1711.01693 arXiv:1711.01693, arXiv: 1711.01693 [astro-ph.IM] (cit. on pp. 29, 30).

Angulo, R. E. et al. (2012), *Scaling relations for galaxy clusters in the Millennium-XXL simulation*, MNRAS **426** 2046, arXiv: 1203.3216 [astro-ph.CO] (cit. on pp. 44, 86).

Angus, G. W. (2009), *Is an 11eV sterile neutrino consistent with clusters, the cosmic microwave background and modified Newtonian dynamics?*, MNRAS **394** 527, arXiv: 0805.4014 [astro-ph] (cit. on pp. 3, 59, 63, 99).

Angus, G. W. and A. Diaferio (2011), *The abundance of galaxy clusters in modified Newtonian dynamics: cosmological simulations with massive neutrinos*, MNRAS **417** 941, arXiv: 1104.5040 [astro-ph.CO] (cit. on pp. 60, 63, 316).

Angus, G. W., A. Diaferio and P. Kroupa (2011), *Using dwarf satellite proper motions to determine their origin*, MNRAS **416** 1401, arXiv: 1108.3697 [astro-ph.CO] (cit. on pp. 49, 63, 64, 103, 131, 173).

Appenzeller, I. (2009), *KOSMOLOGIE-Carl Wirtz und die Hubble-Beziehung-Wenig bekannt ist das Wirken dieses Astronomen im Hinblick auf die Theorien zur Expansion des Alls.*, Sterne und Weltraum **48** 44 (cit. on pp. 27, 29).

Argelander, F. W. A. (1903), *Bonner Durchmusterung des nordlichen Himmels.*, Eds Marcus and Weber's Verlag 0 (cit. on p. 22).

Asencio, E., I. Banik and P. Kroupa (2023), *The El Gordo galaxy cluster challenges ΛCDM for any plausible collision velocity*, arXiv e-prints, arXiv:2308.00744 arXiv:2308.00744, arXiv: 2308.00744 [astro-ph.CO] (cit. on pp. 53, 175).

Asencio, E., I. Banik and P. Kroupa (2021), *A massive blow for ΛCDM - the high redshift, mass, and collision velocity of the interacting galaxy cluster El Gordo contradicts concordance cosmology*, MNRAS **500** 5249, arXiv: 2012.03950 [astro-ph.CO] (cit. on pp. 52, 53, 59, 111, 129, 175).

Asencio, E. et al. (2022), *The distribution and morphologies of Fornax Cluster dwarf galaxies suggest they lack dark matter*, MNRAS **515** 2981, arXiv: 2208.02265 [astro-ph.GA] (cit. on pp. 131, 174).

Asplund, M., N. Grevesse, A. J. Sauval and P. Scott (2009), *The Chemical Composition of the Sun*, ARA&A **47** 481, arXiv: 0909.0948 [astro-ph.SR] (cit. on pp. 67, 147).

Atek, H. et al. (2023), *Revealing galaxy candidates out to z 16 with JWST observations of the lensing cluster SMACS0723*, MNRAS **519** 1201, arXiv: 2207.12338 [astro-ph.GA] (cit. on pp. 76, 95, 175).

Atkinson, R. J. C. (1978), *Some new measurements on Stonehenge*, Nature **275** 50 (cit. on p. 10).

Babcock, H. W. (1938), *On the Rotation of the Andromenda Nebula.*, PhD thesis: University of California, Berkeley (cit. on pp. 2, 31).

– (1939), *The rotation of the Andromeda Nebula*, Lick Observatory Bulletin **498** 41 (cit. on pp. 2, 31).

Balakrishna Subramani, V., P. Kroupa, H. Shenavar and V. Muralidhara (2019), *Pseudo-evolution of galaxies in Λ CDM cosmology*, MNRAS **488** 3876, arXiv: 1907.09486 [astro-ph.GA] (cit. on p. 143).
Baldry, I. K. et al. (2018), *Galaxy And Mass Assembly: the G02 field, Herschel-ATLAS target selection and data release 3*, MNRAS **474** 3875, arXiv: 1711.09139 [astro-ph.GA] (cit. on pp. 92, 135).
Banerjee, S. and P. Kroupa (2012), *On the true shape of the upper end of the stellar initial mass function. The case of R136*, A&A **547**, A23 A23, arXiv: 1209.4079 [astro-ph.GA] (cit. on p. 67).
Banerjee, S., P. Kroupa and S. Oh (2012a), *Runaway Massive Stars from R136: VFTS 682 is Very Likely a "Slow Runaway"*, ApJ **746**, 15 15, arXiv: 1111.0291 [astro-ph.GA] (cit. on p. 146).
– (2012b), *The emergence of super-canonical stars in R136-type starburst clusters*, MNRAS **426** 1416, arXiv: 1208.0826 [astro-ph.SR] (cit. on p. 146).
Banik, I., M. Haslbauer, M. S. Pawlowski, B. Famaey and P. Kroupa (2021), *On the absence of backsplash analogues to NGC 3109 in the ΛCDM framework*, MNRAS **503** 6170, arXiv: 2105.04575 [astro-ph.GA] (cit. on pp. 52, 103, 109, 124, 173, 174, 328).
Banik, I., D. O'Ryan and H. Zhao (2018), *Origin of the Local Group satellite planes*, MNRAS **477** 4768, arXiv: 1802.00440 [astro-ph.GA] (cit. on pp. 103, 128, 131).
Banik, I., C. Pittordis and W. J. Sutherland (2021), *Detailed numerical implementation of the wide binary test*, arXiv e-prints, arXiv:2109.03827 arXiv:2109.03827, arXiv: 2109.03827 [astro-ph.GA] (cit. on p. 176).
Banik, I. et al. (2023), *Strong constraints on the gravitational law from Gaia DR3 wide binaries*, arXiv e-prints, arXiv:2311.03436 arXiv:2311.03436, arXiv: 2311.03436 [astro-ph.SR] (cit. on pp. 176, 177).
Banik, I. et al. (2022), *3D hydrodynamic simulations for the formation of the Local Group satellite planes*, MNRAS **513** 129, arXiv: 2204.09687 [astro-ph.GA] (cit. on pp. 128, 131, 173).
Banik, I. and H. Zhao (2018a), *Testing gravity with wide binary stars like α Centauri*, MNRAS **480** 2660, arXiv: 1805.12273 [astro-ph.GA] (cit. on p. 129).
– (2018b), *Testing gravity with wide binary stars like α Centauri*, MNRAS **480** 2660, arXiv: 1805.12273 [astro-ph.GA] (cit. on p. 176).
– (2022), *From Galactic Bars to the Hubble Tension: Weighing Up the Astrophysical Evidence for Milgromian Gravity*, Symmetry **14** 1331, arXiv: 2110.06936 [astro-ph.CO] (cit. on pp. 57, 59, 60, 78, 103, 172).
Barnes, J. E. and L. Hernquist (1992), *Dynamics of interacting galaxies.*, ARA&A **30** 705 (cit. on pp. 52, 123).
Baumgardt, H. and J. Makino (2003), *Dynamical evolution of star clusters in tidal fields*, MNRAS **340** 227, arXiv: astro-ph/0211471 [astro-ph] (cit. on p. 134).
Begeman, K. G., A. H. Broeils and R. H. Sanders (1991), *Extended rotation curves of spiral galaxies : dark haloes and modified dynamics.*, MNRAS **249** 523 (cit. on p. 58).
Behr, A. (1951), *Zur Entfernungsskala der extragalaktischen Nebel*, Astronomische Nachrichten **279** 97 (cit. on p. 27).
Bekenstein, J. D. (2004), *Relativistic gravitation theory for the modified Newtonian dynamics paradigm*, PhRvD **70**, 083509 083509, arXiv: astro-ph/0403694 [astro-ph] (cit. on pp. 32, 59).
Bekenstein, J. D. and M. Milgrom (1984), *Does the missing mass problem signal the breakdown of Newtonian gravity?*, ApJ **286** 7 (cit. on pp. 58, 128).

Bellstedt, S. et al. (2020), *Galaxy And Mass Assembly (GAMA): a forensic SED reconstruction of the cosmic star formation history and metallicity evolution by galaxy type*, MNRAS **498** 5581, arXiv: 2005.11917 [astro-ph.GA] (cit. on p. 50).

Beltz-Mohrmann, G. D. and A. A. Berlind (2021), *The Impact of Baryonic Physics on the Abundance, Clustering, and Concentration of Halos*, ApJ **921**, 112 112, arXiv: 2103.05076 [astro-ph.CO] (cit. on p. 46).

Besla, G. (2015), *The Orbits and Total Mass of the Magellanic Clouds*, ArXiv e-prints **Arxiv**, arXiv:1511.03346, arXiv: 1511.03346 [astro-ph.GA] (cit. on p. 129).

Besla, G. et al. (2007), *Are the Magellanic Clouds on Their First Passage about the Milky Way?*, ApJ **668** 949, arXiv: astro-ph/0703196 [astro-ph] (cit. on p. 106).

Bessel, F. W. (1838), *On the parallax of 61 Cygni*, MNRAS **4** 152 (cit. on p. 15).

Bessell, M. S. (1990), *UBVRI passbands.*, PASP **102** 1181 (cit. on pp. 140, 152, 168, 177, 267).

Bevins, R. E. et al. (2023), *The Stonehenge Altar Stone was probably not sourced from the Old Red Sandstone of the Anglo-Welsh Basin: Time to broaden our geographic and stratigraphic horizons?*, Journal of Archaeological Science: Reports **51** 104215, ISSN: 2352-409X, URL: https://www.sciencedirect.com/science/article/pii/S2352409X23003905 (cit. on p. 10).

Bílek, M., I. Thies, P. Kroupa and B. Famaey (2018), *MOND simulation suggests an origin for some peculiarities in the Local Group*, A&A **614**, A59 A59, arXiv: 1712.04938 [astro-ph.GA] (cit. on pp. 103, 128, 131).

Bílek, M., I. Thies, P. Kroupa and B. Famaey (2021), *Are Disks of Satellites Comprised of Tidal Dwarf Galaxies?*, Galaxies **9** 100, arXiv: 2111.05306 [astro-ph.GA] (cit. on pp. 103, 127, 131, 173).

Binney, J. and S. Tremaine (2008), *Galactic Dynamics: Second Edition*, Princeton University Press (cit. on pp. 4, 24, 47).

Block, D. L. and K. C. Freeman (2008), *Shrouds of the Night: Masks of the Milky Way and our Awesome new View of Galaxies*, Springer (cit. on pp. 25, 26, 314).

– (2015), "A Walk with Dr Allan Sandage—Changing the History of Galaxy Morphology, Forever: A Conference in honour of David Block and Bruce Elmegreen", *Lessons from the Local Group: A Conference in honor of David Block and Bruce Elmegreen* 1 (cit. on pp. 25, 26, 29, 314).

Blount, T. (1670), *Glossographia: Or, A Dictionary, Interpreting the Hard Words of Whatsoever Language, Now Used in Our Refined English Tongue; with Etymologies, Definitions, and Historical Observations on the Same. Also the Terms of Divinity, Law, Physick, Mathematicks, War, Music, and Other Arts and Sciences Explicated ...* Early English Books Online / EEBO, Tho. Newcomb, and are to be sold by John Martyn, at the Bell without Temple Bar, URL: https://books.google.de/books?id=eCFull-wGrYC (cit. on p. 8).

Bode, J. E. (1768), *Anleitung zur Kenntniss des gestirnten Himmels* (cit. on p. 22).

Böhringer, H., G. Chon, M. Bristow and C. A. Collins (2015), *The extended ROSAT-ESO Flux-Limited X-ray Galaxy Cluster Survey (REFLEX II). V. Exploring a local underdensity in the southern sky*, A&A **574**, A26 A26, arXiv: 1410.2172 [astro-ph.CO] (cit. on pp. 53, 78, 85, 174).

Böhringer, H., G. Chon and C. A. Collins (2020), *Observational evidence for a local underdensity in the Universe and its effect on the measurement of the Hubble constant*, A&A **633**, A19 A19, arXiv: 1907.12402 [astro-ph.CO] (cit. on pp. 53, 78, 85, 174).

Bondi, H. and T. Gold (1948), *The Steady-State Theory of the Expanding Universe*, MNRAS **108** 252 (cit. on p. 32).

Bondi, H. (1967), *Assumption and myth in physical theory: the tarner lectures delivered at Cambridge in November 1965*, CUP Archive (cit. on p. 1).

Boran, S., S. Desai, E. O. Kahya and R. P. Woodard (2018), *GW170817 falsifies dark matter emulators*, PhRvD **97**, 041501 041501, arXiv: 1710.06168 [astro-ph.HE] (cit. on p. 59).

Bosma, A. (1981), *21-cm line studies of spiral galaxies. I. Observations of the galaxies NGC 5033, 3198, 5055, 2841, and 7331.*, AJ **86** 1791 (cit. on pp. 2, 31).

Bournaud, F. (2010), "Star Formation and Structure Formation in Galaxy Interactions and Mergers", *Galaxy Wars: Stellar Populations and Star Formation in Interacting Galaxies*, ed. by B. Smith, J. Higdon, S. Higdon and N. Bastian, vol. 423, Astronomical Society of the Pacific Conference Series 177, arXiv: 0909.1812 [astro-ph.CO] (cit. on p. 52).

Bournaud, F. et al. (2007), *Missing Mass in Collisional Debris from Galaxies*, Science **316** 1166, arXiv: 0705.1356 [astro-ph] (cit. on p. 177).

Boylan-Kolchin, M. (2023), *Stress testing ΛCDM with high-redshift galaxy candidates*, Nature Astronomy, arXiv: 2208.01611 [astro-ph.CO] (cit. on pp. 55, 96).

Boylan-Kolchin, M., G. Besla and L. Hernquist (2011), *Dynamics of the Magellanic Clouds in a Lambda cold dark matter universe*, MNRAS **414** 1560, arXiv: 1010.4797 [astro-ph.GA] (cit. on pp. 49, 106, 116, 118, 119, 130).

Boylan-Kolchin, M., V. Springel, S. D. M. White and A. Jenkins (2010), *There's no place like home? Statistics of Milky Way-mass dark matter haloes*, MNRAS **406** 896, arXiv: 0911.4484 [astro-ph.CO] (cit. on p. 124).

Boylan-Kolchin, M., V. Springel, S. D. M. White, A. Jenkins and G. Lemson (2009), *Resolving cosmic structure formation with the Millennium-II Simulation*, MNRAS **398** 1150, arXiv: 0903.3041 [astro-ph.CO] (cit. on pp. 44, 118).

Bressan, A. et al. (2012), *PARSEC: stellar tracks and isochrones with the PAdova and TRieste Stellar Evolution Code*, MNRAS **427** 127, arXiv: 1208.4498 [astro-ph.SR] (cit. on pp. 140, 145, 150, 151).

Brinchmann, J. et al. (2004), *The physical properties of star-forming galaxies in the low-redshift Universe*, MNRAS **351** 1151, arXiv: astro-ph/0311060 [astro-ph] (cit. on p. 144).

Bringmann, T. (2009), *Particle models and the small-scale structure of dark matter*, New Journal of Physics **11**, 105027 105027, arXiv: 0903.0189 [astro-ph.CO] (cit. on p. 2).

Brown, M. (2010), *How I Killed Pluto and Why It Had It Coming*, Random House Publishing Group, ISBN: 9780385531092 (cit. on p. 22).

Brown, M. J. I. et al. (2017), *Calibration of Ultraviolet, Mid-infrared, and Radio Star Formation Rate Indicators*, ApJ **847**, 136 136, arXiv: 1709.00183 [astro-ph.GA] (cit. on p. 144).

Buat, V., J. M. Deharveng and J. Donas (1989), *Star formation rate and gas surface density in late-type galaxies.*, A&A **223** 42 (cit. on p. 144).

Bührke, T. (2022), *Die Verfolgten: Geniale und geächtete Wissenschaftler von Giordano Bruno bis Alan Turing*, Klett-Cotta (cit. on p. 18).

Bullock, J. S. and M. Boylan-Kolchin (2017), *Small-Scale Challenges to the ΛCDM Paradigm*, ARA&A **55** 343, arXiv: 1707.04256 [astro-ph.CO] (cit. on pp. 49, 78, 173).

Busha, M. T., P. J. Marshall, R. H. Wechsler, A. Klypin and J. Primack (2011), *The Mass Distribution and Assembly of the Milky Way from the Properties of the Magellanic Clouds*, ApJ **743**, 40 40, arXiv: 1011.2203 [astro-ph.GA] (cit. on pp. 106, 118).

Busha, M. T. et al. (2011), *Statistics of Satellite Galaxies around Milky-Way-like Hosts*, ApJ **743**, 117 117, arXiv: 1011.6373 [astro-ph.CO] (cit. on p. 119).

Calzetti, D. (2013), "Star Formation Rate Indicators", *Secular Evolution of Galaxies*, ed. by J. Falcón-Barroso and J. H. Knapen 419 (cit. on p. 144).

Camarena, D. and V. Marra (2020), *Local determination of the Hubble constant and the deceleration parameter*, Physical Review Research **2**, 013028 013028, arXiv: 1906.11814 [astro-ph.CO] (cit. on pp. 54, 87, 88, 319).

Capak, P. et al. (2011), *Spectroscopy of Luminous $z > 7$ Galaxy Candidates and Sources of Contamination in $z > 7$ Galaxy Searches*, ApJ **730**, 68 68, arXiv: 0910.0444 [astro-ph.CO] (cit. on p. 64).

Capak, P. et al. (2011), *A massive protocluster of galaxies at a redshift of $z\sim5.3$*, Nature **470** 233, arXiv: 1101.3586 [astro-ph.CO] (cit. on p. 64).

Carnall, A. C. et al. (2023), *A first look at the SMACS0723 JWST ERO: spectroscopic redshifts, stellar masses, and star-formation histories*, MNRAS **518** L45, arXiv: 2207.08778 [astro-ph.GA] (cit. on p. 76).

Carnall, A. C. et al. (2019), *How to Measure Galaxy Star Formation Histories. I. Parametric Models*, ApJ **873**, 44 44, arXiv: 1811.03635 [astro-ph.GA] (cit. on p. 135).

Carr, B. (1994), *Baryonic Dark Matter*, ARA&A **32** 531 (cit. on pp. 2, 4).

Carroll, S. M. (1997), *Lecture Notes on General Relativity*, arXiv e-prints, gr-qc/9712019 gr, arXiv: gr-qc/9712019 [gr-qc] (cit. on p. 37).

Cebrián, S. (2023), "Review on dark matter searches", *Journal of Physics Conference Series*, vol. 2502, Journal of Physics Conference Series 012004 012004, arXiv: 2205.06833 [physics.ins-det] (cit. on p. 2).

Chabrier, G. (2003), *Galactic Stellar and Substellar Initial Mass Function*, PASP **115** 763, arXiv: astro-ph/0304382 [astro-ph] (cit. on pp. 4, 66, 76, 81, 97, 98, 172, 176, 320).

Chae, K.-H. (2023a), *Breakdown of the Newton-Einstein Standard Gravity at Low Acceleration in Internal Dynamics of Wide Binary Stars*, arXiv e-prints, arXiv:2305.04613 arXiv:2305.04613, arXiv: 2305.04613 [astro-ph.GA] (cit. on pp. 176, 177).

– (2023b), *Robust Evidence for the Breakdown of Standard Gravity at Low Acceleration from Statistically Pure Binaries Free of Hidden Companions*, arXiv e-prints, arXiv:2309.10404 arXiv:2309.10404, arXiv: 2309.10404 [astro-ph.GA] (cit. on pp. 176, 177).

Chae, K.-H., H. Desmond, F. Lelli, S. S. McGaugh and J. M. Schombert (2021), *Testing the Strong Equivalence Principle. II. Relating the External Field Effect in Galaxy Rotation Curves to the Large-scale Structure of the Universe*, ApJ **921**, 104 104, arXiv: 2109.04745 [astro-ph.GA] (cit. on p. 59).

Chae, K.-H. et al. (2020), *Testing the Strong Equivalence Principle: Detection of the External Field Effect in Rotationally Supported Galaxies*, ApJ **904**, 51 51, arXiv: 2009.11525 [astro-ph.GA] (cit. on p. 59).

Chandrasekhar, S. (1943a), *Dynamical Friction. I. General Considerations: the Coefficient of Dynamical Friction.*, ApJ **97** 255 (cit. on pp. 4, 47).

– (1943b), *Dynamical Friction. II. The Rate of Escape of Stars from Clusters and the Evidence for the Operation of Dynamical Friction.*, ApJ **97** 263 (cit. on pp. 4, 47).

– (1943c), *Dynamical Friction. III. a More Exact Theory of the Rate of Escape of Stars from Clusters.*, ApJ **98** 54 (cit. on pp. 4, 47).

Chandrasekhar, S. (1942), *Principles of stellar dynamics* (cit. on pp. 4, 47).

Chruślińska, M., T. Jeřábková, G. Nelemans and Z. Yan (2020), *The effect of the environment-dependent IMF on the formation and metallicities of stars over the cosmic history*, A&A **636**, A10 A10, arXiv: 2002.11122 [astro-ph.GA] (cit. on p. 178).

Cimatti, A. and M. Moresco (2023), *Revisiting the Oldest Stars as Cosmological Probes: New Constraints on the Hubble Constant*, ApJ **953**, 149 149, arXiv: 2302.07899 [astro-ph.CO] (cit. on p. 42).
Clarke, C. J. (2020), *The distribution of relative proper motions of wide binaries in Gaia DR2: MOND or multiplicity?*, MNRAS **491** L72, arXiv: 1910.10256 [astro-ph.SR] (cit. on p. 176).
Cohen, I. B. and G. E. Smith (2002), *The Cambridge Companion to Newton*, Cambridge University Press (cit. on p. 21).
Cohen, M., W. A. Wheaton and S. T. Megeath (2003), *Spectral Irradiance Calibration in the Infrared. XIV. The Absolute Calibration of 2MASS*, AJ **126** 1090, arXiv: astro-ph/0304350 [astro-ph] (cit. on pp. 140, 151, 152, 168, 177, 267).
Cole, S. et al. (2001), *The 2dF galaxy redshift survey: near-infrared galaxy luminosity functions*, MNRAS **326** 255, arXiv: astro-ph/0012429 [astro-ph] (cit. on pp. 81, 133).
Colin, J., R. Mohayaee, M. Rameez and S. Sarkar (2019), *Evidence for anisotropy of cosmic acceleration*, A%A **631**, L13 L13, arXiv: 1808.04597 [astro-ph.CO] (cit. on p. 55).
Combes, F. and D. Pfenniger (1997), *Perspectives for detecting cold H_2_ in outer galactic disks.*, A&A **327** 453, arXiv: astro-ph/9707217 [astro-ph] (cit. on p. 2).
Condon, J. J. (1992), *Radio emission from normal galaxies.*, ARA&A **30** 575 (cit. on p. 144).
Conroy, C. and P. G. van Dokkum (2012), *The Stellar Initial Mass Function in Early-type Galaxies From Absorption Line Spectroscopy. II. Results*, ApJ **760**, 71 71, arXiv: 1205.6473 [astro-ph.CO] (cit. on p. 67).
Cooper, B. (2001), *Beethoven's 'Abendlied' and the 'Wiener Zeitschrift'*, Music Letters **82** 234, ISSN: 00274224, 14774631, URL: http://www.jstor.org/stable/3526060 (visited on 13/11/2023) (cit. on p. 22).
Copernicus, N. and J. G. Rhaticus (1566), *De revolvtionibus orbium coelestium* (cit. on pp. 17, 313).
Correa Magnus, L. and E. Vasiliev (2022), *Measuring the Milky Way mass distribution in the presence of the LMC*, MNRAS **511** 2610, arXiv: 2110.00018 [astro-ph.GA] (cit. on p. 121).
Cowie, L. L., A. Songaila, E. M. Hu and J. G. Cohen (1996), *New Insight on Galaxy Formation and Evolution From Keck Spectroscopy of the Hawaii Deep Fields*, AJ **112** 839, arXiv: astro-ph/9606079 [astro-ph] (cit. on p. 50).
Crain, R. A. et al. (2015), *The EAGLE simulations of galaxy formation: calibration of subgrid physics and model variations*, MNRAS **450** 1937, arXiv: 1501.01311 [astro-ph.GA] (cit. on pp. 34, 45, 92, 96).
Crain, R. A. and F. van de Voort (2023), *Hydrodynamical Simulations of the Galaxy Population: Enduring Successes and Outstanding Challenges*, ARA&A **61** 473 (cit. on p. 173).
Croton, D. J. (2013), *Damn You, Little h! (Or, Real-World Applications of the Hubble Constant Using Observed and Simulated Data)*, Publ. Astron. Soc. Australia **30**, e052 e052, arXiv: 1308.4150 [astro-ph.CO] (cit. on pp. 37, 40).
Croton, D. J. et al. (2006), *The many lives of active galactic nuclei: cooling flows, black holes and the luminosities and colours of galaxies*, MNRAS **365** 11, arXiv: astro-ph/0508046 [astro-ph] (cit. on p. 44).
Croton, D. J. et al. (2016), *Semi-Analytic Galaxy Evolution (SAGE): Model Calibration and Basic Results*, ApJS **222**, 22 22, arXiv: 1601.04709 [astro-ph.GA] (cit. on p. 44).
Crowther, P. A. et al. (2010), *The R136 star cluster hosts several stars whose individual masses greatly exceed the accepted 150M_{solar} stellar mass limit*, MNRAS **408** 731, arXiv: 1007.3284 [astro-ph.SR] (cit. on p. 146).

Cruz, M., E. Martınez-González, P. Vielva and L. Cayón (2005), *Detection of a non-Gaussian spot in WMAP*, MNRAS **356** 29, arXiv: astro-ph/0405341 [astro-ph] (cit. on p. 55).
Cullinane, L. R. et al. (2022a), *The Magellanic Edges Survey - II. Formation of the LMC's northern arm*, MNRAS **510** 445, arXiv: 2106.03274 [astro-ph.GA] (cit. on p. 116).
– (2022b), *The Magellanic Edges Survey - III. Kinematics of the disturbed LMC outskirts*, MNRAS **512** 4798, arXiv: 2203.05450 [astro-ph.GA] (cit. on p. 116).
D'Onghia, E. and A. J. Fox (2016), *The Magellanic Stream: Circumnavigating the Galaxy*, ARA&A **54** 363, arXiv: 1511.05853 [astro-ph.GA] (cit. on pp. 106, 116).
D'Onghia, E. and G. Lake (2008), *Small Dwarf Galaxies within Larger Dwarfs: Why Some Are Luminous while Most Go Dark*, ApJL **686** L61, arXiv: 0802.0001 [astro-ph] (cit. on p. 121).
Dabringhausen, J., M. Hilker and P. Kroupa (2008), *From star clusters to dwarf galaxies: the properties of dynamically hot stellar systems*, MNRAS **386** 864, arXiv: 0802.0703 [astro-ph] (cit. on p. 24).
Dabringhausen, J. and P. Kroupa (2013), *Dwarf elliptical galaxies as ancient tidal dwarf galaxies*, MNRAS **429** 1858, arXiv: 1211.1382 [astro-ph.CO] (cit. on p. 52).
Dabringhausen, J., P. Kroupa and H. Baumgardt (2009), *A top-heavy stellar initial mass function in starbursts as an explanation for the high mass-to-light ratios of ultra-compact dwarf galaxies*, MNRAS **394** 1529, arXiv: 0901.0915 [astro-ph.GA] (cit. on pp. 67, 144).
Dabringhausen, J., P. Kroupa, J. Pflamm-Altenburg and S. Mieske (2012), *Low-mass X-Ray Binaries Indicate a Top-heavy Stellar Initial Mass Function in Ultracompact Dwarf Galaxies*, ApJ **747**, 72 72, arXiv: 1110.2779 [astro-ph.CO] (cit. on pp. 67, 144).
Dainotti, M. G. et al. (2021), *On the Hubble Constant Tension in the SNe Ia Pantheon Sample*, ApJ **912**, 150 150, arXiv: 2103.02117 [astro-ph.CO] (cit. on p. 175).
David, L. P., C. Jones and W. Forman (1992), *X-Ray Properties of Bright Far-Infrared Galaxies*, ApJ **388** 82 (cit. on p. 144).
De Lucia, G., V. Springel, S. D. M. White, D. Croton and G. Kauffmann (2006), *The formation history of elliptical galaxies*, MNRAS **366** 499, arXiv: astro-ph/0509725 [astro-ph] (cit. on p. 44).
de Vaucouleurs, G. (1959), *Classification and Morphology of External Galaxies.*, Handbuch der Physik **53** 275 (cit. on p. 26).
de Vaucouleurs, G. et al. (1991), *Third Reference Catalogue of Bright Galaxies* (cit. on p. 26).
Deason, A. J. et al. (2011), *Mismatch and misalignment: dark haloes and satellites of disc galaxies*, MNRAS **415** 2607, arXiv: 1101.0816 [astro-ph.CO] (cit. on p. 122).
Delgado-Serrano, R. et al. (2010), *How was the Hubble sequence 6 Gyr ago?*, A&A **509**, A78 A78, arXiv: 0906.2805 [astro-ph.CO] (cit. on pp. 46, 50, 75, 77, 92, 173, 317).
Dennefeld, M. (2020), *A History of the Magellanic Clouds and the European Exploration of the Southern Hemisphere*, The Messenger **181** 37, arXiv: 2009.04973 [physics.hist-ph] (cit. on p. 101).
Di Teodoro, E. M., L. Posti, P. M. Ogle, S. M. Fall and T. Jarrett (2021), *Rotation curves and scaling relations of extremely massive spiral galaxies*, MNRAS **507** 5820, arXiv: 2109.03828 [astro-ph.GA] (cit. on p. 178).
Di Valentino, E. (2022), *Challenges of the Standard Cosmological Model*, Universe **8** 399 (cit. on pp. 34, 37, 47).
Di Valentino, E., L. A. Anchordoqui, Ö. Akarsu, Y. Ali-Haimoud, L. Amendola, N. Arendse, M. Asgari, M. Ballardini, S. Basilakos, E. Battistelli, M. Benetti, S. Birrer, F. R. Bouchet, M. Bruni, E. Calabrese, D. Camarena, S. Capozziello, A. Chen, J. Chluba, A. Chudaykin, E. Ó. Colgáin,

F.-Y. Cyr-Racine, P. de Bernardis, J. de Cruz Pérez, J. Delabrouille, J. Dunkley, C. Escamilla-Rivera, A. Ferté, F. Finelli, W. Freedman, N. Frusciante, E. Giusarma, A. Gómez-Valent, J. Guy et al. (2021), *Cosmology Intertwined II: The hubble constant tension*, Astroparticle Physics **131**, 102605 102605, arXiv: 2008.11284 [astro-ph.CO] (cit. on p. 53).

Di Valentino, E., L. A. Anchordoqui, Ö. Akarsu, Y. Ali-Haimoud, L. Amendola, N. Arendse, M. Asgari, M. Ballardini, S. Basilakos, E. Battistelli, M. Benetti, S. Birrer, F. R. Bouchet, M. Bruni, E. Calabrese, D. Camarena, S. Capozziello, A. Chen, J. Chluba, A. Chudaykin, E. Ó. Colgáin, F.-Y. Cyr-Racine, P. de Bernardis, J. de Cruz Pérez, J. Delabrouille, J. Dunkley, C. Escamilla-Rivera, A. Ferté, F. Finelli, W. Freedman, N. Frusciante, E. Giusarma, A. Gómez-Valent, W. Handley et al. (2021), *Cosmology Intertwined III: $f\sigma_8$ and S_8*, Astroparticle Physics **131**, 102604 102604, arXiv: 2008.11285 [astro-ph.CO] (cit. on p. 54).

Di Valentino, E., A. Melchiorri and J. Silk (2020), *Planck evidence for a closed Universe and a possible crisis for cosmology*, Nature Astronomy **4** 196, arXiv: 1911.02087 [astro-ph.CO] (cit. on p. 37).

Di Valentino, E. et al. (2021), *In the realm of the Hubble tension-a review of solutions*, Classical and Quantum Gravity **38**, 153001 153001, arXiv: 2103.01183 [astro-ph.CO] (cit. on pp. 53, 86).

Dicke, R. H. (1969), *Gravitation and the universe.* (Cit. on p. 32).

Diller, A. (1949), *The ancient measurements of the Earth*, Isis **40** 6 (cit. on p. 15).

Dinnbier, F., P. Kroupa and R. I. Anderson (2022), *Do the majority of stars form as gravitationally unbound?*, A&A **660**, A61 A61, arXiv: 2201.06582 [astro-ph.GA] (cit. on p. 148).

Dolag, K., S. Borgani, G. Murante and V. Springel (2009), *Substructures in hydrodynamical cluster simulations*, MNRAS **399** 497, arXiv: 0808.3401 [astro-ph] (cit. on p. 108).

Donas, J. and J. M. Deharveng (1984), *Ultraviolet luminosities and colors of spiral and irregular galaxies. The present-day star formation rate.*, A&A **140** 325 (cit. on p. 144).

Dooley, G. A. et al. (2017), *The predicted luminous satellite populations around SMC- and LMC-mass galaxies - a missing satellite problem around the LMC?*, MNRAS **472** 1060, arXiv: 1703.05321 [astro-ph.GA] (cit. on p. 124).

Dreyer, J. L. E. (1888), *A New General Catalogue of Nebulæ and Clusters of Stars, being the Catalogue of the late Sir John F. W. Herschel, Bart, revised, corrected, and enlarged*, Mem. RAS **49** 1 (cit. on p. 22).

Driver, S. P. et al. (2009), *GAMA: towards a physical understanding of galaxy formation*, Astronomy and Geophysics **50** 5.12, arXiv: 0910.5123 [astro-ph.CO] (cit. on p. 135).

Driver, S. P. et al. (2016), *Galaxy And Mass Assembly (GAMA): Panchromatic Data Release (far-UV-far-IR) and the low-z energy budget*, MNRAS **455** 3911, arXiv: 1508.02076 [astro-ph.GA] (cit. on p. 135).

Dubinski, J. and R. G. Carlberg (1991), *The Structure of Cold Dark Matter Halos*, ApJ **378** 496 (cit. on p. 49).

Duc, P.-A. et al. (2014), *Identification of old tidal dwarfs near early-type galaxies from deep imaging and H I observations*, MNRAS **440** 1458, arXiv: 1403.0626 [astro-ph.GA] (cit. on p. 177).

Duerbeck, H. W. (1989), "Carl Wirtz — An early observational cosmologist", *Morphological Cosmology*, ed. by P. Flin and H. W. Duerbeck, Berlin, Heidelberg: Springer Berlin Heidelberg 405, ISBN: 978-3-540-46179-1 (cit. on p. 29).

Dyson, F. W., A. S. Eddington and C. Davidson (1920), *A Determination of the Deflection of Light by the Sun's Gravitational Field, from Observations Made at the Total Eclipse of May 29, 1919*, Philosophical Transactions of the Royal Society of London Series A **220** 291 (cit. on p. 26).

Eappen, R., P. Kroupa, N. Wittenburg, M. Haslbauer and B. Famaey (2022), *The formation of early-type galaxies through monolithic collapse of gas clouds in Milgromian gravity*, MNRAS **516** 1081, arXiv: 2209.00024 [astro-ph.GA] (cit. on pp. 75, 173).

Eckert, D. et al. (2017), *The XMM cluster outskirts project (X- COP)*, Astronomische Nachrichten **338** 293, arXiv: 1611.05051 [astro-ph.CO] (cit. on p. 63).

Eckert, D., S. Ettori, E. Pointecouteau, R. F. J. van der Burg and S. I. Loubser (2022), *The gravitational field of X-COP galaxy clusters*, A&A **662**, A123 A123, arXiv: 2205.01110 [astro-ph.CO] (cit. on p. 63).

Eddington, A. S. (1919), *The total eclipse of 1919 May 29 and the influence of gravitation on light*, The Observatory **42** 119 (cit. on p. 26).

Efstathiou, G., W. J. Sutherland and S. J. Maddox (1990), *The cosmological constant and cold dark matter*, Nature **348** 705 (cit. on pp. 2, 33).

Ehser, A., G. Borg and E. Pernicka (2011), *Provenance of the gold of the Early Bronze Age Nebra Sky Disk, central Germany: geochemical characterization of natural gold from Cornwall*, European Journal of Mineralogy **23** 895 (cit. on p. 10).

Einstein, A. (1905), *Zur Elektrodynamik bewegter Körper*, Annalen der Physik **322** 891 (cit. on p. 26).

– (1916), *Die Grundlage der allgemeinen Relativitätstheorie*, Annalen der Physik **354** 769 (cit. on p. 2).

Einstein, A. (1915), *Die Feldgleichungen der Gravitation*, Sitzungsberichte der Königlich Preussischen Akademie der Wissenschaften 844 (cit. on pp. 2, 26).

Enea Romano, A. (2016), *Hubble trouble or Hubble bubble?*, arXiv e-prints, arXiv:1609.04081 arXiv:1609.04081, arXiv: 1609.04081 [astro-ph.CO] (cit. on p. 86).

Eriksen, H. K., F. K. Hansen, A. J. Banday, K. M. Górski and P. B. Lilje (2004), *Asymmetries in the Cosmic Microwave Background Anisotropy Field*, ApJ **605** 14, arXiv: astro-ph/0307507 [astro-ph] (cit. on p. 55).

Esa, 1. (1997), *VizieR Online Data Catalog: The Hipparcos and Tycho Catalogues (ESA 1997)*, VizieR Online Data Catalog, I/239 I/239 (cit. on p. 15).

Evelyn-White, H. G. et al. (2006), *Works and Days, Theogony and the Shield of Heracles*, Courier Corporation (cit. on p. 9).

Event Horizon Telescope Collaboration et al. (2019), *First M87 Event Horizon Telescope Results. I. The Shadow of the Supermassive Black Hole*, ApJL **875**, L1 L1, arXiv: 1906.11238 [astro-ph.GA] (cit. on p. 26).

Faber, S. M. and R. E. Jackson (1976), *Velocity dispersions and mass-to-light ratios for elliptical galaxies.*, ApJ **204** 668 (cit. on p. 61).

Famaey, B. and S. S. McGaugh (2013), "Challenges for ΛCDM and MOND", *Journal of Physics Conference Series*, vol. 437, Journal of Physics Conference Series 012001 012001, arXiv: 1301.0623 [astro-ph.CO] (cit. on p. 47).

Famaey, B. and S. S. McGaugh (2012), *Modified Newtonian Dynamics (MOND): Observational Phenomenology and Relativistic Extensions*, Living Reviews in Relativity **15**, 10 10, arXiv: 1112.3960 [astro-ph.CO] (cit. on pp. 46, 57, 60, 99).

Farhang, A., H. G. Khosroshahi, G. A. Mamon, A. A. Dariush and M. Raouf (2017), *Evolution of Compact and Fossil Groups of Galaxies from Semi-analytical Models of Galaxy Formation*, ApJ **840**, 58 58 (cit. on p. 173).

Farr, W. M. et al. (2018), *Aldebaran b's Temperate Past Uncovered in Planet Search Data*, ApJL **865**, L20 L20, arXiv: 1802.09812 [astro-ph.SR] (cit. on p. 9).

Feng, J. L. (2010), *Dark Matter Candidates from Particle Physics and Methods of Detection*, ARA&A **48** 495, arXiv: 1003.0904 [astro-ph.CO] (cit. on p. 2).
Ferreira, L. et al. (2022), *Panic! at the Disks: First Rest-frame Optical Observations of Galaxy Structure at $z > 3$ with JWST in the SMACS 0723 Field*, ApJL **938**, L2 L2, arXiv: 2207.09428 [astro-ph.GA] (cit. on p. 173).
Ferreira, L. et al. (2022), *The JWST Hubble Sequence: The Rest-Frame Optical Evolution of Galaxy Structure at* $1.5 < z < 8$, arXiv e-prints, arXiv:2210.01110 arXiv:2210.01110, arXiv: 2210.01110 [astro-ph.GA] (cit. on p. 173).
Feynman, R., R. Leighton and M. Sands (1963), *The Feynman Lectures on Physics*, The Feynman Lectures on Physics Bd. 1;Bd. 3, Addison-Wesley Publishing Company, URL: https://books.google.de/books?id=_ZUfAQAAMAAJ (cit. on p. 65).
Figer, D. F. (2005), *An upper limit to the masses of stars*, Nature **434** 192, arXiv: astro-ph/0503193 [astro-ph] (cit. on p. 146).
Fioc, M., D. Le Borgne and B. Rocca-Volmerange (2011), *PÉGASE: Metallicity-consistent Spectral Evolution Model of Galaxies*, Astrophysics Source Code Library, record ascl:1108.007, ascl: 1108.007 (cit. on pp. 140, 158, 168).
Fioc, M. and B. Rocca-Volmerange (1999), *PEGASE.2, a metallicity-consistent spectral evolution model of galaxies: the documentation and the code*, arXiv e-prints, astro-ph/9912179 astro, arXiv: astro-ph/9912179 [astro-ph] (cit. on pp. 140, 158, 168).
Flores, R. A. and J. R. Primack (1994), *Observational and Theoretical Constraints on Singular Dark Matter Halos*, ApJ **427** L1, arXiv: astro-ph/9402004 [astro-ph] (cit. on p. 49).
Fontanot, F., G. De Lucia, P. Monaco, R. S. Somerville and P. Santini (2009), *The many manifestations of downsizing: hierarchical galaxy formation models confront observations*, MNRAS **397** 1776, arXiv: 0901.1130 [astro-ph.CO] (cit. on p. 145).
Fontanot, F., F. La Barbera, G. De Lucia, A. Pasquali and A. Vazdekis (2018), *On the shape and evolution of a cosmic-ray-regulated galaxy-wide stellar initial mass function*, MNRAS **479** 5678, arXiv: 1807.01319 [astro-ph.GA] (cit. on p. 144).
Forbes, D. A. and P. Kroupa (2011), *What Is a Galaxy? Cast Your Vote Here*, Publ. Astron. Soc. Australia **28** 77, arXiv: 1101.3309 [astro-ph.GA] (cit. on p. 24).
Frenk, C. S. and S. D. M. White (2012), *Dark matter and cosmic structure*, Annalen der Physik **524** 507, arXiv: 1210.0544 [astro-ph.CO] (cit. on p. 34).
Friedmann, A. (1922), *Über die Krümmung des Raumes*, Zeitschrift fur Physik **10** 377 (cit. on pp. 27, 37).
Frith, W. J., G. S. Busswell, R. Fong, N. Metcalfe and T. Shanks (2003), *The local hole in the galaxy distribution: evidence from 2MASS*, MNRAS **345** 1049, arXiv: astro-ph/0302331 [astro-ph] (cit. on p. 78).
Frith, W. J., N. Metcalfe and T. Shanks (2006), *New H-band galaxy number counts: a large local hole in the galaxy distribution*, MNRAS **371** 1601, arXiv: astro-ph/0509875 [astro-ph] (cit. on p. 78).
Gaia Collaboration (2016), *The Gaia mission*, A&A **595**, A1 A1, arXiv: 1609.04153 [astro-ph.IM] (cit. on pp. 102, 105, 106, 129).
– (2018a), *Gaia Data Release 2. Kinematics of globular clusters and dwarf galaxies around the Milky Way*, A&A **616**, A12 A12, arXiv: 1804.09381 [astro-ph.GA] (cit. on pp. 102, 105–107, 119, 129, 130, 327).

Gaia Collaboration (2018b), *Gaia Data Release 2. Summary of the contents and survey properties*, A&A **616**, A1 A1, arXiv: 1804.09365 [astro-ph.GA] (cit. on pp. 102, 105, 106, 130).

Galilei, G. (1610), *Sidereus nuncius magna, longeque admirabilia spectacula pandens lunae facie, fixis innumeris, lacteo circulo, stellis nebulosis, ... Galileo Galileo : nuper a se reperti beneficio sunt observata in apprime vero in quatuor planetis circa Iovis stellam disparibus intervallis, atque periodis, celeritate mirabili circumvolutis ... atque Medicea sidera nuncupandos decrevit* (cit. on pp. 18, 139).

– (2016), *Sidereus Nuncius, or the sidereal messenger*, University of Chicago Press (cit. on p. 18).

Gallazzi, A., S. Charlot, J. Brinchmann, S. D. M. White and C. A. Tremonti (2005), *The ages and metallicities of galaxies in the local universe*, MNRAS **362** 41, arXiv: astro-ph/0506539 [astro-ph] (cit. on pp. 153, 154, 323).

Galle, J. G. (1846), *Account of the discovery of Le Verrier's planet Neptune, at Berlin, Sept. 23, 1846*, MNRAS **7** 153 (cit. on p. 22).

Garaldi, E., E. Romano-Dıaz, C. Porciani and M. S. Pawlowski (2018), *Radial Acceleration Relation of* Λ *CDM Satellite Galaxies*, Phys. Rev. Lett. **120**, 261301 261301, arXiv: 1712.04448 [astro-ph.GA] (cit. on p. 63).

Garavito-Camargo, N. et al. (2021), *The Clustering of Orbital Poles Induced by the LMC: Hints for the Origin of Planes of Satellites*, ApJ **923**, 140 140, arXiv: 2108.07321 [astro-ph.GA] (cit. on p. 121).

Geffert, M. (2020), *Ludwig van Beethoven und die Astronomie*, (cit. on pp. 22, 23).

Geha, M. et al. (2013), *The Stellar Initial Mass Function of Ultra-faint Dwarf Galaxies: Evidence for IMF Variations with Galactic Environment*, ApJ **771**, 29 29, arXiv: 1304.7769 [astro-ph.CO] (cit. on pp. 67, 144, 148, 166).

Gennaro, M. et al. (2018), *Evidence of a Non-universal Stellar Initial Mass Function. Insights from HST Optical Imaging of Six Ultra-faint Dwarf Milky Way Satellites*, ApJ **855**, 20 20, arXiv: 1801.06195 [astro-ph.GA] (cit. on pp. 67, 144, 166).

Gentile, G. et al. (2007), *Tidal dwarf galaxies as a test of fundamental physics*, A&A **472** L25, arXiv: 0706.1976 [astro-ph] (cit. on p. 177).

Gentile, G., B. Famaey and W. J. G. de Blok (2011), *THINGS about MOND*, A&A **527**, A76 A76, arXiv: 1011.4148 [astro-ph.CO] (cit. on p. 58).

Gentile, G., P. Salucci, U. Klein, D. Vergani and P. Kalberla (2004), *The cored distribution of dark matter in spiral galaxies*, MNRAS **351** 903, arXiv: astro-ph/0403154 [astro-ph] (cit. on p. 49).

Gerbal, D., F. Durret, M. Lachieze-Rey and G. Lima-Neto (1992), *Analysis of X-ray galaxy clusters in the framework of modified Newtonian dynamics.*, A%A **262** 395 (cit. on p. 63).

Gilder, J. and A.-L. Gilder (2005), *Heavenly intrigue: Johannes Kepler, Tycho Brahe, and the murder behind one of history's greatest scientific discoveries*, Anchor (cit. on p. 18).

Gilmore, G. and G. Tausch-Pebody (2022), *The 1919 eclipse results that verified general relativity and their later detractors: a story re-told*, Notes and Records: the Royal Society Journal of the History of Science **76** 155, eprint: https://royalsocietypublishing.org/doi/pdf/10.1098/rsnr.2020.0040, URL: https://royalsocietypublishing.org/doi/abs/10.1098/rsnr.2020.0040 (cit. on p. 26).

Girardi, L. and G. Bertelli (1998), *The evolution of theV-Kcolours of single stellar populations*, MNRAS **300** 533, arXiv: astro-ph/9801145 [astro-ph] (cit. on p. 153).

Girardi, L., P. Marigo, A. Bressan and P. Rosenfield (2013), *The Insidious Boosting of Thermally Pulsing Asymptotic Giant Branch Stars in Intermediate-age Magellanic Cloud Clusters*, ApJ **777**, 142 142, arXiv: 1308.6088 [astro-ph.SR] (cit. on pp. 151, 153).

Gleick, J. (1992), *Genius: The life and science of Richard Feynman* (cit. on p. 2).

Gómez-Valent, A., A. Favale, M. Migliaccio and A. A. Sen (2023), *Late-time phenomenology required to solve the H_0 tension in view of the cosmic ladders and the anisotropic and angular BAO data sets*, arXiv e-prints, arXiv:2309.07795 arXiv:2309.07795, arXiv: 2309.07795 [astro-ph.CO] (cit. on p. 175).

Grazian, A. et al. (2015), *The galaxy stellar mass function at 3.5 ≤z ≤ 7.5 in the CANDELS/UDS, GOODS-South, and HUDF fields*, A&A **575**, A96 A96, arXiv: 1412.0532 [astro-ph.GA] (cit. on pp. 136, 166, 322).

Griffiths, M. and M. Boroughs (1913), *The Stars and Their Stories: A Book for Young People*, H. Holt, ISBN: 9781548800017, URL: https://books.google.de/books?id=E4IRAAAAYAAJ (cit. on p. 10).

Groenewegen, M. A. T. (2006), *The mid- and far-infrared colours of AGB and post-AGB stars*, A&A **448** 181, arXiv: astro-ph/0511475 [astro-ph] (cit. on pp. 140, 151, 152, 168, 177, 267).

Gunawardhana, M. L. P. et al. (2011), *Galaxy and Mass Assembly (GAMA): the star formation rate dependence of the stellar initial mass function*, MNRAS **415** 1647, arXiv: 1104.2379 [astro-ph.CO] (cit. on pp. 67, 144, 162).

Guo, Q. et al. (2011), *From dwarf spheroidals to cD galaxies: simulating the galaxy population in a ΛCDM cosmology*, MNRAS **413** 101, arXiv: 1006.0106 [astro-ph.CO] (cit. on p. 44).

Guth, A. H. (1981), *Inflationary universe: A possible solution to the horizon and flatness problems*, Phys. Rev. D **23** 347 (cit. on p. 32).

Haghi, H. et al. (2019), *A new formulation of the external field effect in MOND and numerical simulations of ultra-diffuse dwarf galaxies - application to NGC 1052-DF2 and NGC 1052-DF4*, MNRAS **487** 2441, arXiv: 1906.03268 [astro-ph.GA] (cit. on p. 53).

Hammer, F., Y. B. Yang, H. Flores, M. Puech and S. Fouquet (2015), *The Magellanic Stream System. I. Ram-Pressure Tails and the Relics of the Collision Between the Magellanic Clouds*, ApJ **813**, 110 110, arXiv: 1510.00096 [astro-ph.GA] (cit. on p. 106).

Harikane, Y. et al. (2023), *A Comprehensive Study of Galaxies at z 9-16 Found in the Early JWST Data: Ultraviolet Luminosity Functions and Cosmic Star Formation History at the Pre-reionization Epoch*, ApJS **265**, 5 5, arXiv: 2208.01612 [astro-ph.GA] (cit. on pp. 76, 95, 99, 175).

Hartsuiker, L. and S. Ploeckinger (2020), *Abundance and group coalescence time-scales of compact groups of galaxies in the EAGLE simulation*, MNRAS **491** L66, arXiv: 1911.02025 [astro-ph.GA] (cit. on p. 173).

Haslbauer, M., J. Dabringhausen, P. Kroupa, B. Javanmardi and I. Banik (2019), *Galaxies lacking dark matter in the Illustris simulation*, A&A **626**, A47 A47, arXiv: 1905.03258 [astro-ph.GA] (cit. on pp. 52, 110, 123, 177).

Haslbauer, M., I. Banik and P. Kroupa (2020), *The KBC void and Hubble tension contradict ΛCDM on a Gpc scale - Milgromian dynamics as a possible solution*, MNRAS **499** 2845, arXiv: 2009.11292 [astro-ph.CO] (cit. on pp. 53–55, 59, 78, 80, 85–88, 99, 129, 172, 174, 175, 318, 319).

Haslbauer, M., I. Banik, P. Kroupa and K. Grishunin (2019), *The ultra-diffuse dwarf galaxies NGC 1052-DF2 and 1052-DF4 are in conflict with standard cosmology*, MNRAS **489** 2634, arXiv: 1909.04663 [astro-ph.GA] (cit. on pp. 52, 177).

Haslbauer, M., I. Banik, P. Kroupa, N. Wittenburg and B. Javanmardi (2022), *The High Fraction of Thin Disk Galaxies Continues to Challenge ΛCDM Cosmology*, ApJ **925**, 183 183, arXiv: 2202.01221 [astro-ph.GA] (cit. on pp. 49–51, 75, 76, 91–94, 131, 173, 316, 319).

Haslbauer, M., I. Banik, P. Kroupa and H. Zhao (submitted), *The Magellanic Clouds are very rare in the IllustrisTNG simulation*, (cit. on pp. 75, 101, 102, 104).

Haslbauer, M., P. Kroupa and T. Jerabkova (2023), *The cosmological star formation history from the Local Cosmological Volume of galaxies and constraints on the matter homogeneity*, MNRAS **524** 3252, arXiv: 2306.16436 (cit. on pp. 54, 80, 81, 133–137, 161, 167, 174–176, 322).

Haslbauer, M., P. Kroupa, A. H. Zonoozi and H. Haghi (2022), *Has JWST Already Falsified Dark-matter-driven Galaxy Formation?*, ApJL **939**, L31 L31, arXiv: 2210.14915 [astro-ph.GA] (cit. on pp. 55, 59, 64, 65, 76, 77, 95–99, 143, 167, 175, 176, 178, 320).

Haslbauer, M. et al. (submitted), *The effect of the environment-dependent stellar initial mass function on local star-forming galaxies*, (cit. on pp. 83, 139, 141).

Hawkins, G. S. (1963), *Stonehenge decoded*, Nature **200** 306 (cit. on p. 10).

Heithausen, A. (2004), *Molecular Hydrogen as Baryonic Dark Matter*, ApJ **606** L13, arXiv: astro-ph/0403514 [astro-ph] (cit. on p. 2).

Henderson, T. (1839), *On the parallax of α Centauri*, MNRAS **4** 168 (cit. on p. 15).

Hernandez, X. (2023), *Internal kinematics of Gaia DR3 wide binaries: anomalous behaviour in the low acceleration regime*, MNRAS **525** 1401, arXiv: 2304.07322 [astro-ph.GA] (cit. on pp. 176, 177).

Hernandez, X., S. Cookson and R. A. M. Cortés (2022), *Internal kinematics of Gaia eDR3 wide binaries*, MNRAS **509** 2304, arXiv: 2107.14797 [astro-ph.GA] (cit. on p. 176).

Hernández-Aguayo, C. et al. (2023), *The MillenniumTNG Project: high-precision predictions for matter clustering and halo statistics*, MNRAS **524** 2556, arXiv: 2210.10059 [astro-ph.CO] (cit. on pp. 34, 96, 175).

Herschel, J. F. W. (1864), *A General Catalogue of Nebulae and Clusters of Stars*, Philosophical Transactions of the Royal Society of London Series I **154** 1 (cit. on p. 22).

Herschel, W. (1781), *XXXII. Account of a comet* (cit. on p. 22).

– (1786), *Catalogue of One Thousand New Nebulae and Clusters of Stars. By William Herschel, LL.D. F. R. S.*, Philosophical Transactions of the Royal Society of London Series I **76** 457 (cit. on p. 22).

– (1789), *Catalogue of a Second Thousand of New Nebulae and Clusters of Stars; With a Few Introductory Remarks on the Construction of the Heavens. By William Herschel, L L. D. F. R. S.*, Philosophical Transactions of the Royal Society of London Series I **79** 212 (cit. on p. 22).

– (1802), *Catalogue of 500 New Nebulae, Nebulous Stars, Planetary Nebulae, and Clusters of Stars; With Remarks on the Construction of the Heavens*, Philosophical Transactions of the Royal Society of London Series I **92** 477 (cit. on p. 22).

Hetherington, N. S. (2014), *Encyclopedia of cosmology (Routledge revivals): Historical, philosophical, and scientific foundations of modern cosmology*, Routledge (cit. on p. 8).

Heymans, C. et al. (2021), *KiDS-1000 Cosmology: Multi-probe weak gravitational lensing and spectroscopic galaxy clustering constraints*, A&A **646**, A140 A140, arXiv: 2007.15632 [astro-ph.CO] (cit. on p. 54).

Hickson, P. (1982), *Systematic properties of compact groups of galaxies*, ApJ **255** 382 (cit. on p. 173).

Higgins, E. R., J. S. Vink, G. N. Sabhahit and A. A. C. Sander (2022), *The hydrogen clock to infer the upper stellar mass*, MNRAS **516** 4052, arXiv: 2209.00667 [astro-ph.SR] (cit. on p. 146).

Hinshaw, G. et al. (2013), *Nine-year Wilkinson Microwave Anisotropy Probe (WMAP) Observations: Cosmological Parameter Results*, ApJS **208**, 19 19, arXiv: 1212.5226 [astro-ph.CO] (cit. on p. 44).
Hodge, J. A., C. L. Carilli, F. Walter, E. Daddi and D. Riechers (2013), *High-resolution Spectroscopic Imaging of CO in a $z = 4.05$ Proto-cluster*, ApJ **776**, 22 22, arXiv: 1307.4763 [astro-ph.CO] (cit. on p. 64).
Hopkins, A. M. (2018), *The Dawes Review 8: Measuring the Stellar Initial Mass Function*, PASA **35**, e039 e039, arXiv: 1807.09949 [astro-ph.GA] (cit. on p. 143).
Hopkins, A. M. and J. F. Beacom (2006), *On the Normalization of the Cosmic Star Formation History*, ApJ **651** 142, arXiv: astro-ph/0601463 [astro-ph] (cit. on p. 166).
– (2008), *Erratum: "On the Normalization of the Cosmic Star Formation History" (ApJ, 651, 142 [20067])*, ApJ **682**, 1486 1486 (cit. on p. 166).
Hopkins, P. F. et al. (2014), *Galaxies on FIRE (Feedback In Realistic Environments): stellar feedback explains cosmologically inefficient star formation*, MNRAS **445** 581, arXiv: 1311.2073 [astro-ph.CO] (cit. on p. 34).
Hopkins, P. F. et al. (2018), *FIRE-2 simulations: physics versus numerics in galaxy formation*, MNRAS **480** 800, arXiv: 1702.06148 [astro-ph.GA] (cit. on p. 34).
Hopkins, P. F. et al. (2023), *FIRE-3: updated stellar evolution models, yields, and microphysics and fitting functions for applications in galaxy simulations*, MNRAS **519** 3154, arXiv: 2203.00040 [astro-ph.GA] (cit. on p. 34).
Hoscheit, B. L. and A. J. Barger (2018), *The KBC Void: Consistency with Supernovae Type Ia and the Kinematic SZ Effect in a ΛLTB Model*, ApJ **854**, 46 46, arXiv: 1801.01890 [astro-ph.CO] (cit. on p. 86).
Hoskin, M. (1985), *Stukeley's Cosmology and the Newtonian Origins of Olbers's Paradox*, Journal for the History of Astronomy **16** 77 (cit. on p. 22).
Hossenfelder, S. (2022), *Existential Physics: A Scientist's Guide to Life's Biggest Questions*, Atlantic Books (cit. on p. 133).
Hoversten, E. A. and K. Glazebrook (2008), *Evidence for a Nonuniversal Stellar Initial Mass Function from the Integrated Properties of SDSS Galaxies*, ApJ **675** 163, arXiv: 0711.1309 [astro-ph] (cit. on p. 67).
Hoyle, F. (1948), *A New Model for the Expanding Universe*, MNRAS **108** 372 (cit. on p. 32).
Hoyle, F. (1966), *Speculations on Stonehenge*, Antiquity **40** 262 (cit. on p. 10).
Hu, W., R. Barkana and A. Gruzinov (2000), *Fuzzy Cold Dark Matter: The Wave Properties of Ultralight Particles*, PhysRevLett **85** 1158, arXiv: astro-ph/0003365 [astro-ph] (cit. on p. 2).
Hubble, E. P. (1929), *A Relation between Distance and Radial Velocity among Extra-Galactic Nebulae*, Proceedings of the National Academy of Science **15** 168 (cit. on pp. 27, 28, 314).
– (1936), *Realm of the Nebulae* (cit. on pp. 25, 314).
Humboldt, A. von (1869), *Kosmos: Entwurf einer physischen Weltbeschreibung*, Bd. 1, Cotta, URL: https://books.google.de/books?id=FmJuAAAAIAAJ (cit. on p. 101).
Ibata, R. A. et al. (2014), *A Thousand Shadows of Andromeda: Rotating Planes of Satellites in the Millennium-II Cosmological Simulation*, ApJL **784**, L6 L6, arXiv: 1403.2389 [astro-ph.GA] (cit. on pp. 52, 124, 131, 174, 328).
Ibata, R. A. et al. (2013), *A vast, thin plane of corotating dwarf galaxies orbiting the Andromeda galaxy*, Nature **493** 62, arXiv: 1301.0446 [astro-ph.CO] (cit. on pp. 52, 174).

Inoue, K. T. and J. Silk (2006), *Local Voids as the Origin of Large-Angle Cosmic Microwave Background Anomalies. I.*, ApJ **648** 23, arXiv: astro-ph/0602478 [astro-ph] (cit. on p. 55).
– (2007), *Local Voids as the Origin of Large-Angle Cosmic Microwave Background Anomalies: The Effect of a Cosmological Constant*, ApJ **664** 650, arXiv: astro-ph/0612347 [astro-ph] (cit. on p. 55).
Jarrett, T. H. et al. (2000), *2MASS Extended Source Catalog: Overview and Algorithms*, AJ **119** 2498, arXiv: astro-ph/0004318 [astro-ph] (cit. on p. 151).
Jarrett, T. H., T. Chester, R. Cutri, S. E. Schneider and J. P. Huchra (2003), *The 2MASS Large Galaxy Atlas*, AJ **125** 525 (cit. on p. 151).
Javanmardi, B. and P. Kroupa (2017), *Anisotropy in the all-sky distribution of galaxy morphological types*, A&A **597**, A120 A120, arXiv: 1609.06719 [astro-ph.GA] (cit. on p. 55).
Jeans, J. H. (1928), *Astronomy and cosmogony* (cit. on pp. 25, 26, 314).
– (1929), *Astronomy and cosmogony*, CUP Archive (cit. on p. 32).
Jerábková, T. (2020), *Stellar populations in gravitationally bound systems*, PhD thesis: Rheinische Friedrich Wilhelms University of Bonn, Germany (cit. on p. 66).
Jeřábková, T. et al. (2018), *Impact of metallicity and star formation rate on the time-dependent, galaxy-wide stellar initial mass function*, A&A **620**, A39 A39, arXiv: 1809.04603 [astro-ph.GA] (cit. on pp. 67, 69–71, 81, 140, 141, 144–149, 157, 158, 165, 166, 168, 317, 323).
Joeveer, M. (2007), "Wirtz, Carl Wilhelm", *The Biographical Encyclopedia of Astronomers*, ed. by T. Hockey et al., New York, NY: Springer New York 1233, ISBN: 978-0-387-30400-7, URL: https://doi.org/10.1007/978-0-387-30400-7_1491 (cit. on p. 29).
Kalari, V. M., G. Carraro, C. J. Evans and M. Rubio (2018), *The Magellanic Bridge Cluster NGC 796: Deep Optical AO Imaging Reveals the Stellar Content and Initial Mass Function of a Massive Open Cluster*, ApJ **857**, 132 132, arXiv: 1801.01490 [astro-ph.SR] (cit. on p. 67).
Kallivayalil, N., R. P. van der Marel and C. Alcock (2006), *Is the SMC Bound to the LMC? The Hubble Space Telescope Proper Motion of the SMC*, ApJ **652** 1213, arXiv: astro-ph/0606240 [astro-ph] (cit. on pp. 101, 105).
Kallivayalil, N. et al. (2006), *The Proper Motion of the Large Magellanic Cloud Using HST*, ApJ **638** 772, arXiv: astro-ph/0508457 [astro-ph] (cit. on pp. 101, 105).
Kallivayalil, N., R. P. van der Marel, G. Besla, J. Anderson and C. Alcock (2013), *Third-epoch Magellanic Cloud Proper Motions. I. Hubble Space Telescope/WFC3 Data and Orbit Implications*, ApJ **764**, 161 161, arXiv: 1301.0832 [astro-ph.CO] (cit. on pp. 101, 105–107, 119, 129, 327).
Kanas, N. (2009), *Star Maps: History, Artistry, and Cartography*, Springer Praxis Books, Praxis, ISBN: 9780387716688, URL: https://books.google.de/books?id=xepttjhzaH8C (cit. on p. 15).
Kannan, R. et al. (2023), *The MillenniumTNG project: the galaxy population at $z \geq 8$*, MNRAS **524** 2594, arXiv: 2210.10066 [astro-ph.GA] (cit. on pp. 96, 175).
Kant, I. (1755), *Allgemeine Naturgeschichte und Theorie des Himmels, nach Newtonischen Grundsätzen abgehandelt*, URL: https://books.google.de/books?id=zbFDAAAAcAAJ (cit. on p. 95).
Karachentsev, I. D. (2012), *Missing dark matter in the local universe*, Astrophysical Bulletin **67** 123, arXiv: 1204.3377 [astro-ph.CO] (cit. on pp. 53, 78, 79, 174, 317).
Karachentsev, I. D., E. I. Kaisina and D. I. Makarov (2018), *Morphological properties of galaxies in different Local Volume environments*, MNRAS **479** 4136, arXiv: 1806.09822 [astro-ph.GA] (cit. on p. 92).

Karachentsev, I. D. and K. N. Telikova (2018), *Stellar and dark matter density in the Local Universe*, Astronomische Nachrichten **339** 615, arXiv: 1810.06326 [astro-ph.GA] (cit. on pp. 53, 78, 109, 174).
Karachentsev, I. D. and E. I. Kaisina (2013), *Star Formation Properties in the Local Volume Galaxies via Hα and Far-ultraviolet Fluxes*, AJ **146**, 46 46, arXiv: 1305.4791 [astro-ph.CO] (cit. on pp. 139, 159).
Karachentsev, I. D., V. E. Karachentseva, W. K. Huchtmeier and D. I. Makarov (2004), *A Catalog of Neighboring Galaxies*, AJ **127** 2031 (cit. on pp. 53, 80, 91, 133, 139, 141, 145, 151, 159, 162, 168, 169, 324).
Karachentsev, I. D., D. I. Makarov and E. I. Kaisina (2013), *Updated Nearby Galaxy Catalog*, AJ **145**, 101 101, arXiv: 1303.5328 [astro-ph.CO] (cit. on pp. 53, 80, 91, 133, 135, 139, 142, 145, 151, 159, 162, 168, 169, 324).
Karwal, T. and M. Kamionkowski (2016), *Dark energy at early times, the Hubble parameter, and the string axiverse*, PhysRevD **94**, 103523 103523, arXiv: 1608.01309 [astro-ph.CO] (cit. on p. 86).
Kashlinsky, A., F. Atrio-Barandela and H. Ebeling (2011), *Measuring the Dark Flow with Public X-ray Cluster Data*, ApJ **732**, 1 1, arXiv: 1012.3214 [astro-ph.CO] (cit. on p. 175).
Kashlinsky, A., F. Atrio-Barandela, D. Kocevski and H. Ebeling (2008), *A Measurement of Large-Scale Peculiar Velocities of Clusters of Galaxies: Results and Cosmological Implications*, ApJ **686** L49, arXiv: 0809.3734 [astro-ph] (cit. on p. 175).
Katrin Collaboration Aker, M. et al. (2022), *Direct neutrino-mass measurement with sub-electronvolt sensitivity*, Nature Physics **18** 160 (cit. on p. 59).
Keenan, R. C., A. J. Barger and L. L. Cowie (2013), *Evidence for a ∼300 Megaparsec Scale Under-density in the Local Galaxy Distribution*, ApJ **775**, 62 62, arXiv: 1304.2884 [astro-ph.CO] (cit. on pp. 53, 78–80, 85–87, 174, 317–319).
Keenan, R. C. et al. (2012), *Testing for a Large Local Void by Investigating the Near-infrared Galaxy Luminosity Function*, ApJ **754**, 131 131, arXiv: 1207.1588 [astro-ph.CO] (cit. on pp. 79, 317).
Keller, B. W. and J. W. Wadsley (2017), *ΛCDM is Consistent with SPARC Radial Acceleration Relation*, ApJL **835**, L17 L17, arXiv: 1610.06183 [astro-ph.GA] (cit. on p. 47).
Kelvin, W. T. B. (2010), *Baltimore lectures on molecular dynamics and the wave theory of light*, Cambridge University Press (cit. on pp. 30, 31).
Kennicutt R. C., J. (1983), *The rate of star formation in normal disk galaxies.*, ApJ **272** 54 (cit. on p. 144).
– (1998), *Star Formation in Galaxies Along the Hubble Sequence*, ARA&A **36** 189, arXiv: astro-ph/9807187 [astro-ph] (cit. on pp. 81, 139, 144, 145, 157–160, 168, 177, 324).
Kennicutt R. C., J. and N. J. Evans (2012), *Star Formation in the Milky Way and Nearby Galaxies*, ARA&A **50** 531, arXiv: 1204.3552 [astro-ph.GA] (cit. on p. 144).
Kepler, J. (1609), *Astronomia nova ..., seu physica coelestis, tradita commentariis de motibus stellae martis* ... lat, Heidelberg: Voegelin (cit. on p. 19).
– (1619), *Ioannis Keppleri harmonices mundi libri V: quorum primus geometricus ... secundus architectonicus ... tertius proprie harmonicus ... quartus metaphysicus, psychologicus et astrologicus ... quintus astronomicus metaphysicus ... : appendix habet comparationem huius operis cum harmonices Cl. Ptolemaei libro III cumque Roberti de Fluctibus ... speculationibus harmonicis, operi de macrocosmo microcosmo insertis*, lat, Lincii Austriae [Linz]: sumptibus Godofredi Tampachii ... excudebat Ioannes Plancus (cit. on p. 19).

Kewley, L. J., M. J. Geller, R. A. Jansen and M. A. Dopita (2002), *The Hα and Infrared Star Formation Rates for the Nearby Field Galaxy Survey*, AJ **124** 3135, arXiv: astro-ph/0208508 [astro-ph] (cit. on p. 144).

Kim, J. et al. (2021), *Head-to-Toe Measurement of El Gordo: Improved Analysis of the Galaxy Cluster ACT-CL J0102-4915 with New Wide-field Hubble Space Telescope Imaging Data*, ApJ **923**, 101 101, arXiv: 2106.00031 [astro-ph.CO] (cit. on p. 53).

King, H. (2003), *The History of the Telescope*, Dover Books on Astronomy Series, Dover Publications, ISBN: 9780486432656, URL: https://books.google.de/books?id=KAWwzHlDVksC (cit. on p. 18).

Kirby, E. N. et al. (2013), *The Universal Stellar Mass-Stellar Metallicity Relation for Dwarf Galaxies*, ApJ **779**, 102 102, arXiv: 1310.0814 [astro-ph.GA] (cit. on pp. 153, 154, 323).

Kirshner, R. P. (2004), *Hubble's diagram and cosmic expansion*, Proceedings of the National Academy of Science **101** 8 (cit. on pp. 28, 314).

Klimentowski, J. et al. (2010), *The grouping, merging and survival of subhaloes in the simulated Local Group*, MNRAS **402** 1899, arXiv: 0909.1916 [astro-ph.CO] (cit. on p. 122).

Klypin, A. A., A. V. Kravtsov, O. Valenzuela and F. Prada (1999), *Where Are the Missing Galactic Satellites?*, ApJ **522** 82, arXiv: astro-ph/9901240 [astro-ph] (cit. on p. 49).

Klypin, A. A., S. Trujillo-Gomez and J. R. Primack (2011), *Dark Matter Halos in the Standard Cosmological Model: Results from the Bolshoi Simulation*, ApJ **740**, 102 102, arXiv: 1002.3660 [astro-ph.CO] (cit. on p. 119).

Koen, C. (2006), *On the upper limit on stellar masses in the Large Magellanic Cloud cluster R136*, MNRAS **365** 590 (cit. on p. 146).

Kogut, A. et al. (1993), *Dipole Anisotropy in the COBE Differential Microwave Radiometers First-Year Sky Maps*, ApJ **419** 1, arXiv: astro-ph/9312056 [astro-ph] (cit. on p. 87).

Köppen, J., C. Weidner and P. Kroupa (2007), *A possible origin of the mass-metallicity relation of galaxies*, MNRAS **375** 673, arXiv: astro-ph/0611723 [astro-ph] (cit. on p. 144).

Koupelis, T. and K. Kuhn (2007), *In Quest of the Universe*, Jones and Bartlett Publishers, ISBN: 9780763743871, URL: https://books.google.de/books?id=6rTttN4ZdyoC (cit. on p. 37).

Krafft, F. (2007), *Die bedeutendsten Astronomen*, marixwissen, marixverlag, ISBN: 9783843802321, URL: https://books.google.de/books?id=TZd4DwAAQBAJ (cit. on pp. 9, 11, 15, 16).

Kragh, H. (2012), *"The most philosophically of all the sciences": Karl Popper and physical cosmology*, URL: http://philsci-archive.pitt.edu/9062/ (cit. on p. 21).

– (2021), "Karl Popper and Modern Cosmology: His Thoughts and Their Impact", *Karl Popper's Science and Philosophy*, ed. by Z. Parusniková and D. Merritt, Cham: Springer International Publishing 53, ISBN: 978-3-030-67036-8, URL: https://doi.org/10.1007/978-3-030-67036-8_4 (cit. on p. 32).

Kraljic, D. and S. Sarkar (2015), *How rare is the Bullet Cluster (in a ΛCDM universe)?*, JCAP **2015** 050, arXiv: 1412.7719 [astro-ph.CO] (cit. on p. 53).

Krauss, L. M. and M. S. Turner (1995), *The cosmological constant is back*, General Relativity and Gravitation **27** 1137, arXiv: astro-ph/9504003 [astro-ph] (cit. on p. 33).

Kravtsov, A. (2010), *The Dark Matter Annihilation Signal from Dwarf Galaxies and Subhalos*, Advances in Astronomy **2010**, 281913 281913, arXiv: 0906.3295 [astro-ph.CO] (cit. on p. 49).

Krishnan, C., E. Ó. Colgáin, A. A. Ruchika Sen, M. M. Sheikh-Jabbari and T. Yang (2020), *Is there an early Universe solution to Hubble tension?*, Phys. Rev. D **102**, 103525 103525, arXiv: 2002.06044 [astro-ph.CO] (cit. on p. 175).

Kroupa, P. (2005), "The Fundamental Building Blocks of Galaxies", *The Three-Dimensional Universe with Gaia*, ed. by C. Turon, K. S. O'Flaherty and M. A. C. Perryman, vol. 576, ESA Special Publication 629, arXiv: astro-ph/0412069 [astro-ph] (cit. on pp. 4, 9, 69, 82, 171, 318).
– (2012), *The Dark Matter Crisis: Falsification of the Current Standard Model of Cosmology*, Publ. Astron. Soc. Australia **29** 395, arXiv: 1204.2546 [astro-ph.CO] (cit. on pp. 3, 34, 37, 47, 50, 52, 74, 127, 177).
Kroupa, P. et al. (2010), *Local-Group tests of dark-matter concordance cosmology . Towards a new paradigm for structure formation*, A&A **523**, A32 A32, arXiv: 1006.1647 [astro-ph.CO] (cit. on pp. 3, 34, 37, 47, 49, 74).
Kroupa, P., M. Haslbauer, I. Banik, S. T. Nagesh and J. Pflamm-Altenburg (2020), *Constraints on the star formation histories of galaxies in the Local Cosmological Volume*, MNRAS **497** 37, arXiv: 2007.07905 [astro-ph.GA] (cit. on pp. 80, 133–135, 153, 161–163, 167, 169, 175, 324).
Kroupa, P., M. S. Pawlowski and M. Milgrom (2012), *The Failures of the Standard Model of Cosmology Require a New Paradigm*, International Journal of Modern Physics D **21**, 1230003 1230003, arXiv: 1301.3907 [astro-ph.CO] (cit. on pp. 34, 47).
Kroupa, P., S. Röser and U. Bastian (1994), *On the motion of the Magellanic Clouds*, MNRAS **266** 412 (cit. on p. 105).
Kroupa, P., C. Theis and C. M. Boily (2005), *The great disk of Milky-Way satellites and cosmological sub-structures*, A&A **431** 517, arXiv: astro-ph/0410421 [astro-ph] (cit. on pp. 50, 52, 120, 174).
Kroupa, P. (1995), *The dynamical properties of stellar systems in the Galactic disc*, MNRAS **277** 1507, arXiv: astro-ph/9508084 [astro-ph] (cit. on p. 148).
– (1997), *Dwarf spheroidal satellite galaxies without dark matter*, New Astron. **2** 139 (cit. on pp. 63, 105).
– (1998), *The dynamical evolution of stellar superclusters*, MNRAS **300** 200, arXiv: astro-ph/9806206 [astro-ph] (cit. on p. 24).
– (2001), *On the variation of the initial mass function*, MNRAS **322** 231, arXiv: astro-ph/0009005 [astro-ph] (cit. on pp. 4, 66, 68, 71, 76, 81, 146, 147, 149, 153, 268, 316, 317, 323, 325).
– (2002), *The Initial Mass Function of Stars: Evidence for Uniformity in Variable Systems*, Science **295** 82, arXiv: astro-ph/0201098 [astro-ph] (cit. on pp. 66, 67, 147).
– (2015), *Galaxies as simple dynamical systems: observational data disfavor dark matter and stochastic star formation*, Canadian Journal of Physics **93** 169, arXiv: 1406.4860 [astro-ph.GA] (cit. on pp. 3, 4, 34, 37, 47, 49, 52, 74, 79, 89, 103, 105, 121, 123, 127, 131, 172, 173, 179, 317).
Kroupa, P. et al. (2023), *The many tensions with dark-matter based models and implications on the nature of the Universe*, arXiv e-prints, arXiv:2309.11552 arXiv:2309.11552, arXiv: 2309.11552 [astro-ph.CO] (cit. on pp. 3, 34, 37, 42, 47, 55, 63, 74, 97, 176, 320).
Kroupa, P. et al. (2018), *Does the galaxy NGC1052-DF2 falsify Milgromian dynamics?*, Nature **561** E4 (cit. on p. 53).
Kroupa, P. and T. Jerabkova (2019), *The Salpeter IMF and its descendants*, Nature Astronomy **3** 482, arXiv: 1910.01126 [astro-ph.SR] (cit. on pp. 4, 66, 70).
– (2021), *The initial mass function of stars and the star-formation rates of galaxies*, arXiv e-prints, arXiv:2112.10788 arXiv:2112.10788, arXiv: 2112.10788 [astro-ph.GA] (cit. on pp. 65, 68, 70, 81, 140, 144, 145, 161, 166, 178, 316).

Kroupa, P. et al. (2022), *Asymmetrical tidal tails of open star clusters: stars crossing their cluster's práh challenge Newtonian gravitation*, MNRAS **517** 3613, arXiv: 2210.13472 [astro-ph.GA] (cit. on pp. 57, 131).

Kroupa, P., L. Subr, T. Jerabkova and L. Wang (2020), *Very high redshift quasars and the rapid emergence of supermassive black holes*, MNRAS **498** 5652, arXiv: 2007.14402 [astro-ph.GA] (cit. on p. 145).

Kroupa, P. and C. Weidner (2003), *Galactic-Field Initial Mass Functions of Massive Stars*, ApJ **598** 1076, arXiv: astro-ph/0308356 [astro-ph] (cit. on pp. 4, 65, 69, 82, 139, 144, 146–148, 168, 318).

Kroupa, P. et al. (2013), "The Stellar and Sub-Stellar Initial Mass Function of Simple and Composite Populations", *Planets, Stars and Stellar Systems. Volume 5: Galactic Structure and Stellar Populations*, ed. by T. D. Oswalt and G. Gilmore, vol. 5 115 (cit. on pp. 4, 144, 146).

Kučera, J. et al. (2017), *Was He Murdered or Was He Not?—Part II: Multi-Elemental Analyses of Hair and Bone Samples from Tycho Brahe and Histopathology of His Bones*, Archaeometry **59** 918 (cit. on p. 19).

Kuhn, T. S. (1992), *The Copernican revolution: Planetary astronomy in the development of Western thought*, Harvard University Press (cit. on p. 18).

– (1997), *The structure of scientific revolutions*, vol. 962, University of Chicago press Chicago (cit. on p. 8).

Labbé, I. et al. (2023), *A population of red candidate massive galaxies 600 Myr after the Big Bang*, Nature **616** 266, arXiv: 2207.12446 [astro-ph.GA] (cit. on pp. 55, 64, 76, 95, 96, 175).

Lada, C. J. and E. A. Lada (2003), *Embedded Clusters in Molecular Clouds*, ARA&A **41** 57, arXiv: astro-ph/0301540 [astro-ph] (cit. on pp. 147, 148).

Lavaux, G. and M. J. Hudson (2011), *The 2M++ galaxy redshift catalogue*, MNRAS **416** 2840, arXiv: 1105.6107 [astro-ph.CO] (cit. on pp. 78, 85, 174).

Leavitt, H. S. and E. C. Pickering (1912), *Periods of 25 Variable Stars in the Small Magellanic Cloud.*, Harvard College Observatory Circular **173** 1 (cit. on p. 24).

Lee, J. C. et al. (2009), *Comparison of Hα and UV Star Formation Rates in the Local Volume: Systematic Discrepancies for Dwarf Galaxies*, ApJ **706** 599, arXiv: 0909.5205 [astro-ph.CO] (cit. on pp. 67, 144).

Lee, J. and E. Komatsu (2010), *Bullet Cluster: A Challenge to ΛCDM Cosmology*, ApJ **718** 60, arXiv: 1003.0939 [astro-ph.CO] (cit. on p. 53).

Lee, M. G., A. Aparicio, N. Tikonov, Y.-I. Byun and E. Kim (1999), *Stellar Populations and the Local Group Membership of the Dwarf Galaxy DDO 210*, AJ **118** 853, arXiv: astro-ph/9905060 [astro-ph] (cit. on p. 165).

Leja, J., A. C. Carnall, B. D. Johnson, C. Conroy and J. S. Speagle (2019), *How to Measure Galaxy Star Formation Histories. II. Nonparametric Models*, ApJ **876**, 3 3, arXiv: 1811.03637 [astro-ph.GA] (cit. on p. 135).

Leja, J., P. G. van Dokkum, M. Franx and K. E. Whitaker (2015), *Reconciling the Observed Star-forming Sequence with the Observed Stellar Mass Function*, ApJ **798**, 115 115, arXiv: 1407.1842 [astro-ph.GA] (cit. on p. 166).

Lelli, F., S. S. McGaugh and J. M. Schombert (2016), *The Small Scatter of the Baryonic Tully-Fisher Relation*, ApJL **816**, L14 L14, arXiv: 1512.04543 [astro-ph.GA] (cit. on p. 70).

Lelli, F., S. S. McGaugh, J. M. Schombert, H. Desmond and H. Katz (2019), *The baryonic Tully-Fisher relation for different velocity definitions and implications for galaxy angular momentum*, MNRAS **484** 3267, arXiv: 1901.05966 [astro-ph.GA] (cit. on pp. 47, 61, 62, 70, 178, 316).
Lelli, F., S. S. McGaugh, J. M. Schombert and M. S. Pawlowski (2017), *One Law to Rule Them All: The Radial Acceleration Relation of Galaxies*, ApJ **836**, 152 152, arXiv: 1610.08981 [astro-ph.GA] (cit. on pp. 47, 60–63, 316).
Lemaître, G. (1927), *Un Univers homogène de masse constante et de rayon croissant rendant compte de la vitesse radiale des nébuleuses extra-galactiques*, Annales de la Societe Scientifique de Bruxelles **47** 49 (cit. on pp. 27, 37).
– (1931), *A homogeneous universe of constant mass and increasing radius accounting for the radial velocity of extra-galactic nebulae*, MNRAS **91** 483 (cit. on pp. 27, 38).
Li, H., M. Vogelsberger, F. Marinacci, L. V. Sales and P. Torrey (2020), *The effects of subgrid models on the properties of giant molecular clouds in galaxy formation simulations*, MNRAS **499** 5862, arXiv: 2001.07214 [astro-ph.GA] (cit. on p. 143).
Li, J. et al. (2023), *Stellar initial mass function varies with metallicity and time*, Nature **613** 460, arXiv: 2301.07029 [astro-ph.GA] (cit. on pp. 67, 144).
Li, P. et al. (2023), *Measuring galaxy cluster mass profiles into the low-acceleration regime with galaxy kinematics*, A&A **677**, A24 A24, arXiv: 2303.10175 [astro-ph.CO] (cit. on p. 63).
Li, Y.-S. and A. Helmi (2008), *Infall of substructures on to a Milky Way-like dark halo*, MNRAS **385** 1365, arXiv: 0711.2429 [astro-ph] (cit. on p. 121).
Li, Y.-S. and S. D. M. White (2008), *Masses for the Local Group and the Milky Way*, MNRAS **384** 1459, arXiv: 0710.3740 [astro-ph] (cit. on pp. 109, 128).
Libeskind, N. I. et al. (2011), *The preferred direction of infalling satellite galaxies in the Local Group*, MNRAS **411** 1525, arXiv: 1010.1531 [astro-ph.CO] (cit. on p. 122).
Licquia, T. C. and J. A. Newman (2015), *Improved Estimates of the Milky Way's Stellar Mass and Star Formation Rate from Hierarchical Bayesian Meta-Analysis*, ApJ **806**, 96 96, arXiv: 1407.1078 [astro-ph.GA] (cit. on pp. 46, 48, 109, 117, 315, 327).
Lieberz, P. and P. Kroupa (2017), *On the origin of the Schechter-like mass function of young star clusters in disc galaxies*, MNRAS **465** 3775 (cit. on pp. 69, 147).
Lilly, S. J., O. Le Fevre, F. Hammer and D. Crampton (1996), *The Canada-France Redshift Survey: The Luminosity Density and Star Formation History of the Universe to Z approximately 1*, ApJL **460** L1, arXiv: astro-ph/9601050 [astro-ph] (cit. on pp. 80, 133).
Linde, A. D. (1982), *A new inflationary universe scenario: A possible solution of the horizon, flatness, homogeneity, isotropy and primordial monopole problems*, Physics Letters B **108** 389 (cit. on p. 32).
Liu, L., B. F. Gerke, R. H. Wechsler, P. S. Behroozi and M. T. Busha (2011), *How Common are the Magellanic Clouds?*, ApJ **733**, 62 62, arXiv: 1011.2255 [astro-ph.CO] (cit. on p. 119).
Livio, M. and T. M. Brown (2006), *The Local Group as an Astrophysical Laboratory*, Space Telescope Science Institute Symposium Series 17, Cambridge University Press (cit. on p. 110).
Lodes, B. (1997), *Das Gloria in Beethovens Missa Solemnis*, vol. 54, Schneider (cit. on p. 22).
Longhorn, M. and S. Hughes (2015), *Modern replication of Eratosthenes' measurement of the circumference of Earth*, Physics Education **50** 175 (cit. on p. 12).
Lonoce, I., W. L. Freedman and A. Feldmeier-Krause (2023), *The Initial Mass Function and Other Stellar Properties Across the Core of the Hydra I Cluster*, ApJ **948**, 65 65, arXiv: 2303.00044 [astro-ph.GA] (cit. on p. 166).

López-Corredoira, M., J. E. Betancort-Rijo, R. Scarpa and Ž. Chrobáková (2022), *Virial theorem in clusters of galaxies with MOND*, MNRAS **517** 5734, arXiv: 2210.13961 [astro-ph.GA] (cit. on p. 63).

López-Corredoira, M. (2022), *Fundamental Ideas in Cosmology*, 2053-2563, IOP Publishing, ISBN: 978-0-7503-3775-5, URL: https://dx.doi.org/10.1088/978-0-7503-3775-5 (cit. on pp. 9, 21, 33).

Lorenz, R. (2019), *Exploring Planetary Climate: A History of Scientific Discovery on Earth, Mars, Venus and Titan*, Cambridge University Press, ISBN: 9781108645331, URL: https://books.google.de/books?id=75CFDwAAQBAJ (cit. on p. 91).

Lovell, C. C., I. Harrison, Y. Harikane, S. Tacchella and S. M. Wilkins (2023), *Extreme value statistics of the halo and stellar mass distributions at high redshift: are JWST results in tension with ΛCDM?*, MNRAS **518** 2511, arXiv: 2208.10479 [astro-ph.GA] (cit. on p. 55).

Lovell, M. R., V. R. Eke, C. S. Frenk and A. Jenkins (2011), *The link between galactic satellite orbits and subhalo accretion*, MNRAS **413** 3013, arXiv: 1008.0484 [astro-ph.CO] (cit. on p. 122).

Lucchini, S. et al. (2020), *The Magellanic Corona as the key to the formation of the Magellanic Stream.*, Nature **585** 203, arXiv: 2009.04368 [astro-ph.GA] (cit. on pp. 116, 131).

Lucchini, S., E. D'Onghia and A. J. Fox (2021), *The Magellanic Stream at 20 kpc: A New Orbital History for the Magellanic Clouds*, ApJL **921**, L36 L36, arXiv: 2110.11355 [astro-ph.GA] (cit. on p. 131).

Ludlow, A. D. et al. (2017), *Mass-Discrepancy Acceleration Relation: A Natural Outcome of Galaxy Formation in Cold Dark Matter Halos*, Phys. Rev. Lett. **118**, 161103 161103, arXiv: 1610.07663 [astro-ph.GA] (cit. on p. 47).

Ludlow, A. D., S. M. Fall, J. Schaye and D. Obreschkow (2021), *Spurious heating of stellar motions in simulated galactic discs by dark matter halo particles*, MNRAS **508** 5114, arXiv: 2105.03561 [astro-ph.GA] (cit. on p. 93).

Lüghausen, F., B. Famaey and P. Kroupa (2015), *Phantom of RAMSES (POR): A new Milgromian dynamicsN-body code*, Canadian Journal of Physics **93** 232, arXiv: 1405.5963 [astro-ph.GA] (cit. on p. 168).

Luminet, J.-P. (2008), *The wraparound universe*, CRC Press (cit. on p. 8).

Lundmark, K. (1924), *The determination of the curvature of space-time in de Sitter's world*, MNRAS **84** 747 (cit. on p. 29).

Madau, P. and M. Dickinson (2014), *Cosmic Star-Formation History*, ARA&A **52** 415, arXiv: 1403.0007 [astro-ph.CO] (cit. on pp. 81, 133–137, 166, 167, 322).

Madau, P. et al. (1996), *High-redshift galaxies in the Hubble Deep Field: colour selection and star formation history to z∼4*, MNRAS **283** 1388, arXiv: astro-ph/9607172 [astro-ph] (cit. on pp. 81, 133).

Madau, P. and T. Fragos (2017), *Radiation Backgrounds at Cosmic Dawn: X-Rays from Compact Binaries*, ApJ **840**, 39 39, arXiv: 1606.07887 [astro-ph.GA] (cit. on pp. 81, 133).

Madau, P., L. Pozzetti and M. Dickinson (1998), *The Star Formation History of Field Galaxies*, ApJ **498** 106, arXiv: astro-ph/9708220 [astro-ph] (cit. on pp. 81, 133).

Maddox, S. J., W. J. Sutherland, G. Efstathiou, J. Loveday and B. A. Peterson (1990), *Galaxy Evolution at Low Redshift*, MNRAS **247** 1P (cit. on pp. 53, 78, 85, 174).

Mahajan, S. et al. (2019), *The Star Formation Reference Survey - III. A multiwavelength view of star formation in nearby galaxies*, MNRAS **482** 560, arXiv: 1810.01336 [astro-ph.GA] (cit. on p. 144).

Maino, D., S. Donzelli, A. J. Banday, F. Stivoli and C. Baccigalupi (2007), *Cosmic microwave background signal in Wilkinson Microwave Anisotropy Probe three-year data with FASTICA*, MNRAS **374** 1207, arXiv: astro-ph/0609228 [astro-ph] (cit. on p. 55).
Maíz Apellániz, J. (2006), *A Recalibration of Optical Photometry: Tycho-2, Strömgren, and Johnson Systems*, AJ **131** 1184, arXiv: astro-ph/0510785 [astro-ph] (cit. on pp. 152, 168, 177, 267).
Maız Apellániz, J., N. R. Walborn, N. I. Morrell, V. S. Niemela and E. P. Nelan (2007), *Pismis 24-1: The Stellar Upper Mass Limit Preserved*, ApJ **660** 1480, arXiv: astro-ph/0612012 [astro-ph] (cit. on p. 146).
Malekjani, M., S. Rahvar and H. Haghi (2009), *Spherical Collapse in Modified Newtonian Dynamics*, ApJ **694** 1220, arXiv: 0811.1833 [astro-ph] (cit. on p. 99).
Marigo, P., A. Bressan, A. Nanni, L. Girardi and M. L. Pumo (2013), *Evolution of thermally pulsing asymptotic giant branch stars - I. The COLIBRI code*, MNRAS **434** 488, arXiv: 1305.4485 [astro-ph.SR] (cit. on pp. 140, 145, 150, 151).
Marinacci, F. et al. (2018), *First results from the IllustrisTNG simulations: radio haloes and magnetic fields*, MNRAS **480** 5113, arXiv: 1707.03396 [astro-ph.CO] (cit. on pp. 34, 44, 92, 96, 102, 108).
Marks, M., P. Kroupa, J. Dabringhausen and M. S. Pawlowski (2012), *Evidence for top-heavy stellar initial mass functions with increasing density and decreasing metallicity*, MNRAS **422** 2246, arXiv: 1202.4755 [astro-ph.GA] (cit. on pp. 67, 69, 70, 144, 147, 148, 168).
– (2014), *Erratum: Evidence for top-heavy stellar initial mass functions with increasing density and decreasing metallicity*, MNRAS **442** 3315 (cit. on pp. 67, 69, 70, 147).
Marriage, T. A. et al. (2011), *The Atacama Cosmology Telescope: Sunyaev-Zel'dovich-Selected Galaxy Clusters at 148 GHz in the 2008 Survey*, ApJ **737**, 61 61, arXiv: 1010.1065 [astro-ph.CO] (cit. on p. 53).
Martın-Navarro, I. et al. (2019), *Fornax 3D project: a two-dimensional view of the stellar initial mass function in the massive lenticular galaxy FCC 167*, A&A **626**, A124 A124, arXiv: 1903.10514 [astro-ph.GA] (cit. on pp. 67, 144, 166).
Mason, C. A., M. Trenti and T. Treu (2023), *The brightest galaxies at cosmic dawn*, MNRAS **521** 497, arXiv: 2207.14808 [astro-ph.GA] (cit. on p. 99).
Massana, P. et al. (2022), *The synchronized dance of the magellanic clouds' star formation history*, MNRAS **513** L40, arXiv: 2203.09523 [astro-ph.GA] (cit. on p. 106).
Matteucci, F. (1994), *Abundance ratios in ellipticals and galaxy formation.*, A&A **288** 57 (cit. on p. 66).
Matteucci, F. and E. Brocato (1990), *Metallicity Distribution and Abundance Ratios in the Stars of the Galactic Bulge*, ApJ **365** 539 (cit. on p. 66).
Mazurenko, S., I. Banik, P. Kroupa and M. Haslbauer (2023), *A simultaneous solution to the Hubble tension and observed bulk flow within 250 h^{-1} Mpc*, MNRAS (cit. on p. 175).
Mazzi, A. et al. (2021), *The VMC survey - XLIII. The spatially resolved star formation history across the Large Magellanic Cloud*, MNRAS **508** 245, arXiv: 2108.07225 [astro-ph.GA] (cit. on p. 106).
McAlpine, S. et al. (2016), *The EAGLE simulations of galaxy formation: Public release of halo and galaxy catalogues*, Astronomy and Computing **15** 72, arXiv: 1510.01320 [astro-ph.GA] (cit. on pp. 34, 45, 46, 92, 96).

McConnachie, A. W. (2012), *The Observed Properties of Dwarf Galaxies in and around the Local Group*, AJ **144**, 4 4, arXiv: 1204.1562 [astro-ph.CO] (cit. on pp. 49, 101, 105, 107, 109, 110, 117, 121, 327).
McGaugh, S. S. (2008), *Milky Way Mass Models and MOND*, ApJ **683** 137, arXiv: 0804.1314 [astro-ph] (cit. on p. 61).
– (2014), *The Third Law of Galactic Rotation*, Galaxies **2** 601, arXiv: 1412.3767 [astro-ph.GA] (cit. on p. 61).
– (2015), *A tale of two paradigms: the mutual incommensurability of ΛCDM and MOND*, Canadian Journal of Physics **93** 250, arXiv: 1404.7525 [astro-ph.CO] (cit. on p. 3).
– (2020), *Predictions and Outcomes for the Dynamics of Rotating Galaxies*, Galaxies **8** 35, arXiv: 2004.14402 [astro-ph.GA] (cit. on p. 60).
McGaugh, S. S., F. Lelli and J. M. Schombert (2016), *Radial Acceleration Relation in Rotationally Supported Galaxies*, PhRvL **117**, 201101 201101, arXiv: 1609.05917 [astro-ph.GA] (cit. on pp. 47, 60–62, 316).
McGaugh, S. S. and M. Milgrom (2013a), *Andromeda Dwarfs in Light of MOND. II. Testing Prior Predictions*, ApJ **775**, 139 139, arXiv: 1308.5894 [astro-ph.CO] (cit. on pp. 123, 127).
McGaugh, S. S. and M. Milgrom (2013b), *Andromeda Dwarfs in Light of Modified Newtonian Dynamics*, ApJ **766**, 22 22, arXiv: 1301.0822 [astro-ph.CO] (cit. on pp. 123, 127).
McGaugh, S. S., J. M. Schombert, G. D. Bothun and W. J. G. de Blok (2000), *The Baryonic Tully-Fisher Relation*, ApJL **533** L99, arXiv: astro-ph/0003001 [astro-ph] (cit. on pp. 47, 61, 70).
McGaugh, S. S. and J. M. Schombert (2014), *Color-Mass-to-light-ratio Relations for Disk Galaxies*, AJ **148**, 77 77, arXiv: 1407.1839 [astro-ph.GA] (cit. on pp. 133, 160).
– (2015), *Weighing Galaxy Disks With the Baryonic Tully-Fisher Relation*, ApJ **802**, 18 18, arXiv: 1501.06826 [astro-ph.GA] (cit. on pp. 70, 72, 178).
McGaugh, S. S., J. M. Schombert and F. Lelli (2017), *The Star-forming Main Sequence of Dwarf Low Surface Brightness Galaxies*, ApJ **851**, 22 22, arXiv: 1710.11236 [astro-ph.GA] (cit. on pp. 134, 135, 161).
McGaugh, S. S. and J. Wolf (2010), *Local Group Dwarf Spheroidals: Correlated Deviations from the Baryonic Tully-Fisher Relation*, ApJ **722** 248, arXiv: 1003.3448 [astro-ph.CO] (cit. on pp. 123, 127).
McQuinn, K. B. W., M. Boyer, E. D. Skillman and A. E. Dolphin (2019), *Using the Tip of the Red Giant Branch As a Distance Indicator in the Near Infrared*, ApJ **880**, 63 63 (cit. on p. 267).
Melia, F. and A. S. H. Shevchuk (2012), *The R_h=ct universe*, MNRAS **419** 2579, arXiv: 1109.5189 [astro-ph.CO] (cit. on p. 55).
Melia, F. (2023), *The cosmic timeline implied by the JWST high-redshift galaxies*, MNRAS **521** L85, arXiv: 2302.10103 [astro-ph.CO] (cit. on pp. 55, 64, 76, 99, 175).
Menanteau, F. et al. (2010), *The Atacama Cosmology Telescope: Physical Properties and Purity of a Galaxy Cluster Sample Selected via the Sunyaev-Zel'dovich Effect*, ApJ **723** 1523, arXiv: 1006.5126 [astro-ph.CO] (cit. on p. 53).
Mercado, F. J. et al. (2023), *Hooks & Bends in the Radial Acceleration Relation: Tests for Dark Matter and Challenges for MOND*, arXiv e-prints, arXiv:2307.09507 arXiv:2307.09507, arXiv: 2307.09507 [astro-ph.GA] (cit. on p. 63).
Merritt, D. (2020), *A philosophical approach to MOND: Assessing the Milgromian research program in cosmology*, Cambridge University Press (cit. on pp. 9, 57).

Messier, C. (1781), *Catalogue des Nébuleuses et des Amas d'Étoiles (Catalog of Nebulae and Star Clusters)*, Connoissance des Temps ou des Mouvements Célestes, for 1784, p. 227-267 (cit. on p. 22).
Metz, M., P. Kroupa and H. Jerjen (2007), *The spatial distribution of the Milky Way and Andromeda satellite galaxies*, MNRAS **374** 1125, arXiv: astro-ph/0610933 [astro-ph] (cit. on p. 120).
Meurer, G. R. et al. (2009), *Evidence for a Nonuniform Initial Mass Function in the Local Universe*, ApJ **695** 765, arXiv: 0902.0384 [astro-ph.GA] (cit. on pp. 67, 144).
Migkas, K. et al. (2021), *Cosmological implications of the anisotropy of ten galaxy cluster scaling relations*, A&A **649**, A151 A151, arXiv: 2103.13904 [astro-ph.CO] (cit. on pp. 54, 175).
Migkas, K. et al. (2020), *Probing cosmic isotropy with a new X-ray galaxy cluster sample through the L_X-T scaling relation*, A&A **636**, A15 A15, arXiv: 2004.03305 [astro-ph.CO] (cit. on p. 175).
Milgrom, M. (1983a), *A modification of the Newtonian dynamics - Implications for galaxies.*, ApJ **270** 371 (cit. on pp. 57, 60).
– (1983b), *A modification of the newtonian dynamics : implications for galaxy systems.*, ApJ **270** 384 (cit. on pp. 57, 60).
– (1983c), *A modification of the Newtonian dynamics as a possible alternative to the hidden mass hypothesis.*, ApJ **270** 365 (cit. on pp. 3, 31, 57, 61, 128, 131, 168).
– (1986), *Solutions for the Modified Newtonian Dynamics Field Equation*, ApJ **302** 617 (cit. on p. 59).
Milgrom, M. (2002), *Does Dark Matter Really Exist?*, Scientific American **287** 42 (cit. on p. 57).
– (2010), *Quasi-linear formulation of MOND*, MNRAS **403** 886, arXiv: 0911.5464 [astro-ph.CO] (cit. on p. 58).
Miller, G. E. and J. M. Scalo (1979), *The Initial Mass Function and Stellar Birthrate in the Solar Neighborhood*, ApJS **41** 513 (cit. on pp. 4, 66).
Mirabel, I. F., H. Dottori and D. Lutz (1992), *Genesis of a dwarf galaxy from the debris of the Antennae.*, A&A **256** L19 (cit. on p. 122).
Misner, C., K. Thorne, J. Wheeler and D. Kaiser (2017), *Gravitation*, Princeton University Press, ISBN: 9781400889099, URL: https://books.google.de/books?id=zAAuDwAAQBAJ (cit. on p. 26).
Moore, B. (1994), *Evidence against dissipation-less dark matter from observations of galaxy haloes*, Nature **370** 629 (cit. on p. 49).
Moore, B. et al. (1999), *Dark Matter Substructure within Galactic Halos*, ApJL **524** L19, arXiv: astro-ph/9907411 [astro-ph] (cit. on p. 49).
Morgan, W. W. (1958), *A Preliminary Classification of the Forms of Galaxies According to Their Stellar Population*, PASP **70** 364 (cit. on p. 26).
– (1959), *Preliminary Classification of the Forms of Galaxies According to Their Stellar Population. II*, PASP **71** 394 (cit. on p. 26).
Morgan, W. W. and N. U. Mayall (1957), *A Spectral Classification of Galaxies*, PASP **69** 291 (cit. on p. 26).
Morishita, T. et al. (2023), *Early Results from GLASS-JWST. XIV. A Spectroscopically Confirmed Protocluster 650 Million Years after the Big Bang*, ApJL **947**, L24 L24, arXiv: 2211.09097 [astro-ph.GA] (cit. on p. 64).
Moster, B. P., T. Naab and S. D. M. White (2013), *Galactic star formation and accretion histories from matching galaxies to dark matter haloes*, MNRAS **428** 3121, arXiv: 1205.5807 [astro-ph.CO] (cit. on p. 124).
Moster, B. P. et al. (2010), *Constraints on the Relationship between Stellar Mass and Halo Mass at Low and High Redshift*, ApJ **710** 903, arXiv: 0903.4682 [astro-ph.CO] (cit. on pp. 48, 315).

Moustakas, J., J. Kennicutt Robert C. and C. A. Tremonti (2006), *Optical Star Formation Rate Indicators*, ApJ **642** 775, arXiv: astro-ph/0511730 [astro-ph] (cit. on p. 144).
Mozel, P. (2003), *The Sky Disk of Nebra*, J. R. Astron. Soc. Canada **97** 245 (cit. on p. 10).
Mucciarelli, A. et al. (2021), *A relic from a past merger event in the Large Magellanic Cloud*, Nature Astronomy **5** 1247, arXiv: 2110.10561 [astro-ph.GA] (cit. on pp. 67, 144).
Müller, O. (2023), *Planes of satellites in the nearby Universe*, arXiv e-prints, arXiv:2304.13582 arXiv:2304.13582, arXiv: 2304.13582 [astro-ph.GA] (cit. on pp. 50, 52, 174).
Müller, O., M. S. Pawlowski, H. Jerjen and F. Lelli (2018), *A whirling plane of satellite galaxies around Centaurus A challenges cold dark matter cosmology*, Science **359** 534, arXiv: 1802.00081 [astro-ph.GA] (cit. on pp. 52, 174).
Murphy, T. W. (2013), *Lunar laser ranging: the millimeter challenge*, Reports on Progress in Physics **76**, 076901 076901, arXiv: 1309.6294 [gr-qc] (cit. on p. 15).
Nadathur, S., M. Lavinto, S. Hotchkiss and S. Räsänen (2014), *Can a supervoid explain the cold spot?*, Phys. Rev. D **90**, 103510 103510, arXiv: 1408.4720 [astro-ph.CO] (cit. on p. 55).
Naddaf, G. (1998), *On the origin of Anaximander's Cosmological Model*, Journal of the History of Ideas **59** 1 (cit. on p. 12).
Nagesh, S. T. et al. (2023), *Simulations of star-forming main-sequence galaxies in Milgromian gravity*, MNRAS **519** 5128, arXiv: 2212.07447 [astro-ph.GA] (cit. on p. 46).
Naidu, R. P. et al. (2022), *Schrodinger's Galaxy Candidate: Puzzlingly Luminous at $z \approx 17$, or Dusty/Quenched at $z \approx 5$?*, arXiv e-prints, arXiv:2208.02794 arXiv:2208.02794, arXiv: 2208.02794 [astro-ph.GA] (cit. on pp. 55, 64, 76, 95, 96, 175).
Naidu, R. P. et al. (2022), *Two Remarkably Luminous Galaxy Candidates at $z \approx 10$-12 Revealed by JWST*, ApJL **940**, L14 L14, arXiv: 2207.09434 [astro-ph.GA] (cit. on pp. 55, 64, 76, 95–97, 99, 175, 320).
Naiman, J. P. et al. (2018), *First results from the IllustrisTNG simulations: a tale of two elements - chemical evolution of magnesium and europium*, MNRAS **477** 1206, arXiv: 1707.03401 [astro-ph.GA] (cit. on pp. 34, 44, 92, 96, 102, 108).
Navarro, J. F. and W. Benz (1991), *Dynamics of Cooling Gas in Galactic Dark Halos*, ApJ **380** 320 (cit. on pp. 50, 91).
Navarro, J. F. and M. Steinmetz (2000), *Dark Halo and Disk Galaxy Scaling Laws in Hierarchical Universes*, ApJ **538** 477, arXiv: astro-ph/0001003 [astro-ph] (cit. on p. 91).
Navarro, J. F. and S. D. M. White (1994), *Simulations of dissipative galaxy formation in hierarchically clustering universes-2. Dynamics of the baryonic component in galactic haloes*, MNRAS **267** 401 (cit. on p. 91).
Nelson, D. et al. (2015), *The illustris simulation: Public data release*, Astronomy and Computing **13** 12, arXiv: 1504.00362 [astro-ph.CO] (cit. on pp. 34, 44, 108).
Nelson, D. et al. (2019), *First results from the TNG50 simulation: galactic outflows driven by supernovae and black hole feedback*, MNRAS **490** 3234, arXiv: 1902.05554 [astro-ph.GA] (cit. on pp. 34, 44, 92, 96, 102, 108).
Nelson, D. et al. (2018), *First results from the IllustrisTNG simulations: the galaxy colour bimodality*, MNRAS **475** 624, arXiv: 1707.03395 [astro-ph.GA] (cit. on pp. 34, 44, 92, 96, 102, 108).
Nelson, D. et al. (2019), *The IllustrisTNG simulations: public data release*, Computational Astrophysics and Cosmology **6**, 2 2, arXiv: 1812.05609 [astro-ph.GA] (cit. on pp. 34, 44, 92, 96, 102, 106, 108, 130).

Neugebauer, O. (1969), *The Exact Sciences in Antiquity*, Acta historica scientiarum naturalium et medicinalium, Dover Publications, ISBN: 9780486223322, URL: https://books.google.de/books?id=JVhTtVA2zr8C (cit. on p. 11).
Newton, I. (1687), *Philosophiae Naturalis Principia Mathematica.* (Cit. on p. 21).
Nichols, M. and J. Bland-Hawthorn (2011), *Gas Depletion in Local Group Dwarfs on ∼250 kpc Scales: Ram Pressure Stripping Assisted by Internal Heating at Early Times*, ApJ **732**, 17 17, arXiv: 1102.4849 [astro-ph.GA] (cit. on p. 121).
Nidever, D. L., S. R. Majewski, W. Butler Burton and L. Nigra (2010), *The 200° Long Magellanic Stream System*, ApJ **723** 1618, arXiv: 1009.0001 [astro-ph.GA] (cit. on p. 106).
Noirot, G. et al. (2023), *The first large catalogue of spectroscopic redshifts in Webb's first deep field, SMACS J0723.3-7327*, MNRAS **525** 1867, arXiv: 2212.07366 [astro-ph.GA] (cit. on p. 76).
Nurisso, G. C. and E. S. Prescott (2017), *The 1970s origins of too big to fail*, Economic Commentary (cit. on p. 49).
Nusser, A. (2002), *Modified Newtonian dynamics of large-scale structure*, MNRAS **331** 909, arXiv: astro-ph/0109016 [astro-ph] (cit. on p. 59).
O'Grady, P. (2017), *Thales of Miletus: The Beginnings of Western Science and Philosophy*, Western Philosophy Series, Taylor & Francis, ISBN: 9781351895378, URL: https://books.google.de/books?id=ZTUlDwAAQBAJ (cit. on p. 11).
O'Raifeartaigh, C. and S. Mitton (2018), *Interrogating the Legend of Einstein's "Biggest Blunder"*, Physics in Perspective **20** 318 (cit. on p. 26).
Oehm, W., I. Thies and P. Kroupa (2017), *Constraints on the dynamical evolution of the galaxy group M81*, MNRAS **467** 273, arXiv: 1701.01441 [astro-ph.GA] (cit. on pp. 49, 103, 130, 131, 172, 173).
Oesch, P. A. et al. (2016), *A Remarkably Luminous Galaxy at z=11.1 Measured with Hubble Space Telescope Grism Spectroscopy*, ApJ **819**, 129 129, arXiv: 1603.00461 [astro-ph.GA] (cit. on pp. 64, 97, 320).
Oey, M. S. and C. J. Clarke (2005), *Statistical Confirmation of a Stellar Upper Mass Limit*, ApJL **620** L43, arXiv: astro-ph/0501135 [astro-ph] (cit. on p. 146).
Ogle, P. M. et al. (2019), *A Break in Spiral Galaxy Scaling Relations at the Upper Limit of Galaxy Mass*, ApJL **884**, L11 L11, arXiv: 1909.09080 [astro-ph.GA] (cit. on p. 178).
Okazaki, T. and Y. Taniguchi (2000), *Dwarf Galaxy Formation Induced by Galaxy Interactions*, ApJ **543** 149, arXiv: astro-ph/0006006 [astro-ph] (cit. on p. 52).
Ostriker, J. P. and P. J. E. Peebles (1973), *A Numerical Study of the Stability of Flattened Galaxies: or, can Cold Galaxies Survive?*, ApJ **186** 467 (cit. on p. 31).
Ostriker, J. P. and P. J. Steinhardt (1995), *The observational case for a low-density Universe with a non-zero cosmological constant*, Nature 600 (cit. on pp. 2, 33).
Oteo, I. et al. (2018), *An Extreme Protocluster of Luminous Dusty Starbursts in the Early Universe*, ApJ **856**, 72 72, arXiv: 1709.02809 [astro-ph.GA] (cit. on p. 64).
Papadopoulos, P. P., W.-F. Thi, F. Miniati and S. Viti (2011), *Extreme cosmic ray dominated regions: a new paradigm for high star formation density events in the Universe*, MNRAS **414** 1705, arXiv: 1009.2496 [astro-ph.CO] (cit. on p. 144).
Papadopoulos, P. P. and W.-F. Thi (2013), "The Initial Conditions of Star Formation: Cosmic Rays as the Fundamental Regulators", *Cosmic Rays in Star-Forming Environments*, ed. by D. F. Torres and O. Reimer, vol. 34, Astrophysics and Space Science Proceedings 41, arXiv: 1207.2048 [astro-ph.HE] (cit. on p. 144).

Parikh, T. et al. (2018), *SDSS-IV MaNGA: the spatially resolved stellar initial mass function in ~400 early-type galaxies*, MNRAS **477** 3954, arXiv: 1803.08515 [astro-ph.GA] (cit. on pp. 67, 144, 148).

Pastorelli, G. et al. (2020), *Constraining the thermally pulsing asymptotic giant branch phase with resolved stellar populations in the Large Magellanic Cloud*, MNRAS **498** 3283, arXiv: 2008.08595 [astro-ph.SR] (cit. on p. 151).

Pastorelli, G. et al. (2019), *Constraining the thermally pulsing asymptotic giant branch phase with resolved stellar populations in the Small Magellanic Cloud*, MNRAS **485** 5666, arXiv: 1903.04499 [astro-ph.SR] (cit. on p. 151).

Pawlowski, M. S. (2021a), *It's time for some plane speaking*, Nature Astronomy **5** 1185 (cit. on pp. 50, 122).

– (2021b), *Phase-Space Correlations among Systems of Satellite Galaxies*, Galaxies **9** 66, arXiv: 2109.02654 [astro-ph.GA] (cit. on pp. 50, 103, 121, 129, 131).

Pawlowski, M. S. et al. (2014), *Co-orbiting satellite galaxy structures are still in conflict with the distribution of primordial dwarf galaxies*, MNRAS **442** 2362, arXiv: 1406.1799 [astro-ph.GA] (cit. on p. 122).

Pawlowski, M. S. and P. Kroupa (2020), *The Milky Way's disc of classical satellite galaxies in light of Gaia DR2*, MNRAS **491** 3042, arXiv: 1911.05081 [astro-ph.GA] (cit. on pp. 52, 102, 106, 107, 117, 119, 120, 122, 124, 129, 131, 174, 327, 328).

Pawlowski, M. S., P. Kroupa and H. Jerjen (2013), *Dwarf galaxy planes: the discovery of symmetric structures in the Local Group*, MNRAS **435** 1928, arXiv: 1307.6210 [astro-ph.CO] (cit. on pp. 127, 128, 174).

Pawlowski, M. S., P.-A. Oria, S. Taibi, B. Famaey and R. Ibata (2022), *On the Effect of the Large Magellanic Cloud on the Orbital Poles of Milky Way Satellite Galaxies*, ApJ **932**, 70 70, arXiv: 2111.05358 [astro-ph.GA] (cit. on p. 121).

Pawlowski, M. S., J. Pflamm-Altenburg and P. Kroupa (2012), *The VPOS: a vast polar structure of satellite galaxies, globular clusters and streams around the Milky Way*, MNRAS **423** 1109, arXiv: 1204.5176 [astro-ph.GA] (cit. on pp. 106, 120, 122).

Pedersen, O. and A. Jones (2010), *A Survey of the Almagest: With Annotation and New Commentary by Alexander Jones*, Sources and Studies in the History of Mathematics and Physical Sciences, Springer New York, ISBN: 9780387848266, URL: https://books.google.de/books?id=8eaHxE9jUrwC (cit. on p. 12).

Peebles, P. J. E. and A. Nusser (2010), *Nearby galaxies as pointers to a better theory of cosmic evolution*, Nature **465** 565, arXiv: 1001.1484 [astro-ph.CO] (cit. on pp. 53, 78, 174).

Penzias, A. A. and R. W. Wilson (1965), *A Measurement of Excess Antenna Temperature at 4080 Mc/s.*, ApJ **142** 419 (cit. on p. 32).

Perivolaropoulos, L. and F. Skara (2022), *Challenges for ΛCDM: An update*, New Astron. Rev. **95**, 101659 101659, arXiv: 2105.05208 [astro-ph.CO] (cit. on pp. 34, 37, 47).

Perlmutter, S. et al. (1998), *Discovery of a supernova explosion at half the age of the Universe*, Nature **391** 51, arXiv: astro-ph/9712212 [astro-ph] (cit. on p. 33).

Perryman, M. A. C. et al. (1997), *The Hipparcos Catalogue.*, A&A **500** 501 (cit. on p. 105).

Peuerbach, G. von (1508), *Theorica nova planetarum*, URL: https://books.google.de/books?id=SUpRAAAAcAAJ (cit. on p. 16).

Pfenniger, D., F. Combes and L. Martinet (1994), *Is dark matter in spiral galaxies cold gas? I. Observational constraints and dynamical clues about galaxy evolution*, A **285** 79, arXiv: astro-ph/9311043 [astro-ph] (cit. on p. 2).
Pflamm-Altenburg, J. and P. Kroupa (2008), *Clustered star formation as a natural explanation for the Hα cut-off in disk galaxies*, Nature **455** 641, arXiv: 0905.0898 [astro-ph.GA] (cit. on pp. 67, 144).
– (2009), *The Fundamental Gas Depletion and Stellar-Mass Buildup Times of Star-Forming Galaxies*, ApJ **706** 516, arXiv: 0910.1089 [astro-ph.CO] (cit. on pp. 140, 145, 147, 159, 162, 163, 165, 167–169).
Pflamm-Altenburg, J., C. Weidner and P. Kroupa (2007), *Converting Hα Luminosities into Star Formation Rates*, ApJ **671** 1550, arXiv: 0705.3177 [astro-ph] (cit. on p. 157).
– (2009), *Diverging UV and Hα fluxes of star-forming galaxies predicted by the IGIMF theory*, MNRAS **395** 394, arXiv: 0901.4335 [astro-ph.GA] (cit. on pp. 81, 144, 145, 157).
Pillepich, A. et al. (2019), *First results from the TNG50 simulation: the evolution of stellar and gaseous discs across cosmic time*, MNRAS **490** 3196, arXiv: 1902.05553 [astro-ph.GA] (cit. on pp. 34, 44, 92, 96, 102, 108).
Pillepich, A. et al. (2018a), *Simulating galaxy formation with the IllustrisTNG model*, MNRAS **473** 4077, arXiv: 1703.02970 [astro-ph.GA] (cit. on pp. 34, 44, 92, 96, 102, 106, 108, 130).
– (2018b), *Simulating galaxy formation with the IllustrisTNG model*, MNRAS **473** 4077, arXiv: 1703.02970 [astro-ph.GA] (cit. on pp. 34, 44, 92, 96, 102, 108).
Piontek, F. and M. Steinmetz (2011), *The modelling of feedback processes in cosmological simulations of disc galaxy formation*, MNRAS **410** 2625, arXiv: 0909.4156 [astro-ph.CO] (cit. on p. 50).
Pittordis, C. and W. J. Sutherland (2018), *Testing modified-gravity theories via wide binaries and GAIA*, MNRAS **480** 1778, arXiv: 1711.10867 [astro-ph.CO] (cit. on p. 176).
– (2019), *Testing modified gravity with wide binaries in Gaia DR2*, MNRAS **488** 4740, arXiv: 1905.09619 [astro-ph.CO] (cit. on p. 176).
– (2023), *Wide Binaries from GAIA EDR3: preference for GR over MOND?*, The Open Journal of Astrophysics **6**, 4 4, arXiv: 2205.02846 [astro-ph.GA] (cit. on pp. 176, 177).
Planck Collaboration et al. (2014), *Planck 2013 results. I. Overview of products and scientific results*, A&A **571**, A1 A1, arXiv: 1303.5062 [astro-ph.CO] (cit. on pp. 46, 55).
Planck Collaboration VI (2020a), *Planck 2018 results. VI. Cosmological parameters*, A&A **641**, A6 A6, arXiv: 1807.06209 [astro-ph.CO] (cit. on pp. 2, 34, 53).
– (2020b), *Planck 2018 results. VI. Cosmological parameters*, A&A **641**, A6 A6, arXiv: 1807.06209 [astro-ph.CO] (cit. on pp. 54, 87, 88, 319).
Planck Collaboration XIII (2016), *Planck 2015 results. XIII. Cosmological parameters*, A&A **594**, A13 A13, arXiv: 1502.01589 [astro-ph.CO] (cit. on pp. 2, 42–44, 53, 54, 95, 108, 133, 136, 145, 153, 163, 165, 315, 322, 324, 325).
Ploeckinger, S., G. Hensler, S. Recchi, N. Mitchell and P. Kroupa (2014), *Chemo-dynamical evolution of tidal dwarf galaxies. I. Method and IMF dependence*, MNRAS **437** 3980, arXiv: 1311.2932 [astro-ph.CO] (cit. on pp. 167, 178).
Ploeckinger, S., S. Recchi, G. Hensler and P. Kroupa (2015), *Chemodynamical evolution of tidal dwarf galaxies - II. The long-term evolution and influence of a tidal field*, MNRAS **447** 2512, arXiv: 1412.3450 [astro-ph.GA] (cit. on pp. 167, 178).
Ploeckinger, S. et al. (2018), *Tidal dwarf galaxies in cosmological simulations*, MNRAS **474** 580, arXiv: 1710.09380 [astro-ph.GA] (cit. on pp. 46, 52, 110, 123).

Poincaré, H. (1906a), *La Voie lactée et la théorie des gaz*, Bulletin de la société astronomique de France **20** 153 (cit. on p. 31).
– (1906b), *The Milky Way and the Theory of Gases*, Popular Astronomy **14** 475 (cit. on p. 31).
Pointecouteau, E. and J. Silk (2005), *New constraints on modified Newtonian dynamics from galaxy clusters*, MNRAS **364** 654, arXiv: astro-ph/0505017 [astro-ph] (cit. on p. 63).
Ponman, T. J. et al. (1994), *A possible fossil galaxy group*, Nature **369** 462 (cit. on p. 173).
Popper, K. R. (1957), *The Poverty of Historicism*, London: Routledge (cit. on p. 1).
– (1959), *The Logic of Scientific Discovery*, London: Hutchinson (cit. on p. 73).
– (1994), *Alles Leben ist Problemlösen: Über Erkenntnis*, Geschichte und Politik **3** (cit. on p. 171).
– (2014), *Conjectures and refutations: The growth of scientific knowledge*, routledge (cit. on p. 1).
Portegies Zwart, S. F., S. L. W. McMillan, P. Hut and J. Makino (2001), *Star cluster ecology - IV. Dissection of an open star cluster: photometry*, MNRAS **321** 199, arXiv: astro-ph/0005248 [astro-ph] (cit. on p. 9).
Poulin, V., J. L. Bernal, E. D. Kovetz and M. Kamionkowski (2023), *Sigma-8 tension is a drag*, Phys. Rev. D **107**, 123538 123538, arXiv: 2209.06217 [astro-ph.CO] (cit. on p. 54).
Poulin, V., T. L. Smith, T. Karwal and M. Kamionkowski (2019), *Early Dark Energy can Resolve the Hubble Tension*, PhysRevLett **122**, 221301 221301, arXiv: 1811.04083 [astro-ph.CO] (cit. on p. 86).
Querejeta, M. (2013), *On the Eclipse of Thales, Cycles and Probabilities*, arXiv e-prints, arXiv:1307.2095 arXiv:1307.2095, arXiv: 1307.2095 [physics.hist-ph] (cit. on p. 11).
Randall, L. (2012), *Knocking on Heaven's Door: How Physics and Scientific Thinking Illuminate Our Universe*, Random House (cit. on p. 85).
Raouf, M., S. S. Shabala, D. J. Croton, H. G. Khosroshahi and M. Bernyk (2017), *The many lives of active galactic nuclei-II: The formation and evolution of radio jets and their impact on galaxy evolution*, MNRAS **471** 658, arXiv: 1706.06595 [astro-ph.GA] (cit. on p. 44).
Rappenglück, M. (1997), "The Pleiades in the "Salle des Taureaux", grotte de Lascaux. Does a rock picture in the cave of Lascaux show the open star cluster of the Pleiades at the Magdalénien era (ca 15.300 BC?"", *Astronomy and Culture* 217 (cit. on pp. 9, 10).
Recchi, S., F. Calura and P. Kroupa (2009), *The chemical evolution of galaxies within the IGIMF theory: the [α/Fe] ratios and downsizing*, A&A **499** 711, arXiv: 0903.2395 [astro-ph.CO] (cit. on pp. 144, 148).
Reid, M. J. and K. M. Menten (2020), *The first stellar parallaxes revisited*, Astronomische Nachrichten **341** 860, arXiv: 2009.11913 [astro-ph.SR] (cit. on p. 15).
Renaud, F., B. Famaey and P. Kroupa (2016), *Star formation triggered by galaxy interactions in modified gravity*, MNRAS **463** 3637, arXiv: 1609.04407 [astro-ph.GA] (cit. on p. 128).
Reynolds, J. H. (1920), *Photometric measures of the nuclei of some typical spiral nebulæ*, MNRAS **80** 746 (cit. on pp. 25, 26, 314).
Rieke, G. H. et al. (2009), *Determining Star Formation Rates for Infrared Galaxies*, ApJ **692** 556, arXiv: 0810.4150 [astro-ph] (cit. on p. 144).
Riess, A. G., S. Casertano, W. Yuan, L. M. Macri and D. Scolnic (2019), *Large Magellanic Cloud Cepheid Standards Provide a 1% Foundation for the Determination of the Hubble Constant and Stronger Evidence for Physics beyond ΛCDM*, ApJ **876**, 85 85, arXiv: 1903.07603 [astro-ph.CO] (cit. on pp. 53, 87, 319).
Riess, A. G. et al. (1998), *Observational Evidence from Supernovae for an Accelerating Universe and a Cosmological Constant*, AJ **116** 1009, arXiv: astro-ph/9805201 [astro-ph] (cit. on p. 33).

Riess, A. G. et al. (2022), *A Comprehensive Measurement of the Local Value of the Hubble Constant with 1 km s^{-1} Mpc^{-1} Uncertainty from the Hubble Space Telescope and the SH0ES Team*, ApJL **934**, L7 L7, arXiv: 2112.04510 [astro-ph.CO] (cit. on pp. 27, 28, 314).
Rindler, W. (1956), *Visual horizons in world models*, MNRAS **116** 662 (cit. on p. 32).
Robertson, H. P. (1935), *Kinematics and World-Structure*, ApJ **82** 284 (cit. on p. 38).
Rodriguez-Gomez, V. et al. (2015), *The merger rate of galaxies in the Illustris simulation: a comparison with observations and semi-empirical models*, MNRAS **449** 49, arXiv: 1502.01339 [astro-ph.GA] (cit. on pp. 108, 114).
Rosenfield, P. et al. (2016), *Evolution of Thermally Pulsing Asymptotic Giant Branch Stars. V. Constraining the Mass Loss and Lifetimes of Intermediate-mass, Low-metallicity AGB Stars*, ApJ **822**, 73 73, arXiv: 1603.05283 [astro-ph.SR] (cit. on p. 151).
Röser, S. and U. Bastian (1993), *The Final PPM Star Catalogue for Both Hemispheres*, Bulletin d'Information du Centre de Donnees Stellaires **42** 11 (cit. on p. 105).
Roshan, M. et al. (2021), *Barred spiral galaxies in modified gravity theories*, MNRAS **503** 2833, arXiv: 2103.01794 [astro-ph.GA] (cit. on p. 131).
Roshan, M. et al. (2021), *Fast galaxy bars continue to challenge standard cosmology*, MNRAS **508** 926, arXiv: 2106.10304 [astro-ph.GA] (cit. on pp. 49, 103, 131, 173).
Rubart, M. and D. J. Schwarz (2013), *Cosmic radio dipole from NVSS and WENSS*, A&A **555**, A117 A117, arXiv: 1301.5559 [astro-ph.CO] (cit. on pp. 53, 78, 85, 174).
Rubart, M., D. Bacon and D. J. Schwarz (2014), *Impact of local structure on the cosmic radio dipole*, A&A **565**, A111 A111, arXiv: 1402.0376 [astro-ph.CO] (cit. on pp. 53, 78, 85, 174).
Rubin, V. C., D. Burstein, J. Ford W. K. and N. Thonnard (1985), *Rotation velocities of 16 SA galaxies and a comparison of Sa, SB and SC rotation properties.*, ApJ **289** 81 (cit. on pp. 2, 31).
Rubin, V. C., J. Ford W. K. and N. Thonnard (1978), *Extended rotation curves of high-luminosity spiral galaxies. IV. Systematic dynamical properties, Sa -> Sc.*, ApJL **225** L107 (cit. on pp. 2, 31).
– (1980), *Rotational properties of 21 SC galaxies with a large range of luminosities and radii, from NGC 4605 (R=4kpc) to UGC 2885 (R=122kpc).*, ApJ **238** 471 (cit. on pp. 2, 31).
Rubin, V. C. and J. Ford W. K. (1970), *Rotation of the Andromeda Nebula from a Spectroscopic Survey of Emission Regions*, ApJ **159** 379 (cit. on pp. 2, 31).
Ruggles, C., B. Cunliffe and C. Renfrew (1997), "Astronomy and Stonehenge", *Proceedings-British Academy*, vol. 92, OXFORD UNIVERSITY PRESS INC. 203 (cit. on p. 10).
Safarzadeh, M. and A. Loeb (2021), *The Challenge to MOND from Ultra-faint Dwarf Galaxies*, ApJL **914**, L37 L37, arXiv: 2104.13961 [astro-ph.GA] (cit. on p. 63).
Sakstein, J. and M. Trodden (2020), *Early Dark Energy from Massive Neutrinos as a Natural Resolution of the Hubble Tension*, PhRvL **124**, 161301 161301, arXiv: 1911.11760 [astro-ph.CO] (cit. on p. 86).
Salpeter, E. E. (1955), *The Luminosity Function and Stellar Evolution.*, ApJ **121** 161 (cit. on pp. 4, 65, 66, 139, 146, 157).
Samuel, J. et al. (2021), *Planes of satellites around Milky Way/M31-mass galaxies in the FIRE simulations and comparisons with the Local Group*, MNRAS **504** 1379, arXiv: 2010.08571 [astro-ph.GA] (cit. on p. 121).
Sancisi, R. (2004), "The visible matter – dark matter coupling", *Dark Matter in Galaxies*, ed. by S. Ryder, D. Pisano, M. Walker and K. Freeman, vol. 220 233, arXiv: astro-ph/0311348 [astro-ph] (cit. on pp. 46, 47).

Sandage, A. (1957), *Observational Approach to Evolution. I. Luminosity Functions.*, ApJ **125** 422 (cit. on pp. 4, 66).
Sanders, R. H. (1994), *A Faber-Jackson relation for clusters of galaxies: implications for modified dynamics.*, A&A **284** L31 (cit. on p. 63).
– (1998), *Cosmology with modified Newtonian dynamics (MOND)*, MNRAS **296** 1009, arXiv: astro-ph/9710335 [astro-ph] (cit. on p. 59).
– (1999), *The Virial Discrepancy in Clusters of Galaxies in the Context of Modified Newtonian Dynamics*, ApJL **512** L23, arXiv: astro-ph/9807023 [astro-ph] (cit. on p. 63).
– (2001), *The Formation of Cosmic Structure with Modified Newtonian Dynamics*, ApJ **560** 1, arXiv: astro-ph/0011439 [astro-ph] (cit. on p. 59).
– (2003), *Clusters of galaxies with modified Newtonian dynamics*, MNRAS **342** 901, arXiv: astro-ph/0212293 [astro-ph] (cit. on pp. 59, 63).
– (2007), *Neutrinos as cluster dark matter*, MNRAS **380** 331, arXiv: astro-ph/0703590 [astro-ph] (cit. on p. 63).
Sanders, R. H. (2010), *The Dark Matter Problem: A Historical Perspective* (cit. on p. 9).
Santos-Santos, I. M. E., A. Fattahi, L. V. Sales and J. F. Navarro (2021), *Magellanic satellites in ΛCDM cosmological hydrodynamical simulations of the Local Group*, MNRAS **504** 4551, arXiv: 2011.13500 [astro-ph.GA] (cit. on pp. 106, 118, 121, 131).
Sawala, T. et al. (2022), *The Milky Way's plane of satellites is consistent with ΛCDM*, Nature Astronomy, arXiv: 2205.02860 [astro-ph.GA] (cit. on p. 52).
Scannapieco, C. et al. (2012), *The Aquila comparison project: the effects of feedback and numerical methods on simulations of galaxy formation*, MNRAS **423** 1726, arXiv: 1112.0315 [astro-ph.GA] (cit. on pp. 50, 91).
Scarpa, R., R. Ottolina, R. Falomo and A. Treves (2017), *Dynamics of wide binary stars: A case study for testing Newtonian dynamics in the low acceleration regime*, International Journal of Modern Physics D **26**, 1750067 1750067, arXiv: 1611.08635 [astro-ph.GA] (cit. on p. 176).
Schaye, J. et al. (2015), *The EAGLE project: simulating the evolution and assembly of galaxies and their environments*, MNRAS **446** 521, arXiv: 1407.7040 [astro-ph.GA] (cit. on pp. 34, 45, 46, 92, 96).
Schilling, G. and L. L. Christensen (2013), *Europe to the stars: ESO's first 50 years of exploring the southern sky*, European Southern Observatory Willey-VCH Verlag Co. (cit. on p. 32).
Schneider, F. R. N. et al. (2018), *An excess of massive stars in the local 30 Doradus starburst*, Science **359** 69, arXiv: 1801.03107 [astro-ph.SR] (cit. on pp. 67, 144, 146).
Schneider, P. (2015), *Extragalactic Astronomy and Cosmology: An Introduction* (cit. on pp. 32, 37).
Schombert, J. M., S. S. McGaugh and F. Lelli (2019), *The mass-to-light ratios and the star formation histories of disc galaxies*, MNRAS **483** 1496, arXiv: 1811.10579 [astro-ph.GA] (cit. on pp. 134, 135, 161, 169).
Schwarz, D. J., C. J. Copi, D. Huterer and G. D. Starkman (2016), *CMB anomalies after Planck*, Classical and Quantum Gravity **33**, 184001 184001, arXiv: 1510.07929 [astro-ph.CO] (cit. on p. 55).
Scolnic, D. M. et al. (2018), *The Complete Light-curve Sample of Spectroscopically Confirmed SNe Ia from Pan-STARRS1 and Cosmological Constraints from the Combined Pantheon Sample*, ApJ **859**, 101 101, arXiv: 1710.00845 [astro-ph.CO] (cit. on pp. 54, 86).

Seneca, L. and L. Reynolds (1965), *L. Annaei Senecae Ad Lucilium epistulae morales*, Ad Lucilium epistulae morales Bd. 1, E Typographeo Clarendoniano, ISBN: 9780198146445, URL: https://books.google.de/books?id=_kj1wqwQ81UC (cit. on p. 7).
Shajib, A. J. et al. (2020), *STRIDES: a 3.9 per cent measurement of the Hubble constant from the strong lens system DES J0408-5354*, MNRAS **494** 6072, arXiv: 1910.06306 [astro-ph.CO] (cit. on p. 87).
Shanks, T., L. M. Hogarth and N. Metcalfe (2019), *Gaia Cepheid parallaxes and 'Local Hole' relieve H_0 tension*, MNRAS **484** L64, arXiv: 1810.02595 [astro-ph.CO] (cit. on p. 78).
Shanks, T., L. M. Hogarth, N. Metcalfe and J. Whitbourn (2019), *Local Hole revisited: evidence for bulk motions and self-consistent outflow*, MNRAS **490** 4715, arXiv: 1909.01878 [astro-ph.CO] (cit. on pp. 78, 86).
Shao, S., M. Cautun, A. J. Deason, C. S. Frenk and T. Theuns (2018), *Evolution of LMC/M33-mass dwarf galaxies in the EAGLE simulation*, MNRAS **479** 284, arXiv: 1803.07269 [astro-ph.GA] (cit. on p. 124).
Shao, S. et al. (2018), *The multiplicity and anisotropy of galactic satellite accretion*, MNRAS **476** 1796, arXiv: 1712.05409 [astro-ph.GA] (cit. on p. 122).
Shapley, H. and H. D. Curtis (1921), *The Scale of the Universe*, Bulletin of the National Research Council **2** 171 (cit. on p. 24).
Shipp, N. et al. (2021), *Measuring the Mass of the Large Magellanic Cloud with Stellar Streams Observed by S*^{5}, ApJ **923**, 149 149, arXiv: 2107.13004 [astro-ph.GA] (cit. on pp. 103, 123–127, 131, 321, 322, 328).
Simek, R. and K. Chlench (2006), *Johannes von Gmunden (ca. 1384-1442): Astronom und Mathematiker*, Studia medievalia septentrionalia, Fassbaender, ISBN: 9783900538958, URL: https://books.google.de/books?id=a%5C_4fAQAAIAAJ (cit. on p. 15).
Simek, R. and M. Klein (2012), *Johannes von Gmunden: –zwischen Astronomie und Astrologie*, Studia medievalia Septentrionalia, Fassbaender, ISBN: 9783902575470, URL: https://books.google.de/books?id=vazRlgEACAAJ (cit. on p. 15).
Simonyi, K. (2001), *Kulturgeschichte der Physik: Von den Anfängen bis heute*, Harri Deutsch Verlag (cit. on p. 9).
Skillman, E. D., S. Côté and B. W. Miller (2003), *Star Formation in Sculptor Group Dwarf Irregular Galaxies and the Nature of "Transition" Galaxies*, AJ **125** 593, arXiv: astro-ph/0211447 [astro-ph] (cit. on p. 159).
Skordis, C. and T. Złośnik (2019), *Gravitational alternatives to dark matter with tensor mode speed equaling the speed of light*, Phys. Rev. D **100**, 104013 104013, arXiv: 1905.09465 [gr-qc] (cit. on p. 59).
– (2021), *New Relativistic Theory for Modified Newtonian Dynamics*, Phys. Rev. Lett. **127**, 161302 161302, arXiv: 2007.00082 [astro-ph.CO] (cit. on p. 59).
Slipher, V. M. (1913), *The radial velocity of the Andromeda Nebula*, Lowell Observatory Bulletin **2** 56 (cit. on p. 27).
– (1917), *Nebulae*, Proceedings of the American Philosophical Society **56** 403 (cit. on pp. 27, 28, 314).
Smith, R. J. (2020), *Evidence for Initial Mass Function Variation in Massive Early-Type Galaxies*, ARA&A **58** 577 (cit. on pp. 67, 144).
Sneppen, A. et al. (2022), *Implications of a Temperature-dependent Initial Mass Function. I. Photometric Template Fitting*, ApJ **931**, 57 57, arXiv: 2205.11536 [astro-ph.GA] (cit. on p. 144).

Sohn, J. et al. (2015), *Compact Groups of Galaxies with Complete Spectroscopic Redshifts in the Local Universe*, Journal of Korean Astronomical Society **48** 381, arXiv: 1601.02646 (cit. on p. 173).

Sohn, J., M. J. Geller, H. S. Hwang, H. J. Zahid and M. G. Lee (2016), *Catalogs of Compact Groups of Galaxies from the Enhanced SDSS DR12*, ApJS **225**, 23 23, arXiv: 1603.06583 [astro-ph.GA] (cit. on p. 173).

Speagle, J. S., C. L. Steinhardt, P. L. Capak and J. D. Silverman (2014), *A Highly Consistent Framework for the Evolution of the Star-Forming "Main Sequence" from z ~0-6*, ApJS **214**, 15 15, arXiv: 1405.2041 [astro-ph.GA] (cit. on pp. 134, 140, 145, 153, 161, 162, 166, 167, 169, 322, 324).

Spergel, D. N. et al. (2003), *First-Year Wilkinson Microwave Anisotropy Probe (WMAP) Observations: Determination of Cosmological Parameters*, ApJS **148** 175, arXiv: astro-ph/0302209 [astro-ph] (cit. on p. 44).

Springel, V. (2005), *The cosmological simulation code GADGET-2*, MNRAS **364** 1105, arXiv: astro-ph/0505010 [astro-ph] (cit. on p. 45).

– (2010), *E pur si muove: Galilean-invariant cosmological hydrodynamical simulations on a moving mesh*, MNRAS **401** 791, arXiv: 0901.4107 [astro-ph.CO] (cit. on p. 45).

Springel, V. et al. (2018), *First results from the IllustrisTNG simulations: matter and galaxy clustering*, MNRAS **475** 676, arXiv: 1707.03397 [astro-ph.GA] (cit. on pp. 34, 37, 44, 92, 96, 102, 108).

Springel, V. et al. (2005), *Simulations of the formation, evolution and clustering of galaxies and quasars*, Nature **435** 629, arXiv: astro-ph/0504097 [astro-ph] (cit. on pp. 34, 44).

Springel, V., S. D. M. White, G. Tormen and G. Kauffmann (2001), *Populating a cluster of galaxies - I. Results at [formmu2]z=0*, MNRAS **328** 726, arXiv: astro-ph/0012055 [astro-ph] (cit. on p. 108).

Starobinsky, A. A. (1982), *Dynamics of phase transition in the new inflationary universe scenario and generation of perturbations*, Physics Letters B **117** 175 (cit. on p. 32).

Steer, I. (2012), *History: Who discovered Universe expansion?*, Nature **490** 176 (cit. on p. 29).

Stukeley, W. (1752), *Memoirs of Sir Isaac Newton's life* (cit. on p. 21).

Tenneti, A. et al. (2018), *The radial acceleration relation in disc galaxies in the MassiveBlack-II simulation*, MNRAS **474** 3125, arXiv: 1703.05287 [astro-ph.GA] (cit. on p. 47).

Tetzlaff, A. (2021), *" von kunst gewinnt man tugent"-Überlegungen zum Artes-liberales-Zyklus im Welschen Gast des Thomasin von Zerklaere*, (cit. on p. 7).

The, L. S. and S. D. M. White (1988), *Modified Newtonian Dymanics and the Coma Cluster*, AJ **95** 1642 (cit. on p. 63).

The EAGLE team (2017), *The EAGLE simulations of galaxy formation: Public release of particle data*, arXiv e-prints, arXiv:1706.09899 arXiv:1706.09899, arXiv: 1706.09899 [astro-ph.GA] (cit. on pp. 45, 46).

The Initial Mass Function 50 years later (2005), vol. 327, Astrophysics and Space Science Library (cit. on p. 67).

Tiesinga, E., P. J. Mohr, D. B. Newell and B. N. Taylor (2021), *CODATA recommended values of the fundamental physical constants: 2018**, Reviews of Modern Physics **93**, 025010 025010 (cit. on p. 21).

Tombaugh, C. W. (1946), *The Search for the Ninth Planet, Pluto*, Leaflet of the Astronomical Society of the Pacific **5** 73 (cit. on p. 22).

Tomczak, A. R. et al. (2016), *The SFR-M* Relation and Empirical Star-Formation Histories from ZFOURGE* at 0.5 < z < 4*, ApJ **817**, 118 118, arXiv: 1510.06072 [astro-ph.GA] (cit. on p. 167).

Tomozeiu, M., L. Mayer and T. Quinn (2016), *Tidal Stirring of Satellites with Shallow Density Profiles Prevents Them from Being Too Big to Fail*, ApJL **827**, L15 L15, arXiv: 1605.00004 [astro-ph.GA] (cit. on p. 50).
Toomer, G. J. (1974), *Hipparchus on the Distances of the Sun and Moon*, Archive for History of Exact Sciences **14** 126, ISSN: 00039519, 14320657, URL: http://www.jstor.org/stable/41133426 (visited on 13/11/2023) (cit. on p. 15).
Trabucchi, M. et al. (2021), *Modelling long-period variables - II. Fundamental mode pulsation in the non-linear regime*, MNRAS **500** 1575, arXiv: 2010.13654 [astro-ph.SR] (cit. on p. 151).
Trujillo-Gomez, S., A. Klypin, J. R. Primack and A. J. Romanowsky (2011), *Galaxies in ΛCDM with Halo Abundance Matching: Luminosity-Velocity Relation, Baryonic Mass-Velocity Relation, Velocity Function, and Clustering*, ApJ **742**, 16 16, arXiv: 1005.1289 [astro-ph.CO] (cit. on p. 119).
Tsujikawa, S. (2013), *Quintessence: a review*, Classical and Quantum Gravity **30**, 214003 214003, arXiv: 1304.1961 [gr-qc] (cit. on p. 41).
Tucker, W. et al. (1998), *1E 0657-56: A Contender for the Hottest Known Cluster of Galaxies*, ApJ **496** L5, arXiv: astro-ph/9801120 [astro-ph] (cit. on p. 53).
Tully, R. B. and J. R. Fisher (1977), *A new method of determining distances to galaxies.*, A&A **54** 661 (cit. on pp. 47, 57, 61, 70).
van den Bergh, S. (1959), *A Catalogue of Dwarf Galaxies*, Publications of the David Dunlap Observatory **2** 147 (cit. on p. 165).
van den Bosch, F. C. (2001), *The origin of the density distribution of disc galaxies: a new problem for the standard model of disc formation*, MNRAS **327** 1334, arXiv: astro-ph/0107195 [astro-ph] (cit. on p. 91).
van Dokkum, P. G. and C. Conroy (2010), *A substantial population of low-mass stars in luminous elliptical galaxies*, Nature **468** 940, arXiv: 1009.5992 [astro-ph.CO] (cit. on p. 67).
– (2021), *Variation in the Stellar Initial Mass Function from the Chromospheric Activity of M Dwarfs in Early-type Galaxies*, ApJ **923**, 43 43, arXiv: 2109.14632 [astro-ph.GA] (cit. on pp. 67, 144).
van Dokkum, P. G. et al. (2018), *A galaxy lacking dark matter*, Nature **555** 629, arXiv: 1803.10237 [astro-ph.GA] (cit. on p. 52).
Van Helden, A. (2010), *Measuring the Universe: Cosmic Dimensions from Aristarchus to Halley*, University of Chicago Press, ISBN: 9780226848907, URL: https://books.google.de/books?id=L-yb7GX9mQIC (cit. on pp. 12, 14, 312).
Vanderburgh, W. L. (2014), *Putting a New Spin on Galaxies: Horace W. Babcock, the Andromeda Nebula, and the Dark Matter Revolution*, Journal for the History of Astronomy **45** 141 (cit. on p. 31).
Vazdekis, A., R. F. Peletier, J. E. Beckman and E. Casuso (1997), *A New Chemo-evolutionary Population Synthesis Model for Early-Type Galaxies. II. Observations and Results*, ApJS **111** 203, arXiv: astro-ph/9701036 [astro-ph] (cit. on p. 66).
Vielva, P., E. Martınez-González, R. B. Barreiro, J. L. Sanz and L. Cayón (2004), *Detection of Non-Gaussianity in the Wilkinson Microwave Anisotropy Probe First-Year Data Using Spherical Wavelets*, ApJ **609** 22, arXiv: astro-ph/0310273 [astro-ph] (cit. on p. 55).
Vogelsberger, M. et al. (2014a), *Properties of galaxies reproduced by a hydrodynamic simulation*, Nature **509** 177, arXiv: 1405.1418 [astro-ph.CO] (cit. on pp. 34, 50, 51, 75, 91, 92, 173, 316).
– (2014b), *Properties of galaxies reproduced by a hydrodynamic simulation*, Nature **509** 177, arXiv: 1405.1418 [astro-ph.CO] (cit. on pp. 44, 108).

von Struve, O. W. (1840), *Über die Parallaxe des Sterns α Lyrae nach Micrometermessungen am großen Refractor der Dorpater Sternwarte.*, Astronomische Nachrichten **17** 177 (cit. on p. 15).
Walker, A. G. (1937), *On Milne's Theory of World-Structure*, Proceedings of the London Mathematical Society **42** 90 (cit. on p. 38).
Walter, F. et al. (2012), *The intense starburst HDF 850.1 in a galaxy overdensity at $z \approx 5.2$ in the Hubble Deep Field*, Nature **486** 233, arXiv: 1206.2641 [astro-ph.CO] (cit. on p. 64).
Wang, G. C. P. et al. (2021), *Overdensities of submillimetre-bright sources around candidate protocluster cores selected from the South Pole Telescope survey*, MNRAS **508** 3754, arXiv: 2010.02909 [astro-ph.CO] (cit. on p. 64).
Watkins, R. et al. (2023), *Analysing the large-scale bulk flow using cosmicflows4: increasing tension with the standard cosmological model*, MNRAS **524** 1885, arXiv: 2302.02028 [astro-ph.CO] (cit. on p. 175).
Watts, A. B. et al. (2018), *Star formation in the outskirts of DDO 154: a top-light IMF in a nearly dormant disc*, MNRAS **477** 5554, arXiv: 1804.07072 [astro-ph.GA] (cit. on pp. 67, 144).
Weidner, C. and P. Kroupa (2004), *Evidence for a fundamental stellar upper mass limit from clustered star formation*, MNRAS **348** 187, arXiv: astro-ph/0310860 [astro-ph] (cit. on pp. 146, 168).
Weidner, C., P. Kroupa and I. A. D. Bonnell (2010), *The relation between the most-massive star and its parental star cluster mass*, MNRAS **401** 275, arXiv: 0909.1555 [astro-ph.SR] (cit. on p. 168).
Weidner, C., P. Kroupa and S. S. Larsen (2004), *Implications for the formation of star clusters from extragalactic star formation rates*, MNRAS **350** 1503, arXiv: astro-ph/0402631 [astro-ph] (cit. on pp. 147, 148, 168).
Weidner, C. and P. Kroupa (2006), *The maximum stellar mass, star-cluster formation and composite stellar populations*, MNRAS **365** 1333, arXiv: astro-ph/0511331 [astro-ph] (cit. on pp. 146, 147, 168).
Weinberg, D. H., J. S. Bullock, F. Governato, R. Kuzio de Naray and A. H. G. Peter (2015), *Cold dark matter: Controversies on small scales*, Proceedings of the National Academy of Science **112** 12249, arXiv: 1306.0913 [astro-ph.CO] (cit. on pp. 78, 173).
Weisz, D. R., A. E. Dolphin, E. D. Skillman, J. Holtzman, J. J. Dalcanton et al. (2013), *Comparing the ancient star formation histories of the Magellanic Clouds*, MNRAS **431** 364, arXiv: 1301.7422 [astro-ph.CO] (cit. on p. 106).
Weisz, D. R., A. E. Dolphin, E. D. Skillman, J. Holtzman, K. M. Gilbert et al. (2014), *The Star Formation Histories of Local Group Dwarf Galaxies. II. Searching For Signatures of Reionization*, ApJ **789**, 148 148, arXiv: 1405.3281 [astro-ph.GA] (cit. on p. 135).
Wetzstein, M., T. Naab and A. Burkert (2007), *Do dwarf galaxies form in tidal tails?*, MNRAS **375** 805, arXiv: astro-ph/0510821 [astro-ph] (cit. on pp. 52, 123).
Wheeler, J. A. and K. Ford (1998), *Geons, black holes and quantum foam : a life in physics* (cit. on p. 26).
Whitbourn, J. R. and T. Shanks (2014), *The local hole revealed by galaxy counts and redshifts*, MNRAS **437** 2146, arXiv: 1307.4405 [astro-ph.CO] (cit. on p. 78).
Wilkins, S. M., N. Trentham and A. M. Hopkins (2008), *The evolution of stellar mass and the implied star formation history*, MNRAS **385** 687, arXiv: 0801.1594 [astro-ph] (cit. on p. 166).
Williams, A. A., V. Belokurov, A. R. Casey and N. W. Evans (2017), *On the run: mapping the escape speed across the Galaxy with SDSS*, MNRAS **468** 2359, arXiv: 1701.01444 [astro-ph.GA] (cit. on p. 128).

Willmer, C. N. A. (2018), *The Absolute Magnitude of the Sun in Several Filters*, ApJS **236**, 47 47, arXiv: 1804.07788 [astro-ph.SR] (cit. on p. 151).
Wirtz, C. (1916), *Die Trift der Nebelflecke*, Astronomische Nachrichten **203** 197 (cit. on p. 29).
– (1917), *Über die Eigenbewegungen der Nebelflecke*, Astronomische Nachrichten **204** 23 (cit. on p. 29).
– (1922a), *Einiges zur Statistik der Radialbewegungen von Spiralnebeln und Kugelsternhaufen*, Astronomische Nachrichten **215** 349 (cit. on pp. 28, 29, 314).
– (1922b), *Notiz zur Radialbewegung der Spiralnebel*, Astronomische Nachrichten **216** 451 (cit. on pp. 28, 314).
– (1924), *De Sitters Kosmologie und die Radialbewegungen der Spiralnebel*, Astronomische Nachrichten **222** 21 (cit. on pp. 28, 29, 314).
Wirtz, C. (1911a), *Beobachtungen von Nebelflecken am 49 cm-Refraktor. III. Teil. 1902 April bis 1910 März*, Annalen der Kaiserlichen Universitats-Sternwarte in Strassburg **4** 1 (cit. on p. 29).
– (1911b), *Vergleichung des Generalkatalogs der am großen Refraktor in Straßbur beobachteten Nebelflecke mit andern Nebelverzeichnissen*, Annalen der Kaiserlichen Universitats-Sternwarte in Strassburg **4** 113 (cit. on p. 29).
Wittenburg, N., P. Kroupa, I. Banik, G. Candlish and N. Samaras (2023), *Hydrodynamical structure formation in Milgromian cosmology*, MNRAS **523** 453, arXiv: 2305.05696 [astro-ph.CO] (cit. on pp. 59, 64, 99, 176, 179).
Wittenburg, N., P. Kroupa and B. Famaey (2020), *The Formation of Exponential Disk Galaxies in MOND*, ApJ **890**, 173 173, arXiv: 2002.01941 [astro-ph.GA] (cit. on pp. 93, 94, 128).
Wolf, M. (1908), *Die Klassifizierung der kleinen Nebelflecken*, Publikationen des Astrophysikalischen Instituts Koenigstuhl-Heidelberg **3** 109 (cit. on p. 24).
Wong, J. H. W., T. Shanks, N. Metcalfe and J. R. Whitbourn (2022), *The local hole: a galaxy underdensity covering 90 per cent of sky to ≈200 Mpc*, MNRAS **511** 5742, arXiv: 2107.08505 [astro-ph.CO] (cit. on pp. 53, 78).
Wong, K. C. et al. (2020), *H0LiCOW - XIII. A 2.4 per cent measurement of H_0 from lensed quasars: 5.3σ tension between early- and late-Universe probes*, MNRAS **498** 1420, arXiv: 1907.04869 [astro-ph.CO] (cit. on pp. 53, 87, 175, 319).
Wu, X., B. Famaey, G. Gentile, H. Perets and H. Zhao (2008), *Milky Way potentials in cold dark matter and MOdified Newtonian Dynamics. Is the Large Magellanic Cloud on a bound orbit?*, MNRAS **386** 2199, arXiv: 0803.0977 [astro-ph] (cit. on p. 128).
Xu, Y., X. Kang and N. I. Libeskind (2023), *A Rotating Satellite Plane around Milky Way-like Galaxy from the TNG50 Simulation*, ApJ **954**, 128 128, arXiv: 2303.00441 [astro-ph.GA] (cit. on p. 52).
Yadav, J. K., J. S. Bagla and N. Khandai (2010), *Fractal dimension as a measure of the scale of homogeneity*, MNRAS **405** 2009, arXiv: 1001.0617 [astro-ph.CO] (cit. on pp. 37, 78).
Yagi, M. et al. (2010), *A Dozen New Galaxies Caught in the Act: Gas Stripping and Extended Emission Line Regions in the Coma Cluster*, AJ **140** 1814, arXiv: 1005.3874 [astro-ph.CO] (cit. on p. 52).
Yan, Z., T. Jerabkova and P. Kroupa (2017), *The optimally sampled galaxy-wide stellar initial mass function. Observational tests and the publicly available GalIMF code*, A&A **607**, A126 A126, arXiv: 1707.04260 [astro-ph.GA] (cit. on pp. 71, 72, 81, 140, 141, 144, 145, 147–150, 168, 169, 177, 317, 323).
– (2019), *The star formation timescale of elliptical galaxies. Fitting [Mg/Fe] and total metallicity simultaneously*, A&A **632**, A110 A110, arXiv: 1911.02568 [astro-ph.GA] (cit. on p. 144).

Yan, Z., T. Jerabkova and P. Kroupa (2020), *Chemical evolution of ultra-faint dwarf galaxies in the self-consistently calculated integrated galactic IMF theory*, A&A **637**, A68 A68, arXiv: 2003.11029 [astro-ph.GA] (cit. on pp. 67, 69, 70, 144, 147, 148, 168).

– (2023), *The most massive stars in very young star clusters with a limited mass: Evidence favours significant self-regulation in the star formation processes*, A&A **670**, A151 A151, arXiv: 2211.13244 [astro-ph.GA] (cit. on pp. 69, 70, 144, 146, 168).

Yan, Z., T. Jerabkova, P. Kroupa and A. Vazdekis (2019), *Chemical evolution of elliptical galaxies with a variable IMF. A publicly available code*, A&A **629**, A93 A93, arXiv: 1907.10614 [astro-ph.GA] (cit. on pp. 72, 81, 140, 141, 145, 150, 152, 168, 169, 177, 179, 323).

Yan, Z., T. Jeřábková and P. Kroupa (2021), *Downsizing revised: Star formation timescales for elliptical galaxies with an environment-dependent IMF and a number of SNIa*, A&A **655**, A19 A19, arXiv: 2107.03388 [astro-ph.GA] (cit. on pp. 67, 69–71, 96, 139, 141, 144–150, 153, 166, 168, 177, 317, 323).

Ying, J. M. et al. (2023), *The Absolute Age of M92*, AJ **166**, 18 18, arXiv: 2306.02180 [astro-ph.SR] (cit. on p. 42).

York, D. G. et al. (2000), *The Sloan Digital Sky Survey: Technical Summary*, AJ **120** 1579, arXiv: astro-ph/0006396 [astro-ph] (cit. on pp. 75, 92).

Yoshida, M. et al. (2008), *Strange Filamentary Structures ("Fireballs") around a Merger Galaxy in the Coma Cluster of Galaxies*, ApJ **688** 918, arXiv: 0807.2573 [astro-ph] (cit. on p. 52).

Yoshii, Y. and B. A. Peterson (1995), *Interpretation of the Faint Galaxy Number Counts in the K Band*, ApJ **444** 15 (cit. on p. 33).

Yu, H. and F. Y. Wang (2016), *On the Inconsistency between Cosmic Stellar Mass Density and Star Formation Rate up to $z \sim 8$*, ApJ **820**, 114 114, arXiv: 1602.01985 [astro-ph.GA] (cit. on pp. 135, 136, 167, 178, 322).

Yun, M. S., N. A. Reddy and J. J. Condon (2001), *Radio Properties of Infrared-selected Galaxies in the IRAS 2 Jy Sample*, ApJ **554** 803, arXiv: astro-ph/0102154 [astro-ph] (cit. on p. 144).

Zhang, Z.-Y., D. Romano, R. J. Ivison, P. P. Papadopoulos and F. Matteucci (2018), *Stellar populations dominated by massive stars in dusty starburst galaxies across cosmic time*, Nature **558** 260, arXiv: 1806.01280 [astro-ph.GA] (cit. on pp. 67, 144).

Zhao, H., B. Famaey, F. Lüghausen and P. Kroupa (2013), *Local Group timing in Milgromian dynamics. A past Milky Way-Andromeda encounter at $z > 0.8$*, A&A **557**, L3 L3, arXiv: 1306.6628 [astro-ph.GA] (cit. on pp. 103, 128, 129, 131).

Zhou, S. et al. (2019), *SDSS-IV MaNGA: stellar initial mass function variation inferred from Bayesian analysis of the integral field spectroscopy of early-type galaxies*, MNRAS **485** 5256, arXiv: 1811.09799 [astro-ph.GA] (cit. on pp. 67, 144, 148).

Zinner, E., H. M. Nobis and F. Schmeidler (1988), *Entstehung und Ausbreitung der copernicanischen Lehre*. (Cit. on p. 18).

Zonoozi, A. H., H. Mahani and P. Kroupa (2019), *Was the Milky Way a chain galaxy? Using the IGIMF theory to constrain the thin-disc star formation history and mass*, MNRAS **483** 46, arXiv: 1810.00034 [astro-ph.GA] (cit. on pp. 100, 150).

Zucca, E. et al. (1997), *The ESO Slice Project (ESP) galaxy redshift survey. II. The luminosity function and mean galaxy density.*, A&A **326** 477, arXiv: astro-ph/9705096 [astro-ph] (cit. on pp. 53, 78, 85, 174).

Zwicky, F. (1933), *Die Rotverschiebung von extragalaktischen Nebeln*, Helvetica Physica Acta **6** 110 (cit. on pp. 2, 29, 30).

– (1937), *On the Masses of Nebulae and of Clusters of Nebulae*, ApJ **86** 217 (cit. on p. 31).

List of Figures

2.1 Prehistoric paintings in the “Hall of the Bulls” (French: “Salle des taureaux”) in the cave of Lascaux (France). *Left:* The wall painting prominently shows a bull with two horns. The seven black dots above the head of the bulls might resemble the stars of the open star cluster Pleiades. The stars arranged in one line below left to the head of the bull could be the belt stars of the Orion constellation. The stars in the head of the bull could be the members of the star cluster Hyades with the star Aldebaran being the eye of the bull. Credit: Elke Wetzig (downloaded from Wikipedia on 15.08.2023), CC BY-SA 4.0. *Right:* Prehistoric painting “Shaft scence” in the cave of Lascaux showing a bison, a man with a bird head, and a bird forming the Summer Triangle consisting of the stars Vega, Altair, and Deneb (argument by Michael Rappenglueck as documented e.g. in the BBC article `http://news.bbc.co.uk/2/hi/science/nature/871930.stm` (published on 09.08.2000; website visited on 22.11.2023)). Credit: Peter80 (downloaded from Wikipedia on 15.08.2023), CC BY-SA 3.0. . . . 10

2.2 Astronomy in prehistoric times. *Left:* The prehistoric stone monument Stonehenge constructed between 3000 BC and 2000 BC in Wiltshire (England). Credit: Operarius (downloaded from Wikipedia on 15.08.2023), CC BY-SA 3.0. *Right:* Image of the Nebra sky disk (in German: Himmelsscheibe von Nebra) from c. 1800–1600 BCE showing the Full Moon (middle left), the Waxing Moon (right), the seven visible stars of the Pleiades (top middle left), the rising and setting Sun (left and right), and a Solar barque (bottom). The deformations at the left edge of the disk were caused during the archaeological excavations. Credit: Frank Vincentz (downloaded from Wikipedia on 15.08.2023), CC BY-SA 4.0. 11

2.3 Illustration of Aristotle's (left) and Ptolemaic (right) geocentric model of the Universe. *Left:* Aristotle's model assumes that the Earth (blue dot) is at the exact centre of the Universe being surrounded by perfect circles on which move with uniform speed the Moon (first black circle), Sun (red circle), the five planets known at ancient times (i.e. from closest to furthest from Earth: Mercury, Venus, Mars, Jupiter, Saturn; black circles), the sphere of the fixed stars (yellow circle), and the Prime Mover (green circle). *Right:* The Ptolemy model is a modification of the Aristotle's model (left) by introducing "deferents" (solid circle) and "epicycles" (dotted circle) to explain the motion of a planet (black dot). The planet orbits around the centre of the epicycle, which itself follows on a circular motion the deferent. The centre of the deferent is called "eccentrix" (X mark symbol) while the Earth is slightly off-centered. On the opposite position of the Earth is the so-called "equant" (red dot) from which the centre of the epicycle has a constant angular velocity. Note that both diagrams are not to scale. Credit: Illustration made by the author of the thesis, but based on the diagrams presented on the websites `https://www.pas.rochester.edu/~blackman/ast104/aristotle8.html` (left) and `https://www.britannica.com/science/Ptolemaic-system` (right). 13

2.4 Schematically illustration of the derivation of the Earth's circumference by Eratosthenes of Cyrene (c. 276–c. 195/194 BC). Cyene is located close to the Tropic of Cancer such that the Sun ray's fall exactly parallel (orange dashed lines) in a well only at Solistice. Cyence and Alexandria are located roughly at the same meridian and are separated by $\approx$ 5 000 Stadia which corresponds to $\approx$ 800 km. At Solistice, a pole or tower located in Alexandria (green solid line) throws a shadow of $\alpha = 7.2^\circ$ from vertical such that Eratosthenes derived a Earth's circumference of $d_{\text{Earth}} \approx 250\,000$ Stadia corresponding to $\approx$ 40 000 km (see e.g. the documentation in Van Helden 2010). Note that the illustration is not to scale. Credit: figure made by the author of this thesis but based on the image from "cmglee, David Monniaux, jimht at shaw dot ca" from Wikipedia (webpage visited on 13.08.2023), Attribution-ShareAlike 4.0 International (CC BY-SA 4.0 Deed). 14

2.5 Astronomy in Gmunden (Austria). *Left:* Memoriam of Johannes von Gmunden (c. 1380/84–1442) mounted in front of the city hall at the Rathaus-Platz 1 in Gmunden. The top plaque reads "Zur Erinnerung an den in dieser Stadt geborenen berühmten Mathematiker und Astronomen Canonicus Johannes von Gmunden eine Zierde der Wiener Universität, an welcher er als Magister und Vice Kanzler 1408 bis 1435 thätig [sic!] war. Er starb am 23. Februar 1442 als Pfarrer von Laa in Nied Oesterr." which translates to "In memory of the famous Mathematician and Astronomer born in this city Canonicus Johannes von Gmunden adornment from the University of Vienna at which he acted as a magister and vice-chancellor from 1408 to 1435. He died in February 1442 as a pastor in Laa in Lower Austria" (translated from German into English by the author of this thesis). The bottom plague announces the timings of the famous "Keramik Glockenspiel" (ceramic bells) at the Gmundner city hall. Credit: Photo taken by the author of this thesis (September 2023). *Right:* Observatory of Gmunden located at the Kalvarienbergweg 3 which was originally a former tower for gunpowder constructed in 1844 and was rebuilt to an observatory by Johannes Eisner (1915–1993) in 1949. Nowadays the observatory is aimed for public guiding tours organized by the club "AURIGA-Traunseeastronomie e.V." led by Hagen Tolle. Credit: Peter Petz 16

2.6 "De revolutionibus orbium coelestium" published in 1543 by Nicolaus Copernicus (1473–1543). *Left:* Title page of the 2nd edition (1566) of "De revolutionibus orbium coelestium" (Copernicus and Rhaticus 1566). Credit: Copernicus and Rhaticus (1566) (image of the title page downloaded from Wikipedia on 18.09.2023), Public domain. *Right:* Illustration of the heliocentric model proposed by Nicolaus Copernicus in "De revolutionibus orbium coelestium" in which the Sun is at the centre of the known Universe surrounded (from the inside out) by the planets Mercury, Venus, Earth with Moon, Mars, Jupiter, Saturn, and the fix stars. Credit: Own work from Copernicus 1543 (downloaded from Wikipedia on 18.09.2023), Public domain. 17

2.7 History of astronomy in Prague. *Left:* The tomb of Tycho Brahe (1546–1601) is located next to the altar of the Church of Mother of God before Týn (Kostel Matky Boží před Týnem) which is located at the old town square of Prague (Czech Republic). Credit: Photo taken by the author of the thesis during a research visit in Prague (October 2019). *Right:* House of Johannes Kepler (1571–1630) located in the Karlova street number 4 in Prague (Czech Republic). The plaque above the door states in Czech language "zde žil v letech 1607 až 1612 JOHANNES KEPLER v té době objevil první dva zákony o pohybu planet kolem slunce", which translates: "Here lived from 1607 until 1612 Johannes Kepler. During this period he discovered [the first] two laws concerning the motion of planets around the [S]un." (Wolfgang Volk, `http://www.w-volk.de/museum/plaque05.htm` (webpage visited on 14.11.2023)). Credit: Photo taken by the author of the thesis during a research visit in Prague (September 2022). 20

2.8 History of astronomy in Bonn. *Left:* Old observatory located in the Poppelsdorfer Allee 47 at Bonn, where Friedrich Wilhelm August Argelander (1799–1875) performed with Eduard Schönfeld (1828–1891) the famous Bonner Durchmusterung from 1859 to 1863. Credit: Photo taken by the author of the thesis (September 2023). *Right:* Tomb of Friedrich Wilhelm August Argelander (1799–1875) at the old cemetery in Bonn. Credit: Photo taken by the author of the thesis (August 2023). 23

2.9 Original Hubble diagram published in Hubble (1936), which divides galaxies in ellipticals (E), lentriculars (S0), unbarred (Sa–Sc), and barred (Sba–Sbc) spirals. This diagram was mainly influenced by the works of John Reynolds and James Jeans (Block and Freeman 2008; Block and Freeman 2015) insofar as J. H. Reynolds (1920) already divided spiral galaxies into seven different groups and Jeans (1928) proposed the tuning fork diagram to distinguish different galaxy types. Credit: Scan of figure 1 of Hubble (1936). 25

2.10 The famous Hubble diagram published in this form by Hubble (1929) which shows a correlation between the distance and velocity (redshift) of 24 galaxies (see also Equation 2.8). Note that the unit of the y-axis for the velocity is given in "km" but should be correctly "km/s". It is often stated that this is a typo made by Edwin Hubble (Kirshner 2004), but I would like to highlight that also e.g. Wirtz (1922a), Wirtz (1922b), Wirtz (1924), or Slipher (1917) used in their studies the labeling "km" instead of "km/s" for velocities. Therefore, although the unit "km" for the velocity is incorrect, there is also the possibility that this labeling was "just" a convention or a bad habit in the early 20th century. The x-axis shows the distance from the MW in parsec (1 parsec [1 pc] corresponds to 3.086×10^{13} km). The black circles (solid line) correspond to individual galaxies ("nebulae"), while the open circles are galaxies binned in groups. The black cross refers to the mean velocity and mean distance of 22 nebulae. Hubble (1929) derived a Hubble constant of $H_0 = 500\,\mathrm{km\,s^{-1}\,Mpc^{-1}}$, which is significantly higher than the current locally measured value of $H_0 = 73.04 \pm 1.04\,\mathrm{km\,s^{-1}\,Mpc^{-1}}$ based on Cepheid and SN Ia data (Riess et al. 2022). Credit: figure 1 of Hubble (1929). 28

2.11 *Left:* Image of Carl Wirtz (1876–1939) who studied astronomy in Bonn and is the actual discoverer of the expansion of the Universe. Credit: Austrian Academy of Sciences Press/Communications in Asteroseismology, Vienna Observatory, Volume 149, December 2008, p. 127/Institut für Astronomie der Universität Wien (downloaded from Wikipedia on 15.09.2023), Public domain. *Right:* Amusing coincidence of the name "K[C]arl Wirtz" printed on a construction site barrier at the Wiesenweg in Bonn. Credit: Photo taken by the author of the thesis in Bonn (June 2023). 30

2.12 European Southern Observatory (ES0) in Garching bei München (Germany). *Left:* Headquarters of ESO in Garching bei München (Germany). Credit: Photo taken by the author of this thesis during a research visit (October 2022). *Right:* Supernova exhibition next to the ESO headquarter in Garching. Credit: Photo taken by the author of this thesis during a research visit (July 2019). 33

2.13 Artistic images of selected telescopes and space missions of the 21st century. *Top left (a):* The James Webb Space Telescope (JWST), which is named after the former administrator of NASA James Edwin Webb (1906–1992), was launched in December 2021 and started its science programme in July 2022. Credit: NASA (downloaded from Wikipedia on 30.10.2023), Public domain. *Top right (b):* Euclid, which is named after the mathematician Euclid (fl. 300 BC), was launched in July 2023. Credit: ESA (downloaded from Wikipedia on 30.10.2023), CC BY-SA IGO 3.0. *Bottom left (c):* Rendering of the Extremely Large Telescope (ELT) operated by ESO and located at the Cerro Armazones (Chile). The first light of the ELT is expected for 20281615[16]. The primary mirror with a diameter of 39.3 m would allow to study e.g. the formation of galaxies in the very early Universe. Credit: ESO/L. Calçada (downloaded from Wikipedia on 30.10.2023), CC BY 4.0. *Bottom right (d):* The Jupiter Icy Moons Explorer (JUICE) was launched in April 2023 and will explore the moons of the planet Jupiter. Credit: ESA (downloaded from Wikipedia on 30.10.2023), CC BY-SA IGO 3.0. 35

3.1 Cosmic evolution of the density parameters of the total matter (black), baryonic matter (green), radiation (red), and dark energy (blue) within the ΛCDM framework assuming a standard ΛCDM cosmology with $H_0 = 67.74\,\mathrm{km\,s^{-1}\,Mpc^{-1}}$, $\Omega_{\mathrm{m},0} = 0.3089$, $\Omega_{\mathrm{b},0} = 0.049$, $\Omega_{\mathrm{rad},0} = 9.16 \times 10^{-5}$, and $\Omega_{\Lambda,0} = 0.6911$, respectively (Planck Collaboration XIII 2016). The *left* panel shows the density parameters in the International System of Units (SI), while the *right* panel shows the density parameters scaled by the critical density ρ_{crit} (Equation 3.22). The Universe was radiation dominates at $z \gtrsim 3400$ (Equation 3.42), dark matter-dominated between $3400 \gtrsim z \geq 0.31$, and became dark energy-dominated at $z \leq 0.31$ (Equation 3.44) as highlighted by the vertical dashed lines. The vertical dotted line marks the redshift $z = 0.65$ (Equation 3.47) when the Universe started to accelerate. Credit: figure made by the author of this thesis. 43

3.2 The Illustris The Next Generation (IllustrisTNG or TNG) project consists of different simulation runs with different resolution realizations and box sizes. The TNG50, TNG100, and TNG100 runs have 51.7 cMpc, 110.7 cMpc, and 302.6 cMpc per cubic side, respectively (see text). The images show the projected density contrast (the brighter the higher the density contrast) revealing the cosmic web in the simulations. The most massive galaxy clusters form in the knots of the cosmic web. Credit: TNG Collaboration (downloaded from the website of the IllustrisTNG project `https://www.tng-project.org/media/` on 10.11.2023). 45

3.3 The stellar-to-halo mass ($M_* - M_{200}$) relation for haloes with a central subhalo with $M_* > 10^8\,M_\odot$ at redshift $z = 0$ in the flagship runs TNG50-1 (top left), TNG100-1 (top right), TNG300-1 (bottom left), and EAGLE Ref-L0100N1054 (bottom right). The red horizontal solid line marks the MW with a stellar mass of $M_* = (6.08 \pm 1.14) \times 10^{10}\,M_\odot$ (Licquia and Newman 2015) and the red shaded area highlights the corresponding uncertainty. Note that the relation provides a wide range of different M_{200} values for a given value of M_* (see text). The green dashed line refers to equation 2 of Moster et al. (2010). Credit: figure made by the author of this thesis using the IllustrisTNG and EAGE subhalo and halo catalogues (see the Sections 3.2.2-3.2.3). 48

3.4 Hubble diagram (see also Section 2.5 for a historical overview) based on simulated galaxies formed in the Illustris-1 simulation. The simulation produce a mix of elliptical (top left), barred (bottom right) and non-barred (top right) disk, and irregular (bottom left) galaxies (Vogelsberger et al. 2014a) but cannot reproduce the correct fraction of the observed galaxy types (Haslbauer et al. 2022). This problem is considered in more detail in the Chapter 8 and in the corresponding publications attached in Appendix B. Credit: top panel of figure 1 of Vogelsberger et al. (2014a). 51

4.1 *Left:* Angular power spectrum of the cosmic microwave background (CMB) of the ΛCDM model (red line) and the νHDM model (blue line). The cosmological parameters of these models are listed in the top middle (ΛCDM) and top right (νHDM) of the panel. The points refer to the 7-year data release of the Wilkinson Microwave Anisotropy Probe (WMAP-7; black), Atacama Cosmology Telescope (ACT; turquoise data points), and the Arcminute Cosmology Bolometer Array Receiver (ACBAR; green). Credit: figure 1 of Angus and Diaferio (2011). *Right:* Power spectrum of the ΛCDM (dotted line) and the νHDM (solid line) model at redshift $z = 254.1$ using the Code for Anisotropies in the Microwave Background (CAMB). The dashed line shows the power spectrum of the N-body simulation by Angus and Diaferio (2011). Credit: figure 2 of Angus and Diaferio (2011). 60

4.2 *Left:* Radial acceleration relation (RAR) which shows the observed centripetal acceleration, $g_{\rm obs}$ (y-axis), in dependence of the centripetal acceleration implied from the observed baryons, $g_{\rm bar}$ (x-axis), for X-ray ETGs (red circles), rotating ETGs (orange diamonds), binned LTGs (blue squares; see also figure 3 of McGaugh, Lelli and Schombert 2016), and binned dSphs (green hexagons). The dotted black line shows the identity line on which dark matter-free galaxies (e.g. TDGs; Section 3.3.8) are expected to lie if Newtonian dynamics is valid. Credit: left panel of figure 12 of Lelli et al. (2017). *Right:* Baryonic Tully-Fisher relation (BTFR) which shows a relation between the velocity of the flat part of the rotation curve, $V_{\rm f}$, and the baryonic mass, $M_{\rm b}$, for 123 galaxies of the SPARC database. The data are fitted in the $\log_{10}$-space with a linear fit of the form $\log_{10}(M_{\rm b}/M_\odot) = s\log_{10}(V_{\rm f}/[{\rm km\,s^{-1}}]) + I$, where the best fitting parameters are $s = 3.85 \pm 0.09$ and $I = 1.99 \pm 0.18$. The BTFR has a orthogonal scatter of only $\sigma_\perp = 0.026 \pm 0.007$. The colorbar represents the gas fraction of the galaxies defined as $F_{\rm g} \equiv M_{\rm g}/M_{\rm b}$, where $M_{\rm g}$ and $M_{\rm b}$ are the gas and baryonic mass, respectively. The BTFR follows from the RAR but not vice versa (see text). Credit: top left panel of figure 2 of Lelli et al. (2019). 62

5.1 Schematic illustration of the concept of a varying IMF. The black solid line shows the canonical IMF (Equation 5.2) formulated by Kroupa (2001). A bottom-heavy IMF (red dotted) has more, while a bottom-light IMF (orange dotted) has fewer low mass stars (here at $m \lesssim 0.5\,M_\odot$) relative to the canonical IMF. A top-heavy IMF (blue dotted) has more, while a top-light IMF (green dotted) has fewer massive stars (here at $m \gtrsim 0.5\,M_\odot$) relative to the canonical IMF. Note that the y-axis shows arbitrary numbers/unit but a more quantitative analysis of the gwIMF within the IGIMF framework can be found in Figure 5.2 and in Chapter 12. Credit: figure made by the author of the thesis, but based on figure 1.2 of Kroupa and Jerabkova (2021). . 68

5.2 Grid of gwIMFs in dependence of the SFR (from left to right: $\psi = 10^{-5}, 1, 10^{4}\,M_\odot\,yr^{-1}$) and metallicity (from bottom to top: [Z]= -5,-3,0,1) for the IGIMF formulation of Yan, Jeřábková and Kroupa (2021) (blue dot-dashed lines) and the canonical IMF (dashed black lines; Kroupa 2001). The gwIMFs are normalized by the mass formed over 10 Myr. The light green arrow schematically illustrates the time evolution of the gwIMF in a typical early type galaxy starting with a low SFR and metallicity (bottom left panel). A more detailed discussion of the time evolution of the gwIMF can be found in Chapter 12 and figure 2 in Jeřábková et al. (2018). Credit: figure made by the author of this thesis based on figure 2 of Jeřábková et al. (2018) and Figure 12.1 in Chapter 12 using the Python 3 module "GalIMF" developed by Yan, Jerabkova and Kroupa (2017). 71

6.1 Morphological distribution of local galaxies with stellar masses $M_* > 1.5 \times 10^{10}\,M_\odot$ from the SDSS. I.e., 72±8 per cent are spirals, 10±3 per cent are peculiar, 15±4 per cent are lentriculars (S0), and only 3 ± 1 per cent are ellipticals (table 3 of Delgado-Serrano et al. 2010). The galaxy morphological types can be used as a test of galaxy evolution models (see text). Credit: Top panel of figure 5 of Delgado-Serrano et al. (2010). . . 77

6.2 Observed density contrast, $\langle\rho\rangle/\rho_0$, in dependence of the co-moving radial distance assuming $H_0 = 70\,km\,s^{-1}\,Mpc^{-1}$ and $h_{70} = 1$. The light blue data point marks $\langle\rho\rangle/\rho_0 = 0.54 \pm 0.06$, which has been derived over the redshift range of $0.01 < z < 0.07$ (corresponding to a co-moving radial distance range of 40-300 cMpc) based on the 2M++ catalogue with a limiting magnitude of $K_s < 14.36$ in the Ks-band covering 90 per cent of the sky (see figure 9 and table 1 of Keenan, Barger and Cowie 2013). The orange square refers to the measured density within a sphere with a radius of 50 Mpc (Karachentsev 2012, and see also Section 3.3.9). The black and red circles have been obtained from the GAMA survey with a limiting K-band magnitude of $K < 17$ and UKIDSS/SDSS with $K < 16.3$ (Keenan, Barger and Cowie 2013). The violet up-pointing triangle is taken from Keenan et al. (2012). The grey shaded region estimates the density fluctuations expected in the ΛCDM model but see Chapter 7 for a more sophisticated and quantitatively comparison between the observations and the ΛCDM model. Credit: figure 1 of Kroupa (2015). 79

6.3 Concept outline of the research project published in Haslbauer, Banik and Kroupa (2020) in which we study the formation of the locally observed KBC void (see Figure 6.2) and its implication on the Hubble tension (Section 3.3.10) in both the ΛCDM (Section 3) and MOND (νHDM; Section 4.2) framework. Starting with the initial conditions defined by the CMB at redshift $z = 1100$, we first quantified the likelihood of the existence of KBC-void-like structures at $z = 0$ in the ΛCDM framework by mimicking the observations by Keenan, Barger and Cowie (2013) in the MXXL simulation (Section 3.2.1). We investigate if outflows (illustrated by the red arrows) from the void centre (yellow star) would explain the locally measured higher value of H_0. Secondly, we tested if both the KBC void and Hubble tension can be explained in the νHDM model. The main results of the project are summarized in the Chapter 7 and the corresponding paper is attached in Appendix A. Credit: Figure made by the author of the thesis based on figure 3 of the blog post "Solving both crises in cosmology: the KBC-void and the Hubble-Tension" published on the science blog "The Dark Matter Crisis – The rise and fall of cosmological hypotheses" using the heat map of the CMB by the 9th year WMAP (credit: NASA/WMAP Science Team (downloaded from Wikipedia on 16.09.2023), Public Domain) and the projected density map of the TNG100-1 simulation box (credit: TNG Collaboration (downloaded from the TNG project website on 30.10.2023), the red arrows and yellow star have been added by the author of the thesis). 80

6.4 The galaxy-wide IMF (gwIMF) in a cosmology context. Star formation occurs in embedded clusters some of which evolve to young open star clusters formed out of giant molecular clouds. The stellar IMF depends on the properties of the embedded cluster (Section 5.3). Considering that the embedded clusters are the fundamental building blocks of galaxies (Kroupa 2005), the IGIMF theory allows of the calculations of the gwIMF by summing up the stellar IMFs of all embedded clusters (Kroupa and Weidner 2003). Thus, the properties of galaxies are affected by the underlying cosmological paradigm and the stellar IMF which both influence the stellar population, chemical enrichment, and galactic and cosmic matter cylce (see text). Comparing observations with galaxy formation and evolution simulations requires assumptions about the stellar IMF (see e.g. also the Chapters 9 and 12). Credits: Figure made by the author of the thesis using an illustration of the ELT (Credit: ESO/L. Calçada (downloaded from Wikipedia on 30.10.2023), CC BY 4.0) and an image of the galaxy M101/NGC 5457 taken by the HST (Credit: ESA/Hubble (downloaded from Wikipedia on 30.10.2023), CC BY 4.0 Deed). 82

7.1 The KBC void and Hubble tension in the ΛCDM framework. *Left:* Apparent density distribution, $\tilde{\delta}$, of spherical shells with an inner radius of 40 cMpc and an outer radius of 300 cMpc for 10^6 vantage points at redshift $z = 0$ in the MXXL simulation (blue histograms) which is fitted with a Gaussian function (black solid line). The red line shows the KBC void with an observed density contrast of $\delta_{\rm obs} = 0.46$ and an observational uncertainty of $\sigma_{\rm obs} = 0.06$ (Gaussian error). Credit: figure 1 of Haslbauer, Banik and Kroupa (2020). *Right:* Relation between the apparent density contrast, $\tilde{\delta}$, and the local Hubble constant scaled by the value of the global Hubble constant, $H_0^{\rm local}/H_0^{\rm gobal}$. The green dot refers to the cosmic mean density such that $\tilde{\delta} = 0$ and to the global Hubble constant value of $H_0^{\rm global} = 67.4 \pm 0.5\,{\rm km\,s^{-1}\,Mpc^{-1}}$ (Planck Collaboration VI 2020b) while the red dot marks the locally observed KBC void with $\delta_{\rm obs} = 0.46 \pm 0.06$ (Keenan, Barger and Cowie 2013) and locally measured $H_0^{\rm local} = 73.8^{+1.1}_{-1.1}\,{\rm km\,s^{-1}\,Mpc^{-1}}$ (Riess et al. 2019; K. C. Wong et al. 2020). The grey contour lines show the corresponding confidence levels. The blue dots on the straight blue line mark the confidence levels of the expected apparent cosmic variance in the ΛCDM framework. Credit: figure 2 of Haslbauer, Banik and Kroupa (2020). 87

7.2 The KBC void and Hubble tension in the νHDM framework. *Left:* Comparison of structure formation in the ΛCDM (red dashed line) and our best-fitting MOND (blue solid line) model by showing the true density evolution of a sphere with a co-moving radius of 300 cMpc for an initial density fluctuation of $\alpha_{\rm v} = 3.76 \times 10^{-5}$ at redshift $z = 9$ which corresponds to a cosmic scale factor of $a = 0.1$. Credit: modified version of the right panel of figure 5 of Haslbauer, Banik and Kroupa (2020) by showing only models with the same initial density fluctuation and a time-independent external field effect (EFE). *Right:* Comparison of the Hubble constant, H_0, and the acceleration parameter, $\overline{q}_0 \equiv -q_0$ (see the definition of q_0 in Section 3.3.12), jointly derived over the redshift range of $0.023 \leq z \leq 0.15$. The black dot shows the jointly derived values obtained by Camarena and Marra (2020) from the Pantheon SNe, while the blue point refers to our best-fitting MOND model. The green dot marks the global values derived from the CMB (Planck Collaboration VI 2020b), which differ with the observations by Camarena and Marra (2020) at 4.39σ. Credit: modified version of figure 6 of Haslbauer, Banik and Kroupa (2020) by showing only the best-fitting MOND model. 88

8.1 Sky-projected aspect ratio, $q_{\rm sky}$, distributions of observed and simulated galaxies with $10.0 < \log_{10}(M_*/M_\odot) \leq 11.65$ formed in the TNG50-1 (blue solid line in the left and right panels), TNG100-1 (red dashed line in the left panel), Illustris-1 (green dotted-dashed in the left panel), Ref-L0050N0752 (hereafter EAGLE50; red dashed in the right panel), and Ref-L0100N1504 (hereafter EAGLE100; green dotted-dashed in the right panel). The black solid line and grey dashed line in both panels refer to the observed sky-projected aspect ratio distributions of galaxies in the GAMA DR3 and SDSS DR16, respectively. An thin disk galaxy observed edge-on would have $q_{\rm sky} \lesssim 0.2$ and a perfect spherical galaxy has $q_{\rm sky} = 1$. Credit: figure 4 of Haslbauer et al. (2022). 92

9.1 Comparison of the high-redshift galaxy candidates (grey and black errorbars) with the stellar mass buildup of the ΛCDM framework by showing the most massive subhaloes in terms of their stellar masses formed in the TNG50-1 (red circles), TNG100-1 (green squares), and different EAGLE (blue symbols) simulation runs in dependence of redshift assuming an invariant canonical IMF (Chabrier 2003). The black errorbars refer to the galaxy candidates ID 14924, ID 1514, GL-z11, GL-z13, CEERS-1749 detected by the JWST and to the spectroscopically confirmed galaxy GN-z11 (GN-z11; Oesch et al. 2016) by the HST. After the acceptance of our paper, the two galaxy candidates GL-z11 and GL-z13 have been renamed to GL-z10 and GL-z12, respectively, because of a slight revision of their physical properties by Naidu et al. (2022). In order to show these changes to the previous results, we added the two grey errorbars which refer to the updated values of $\log_{10}(M_*/M_\odot) = 9.6^{+0.2}_{-0.4}$ at $z_{\rm phot} = 10.4^{+0.4}_{-0.5}$ (GL-z10) and $\log_{10}(M_*/M_\odot) = 9.1^{+0.3}_{-0.4}$ at $z_{\rm phot} = 12.4^{+0.1}_{-0.3}$ (GL-z12; see their table 3). Credits: modified version of figure 2 of Haslbauer et al. (2022) by including the updated values of GL-z11 (now named as GL-z10 in Naidu et al. 2022) and GL-z13 (now named as GL-z12), figure 7 of Kroupa et al. (2023), and figure 3 of the blog post "The James Webb Space Telescope, and the early Universe" by **Moritz Haslbauer** and Pavel Kroupa on the science blog "The Dark Matter Crisis – The rise and fall of cosmological hypotheses". 97

9.2 Stellar masses of the galaxy candidates ID 1514 (blue), GL-z11 (red), GL-z13 (orange), and CEERS-1749 (green) for an invariant canonical IMF (star symbols) and a systematically varying gwIMF within the IGIMF context (circles). For simplicity, the IGIMF models assume a constant metallicity of [Fe/H]= −2 and constant SFH starting 200 Myrs after the Big Bang as indicated by the dashed vertical black line. The colored squares show the most massive subhaloes in term of their stellar masses identified in the here-assessed ΛCDM simulations which adopt an invariant canonical IMF (Chabrier 2003). Galaxies with an invariant canonical IMF populate the grey shaded region in the ΛCDM simulation. Credit: right panel of figure 4 of Haslbauer et al. (2022). 98

10.1 Image of the Small and Large Magellanic Clouds taken in front of the Auxiliary Telescopes of the Very Large Telescope (VLT) in Paranal (Chile). Credit: J. C. Muñoz/ESO (downloaded from the website `https://www.eso.org/public/austria/images/ATs_Magellanic_Clouds_hires-CC/?lang` on 16.09.2023), Creative Commons Attribution 4.0 International License. 102

10.2 Distribution of the specific phase-space density of the MCs ($f_{\rm MCs}$; Equation 10.1) and the inverse kinematic timescale of the LMC ($\Omega_{\rm LMC}$; Equation 10.3) for systems with $50\,{\rm kpc} \leq d_{\rm MW-LMC} \leq 100\,{\rm kpc}$ in the ΛCDM cosmological simulations TNG50-1 (46 objects; left), TNG100-1 (118 objects; middle), and TNG300-1 (191 objects; right). The red cross shows the observed values, i.e. $f_{\rm MCs,obs} = 9.10 \times 10^{-11}\,{\rm km^{-3}\,s^3\,kpc^{-3}}$ and $\Omega_{\rm LMC,obs} = 6.48\,{\rm km\,s^{-1}\,kpc^{-1}}$. None of the 355 analogues in the three TNG runs have $f_{\rm MCs} \geq f_{\rm MCs,obs}$ and $\Omega_{\rm LMC} \geq \Omega_{\rm LMC,obs}$, as indicated by the grey shaded region at the top right of each panel. 112

10.3 Cumulative distribution of $f_{\rm MCs}$ obtained from the TNG50-1 run fitted with a linear (dashed black line) and a quadratic (solid black line) function in $\log_{10}$-space. The red dashed line marks the observed value of $f_{\rm MCs,obs} = 9.10 \times 10^{-11}\,{\rm km}^{-3}\,{\rm s}^{3}\,{\rm kpc}^{-3}$. The intersection between the linear (quadratic) fit and the red dashed line yields a P-value of 1.62×10^{-3} (7.81×10^{-5}), which corresponds to a 3.15σ (3.95σ) tension for a single Gaussian variable (see also Table 10.2 for TNG100-1 and TNG300-1). 113

10.4 Estimated tension of the MCs' phase-space density in dependence of the minimum value of $f_{\rm MCs}$ beyond which the cumulative $f_{\rm MCs}$ distribution of the simulations is fitted with a linear (left panel) and quadratic (right panel) function. The horizontal lines correspond to the null detection of analogues as equivalent to an upper limit on the frequency of analogues. 114

10.5 Time evolution of the physical separation between the MW-LMC (blue), MW-SMC (red), and LMC-SMC (green) in analogue system 1 (left panel) and 2 (right panel) identified at a lookback time of 3.1 Gyr ($z = 0.26$) in the TNG100-1 simulation and 2.7 Gyr ($z = 0.21$) in the TNG300-1 simulation, respectively. Systems 2 and 3 consist of the same system identified as an analogue to the MCs at slightly different times (the larger lookback time is plotted here as the former would overlap with the 2.5 Gyr gridline). The formation of the MS requires a close interaction between the MCs before identification (see the text), for which we show a solid black horizontal line at 30 kpc and shade the time period $1 - 4$ Gyr before identification (dashed vertical line). *Left panel:* Since there is no close (< 30 kpc) interaction within this period, this system would not form an MS-like structure. *Right panel:* The LMC and SMC have a pericentre passage wrt. each other about 1.5 Gyr before identification with $d_{\rm LMC-SMC} = 29.9$ kpc, in principle marginally allowing the formation of an MS-like structure. The physical properties of these galaxies are listed in Table 10.3. 118

10.6 Distribution of the number of subhaloes with $M_\star > 10^5\,M_\odot$ within 20 kpc (blue), 25 kpc (orange), or 50 kpc (green) of pre-infall LMC analogues with $d_{\rm MW-LMC} > 100$ kpc in the initial LMC sample (Section 10.2.4) in the high-resolution realization TNG50-1 (248 objects). 123

10.7 Histograms showing the total mass of LMC analogues with different distance criteria in TNG50-1 (top left), TNG100-1 (top right), and TNG300-1 (bottom left), with the combined sample shown in the bottom right panel. The solid blue histograms refer to the initial sample of analogues to the LMC. The dotted red and dashed green histograms show the results when we also require the LMC to be within 50 kpc or between $50 - 100$ kpc, respectively, of the MW analogue. The sample sizes of the different distributions are given in brackets in the panel legends. The dashed vertical line and grey shaded region mark the total mass of the LMC and its uncertainty as deduced from five Galactic stellar streams near the LMC (these give $M^{\rm dyn}_{\rm LMC} = 18.8^{+3.5}_{-4.0} \times 10^{10}\,M_\odot$; Shipp et al. 2021). The solid vertical line shows the total mass of the LMC expected from abundance matching ($M_{\rm LMC} \approx 2 \times 10^{11}\,M_\odot$). Constraining the total mass of the LMC with the LG timing argument gives similar results (see the text). Table 10.5 lists the number of LMC analogues with a total mass equal to at least the 1σ lower limit of the analysis by Shipp et al. (2021). 125

10.8 Distribution of the MW-LMC distance and the total LMC mass of analogues in the combined sample of the three TNG runs (5568 objects). The red dot with vertical error bar refers to the observed $d_{\mathrm{MW-LMC}} = 50.0$ kpc and the total LMC mass deduced from five Galactic stellar streams near the LMC (these give $M_{\mathrm{LMC}} = 18.8^{+3.5}_{-4.0} \times 10^{10}\,M_{\odot}$; Shipp et al. 2021). None of the 5568 simulated objects have a lower Galactocentric distance and higher mass. 126

11.1 Star-formation rates of galaxies located in the Local Volume. *Left:* Present-day SFRs in dependence of the present-day stellar masses of LV galaxies. The black solid line refers to a constant SFH over a star-forming time-scale of 13.6 Gyr assuming a mass-loss factor of 1.3. The red solid line shows the present-day main-sequence of star-forming galaxies with $10^{9.7} < M_{*}/M_{\odot} < 10^{11.1}$ and an uncertainty of ±0.2 dex highlighted by the red shaded region (equation 28 of Speagle et al. 2014). The red dashed line extrapolates the main-sequence to higher and lower stellar masses. The green star shows the position of the Milky Way with $M_{*} = 3.6 \times 10^{10}\,M_{\odot}$ and $SFR_0 = 1.7\,\mathrm{M_{\odot}\,yr^{-1}}$, which lies as expected on the main-sequence. *Right:* Distribution of the parameter $\log_{10}(\overline{SFR}/SFR_0)$ of LV galaxies, which has a mean and median of 0.67 (dashed line) and 0.39 (solid line), respectively. Credits: figure 3 of Haslbauer, Kroupa and Jerabkova (2023). 134

11.2 Evolution of the co-moving SFRD (*top*) and SMD (*bottom*) of the Universe assuming a standard ΛCDM cosmology (Planck Collaboration XIII 2016). The green, red, and blue shaded regions refer to the cosmic SFRDs and SMDs derived from the LV assuming the power-law, delayed-τ, and combined SFH model, respectively. *Top Left:* The "Lilly-Madau" plot. The black solid line is the best fit (equation 15 of Madau and Dickinson 2014) to the measured SFRDs marked with the grey crosses (table 2 of Madau and Dickinson 2014). *Top right:* Ratio between the SFRD of Madau and Dickinson (2014) and the SFRD derived from the LV for the thee different SFH models. The vertical dashed black line marks the peak of the Lilly-Madau plot at $z = 1.86$. *Bottom Left:* The black solid line shows the cosmic SMD implied from the best fit to the measured SFRDs (black line and grey crosses in the left panel). The grey circles and crosses are the measured SMDs taken from Madau and Dickinson (2014) and Grazian et al. (2015), respectively. Yu and F. Y. Wang (2016) reported a tension between the SMDs derived from the measured SFRDs and the measured SMDs over the redshift range of $0.5 < z < 6$ as evident also in the right panel (see the difference between the black solid line and data points). *Bottom right:* Ratio between the SMD derived from Madau and Dickinson (2014) and the SMD derived from the LV for the thee different SFH models. Credit: figure 5 of Haslbauer, Kroupa and Jerabkova (2023). 136

12.1 Grid of simulated gwIMFs in dependence of the SFR (from left to right: $\psi = 10^{-5}, 1, 10^{4}$ $M_\odot\,yr^{-1}$) and metallicity (from top to bottom: [Z] = 1,0,-3,-5) for the IGIMF-2021 formulation (solid red line) by Yan, Jeřábková and Kroupa (2021) using the GalIMF code (Yan, Jerabkova and Kroupa 2017) in comparison with the canonical IMF (dashed black) with the power-law indices $\alpha = 1.3$ for stars in the mass range of $0.08 - 0.5\,M_\odot$ and $\alpha = 2.3$ for stars with $> 0.5\,M_\odot$ (Kroupa 2001). This grid is similar to figure 2 of Jeřábková et al. (2018) but includes only the IGIMF-2021 formulations which is adopted throughout the analysis presented in this study. 149

12.2 Flowchart of the photGalIMF code, which is an extension of the GalIMF code (Yan et al. 2019) by coupling it with stellar isochrones in order to calculate photometric properties of galaxies. The GalIMF code calculates the stellar population of a galaxy for a given SFH, g_{conv}, and the gwIMF model at different times. The metallicity, masses, and ages of the living stars are then transferred to the photometric module, which calculates the luminosity for the selected photometric bands (see text) and each $\delta t = 10$ Myr time interval. 152

12.3 Present-day stellar (including remnants) mass–metallicity relation for galaxies with different constant SFRs over a time-span of 13.6 Gyr, adopting $g_{conv} = 0.10$ (red line) and $g_{conv} = 0.25$ (blue line), within the IGIMF-2021 context. The green stars refer to dwarf galaxies of the MW and M31 galaxies (table 4 of Kirby et al. 2013). The solid black line shows the median while the dashed lines the 16th and 84th percentiles of the metallicity distribution of galaxies in the Sloan Digital Sky Survey Data Release 2 (table 1 of Gallazzi et al. 2005). Note that the shown stellar masses of Kirby et al. (2013) and Gallazzi et al. (2005) are derived for the canonical gwIMF but the simulated mass–metallicity relations (red and blue lines) refers to a varying gwIMF within the IGIMF theory (see text). 154

12.4 Time evolution of the Ks-band mass-to-light ratio, M/L_{Ks}, assuming constant metallicities for single stellar populations (SSP; solid red) and constant SFRs (dashed blue) for a chemical evolution model adopting $g_{conv} = 0.25$. The sharp drop in the SSP models of M/L_{Ks} at $t \approx 2 \times 10^9$ yr is caused by a significant increase of the number of AGB stars. 155

12.5 Time evolution of the gwIMF (right panels) and the mass-to-light ratio, M/L_{Ks}, in the Ks-band (left panels) assuming a constant SFH of $\psi = 10^3\,M_\odot\,yr^{-1}$ (top panels), $1\,M_\odot\,yr^{-1}$ (middle panels), and $10^{-3}\,M_\odot\,yr^{-1}$ (bottom panels) over a timescale of 14 Gyr in the canonical IMF (dashed black lines in the left and right panels) and IGIMF-2021 (solid black line in the left panels and colored lines in the right panels) framework. The chemical evolution model adopts $g_{conv} = 0.25$. The M/L_{Ks} values evaluated at an age of 13.6 Gyr are shown in Figure 12.6. 156

12.6 Mass-to-light ratio, M/L_{Ks}, in the Ks-band in dependence of L_{Ks} for galaxies with an age of 13.6 Gyr assuming $g_{conv} = 25\%$ (red line) and 10% in the IGIMF-2021 context. The dashed black line shows the mean M/L_{Ks} of the two different chemical enrichment models (red and blue lines). 157

12.7 Left panel: Star formation rate in dependence of the Hα luminosity assuming a canonical IMF (solid black line; Kennicutt 1998) and the IGIMF-2021 theory (colored lines) for different metallicities calculated with the PÉGASE code (see text). Right panel: Conversion factor of the SFRs, $\Phi = \frac{\psi_{\rm IGIMF}}{\psi_{\rm K98}}$, in dependence of the H$\alpha$ luminosity. The solid black line refers to $\psi_{\rm IGIMF} = \psi_{\rm K98}$. The fitting parameters are listed in Table F.1. 159

12.8 Similar to the relations presented in the panels of Figure 12.7 by showing explicitly the relation between $\psi_{\rm K98}$ (Kennicutt 1998) and the SFRs of the IGIMF-2021 formalism for different metallicities (colored lines). The dashed black line shows the identity line. The fitting parameters are listed in Table F.1. 160

12.9 Star formation rate in dependence of the stellar mass derived from the Ks-band luminosity of local galaxies in the canonical IMF (left panels) and IGIMF-2021 (right panels) context. The observed SFR values have an estimated uncertainty of about 30% (see figure 1 of Kroupa et al. 2020) due to distance uncertainties (Karachentsev et al. 2004; Karachentsev, Makarov and Kaisina 2013). The errorbars of the IGIMF-corrected stellar mass values refer to the two different applied chemical enrichment models (Section 12.2.2.1) and the errobars of the IGIMF-corrected SFR values refer to metallicities of $[Z] = -2.20$ (lower limit) and $[Z] = 0.45$ (upper limit; see Section 12.2.5 for further details). The solid green lines show the present-day main sequence of star-forming galaxies with $10^{9.7} < M_*/M_\odot < 10^{11.1}$ and a scatter of ± 0.2 dex highlighted by the red shaded area (i.e. Equation (28) of Speagle et al. 2014, and Equation (12.22)). The dashed green lines are extrapolations beyond the adopted fitted range of the stellar masses. The solid red lines show the IGIMF-corrected main sequence of star-forming galaxies (green line; Equation (12.23)) of Speagle et al. (2014) by using Equation (12.19) for $[Z] = 0$. 162

12.10 Gas depletion timescale in dependence of the gas mass of local galaxies in the canonical IMF (left panel) and IGIMF-2021 (right panel) context. The dashed red line shows the age of the Universe $\tau_{\rm gas} = \tau_{\rm h} = 13.8$ Gyr assuming the standard ΛCDM cosmology (Planck Collaboration XIII 2016). The error on the IGIMF-corrected $\tau_{\rm gas}$ values (right panel) is estimated by adopting the SFR values for $[Z] = -2.20$ (upper limit) and $[Z] = 0.45$ (lower limit). The solid red line is a fit (Equation (12.25)) to the IGIMF-2021 data in linear-space. 163

12.11 Distribution of the gas depletion timescale, $\tau_{\rm gas}$, in the canonical IMF (blue) and IGIMF-2021 (green) context in the $\log_{10}$-space. The $\tau_{\rm gas}$ are calculated by adopting the IGIMF-corrected SFR values for a Solar metallicity. The histograms are fitted with a Gaussian (solid red lines) with expected values of $\mu = \log_{10}(\tau_{\rm gas}/{\rm Gyr}) = 1.12$ (13.25 Gyr; canonical IMF) and $\mu = \log_{10}(\tau_{\rm gas}/{\rm Gyr}) = 0.67$ (4.72 Gyr; IGIMF-2021) and variances of $\sigma = 0.60$ Gyr (canonical IMF) and $\sigma = 0.41$ Gyr (IGIMF-2021). . . 164

12.12 Stellar mass buildup timescale normalized by the age of the Universe of $\tau_{\rm h} = 13.8\,{\rm Gyr}$ (Planck Collaboration XIII 2016) in dependence of the stellar mass of local galaxies in the canonical IMF (left panel) and IGIMF-2021 (right panel) context. The dashed red line refers to a stellar mass buildup timescale equal to $\tau_{\rm h} = 13.8\,{\rm Gyr}$. The upper and lower limits of the IGIMF-corrected τ_* values (right panel) are estimated by adopting $\tau_{\rm up,*} = M_{\rm upper,*}/\psi([Z] = -2.20)$ and $\tau_{\rm low,*} = M_{\rm low,*}/\psi([Z] = 0.45)$, respectively. $\psi([Z] = -2.20)$ and $\psi([Z] = 0.45)$ refer to the IGIMF-corrected SFR values for $[Z] = -2.20$ and $[Z] = 0.45$. $M_{\rm up,*}$ and $M_{\rm low,*}$ refer to the upper and lower IGIMF-corrected stellar masses by applying the maximum and minimum $M/L_{\rm Ks}$ values (Section 12.2.5). The solid (dashed) red line shows the fit of Equation (12.28) to the IGIMF-2021 data in linear-space. 165

E.1 Same as Figure 10.2 but for the low-resolution runs TNG50-2 (8 objects; left), TNG50-3 (1 object; middle), and TNG100-2 (22 objects; right). 264

E.2 *Left panel*: Similar to Figure 10.2, but here the black dots show the results of TNG50-1 (46 objects), TNG50-2 (8 objects), TNG50-3 (one object), TNG100-1 (118 objects), TNG100-2 (22 objects), and TNG300-1 (191 objects). The colored symbols mark the medians of the different resolution runs: $\log_{10}\left(f_{\rm MCs}/\left[{\rm km}^{-3}\,{\rm s}^{3}\,{\rm kpc}^{-3}\right]\right) = -14.07$ (TNG50-1), -12.83 (TNG50-2), -15.30 (TNG50-3), -13.92 (TNG100-1), -13.95 (TNG100-2), and -13.75 (TNG300-1). *Right panel:* Cumulative distribution of the specific phase-space density of the MCs ($f_{\rm MCs}$; Equation 10.1). In both panels, the red cross shows the observed value of $f_{\rm MCs,obs} = 9.10 \times 10^{-11}\,{\rm km}^{-3}\,{\rm s}^{3}\,{\rm kpc}^{-3}$. 265

E.3 Similar to Figure 10.2, but for analogues to the MCs with $d_{\rm MW-LMC} \geq 50\,{\rm kpc}$. None of the 143 (TNG50-1), 20 (TNG50-2), 29 (TNG50-3), 431 (TNG100-1), 49 (TNG100-2), or 521 (TNG300-1) analogues have $f_{\rm MCs} \geq f_{\rm MCs,obs}$ and $\Omega_{\rm LMC} \geq \Omega_{\rm LMC,obs}$. One of the 1193 analogues has $f_{\rm MCs} \geq f_{\rm MCs,obs}$. 266

F.1 Mass-to-light ratios in the Ks- (blue), $K_{3.6\mu{\rm m}}$- (red), and V- (green) band evaluated at 13.6 Gyr in dependence of the metallicity assuming constant SFRs and metallicities for a canonical IMF (Kroupa 2001). 268

F.2 Same as Figure 12.1 but showing gwIMFs for high metallicities of [Z]≥ 0.4. 269

F.1 The observatory and night sky of Gmunden during a public guiding tour. Credit: Thomas Kurat/moefotografie 331

List of Tables

10.1 Observational properties of the MCs based on tables 1 and 2 of Pawlowski and Kroupa (2020). The proper motions are a combination of data from Gaia DR2 (Gaia Collaboration 2018a) and the HST (Kallivayalil et al. 2013), as discussed further in section 2.1 of Pawlowski and Kroupa (2020). From left to right: stellar mass; position $\boldsymbol{r}$ in Galactocentric Cartesian coordinates; distance to the Galactic centre; velocity $\boldsymbol{v}$ in Galactocentric Cartesian coordinates; total velocity wrt. the MW; and absolute specific angular momentum $h \equiv |\boldsymbol{r} \times \boldsymbol{v}|$. The stellar masses of the LMC and SMC are taken from table 4 of McConnachie (2012). 107

10.2 Analogues to the MCs (i.e., systems with satellites analogous to both the LMC and the SMC) in the redshift range $0 \leq z \leq 0.26$ in the TNG50-1, TNG100-1, and TNG300-1 simulation for different selection criteria. The table lists the number of analogues, their frequency relative to the total number of selected MW-like galaxies hosting analogues to both MCs, and the corresponding equivalent number of standard deviations for a single Gaussian variable (Equation 10.5). The first part summarizes the initial samples of analogues to the MW, LMC, SMC, and both MCs as defined in Sections 10.2.3 and 10.2.4. The other parts list the results if additional selection criteria (indicated by the plus symbol in the first column) are applied to the initial sample of analogues to the MCs. The last part of the table gives the combined likelihood of the MCs by adding up the χ^2 values of their phase-space density (Section 10.3.1) and the alignment of the LMC orbital pole with that of the DoS. The corresponding P-value is calculated for two degrees of freedom (Section 10.4.3.2). As explained in Section 10.3.1, the linear extrapolation underestimate the tension because the fit does not account for the curvature for data with $\log_{10}\left(f_{\mathrm{MCs,min}}/\left[\mathrm{km}^{-3}\,\mathrm{s}^{3}\,\mathrm{kpc}^{-3}\right]\right) \gtrsim -13$. 115

10.3 Physical properties of the observed MW, LMC, and SMC and their analogues which fulfil $f_{\mathrm{MCs}} \geq f_{\mathrm{MCs,obs}} = 9.1 \times 10^{-11}\,\mathrm{km}^{-3}\,\mathrm{s}^{3}\,\mathrm{kpc}^{-3}$ at redshift $z = 0.26$ (system 1), $z = 0.21$ (system 2), and $z = 0.20$ (system 3). Systems 2 and 3 consist of the same objects identified at different timesteps (snapshots). The last two rows list the alignment of the orbital poles, where $\widehat{\boldsymbol{h}}$ is the normalized specific angular momentum vector. The observed stellar masses of the MW and the MCs are taken from Licquia and Newman (2015) and McConnachie (2012), respectively. The distances and velocities of the MCs are taken from Pawlowski and Kroupa (2020). The dark matter and total masses of these galaxies are not listed because these parameters are very sensitive to the applied measurement method (though see Section 10.4.4). 117

10.4 Level of tension for different LG observations in the ΛCDM framework. The frequency of the MW DoS in ΛCDM is taken from section 4.2 of Pawlowski and Kroupa (2020), who considered 2548 MW-like galaxies and found one with a similar satellite system. We therefore assume that its likelihood in ΛCDM is $1/2548 = 3.92 \times 10^{-4}$. For M31, we use figure 2 of R. A. Ibata et al. (2014), which shows that 3 out of 7757 M31-like galaxies in the MS-II have a satellite system similar to that of M31. The likelihood of the backsplash galaxy NGC 3109 in ΛCDM has been quantified in Banik et al. (2021), who found no such analogues in 13225 galaxies similar to the MW or M31 in the TNG300-1 simulation. This implies a likelihood below $1/13225 = 7.56 \times 10^{-5}$. The last row gives the significance of the MCs as quantified using TNG50-1 in Sections 10.3.1 and 10.4.3. 124

10.5 Statistics of analogues to the LMCs (i.e., systems with a satellite analogous to the LMC) in the redshift range $0 \leq z \leq 0.26$ in the TNG50-1, TNG100-1, and TNG300-1 simulation with a total mass higher than the 1σ lower limit of the observationally inferred LMC mass ($M_{\rm LMC}^{\rm dyn} = 18.8^{+3.5}_{-4.0} \times 10^{10}\,M_{\odot}$; Shipp et al. 2021). We show results for different distance criteria. Similarly to Table 10.2, we list the number of analogues, their frequency relative to the total number of selected MW-like analogues, and the corresponding equivalent number of standard deviations for a single Gaussian variable (Equation 10.5). The distributions of the total LMC mass for these three samples are presented in Figure 10.7. The last two parts of the table list the statistical analysis of Figure 10.8. 127

F.1 Polynomial coefficients of the fitting functions Equations (12.16), (12.18), and (12.19) to the SFR–Hα and $\Phi - L_{\rm H\alpha}$, $SFR_{\rm K98} - SFR_{\rm IGIMF}$ relations, respectively, for different metallicities. The fitting relations of the SFR–Hα and $\Phi - L_{\rm H\alpha}$ are defined for the Hα luminosity range of $-6 < \log_{10}\left(L_{\rm H\alpha}/(10^{41}\,{\rm erg\,s^{-1}})\right) < 4$ and $SFR_{\rm K98} - SFR_{\rm IGIMF}$ relations for SFRs derived from the Kennicutt law in the range of $-6 < \log_{10}\left(\psi_{\rm K98}/({\rm M_{\odot}\,yr^{-1}})\right) < 4$ (Sect. 12.2.3).
*Using the relation $[Z] = \log_{10}(Z/Z_{\odot})$, where $Z_{\odot} = 0.0142$ (Sect. 12.2.1). 270

Acknowledgements

"The purpose of life is the investigation of the Sun, the Moon, and the heavens."
(Anaxagoras)

During my studies I sometimes had the feeling that my office became the cockpit of a space ship in which I am sitting only in front of my computer trying to fly through the stars and galaxies safely by applying the correct law of gravity. The "mission PhD" has been a challenging part of my life but at the same time, astronomy allowed me meeting and working with great people from all over the world. Thinking about the Universe and doing fundamental research is a privilege - especially in these days. The PhD journey will now come to an end but not without thanking my companions, "co-astronauts" (aka co-authors), and technicians on this space flight.

First of all, I would like to thank my PhD supervisor Prof. Dr. Pavel Kroupa for all his support and scientific guidance during my studies in Bonn. I am especially grateful that he always communicated with me in a respectful way and at eye level. He learned me thinking outside the box by keeping questioning well-established theories. I also appreciated our discussions beyond physics and astronomy in which we covered especially sociological and historical topics. This period of my life was an extremely valuable experience and development of my own personality. Dear Pavel, thank you very much for your time, so that I am seeing the sky now with other eyes!

I am very thankful to Prof. Dr. Karl Menten for his support and giving me the possibility being part of the Max-Planck-Institut für Radioastronomie (MPIfR) in Bonn. The personal interaction with him and also with all the members of his research group at the MPIfR and the resulting feedback and inputs were extremely helpful to improve my manuscripts. Dear Prof. Dr. Karl Menten, thank you very much for supporting me!

During my studies I had many encounters with several physicists and astrophysicists. Especially, I would like to thank my colleague Dr. Indranil Banik for long and intense discussions on Milgromian dynamics and the challenges faced by the ΛCDM paradigm. Our organization of the international conference "BonnGravity2019 – The functioning of galaxies: challenges for Newtonian and Milgromian dynamics" in September 2019 was a great experience. Dear Indranil, thank you very much for all the meetings and introducing me to the concept of MOND! A special thank you goes to Dr. Tereza Jerabkova for supporting me during my four months visit at the European Southern Observatory (ESO) in Garching bei München from October 2022 to January 2023. During this time we explored the galaxy evolution in the context of the integrated galaxy initial mass function (IGIMF) theory. I really enjoyed the open-minded atmosphere at ESO and the vital discussions during the science coffee breaks, galaxy evolution coffees or journal club. On this occasion, I also would like to thank Dr. Zhiqiang Yan, who collaborated with us on the IGIMF projects. I have learned a lot during our weekly

online meetings in which we especially discussed the mass-to-light ratio of galaxies in the context of the invariant canonical IMF and varying gwIMF within the IGIMF theory. Dear Tereza and Yan, thank you very much for collaborating with me on the IGIMF in a cosmological context. I am looking forward putting all our ideas down on paper and publishing our projects. I acknowledge support from the ESO Early-Career Visitor Programme which enabled my visits at ESO and the IGIMF projects on stellar populations of nearby galaxies in a cosmological context. I thank my bachelor supervisor Prof. Dr. Gerhard Hensler from the University of Vienna who introduced me to the challenges of the ΛCDM framework and who encouraged me to do my Master studies at the University of Bonn.

I am also grateful to Prof. Dr. Hosein Haghi, Prof. Dr. Akram Hasani Zonoozi, Prof. Dr. Tom Richtler, Prof. Dr. Wolfgang Kundt, Dr. Javanmardi Behnam, Dr. Wolfgang Oehm, Dr. Jörg Dabringhausen, Dr. Alice Concas, Dr. Eda Gjergo, Nikolaus Sulzenauer, Dr. Cosima Eibensteiner, Dr. Sven Heydenreich, Davit Alkhanishvilli, Nils Wittenburg, Elena Asencio, Srikanth T. Nagesh, and Nick Samaras for interesting and useful conversations on several astronomical topics. I thank Dr. Michael Geffert for interesting discussions on the history of astronomy in Bonn. A particular thank you goes to my former office colleagues Dr. Patrick Lieberz, Dr. Jan Pflamm-Altenburg, and Dr. Vikrant V. Jadhav for a positive working atmosphere.

In this regard, I thank all the other former and current members of The Stellar Populations and Dynamics Research Group (SPODYR) group lead by Prof. Dr. Kroupa at the Helmholtz-Institut für Strahlen-und Kernphysik (HISKP) and the Millimeter and Submillimeter Astronomy group lead by Prof. Dr. Menten at the MPIfR in Bonn. I really enjoyed the vital discussions during our several group meetings and appreciated your feedback on my work. I would like to thank the SPODYR group at the Bonn University for a studentship. However, all our scientific research would not have been possible without the work done by the technical requirements and the administrative staff of the Argelander Institut für Astronomie (AIfA), HISKP, and MPIfR. In particular, I thank the secretaries Sabine Derdau, Elisabeth Kramer, Ellen Fuhrmann, Christa Börsch, and Eva Schmelmer, and the IT-team Andreas Bödewig, Dr. Ole Marggraf, and Dr. Oliver-Mark Cordes. On this occasion I should also thank my own laptop, which wanted to finish a little bit earlier than me and gave up just two months before submitting this thesis causing with its decision some troubles. Mark Twain was saying "Humor is tragedy plus time" – I fear that time still has to pass a bit more.

I acknowledge the Deutscher Akademischer Austauschdienst (DAAD) Eastern-European exchange programme for financing visits at the Charles University of Prague during which my colleagues and I discussed several topics ranging from cosmology to stellar populations. The atmosphere in Prague with its unique astronomical history mainly characterized by Johannes Kepler, Tycho Brahe, and Albert Einstein was a special motivation during my Master and PhD studies.

On a more personal side, special thanks go to Hagen Tolle, Thomas Kurat, Peter Petz, Rolf Löhr, and the all the other members of the "AURIGA-Traunseeastronomie e.V." who are with me from the very beginning of my astronomical journey. I am looking forward to attend again our guiding tours at the local observatory in Gmunden. I am grateful to my friends Rita and Petra Viechtbauer, Anni Oberndorfer, Verena Haslbauer, David Lugmayr, Christoph Spat, Michael Eichler, Igor Kraut, and Klemens Gelbenegger with whom I enjoyed long telephone and video calls while being away from Austria. I would not wish to deny that your sympathetic ear was an extremely helpful mental support. A special thank you to Igor Kraut and Klemens Gelbenegger, who started with me the physics journey in Vienna some years back. I thank my colleagues and friends from the athletic group of the SSF Bonn for keeping me (more or less) physically and mentally fit over the last years.

I thank my grandparents Renate and Ferdinand Ganzenbacher-Waldl and Friederike and Alois Haslbauer and Franz Nußbaumer for encouraging and accompanying me through my life. Finally, I deeply thank my parents, Helga and Gerhard, for their tireless support since I am alive. I dedicate this work to my parents and grand parents.

Figure F.1: The observatory and night sky of Gmunden during a public guiding tour. Credit: Thomas Kurat/moefotografie

It is often said that "All good things come to an end" but at the same time new ways open. Personally, I am looking forward observing again the night sky of Gmunden (not only my own but also the birth place of the Medival astronomer Johannes von Gmunden) as shown Figure F.1 but this time with new knowledge on the functioning of our Universe. Meanwhile, I am still sitting in my office at the Argelander Institute for Astronomy finalizing my doctoral thesis while listening to Ludwig van Beethoven's "Abendlied unterm gestirnten Himmel" and looking out of the window observing the shining stars in the dark sky. Bonn, thank you for having me.

Moritz Haslbauer (November 2023)

“Abendlied unterm gestirnten Himmel”

Wenn die Sonne niedersinket,
Und der Tag zur Ruh sich neigt,
Luna freundlich leise winket,
Und die Nacht herniedersteigt;

Wenn die Sterne prächtig schimmern,
Tausend Sonnenstrahlen flimmern:
Fühlt die Seele sich so groß,
Windet sich vom Staube los.

Schaut so gern nach jenen Sternen,
Wie zurück ins Vaterland,
Hin nach jenen lichten Fernen,
Und vergißt der Erde Tand;

Will nur ringen, will nur streben,
Ihre Hülle zu entschweben:
Erde ist ihr eng und klein,
Auf den Sternen möcht sie sein.

Ob der Erde Stürme toben,
Falsches Glück den Bösen lohnt:
Hoffend blicket sie nach oben,
Wo der Sternenrichter thront.

Keine Furcht kann sie mehr quälen,
Keine Macht kann ihr befehlen;
Mit verklärtem Angesicht,
Schwingt sie sich zum Himmelslicht.

Eine leise Ahnung schauert
Mich aus jenen Welten an;
Lange nicht mehr dauert
Meine Erdenpilgerbahn,

Bald hab ich das Ziel errungen,
Bald zu euch mich aufgeschwungen,
Ernte bald an Gottes Thron
Meiner Leiden schönen Lohn.

(Text by Heinrich Goeble and music by Ludwig van Beethoven)